UNIVERSIDAD DE LA RIOJA

TESIS DOCTORAL

Título
Diseño de sistemas pentafluorofenil-ciclometalados de Pt^{II} y Pt^{IV}. Estudio de sus propiedades
Autor/es
Nora Giménez Lizardi
Director/es
Elena Lalinde Peña y María Teresa Moreno García
Facultad
Facultad de Ciencia y Tecnología
Titulación
Departamento
Química
Curso Académico

Diseño de sistemas pentafluorofenil-ciclometalados de Pt^{II} y Pt^{IV}. Estudio de sus propiedades

Design of pentafluorophenyl-cyclometalated Pt^{II} and Pt^{IV} complexes. Study of their properties

Memoria presentada en el Departamento de Química de la Universidad de La Rioja para optar al título de Doctor por la licenciada:

Nora Giménez Lizardi

Universidad de La Rioja-2019

GOBIERNO DE ESPAÑA MINISTERIO DE ECONOMÍA Y COMPETITIVIDAD

UNIVERSIDAD DE LA RIOJA

CISQ CENTRO DE INVESTIGACIÓN EN SÍNTESIS QUÍMICA UNIVERSIDAD DE LA RIOJA

ELENA LALINDE PEÑA, Catedrática de Química Inorgánica de la Universidad de La Rioja.

Mª TERESA MORENO GARCÍA, Catedrática de Química Inorgánica de la Universidad de La Rioja.

CERTIFICAN:

Que el presente trabajo de investigación titulado **"Diseño de sistemas pentafluorofenil-ciclometalados de Pt^{II} y Pt^{IV}. Estudio de sus propiedades"** ha sido realizado en el Departamento de Química-Centro de Investigación en Síntesis Química (C.I.S.Q) de la Universidad de La Rioja bajo nuestra dirección por la Licenciada en Química Nora Giménez Lizardi y autorizan su presentación para que sea calificado como Tesis Doctoral.

Logroño, Junio de 2019

Fdo.: Prof. Elena Lalinde Peña **Fdo.: Prof. Mª Teresa Moreno García**

ÍNDICE

ABBREVIATIONS AND ACRONYMS / *ABREVIATURAS Y SIGLAS*

Hthpy	2-(2-tienyl)pyridine / *2-(2-tienil)piridina*
Hpbt	2-phenylbenzothiazole / *2-fenilbenzotiazol*
Hpq	2-phenylquinoline / *2-fenilquinoleína*
Hdfppy	2-(2,4-difluorophenyl)pyridine / *2-(2,4-difluorofenil)piridina*
Hbzq	7,8-benzoquinoline / *7,8-benzoquinoleína*
Hoxd	2,5-diphenyl-1,3,4-oxadiazole / *2,5-difenil-1,3,4-oxadiazol*
Hpypy	1-(2-pyridyl)pyrene (pypy) / *1-(2-piridil)pireno*
CN^-	cyanide / *cianuro*
Mepy	4-Methylpyridine / *4-Metilpiridina*
bpe	1,2-bi(4-pyridyl)ethylene / *1,2-Bis(4-piridil)etileno*
dmso	Dimethyl sulfoxide / *dimetilsulfóxido*
thf	Tetrahydrofuran / *tetrahidrofurano*
tht	Tetrahydrothiophene / *tetrahidrotiofeno*
HDA	Hexadeuteroacetone / *Hexadeuteroacetona*
LEDs	light-emitting diode / *Dispositivo emisor de luz*
OLED	Organic light-emitting diode / *Dispositivo orgánico emisor de luz*
o-	ortho / *orto*
m-	meta
p-	para
i. e. / *ej.*	In example / *ejemplo*
IR	Infrared radiation / *Infrarrojo*

vs / *mf*	very strong / *Muy fuerte*
s / *f*	strong / *Fuerte*
m	medium / *medio*
w / *d*	weak / *débil*
UV-Vis	Ultraviolet–visible / *Ultravioleta-visible*
sh / *h*	shoulder / *hombro*
br / *a*	broad / *ancho*
nm	nanometer (10^{-9} meters) / *nanómetro*
max	maximum / *máximo*
λ	Wavelength / *longitud de onda*
λ_{abs}	Absorption wavelength / *Longitud de onda de absorción*
λ_{em}	Emission wavelength / *Longitud de onda emisión*
λ_{exc}	Excitation wavelength / *Longitud de onda de excitación*
ε	molar extinction coefficient / *coeficiente de absorción molar*
τ	Emission lifetime / *Tiempo de vida de emisión*
Φ	quantum yield / *rendimiento cuántico*
k_r	radiative rate constant / *constante radiativa*
k_{nr}	non-radiative rate constant / *constante no-radiativa*
ESI	Electrospray ionization
MALDI	Matrix-assisted laser desorption ionization
TOF	Time of flight
E	Potential
RT	Room Temperature / Temperatura ambiente

NMR / *RMN*	Nuclear Magnetic Resonance / *Resonancia Magnética Nuclear*
COSY	Correlation spectroscopy
TOCSY	Total Correlation Spectroscopy
HSQC	Heteronuclear single quantum coherence
HMBC	Heteronuclear multiple bond coherence
δ	NMR chemical shift / *desplazamiento químico en RMN*
s	singlet / *singlete*
d	doublet / *doblete*
t	triplet / *triplete*
q	quatriplet / *cuatriplete*
sept	septuplet / *septuplete*
m	Multiplet / *multiplete*
ISC	intersystem crossing / *cruce intersistémico*
IC	Internal conversion / *conversión interna (IC)*
VR	vibrational relaxation / *relajación vibracional*
IL	Intraligand / *intraligando*
ILCT	Intraligand charge transfer / *Transferencia de carga intraligando*
LL'CT	Ligand to ligand charge transfer / *Transferencia de carga de un ligando a otro ligando*
MLCT	Metal to ligand charge transfer / *Transferencia de carga del metal al ligando*
MC	Metal-centered / *centrado en el metal*
HOMO	High occuped molecular orbital
LUMO	Low unoccuped molecular orbital

SOMO	single occuped molecular orbital
TD-DFT	Time Dependent-Density Functional Theory
DFT	Density Functional Theory
PCM	Polarizable continuum model
$\mathbf{S_0}$	ground state / *estado fundamental*
$\mathbf{S_n}$	singlet excited state / *estado excitado singlete*
$\mathbf{T_n}$	triplet excited state / *estado excitado triplete*
f	oscillator strength / *fuerza del oscilador*

Introducción

Introducción

El interés en el estudio de compuestos luminiscentes de metales de transición ha crecido de manera significativa en los últimos años, debido a sus interesantes propiedades ópticas. Muchos de los compuestos con metales de la tercera serie de transición y algunos de la segunda presentan fosforescencias muy eficientes, con largas vidas medias, grandes desplazamientos de Stokes y estados excitados modulables. La eficiencia de la fosforescencia a temperatura ambiente se atribuye al efecto del átomo pesado, que induce un fuerte acoplamiento espín-órbita, facilitando que el cruce intersistémico (ISC) desde un estado singlete a un estado triplete se produzca de manera eficiente y rápida.[1] Además, el efecto del átomo pesado es mayor cuando éste está implicado en los orbitales que participan en la correspondiente transición electrónica o está interaccionando con un átomo que contribuye a la fosforescencia.[2]

De acuerdo con el diagrama de niveles de energía de Perrin-Jablonski (Figura I.1), cuando una molécula se excita por absorción de luz, pasa de un estado fundamental singlete (S_0) a estados excitados. Esta absorción es muy rápida (10^{-15} s) y, debido a que el cambio de multiplicidad de spin está prohibido por las reglas de selección, los estados que se pueblan son estados excitados singlete S_1, S_2, etc. Hay que tener en cuenta que la pérdida de energía mediante conversión interna (IC) permite alcanzar el estado excitado singlete más bajo en energía, y que el camino más probable hacia el estado fundamental es aquel que implica menor tiempo de vida media del estado excitado.[3]

Por lo tanto, si el acoplamiento espín-órbita no es bueno, la desactivación al estado fundamental se produce desde el estado S_1, bien a través de un proceso emisivo de espín permitido, denominado fluorescencia, o mediante procesos no radiantes (relajación vibracional y conversión interna). Sin embargo, para los estados excitados singlete con una importante contribución del metal en los orbitales implicados, el cruce entre sistemas (ISC) es más rápido (~ 10^{-12} s)[4] que el proceso de desactivación desde el estado excitado singlete (~10^{-8} s).[5] Por lo tanto, se elimina la fluorescencia y la desactivación al estado fundamental se produce a través de un estado triplete T_1, siendo esta transición formalmente prohibida por el espín, ya que implica una transición entre estados con diferente multiplicidad. A la desactivación con emisión de luz desde el estado excitado T_1 se le denomina fosforescencia.

El tiempo de vida de fosforescencia es relativamente largo (τ 10^{-6} – 10^{-3} s) en comparación con los tiempos de vida de fluorescencia (τ 10^{-9} – 10^{-7} s), debido a que la fosforescencia requiere el cruce intersistémico entre los estados S_1 y T_1.[6] En los compuestos puramente orgánicos, el estado triplete se desactiva mediante procesos no radiantes, ya que son mucho más rápidos que las transiciones radiantes triplete (excitado) → singlete (fundamental) (constante de velocidad ~ 10^3 s^{-1}). Además, es importante mencionar que el 25 % de los estados excitados que se generan son estados singlete y el 75 % tripletes, y que, por lo tanto, en los sistemas orgánicos fluorescentes solo contribuyen a la emisión de luz el 25 % de los posibles estados excitados, por lo que estadísticamente la eficiencia cuántica interna máxima sería del 25 %.[7] Todas estas características hacen que los compuestos de metales de transición fosforescentes sean muy adecuados para utilizarlos como dopantes en dispositivos OLEDs (organic light-emitting diodes), ya que la participación de los estados excitados en la emisión podría ser hasta del 100 %.[6, 8]

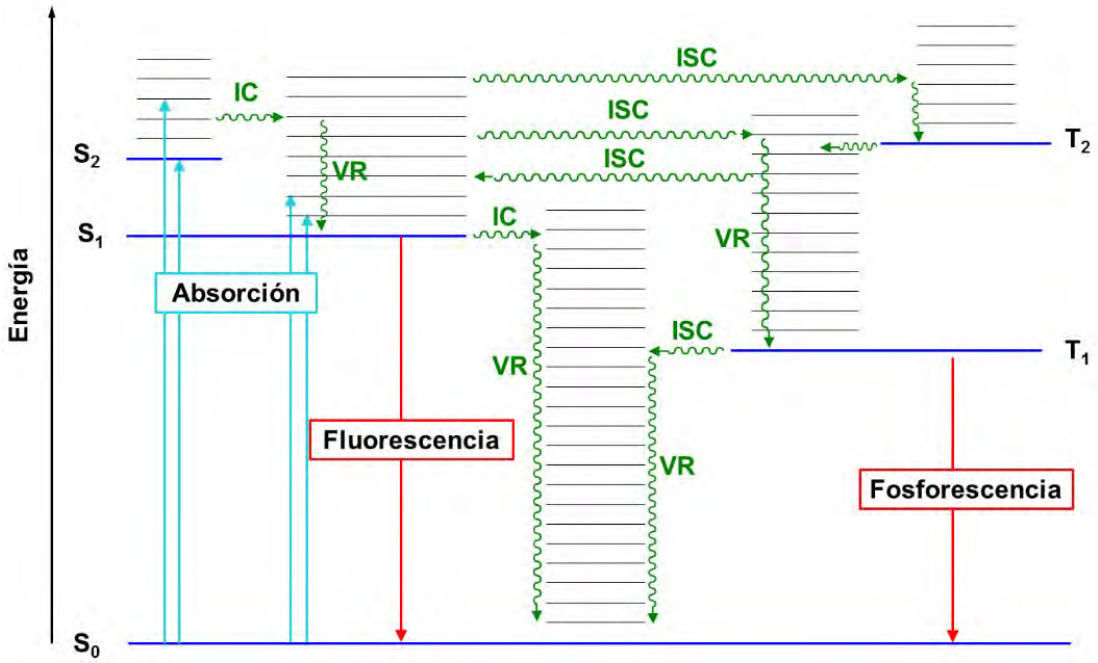

Figura I.1. Diagrama de Perrin-Jablonski: IC – conversión interna, ISC – cruce intersistemas, VR – relajación vibracional, S – estado singlete, T – estado triplete. Las flechas rectas y las flechas curvilíneas representan transiciones radiativas y no radiativas, respectivamente.

Un buen número de compuestos de metales de transición fosforescentes se han empleado en el desarrollo de OLEDs,[6-9] así como en fotocatálisis,[10] celdas solares,[10g, 11] quimiosensores[12] o bioimagen[13] (Figura I.2).

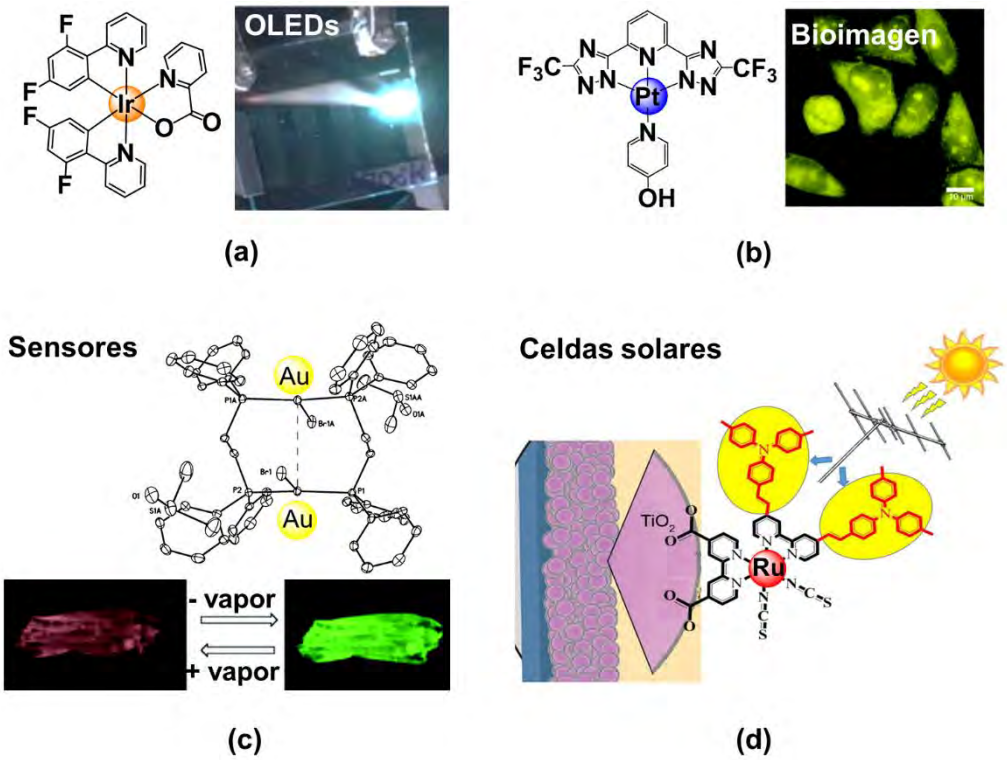

Figura I.2. Diferentes aplicaciones de compuestos con metales de transición: (a) OLEDs,[9j] (b) bioimagen,[13l] (c) sensores químicos,[12h] (d) celdas solares.[11k]

El desarrollo de este campo ha sido muy intenso en las dos últimas décadas y hay numerosas revisiones recientes en la bibliografía sobre las propiedades fotofísicas y fotoquímicas de compuestos de metales de transición, particularmente de compuestos de iones metálicos d^6 [Ru(II), Os(II), Ir(III)][10g, 11b, 14] y d^8 [Pt(II), Au(III)],[3, 8, 9g, 15] con geometrías octaédrica y plano-cuadrada, respectivamente.

1. Luminiscencia en complejos plano-cuadrados de Pt(II) (d^8)

En particular, el Pt, elemento de la tercera serie de transición, presenta la segunda constante de acoplamiento espín-órbita más grande (ξ 4481 cm^{-1}).[16] Este hecho, unido a la geometría plano-cuadrada de los complejos de Pt(II), son los responsables de muchos de los procesos fundamentales que influyen en la absorción, luminiscencia y otras propiedades del estado excitado y, por tanto, en las interesantes propiedades fotofísicas de los compuestos de Pt(II).

Un factor decisivo que afecta a las propiedades emisivas de estos compuestos de Pt(II) es el desdoblamiento de campo ligando que generan los ligandos coordinados al centro metálico. La Figura I.3 representa un esquema de los diagramas de orbitales moleculares simplificados en compuestos d^8 plano-cuadrados de Pt(II), con las situaciones electrónicas más frecuentes que se pueden encontrar dependiendo de las características de los ligandos coordinados al metal. Con ligandos de campo débil (como aminas, fosfinas, halogenuros, etc., Figura I.3A) los compuestos generalmente no son luminiscentes en disolución. Este comportamiento se debe a que las transiciones centradas en el metal (MC) o transiciones d-d suelen ser no emisivas, ya que el orbital LUMO que se puebla después de la excitación, es un orbital $d_{x^2-y^2}$ centrado en el metal y con un carácter fuertemente antienlazante. Tras su población, se produce una distorsión en la geometría de la molécula, provocando que el mínimo de energía de la superficie de energía potencial esté considerablemente desplazado respecto al del estado fundamental. Según el principio de Frank-Condon, este hecho favorece que el estado excitado se desactive a través de procesos no radiantes (sin emisión de luz), como los procesos de conversión interna (IC) o el cruce entre sistemas (ISC). Esta distorsión se favorece en disolución a temperatura ambiente, ya que en estado sólido o a bajas temperaturas, ésta puede atenuarse y observarse una emisión débil.

Por lo tanto, para conseguir desactivación con emisión de luz, hay que evitar la población de este orbital $d_{x^2-y^2}$, incrementando su energía para que no sea accesible a temperatura ambiente y aumentando así el salto energético d-d. Una buena estrategia a seguir es la coordinación de ligandos al centro metálico de carácter fuertemente dador (cianuros, acetiluros…), ligandos aromáticos conjugados (ciclometalados, polipiridilos…) y/o ligandos quelato, ya que aumentan la rigidez del sistema. La coordinación de este tipo de ligandos provoca un aumento en la energía del orbital vacío centrado en el metal ($d_{x^2-y^2}$), reduciendo los procesos no radiantes y la formación de un orbital LUMO centrado en los ligandos (niveles energéticos π^*), permitiendo la formación de estados excitados de transferencia de carga metal-ligando (MLCT), como se ilustra en la Figura I.3B. Si además se produce una estabilización del orbital ocupado d_{xy} centrado en el metal (Figura I.3C), la transición puede ser centrada en el ligando (IL) del tipo $\pi \rightarrow \pi^*$, de transferencia de carga intraligando (ILCT) o de transferencia de carga ligando-ligando (LLCT). En estas situaciones, la desactivación se produce con emisión de luz (en algunos casos incluso en disolución a temperatura ambiente). Es interesante

mencionar que los estados triplete de carácter MLCT tienen un mejor acoplamiento spin-órbita inducido por el metal y, generalmente, presentan emisiones con tiempos de vida cortos y constantes radiativas altas, mientras que los estados triplete de carácter IL muestran tiempos de vida largos y constantes radiativas bajas.[17]

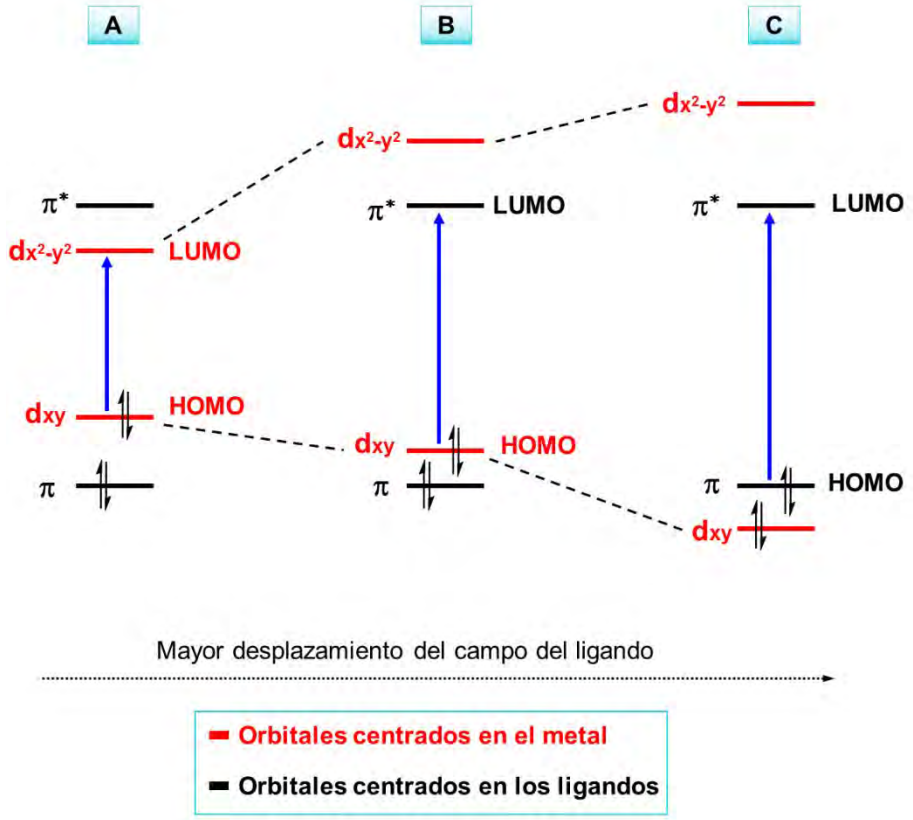

Figura I.3. Representación esquemática de las transiciones HOMO (Orbital ocupado de mayor energía) – LUMO (Orbital vacío de menor energía) en función del tipo de ligandos coordinados en un complejo plano-cuadrado de platino(II).

Otro factor que afecta a la eficiencia de la emisión en compuestos de Pt(II) es la diferencia estructural entre la geometría en el estado excitado respecto a la del estado fundamental. Así, moléculas con distorsiones geométricas en el estado excitado aceleran el decaimiento no radiativo a través de acoplamientos vibracionales entre el estado excitado y el estado fundamental. Por lo tanto, es conveniente coordinar al centro metálico ligandos que produzcan distorsiones mínimas en el estado excitado (T_1) en relación al fundamental (S_0). Así, los complejos que contienen ligandos rígidos son ventajosos en el diseño de materiales luminiscentes con altas eficiencias.[8]

Además, la geometría plano-cuadrada de los compuestos de Pt(II), especialmente con ligandos no voluminosos, facilita la formación de interacciones axiales Pt···Pt, lo que permite establecer apilamientos *inter*moleculares (agregados si se forman en el estado

fundamental y excímeros o exciplejos en el estado excitado).[1a, 9f, 18] En complejos multinucleares, que incorporan dos o más unidades de Pt(II) distintas unidas covalentemente, tales interacciones son posibles dentro de la molécula (interacciones *intra*moleculares). La interacción Pt···Pt se produce por solapamiento de los orbitales $6p_z$ y $5d_z^2$, que da lugar a nuevos orbitales moleculares enlazantes (pσ, dσ) y antienlazantes (pσ*, dσ*) (Figura I.4).[19] Aunque formalmente el orden de enlace Pt-Pt es cero debido a que los orbitales dσ y dσ* están ocupados, la interacción neta, aunque débil, es energéticamente favorable y la especie resultante es más estable que la molécula aislada.

Si los ligandos son esencialmente planos y con sistemas σ-dadores-π conjugados como diiminas, tert-piridilos, ligandos ciclometalados [(C^N, C^N^N, N^C^N…) o carbenos N-heterocíclicos (NHCs)], se facilita la presencia de interacciones π···π adicionales, que determinan la estructura y, además, las propiedades ópticas. La Figura I.4 muestra el diagrama de energía para sistemas dinucleares (Pt_2) con interacciones Pt···Pt y/o π···π. Como se observa, el orbital ocupado de mayor energía (HOMO) está formado principalmente por el orbital antienlazante (dσ*) y el LUMO se localiza principalmente en los orbitales π* de los ligandos.

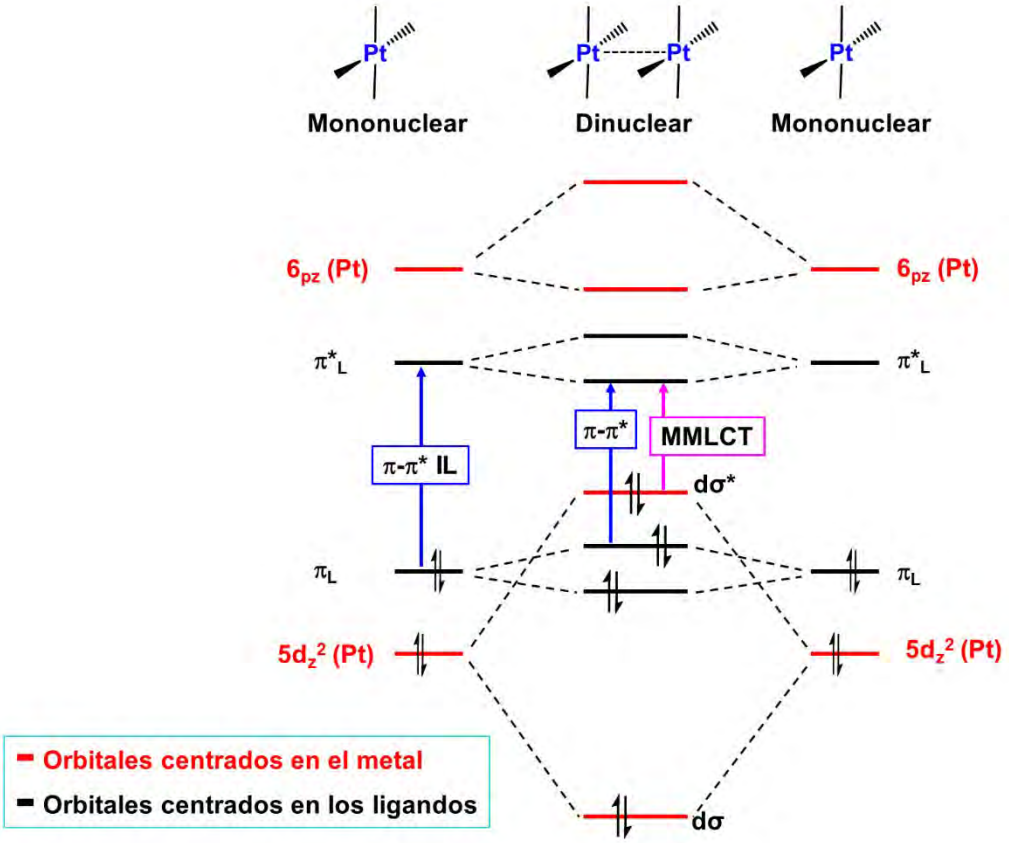

Figura I.4. Diagrama simplificado de orbitales moleculares de un complejo dinuclear d^8 de Pt(II) con interacciones Pt···Pt y π···π.

Estas interacciones Pt···Pt y/o π···π juegan un papel importante en las propiedades fotofísicas de los compuestos de Pt(II). Como resultado, estos sistemas pueden presentar emisiones que provienen de estados excitados metal-metal-ligando (^{3}MMLCT) (como consecuencia de la transición desde el orbital dσ*(Pt) al orbital π* del ligando aromático) y/o estados excitados exciméricos ligando-ligando (^{3}ππ*).[1a, 9f, 18] Como consecuencia, la emisión aparece desplazada al rojo respecto al monómero, desplazándose hacia menores energías a media que aumenta la interacción Pt···Pt y/o π···π*, favorecida en estado sólido y disoluciones concentradas. En ocasiones, las interacciones π···π son desactivantes por el fenómeno denominado Agregation Induced Quenching (AIQ) o, por el contrario, incrementan la rigidez y aumentan la eficiencia de las emisiones (Agregation Induced Emission, AIE o Agregation Induced Enhanced Emission, AIEE).

Además, estas emisiones son en general muy sensibles a estímulos externos. De hecho, muchos compuestos de Pt(II) muestran cambios de color y/o del color de la emisión por la acción de vapores de un disolvente o gas (vapocromismo/vapoluminiscencia),[12g, 12h, 18d, 20] de una fuerza mecánica (mecanocromismo)[12h, 20c, 21] o la temperatura (termocromismo).[20d, 22]

1.1 Derivados luminiscentes de Pt(II) con ligandos ciclometalados

La incorporación de ligandos ciclometalados al centro de platino mejora, en general, las propiedades emisivas. Estos ligandos actúan como ligandos quelato, uniéndose al metal mediante el átomo de carbono (formalmente aniónico, C^-) y un heteroátomo (generamente N). Por lo tanto, la ciclometalación es la coordinación de un ligando heteroaromático quelato a un centro metálico mediante un enlace covalente metal-carbono, implicando la desprotonación de un protón aromático y la formación de ligandos ciclometalados aniónicos.[7b] Estos ligandos no sólo aumentan la rigidez del sistema sino que, la presencia de un átomo de carbono fuertemente σ-dador y un grupo piridínico π-aceptor, genera un aumento del desdoblamiento del campo elevando la energía de los estados d-d centrados en el metal (tipo MC) comentados anteriormente y favoreciendo la generación de estados excitados triplete ^{3}MLCT o ^{3}IL.[15a] Además, el enlace metal-carbono formado en el proceso de ciclometalación aumenta la estabilidad del complejo.[15c]

Los primeros estudios sobre las propiedades luminiscentes en compuestos de Pt(II) con ligandos ciclometalados los llevaron a cabo von Zelewsky y *col.* en 1985,[23] sobre los compuestos *cis*-[Pt(ppy)$_2$], *cis*-[Pt(thpy)$_2$], *cis*-[Pt(bzq)$_2$], sintetizados vía especies litiadas.[24] Estos derivados presentan emisiones intensas y estructuradas que fueron atribuidas a transiciones ^{3}MLCT. Debido a la tendencia del átomo de C$^-$ a situarse en posición *trans* al átomo de nitrógeno, estos compuestos corresponden al isómero *cis* (Figura I.5). Sin embargo, este tipo de compuestos no son estables en disolventes halogenados ya que muestran reactividad fotoquímica con moléculas que contienen halógenos para formar los correspondientes compuestos de Pt(IV), con fosforescencia desplazada hacia el azul.[25] Desde entonces, el número de estudios sobre compuestos luminiscentes de Pt(II) con ligandos C^N bidentados ha sido muy elevado.[14a, 15b, 15c, 26]

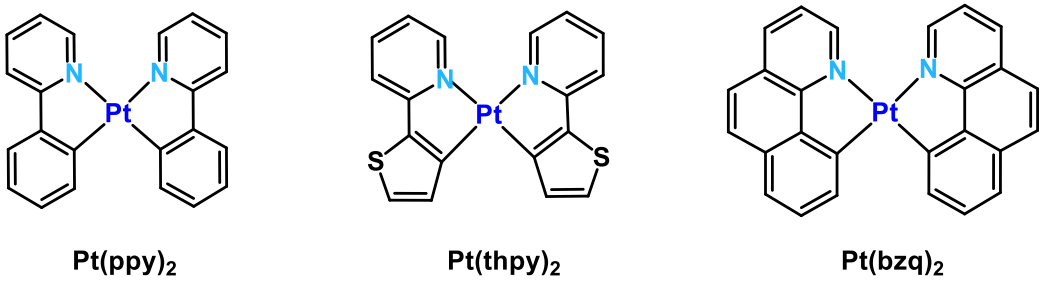

Figura I.5. Estructuras moleculares de los compuestos *cis*-[Pt(ppy)$_2$], *cis*-[Pt(thpy)$_2$] y *cis*-[Pt(bzq)$_2$].

Los compuestos plano-cuadrados d^8 de Pt(II) con ligandos ciclometalados presentan emisiones fosforescentes altamente eficientes incluso en disolución a temperatura ambiente. Estas emisiones no solo dependen del ligando ciclometalado sino también de los ligandos auxiliares, y en general se atribuyen a estados excitados triplete del tipo ^{3}IL ($\pi\pi^*$), ^{3}MLCT, ^{3}LLCT o a transiciones con mezcla de contribuciones del tipo ^{3}IL/^{3}MLCT o ^{3}LLCT/^{3}MLCT.[1b, 15b, 27] Hasta la fecha se han descrito para estos compuestos interesantes aplicaciones como dopantes en dispositivos OLEDs,[7, 9a-e, 9g-i, 15b-d, 28] fotocatálisis,[10a, 10b, 29] marcadores biológicos, [8, 13g, 13l, 30] sensores ópticos,[12a-c, 12g, 12h, 31] dispositivos basados en óptica no lineal, [32] celdas electroquímicas emisoras de luz de estado sólido[11a, 11d, 11h, 14c, 33] y terapia fotodinámica.[13i, 34]

Los factores que afectan a la energía de la emisión y, en consecuencia, a su modulación y también al rendimiento cuántico en estos sistemas ciclometalados son diversos. Por un lado, afecta la rigidez, ya que como hemos comentado previamente, una distorsión geométrica de la molécula acelera el decaimiento no-radiativo a través de

acoplamiento vibrónico entre el estado excitado y el fundamental. Por otro lado, la diferencia energética π-π* asociada al ligando C^N desempeña un papel muy importante en la energía de la emisión final. Así, los ligandos ciclometalados que contengan heterociclos con átomos de azufre, una conjugación π muy extendida o átomos que retiren (o cedan) densidad electrónica en el anillo piridínico (o fenílico) provocan una emisión desplazada hacia el rojo. Por el contrario, si se introducen en el anillo fenílico átomos que retiren densidad electrónica, como el flúor, se puede provocar un aumento en la diferencia de energía π-π*, y por lo tanto conseguir emisiones azules.[14a] Además, la fortaleza del campo ligando de los ligandos auxiliares y su naturaleza electrónica afecta a su mayor o menor implicación en el estado excitado. Los niveles HOMO y LUMO de los ligandos ciclometalados y los coligandos deben permitir la participación del átomo pesado de Pt en el estado emisivo. Cabe destacar que se pueden introducir modificaciones específicas como usar sustituyentes voluminosos para minimizar el self-quenching dependiente de la concentración, o bien, introducir grupos funcionales orientados a una aplicación particular. Así, la incorporación de sustituyentes hidrofóbicos o hidrofílicos permite controlar la solubilidad de los materiales en disolventes orgánicos para aplicaciones en disolución o mejorar la solubilidad en agua para aplicaciones biológicas.[13l, 35]

Una de las estrategias más generales para la obtención derivados de platino con ligandos ciclometalados C^N se basa en la reacción de K_2PtCl_4 con exceso del correspondiente ligando HC^N, para dar lugar a los derivados dinucleares $[Pt(C^N)(\mu\text{-}Cl)]_2$ y/o a los derivados mononucleares [Pt(C^N)(HC^N)Cl], que presentan un ligando ciclometalado y otro coordinado a través del nitrógeno.[14a, 36] Los derivados dinucleares sufren fácilmente reacciones de ruptura del sistema de puentes cloro con ligandos del tipo L^L (diaminas, diiminas…) o β-dicetonas para dar derivados mononucleares heterolépticos del tipo $[Pt(C^N)(N^N)]^+$ [37] o [Pt(C^N)(O^O)],[14a, 15c, 38] respectivamente, en general más emisivos que los derivados homolépticos.[14a] Además, también se ha publicado recientemente la síntesis de compuestos [Pt(C^N)(ligando N-dador)Cl] a partir de la fácil ruptura de los compuestos dinucleares $[Pt(C^N)(\mu\text{-}Cl)]_2$. Estos derivados resultan ser muy luminiscentes en PMMA (polimetilmetacrilato), con rendimientos cuánticos de fosforescencia de hasta el 72% con potencial aplicación en el campo de la electroluminiscencia (Figura I.6).[39]

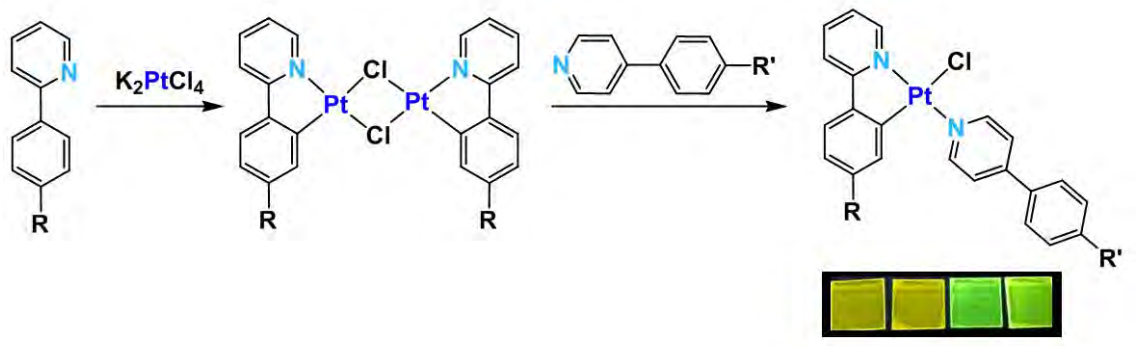

Figura I.6.[39]

En relación a los ligandos ciclometalados bidentados es interesante comentar que, además de los ligandos ya comentados tipo C^N, se han estudiado recientemente ligandos ciclometalados tipo C^C* (carbenos N-heterocíclicos, NHC).[15d, 40] En general, estos derivados con ligandos C^C* emiten intensamente en el azul e incluso en la región de UV, debido a la alta energía del orbital LUMO centrado en el ligando C^C*, y presentan altos rendimientos en films de PMMA, favorecidos por el fuerte campo inducido tanto por el carbeno como por el carbono aniónico (Figura I.7).

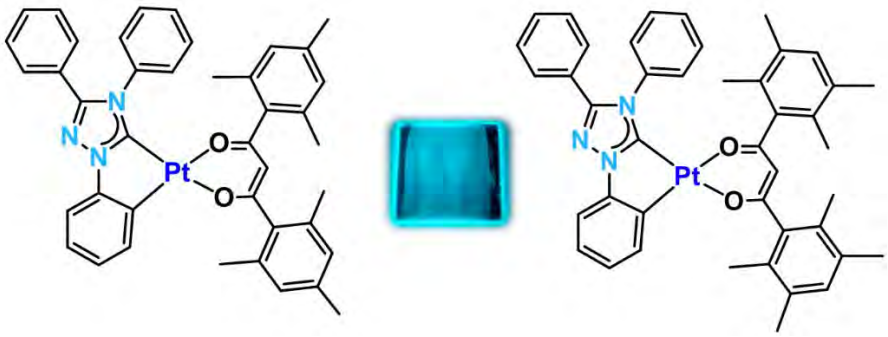

Figura I.7.[40d]

Además de ligandos ciclometalados bidentados, el centro de Pt(II) puede acomodar diferentes tipos de ligandos ciclometalados multidentados y ligandos auxiliares, dando lugar a una gran variedad de compuestos neutros o iónicos.[8, 9c, 9g, 15b, 15c, 29a, 30c] En general, los derivados ciclometalados de Pt(II) con ligandos multidentados se pueden clasificar en tres grupos (Figura I.8).[15c] Los de tipo I tienen un ligando tridentado ciclometalado, que son en general de los tipos N^C^N, C^N^N o C^N^C, y un ligando monodentado. Los tipos II y III, recientemente desarrollados, se basan en ligandos tetradentados, pero el tipo II es un ligando acíclico y el tipo III es uno cíclico. La rigidez y robustez de estos ligandos con átomos fuertemente σ-dadores proporciona compuestos fosforescentes de Pt(II) altamente eficientes y muy robustos. De hecho, se han

desarrollado recientemente compuestos de Pt(II) con eficiencias de emisión de $\phi_p \sim 1$ y una excepcional estabilidad térmica (Td > 400ºC).[41]

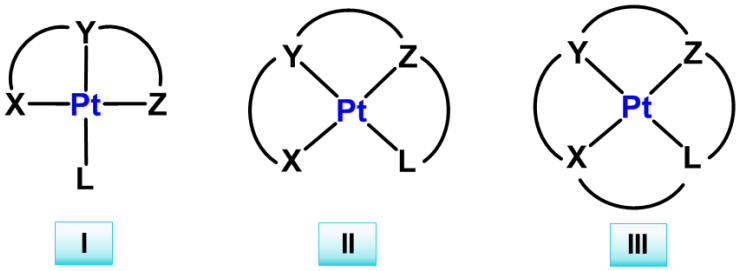

Figura I.8. Clasificación de los compuestos Pt(II) con ligandos ciclometalados multidentados. X, Y, Z, L = unidades estructurales que contienen un átomo dador, siendo al menos uno de ellos el carbono C^- en el ligando ciclometalado.[15c]

1.2 Derivados de Pt(II) con ligandos ciclometalados y grupos C_6F_5

Como se ha comentado, la elección de los coligandos es importante para obtener emisiones eficientes en los compuestos ciclometalados de Pt(II). Así, el grupo C_6F_5 utilizado como coligando en esta Memoria, es un grupo de campo fuerte debido a la presencia del átomo de C sp^2 dador, aumentando la energía de las transiciones no emisivas d-d y, por lo tanto, mejorando las propiedades emisivas de estos compuestos. Además, este grupo forma enlaces Pt-C(sp^2) muy robustos, dando lugar a complejos estables.[27]

Los productos de partida más comunes que se utilizan para la síntesis de derivados mononucleares alquilo y arilo de Pt(II) con ligandos C^N del tipo [Pt(C^N)XS][42] (X = Cl, Br, R; S = SMe_2, SEt_2, disolvente) son especies con ligandos lábiles del tipo *cis*-[PtX_2S_2] (X = Cl, R; S = SMe_2, NCMe, dmso, thf, etc) o compuestos dinucleares [$PtR_2(\mu$-$SMe_2)]_2$ (R = Me, arilo), ya que permiten que el ligando HC^N se coordine inicialmente por el átomo de nitrógeno y producir, en una etapa posterior, la ciclometalación por eliminación de RH. Sin embargo, los ejemplos descritos para la obtención de compuestos ciclometalados que contengan como coligando el grupo pentafluorofenilo a partir de productos de partida tipo [$Pt(C_6F_5)_2S_2$] son muy escasos,[43] probablemente debido a la alta estabilidad que presentan los enlaces Pt-C_6F_5, que dificulta su eliminación como C_6F_5H.

El primer ejemplo descrito en la bibliografía de un compuesto ciclometalado de Pt(II) con ligandos pentafluorofenilo publicado fue el derivado [$Pt(C_6F_5)(C_6H_4C(Ph)$=N-N=$CPh_2)$] publicado en 1992.[43b] El compuesto contiene una azina benzofenona ciclometalada actuando como un ligando tridentado κ^2C,N-η^2fenilo, que se genera por

activación del enlace C-H en un grupo fenilo con eliminación de C_6F_5H (Esquema I.1a). En la misma línea, Crespo, Martínez y *col*. han publicado que la reacción de *cis*-$[Pt(C_6F_5)_2S_2]$ (S = SEt_2, SMe_2) con la imina 2-$BrC_6H_4CH{=}NCH_2$ (4'-ClC_6H_4) (Esquema I.1b) evoluciona con la formación final de los complejos metalados $[PtBr\{(6\text{-}C_6F_5)(2\text{-}C)C_5H_3CHN\text{-}CH_2(4'\text{-}ClC_6H_4)\}S]$.[43a] Sin embargo, estos trabajos se han focalizado solo en estudios de reactividad.

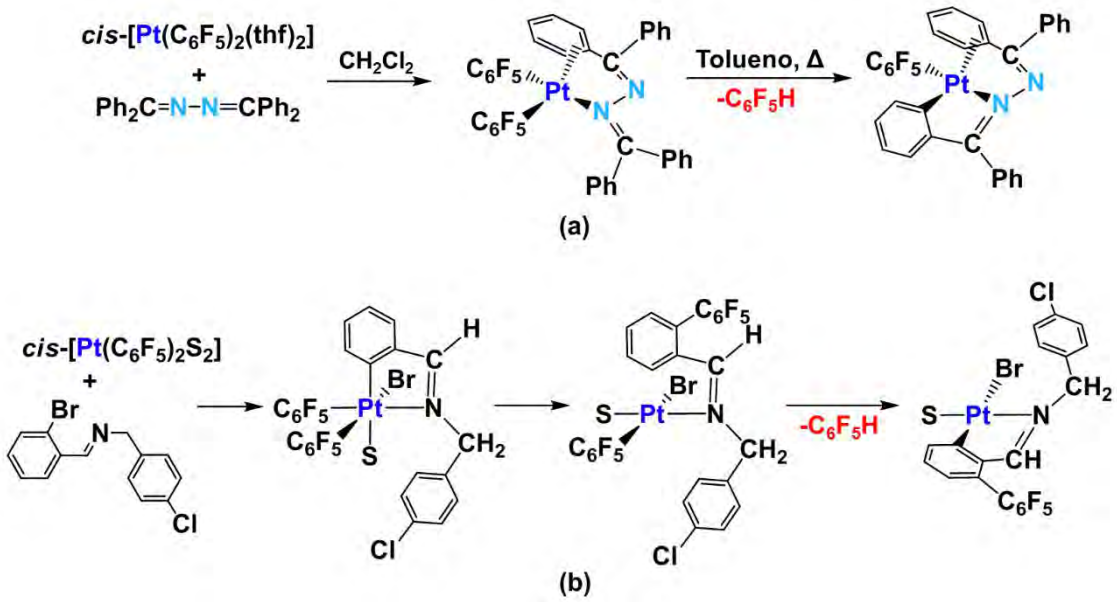

Esquema I.1

Más recientemente, el grupo del Prof. J. Forniés publicó el compuesto aniónico $(NBu_4)[Pt(bzq)(C_6F_5)_2]$ (Hbzq = 7,8-benzoquinoleína),[44] obtenido por activación del enlace C-H del ligando Hbzq utilizando como precursor el derivado $(NBu_4)[Pt(C_6F_5)_3(Hbzq\text{-}\kappa N)]$. El compuesto $(NBu_4)[Pt(bzq)(C_6F_5)_2]$ es interesante, no sólo por su eficaz emisión color verde de naturaleza $^3IL/^3MLCT$, sino porque debido a su naturaleza aniónica, ha resultado ser un excelente precursor para la síntesis de compuestos polimetálicos. Estos derivados polimetálicos están estabilizados por enlaces del tipo dador-aceptor Pt→M (M = Cd,[44] Ag[45]) y, en algunos casos, también con interacciones η^1-C(bzq)···M y presentan propiedades fotofísicas muy interesantes (Figura I.9).[27]

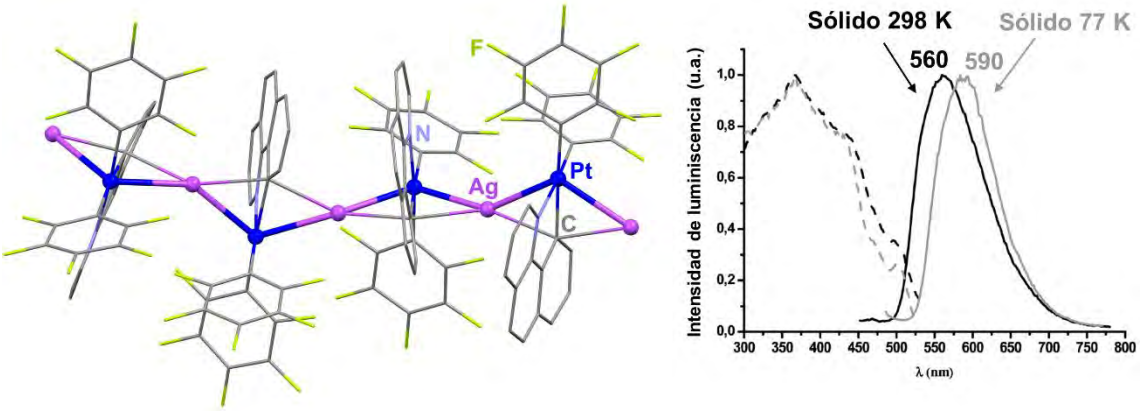

Figura I.9.[45b]

Siguiendo la línea de investigación centrada en la síntesis de compuestos luminiscentes mononucleares de Pt(II) con ligandos ciclometalados C^N y pentafluorofenilo, nuestro grupo de investigación publicó en 2012 que el derivado *cis*-[Pt$(C_6F_5)_2(thf)_2$] (thf = tetrahidrofurano) es capaz de activar un enlace C-H en la molécula de Hbzq en acetona para obtener el solvato complejo [Pt(bzq)(C_6F_5)(acetona)]. El estudio de la reacción permitió demostrar que la metalación ocurre a través de la formación inicial del compuesto saturado *cis*-[Pt$(C_6F_5)_2$(Hbzq-κN$)_2$], que reacciona con el exceso de *cis*-[Pt$(C_6F_5)_2(thf)_2$] para formar [Pt(bzq)(C_6F_5)(acetona)] y HC_6F_5, cuando la reacción se lleva a cabo en acetona a reflujo (Esquema I.2a). Sin embargo, el derivado *cis*-[Pt$(C_6F_5)_2$(Hbzq-κN$)_2$] evoluciona hacia el compuesto ciclometalado *cis*-[Pt(bzq)(Hbzq-κN)(C_6F_5)] cuando la reacción se realiza en CH_2Cl_2 y proporción molar 1:2 (Esquema I.2b).[46] Estos resultados son relevantes en el contexto de esta Memoria, ya que estos derivados son precursores (o análogos de precursores) de muchos de los productos finales descritos en esta Tesis Doctoral.

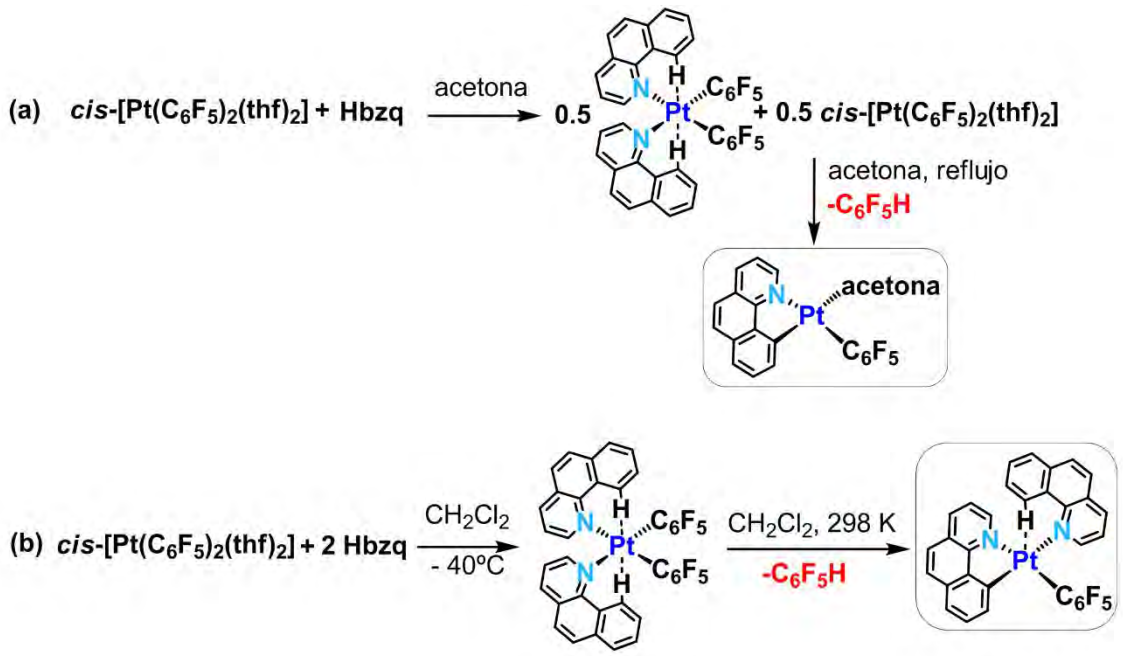

Esquema I.2.

Recientemente, nuestro grupo de investigación ha publicado, a partir de los correspondientes solvatos de dmso, la síntesis y propiedades de compuestos con ligandos fosfina biocompatibles [Pt(C^N)(C_6F_5)(L)] (C^N = ppy, dfppy; L = $PPh_2C_6H_4COOH$ (dpbH); $PPh_2C_6H_4CONHCH_2COOMe$ (dpbGlyOMe); $P(C_6H_4SO_3Na)_3$ (TPPTS)].[47] Además de sus propiedades fotofísicas, se ha estudiado su actividad biológica, examinando su citotoxicidad frente a tres líneas celulares distintas, su localización en la célula por microscopía de fluorescencia, así como un posible mecanismo de acción. Algunos de estos compuestos muestran valores de citotoxicidad muy altos (en el rango μM) y su localización celular se produce principalmente en el citoplasma, de acuerdo con los estudios de electroforesis que indican que estos derivados de platino no muestran evidencias de interacción con el ADN. Estudios complementarios sobre el mecanismo de acción con el compuesto [Pt(dfppy)(dpbH)(C_6F_5)] revelan que éste presenta una potente actividad en la despolimerización de los microtúbulos de la tubulina, inhibiendo la formación de los microtúbulos en la célula (Figura I.10).

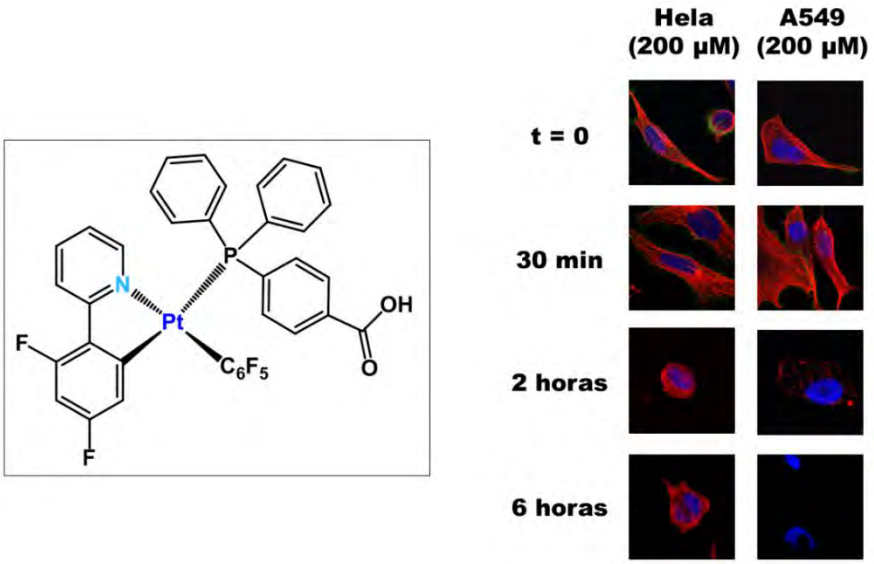

Figura I.10. Compuesto [Pt(dfppy)(dpbH)(C_6F_5)] mostrando su acción en la desestabilización de los microtúbulos de la tubulina en las células HeLa y A549.[47]

El solvato [Pt(bzq)(C_6F_5)(acetona)], que contiene una molécula de acetona lábil, se ha utilizado como precursor para la síntesis de otros derivados [Pt(bzq)(C_6F_5)(L)] (L = PPh_3, $pyPh_2$, tht, MeCN)[48] incluyendo los primeros ejemplos con η^2-alquinos terminales [Pt(bzq)(C_6F_5)(η^2-RC≡CH)].[46] También se han utilizado para generar clústers polimetálicos Pt_2M (M = Pb,[49] Ag[48]) y PtTl[50] con interesantes estructuras y propiedades. Así, algunos de los clústers Pt_2Pb y PtTl soportados por puentes 2-piridintiolato presentan propiedades vapocrómicas y vapoluminiscentes (ver ejemplo en la Figura I.11), causados por cambios en el entorno del heterometal tras la coordinación de diferentes moléculas de disolvente, propiedades mecanocrómicas al ejercer presión o solvatocrómicas con diferentes estructuras y emisiones dependiendo del disolvente y las condiciones de cristalización.

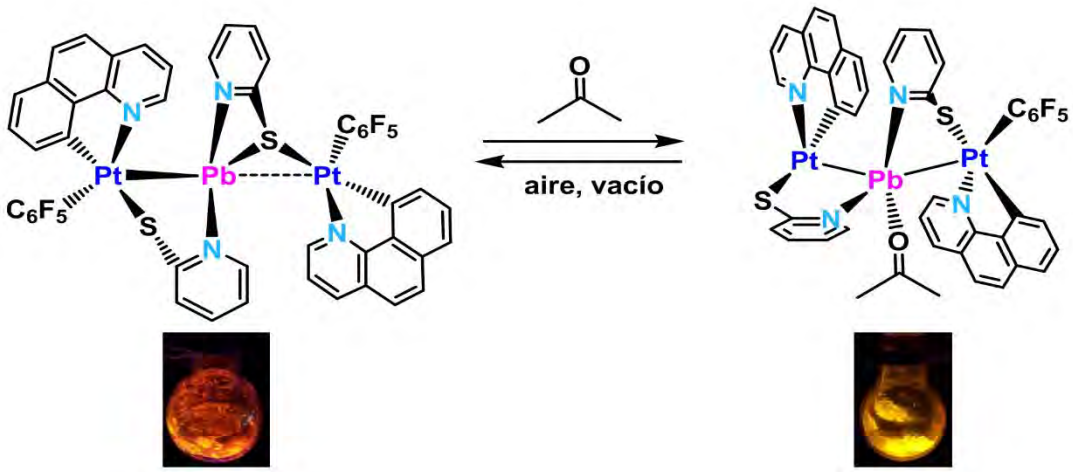

Figura I.11.[49a]

Teniendo en cuenta todo lo anterior, resulta razonable pensar que los compuestos de Pt(II) con ligandos ciclometalados con una posición lábil [Pt(C^N)(C_6F_5)(disolvente)] son muy interesantes para la síntesis de nuevos compuestos luminiscentes.

2. Luminiscencia en complejos octaédricos de Pt(IV) (d^6)

Los compuestos octaédricos d^6 de Pt(IV) se conocen desde hace más de un siglo. Son compuestos de 18 electrones, con la esfera de coordinación completa, lo que les convierte en derivados muy estables y, por lo tanto, su reactividad frente agentes externos es limitada. Los principales estudios sobre compuestos de platino (IV) se han centrado, principalmente, en procesos de adición oxidante/eliminación reductora relevantes para catálisis[51] y en estudios biológicos, por su potencial aplicación como pro-fármacos en tratamientos de quimioterapia.[52]

Frente a la enorme cantidad de estudios publicados en compuestos luminiscentes organometálicos de Pt(II), las propiedades ópticas de los compuestos de Pt(IV) están sorprendentemente casi sin explorar, a pesar de que su entorno octaédrico ofrece seis posibilidades de coordinación, frente a las cuatro de los compuestos de Pt(II) y que la geometría octaédrica da lugar a sistemas rígidos, lo que favorece un aumento del rendimiento cuántico y dificulta la desactivación de la luminiscencia debida a interacciones intermoleculares. Sin embargo, uno de los mayores inconvenientes que se produce en la síntesis de compuestos de Pt(IV) luminiscentes es la inestabilidad que presentan algunos de estos compuestos frente a estímulos fotoquímicos y térmicos, produciéndose fácilmente fotoisomerización y/o la reducción a sistemas de Pt(II).[53]

La escasez en el estudio sobre compuestos de Pt(IV) contrasta también con los extensos estudios que se encuentran en la bibliografía sobre compuestos luminiscentes de otros iones d^6 como Re(I), Ru(II), Os(II) e Ir(III).[10g, 14a, 14j, 54] En particular, los derivados de Ir(III) con ligandos ciclometalados han sido extensamente estudiados por sus interesantes propiedades ópticas. Estos derivados con geometría octaédrica son muy emisivos, debido a que los estados excitados de menor energía se atribuyen generalmente a mezcla de transiciones de transferencia de carga metal-ligando (^{3}MLCT) y centradas en el ligando (^{3}IL), evitándose así que se alcancen los estados no radiativos d-d centrados en el metal (MC).[55] En la Figura I.12A se representa, a modo de ejemplo, el diagrama esquemático de orbitales moleculares de un compuesto d^6 en el que el orbital HOMO está

formado por orbitales centrados en el metal y en el ligando, mientras que el orbital desocupado LUMO se centra en orbitales π* del ligando. Esta situación da lugar generalmente a la formación de estados excitados del tipo MLCT/IL.

Sin embargo, en compuestos de Pt(IV) de geometría también octaédrica, la contribución MLCT al estado excitado es mucho menor, debido a la baja energía de los orbitales *d* centrados en el metal, provocado por la mayor carga del ión metálico (Figura I.12B).[56] Así, tanto el orbital HOMO como el LUMO están centrados generalmente en los ligandos, dando lugar a estados excitados π-π* con un carácter principalmente intraligando (^{3}IL), con tiempos de vida muy largos (desde decenas hasta cientos de microsegundos). Hay que tener en cuenta que, aunque la influencia del metal en los orbitales frontera sea prácticamente nula, éste tiene un papel muy importante en las propiedades emisivas de estos compuestos de Pt(IV). Así, la influencia del metal es generalmente suficiente para que el compuesto presente un acoplamiento spin-órbita eficaz, produciéndose el cruce intersistémico para dar emisiones fosforescentes. Sin embargo, se han encontrado algunos ejemplos de compuestos de Pt(IV) fluorescentes cuando se incorporan al centro metálico cromóforos altamente conjugados.[57]

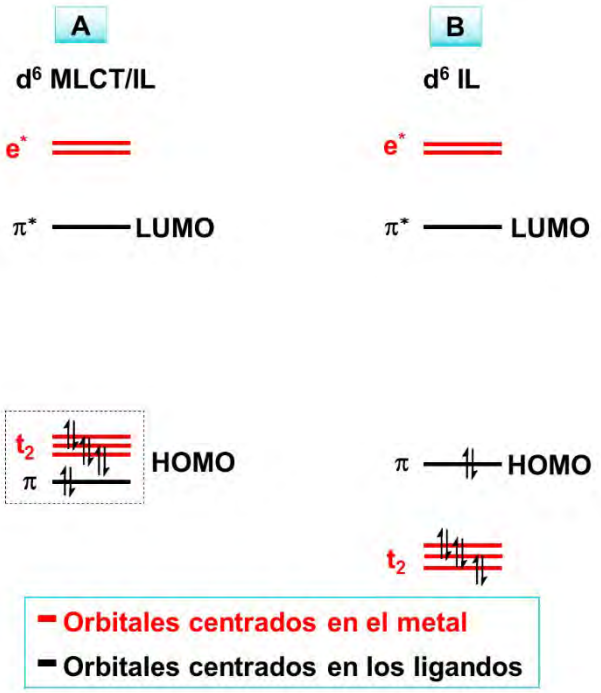

Figura I.12. Diagrama esquemático de orbitales moleculares de compuestos octaédricos d^6 para estados excitados del tipo (a) MLCT/IL y (b) IL.

2.1 Derivados luminiscentes de Pt(IV) con ligandos ciclometalados

Los primeros compuestos organometálicos de Pt(IV) luminiscentes a temperatura ambiente contienen ligandos ciclometalados y fueron publicados por von Zelewsky, Balzani *y col*. en 1986. Observaron que algunos derivados bis-ciclometalados de Pt(II) [Pt(C^N)$_2$] [C^N = 2-fenilpiridina (ppy), 2-(2-tienil)piridina (thpy)] son extremadamente fotosensibles en disolventes orgánicos clorados (CH_2Cl_2, CH_3Cl), debido al carácter nucleofílico del centro metálico,[58] dando lugar a derivados de Pt(IV) [Pt(C^N)$_2$(CH_2Cl)Cl]. A la vista de estos resultados, estudiaron reacciones de adición oxidante utilizando haluros de alquilo para dar derivados del tipo [Pt(C^N)(CH_2R)X], siendo algunos de estos productos intensamente luminiscentes con emisiones atribuidas a transiciones puramente intraligando (^{3}IL), con luminiscencia en la zona azul o verde del espectro visible.[25, 59]

El estudio de estas reacciones indicó que la adición oxidante se produce principalmente a través de un mecanismo del tipo S_{N2} para dar un sólo esteroisómero de Pt(IV) de los 11 posibles productos que se pueden formar (Esquema I.3).[59a]

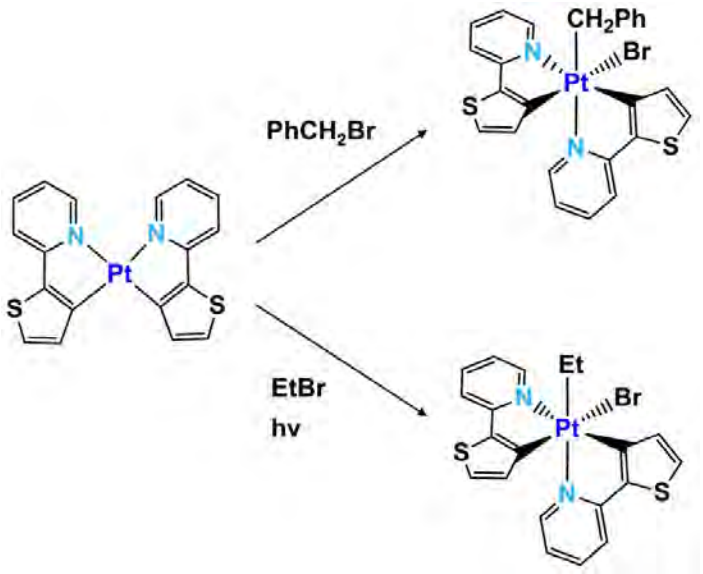

Esquema I.3

Desde entonces, se han publicado varias familias de compuestos luminiscentes de Pt(IV) con ligandos ciclometalados. El grupo de Swager empleó una reacción de oxidación similar a la comentada anteriormente para demostrar que una serie de compuestos [Pt(C^N)$_2$] [C^N = 2-benzotiofen-2-il-piridina (btp), 2-tienilpiridina (thpy)] reacciona en presencia de cianuros de halógeno (X-CN), altamente tóxicos, formando

especies de Pt(IV) con luminiscencia desplazada hacia el azul en comparación con la de los precursores de Pt(II), convirtiendo así estos compuestos en sensores muy interesantes (Figura I.13).[60]

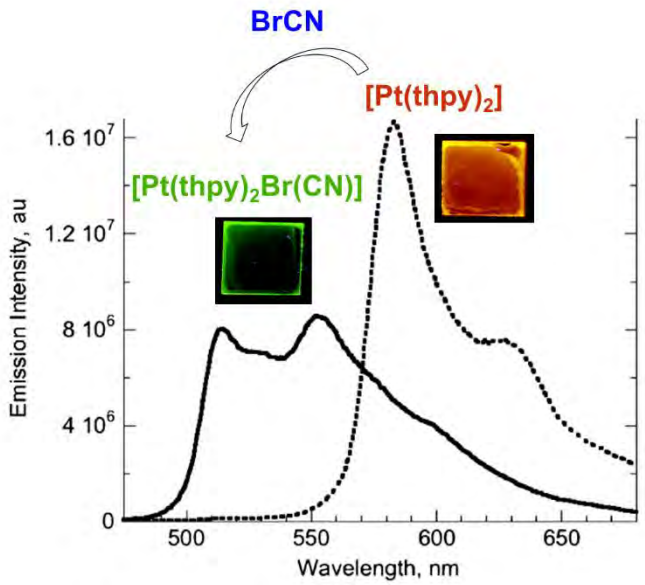

Figura I.13.[60]

Más recientemente, F. Lelj *y col.* publicaron la síntesis de compuestos monociclometalados de Pt(IV) [Pt(C^N)(O^O)I_2] [C^N = fenilpiridina (ppy), dietilamino-5H-benzo[a]-fenoxazin-5-ona (Nile Red, Figura I.14); O^O = acetilacetonato (acac), hexafluoroacetilacetonato (hfacac)] mediante oxidación con I_2 de los precursores de Pt(II). Mientras los derivados de Pt(IV) con ppy no son luminiscentes, el compuesto con el ligando ciclometalado Nile Red (NR) muestra fluorescencia, aunque con menores rendimientos cuánticos que los precursores de Pt(II) (Figura I.14).[61]

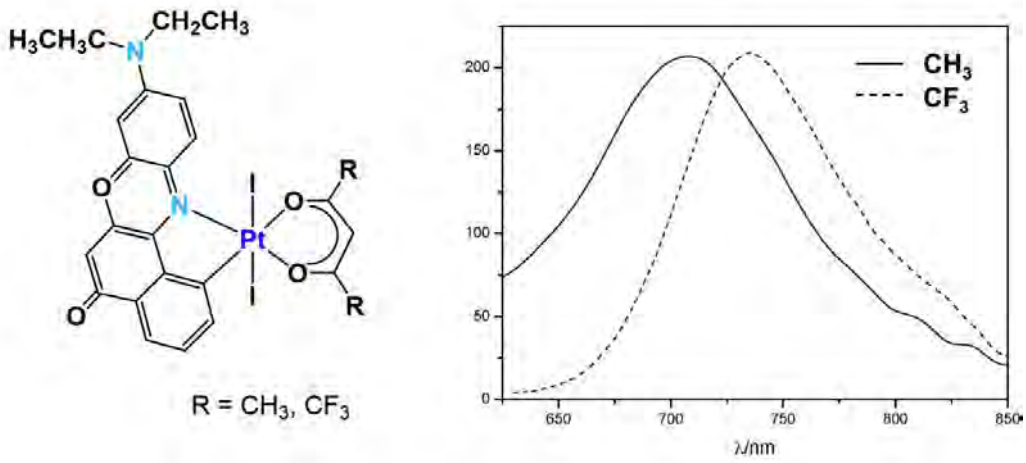

Figura I.14

Simultáneamente, Jenkins y Bernhard publicaron los compuestos bis-ciclometalados $[Pt(C^N)_2Cl_2]$ [C^N = 5-metil-2-(4'-fluorofenil)piridina (F-mppy), 2-fenilpiridina (ppy), 5-metil-2-(4'-metoxifenil)piridina (MeO-mppy)], obtenidos por oxidación de los precursores de Pt(II) [Pt(C^N)(HC^N)(Cl)], que contienen un ligando ciclometalado y otro coordinado a través del nitrógeno, utilizando el oxidante $PhICl_2$. Además, la sustitución de los átomos de Cl por ligandos diimina N^N da lugar a los compuestos $[Pt(C^N)(N^N)][PF_6]_2$ [N^N = 5,5'-difluoro-2,2'–bipiridina (dFbpy), 2,2'-bipiridina (bpy), 4,4'-dimetoxi-2,2'-bipiridina (dMeObpy)], siendo éstos los primeros ejemplos de Pt(IV) publicados con tres ligandos quelato rodeando al centro metálico.[62] Estos derivados muestran emisiones fosforescentes con estados excitados de carácter ^{3}IL centrados en los ligandos ciclometalados (Figura I.15).

Figura I.15.[62]

En general, los oxidantes más utilizados para obtener sistemas de Pt(IV) con ligandos ciclometalados son del tipo $Ph\text{-}I(L)_2$, donde L es un grupo aniónico o un ligando neutro. En estos casos, el I(III) actúa como oxidante de dos electrones, y además, libera los grupos o aniones L a los que está unido.[63] Además, dentro de este grupo de oxidantes, el compuesto con L = Cl ($PhICl_2$) es el más utilizado para la obtención de compuestos bis-ciclometalados.

Teniendo en cuenta los escasos antecedentes que se encontraron en la bibliografía al inicio de esta Tesis, consideramos que la síntesis de compuestos emisivos de Pt(IV) con ligandos ciclometalados y el estudio de sus propiedades luminiscentes podía aportar resultados novedosos y de interés en este campo. De manera simultánea a los estudios sobre compuestos de Pt(IV) luminiscentes que se han llevado a cabo durante la realización de esta Tesis Doctoral, se han publicado varios trabajos donde se estudian las propiedades fosforescentes de compuestos de Pt(IV) con una variedad de ligandos ciclometalados, siendo la mayor parte del tipo C^N.

Los tipos de derivados luminiscentes de Pt(IV) con ligandos ciclometalados C^N publicados durante el desarrollo del trabajo de la Tesis, se recogen en la Figura I.16 y se pueden clasificar de la siguiente manera:

- Compuestos mono-ciclometalados aniónicos: $(NBu_4)[Pt(C^N)(S^S)_2]$[64] (S^S = ligando dianiónico 1,2-bencenoditiolato) (**Tipo A**)
- Compuestos bis-ciclometalados con un eje de simetría C_2 en la unidad $Pt(C^N)_2$ (**Tipo B**): $[Pt(C^N)_2X_2]$[65] (X = haluro, carboxilato)
- Compuestos bis-ciclometalados con la unidad $Pt(C^N)_2$ asimétrica (**Tipo C**): $[Pt(C^N)_2X_2]$[65a] (X = haluro) o $[Pt(C^N)_2(R)(X)]$ (R = alquilo; X = haluro).[66]
- Compuestos tris-ciclometalados (**Tipo D**): homolépticos *mer/fac*-$[Pt(C^N)_3]^+$ y heterolépticos *mer/fac*-$[Pt(C^N)_2(C^N)']^+$.[67]

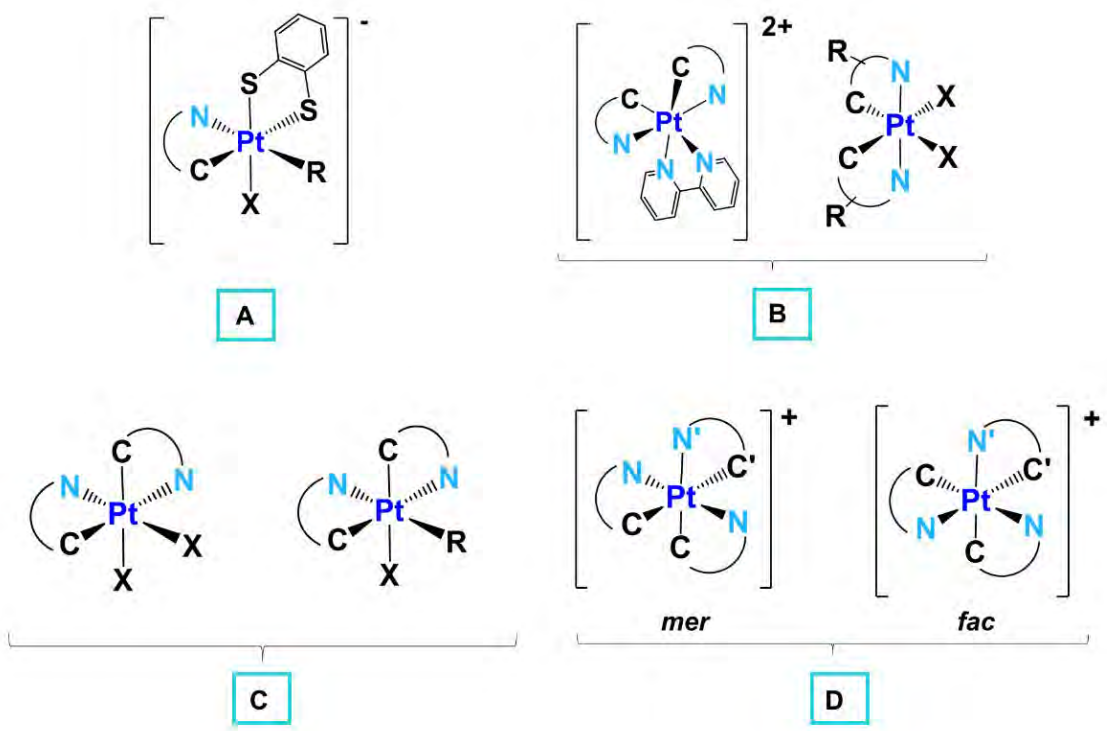

Figura I.16. Clasificación de compuestos de Pt(IV) luminiscentes con ligandos ciclometalados C^N publicados recientemente.

Los derivados que se muestran en la Figura I.16A son los primeros compuestos aniónicos de Pt(IV) con ligandos ciclometalados, y se obtienen por adición de un equivalente 1,2-bencenoditiol $[H_2(Thio)]$ a los precursores aniónicos de Pt(II) $(NBu_4)[(C^N)Pt(S^S)]$.[64] Estos derivados muestran emisión en estado sólido a 298 K con rendimientos cuánticos del orden de 5-10%. Los compuestos *cis*-$[(C^N\text{-}R)_2X_2]$ (R = $OC_{12}H_{25}$; X = Cl, Br), representados en la Figura I.16B, han sido publicados

recientemente por Bruce, Williams, Lyman *y col.*, y son los primeros derivados de Pt(IV) que, además de ser emisivos en disoluciones desoxigenadas ($\phi \sim 10\%$), muestran un comportamiento de cristal líquido, lo que les convierte en una nueva clase de materiales emisivos.[65b]

En la Figura I.16C se muestran los derivados asimétricos bis-ciclometalados publicados por González-Herrero *y col.*[65a, 66] Algunos de estos derivados mostraron emisiones fosforescentes muy eficientes, con rendimientos cuánticos que alcanzan el 81% en disolución a temperatura ambiente (Figura I.17).[66]

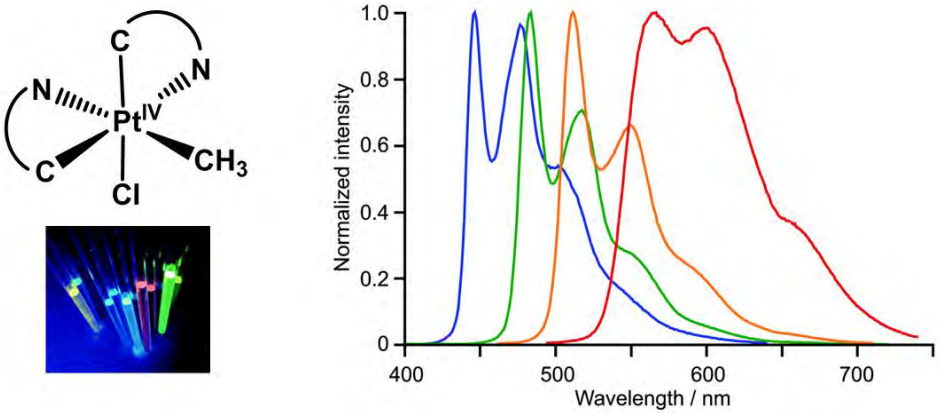

Figura I.17.[66]

En relación a los compuestos del tipo D (Figura I.16D), el grupo de González-Herrero ha demostrado que los isómeros homolépticos *mer*-$[Pt(C^N)_3]^+$ [C^N = 2-fenilpiridina (ppy), 2-(2-tienil)piridina (thpy), 2-2,4-difluorofenil)piridina (dfppy), 1-fenilpirazol (ppz), 2-(9,9-dimetilfluoren-2-il)piridina (flpy)][67a, 67c] y heterolépticos *mer*-$[Pt(dfppy)_2(ppy)]^+$[67b] y *mer*-$[Pt(ppy)_2(flpy)]^+$[67c] isomerizan fácilmente por irradiación con una lámpara de mercurio a los respectivos compuestos *fac*-$[Pt(C^N)_3]^+$ (C^N = ppy, thpy, dfppy, ppt, flpy), *fac*-$[Pt(dfppy)_2(ppy)]^+$ y *fac*-$[Pt(ppy)_2(flpy)]^+$, respectivamente. Además, los rendimientos cuánticos de emisión de los isómeros *fac* son más elevados en todos los casos, con rendimientos cuánticos de hasta el 49% en CH_2Cl_2 a 298 K (ver ejemplos en el Esquema I.4). Como se ha comentado anteriormente, uno de los inconvenientes de los compuestos luminiscentes de Pt(IV) es su limitada estabilidad fotoquímica y térmica. En este sentido, los intentos de preparación de los derivados homolépticos *mer*-$[Pt(C'^N')_3]^+$ o la obtención por fotoisomerización de los heterolépticos *fac*-$[Pt(C^N)_2(C'^N')]^+$ a partir de los *mer*-$[Pt(C^N)_2(C'^N')]^+$ cuando

C'^N' = 2-(2-tienil)piridina (thpy) o 1-fenilisoquinoleína (piq) fueron infructuosos debido a que se produce la reducción a compuestos de Pt(II).[67b]

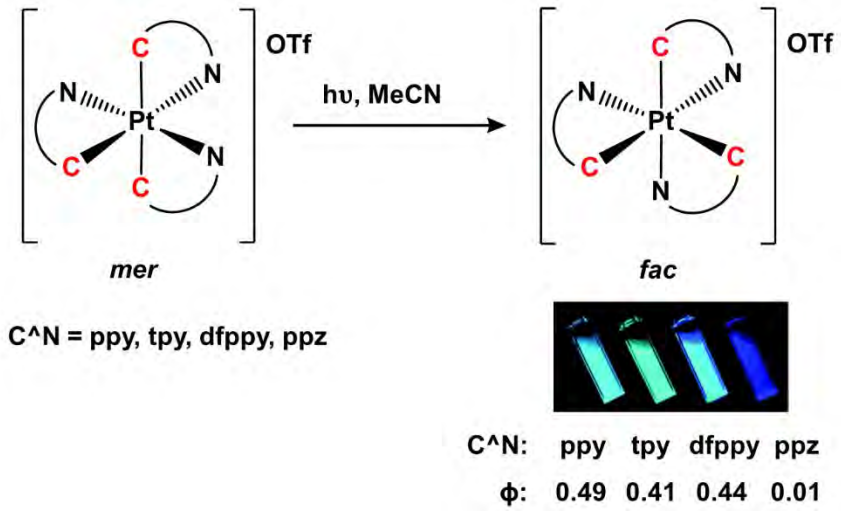

Esquema I.4. Isomerización *mer* – *fac* (C^N = ppy, tpy, dfppy, ppz).[67a]

Los estudios de este grupo han demostrado que las eficiencias de las emisiones de los compuestos de Pt(IV) dependen fundamentalmente de dos factores. Por un lado, influye la contribución de la transición MLCT al estado excitado, de manera que los derivados neutros, aquellos que tienen enlaces Pt-C cortos y los que presentan coligandos π-dadores muestran una mayor contribución MLCT al estado excitado, aumentando la eficiencia de las emisiones. Por otro lado, afecta la existencia de estados excitados térmicos accesibles de tipo LMCT, que pueden provocar la desactivación del estado excitado por procesos no radiantes, desfavorecidos en compuestos con enlaces Pt-C cortos y ligandos con un fuerte carácter σ-dador.[56]

Además, durante este año 2019 ese mismo grupo ha publicado compuestos luminiscentes de Pt(IV) que combinan el ligando ciclometalado C^C* (1,2,3-triazolilideno) y ligandos bis o tridentados 2,6-diarilpiridinas (C^N^CH o C^N^C)[56] (Figura I.18a) y Rodríguez y Crespo han publicado compuestos luminiscentes de Pt(IV) con un ligando imina tridentado (C^N^N') con un sustituyente *para*-fluoro y coligandos metilo o haluro (Figura I.18b).[68]

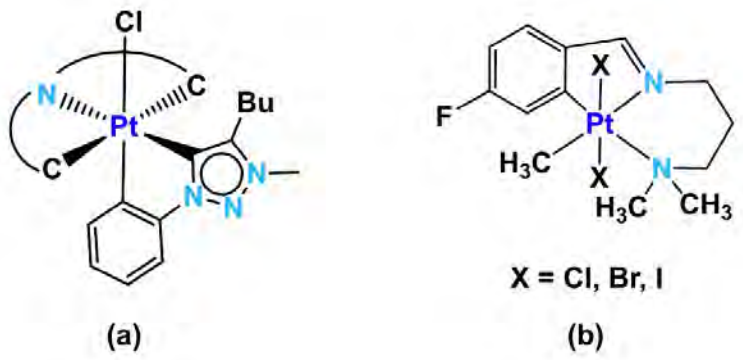

Figura I.18

Hasta la fecha, solo se han publicado dos compuestos de Pt(IV) que son activos en OLEDs basados en polímeros (Figura I.19). Los compuestos contienen un ligando bis-ciclometalado tetradentado basado en la unidad isoquinolina funcionalizada con grupos trifenilamina, que actúan como transportadores de huecos, y dos ligandos auxiliares cloruro que se sitúan en *trans*.[69] Los compuestos muestran luminiscencia en el NIR (λ_{em} ~ 750 nm) en disolución diluida de 2-MeTHF con vidas medias del orden de 0.7 μs de naturaleza ^{3}ILCT/^{3}MLCT. La emisión del dispositivo OLED fabricado en poli(vinilcarbazol) muestra un pico electroluminiscente similar en el NIR (λ_{EL} ~ 750 nm) con una intensidad radiante máxima de 164 μWcm^{-2} y eficiencia cuántica externa (EQE) de 40.85% para el compuesto mostrado en la Figura I.19b,c.

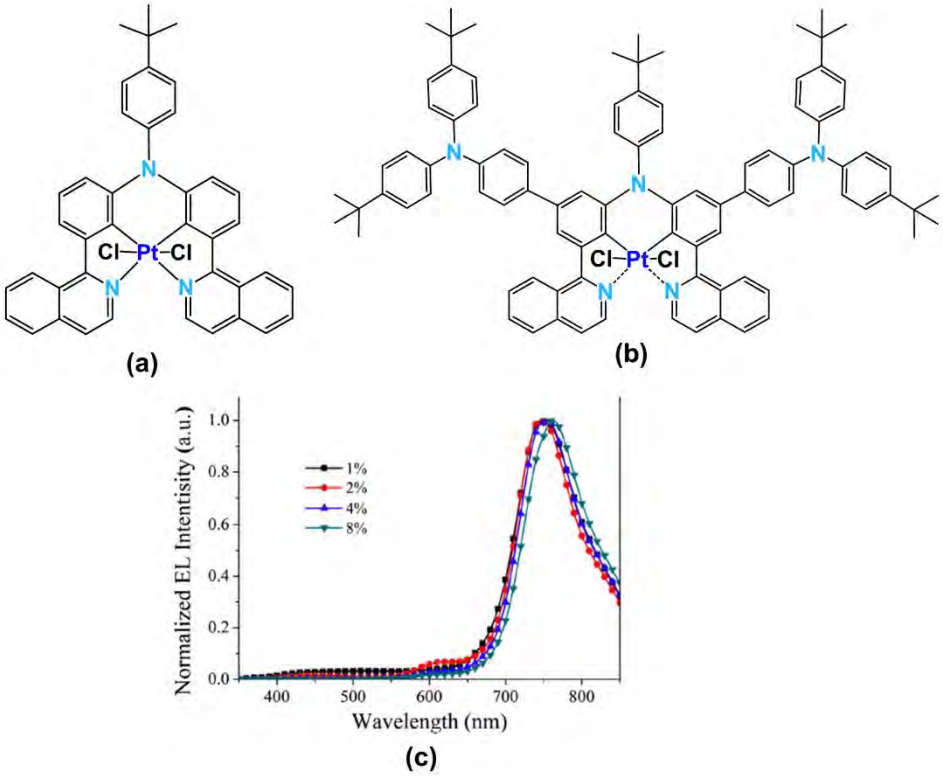

Figura I.19. [69]

Conviene destacar que recientemente se han publicado por primera vez sistemas heterobimetálicos de Pt(IV) luminiscentes [Pt(IV)-O-Re(VII)] (Figura I.20) con emisiones fundamentalmente ^{3}IL con algo de contribución ^{3}MLCT.[70] El estudio demuestra que la coordinación de la unidad ReO_4^- aumenta el rendimiento cuántico de fosforescencia en relación a los precursores monómeros de Pt(IV).

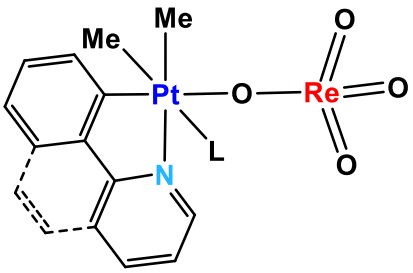

C^N = ppy, bzq; L = PPh_3, $PMePh_2$

Figura I.20

Como se ha comentado anteriormente, el grupo C_6F_5 forma enlaces Pt-C(sp^2) muy robustos por lo que estabiliza compuestos organometálicos en estados de oxidación altos e impide los procesos de reducción y eliminación.[46] Por lo tanto, pensamos que el C_6F_5 sería un coligando adecuado para abordar la síntesis de compuestos ciclometalados de Pt(IV) ya que aumentaría la estabilidad de los sistemas. Por otra parte, es un ligando de campo fuerte capaz de desestabilizar los orbitales vacíos centrados en el metal, desactivantes de la luminisciencia, por lo que es de esperar que se incremente la eficiencia de las emisiones. Por último, queremos destacar que, aunque se conocen pentafluorofenil derivados de Pt(IV),[51d, 71] no se encuentran en la bibliografía estudios relacionados con propiedades luminiscentes.

3. Objetivos

Dada la experiencia del grupo de investigación de "Materiales Moleculares Organometálicos" en la síntesis de compuestos organometálicos de Pt(II) con ligandos ciclometalados y la escasez de compuestos luminiscentes de Pt(IV), se comenzó una línea de investigación dirigida a la obtención de nuevos sistemas de Pt(II) y Pt(IV) con diferentes ligandos ciclometalados, utilizando el ligando pentafluorofenilo como ligando auxiliar. Así, el trabajo descrito en esta Memoria se centra en la síntesis, caracterización

y estudio de las propiedades fotofísicas de compuestos luminiscentes pentafluorofenil-cicloplatinados de Pt(II) y Pt(IV).

En el primer Capítulo (**Capítulo 1**), se continuó una de las líneas de investigación que comenzó el Dr. Sergio Sánchez durante su Tesis Doctoral,[72] dirigida al estudio de las reacciones de oxidación del derivado de Pt(II) [Pt(bzq)(C_6F_5)(η^2-HC≡CFc)] (bzq = 7,8-benzoquinoleína) con oxidantes halogenados. Estas reacciones de oxidación conducían a la formación de dos especies diferentes: por un lado, a los derivados de Pt(II) [Pt{bzq-κN-η^2-CH=C(X)Fc}(C_6F_5)X] (X = Cl, I) con el ligando (*Z*)-10-[1-X,1-ferrocenilvinilo]benzoquinoleína funcionalizado y, por otro lado, a derivados dinucleares de Pt(IV). En base a estos sorprendentes resultados, nos planteamos como primer objetivo la obtención del ligando libre funcionalizado. En segundo lugar, se decidió explorar un camino alternativo para obtener los derivados dinucleares de Pt(IV), así como la obtención de monómeros de Pt(IV) del tipo [Pt(bzq)(C_6F_5)X_2(S)] (S = tht, dmso). Desafortunadamente, todos los derivados de Pt(IV) obtenidos resultaron ser no emisivos.

Con la esperanza de obtener sistemas de Pt(IV) luminiscentes, en el segundo Capítulo de esta Memoria se aborda la síntesis de nuevos pentafluorofenil derivados de Pt(II) que presenten dos cromóforos en su esfera de coordinación y que puedan generar, tras su oxidación, sistemas bis(ciclometalados) de Pt(IV) con el grupo C_6F_5 como ligando auxiliar. Presumiblemente, la rigidez de los ligandos ciclometalados así como el desdoblamiento de campo que ejercen estos dos ligandos y el grupo C_6F_5 serán adecuados para inducir propiedades luminiscentes en los compuestos finales.

Así, la primera parte del **Capítulo 2** se centra en la síntesis y caracterización de compuestos Pt(II) del tipo [Pt(C^N)(HC^N)(C_6F_5)], que contienen un ligando ciclometalado y otro coordinado a través del nitrógeno, obtenidos a partir de los derivados *cis*-[Pt(HC^N)$_2$(C_6F_5)$_2$], usando varios ligandos heterocíclicos diferentes. Se han comparado sus propiedades ópticas y sus variaciones se justifican mediante cálculos teóricos. Además, se prepararon algunos derivados solvato [Pt(C^N)(C_6F_5)(dmso)], que muestran interesantes propiedades biológicas, evaluándose la estabilidad en medio celular-dmso, su citotoxicidad frente a dos líneas celulares distintas y su localización celular mediante microscopía de fluorescencia.

La segunda parte del **Capítulo 2** se centra en la síntesis y caracterización estructural de compuestos homolépticos de Pt(IV) *fac*-[Pt(C^N)$_2$(C_6F_5)Cl] con dos ligandos ciclometalados. Estos compuestos se generan mediante oxidación inicial de los derivados de Pt(II) sintetizados en la primera parte del capítulo [Pt(C^N)(HC^N)(C_6F_5)] con $PhICl_2$, seguido de una fácil metalación del segundo heterociclo. El seguimiento de las reacciones por RMN ha permitido estudiar el mecanismo de formación. Además, con el fin de examinar la influencia de los coligandos en la eficiencia de las emisiones, se plantea la sustitución del átomo de cloro, de campo débil, por ligandos de campo fuerte como los ligandos cianuro (CN^-), 4-Metilpiridina (Mepy) o 1,2-bi(4-piridil)etileno (bpe). Se analiza la geometría de los isómeros obtenidos tanto por RMN multinuclear como por difracción de Rayos-X y se realiza un estudio comparativo de sus propiedades luminiscentes en relación con las de los productos de partida, reforzado con los resultados obtenidos por cálculos teóricos DFT y TD-DFT.

Teniendo en cuenta el interés de los derivados de Pt(IV) homolépticos luminiscentes obtenidos, en el **Capítulo 3** se consideró de interés la síntesis de pentafluorofenil derivados de Pt(IV) con dos ligandos ciclometalados diferentes coordinados al centro metálico por oxidación de los precursores adecuados de Pt(II). Para ello, inicialmente se aborda la síntesis y caracterización de los precursores monociclometalados de Pt(II) con el ligando benzoquinolato y diferentes ligandos heterocíclicos HC^N [Pt(bzq)(HC^N-κN)(C_6F_5)] a partir del solvato de acetona [Pt(bzq)(C_6F_5)(acetona)].[46] También se lleva a cabo un estudio comparativo de las propiedades ópticas con apoyo de cálculos teóricos. En la segunda parte se recoge la preparación de los derivados heterolépticos de Pt(IV) *fac*-[Pt(bzq)(C^N)(C_6F_5)Cl] por oxidación de los precursores de Pt(II) [Pt(bzq)(HC^N-κN)(C_6F_5)] con el oxidante $PhICl_2$. Estos compuestos solo se diferencian en el segundo ligando ciclometalado C^N, por lo que se ha realizado un estudio comparativo de las propiedades ópticas y de cálculos teóricos de estos derivados con el objeto de evaluar la influencia del segundo derivado ciclometalado, observándose emisión dual con ligandos C^N muy deslocalizados.

Siguiendo con nuestro interés en el fragmento "Pt(bzq)(C_6F_5)", en el **Capítulo 4** se propone la síntesis y caracterización del derivado de Pt(II), [Pt(bzq)(dppm)(C_6F_5)], que contiene el ligando bis(difenilfosfino)metano (dppm) actuando como monodentado, y se utiliza como precursor para obtener el derivado heterobimetálico Pt-Au [Pt(bzq)(C_6F_5)(μ-dppm)AuCl], con el ligando dppm puente entre los dos centros metálicos. El impacto en

las propiedades ópticas de la coordinación del Au(I) en el compuesto heterometálico respecto al monometálico es mínima, lo que se atribuye a la ausencia de enlace Pt(II)-Au(I), confirmado por Rayos X y cálculos teóricos. Además, se ha evaluado la actividad citotóxica de estos compuestos frente a varias líneas celulares, comparándolas con la de otros compuestos relacionados, y se han realizado experimentos de localización celular por microscopía de fluorescencia.

Parte de este trabajo de investigación ha dado lugar a las siguientes publicaciones:

1) Unexpected Formation of Ferrocenyl(vinyl)benzoquinoline Ligands by Oxidation of an Alkyne Benzoquinolate Platinum(II) Complex.
Jesús R. Berenguer, Julio Fernández, Nora Giménez, Elena Lalinde, M. Teresa Moreno, and Sergio Sánchez. *Organometallics* **2013**, 32, 3943−3953.

2) Luminescent pentafluorophenyl-cycloplatinated complexes: synthesis, characterization, photophysics, cytotoxicity and cellular imaging.
Jesús R. Berenguer, José García Pichel, Nora Giménez, Elena Lalinde, M. Teresa Moreno and Sergio Piñeiro-Hermida. *Dalton Trans*., **2015**, 44, 18839–18855.

3) Facile Approaches to Phosphorescent Bis(cyclometalated) pentafluorophenyl Pt(IV) Complexes: Photophysics and Computational Studies.
Nora Giménez, Rebeca Lara, M. Teresa Moreno, and Elena Lalinde. *Chem. Eur. J.* **2017**, 23, 5758 – 5771.

4) Design of Luminescent, Heteroleptic, Cyclometalated Pt(II) and Pt(IV) Complexes: Photophysics and Effects of the Cyclometalated Ligands
Nora Giménez, Elena Lalinde, Rebeca Lara, and M. Teresa Moreno. *Chem. Eur. J.* **2019**, 25, 5514 – 5526.

5) Heterobimetallic Pt(II)-Au(I) Complexes Comprising Unsymmetrical 1,1 Bis(diphenylphosphanyl)methane Bridges: Synthesis, Photophysical, and Cytotoxic Studies
Hamid R. Shahsavari, Nora Giménez, Elena Lalinde, M. Teresa Moreno, Masood Fereidoonnezhad, Reza Babadi Aghakhanpour, Mehri Khatami, Foroogh Kalantari, Zahra Jamshidi and Mozhdeh Mohammadpour. *Eur. J. Inorg. Chem*. **2019**, 1360-1373.

Capítulo 1

Reacciones de oxidación de los derivados [Pt(bzq)(C_6F_5)L] (L = HC≡CFc, CH_3COCH_3, tht)

Como se ha adelantado en la Introducción, nuestro grupo de investigación ha publicado la síntesis del solvato neutro luminiscente *cis*-[Pt(bzq)(C_6F_5)(acetona)],[46] con una molécula de acetona coordinada, que ha resultado ser un excelente precursor para la síntesis de nuevos compuestos del tipo [Pt(bzq)(C_6F_5)L],[27] ya que la molécula de acetona se puede desplazar con un equivalente de un alquino terminal HC≡CR (R = Ph, ^{t}Bu, Fc) o difenilacetileno (PhC≡CPh), para dar lugar a los primeros derivados cicloplatinados η^2-alquino [Pt(bzq)(C_6F_5)(η^2-RC≡CR')] (R = H, R' = Ph, ^{t}Bu, Fc; R = R' = Ph) (Esquema 1.1).[46] Con la excepción del derivado de Fc, son compuestos luminiscentes en todos los medios, con emisiones originadas de estados excitados mixtos ^{3}LC/^{3}MLCT.

Esquema 1.1

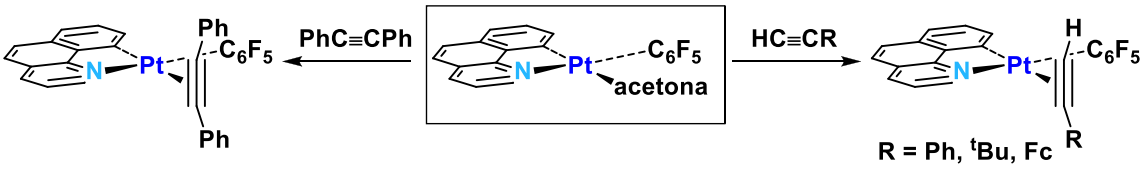

En este contexto, consideramos que el ferrocenilalquino derivado, [Pt(bzq)(C_6F_5)(η^2-HC≡CFc)] podría ser un sustrato idóneo para estudiar su reactividad frente a reacciones de oxidación con halógenos, ya que contiene la unidad "Pt(bzq-$\kappa N,C^{10}$)(C_6F_5)" que presenta alta estabilidad y dos centros redox cercanos Pt(II) y Fe(II) conectados a través de una unidad insaturada η^2-alquino.

Las reacciones de oxidación de Pt(II) para dar compuestos de Pt(IV) han sido muy estudiadas, principalmente debido a la relevancia de estos compuestos de Pt(IV) como especies intermedias en estudios mecanísticos relacionados con activación de enlaces C-H y subsiguiente funcionalización a través de eliminación reductiva de especies con enlaces C-X (X = haluro, C, O, N, P…).[51c, 51e, 59c, 73] Así, en la química de Pt(II), el mecanismo general para la formación de nuevos enlaces bajo condiciones oxidantes generalmente implica la oxidación inicial del centro de Pt(II) dando un intermedio de Pt(IV), que sufre subsiguiente eliminación reductiva para producir enlaces C-C o C-haluro.[51e, 73h-l] Por ejemplo, J. P. Rourke y *col*., han estudiado recientemente la adición

oxidante de compuestos ortometalados de Pt(II) para producir intermedios de Pt(IV) que sufren espontáneamente eliminación reductora con acoplamientos C-C selectivos sp^2-sp^3, en lugar de producirse el acoplamiento C-C sp^3-sp^3 (Esquema 1.2).[73n]

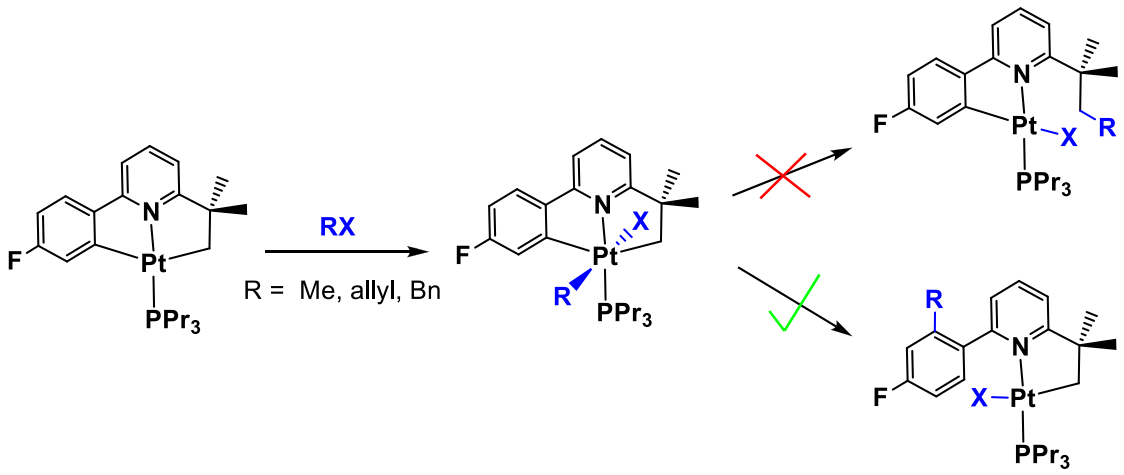

Esquema 1.2

Los primeros estudios sobre la oxidación del sustrato [Pt(bzq)(C_6F_5)(η^2-HC≡CFc)] con $PhICl_2$ o I_2 se llevaron a cabo en nuestro grupo de investigación por Sergio Sánchez, con resultados muy interesantes.[72] Debido a la presencia del ligando ferrocenilalquino, las reacciones de oxidación conducen a los derivados de Pt(II) [Pt{bzq-κN-η^2-CH=C(X)Fc}(C_6F_5)X] (X = Cl **A**, I **B**), que contienen el ligando funcionalizado (*Z*)-10-[1-X,1-ferrocenilvinilo]benzoquinoleína, obtenidos a través de una adición formal electrofílica del oxidante al alquino insaturado con formación simultánea de enlaces C-haluro y C-C (Ecuación 1.1). La disposición *Z* del nuevo ligando funcionalizado formado fue confirmada por difracción de Rayos X para el derivado de cloro. Además, en esta reacción se obtienen, como productos secundarios, pequeñas cantidades de los derivados de Pt(IV) [Pt(bzq)(C_6F_5)X(μ-X)]$_2$ (X = Cl **C**, I **D**), respectivamente.[72]

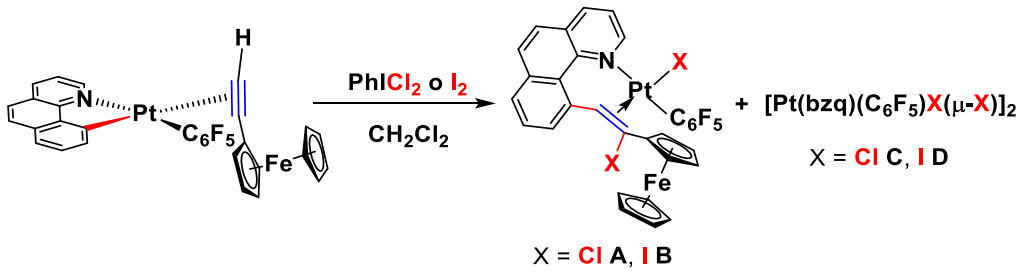

Ecuación 1.1

Los cálculos teóricos DFT que se realizaron para el complejo precursor [Pt(bzq)(C_6F_5)(η^2-HC≡CFc)] revelan que los dos orbitales moleculares ocupados más energéticos están cerca en energía (HOMO -5.49 eV, HOMO-1 -5.54 eV) y están esencialmente localizados en el ligando ferrocenilalquino (Figura 1.1).[46] Además, el complejo exhibe una onda de oxidación cuasi-reversible a 0.70 V, que se asigna al par redox Fc/Fc^+. Esta asignación está de acuerdo con observaciones previas en complejos cicloplatinados de Pt(II), que usualmente exhiben ondas irreversibles debidas al metal [Pt(II) a Pt(III) o Pt(IV)] a potenciales más altos.[74]

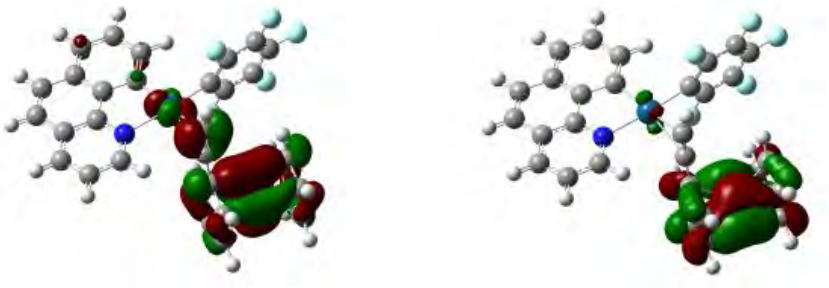

Figura 1.1. HOMO y HOMO-1 en [Pt(bzq)(C_6F_5)(η^2-HC≡CFc)]

Teniendo esto en cuenta, aunque el mecanismo exacto de formación de los compuestos **A** y **B** en la reacción de oxidación del precursor [Pt(bzq-$\kappa N,\kappa C^{10}$)(C_6F_5)(η^2-HC≡CFc) no es del todo claro, se propuso como posible ruta el mecanismo que se muestra en el Esquema 1.3. Como paso inicial, se propuso la oxidación del grupo ferrocenilo, con la formación de átomos Cl· e iones Cl^- dando la especie **X**. La posterior adición de Cl· al triple enlace en un proceso redox asociado concertado, en el que se produce la reducción de Fc^+ a Fc y la oxidación de Pt(II) a Pt(IV) y la simultánea coordinación de $\mathbf{X}^-$, originaría la formación del complejo pentacoordinado cloroferrocenilvinilo Pt(IV) **Y**. Una rápida isomerización de **Y**, favorecida por la fuerte influencia *trans* del átomo de carbono metalado, genera **Z**, que sufriría la etapa final de acoplamiento reductivo C-C. Los dos últimos pasos de este mecanismo tienen muchos precedentes en sistemas de Pt(II)/Pt(IV) que implican oxidantes halogenados.[51c, 51e, 59c, 73a-k] Por otro lado, la conocida resistencia de los enlaces Pt-C(C_6F_5) para sufrir procesos de inserción y acoplamiento podría explicar el acoplamiento selectivo C-C(bzq) observado. Además, la formación *regioselectiva* del ligando (Z)-bzqCH=CClFc se explica por la adición inicial de Cl·, más favorecida en el carbono interno del alquino, que conduce al intermedio vinílico menos impedido estéricamente, que tiene los dos grupos voluminosos (Fc y Cl) lejos del platino.

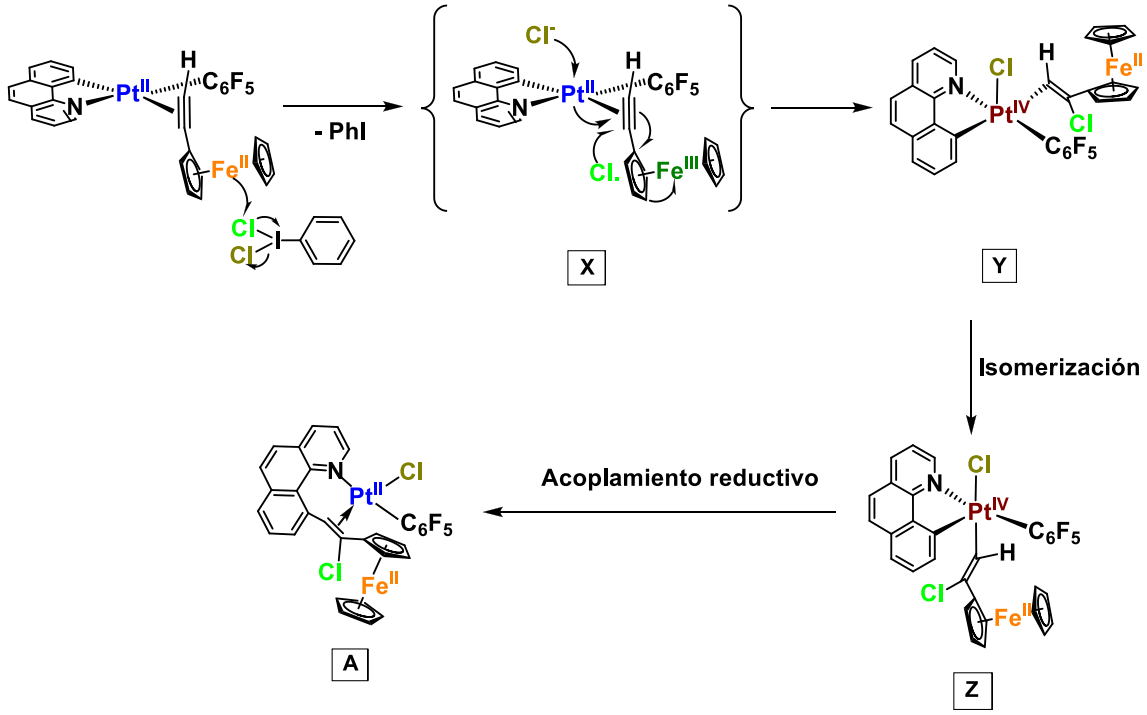

Esquema 1.3

Aunque no se puede descartar un ataque electrófilo directo al alquino para dar **Y**, se ha propuesto que es la oxidación del grupo Fc lo que promueve este ataque. Además, se ha comprobado que en la reacción de HC≡CFc con $PhICl_2$ no se produce el ataque electrófilo, sino que tiene lugar la oxidación del grupo ferrocenilo, lo que apoya el primer paso del mecanismo propuesto. También se realizó la reacción de oxidación del alquino complejo relacionado [Pt(bzq)(C_6F_5)(η^2-HC≡CPh)] con $PhICl_2$, en las mismas condiciones, comprobándose que evoluciona lentamente hacia la formación del derivado de Pt(IV) [Pt(bzq)(C_6F_5)Cl(μ-Cl)]$_2$ **C**. Este resultado es coherente con la labilidad del ligando alquino coordinado y con el papel del grupo ferrocenilo en la formación de **A** y **B**. Es interesante comentar que la coordinación de un alquino terminal a un complejo de Pt(II) convierte el ligando en una especie más electrofílica y, por lo tanto, puede dar lugar a ataques nucleofílicos mediados por el metal para generar nuevas y, a veces, interesantes moléculas.[75] Por lo tanto, la reacción observada del cloro con el η^2-alquino coordinado, mediada probablemente por la presencia del grupo ferrocenilo rico en electrones, resultaría sorprendente y abriría una nueva vía de reacción mediada por centros metálicos.

Varios grupos de investigación han estudiado distintos métodos de síntesis de moléculas benzoquinoleína sustituidas en la posición 10,[73b, 76] mediante la activación de enlaces C-H catalizada por un metal, como una alternativa efectiva a los procedimientos

más tradicionales de ortolitiación electrofílica (Esquema 1.4). Sin embargo, hasta donde nosotros sabemos, esta es la primera ocasión en la que se incorpora un fragmento vinil-haluro, CH=CXR a una benzoquinoleína.

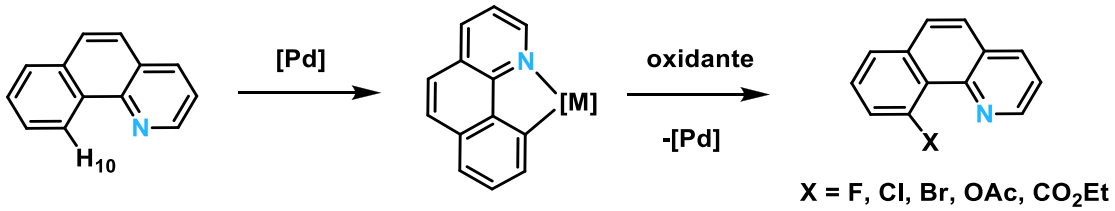

Esquema 1.4

Si nos centramos en la química del platino, Consuelo Fortuño y *col.* publicaron la interesante formación del ligando $bzqPPh_2$ mediante el acoplamiento C(bzq)-P provocado por la reducción de un complejo bimetálico de valencia mixta Pt(II)-Pt(IV) $(NBu_4)[Pt^{II}(C_6F_5)_2(PPh_2)_2Pt^{IV}(bzq)I_2]$[51d] (Figura 1.2).

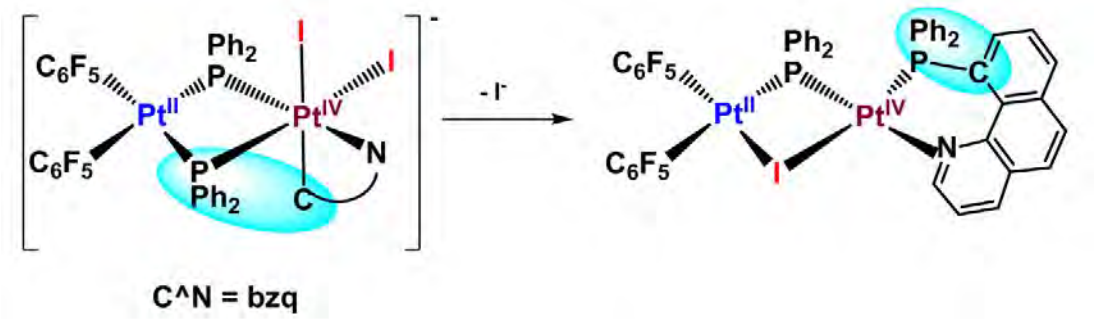

Figura 1.2

Se ha observado que, aunque la inserción de alquinos en complejos ciclometalados es una herramienta útil para la construcción de heterociclos que contienen nitrógeno,[77] la inserción de alquinos en el ligando benzoquinoleína no es muy común.[78] Jones *y col.* han publicado la síntesis de una sal de isoquinoleína, que transcurre a través de una reacción inicial de inserción de dimetilacetilendicarboxilato en [Cp*M(bzq)Cl] (M = Rh, Ir), proporcionando los correspondientes vinil complejos como intermedios de la reacción (Esquema 1.5).[78a] Por otra parte, Cabeza *y col.* han publicado una reacción de inserción similar entre un cluster trirutenio con ligandos carbonilo, que contiene un ligando 2-amino-7,8-benzoquinolato y los alquinos $HC{\equiv}CCH_2X$ (X= OH, $SiMe_3$), dando lugar en este caso a una funcionalización de tipo alílico η^3-C_3 en el C^{10} del ligando.[78b]

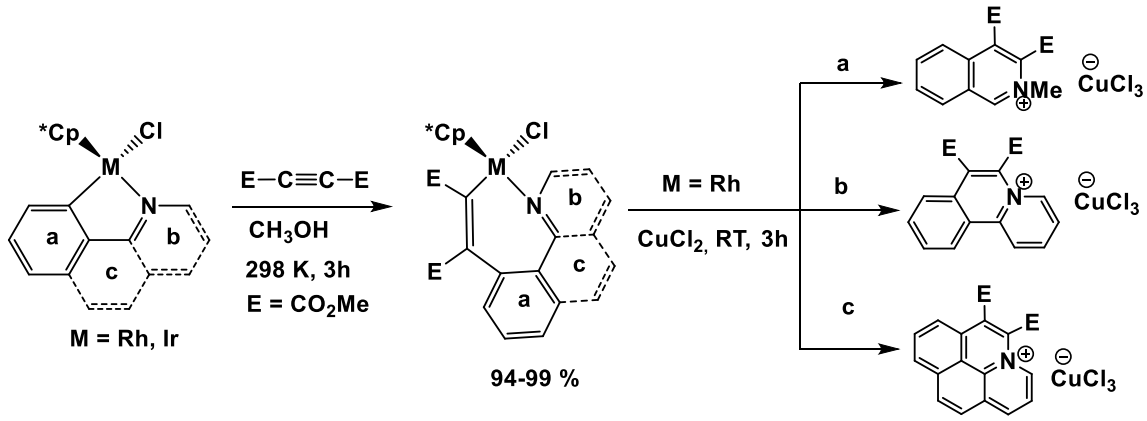

Esquema 1.5

Finalmente, destacar que aunque se han publicado inserciones migratorias de moléculas insaturadas como CO, CNR, alquenos y alquinos en enlaces Pt-H y Pt-R,[75a, 79] hasta la fecha no se conoce una inserción similar en un enlace cicloplatinado Pt-C(bzq).

Teniendo en cuenta los sorprendentes resultados que se obtuvieron en nuestro grupo al realizar las reacciones de oxidación con agentes halogenados del compuesto de Pt(II) [Pt(bzq)(C_6F_5)(η^2-HC≡CFc)] (Ecuación 1.1), en este capítulo nos propusimos los siguientes objetivos:

En primer lugar, se planteó la obtención de los ligandos libres (*Z*)-10-[1-X,1-ferrocenil(vinil)]benzoquinoleína (X = Cl **1**, I **2**) a partir de las especies de Pt(II) [Pt{bzq-*κN*-η^2-CH=C(X)Fc}(C_6F_5)X] (X= Cl **A**, I **B**).

En segundo lugar, dado nuestro interés en el estudio de sistemas de Pt(IV) conteniendo el fragmento cromóforo "Pt(bzq)(C_6F_5)" se decidió explorar un camino alternativo para obtener los derivados dinucleares de Pt(IV), **C** y **D** a partir de la oxidación del solvato [Pt(bzq)(C_6F_5)(acetona)] con agentes halogenados, y extender el procedimiento al análogo dinuclear de bromo [Pt(bzq)(C_6F_5)Br(μ-Br)]$_2$ (**E**). Estos dímeros insolubles reaccionan con el disolvente dador dimetilsulfóxido (dmso) para formar especies monómeras solubles de Pt(IV)-dmso, [Pt(bzq)(C_6F_5)X_2(dmso)] (X = Cl **3**, I **4**, Br **5**) como una mezcla de isómeros *cis* y *trans*.

Finalmente, con fines comparativos, se examinaron las reacciones de oxidación directa del derivado de Pt(II) [Pt(bzq)(C_6F_5)(tht)] para obtener derivados mononucleares de Pt(IV)-tht, [Pt(bzq)(C_6F_5)X_2(tht)] (X = Cl **6**, I **7**, Br **8**).

1.1 Síntesis y caracterización de los ligandos benzoquinoleína funcionalizados libres (Z)-10-[1-X,1-ferrocenil(vinil)]benzoquinoleína (X = Cl, I) (1 y 2)

Las benzoquinonas rígidas funcionalizadas son moléculas con interesantes aplicaciones fotofísicas,[80] usadas en catálisis[81] y con propiedades biológicas.[82] Considerando los resultados obtenidos por nuestro grupo de investigación en las reacciones de oxidación de [Pt(bzq)(C_6F_5)(η^2-HC≡CFc)] con oxidantes halogenados (Ec. 1.1), nuestro primer objetivo fue la obtención de los ligandos libres (*Z*)-10-[1-X,1-ferrocenil(vinil)]benzoquinoleína (X = Cl, I) a partir de los derivados de Pt(II) **A** y **B**.

Con esa finalidad, se exploró la reacción de los compuestos [Pt{bzq-κN-η^2-CH=CFcX(C_6F_5)X] (X = Cl **A**; I **B**) con exceso de PPh_3 en CH_2Cl_2 durante 1 hora. Ambas reacciones transcurren con desplazamiento de los ligandos correspondientes **1** y **2** (Ecuación 1.2) y formación de *trans*-[Pt(C_6F_5)X(PPh_3)$_2$], como se confirma por RMN de $^{31}P\{^1H$ y ^{19}F. Por eliminación del disolvente y adición de Et_2O, el correspondiente compuesto *trans*-[Pt(C_6F_5)X(PPh_3)$_2$] se separa por filtración, mientras que los ligandos **1** y **2** pueden obtenerse puros como sólidos naranjas mediante purificación del filtrado por una columna de cromatografía (SiO_2, *n*-hexano/CH_2Cl_2 8/2).

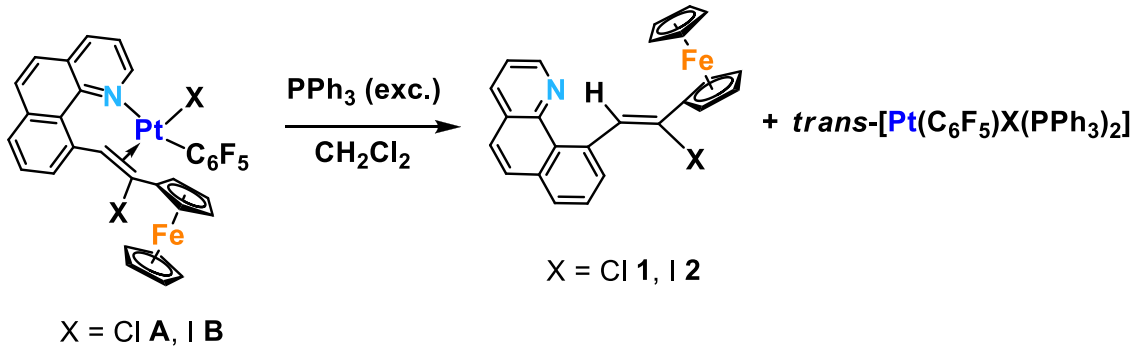

Ecuación 1.2

Los compuestos **1** y **2** son estables al aire y fueron caracterizados mediante los métodos analíticos (análisis elemental C, H, N) y espectroscópicos [IR, espectrometría MALDI-TOF, RMN monodimensional (^1H, $^{13}C\{H\}$ y ^{19}F) y bidimensional] habituales. Además, para el compuesto **1**, se ha confirmado su estructura cristalina mediante difracción de Rayos X.

Los espectros de masas MALDI-TOF (+) de ambos derivados exhiben el pico molecular $[M]^+$ y, en el compuesto **2**, se ha encontrado también el pico molecular correspondiente al fragmento $[M\text{-}I]^+$.

En los espectros de IR se observa una banda intensa a 1374 cm^{-1}, que se asigna, por comparación con los derivados **A** y **B**, a la vibración de tensión ν(C=C) del fragmento oléfinico del ligando {bzq-*κN*-η^2-CH=C(X)Fc}(C_6F_5)X. En el espectro de RMN de ^1H, la señal más significativa corresponde al protón olefínico [δ 8.31 (**1**), 8.19 (**2**)] (ver Figura 1.3b). Esta señal se ve desplazada a frecuencias más altas (~ 2 ppm) en comparación con la señal correspondiente al protón olefínico de sus respectivos precursores [Pt{bzq-*κN*-η^2-CH=C(Cl)Fc}(C_6F_5)Cl] **A** (δ 6.44) y [Pt{bzq-*κN*-η^2-CH=C(I)Fc}(C_6F_5)I] **B** (δ 6.46) (ver Figura 1.3a), en coherencia con la descoordinación al centro de platino. Estos valores están de acuerdo con los escasos datos encontrados para 10-(vinil)benzoquinoleínas en la bibliografía (δ ~ 8.6).[83] En el caso de los ligandos libres **1** y **2**, se observan 2 señales diferentes correspondientes a las resonancias CH (C_5H_4) del grupo ferrocenilo, en lugar de las cuatro señales observadas en los derivados de Pt (**A** y **B**), lo que indica una menor congestión estérica en los ligandos libres, en los que el grupo ferrocenilo tiene libertad de giro alrededor del enlace C-C.

El espectro de RMN de $^{13}C\{^1H\}$ también confirma la estructura de estos compuestos (Figura 1.4). El carbono vinílico *CH* aparece muy cerca en ambos ligandos [δ 127.1 (**1**), 126.0 (**2**)], mientras que el carbono halogenado =*C*(X)Fc resuena, como es de esperar, a más altas frecuencias [δ 134.8 (**1**), 137.3 (**2**)].

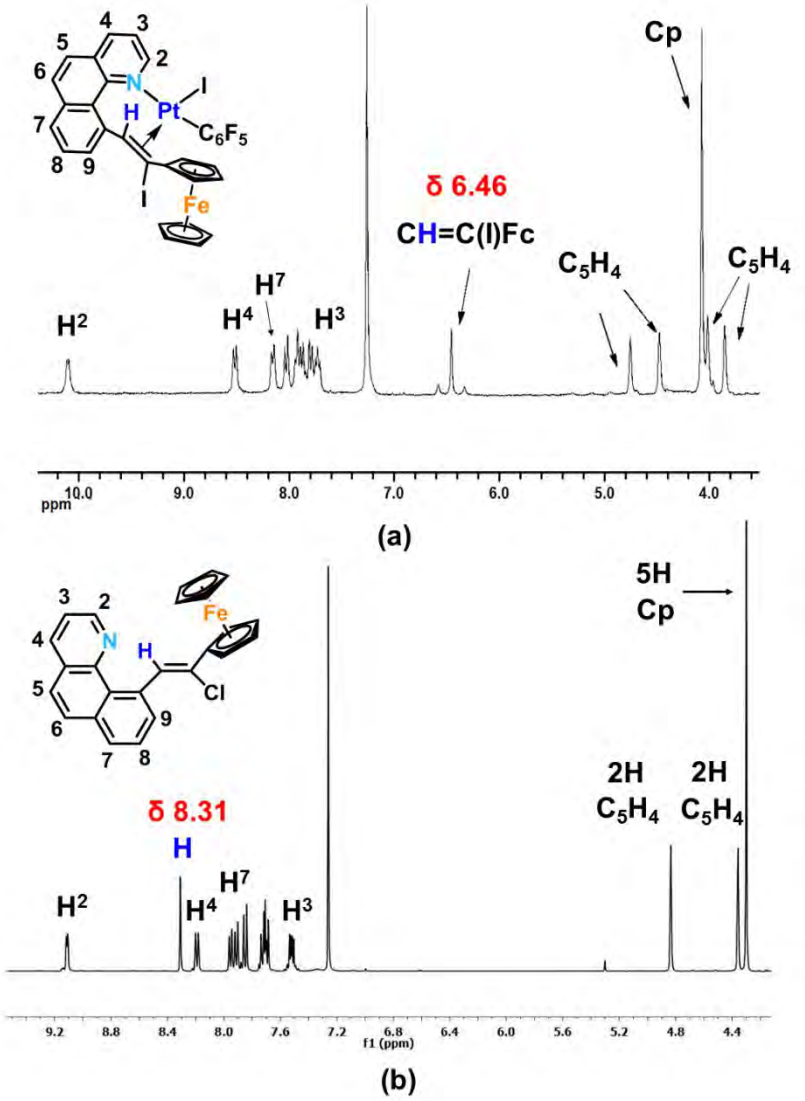

Figura 1.3. Espectro de RMN de ^{1}H en $CDCl_3$ de (a) [Pt{bzq-κ*N*-η^2-CH=C(I)Fc}(C_6F_5)I] **B** y (b) [(*Z*)-bzq-CH=C(Cl)Fc] **1**.

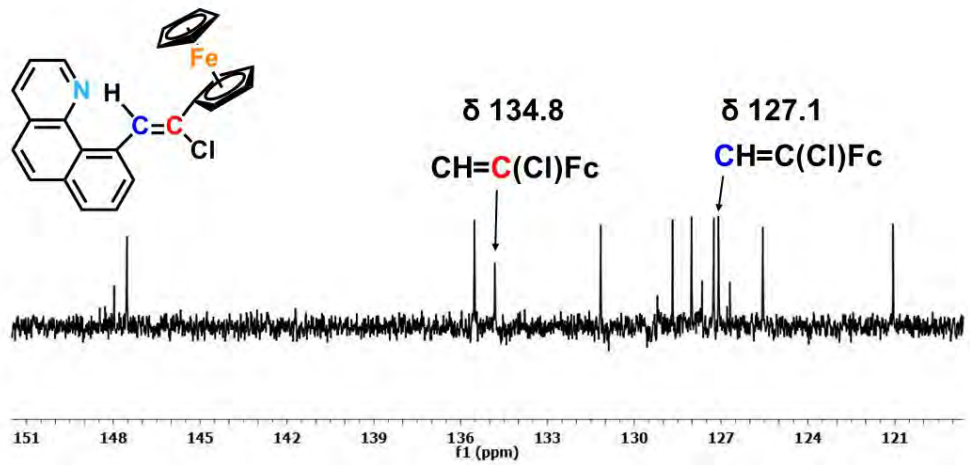

Figura 1.4. Espectro de RMN de $^{13}C\{^{1}H\}$ en $CDCl_3$ de [(*Z*)-bzq-CH=C(Cl)Fc] **1**.

Se ha llevado a cabo un estudio estructural por difracción de Rayos X del derivado **1** (Figura 1.5a), confirmándose la formación del nuevo ligando funcionalizado (*Z*)-10-[1-Cl,1-ferrocenilvinilo]benzoquinoleína. Con fines comparativos, se muestra la estructura de Rayos X del precursor cloroferrocenil(vinil)benzoquinolinil Pt(II) (**A**)[72, 84] (Figura 1.5b), en el que el ligando actúa de quelato $\kappa N{:}\eta^2$ hacia el fragmento "Pt(C_6F_5)Cl". Aunque los datos del cristal del compuesto **1** no son lo suficientemente buenos como para poder hacer una discusión detallada, sí nos han permitido confirmar claramente la conectividad de los átomos en la olefina neutra (*Z*)-cloroferrocenil(vinil)benzoquinoleína y la retención de la geometría con la disposición *geminal* del Fc y el Cloro.

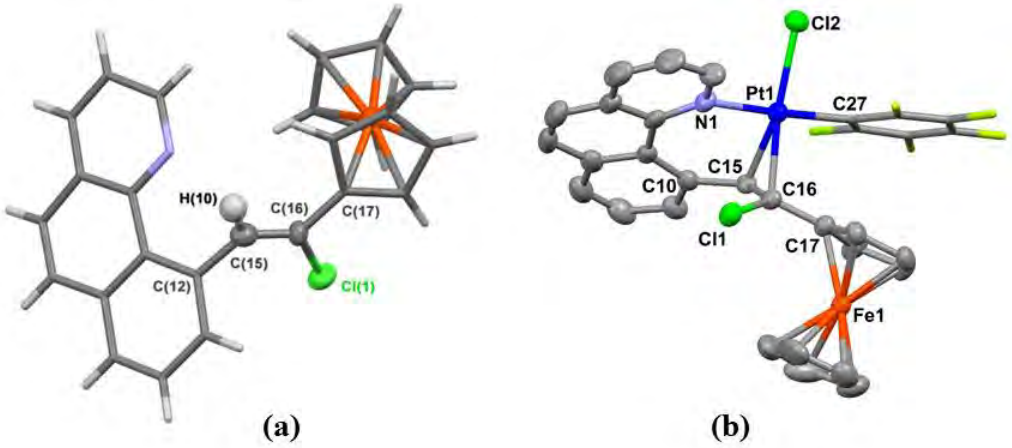

Figura 1.5. Estructura de Rayos X de los compuestos (a) [bzq-CH=C(Cl)Fc] **1** y (b) [Pt{bzq-κ*N*-η^2-CH=C(Cl)Fc}(C_6F_5)Cl] **A**.

Es un hecho establecido que los haluros de vinilo son útiles como sustratos en una gran variedad de reacciones de acoplamiento cruzado. Por lo tanto, la presencia de cloro o yodo en estos ligandos abre la posibilidad de una funcionalización adicional, permitiendo la síntesis de nuevos ligandos que contengan los grupos bzq y Fc. Además, es de esperar que este tipo de moléculas muestren propiedades como interruptores fluorescentes debido a la estabilidad del par redox Fc/Fc^+.[85]

1.2 Síntesis y caracterización de los compuestos de Pt(IV) [Pt(bzq)(C_6F_5)X_2(dmso)] (X=Cl 3, I 4, Br 5)

Como se ha adelantado en la Introducción de este Capítulo, las oxidaciones del sustrato de Pt(II) [Pt(bzq)(C_6F_5)(η^2-HC≡CFc)] con $PhICl_2$ o I_2 producen, además de los compuestos [Pt{bzq-κN-η^2-CH=C(X)Fc}(C_6F_5)X] (X= Cl **A**, I **B**), los derivados dinucleares de Pt(IV) [Pt(bzq)(C_6F_5)X(μ-X)]$_2$ (X = Cl **C**, I **D**). Debemos indicar que, para este trabajo, se intentaron las reacciones de oxidación análogas del sustrato [Pt(bzq)(C_6F_5)(η^2-HC≡CFc)] con Br_2 o Cl_2 (disuelto en CCl_4 o CH_2Cl_2), obteniéndose mezclas complicadas en todos los casos, tanto a temperatura ambiente como a baja temperatura.

Los derivados **C** y **D** son compuestos muy insolubles pero se identificaron, sin ninguna duda, como derivados dinucleares de Pt(IV) por espectrometría de masas, análisis elemental y espectrometría IR. Su formación se debe probablemente a la pérdida del alquino en disolución seguido de un ataque rápido del oxidante al centro de Pt. De hecho, se obtienen de forma directa en alto rendimiento no sólo los compuestos [Pt(bzq)(C_6F_5)X(μ-X)]$_2$ (X = Cl **C**; I **D**), sino también el análogo de bromo [Pt(bzq)(C_6F_5)Br(μ-Br)]$_2$ **E**, por reacción del solvato [Pt(bzq)(C_6F_5)(acetona)] con 1 equivalente del correspondiente oxidante ($PhICl_2$, I_2 o Br_2) en CH_2Cl_2 a 0 ºC (Esquema 1.6).

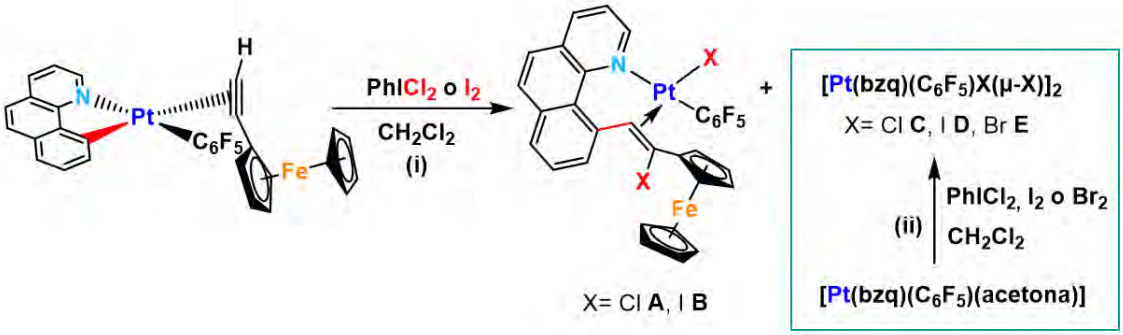

Esquema 1.6

En este contexto, hay que señalar que Yagyu *y col*[86] han publicado dos complejos de yodo similares [Pt(ppy)ArI(μ-I)$_2$]$_2$ [ppy = fenilpiridina, Ar = $C_6H_3Me_2$, $C_6H_3(CF_3)_2$], formados por la adición oxidante de I_2 a los precursores de dmso o acetonitrilo [Pt(ppy)Ar(S)] (S = dmso, NCMe). En este trabajo, se confirmó por difracción de Rayos X la retención de la disposición *meridional* de los grupos ppy y Ar en ambos centros de

Pt (Figura 1.6a). De las dos posibles orientaciones de ambos fragmentos *syn* (I, II) y *anti* (III, IV) (Figura 1.6b), el compuesto [Pt{$C_6H_3(CF_3)_2$-3,5}(Phpy)I_2(μ-I)$_2$] adopta una disposición *anti* de los grupos $C_6H_3(CF_3)_2$, probablemente para minimizar las repulsiones estéricas. Los compuestos **C**, **D** y **E** podrían tener una disposición similar, aunque no se descarta cualquier otro isómero con una disposición *syn* de los grupos C_6F_5 (I y II).

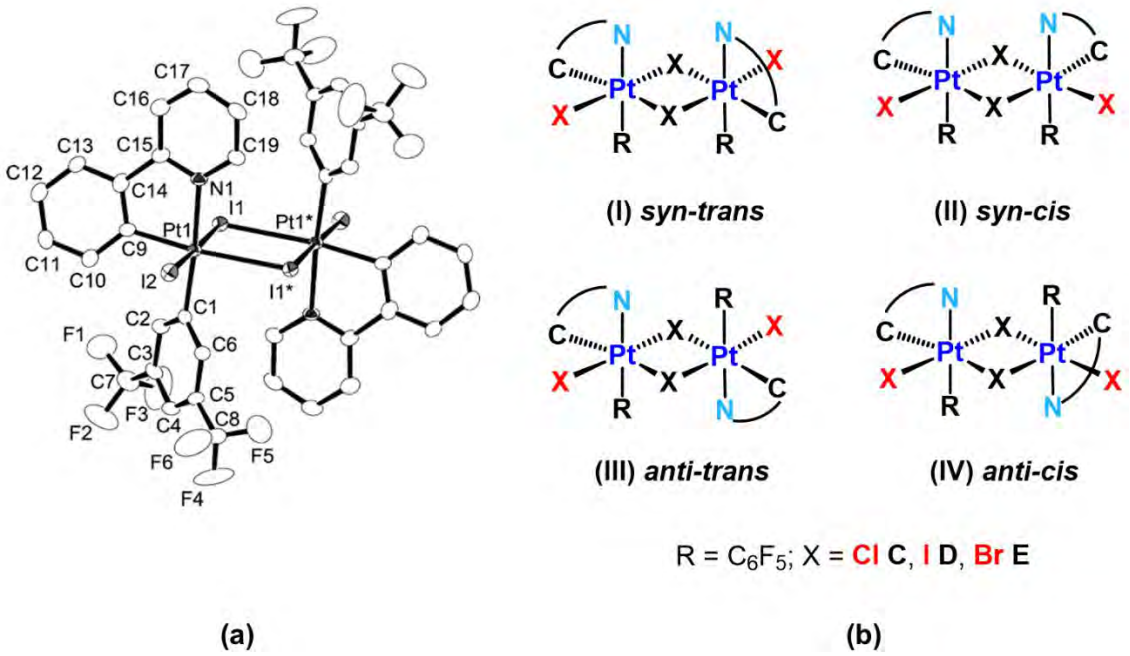

Figura 1.6. (a) Estructura molecular de [Pt{$C_6H_3(CF_3)_2$-3,5}(Phpy)I_2(μ-I)$_2$].[86] (b) Posibles isómeros.

Dado que los compuestos dinucleares de Pt(IV) **C**, **D** y **E** son muy insolubles en los disolventes orgánicos usuales, decidimos utilizar un disolvente fuertemente dador como el dimetilsulfóxido (dmso) para su caracterización. En estas condiciones, observamos que las moléculas de dimetilsulfóxido reaccionan con los compuestos dinucleares [Pt(bzq)(C_6F_5)X(μ-X)]$_2$ (X = Cl **C**, I **D**, Br **E**) dando lugar a los monómeros [Pt(bzq)(C_6F_5)X_2(dmso)] (X = Cl **3**, I **4**, Br **5**), que son más solubles (ver Ecuación 1.3). La reacción es muy lenta a temperatura ambiente, pero se completa en pocos minutos si se calienta a ~50 ºC. El tratamiento de la disolución final con agua causa la precipitación de un sólido amarillo pálido (**3** y **5**) o naranja (**4**), identificados en cada caso como una mezcla de isómeros.

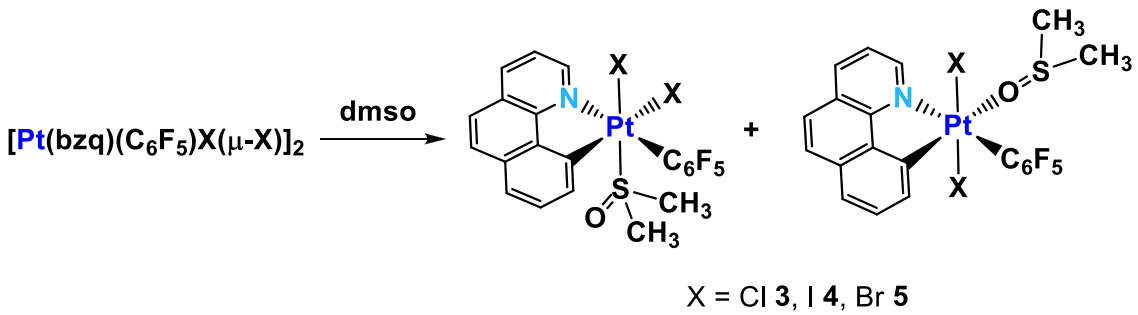

Ecuación 1.3

Aunque sería posible la formación de diferentes isómeros, sólo se observan dos de ellos por RMN de ^{1}H y ^{19}F. El estudio por RMN, difracción de Rayos X y cálculos teóricos DFT apuntan a que los isómeros que se forman son las especies recuadradas ***cis*-(dmso-κ*S*)** y ***trans*-(dmso-κ*O*)** en una relación ~ 1:1 para los derivados de Cl (**3**) y I (**4**) y ~ 2:1 para el derivado de Br (**5**) (Ver Figuras 1.7 y 1.8).

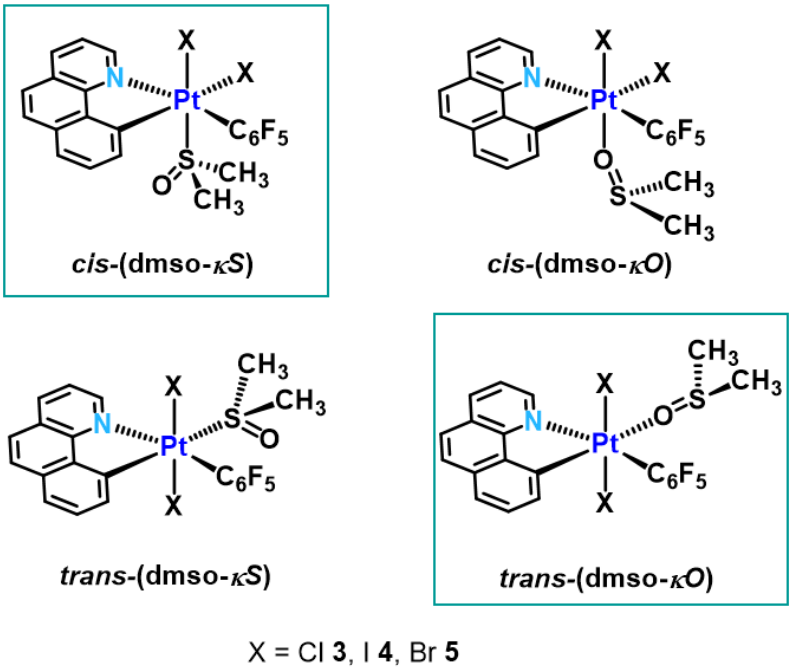

Figura 1.7. Posibles isómeros que se pueden formar como productos de la reacción de la Ecuación 1.3.

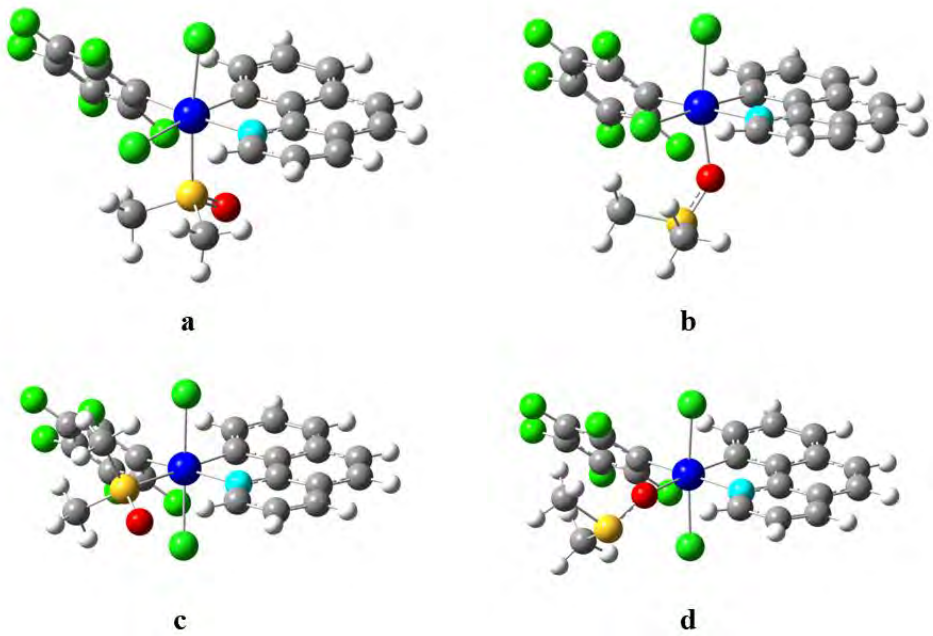

Figura 1.8. Geometrías optimizadas por cálculos DFT de los posibles isómeros **a**, **b**, **c** y **d** del compuesto **3**.

Tabla 1.1 Distancias [Å] y ángulos [deg] seleccionados para los isómeros **a**, **b**, **c** y **d** del compuesto **3** optimizados por cálculos teóricos.

	a	**b**	**c**	**d**
Pt-C(bzq)	2.03265	2.02597	2.02366	2.00160
Pt-N(bzq)	2.14321	2.14101	2.15650	2.12648
Pt-Cl	2.35231	2.32011	2.36728	2.37915
	2.48529	2.49412	2.36350	2.35384
Pt-S(dmso)	2.39449		2.59141	
Pt-O(dmso)		2.13117		2.26992
Cl-Pt-Cl	96.91430	93.7967	173.01821	174.58736
Cl-Pt-S	174.17171		83.64227	
	84.95123		91.74906	
Cl-Pt-O		169.56967		88.37749
		94.22729		90.84857

La optimización de las estructuras de los posibles isómeros del derivado [Pt(bzq)(C_6F_5)Cl_2(dmso)] **3** mediante cálculos teóricos DFT (Figura 1.8 y Tabla 1.1), revelan que las diferencias en las energías del estado fundamental entre los isómeros *cis* y *trans* son muy pequeñas. De los dos isómeros *cis*, el isómero ***cis*-(dmso-*κS*)** es 7.2 kJ/mol más estable que el isómero ***cis*-(dmso-*κO*)**, mientras que, de los dos isómeros *trans*, el isómero ***trans*-(dmso-*κO*)** es más estable que el isómero ***trans*-(dmso-*κS*)** por 4.0 kJ/mol. Estos resultados están de acuerdo con los de otros compuestos ciclometalados

de Pt(IV) con ligandos dmso previamente publicados, que sugieren que el isómero más favorable es el que tiene el oxígeno *trans* al carbono ciclometalado, ya que es el mejor σ dador y π aceptor. Además, estudios teóricos similares muestran que la coordinación *κS* del ligando dmso está favorecida cuando el ligando dmso está en disposición *trans* respecto a un halógeno en compuestos de Pt(IV) (en coherencia con el carácter más blando del S con respecto al O).[87]

Después de muchos intentos, se obtuvieron un pequeño número de cristales del compuesto *trans*-[Pt(bzq)(C_6F_5)Br_2(dmso-*κO*)] **5** mediante lenta difusión de *n*-hexano sobre una disolución del compuesto en acetona. El análisis por difracción de Rayos X de uno de los cristales mostró que éstos correspondían al isómero *trans* con el ligando dmso enlazado a través del oxígeno y en disposición *trans* al carbono ciclometalado del ligando bzq (Figura 1.9). Por lo tanto, se confirma también por difracción de Rayos X que el isómero *trans* contiene el ligando dmso coordinado a través del oxígeno. Las distancias y ángulos de enlaces más relevantes se recogen en la Tabla 1.2.

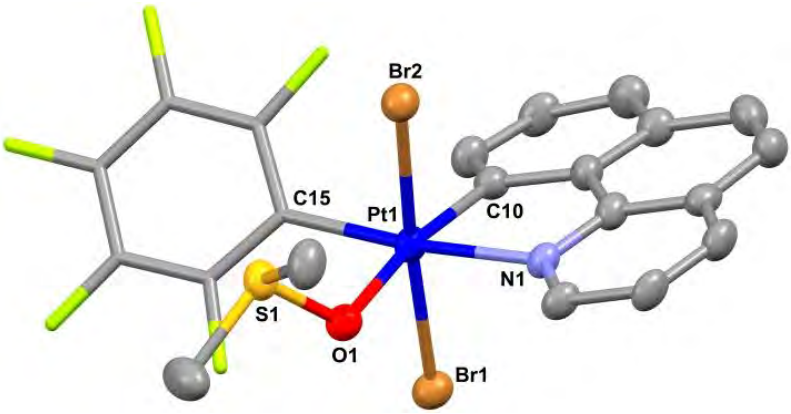

Figura 1.9. Estructura cristalina del derivado *trans*-[Pt(bzq)(C_6F_5)Br_2(dmso-*κO*)] ***trans*-5 (dmso-*κO*)**.

Tabla 1.2. Distancias [Å] y ángulos [º] para el derivado ***trans*-5(dmso-*κO*)**

Distancias [Å]	
Pt(1)-C(10)	2.011(6)
Pt(1)-O(1)	2.197(4)
Pt(1)-Br(1)	2.4504(8)
S(1)-O(1)	1.544(4)
Pt(1)-N(1)	2.111(5)
Pt(1)-C(15)	2.050(6)
Pt(1)-Br(2)	2.4654(7)

Ángulos [º]	
C(10)-Pt(1)-N(1)	81.5(2)
O(1)-Pt(1)-C(15)	92.4(2)
Br(1)-Pt(1)-C(10)	86.0(2)
Br(1)-Pt(1)-O(1)	91.1(1)
Br(2)-Pt(1)-C(10)	94.8(2)
Br(2)-Pt(1)-O(1)	87.4(1)
S(1)-O(1)-Pt(1)	121.1(2)
N(1)-Pt(1)-O(1)	89.6(2)
C(10)-Pt(1)-C(15)	96.8(3)
Br(1)-Pt(1)-N(1)	91.8(1)
Br(1)-Pt(1)-C(15)	93.6(2)
Br(2)-Pt(1)-N(1)	83.3(1)
Br(2)-Pt(1)-C(15)	91.4(2)

Es interesante destacar que, aunque se han propuesto algunas especies de Pt(IV) con ligandos dmso-*κO* como intermedios en reacciones de bromación en disoluciones de dmso,[88] no hay muchos ejemplos de compuestos de platino caracterizados cristalográficamente que contengan una molécula de dmso coordinada a través del oxígeno.[87, 89]

En la estructura del compuesto ***trans*-5(dmso-*κO*)**, el centro de Pt muestra una geometría octaédrica ligeramente distorsionada con los dos átomos de Br en disposición *trans* [Pt(1)-Br(1) 2.4504(8), Pt(1)-Br(2) 2.4654(7) Å]. Las distancias más significativas Pt(1)-O(1) [2.197(4) Å] y S(1)-O(1) [1.544 (4) Å] son similares a las encontradas en otros ejemplos publicados,[87] mientras que el ángulo S(1)-O(1)-Pt(1) [121.1(2)º] es ligeramente mayor. La distancia Pt-C (ortometalado) [Pt(1)-C(10) 2.011(6) Å] es parecida a las que comentaremos para los compuestos ***cis*-7** y ***cis*-8**. No obstante, la distancia Pt-C(C_6F_5) [2.050(6) Å] es ligeramente más corta que en otros complejos de Pt(IV) que contienen ligandos pentafluorofenilo *trans*-[Pt(C_6F_5)$_4$Br(NCPh)]$^-$ [2.106(8)-2.129(9) Å],[71c] hecho que se atribuye a la baja influencia *trans* del átomo dador N.

En las especies **3**, **4** y **5**, la presencia de la mezcla de los dos isómeros ***cis*-(dmso-*κ*S)** y ***trans*-(dmso-*κ*O)** se observa también por espectroscopía de RMN de ^{1}H y ^{19}F en disolución, en una relación molar ~ 1:1 (en **3** y **4**) y ~ 2:1 (en **5**). Es interesante señalar que la relación entre los dos isómeros no cambia con el tiempo una vez que se aíslan. Sin embargo, el aumento del tiempo de reacción en dmso conduce siempre a una mayor proporción del isómero ***trans*-(dmso-*κO*)**. A baja temperatura (223 K), los espectros de

RMN de ^{19}F muestran dos conjuntos de 5 señales diferentes debido a los grupos C_6F_5 de cada uno de los isómeros, lo que indica que la rotación a través del enlace Pt-C_6F_5 está impedida en ambos isómeros (Figura 1.10). Al aumentar la temperatura, se observa que para los compuestos **3** y **5** los dos grupos de *o*-F y *m*-F coalescen y aparecen como una sola señal ($T^a_{coalescencia}$ *o*-F 293 **3**, 313 K **5**) (Figura 1.10a para el derivado de cloro **3**), mientras que en el derivado con el halógeno más voluminoso yodo (**4**), se observan cuatro señales de *o*-F incluso a temperatura ambiente (Figura 1.10b).

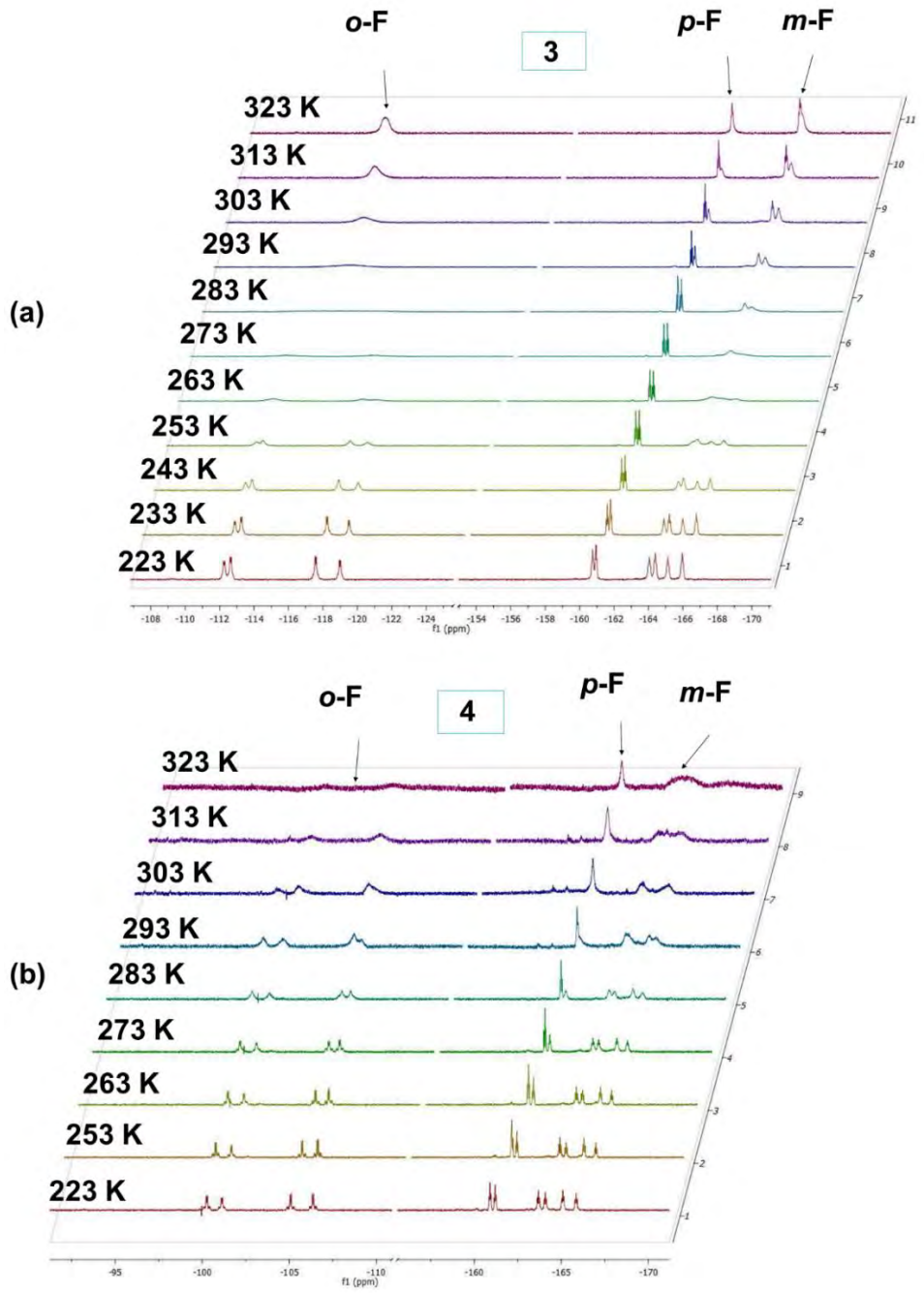

Figura 1.10. Espectros de RMN a temperatura variable de ^{19}F (376.5 MHz) en CD_3COCD_3 de (a) **3** y (b) **4**.

En el espectro de RMN de ^{1}H se pueden observar los dos conjuntos de señales en la zona aromática, asignados al ligando ciclometalado, con algunas de las señales solapadas, lo que indica la presencia de dos isómeros geométricos. En particular, se observa que el protón situado cerca del C ortometalado (H^9) aparece en la zona de campo alto [7.32 **3**; 7.23 ***cis*-4(dmso-*κS*)**, 7.29 ***trans*-4(dmso-*κO*)**; 7.29 ***cis-5(dmso-κS)***, 7.31 ***trans*-5(dmso-*κO*)**], lo que indica que este protón sufre un fuerte apantallamiento debido a su proximidad al grupo aromático C_6F_5, lo que está de acuerdo con una disposición meridional de la unidad "Pt(bzq-$\kappa N,\kappa C^{10}$)(C_6F_5)" (Figura 1.11 para **3**). Además, los valores de la constante de acoplamiento $^3J_{Pt\text{-}H}$ (35-39 Hz) son menores en relación a los precursores de Pt(II) [Pt(bzq)(C_6F_5)(η^2-HC≡CFc)] y [Pt(bzq)(C_6F_5)(acetona)] (~70 Hz), lo que está en coherencia con el cambio en el estado de oxidación de Pt(II) a Pt(IV).

A temperatura ambiente, las señales de resonancia correspondientes a los seis protones de los metilos del ligando dmso aparecen como singletes bien separados para cada isómero [con forma ancha en ***cis*-4(dmso-*κS*)**]. Además, estos singletes están notablemente más desapantallados en los isómeros ***cis*-(dmso-*κS*)** (3.05-3.07 ppm) que en los ***trans*-(dmso-*κO*)** (2.53-2.55 ppm). Esta característica se ha observado previamente en compuestos de Pt(IV) con el ligando dmso unido a través del O y S.[88] Al bajar la temperatura, la señal que se asigna al isómero ***cis-κS*** se ensancha y se resuelve en dos singletes separados (3.09, 3.03 **3**; 3.16, 2.99 **4**; 3.15, 3.01 **5**). Sin embargo, el singlete debido al isómetro ***trans*-(dmso-*κO*)** permanece inalterado (ver Figura 1.10).

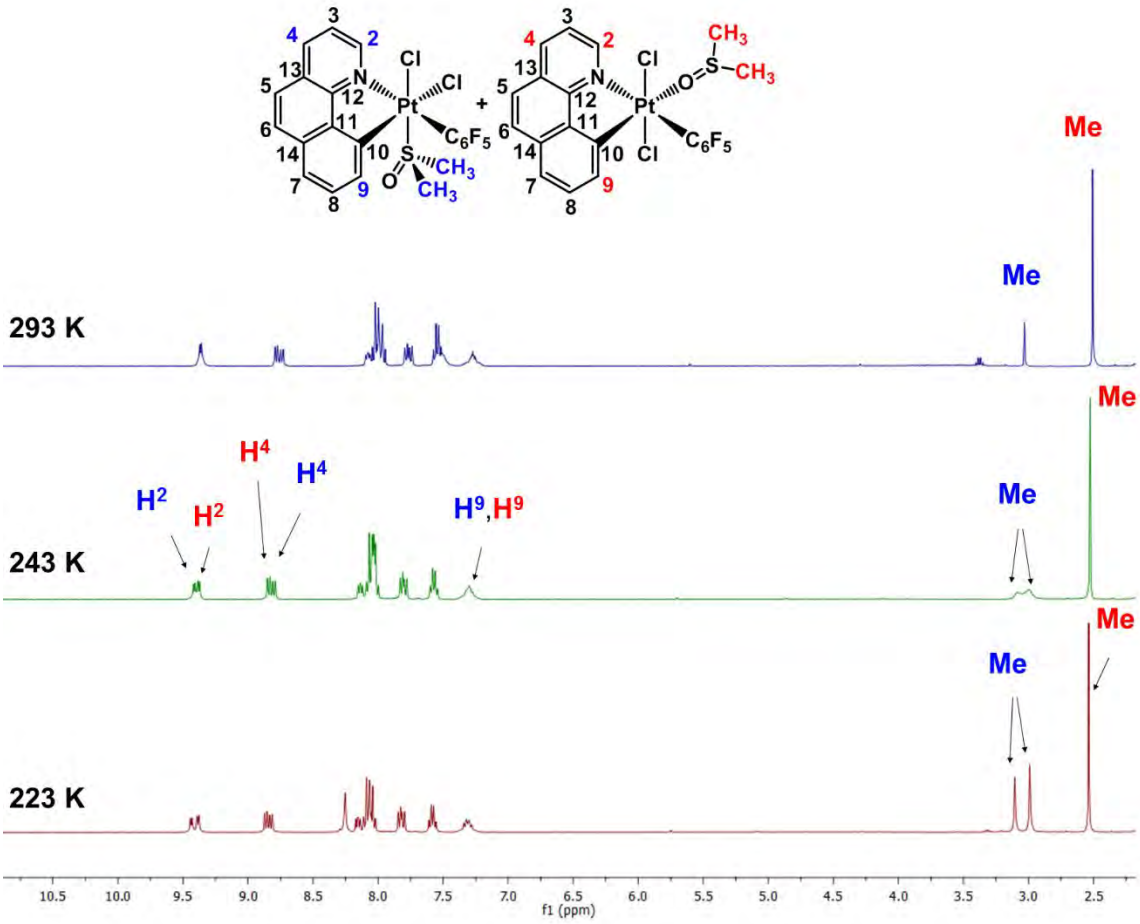

Figura 1.11. Espectros de RMN de ^{1}H en CD_3COCD_3 a temperatura variable de [Pt(bzq)(C_6F_5)Cl_2(dmso)] **3.**

Desafortunadamente, no se han observado satélites de platino en ninguna de las señales de metilos, lo que nos impide corroborar por RMN de ^{1}H la coordinación del dmso a través del S. Sin embargo, la confirmación de la coordinación *κS* del ligando dmso en los isómeros *cis* se obtiene del análisis por RMN de una secuencia de experimentos NOESY y NOE entre el protón H^2 del ligando bzq y las resonancias de los Me del dmso (Figuras 1.12 y 1.13). Así, la falta de acoplamiento NOE entre el metilo y los protones H^2 aromáticos para el isómero *trans* sugiere que el dmso se coordina a través del átomo de oxígeno, mientras que el acoplamiento NOE sugiere la coordinación *κS* del dmso para el isómero *cis*.

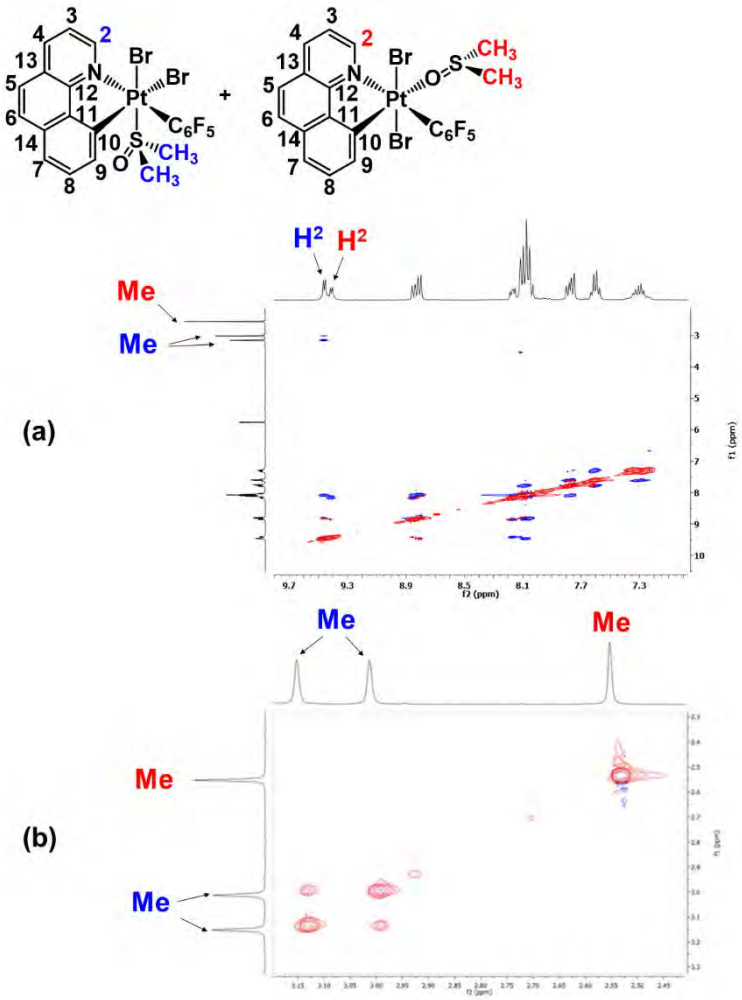

Figura 1.12. Experimento NOESY del compuesto [Pt(bzq)(C_6F_5)Br_2(dmso)] **5** a 223 K, (a) zona aromáticos y zona de metilos y (b) ampliación de zona de metilos.

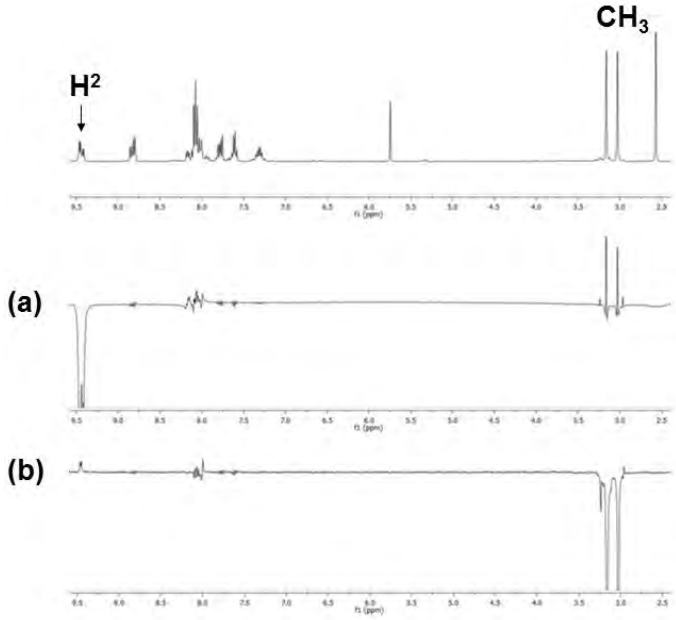

Figura 1.13. Experimentos NOE del compuesto [Pt(bzq)(C_6F_5)Br_2(dmso)] **5** a 223 K, irradiando a (a) 9.40 ppm y (b) 3.20 ppm.

1.3 Síntesis y caracterización de los compuestos de Pt(IV) [Pt(bzq)(C_6F_5)X_2(tht)] (X=Cl 6, I 7, Br 8)

Con fines comparativos, consideramos de interés examinar la oxidación del precursor [Pt(bzq)(C_6F_5)(tht)] con $PhICl_2$, I_2 o Br_2. Estas reacciones se han llevado a cabo en CH_2Cl_2 con 1 equivalente del correspondiente oxidante a temperatura ambiente como se recoge en el Esquema 1.7. Las reacciones tienen lugar con retención de la disposición *meridional* del fragmento "Pt(bzq-$\kappa N,\kappa C^{10}$)(C_6F_5)" y la formación de los derivados [Pt(bzq)(C_6F_5)X_2(tht)] (X = Cl **6**, I **7**, Br **8**), identificados como el isómero *cis* para el compuesto [Pt(bzq)(C_6F_5)Br_2(tht)] **8** y como una mezcla de isómeros *cis* y *trans* en los derivados con cloro y yodo [Pt(bzq)(C_6F_5)Cl_2(tht)] **6** y [Pt(bzq)(C_6F_5)I_2(tht)] **7** (*cis*:*trans* ≈ 7:1 **6**, 5:1 **7**) (Esquema 1.7). Para **7** y **8**, se puede separar el correspondiente isómero mayoritario *cis* puro por cristalización.

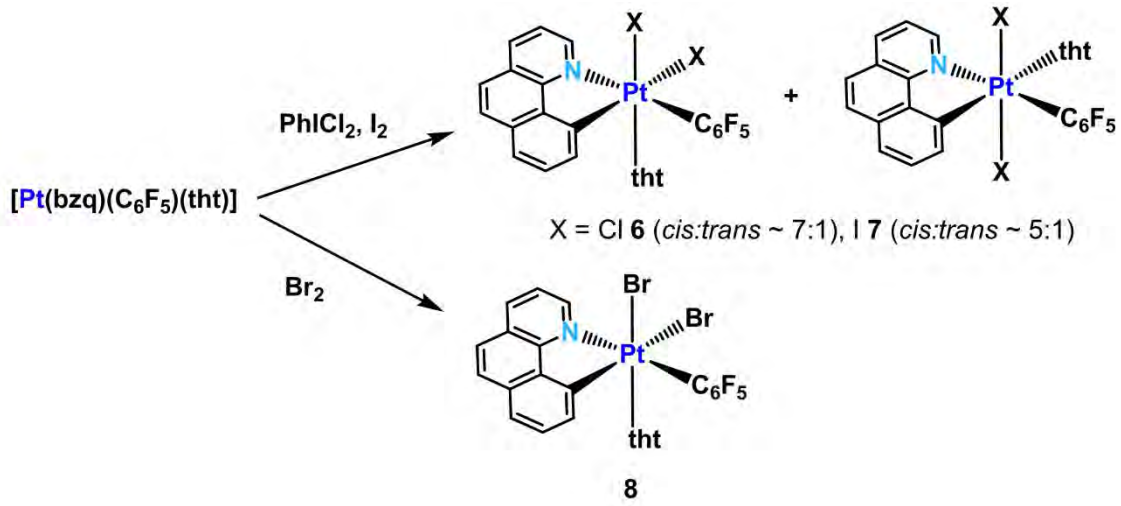

Esquema 1.7

Teniendo en cuenta trabajos anteriormente publicados donde se estudian reacciones análogas de oxidación de complejos de Pt(II) con oxidantes halogenados, se propone el mecanismo recogido en el Esquema 1.8.[71a, 71c] La primera etapa implica la formación de un aducto lineal entre el complejo de Pt(II) y la molécula de halógeno X_2. La formación de este aducto implica una interacción entre el centro básico de Pt dador d_z^2 y el halógeno, que actúa como electrófilo, y suele estar favorecida por la basicidad del centro metálico. La siguiente etapa implica transferencia de densidad electrónica del platino a orbitales antienlazantes del X_2, que produce la ruptura heterolítica del enlace X_2

y la liberación del anión X^-. Formalmente es una oxidación de dos electrones en el metal ($d^8 \rightarrow d^6$) con incorporación del fragmento X^+ y formación de la especie pentacoordinada **F**. Si en la siguiente etapa el X^- se coordina en la posición vacante, se genera el isómero *trans* (Esquema 1.8iii). Sin embargo, también puede ocurrir que el intermedio pentacoordinado **F** isomerice e incorpore el X^- generando el isómero *cis* (Esquema 1.8iv,v). Como se puede ver en el Esquema 1.8iv, en la formación de los compuestos de cloro **6** y yodo **7** es imprescindible que ocurra una reordenación o isomerización de la especie pentacoordinada para dar los isómeros finales *cis*. Cabe destacar que se han observado previamente isomerizaciones similares[51c, 51e, 59c, 71a, 73a-d, 73f, 73g] y que la preferencia por la formación del isómero *cis*, que localiza el azufre en disposición *cis* al átomo de carbono metalado C(bzq), está de acuerdo con el llamado efecto *transfobia*,[90] que consiste en una desestabilización de los isómeros que colocan en *trans* los ligandos de alta influencia *trans*.

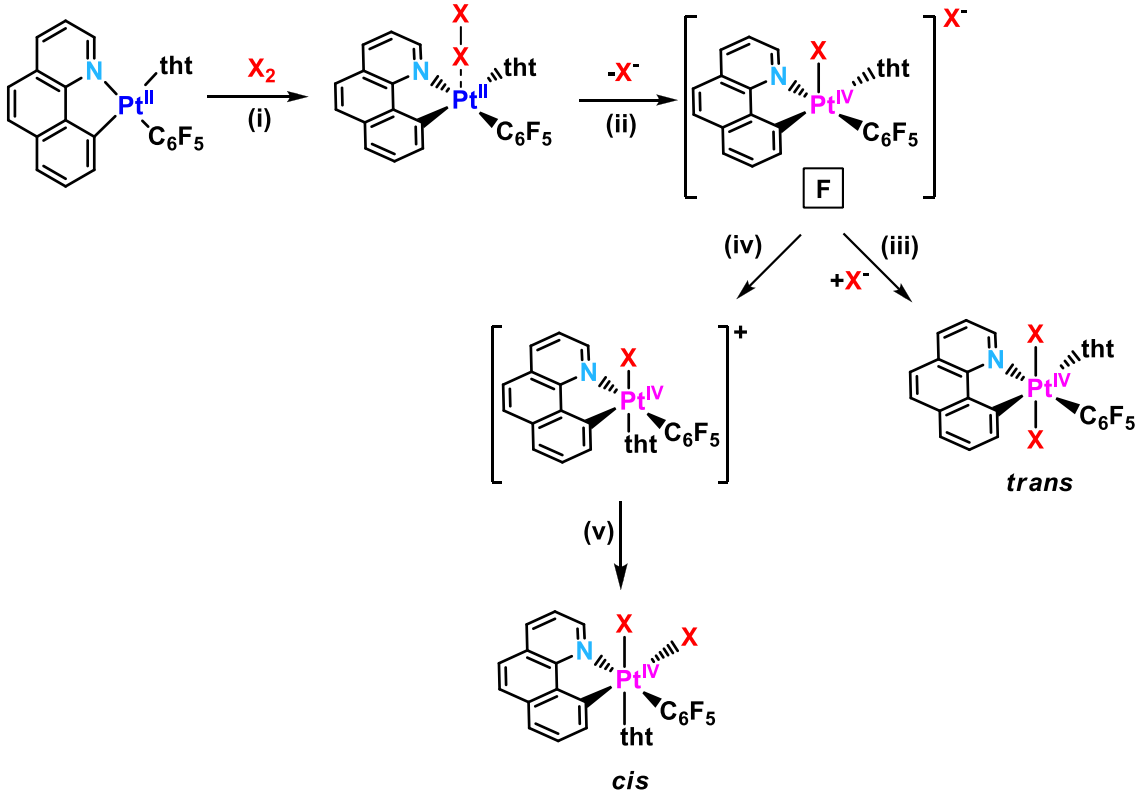

Esquema 1.8

Estos compuestos **6-8** se han caracterizado también mediante MALDI-TOF, análisis Elemental, IR y RMN multinuclear (^{1}H y ^{19}F).

Los espectros de RMN sugieren que los compuestos **6** y **7** se aíslan como una mezcla de los dos isómeros, *cis* y *trans* (*cis:trans* ~7:1 **6**. ~5:1 **7**), mientras que el compuesto de bromo [Pt(bzq)(C_6F_5)Br_2(tht)] **8** se obtiene como el isómero *cis* puro. El espectro de protón del isómero *cis* de los compuestos **6-8** muestra el protón característico H^9, con satélites de ^{195}Pt a campo relativamente alto (δ 7.30-7.45) (Figura 1.14). Este apantallamiento se debe a la proximidad de este protón al grupo C_6F_5 y es coherente con la posición *meridional* del fragmento "Pt(C^N)C_6F_5", que presenta los dos carbonos dadores en *cis*. Los valores menores de la constante de acoplamento $^{3}J_{Pt\text{-}H9}$ en estos compuestos ($^{3}J_{Pt\text{-}H9}$ = 35 **6**, **7**; 40 Hz **8**) en comparación a la observada en el precursor [Pt(bzq)(C_6F_5)(tht)] ($^{3}J_{Pt\text{-}H9}$ = 62 Hz), es coherente con la oxidación de Pt(II) a Pt(IV) con un menor carácter *s* en los enlaces Pt-C.

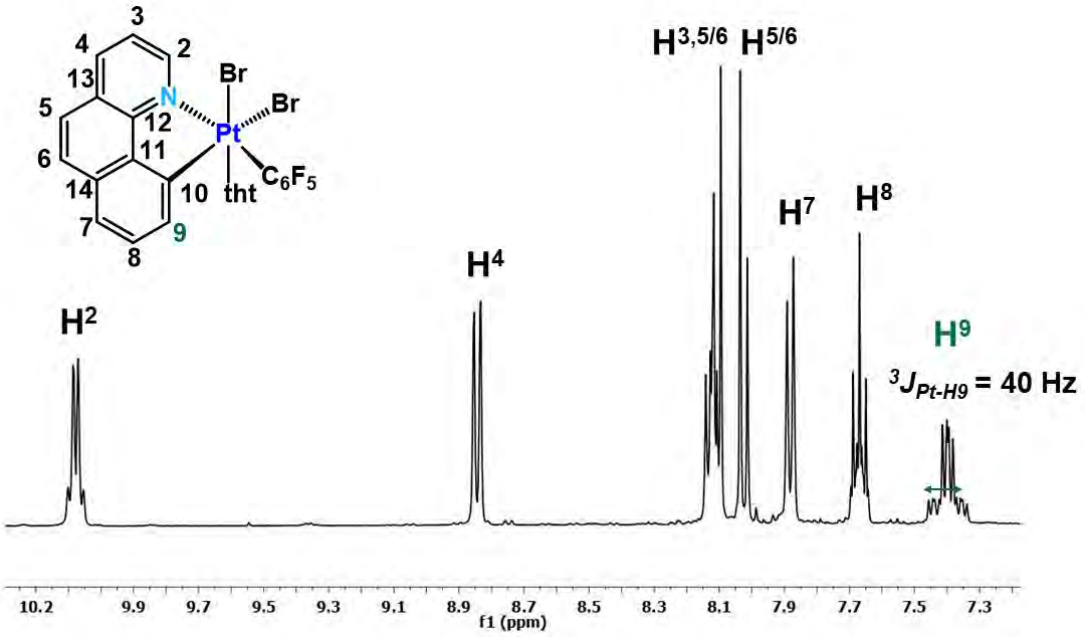

Figura 1.14. Espectro de RMN de ^{1}H en CD_3COCD_3 de [Pt(bzq)(C_6F_5)Br_2(tht)] ***cis*-8**.

El espectro de RMN de ^{19}F muestra que la rotación del anillo pentafluorofenilo está impedida, como sugiere el patrón de cinco señales distintas, con diferente entorno químico para los *o*-F y para los *m*-F. Para estudiar mejor estas señales, se han realizado los espectros de ^{19}F en el rango de temperaturas de 223 a 298 K y se observa que, a baja temperatura, las dos señales correspondientes a los *o*-F se resuelven mejor y el singlete

ancho correspondiente a los *m*-F se separa en dos señales diferentes (Figura 1.15). Los valores de la constante de acoplamiento entre los *o*-F y ^{195}Pt ($^3J_{Pt\text{-}oF}$ 75-113 Hz) son típicos de compuestos de Pt(IV) con anillos pentafluorofenilo,[71a, 71c, 91] e inferiores a los encontrados en los compuestos de Pt(II) [Pt(bzq)(C_6F_5)(η^2-HC≡CFc)][46] y [Pt(bzq)(C_6F_5)(tht)][48] (~510 Hz).

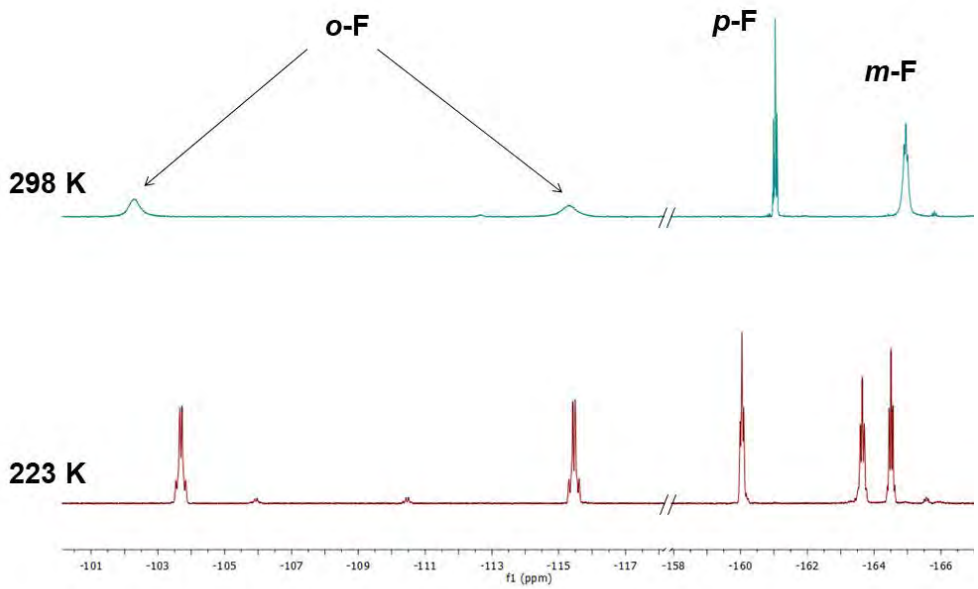

Figura 1.15. Espectros de RMN de ^{19}F (376.5 MHz) en CD_3COCD_3 de [Pt(bzq)(C_6F_5)Br_2(tht)] ***cis*-8** a 298 y 223 K.

Se obtuvieron monocristales adecuados para el estudio por difracción de Rayos X de los compuestos **7** y **8** mediante lenta difusión de *n*-hexano sobre una disolución del compuesto en cloroformo o acetona, respectivamente. En la Figura 1.16 se muestra la estructura molecular de estos compuestos y las distancias y ángulos de enlaces más relevantes se recogen en la Tabla 1.3.

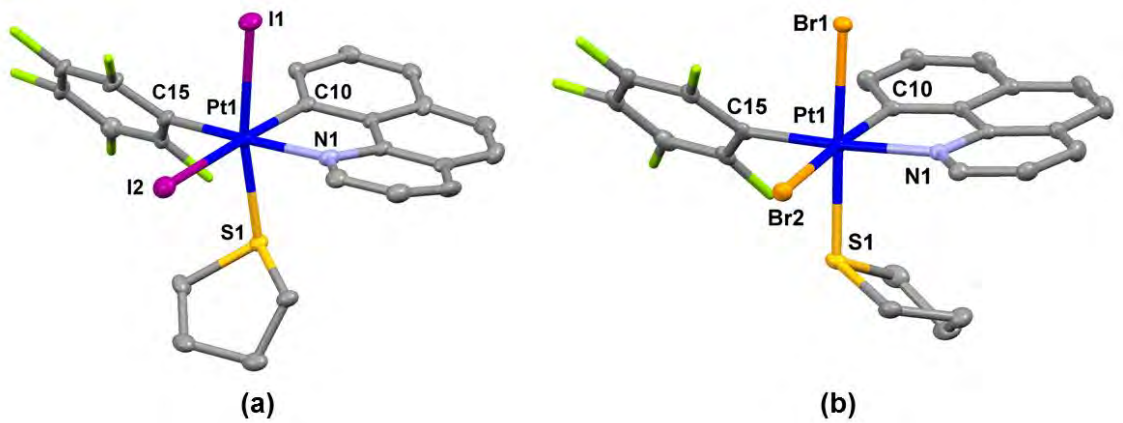

Figura 1.16. Estructuras cristalinas de los derivados (a) *cis*-[Pt(bzq)(C_6F_5)I_2(tht)] ***cis*-7** y (b) *cis*-[Pt(bzq)(C_6F_5)Br_2(tht)] ***cis*-8**.

Tabla 1.3. Distancias [Å] y ángulos [º] para los derivados ***cis*-7** y ***cis*-8**.

		***cis*-7**	
Distancias [Å]			
Pt(1)-C(10)	2.049 (9)	Pt(1)-N(1)	2.119(8)
Pt(1)-S(1)	2.386(2)	Pt(1)-C(15)	2.067(9)
Pt(1)-I(1)	2.6479(7)	Pt(1)-I(2)	2.7550(7)
Ángulos [º]			
C(10)-Pt(1)-N(1)	82.3(3)	C(10)-Pt(1)-S(1)	88.2(2)
C(10)-Pt(1)-I(1)	84.8(2)	N(1)-Pt(1)-S(1)	84.9(2)
N(1)-Pt(1)-I(1)	86.5(2)	C(15)-Pt(1)-S(1)	93.4(3)
C(15)-Pt(1)-I(1)	94.6(3)	C(15)-Pt(1)-C(10)	92.1(4)
C(15)-Pt(1)-I(2)	90.7(3)	S(1)-Pt(1)-I(2)	91.03(6)
I(1)-Pt(1)-I(2)	95.55(2)	N(1)-Pt(1)-I(2)	94.9(2)
		***cis*-8**	
Distancias [Å]			
Pt(1)-C(10)	2.050(4)	Pt(1)-N(1)	2.112(4)
Pt(1)-S(1)	2.363(1)	Pt(1)-C(15)	2.044(5)
Pt(1)-Br(1)	2.4677(5)	Pt(1)-Br(2)	2.5682(5)
Ángulos [º]			
C(10)-Pt(1)-N(1)	81.1(2)	C(10)-Pt(1)-S(1)	96.6(1)
C(10)-Pt(1)-Br(1)	84.6(1)	N(1)-Pt(1)-S(1)	92.7(1)
N(1)-Pt(1)-Br(1)	85.2(1)	C(15)-Pt(1)-S(1)	89.8(1)
C(15)-Pt(1)-Br(1)	92.3(2)	C(15)-Pt(1)-C(10)	95.2(2)
C(15)-Pt(1)-Br(2)	90.1(1)	S(1)-Pt(1)-Br(2)	83.34(3)
Br(1)-Pt(1)-Br(2)	95.25(2)	N(1)-Pt(1)-Br(2)	93.6(1)

Sorprendentemente, una búsqueda de datos en la Base Cristalográfica de Cambridge revela que, aunque el tht es un ligando común para complejos de Pt(II), sólo existe una estructura cristalina de un derivado de Pt(IV) con un ligando tht coordinado.[92] Ambas estructuras (***cis*-7** y ***cis*-8**) son similares y confirman, de acuerdo a los datos de RMN, que los grupos bzq y C_6F_5 retienen la disposición *meridional* del precursor. El platino muestra una geometría octaédrica distorsionada correspondiente a un complejo de

Pt(IV) con los átomos de iodo (**7**) y bromo (**8**) en una disposición mutuamente *cis* y con distancias y ángulos en el mismo rango que en otros derivados de Pt(IV) con esos ligandos (Tabla 1.3).[73k, 86, 93] En ambos compuestos, la distancia Pt-X *trans* al ligando tetrahidrotiofeno [Pt(1)-I(1) 2.6479(7) y Pt(1)-Br(1) 2.4677(5) Å] es significativamente más pequeña que la distancia *trans* al carbono metalado de la bzq [Pt(1)-I(2) 2.7550(7) y Pt(1)-Br(2) 2.5682(5) Å], de acuerdo con la menor influencia *trans* del átomo de azufre.

Las distancias Pt-C(C_6F_5) [2.067(9) **7**; 2.044(5) **8** Å] son ligeramente más cortas que las encontradas en otros compuestos de Pt(IV) con ligandos pentafluorofenilo,[71c] debido a la muy débil influencia *trans* del átomo dador N. Por otro lado, las distancias Pt-S [2.386(2), 2.363(1) Å] son parecidas a la encontrada en el precursor [Pt(bzq)(C_6F_5)(tht)] [2.3719(19) Å],[48] lo que se puede atribuir también a la naturaleza de los ligandos en *trans*. La menor influencia *trans* del haluro en el derivado de Pt(IV) con relación al C(bzq) que se sitúa *trans* al S en el derivado de Pt(II) [Pt(bzq)(C_6F_5)(tht)], queda compensada con el cambio en el estado de oxidación.

Desafortunadamente, ninguno de los compuestos ciclometalados de Pt(IV) sintetizados muestran propiedades luminiscentes. Este hecho, puede ser atribuido a la presencia de estados excitados de baja energía d-d centrados en el metal, que son generalmente estados no radiantes, y seguramente es causado por la presencia de un único ligando ciclometalado bzq y dos ligandos haluro de campo débil.

Chapter 2

Luminescent pentafluorophenyl homoleptic cyclometalated Pt(II) and Pt(IV) compounds

At the beginning of this Thesis, our research group and others had reported some luminescent platinum (II) complexes with cyclometalated ligands using the C_6F_5 group as auxiliary ligand.[44-46, 48, 94] The presence of the C_6F_5 group as auxiliary ligand increases the stability of this type of the complexes avoiding reductive elimination processes and also, significantly improves their emission properties in solution, due to the presence of a strong Pt-C_6F_5 bond. Of particular interest for this work, our group previously reported the preparation of the solvate monopentafluorophenyl cyclometalated complex [Pt(bzq)(C_6F_5)(acetone)],[46] by easy C-H activation of Hbzq (Hbzq = 7,8-benzoquinoline) in acetone using *cis*-[Pt(C_6F_5)$_2$(thf)$_2$] as precursor in a 1:1 molar ratio (Scheme 2.1). The study of the reaction pathway indicated that the metalation involves the initial formation of 0.5 equiv. of the bis(pentafluorophenyl), bis(N^CH) complex *cis*-[Pt(Hbzq-*κN*)$_2$(C_6F_5)$_2$], which subsequently reacts in acetone with the remaining *cis*-[Pt(C_6F_5)(thf)$_2$] to give the solvate acetone complex and HC_6F_5 (Scheme 2.1i). Moreover, *cis*-[Pt(Hbzq)$_2$(C_6F_5)$_2$] undergoes a fast C-H metalation in CH_2Cl_2 to yield the cyclometalated luminescent [Pt(bzq)(Hbzq-*κN*)(C_6F_5)] and HC_6F_5 (Scheme 2.1ii). This complex was also prepared in high yield directly by replacing the acetone molecule in the acetone solvate complex (Scheme 2.1iii).

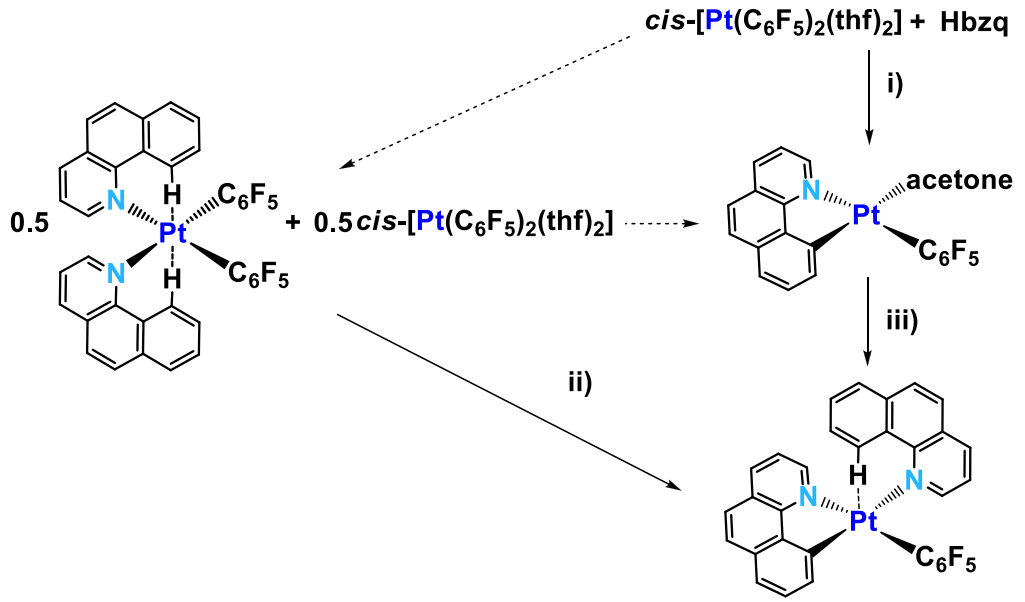

Scheme 2.1. Conditions: i) acetone, reflux, -HC_6F_5; ii) CH_2Cl_2, 298 K, -HC_6F_5; iii) Hbzq, CH_2Cl_2, 298K.

In keeping with these results, we decided to explore the synthesis of mono(pentafluorophenyl)cycloplatinated complexes [Pt(C^N)(HC^N-*κN*)(C_6F_5)] following a similar two-step procedure to that commented in the Scheme 2.1, using as precursors the corresponding compounds with two heterocyclic ligands coordinated through the nitrogen atom [Pt(HC^N-*κN*)$_2$(C_6F_5)$_2$].

Thus, in the **Chapter 2.1** is summarized the synthesis, characterization, photophysics and theoretical calculations of new complexes [Pt(HC^N-*κN*)$_2$(C_6F_5)$_2$] [HC^N = Hthpy (2-(2-thienyl)pyridine) **9a**, Hpbt (2-phenylbenzothiazole) **9b**, Hpq (2-phenylquinoline) **9c** and Hdfppy (2-(2,4-difluorophenyl)pyridine) **9d**], which undergo subsequent C-H activation to give rise to the final cyclometalated complexes [Pt(C^N)(HC^N- *κN*)(C_6F_5)] (C^N = thpy **10a**, pbt **10b**, pq **10c**, dfppy **10d**).

We had envisaged that these new compounds **10** would exhibit desirable absorption and emission in solution under ambient conditions to be used in biological labelling studies. However, studying their properties, we found that in dmso solvent (the most widely used solvent for laboratory-based biological studies), complexes **10** undergo a fast displacement reaction of the non metalated HC^N ligand with the donor S(O)Me_2 molecule. Accordingly, the preparation of complexes [Pt(C^N)(C_6F_5)(dmso)] (C^N = thpy **11a**, pbt **11b**) is also presented in this Chapter.

Furthermore, for complexes **11a**, **11b** and the related complex [Pt(ppy)(C_6F_5)(dmso)] **11-ppy**,[49b] previously prepared by the group, cytotoxicity studies and cellular localization were carried out by the group "Lung Cancer and Respiratory Diseases" led by Dr. José García Pichel in the CIBIR (Centro de Investigación Biomédica de La Rioja).

On the other hand, as has been shown in the **Chapter 1**, the mono(cyclometalated)pentafluorophenyl Pt(IV) derivatives [Pt(bzq)(C_6F_5)X_2L] (L = dmso, X = Cl **3**, I **4**, Br **5**; L = tht, X = Cl **6**, I **7**, Br **8**) were not emissive, which presumably might be due to the presence of only one cyclometalated benzoquinolinyl group as strong field ligand.

In order to prepare Pt(IV) complexes with two cyclometalated groups for improving their luminescent properties, we decided to study the oxidation and metalation of complexes [Pt(C^N)(HC^N-*κN*)(C_6F_5)] **10**, containing an additional HC^N pendant

molecule as auxiliary ligand. Thus, the **Chapter 2.2** presents an easy and successful approach to the preparation of luminescent bis-cyclometalated Pt(IV) complexes featuring C_6F_5 and Cl^- (*fac*-C,C,C_{C6F5} isomer, **12**), CN^- (*mer*-C,C,C_{C6F5} isomer, **13**), Mepy and bpe (*fac*-C,C,C_{C6F5} isomer, **14**, **15**) as auxiliary ligands. All these Pt(IV) complexes are luminescent and their electronic spectra are compared with those of Pt(II) (**9** and **10**), and interpreted with the aid of DFT and time-dependent DFT calculations.

2.1 Luminescent Pt(II) [Pt(C^N)(C_6F_5)L] (L = HC^N, dmso) compounds

2.1.1 Synthesis

In keeping with the previously described two-step process to prepare the cyclometalated complex [Pt(bzq)(Hbzq)(C_6F_5)][46] (Scheme 2.1), we decided to use the same procedure employing 2-(2-thienyl)pyridine (Hthpy), 2-phenylbenzothiazole (Hpbt), 2-phenylquinoline (Hpq) and 2-(2,4-difluorophenyl)pyridine (Hdfppy) as N^CH ligands. Thus, as is shown in Scheme 2.2i, *cis*-[Pt(C_6F_5)$_2$(thf)$_2$] was reacted with 2 equiv. of the corresponding N^CH ligand under mild conditions (CH_2Cl_2, 1.5 to 5 h, room temperature) to give the bis(N^CH) derivatives [Pt(HC^N-κN)$_2$(C_6F_5)$_2$] (HC^N = Hthpy **9a**, Hpbt **9b**, Hpq **9c**, Hdfppy **9d**). The anchoring of both HC^N ligands through the nitrogen atom to the Pt center will allow subsequent C-H activation to afford new cyclometalated complexes. However, these systems require drastic conditions of xylene (**10a-c**) or toluene (**10d**) for 2 hours to successfully afford the final cyclometalated derivatives [Pt(C^N)(HC^N-κN)(C_6F_5)] (**10a-d**) (Scheme 2.2ii).

With the aim of studying the cytotoxicity of the cyclometalated compounds (**10a-c**), we first examined the solubility of the compounds. Unfortunately, these compounds were not soluble in water, but they were soluble in dmso, which is a widely used solvent for cytotoxicity measurements. Thus, we examined the stability of these compounds in dmso-d^6 by ^{1}H NMR and we found that by dissolving **10a-c** in dmso, the N^CH ligand is easily substituted by a molecule of dmso, giving rise to the corresponding dmso solvate [Pt(C^N)(C_6F_5)(dmso)] (C^N = thpy **11a**, pbt **11b**). In the case of the complex **10c**, which contain the 2-phenylquinoline ligand, a complex mixture of species was detected by ^{1}H NMR when it was dissolved in dmso-d^6, in which the expected **11c** was also present. This behaviour should be taken into account when studying the biological activity of related complexes in dmso. For this reason, we decided to isolate and to characterize the dmso solvates. We have also included in the biological studies the complex [Pt(ppy)(C_6F_5)(dmso)] **11-ppy**, previously prepared and published by our group.[49b] The preparation and study of the solvate complex with the dfppy ligand [Pt(dfppy)(C_6F_5)(dmso)] was carried out by Gonzalo Millán and has been recently published,[47] so its preparation and characterization are not described in this Memory.

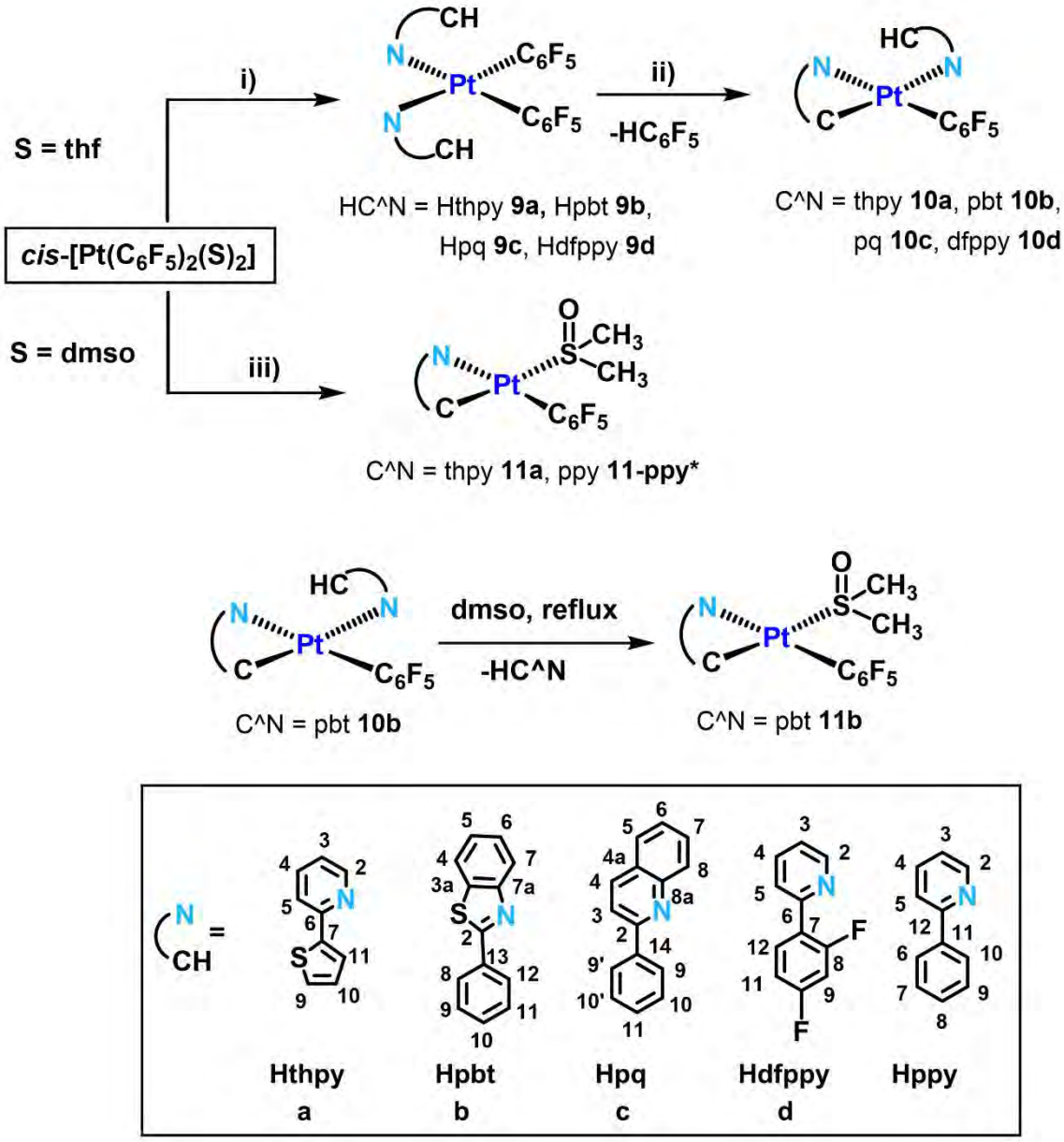

Scheme 2.2. Syntetic routes for **9-11**. Reagents and conditions: (i) HC^N (2 equiv.), CH_2Cl_2, (ii) xylene (**10a-c**) or toluene (**10d**) at reflux, (iii) HC^N (1 equiv.), -HC_6F_5, xylene at reflux. *Lalinde, E. *et al. Inorg. Chem*. **2014**, 53, 8870.

As is shown in Scheme 2.2iii, only the derivative with the thpy ligand (**11a**) could be prepared, as an orange microcrystalline solid, in a similar way to that described for **11-ppy**, by reaction of *cis*-[Pt(C_6F_5)$_2$(dmso)$_2$] with 1 equiv. of Hthpy in refluxing xylene. Considering previous mechanistic studies[43a, 73d, 86, 95] (Scheme 2.3), the reaction leading to **11a** probably takes place with the substitution of one of the coordinated molecules of dmso by the Hthpy ligand to form the species **G**. In this species, the perpendicular orientation of the pyridinic group of the Hthpy ligand to the plane of the platinum likely approximates the *ortho* C^{11}-H bond to the platinum, which is an electron-rich center in

the axial direction, triggering its activation by oxidative addition, leading to the hydride Pt(IV) complex **H**. Subsequent reductive elimination would proceed preferentially with the C_6F_5 group situated in *trans* to the metalated carbon, due to its high *trans* influence,[46, 90] with final formation of **11a**.

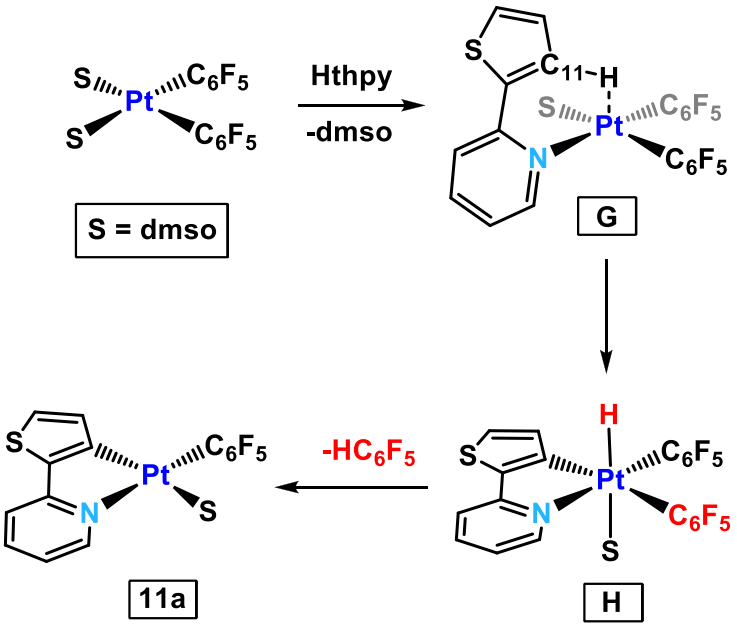

Scheme 2.3

Unfortunately, this method did not work for the corresponding Hpbt or Hpq solvates, as the related reactions evolve with considerable decomposition to platinum(0). However, the solvate complex [Pt(pbt)(C_6F_5)(dmso)] (**11b**) was prepared alternatively by refluxing [Pt(pbt)(Hpbt)(C_6F_5)] (**10b**) in a minimum amount of dmso for 4 h (see Scheme 2.2iv). Unfortunately, all attempts to isolate [Pt(pq)(C_6F_5)(dmso)] as a pure complex were fruitless. It is worth mentioning that in the dmso-solvate complexes, the dmso molecule is *κ-S* coordinated, as is confirmed by X-ray (See below). This is in accordance with the softer character of the S in relation to the O atom. Taking into account the HSAB (hard and soft acids and bases) concept,[96] both Pt(II) and sulfur are considered to be "soft" and therefore expected to form stable bonds, whereas the harder Pt(IV) center shows mainly *κ-O* coordination, although examples with *κ-S* coordination are also known, (for instance, the platinum (IV) complexes described in the Chapter 1 of this Memory).[84]

2.1.2 Characterization and X-ray structures

A combination of crystallography (**9a**, **9c**, **9d**, **10b**, **10d**, **11a** and **11b**), IR spectra, mass spectrometry, NMR spectroscopy and elemental analysis support the formulation proposed for these compounds. The presence of the C_6F_5 group was confirmed by IR, showing, for complexes **9**, two $\nu_{X\text{-sens}}$ vibration bands in agreement with the presence of two C_6F_5 groups in *cis*-disposition. However, for complexes **10** and **11**, with one C_6F_5 group coordinated to the platinum, only one band $\nu_{X\text{-sens}}$ was observed.

These new compounds were fully characterized by multinuclear NMR spectroscopic analysis. All experiments were recorded in $CDCl_3$ and the signals were assigned on the basis of ^{1}H-^{1}H (COSY and TOCSY) and ^{1}H-^{13}C (HSQC and HMBC) correlation experiments.

2.1.2.1 Characterization of complexes 9

For the derivatives with two heterocyclic ligands coordinated through de nitrogen atom (complexes **9**), the ^{1}H, ^{19}F and ^{13}C{^{1}H} NMR spectra confirm the presence of only one set of signals for both N^CH and C_6F_5 ligands at room temperature (Figure 2.1). In these complexes, the most deshielded signal (also deshielded in relation to the free ligand) is attributed to the *ortho* proton of the phenyl (**9b**-**9d**) or thienyl (**9a**) ring, which is located close to the Pt center thus reflecting the anisotropic effect associated with the Pt dz^2 electron density[46] (δ 8.50, H^{11}, **9a**; δ 8.13, H^8, **9b**; δ 8.68, H^9, **9c** at -50ºC; δ 9.28, H^{12}, **9d**). The proton adjacent to the N atom (H^2 in **9a** and **9d**) appears with platinum satellites ($^3J_{Pt\text{-}H}$ = 28 Hz **9a**; 33 Hz **9d**), whereas complexes **9b** and **9c** do not have that proton.

The steric congestion due to the coordination of two bulky Hpq ligands is reflected in the ^{1}H NMR of complex **9c**. The *ortho* (H$^{9,9'}$) and *meta* (H$^{10,10'}$) proton signals of the phenyl ring, are broad and close to coalescence at room temperature and split into four different resonances at 223 K, evidencing that the phenyl ring is rigid on the NMR time scale (Figure 2.2). The congestion is also reflected in the ^{19}F NMR spectra of all complexes, which is consistent with relatively rigid molecules showing five [**9a** (at -45ºC, Figure A2.1), **9b** and **9d** (Figure 2.1b)] or four (**9c**) distinct signals corresponding to the C_6F_5 group, thus indicating that the rotation of the C_6F_5 ring around the Pt-C_{ipso} is hindered due to the steric hindrance of the HC^N ligands.

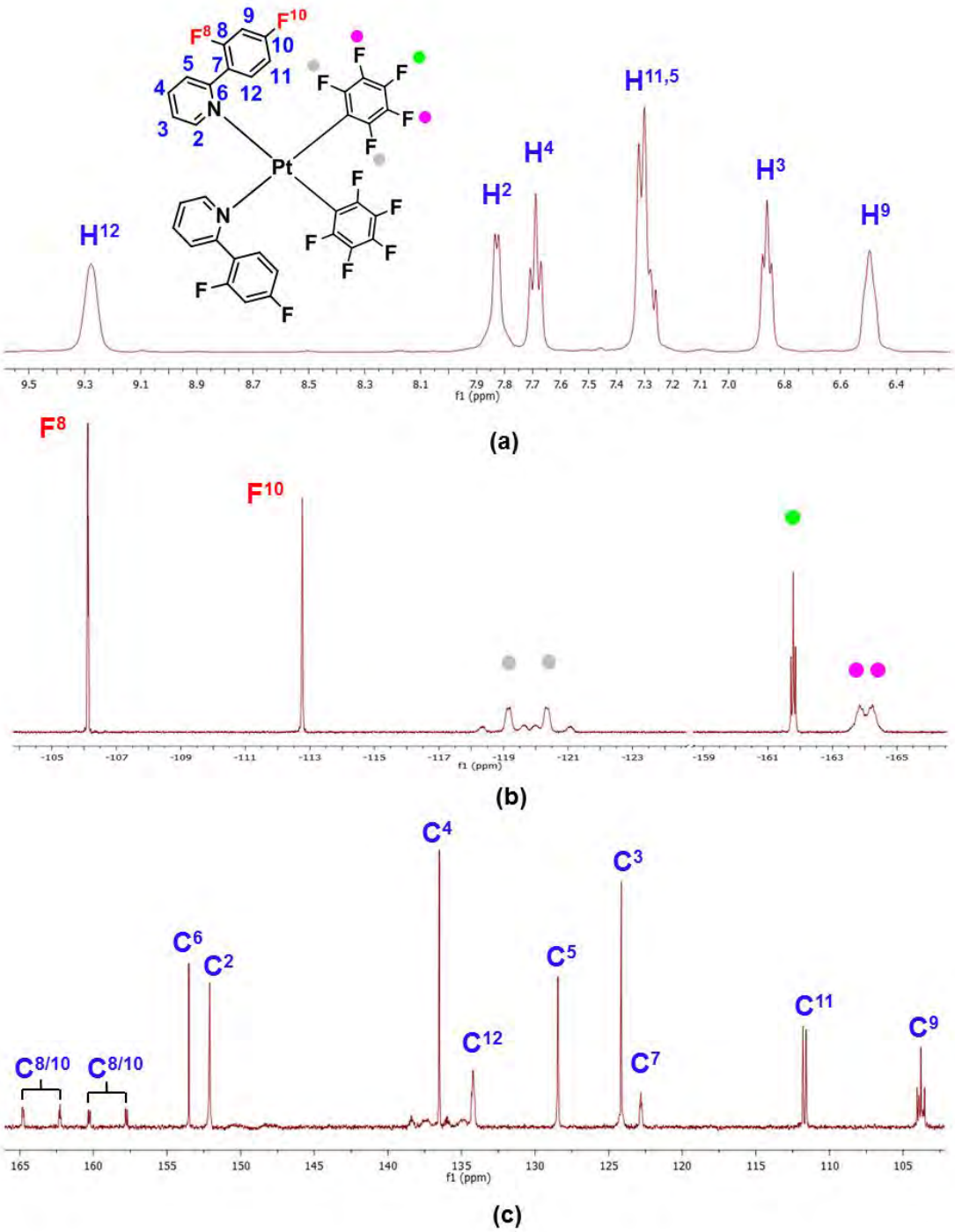

Figure 2.1. (a) ^{1}H, (b) $^{19}F\{^{1}H\}$ and (c) $^{13}C\{^{1}H\}$ spectra of complex **9d** in $CDCl_3$ at 298 K.

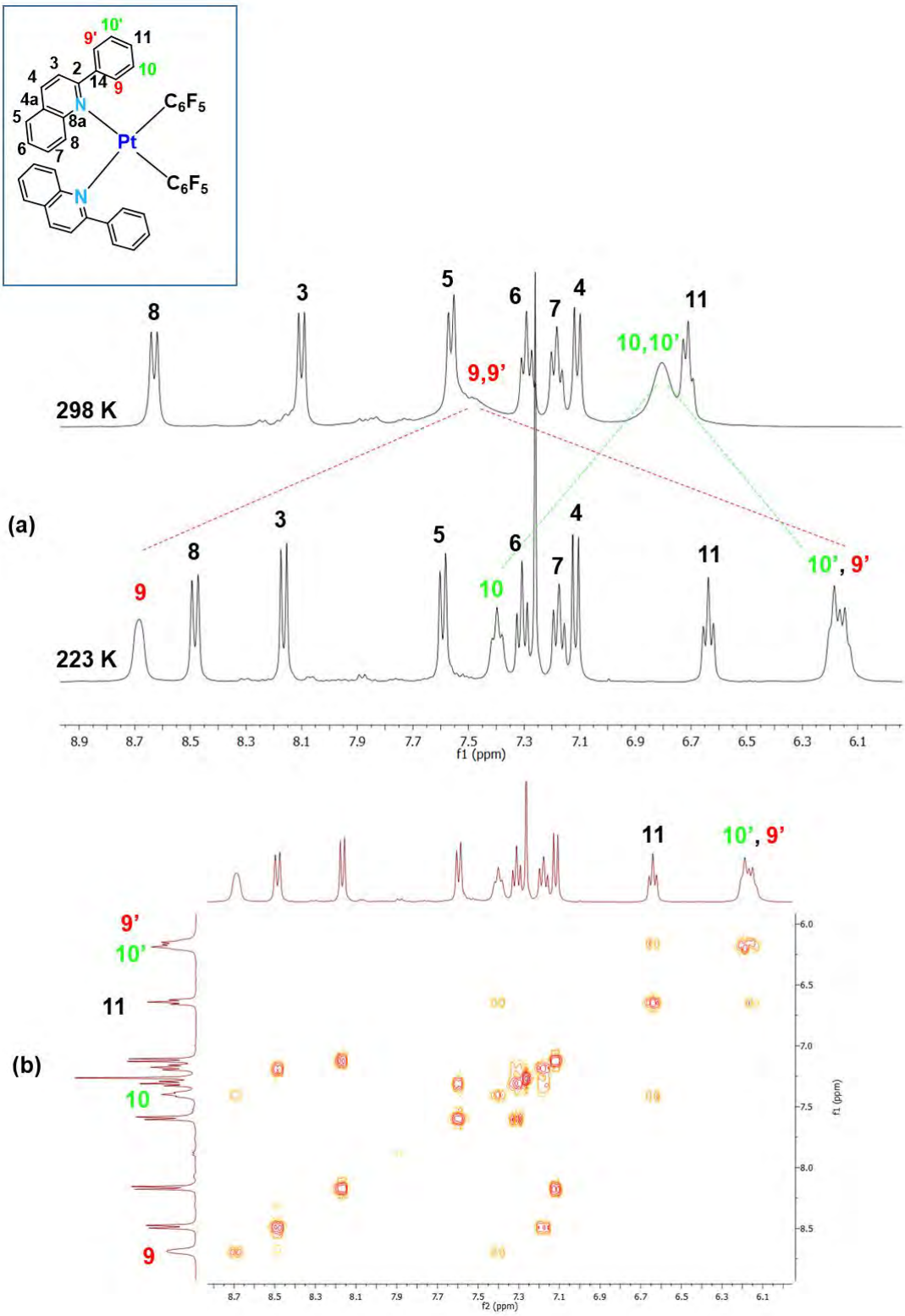

Figure 2.2. (a) ^{1}H NMR spectra at 298 K and 223 K and (b) COSY (^{1}H-^{1}H) spectrum at 223 K of **9c** in $CDCl_3$.

The molecular structures of complexes **9a**, **9c**·0.75CH_2Cl_2 and **9d** were established by X-ray diffraction studies (Figure 2.3, Table 2.1). The compounds show a distorted planar environment for the platinum ($Pt_2N_2C_2$), formed by two *cis* non-chelated thienylpiridine (**9a**), phenylquinoline (**9c**) or difluorophenylpyridine (**9d**) and two C_6F_5 rings. The HC^N ligands adopt a *transoidal* (or *anti*) disposition in relation to the platinum square plane, with dihedral angles between the pyridine groups and the Pt coordination planes of ~55º. The HC^N ligands are not planar exhibiting, in **9a**, interplanar angles between the pyridine group and the thiazoline ring of 38.16º, 39.79º; in **9c**, between the phenyl and quinoline groups of 59.13º, 64.72º and; in **9d**, between the pyridine and the phenyl groups of 48.32º and 52.54º. In **9a**, one of the thienyl ligands locates the C-H (H16) towards the platinum atom with a long distance (3.044 Å). However, in complexes **9c** and **9d**, two of the protons of the quinoline or aryl rings are located in pseudoaxial positions above and below the platinum coordination plane, with short Pt···H distances (Pt-H14/H29 2.773/2.759 Å in **9c**; Pt-H11/H22 2.982/2.897 Å in **9d**). These Pt···H separations are close or shorter than the sum of the van der Waals radii[97] (2.95 Å), and the Pt···H-C angles (116.31, 115.63º in **9c**, 102.9, 101.3º in **9d**) fall within the range of the Pt···H bonding interactions reported in the literature.[46, 98]

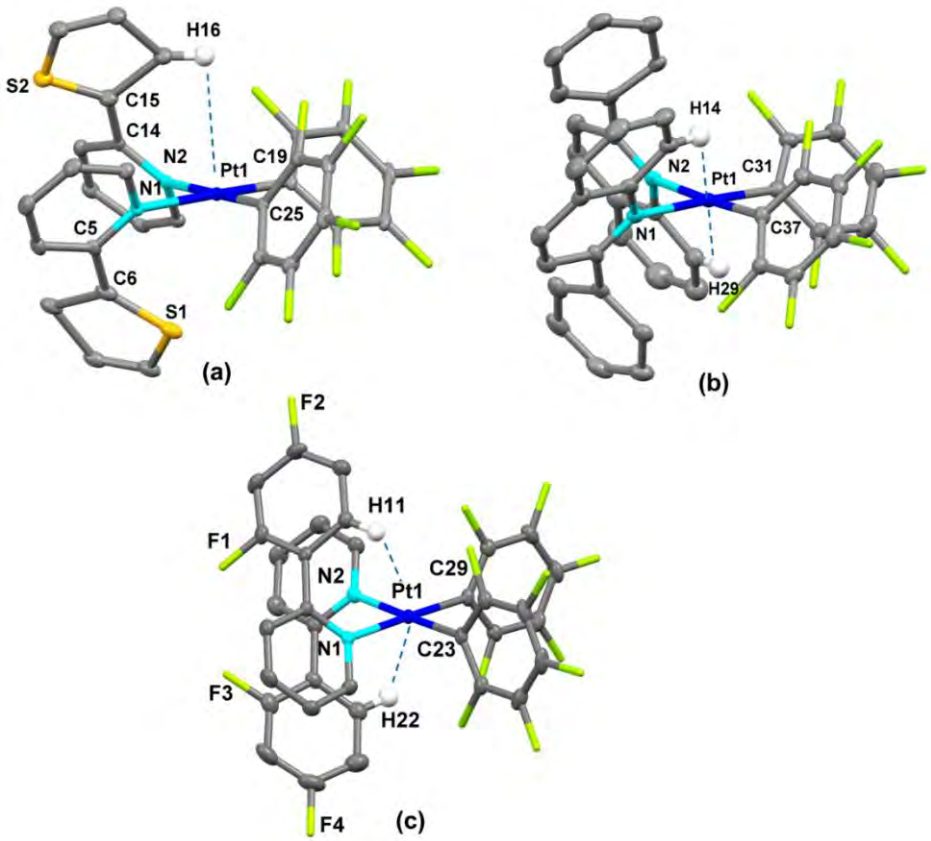

Figure 2.3. View of the molecular structures of (a) **9a**, (b) **9c**·0.75CH_2Cl_2 and (c) **9d**.

Table 2.1: Selected distances (Å) and angles (°) for complexes **9a**, **9c**·0.75CH_2Cl_2, **9d**.

9a			
Distances (Å)		**Angles (°)**	
Pt-N(1)	2.110(3)	N(2)-Pt-N(1)	88.97(12)
Pt-N(2)	2.111(3)	N(2)-Pt-C(19)	88.80(14)
Pt-C(19)	2.012(4)	N(1)-Pt-C(25)	89.79(14)
Pt-C(25)	2.015(4)	C(25)-Pt-C(19)	92.46(16)
C(14)-C(15)	1.464(6)		
H(16)···Pt(1)	3.044		
9c·0.75CH_2Cl_2			
Distances (Å)		**Angles (°)**	
Pt-N(1)	2.173(6)	N(2)-Pt-N(1)	90.1(2)
Pt-N(2)	2.133(5)	C(31)-Pt-N(2)	91.5(2)
Pt-C(31)	2.012(8)	C(31)-Pt-C(37)	87.2(3)
Pt-C(37)	2.011(6)	C(37)-Pt-N(1)	91.4(2)
H(14)···Pt(1)	2.773		
H(29)···Pt(1)	2.759		
9d			
Distances (Å)		**Angles (°)**	
Pt-N(1)	2.117(2)	N(1)-Pt-N(2)	90.82(9)
Pt-N(2)	2.117(2)	C(23)-Pt-N(1)	90.85(10)
Pt-C(23)	2.012(3)	C(29)-Pt-C(23)	86.63(11)
Pt(1)-C(29)	2.013(3)	C(29)-Pt-N(2)	91.71(10)
H(11)···Pt	2.982		
H(22)···Pt	2.897		

In **9a**, the molecules are stacked by weak π···π interactions between Hthpy and C_6F_5 (3.36 Å) ligands and between C_6F_5 groups, supported by secondary F···H and H···S weak intermolecular interactions (Figure 2.4). The molecules in **9c** and **9d** complexes are stacked through weak secondary F···H and F···C interactions (See Figure A2.2).

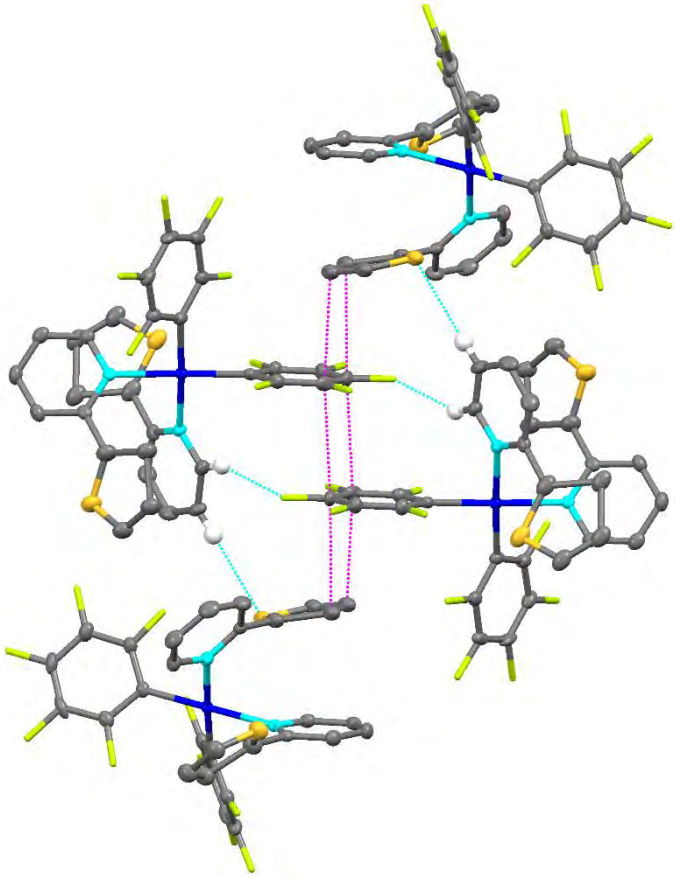

Figure 2.4. Crystal packing of **9a** showing the intermolecular contacts. The supramolecular packing is formed by chains supported by intermolecular π···π (pink lines) involving Hthpy and C_6F_5 ligands with interplanar distances of 3.36 Å. These π···π interactions are supported by $F_{C6F5}\cdots H_{Hthpy}$ (2.38 Å) and $H_{Hthpy}\cdots S_{Hthpy}$ (2.86 Å) secondary interactions (blue lines).

2.1.2.2 Characterization of complexes 10

In complexes **10**, the expected metalated and nonmetalated ligands are observed in their ^{1}H NMR spectra (Figure 2.5). The most distinctive signal is that of the *ortho* proton to the metalated carbon, which appears upfield shifted in relation to complexes **9** (δ 6.75-6.22), with the expected platinum satellites (26 Hz, **10a**; 68 Hz, **10b**; 77 Hz, **10d**). The strong shielding of this signal is attributed to its proximity to the diamagnetic current of the C_6F_5 group, thus supporting the *cis* disposition of the C-metalated atom to the C_6F_5 group. For complex **10c**, the complexity of the ^{1}H and ^{13}C{^{1}H} NMR spectra precluded a detailed assignment of the signals. However, the expected integration in the ^{1}H NMR spectrum of the 21 protons (11 protons of the HC^N ligand and 10 of the C^N cyclometalated ligand) and the downfield shift of one of the signals confirms the orthometalation of one of the ligands.

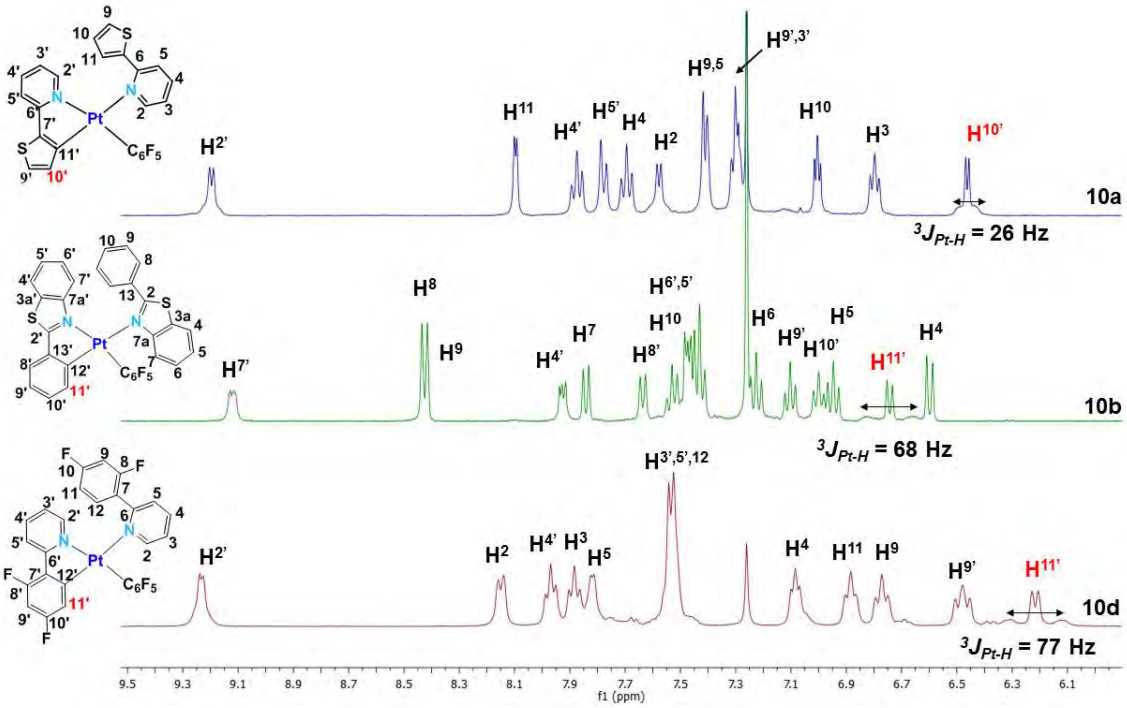

Figure 2.5. ^{1}H NMR spectra of **10a**, **10b** and **10d** in $CDCl_3$.

As in complexes **9**, ^{19}F NMR spectra indicate that the rotation of the C_6F_5 ring around the Pt-C_{ipso} bond is hindered and the high values of the $^3J_{Pt-oF}$ observed (455-503 Hz) are consistent with the relatively low *trans* influence of the pyridine N atom of the C^N metalated ligand. As expected, the ^{19}F{^{1}H} NMR spectrum of **10d** shows the fluorine resonances of the cyclometalated group (dfppy, $F^{10'}$ and $F^{8'}$) with long range four bonds platinum satellites of 66 and 55 Hz, respectively (Figure 2.6), while those of the pendant Hdfppy group (F^{10} and F^{8}) do not show platinum satellites.

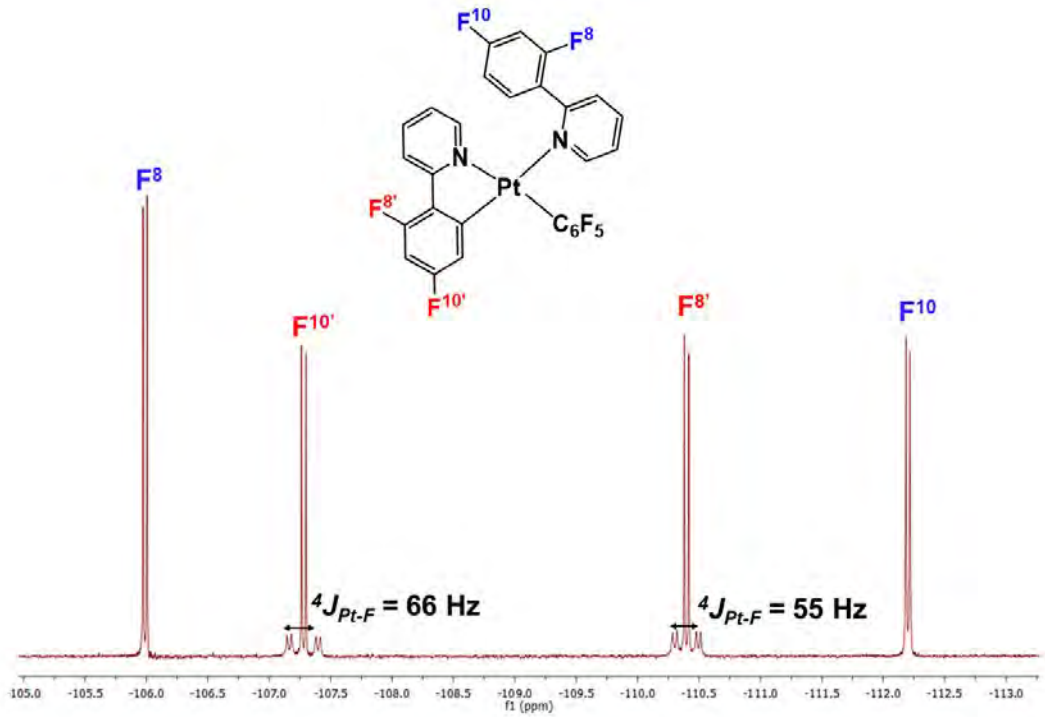

Figure 2.6. Selected region of the $^{19}F\{^1H\}$ NMR spectra of [Pt(dfppy)(Hdfppy)(C_6F_5)] **10d**.

The X-ray diffraction studies of **10b** and **10d** confirm the C-H activation of one of the HC^N ligands (pbt and dfppy, respectively) and the N-coordination of the other one (Hpbt and Hdfppy) (Figure 2.7, Table 2.2 and Table E.3). These compounds represent examples of the few Pt(II) complexes containing a chelated and non-chelated cyclometalated ligand whose crystal structure have been determined.[36, 46, 99] Their structural data are similar to those previously found for [Pt(bzq)(Hbzq)(C_6F_5)].[46] Thus, in accordance with the spectroscopic data, the C_6F_5 ligand is in a *cis* disposition with respect to the metalated atom (C9 in **10b** and C11 in **10d**). The Pt-N2$_{(HC^N)}$ distance [2.152(3) Å (**10b**), 2.153(3) Å (**10d**)] is longer than the Pt-N1$_{(C^N)}$ distance [2.101(3) Å (**10b**), 2.072(2) Å (**10d**)], reflecting the high *trans* influence of the metalated carbon. Along the same lines, the Pt-C$_{(C^N)}$ bond is shorter [Pt-C9, 2.007(3) Å in **10b**; Pt-C11, 1.981(3) Å in **10d**] than the Pt-C$_{(C6F5)}$ bond [2.005(4) Å (**10b**), 2.019(3) Å (**10d**)], which reflects the strong σ-donating and π-accepting character of the cyclometalating C^N moiety. In **10b**, the Hpbt pendant ligand is coordinated almost perpendicular to the Pt coordination plane with a dihedral angle of 83.49º. This causes the location of the H22 and H15 protons close to the Pt center (2.587 and 2.786 Å, respectively), suggesting the presence of Pt···H bonding interactions.[46, 98] In **10d**, the Hdfppy ligand is coordinated forming a dihedral angle of 63.96º with the Pt coordination plane. However, in contrast to that seen in **10b**, the strong twist of the pendant difluorophenyl ring relative to the N-coordinated pyridine

unit (interplanar angle 56º) places the *ortho*-H22 relatively distant from the platinum center (3.058 Å).

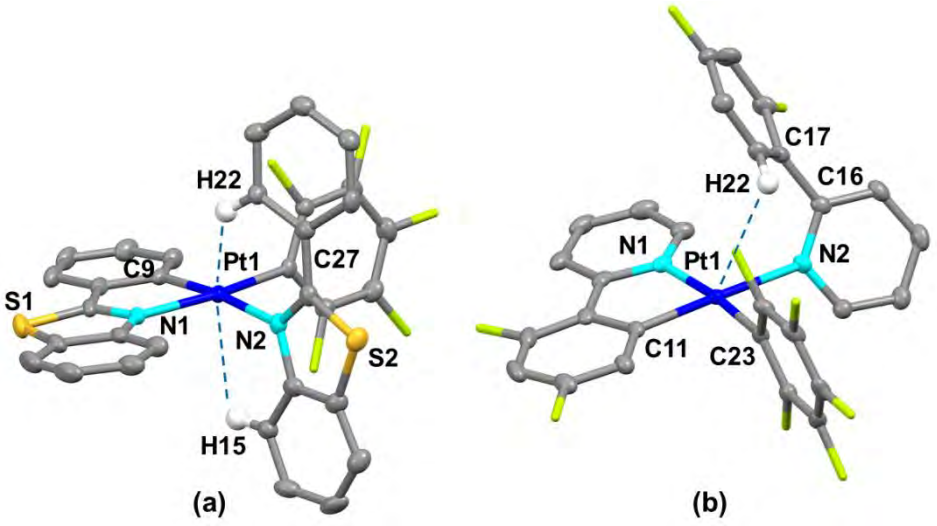

Figure 2.7. Molecular structure of (a) **10b** and (b) **10d**.

Table 2.2: Selected distances (Å) and angles (°) for complexes **10b** and **10d**.

10b			
Distances (Å)		**Angles (°)**	
Pt-N(1)	2.101(3)	N(2)-Pt-N(2)	96.90(12)
Pt-N(2)	2.152(3)	C(9)-Pt-N(1)	81.37(15)
Pt-C(9)	2.007(3)	C(27)-Pt-C(9)	91.20(15)
Pt-C(27)	2.005(4)	C(27)-Pt-N(2)	90.65(12)
Pt···H(22)	2.587		
Pt···H(15)	2.786		
10d			
Distances (Å)		**Angles (°)**	
Pt(1)-N(1)	2.072(2)	N(1)-Pt-N(2)	96.78(10)
Pt(1)-N(2)	2.153(3)	C(11)-Pt-N(1)	80.91(12)
C(5)-C(6)	1.465(5)	C(11)-Pt-C(23)	92.46(13)
Pt(1)-C(11)	1.981(3)	C(23)-Pt-N(2)	89.77(11)
Pt(1)-C(23)	2.019(3)		
C(16)-C(17)	1.487(4)		
H(22)···Pt	3.058		

The analyisis of the packing shows the presence of dimers through moderate intermolecular π···π (Hpbt···Hpbt) (3.31 Å) and S···C (Hpbt) (3.50 Å) interactions in **10b** (Figure 2.8a) and chains supported by π···π intermolecular interactions between dfppy cyclometalated groups in **10d** (Figure 2.8b). Additional weak contacts are shown in Figure A2.3.

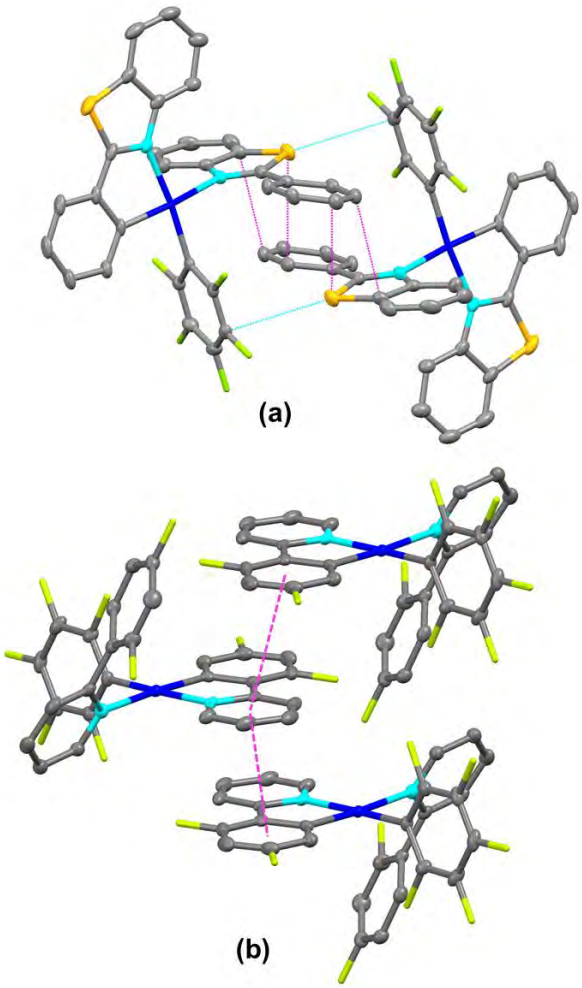

Figure 2.8. Crystal packing of (a) **10b** showing dimers supported by intermolecular π···π interactions (pink lines) involving Hpbt ligands with interplanar distances of 3.31 Å ($C_{Hpbt}\cdots C_{Hpbt}$) and 3.50 Å ($S_{Hpbt}\cdots C_{Hpbt}$) supported by $C_{C6F5}\cdots S_{Hpbt}$ (3.48 Å) secondary interactions (blue) and (b) **10d** showing the effective intermolecular π···π interactions involving the planar dfppy ligands in a head-to-head manner (3.35 - 3.37 Å).

2.1.2.3 Characterization of complexes 11

The solvate complexes [Pt(C^N)(C_6F_5)(dmso)] (C^N = thpy **11a**; pbt **11b)** show in their ^{1}H NMR spectra the signals of the cyclometalated C^N ligand and the methyl resonance corresponding to the coordinated dmso ligand, featuring platinum satellites ($^3J_{Pt\text{-}H}$= 13 - 16 Hz). In the aromatic region, the signal of the *ortho* proton to the metalated

Pt-C bond appears slightly upfield shifted in relation to the complexes [Pt(C^N)(HC^N)(C_6F_5)] **10a** and **10b** (δ $H^{10'}$ 6.04 **11a**, 6.46 **10a**; $H^{11'}$ 6.35 **11b**, 6.75 **10b**) showing similar Pt-H coupling constants ($^3J_{Pt-H}$ = 27 Hz **11a**, 26 Hz **10a**; 63 Hz **11b**, 68 Hz **10b**) (Figure 2.9a). It is worth mentioning that the $^3J_{Pt-H}$ values found for the proton adjacent to the metalated carbon (~26 Hz) in the thienyl derivatives (**10a** and **11a**) are lower than those found for similar protons in the rest of the complexes (~ 65 Hz) featuring orthometalated phenyl rings. The most deshielded resonance corresponds in **11a** to the proton adjacent to the nitrogen of the cyclometalated group which appears with visible Pt satellites (δ $H^{2'}$ 9.46, $^3J_{Pt-H}$ = 28.4 Hz) and to the benzothiazol $H^{7'}$ proton in **11b** (δ 9.07).

The $^{19}F\{^1H\}$ NMR spectra display three signals corresponding to one C_6F_5 group with the equivalents *ortho-F* and *meta-F*, indicating the free rotation of the C_6F_5 ring due to the less steric hindrance of the dmso ligand in comparison to the HC^N-κN ligand im complexes **9** and **10**. The presence of the cyclometalated ligand is also reflected in their $^{13}C\{^1H\}$ NMR spectra. In **11a**, the othometalated $C^{11'}$ signal is seen at 149.9 ppm with the expected short range platinum satellites ($^1J_{Pt-C}$ = 1002 Hz) (Figure 2.9b), whereas at high field appears, in both complexes, the carbon resonance of the methyl groups of the dmso ligand with platinum satellites (δ / $^2J_{Pt-C}$ = 45.2 / 42.4 Hz **11a**; 46.3 / 40 Hz **11b**).

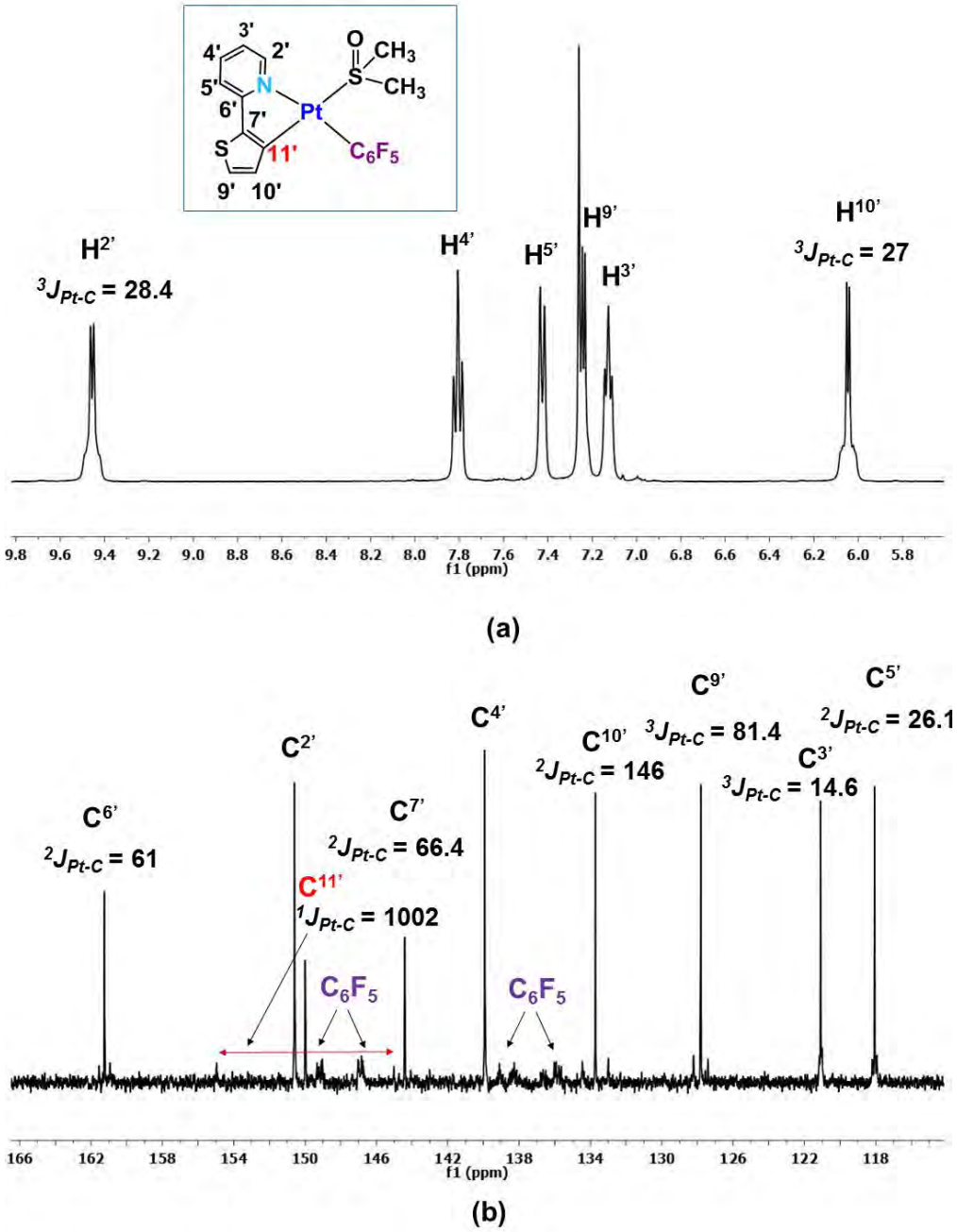

Figure 2.9. NMR spectra (aromatic region) of **11a** in $CDCl_3$: (a) ^1H and (b) $^{13}C\{^1H\}$.

The molecular structures of **11a** and **11b** have been solved by X-ray crystallography (Figure 2.10, Table 2.3 and Table E.4). In both molecules, the Pt atom exhibits a distorted planar environment due to the small bite angle of the C^N cyclometalated ligand [79.0(3)º **11a**, 80.1(2)º **11b**], with the C_6F_5 group coordinated in a *cis*-position to the metalated carbon atom. The dmso molecule shows the expected *S*-coordination usually found in Pt(II) derivatives.[100] The Pt-S distance [2.296(2) Å **11a**, 2.3140(13) **11b**] is slightly larger than the average of this distance in related structures,[88, 100] likely due to the strong *trans* influence of the metalated C-atom.

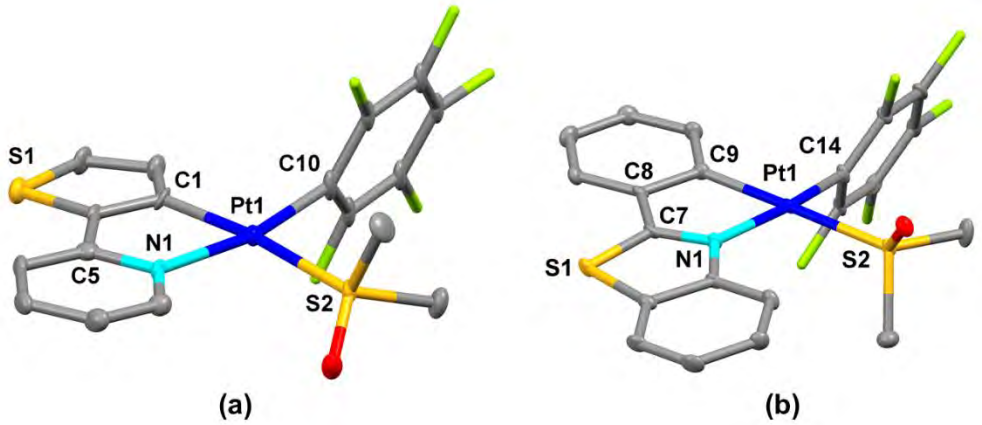

Figure 2.10. Molecular structures of (a) **11a** and (b) **11b**.

Table 2.3: Selected distances (Å) and angles (°) for complexes **11a** and **11b**.

11a			
Distances (Å)		**Angles (°)**	
Pt-N(1)	2.009(7)	C(10)-Pt(1)-C(1)	91.5(4)
Pt-C(1)	2.049(9)	C(1)-Pt(1)-N(1)	79.0(3)
Pt-S(2)	2.296(2)	C(10)-Pt(1)-S(2)	92.0(3)
Pt-C(10)	2.007(10)	N(1)-Pt-S(2)	98.09(18)
O(1)-S(2)	1.472(6)	O(1)-S(2)-Pt(1)	116.9(3)
S(2)-C(16)	1.789(9)		
S(2)-C(17)	1.795(9)		
11b			
Distances (Å)		**Angles (°)**	
Pt-N(1)	2.136(4)	C(14)-Pt(1)-C(9)	89.3(2)
Pt-C(9)	2.041(6)	C(9)-Pt(1)-N(1)	80.1(2)
Pt-C(14)	2.012(5)	C(14)-Pt(1)-S(2)	90.37(15)
Pt-S(2)	2.3140(13)	N(1)-Pt-S(2)	100.14(12)
S(2)-C(20)	1.775(5)	O(1)-S(2)-Pt(1)	118.23(15)
S(2)-C(21)	1.781(6)	O(1)-S(2)-C(20)	105.3(3)
O(1)-S(2)	1.475(4)	O(1)-S(2)-C(21)	109.4(3)
		C(20)-S(2)-C(21)	98.1(3)

Analysis of the crystal packings show that **11a** establishes a supramolecular arrangement through effective π···π intermolecular interactions between cyclometalated thpy groups with an interplanar distance of *ca.* 3.34 Å (Figure 2.11), whereas **11b** only shows intermolecular contacts (F···F, F···H and F···S) involving fluorine atoms from C_6F_5 (Figure 2.12).

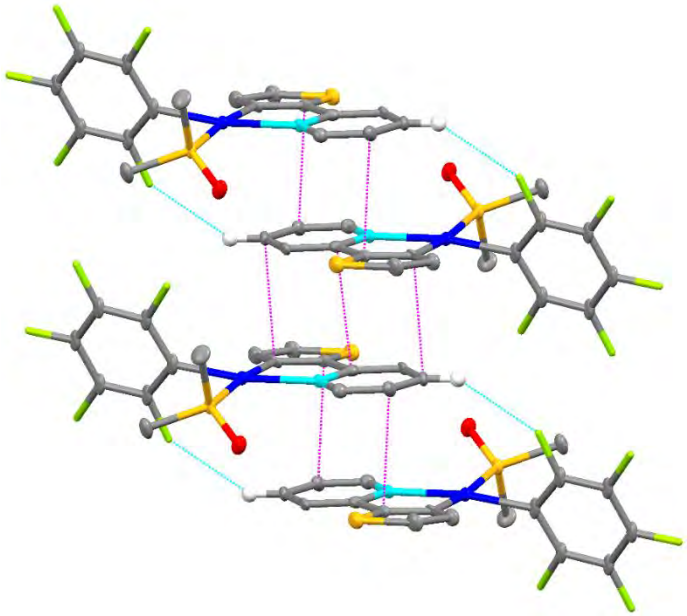

Figure 2.11. Crystal packing of **11a** showing the intermolecular contacts. The supramolecular packing is formed by chains supported by intermolecular π··π (pink lines) involving two thpy ligands (3.33-3.40 Å). These π···π interactions are supported by $F_{C6F5}\cdots H_{thpy}$ (2.60 Å) (blue lines).

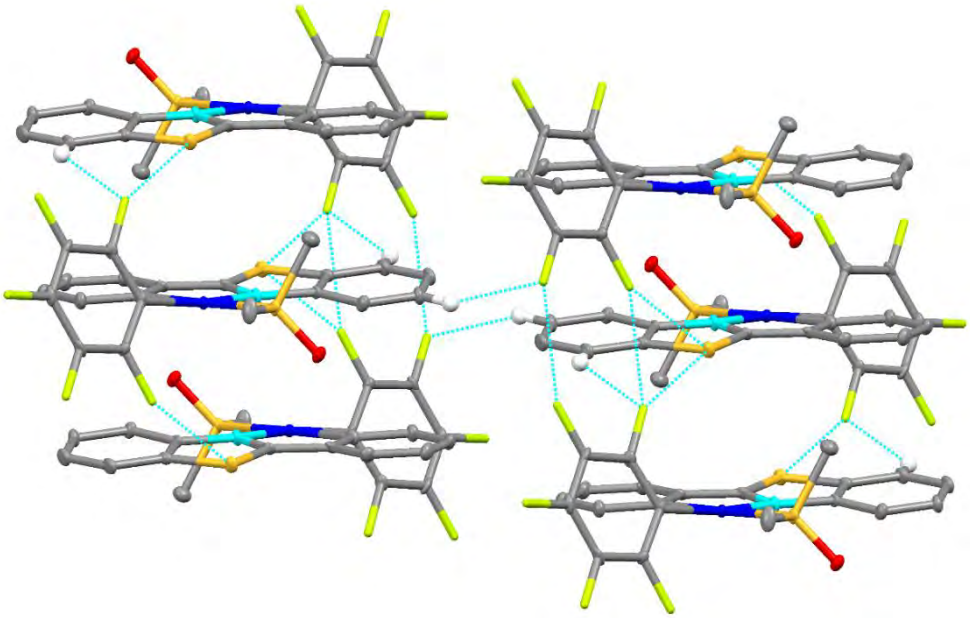

Figure 2.12. View of the secondary interactions present in the structure **11b** showing the interactions $F_{C6F5}\cdots F_{C6F5}$ (2.84 Å), $F_{C6F5}\cdots H_{pbt}$ (2.55-2.64 Å) and $F_{C6F5}\cdots S_{pbt}$ (3.15-3.25 Å).

2.1.3 Photophysical properties

2.1.3.1 Absorption spectroscopy

The UV-vis absorption spectra were examined for all the complexes in CH_2Cl_2 solutions. In selected compounds, the spectra were also recorded in MeCN solutions. All the data are summarized in Table 2.4. The spectra of the series of complexes containing thpy (**9a**, **10a**, **11a**), pbt (**9b**, **10b**, **11b**), pq (**9c**, **10c**) or dfppy (**9d**, **10d**) ligands are represented in Figure 2.13. Besides, for comparison, the absorption spectrum of the corresponding free ligand (Hthpy, Hpbt, Hpq and Hdfppy, respectively) is also included in each of the series (dotted lines in Figure 2.13). All complexes exhibit very intense high-energy absorptions which are mainly attributed to π-π* intraligand ^{1}IL (HC^N, C^N, C_6F_5) transitions.

In detail, as it is displayed in Figure 2.13, the intense bands in complexes **9** [Pt(HC^N-*κN*)$_2$(C_6F_5)$_2$] (represented by blue lines) follow the tendency of the free ligands (302 **9a**, 292 **9b**, 338 **9c**, 275 nm **9d**). According to the results of theoretical calculations for **9a**, **9c** and **9d** (see below), these bands bear a remarkable intraligand ^{1}IL (L = HC^N) with some ligand to ligand charge transfer (C_6F_5 → HC^N) in **9a** or Pt to ligand charge transfer ^{1}MLCT (Pt → HC^N) in **9c** and **9d**. Besides, these complexes exhibit tails of very low intensity, that are not present in the free ligands, ascribed to ^{1}MLCT (Pt → HC^N) transitions with some ^{1}IL (HC^N) contribution.

Complexes **10** and **11**, which contain a cyclometalated ligand, exhibit a characteristic low energy feature (340-430 nm, $\varepsilon = 4.9 - 0.6 \times 10^{-3}$ M^{-1} cm^{-1}) typical of cycloplatinated systems.[26c, 101] These bands are attributed, on the basis of TD-DFT theoretical calculation for **10b**, **10d** and **11a**, to an admixture of ^{1}IL' transition centred in the cyclometalated ligand (L' = C^N) with metal to ligand (Pt → C^N) ^{1}ML'CT contribution, that is higher in complexes **10**. In **10d**, the low energy feature has mixed ^{1}ML'CT/^{1}IL' character, with some d(Pt)/π(C^N) → HC^N contribution. Moreover, it has been studied the solvatochromism for some complexes by performing the UV-vis absoption spectra in a more polar solvent, like acetonitrile. The characteristic low energy band exhibits a solvatochromic shift on increasing the polarity of the solvent (from CH_2Cl_2 to MeCN, Table 2.4), evidencing a charge transfer nature. For complexes **10b-c**, the solvatochromism observed is negative indicating that the ground state is more polar

than the excited state.[102] For complexes **11** the solvatochromism is positive in **11a** and negative in **11b**. It is worth to note that the position of the low energy band follows the order (from high to low energy) dfppy (**d**) > thpy (**a**) > pbt (**b**) > pq (**c**) for complexes **10**, whereas the change of the C^N ligand has very little effect on complexes **11**. As is shown in Figure 2.13a,b, the substitution of HC^N by dmso in the thpy and pbt complexes causes a blue shift in the low energy absorption. This fact is in accordance with the expected stabilization of the HOMO energy level due to the π-acceptor nature of the *S*-dmso ligand.

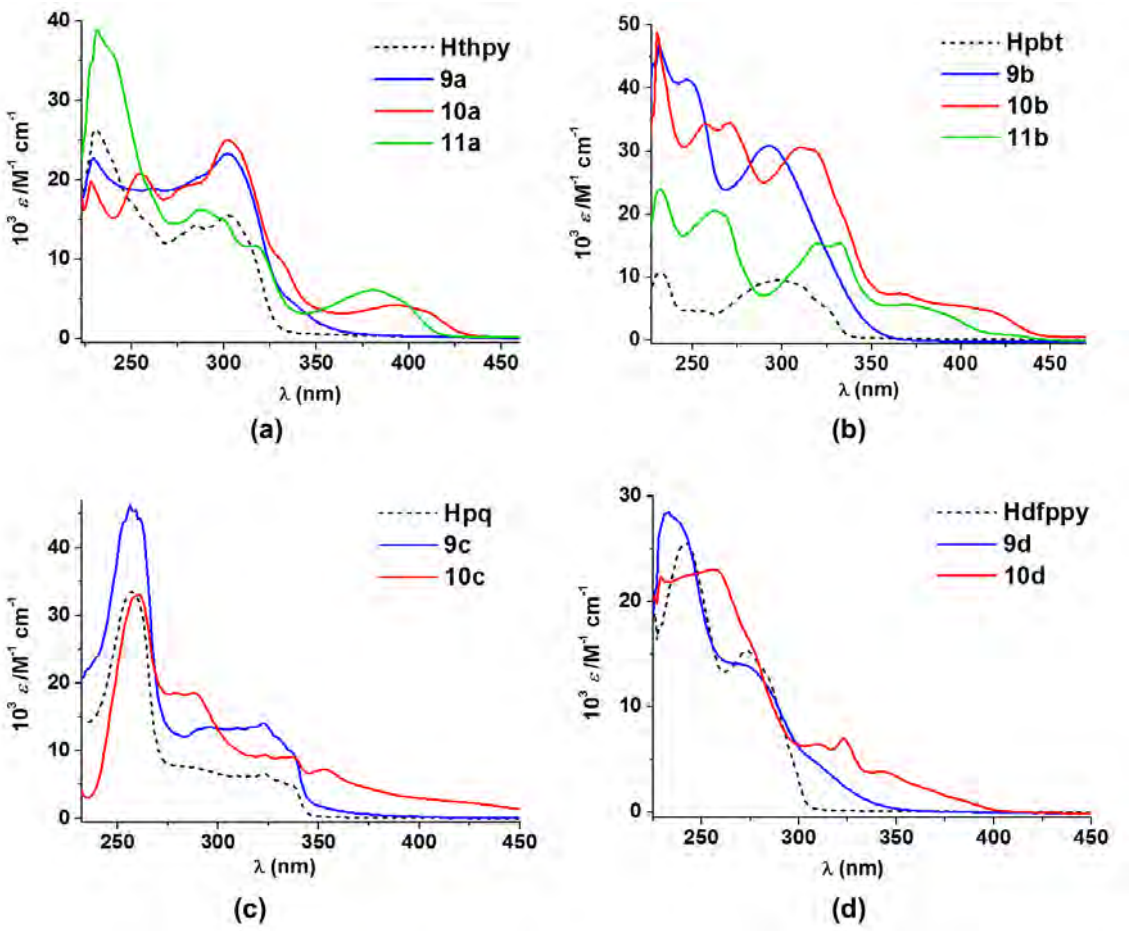

Figure 2.13. Absorption spectra of the series of complexes in CH_2Cl_2 (5×10^{-5} M) at 298 K (a) Hthpy ligand, **9a**, **10a**, **11a** (b) Hpbt ligand, **9b**, **10b**, **11b** (c) Hpq ligand, **9c**, **10c** and (d) Hdfppy ligand, **9d**, **10d**.

Table 2.4. Absorption data for complexes **9**, **10** and **11** in CH_2Cl_2 and MeCN 5×10^{-5} M solutions.

Compound	λ_{abs}/nm (10^3 ε/M^{-1} cm^{-1})
9a	230 (22.6), 262 (18.7), 284_{sh} (19.9), 302 (23.0), 340_{sh} (3.7) (*CH_2Cl_2*) 208 (18), 240 (13.6), 260 (12.5), 300 (15.9), 340 (1.6) (*MeCN*)
9b	231 (47.1), 248 (41.1), 292 (30.1) (*CH_2Cl_2*)[a] 227, 248, 254, 292 (*MeCN*)[b]
9c	258 (45.6), 295 (13.5), 322 (13.9), 338 (9.7) (*CH_2Cl_2*) 205 (69), 219 (53.5), 236 (45.3), 253 (52.0), 309 (5.1), 322 (7.1), 336 (1.4) (*MeCN*)
9d	235 (27.9), 275 (13.5), 312_{sh} (4.0) (*CH_2Cl_2*)
10a	228 (21.2), 255 (22.1), 279_{sh} (20.4), 302 (26.2), 330 (11.2), 392 (4.3), 410 (3.4) (*CH_2Cl_2*) 220 (14.7), 248 (18.4), 274 (17.8), 298 (23.6), 328_{sh} (9.2), 390 (3.3), 410 (2.8) (*MeCN*)
10b	230 (49.6), 257 (35.0), 270 (35.2), 309 (31.2), 320 (30.5), 335 (19.8), 366 (8.1), 397 (6.4), 420 (4.9) (*CH_2Cl_2*) 210 (49.5), 232_{sh} (30.5), 251 (20.2), 267 (23.1), 276 (21.5), 308 (20.0), 326_{sh} (15.1), 358 (3.8), 390 (2.7), 413 (1.9) (*MeCN*)
10c	237 (35), 287 (18.6), 330 (9.1), 355 (7.2), 430 (2.7) (*CH_2Cl_2*) 213 (48.8), 255 (53.5), 274 (26.7), 285 (25.3), 322 (10.6), 336 (10.6), 349 (8.0), 418 (1.9) (*MeCN*)
10d	255 (22), 310 (5.8), 323 (6.3), 345 (3.1), 380_{sh} (0.6) (*CH_2Cl_2*)
11a	231 (38.9), 240_{sh} (36.0), 260 (18.3), 288 (16.3), 300 (15.0), 318 (11.7), 381 (6.1), 398 (4.5) (*CH_2Cl_2*) 215 (20.1), 245 (19.53), 274 (13.0), 295 (15.7), 305 (15.1), 325 (12.2), 393 (5.5), 410 (4.7) (*MeCN*)
11b	231 (24), 261 (20.5), 268_{sh} (19.7), 319 (15.4), 332 (15.5), 370 (5.7), 390_{sh} (4.2), 430 (0.8) (*CH_2Cl_2*) 220 (27.3), 254 (15.9), 265 (18.2), 316 (11.5), 330 (11.3), 358 (4.6), 390 (3.5), 410 (2.7) (*MeCN*)

[a] Tail to 350 nm; [b] Saturated solution.

2.1.3.1 Emission spectroscopy

For comparative purposes, the emission data of all complexes in deoxygenated CH_2Cl_2 solutions are included in Table 2.5, while the solid state data are summarized in Table 2.6.

Complexes **9**, **10** and **11** exhibit long lived luminescence in degassed CH_2Cl_2 solutions with similar profiles in the range from 5×10^{-5} M to 10^{-3} M, thus excluding the formation of aggregates and/or excimers in this range. We note that for **9d**, the emission spectra was recorded in thf because in CH_2Cl_2 a weak emission due to a trace amount of the more emissive complex **10d** was always detected. Notwithstanding, **9d** is not emissive

in thf at 298 K. In the solid state, all complexes are emissive at room temperature and low temperature (77 K) except **11a** which emits only at 77 K.

Table 2.5. Photophysical data for **9-11** in CH_2Cl_2 or thf (**9d**) degassed solutions (5×10^{-5} M).

	T[a] (K)	λ_{em}/nm	ϕ/%[a]	τ/μs	k_r[b]/s^{-1}	K_{nr}[c]/s^{-1}
9a	298	490, 520, 560$_{sh}$ [d]	1.2	0.9	1.3×10^4	1.1×10^6
	77	506, 550, 600$_{sh}$ [d]		234.3 (39%), 29.9 (41%)		
9b	298	370, 540 [e]	1.6 (370) 1.4 (540)	0.12 (53%), 0.02 (47%) (370) 2 (540)	2.2×10^5 7×10^3	1.3×10^7 4.9×10^5
	77	475, 515, 560 [d]		7.5		
9c	298	485, 518, 560$_{sh}$	3.7	0.6 (32%), 3.3 (68%)	1.5×10^4	4.0×10^5
	77	475, 510, 550, 600$_{sh}$		184 (72%), 773 (28%)		
10^{-4} M	298	485, 550, 580				
	77	485, 520, 560				
9d	77 [f]	450		91.12		
10a	298	555, 575, 600, 630$_{sh}$ [d]	1	0.9	1.1×10^4	1.1×10^6
	77	550, 570, 595, 620$_{sh}$, 650$_{sh}$ [d]		31		
10b	298	530, 570, 615$_{sh}$ [d]	4.4	1.1	4×10^4	8.7×10^5
	77	515, 560, 600, 675$_{sh}$ [d]		18		
10c	298	550, 580 [d]	9.7	1.1	8.8×10^4	8.2×10^5
	77	548, 590 [d]		20.4		
10d	298	465$_{max}$, 495$_{max}$, 530 [d]	3.5	1.4	2.5×10^4	6.9×10^5
	77	465$_{max}$, 475, 530 [d]		25.2		
11a	298	435, 550, 595 [d]	0.7 (435) 1.3 (550)	5.2×10^{-3} (59%), 0.11 (41%) (435) 8.5 (550)	1.5×10^5 1.5×10^3	2.1×10^7 1.2×10^5
	77	545, 590 [d]		8.5		
11b	298	530, 570, 610$_{sh}$ [d]	2.9	1.1	2.6×10^4	8.8×10^5
	77	525, 570, 610 [d]		19.4		

[a] Absolute quantum yields determined by the absolute method using an integrated sphere. [b] $k_r = \phi/\tau_{average}$. [c] $k_{nr} = (1 - \phi)/\tau_{average}$. [d] Identical profile at 10^{-4} and 10^{-3} M. [e] The band at 370 nm disappears in concentrated solutions (10^{-3} M) due to self absorption. [f] Non emissive at 298 K.

In fluid CH_2Cl_2 solution, complexes **9a** and **9c** show long-lived low energy structured emissions (490 nm, τ 0.9 μs **9a**; 485 nm, τ 0.6 (32 %), 3.3 (68 %) μs **9c**) (Figure 2.14a), whereas **9b**, bearing the Hpbt ligand, exhibits high-energy fluorescence located on the 2-phenylbenzothiazole Hpbt group [370 nm, τ 120 ns (53 %), 20 ns (47 %)] and a broad low energy phosphorescence centered at 540 nm (τ 2μs) (Figure 2.14a). In **9b**, the presence of dual emission suggests that the intersystem crossing from singlet to triplet state is not very effective in this complex at 298 K.[4, 103] Upon increasing the concentration

to 10^{-3} M, the fluorescence band at 370 nm disappears and just phosphorescence is observed.

As noted before, [Pt(Hdfppy)$_2$(C_6F_5)$_2$] **9d** is not emissive in fluid thf solution. The quenching of the luminescence for this complex at room temperature can be tentatively attributed to a significant structural distortion of one of the dfppy ligands in the T_1 state (see DFT calculations), which likely favours the nonradiative deactivation. Nevertheless, thermal quenching of the emission in solution at 298 K could also be caused by interactions with solvent molecules.[14a]

As is shown in Figure 2.14b, in frozen glasses at 77 K, complexes **9a-c** exhibit highly structured emissions (475-506 nm), whereas **9d** shows a broad band blue shifted (450 nm) in relation to the compounds **9a-c**. On the basis of theoretical calculations of **9a**, **9c** and **9d** (see below), the emissions are attributed to a mixture of metal to ligand ^{3}MLCT (Pt → HC^N) and ^{3}IL (HC^N) excited states with different contributions.

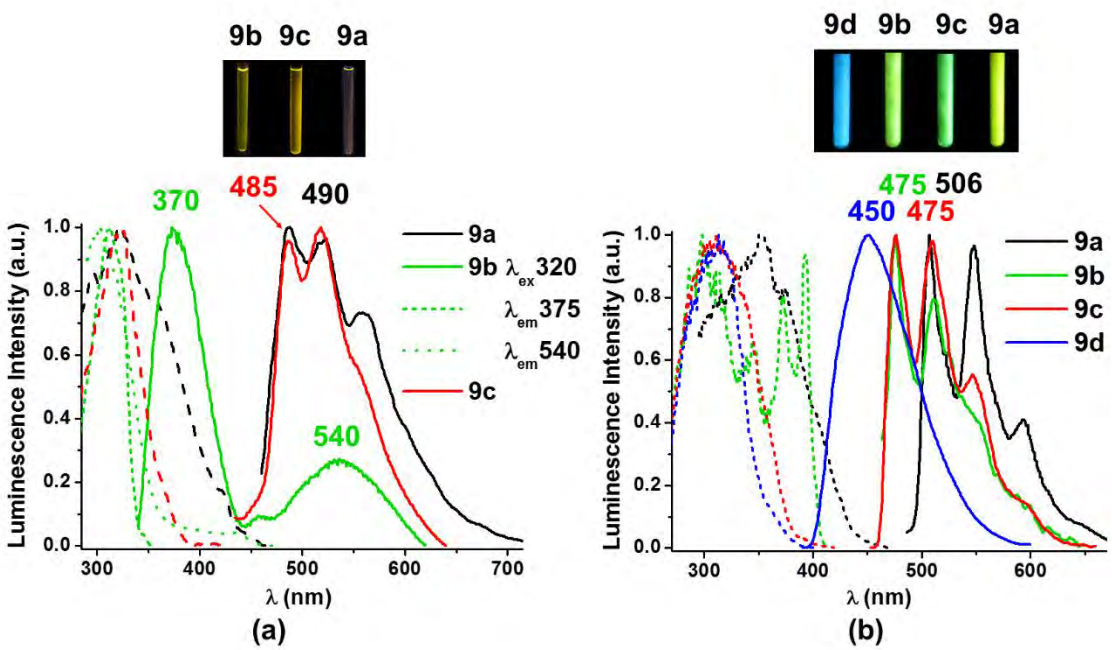

Figure 2.14. Normalized excitation (dotted lines) and emission (solid lines) spectra of (a) **9a-c** in CH_2Cl_2 5 × 10^{-5} M at 298 K and (b) **9a-c** in CH_2Cl_2 and **9d** in thf 5 × 10^{-5} M solutions at 77 K.

In the solid state, complexes **9** show broad emission profiles (460-565 nm) which become slightly structured at 77 K (Figure 2.15). The emission maxima are red-shifted in relation to those observed in glassy media. This fact is not unusual and could be attributed to the solid state effects.[46, 104] Emission lifetimes are in the order of microseconds (4.3–102.8 μs) at 298 K, increasing at 77 K (30.5 – 203.9 μs) (Table 2.6). All of these

characteristics and the large Stokes shifts are indicative of phosphorescence emissions from excited states of an essentially intraligand ^{3}IL character.

Table 2.6. Photophysical data for complexes **9-11** in the solid state.

	T[a] (K)	λ_{em}/nm	ϕ/%[a]	τ/µs	k_r[b]/s^{-1}	k_{nr}[c]/s^{-1}
9a	298	565, 605 (Ground solid) 538 (Crystals) [d]	12.2	20.0	6.1×10^3	4.4×10^4
	77	520, 555, 600 (Ground solid) 520, 545 (Crystals) [d]		83 (75%), 294 (25%)		
9b	298	516	14	102.8	1.4×10^3	8.4×10^3
	77	480, 510_{max}, 550_{sh}		203.9 (510)		
9c	298	560, 595 (Ground solid) 485, 515, 555 (Crystals) [d]	3.6	12.8	4.9×10^3	7.3×10^4
	77	560, 600 (Ground solid) 485, 525, 570 (Crystals) [d]		33.2 (76%), 538 (24%)		
9d	298	460	23	4.3	5.3×10^4	1.8×10^5
	77	430, 455_{max}, 480, 500_{sh}		30.5		
10a	298	550, 570, 600_{max}, 620_{sh}, 650_{sh}	5.1	15.3 (550); 16.3 (600)	3.3×10^3	6.2×10^4
	77	548, 560_{max}, 580, 600, 650_{sh}		16.9		
10b	298	530, 570_{max}, 620	16.5	12.4 (530); 10.8 (570)	1.5×10^4	7.7×10^4
	77	525_{max}, 540, 570_{max}, 620		10.3 (525); 18.0 (570)		
10c	298	550, 580_{max}, 625	1.1	9.2 (580)	1.2×10^4	1.1×10^5
	77	555_{max}, 600		14.9		
10d	298	470, 500_{max}, 530	16.3	12.1	1.3×10^4	6.9×10^4
	77	470_{max}, 500_{max}, 540		18.1		
11a	77 [e]	595, 615, 650		64.1		
11b	298	538, 580, 630_{sh}	2.5	12.4	2.0×10^3	7.9×10^4
	77	545, 580, 630		26.0		

[a] Absolute quantum yields determined by the absolute method using an integrated sphere. [b] $k_r = \phi/\tau_{average}$. [c] $k_{nr} = (1 - \phi)/\tau_{average}$. [d] Crystals obtained from CH_2Cl_2/*n*-hexane. [e] Non emissive at 298 K.

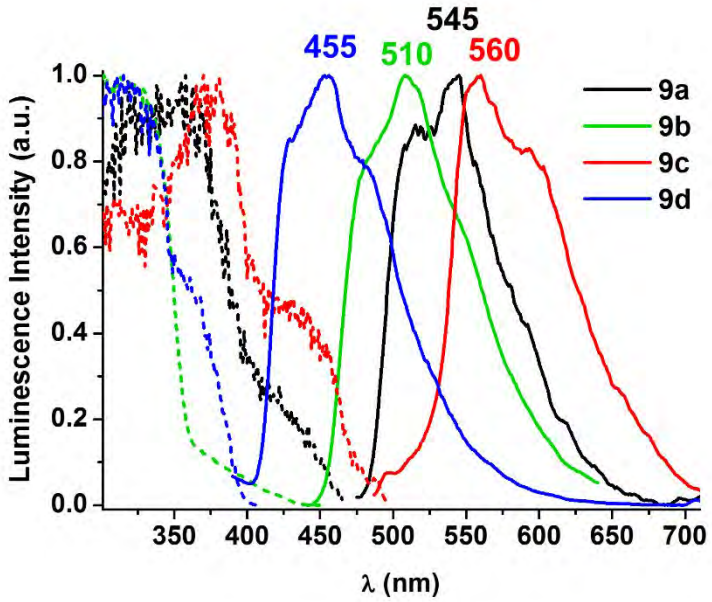

Figure 2.15. Normalized excitation and emission spectra of **9a-d** in the solid state at 77 K.

It should be noted that, for **9a** and **9c**, the shape of the emission band depends on the crystallization conditions. As illustrations, the emission profiles of different solid samples of **9a** or **9c** at 298 K (bulk material, ground solid and crystals obtained from CH_2Cl_2/*n*-hexane) are shown in Figure 2.16.

For **9a**, the as-obtained white solid shows an orange emission with two overlapped structured bands with peak maxima at 520 and 560 nm, respectively (represented by a black line in Figure 2.16a). The excitation spectra monitoring on both maxima are different, suggesting the presence of at least two emitting luminophores, likely associated to conformational isomerism of the two bulky HC^N coordinated ligands in the rigid media. When the bulk material is finely ground and dried in vacuum, the high energy peak at 520 nm essentially disappears, exhibiting only the structured band with a maximum at 560 nm (**9a**-ground, red line). However, the few white crystals of **9a** obtained in a mixture of CH_2Cl_2/*n*-hexane, display a yellow emission with a broad profile centered at 530 nm (Figure 2.16a, blue line). In **9c**, the as-obtained solid and the ground solid have the same emission and excitation spectra, showing a slightly structured band at 560 nm. However, crystals obtained in CH_2Cl_2/*n*-hexane display a blue shifted structured band (485 nm) (Figure 2.16b, blue line). This could be attributed, as for **9a**, to a conformational isomerism of the HC^N ligands. It is reasonable to think that the two

bulky coordinated N-ligands could generate different conformational isomers, as has been previously described in other systems.[38a, 45a, 105]

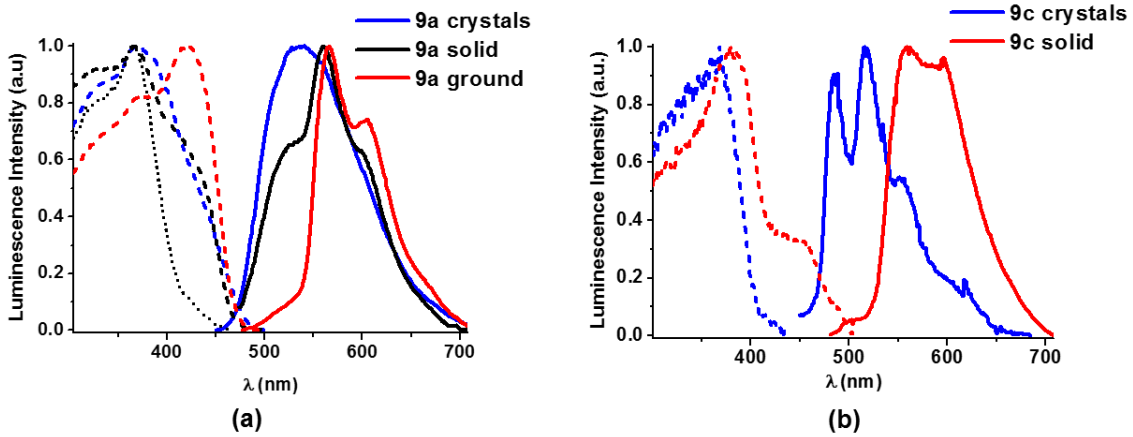

Figure 2.16. Normalized excitation and emission spectra of different samples in the solid state at 298 K of (a) **9a** and (b) **9c** (λ_{ex} 365 nm).

The cyclometalated complexes **10a-d** exhibit vibronically structured spectra in all media with discrete quantum yields (ϕ 5.1-16.5 % solid; 1-9.7 %, CH_2Cl_2) (Figures 2.17 and A2.4, Tables 2.5 and 2.6). The emission profiles and the long-lived lifetimes are characteristic of excited states having mixed ^{3}IL'/^{3}ML'CT character, located on the cyclometalated Pt(C^N) unit, as confirmed by theoretical calculations (see below). The emission maxima are, in general, red-shifted in relation to the bis-(HC^N) derivatives **9** due to the formation of the Pt-C bond. For example, in frozen CH_2Cl_2: 550 **10a** *vs* 506 **9a**; 515 **10b** *vs* 475 **9b**; 548 **10c** *vs* 475 **9c**. Besides, the emission depends on the cyclometalated ligand, following the order **10d** (dfppy) > **10b** (pbt) > **10c** (pq) ~ **10a** (thpy) from more to less energetic in all media. The bathochromic shift observed for example for the pbt derivative **10b** compared with the dfppy **10d** is in line with the lower energy of the π* orbital of the pbt in relation to that of the dfppy.

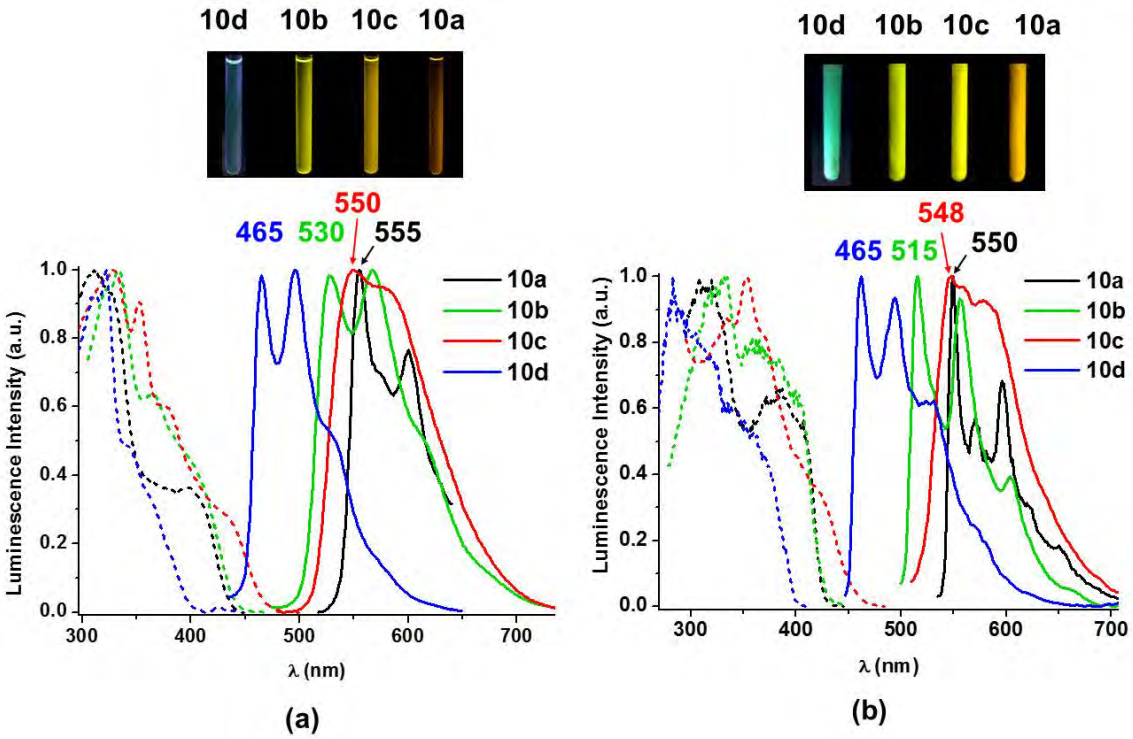

Figure 2.17. Normalized excitation and emission spectra of complexes **10a-d** in CH_2Cl_2 5 × 10^{-5} M at (a) 298 K and (b) 77 K.

The emissive properties of the dmso-complexes **11**, [Pt(C^N)(C_6F_5)(dmso)] (C^N = thpy **11a**, pbt **11b**), have also been studied and compared with their precursors [Pt(C^N)(HC^N)(C_6F_5)] (C^N = thpy **10a**, pbt **10b**). It has been observed that the substitution of the bulky ligands in **10a**,**b** for the small dmso ligand in **11a**,**b** has a negative impact on their luminescent properties. In the solid state, **11a** is not emissive at 298 K while complex **11b**, with the pbt cyclometalated ligand, exhibits a yellow-orange emission (538 nm, 298 K; 545 nm, 77 K) with a remarkable decreasing in the quantum yield value in relation to **10b** (ϕ 2.5 % **11b** *vs* 16.5 % **10b**). The quenching of the luminescence of **11a** at room temperature might be attributed to an "aggregation quenching effect" associated to the presence of close π···π intermolecular contacts between the planar cyclometalated thpy units, as observed in the crystal packing of this complex previously commented in Figure 2.11.[106] Indeed, not similar π···π contacts are found in the crystal packing of **11b** (Figure 2.12). Upon cooling at 77 K, both complexes display intense vibronically structured emissions (Figure 2.18) with long lifetimes (64.1 μs **11a**, 26.0 μs **11b**). These characteristics are indicative of an emitting state with remarkable ^{3}IL' (C^N) character, as was also supported by theoretical calculations on **11a** (see below). According to this assignment, the emission maximum for the thpy-compound **11a** is batochromically shifted in relation to the pbt-compound **11b** (595 nm

11a *vs* 545 **11b**, in solid state at 77 K; 545 nm **11a** *vs* 525 nm **11b**, CH_2Cl_2 at 77 K) due to the smaller energetic gap associated to the thpy ligand.

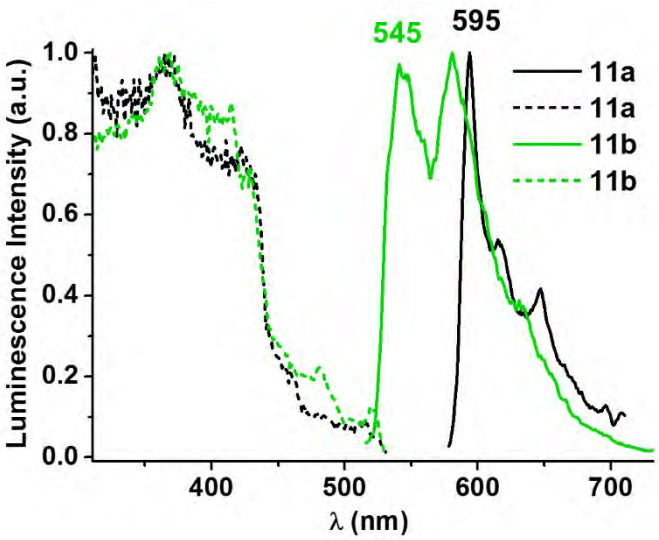

Figure 2.18. Normalized excitation and emission spectra of **11a** and **11b** in the solid state at 77 K.

In frozen degassed CH_2Cl_2 solution, both **11a** and **11b** exhibit similar structured emissions to those of **10a** and **10b** (Figure 2.19b). However, in fluid CH_2Cl_2 solution while **11b** only shows a phosphorescence band at 530 nm similar to **10b**, **11a** exhibits a dual emission: a low band due to phosphorescence (550, 595 nm, τ 8.5 μs), together with an unstructured band at a high energy [435 nm, τ 5.2 (59 %), 110 (41 %) ns] (Figure 2.19a). Due to the small Stokes shift, broad shape and the fact that no quenching was observed upon exposure to air, the band at 435 nm was tentatively ascribed to a fluorescent emission of excimeric origin, as the fluorescence of the free Hthpy ligand in CH_2Cl_2 has a λ_{max} of 358 nm. Besides, the presence of fluorescent emission in **11a** indicates that for this complex, the intersystem crossing is not very effective. This behaviour could be attributed to the weakness of the Pt-C_{thpy} metalated bond.

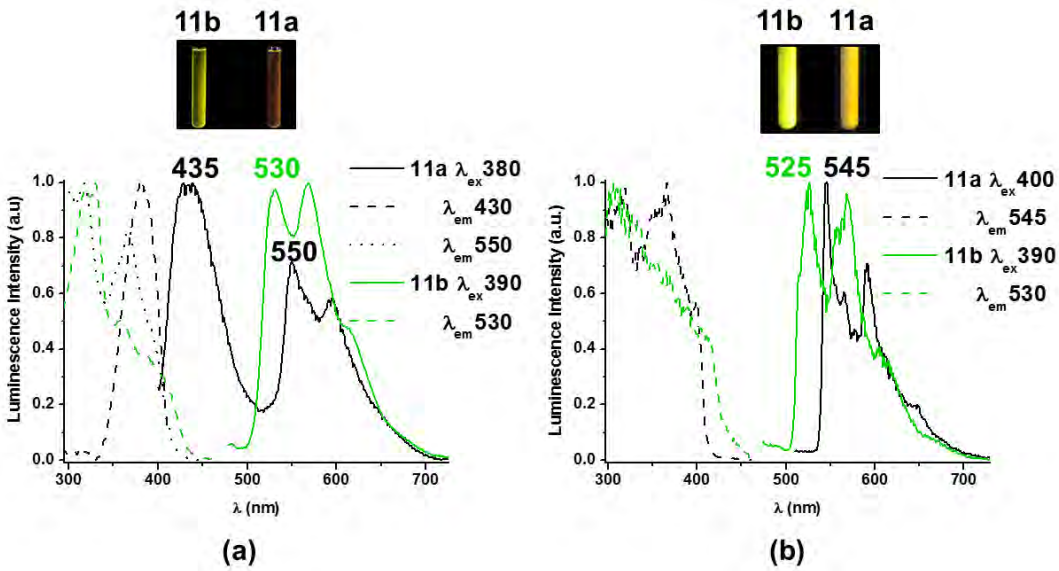

Figure 2.19. Normalized excitation and emission spectra of **11a** and **11b** in CH_2Cl_2 5 × 10^{-5} M solutions at (a) 298 K and (b) 77 K.

2.1.4 Theoretical calculations

Density functional theory (DFT) and time-dependent DFT (TD-DFT) calculations have been performed for complexes **9a**, **9c**, **9d**, **10b**, **10d** and **11a** at the B3LYP/(6-31G**+LANL2DZ) level of theory. The effect of the solvent (CH_2Cl_2) was taken into account using the polarized continuum model (PCM) approach. The geometries of the complexes were fully optimized without imposing any symmetry constraints. Bond distances and angles for the optimized structures (S_0 and T_1) are detailed in Table A2.1 and are generally rather consistent with those obtained by X-ray. Contour plots of frontier orbitals (S_0) for the six calculated complexes in CH_2Cl_2 are displayed in Figures A2.5-A2.10 and the molecular orbital compositions given in Table A2.2. Selected singlets and triplets excitations calculated by TD-DFT at their optimized S_0 geometry in CH_2Cl_2 with detailed descriptions of absorption wavelength, oscillator strength and transition assignments are collected in Table A2.3. For comparison, the calculated singlet excitations and the corresponding experimental absorption spectra are shown in Figure 2.20.

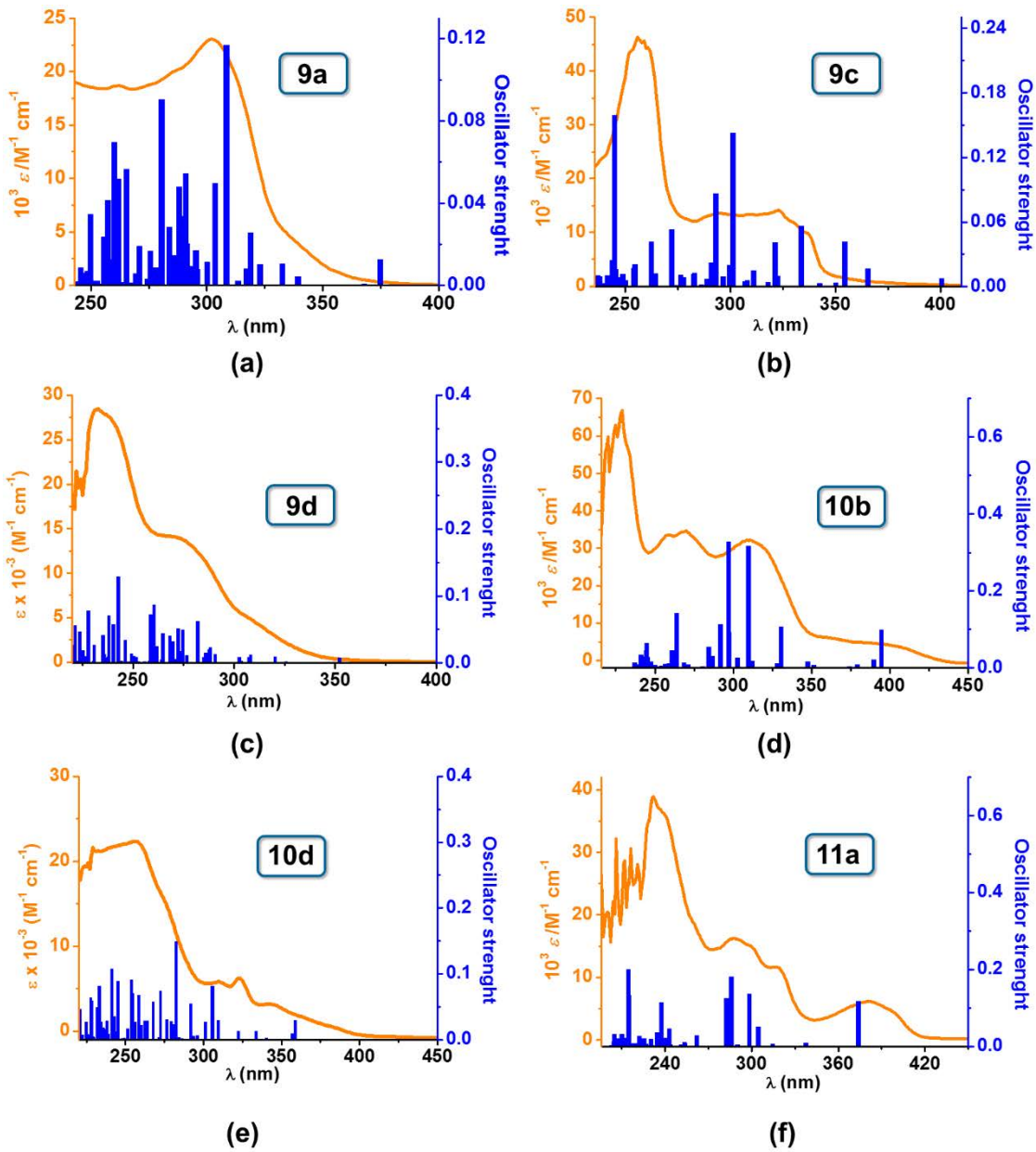

Figure 2.20. Calculated stick absorption spectra of **9a**, **9c**, **9d**, **10b**, **10d** and **11a** compounds in CH_2Cl_2 compared with the experimental absorption spectra.

According to the X-ray structures for the complexes **9a**, **9c** and **9d** in their optimized S_0 geometry, the HC^N ligands are also found mutually *trans*-oriented. The calculated pseudoaxial Pt···H_{ortho} separations are slightly longer than those found in the structure for **9d** (3.065, 3.064 Å calculated *vs* 2.982, 2.897 Å X-ray), whereas they are shorter for **9a** (2.895 Å calculated *vs* 3.044 Å X-ray) and **9c** (2.677, 2.677 Å calculated *vs* 2.773, 2.759 Å X-ray).

For these complexes, the low lying target orbitals from LUMO to LUMO+3 are distributed over both HC^N ligands, mostly in the acceptor pyridine (**9a**, **9d**) or quinoline

(**9c**) groups (see Figures A2.5-A2.7, Table A2.2). The HOMOs of the three complexes are mainly composed of the dz^2 Pt orbital (73 % **9a**, 82 % **9c**, **9d**) with some HC^N (21 % **9a**, 10% **9c**, **9d**) contribution. Moreover, in the corresponding HOMO-1 orbitals there are also a quite large contribution from both C_6F_5 ligands (56-65 %), in addition to the Pt contribution (30-33 %).

A schematic representation of some selected energy levels, transitions and contours of the commented frontier orbitals is displayed in Figure 2.21. The lowest calculated singlet excitation (S_1) in these complexes **9** (375 **9a**, 401 **9c** and 352 nm **9d**) is mainly contributed from the HOMO to LUMO transition, being attributed to ^{1}MLCT (Pt→HC^N) with some intraligand ^{1}IL (HC^N) contribution, larger in **9a**. The next close low-energy transitions S_3 and S_4 (S_2 has a very low oscillator strength, so it has been discarded) are associated with transitions involving the HOMO-1 and the LUMO and LUMO+1 (Figure 2.21) having characteristics of mixed ^{1}MLCT/^{1}L''LCT (Pt→HC^N/C_6F_5→HC^N) nature (Table A2.3) (L'' = C_6F_5). The most intense singlet excitations correspond to transitions largely of ^{1}IL (HC^N) with some ^{1}L''LCT (C_6F_5→HC^N) in **9a** [308 nm (S_9)] and with some ^{1}MLCT in **9c** [334 nm (S_7)] and with ^{1}MLCT/^{1}ML''CT (S_5)/^{1}L''LCT/^{1}MLCT (S_6) in **9d**.

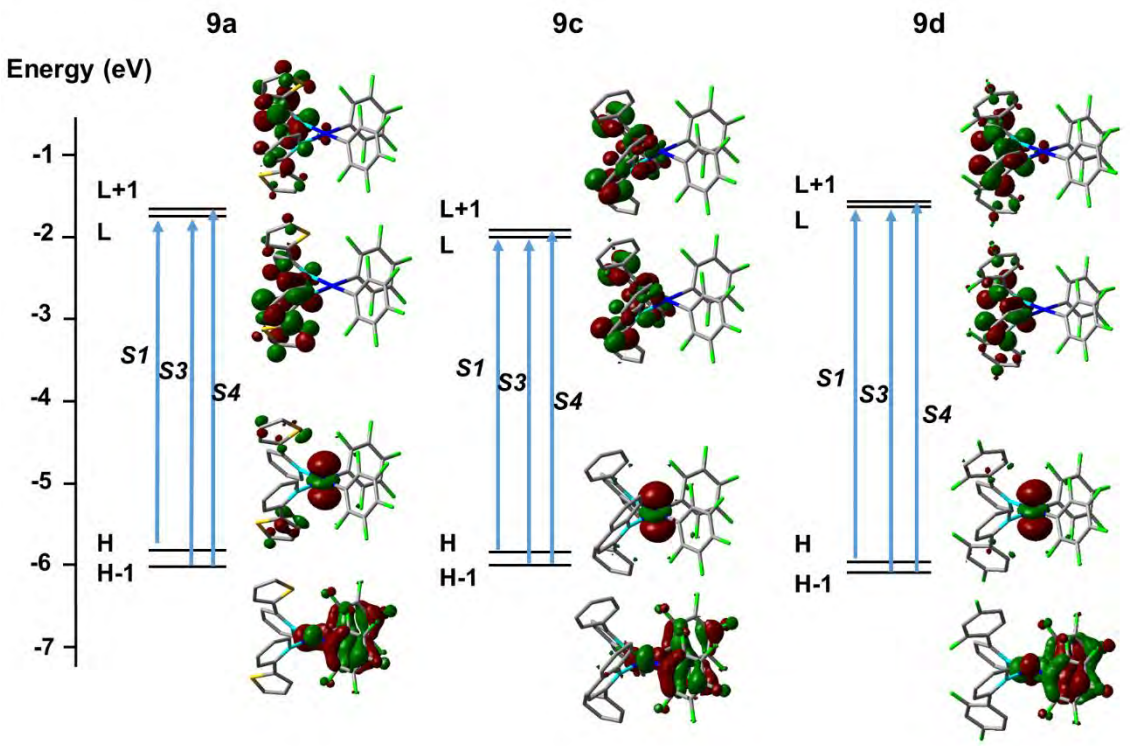

Figure 2.21. Schematic representation of selected energy levels and frontier orbitals of **9a**, **9c** and **9d** in their S_0 state.

For the cyclometalated complexes **10b** and **10d**, the Pt···H (HC^N) distances in the optimized S_0 and T_1 geometries are longer than those obtained by X-ray diffraction (Table A2.1).

The schematic representation of selected energy levels, transitions and contours of the some frontier orbitals is displayed in Figure 2.22. For these complexes, the two calculated low-lying singlet excitations ($S_0 \rightarrow S_1$ and $S_0 \rightarrow S_2$) (359, 357 **10d** < 395, 390 nm **10b**) are in good agreement with the available experimental data in CH_2Cl_2 solution (380 **10d** < 420 nm **10b**) (Figure 2.20d-f, Table A2.3). These excitations primarily arise from HOMO and HOMO-1 to LUMO transitions (contributions: 84 %, 87 % **10b**; 90 %, 95 % **10d**). As is shown in Figure 2.22 and Table A2.2, the HOMOs have a mixed π(C^N) metalated ligand (pbt 63 % **10b**; dfppy 60 % **10d**) and d_π(Pt) (35 % **10b**, 38% **10d**) character, whereas the HOMOs-1 have predominantly platinum (dz^2) character (Pt 87 % **10b**; 89 % **10d**). However, although the LUMOs are primarily formed by π* orbitals of the cyclometalated ligands (pbt 91 % **10b**; dfppy 74 % **10d**), **10d** has also some contribution from the pendant non metalated Hdfppy (21 %). Therefore, the low-energy feature has mixed ^{1}IL'/^{1}ML'CT character (L' = cyclometalated ligand) with some ^{1}[(M+L')→L] d(Pt)/π(C^N)→HC^N contribution in the dfppy derivative **10d**.

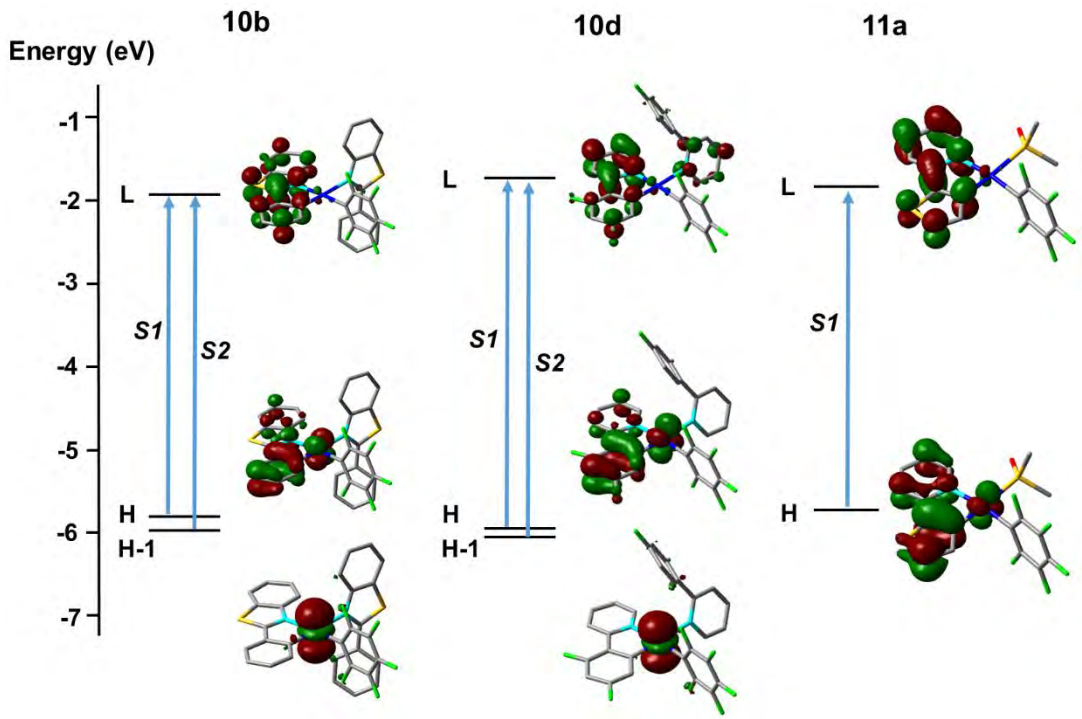

Figure 2.22. Schematic representation of selected energy levels and frontier orbitals of **10b**, **10d** and **11a** in their S_0 states.

In contrast with **10b** and **10d**, for the solvate dmso complex **11a**, the calculated singlet excitation S_2 is well separated from S_1 (S_1 374, S_2 338 nm) and it is also very weak. In this complex, the lowest energy absorption ($S_0 \rightarrow S_1$) compares well with the experimental value (398 nm), and it is derived primarily from the HOMO to LUMO transition. The HOMO has a mixed thpy (85 %) and d_π(Pt) (14 %) contribution and the LUMO is predominantly on the π^* cyclometalated ligand (thpy 89 %). Thus, the low energy absorption has ligand center character (^{1}IL') with minor ^{1}ML'CT contribution (Figure 2.22).

We have also investigated the emitting behaviour of these complexes, analysing their optimized lowest energy triplet state (T_1). Geometry optimization was carried out by means of spin-unrestricted DFT calculations (U-B3LYP) (Table A2.3). The spin density plots are shown in Figures 2.23 and 2.24. The calculated electronic energies relative to the S_0 state at the optimized T_1 state (629 **9a**, 568 **9c**, 625 **10b**, 518 **10d**, 669 nm **11a**) are red-shifted from the experimental values (490 **9a**, 485 **9c**, 530 **10b**, 465 **10d**, 550 nm **11a**, CH_2Cl_2) due to insufficient description of the charge-transfer transitions using DFT calculations. Similar discrepancies have been previously reported.[107] However, they follow the tendency observed in the experimental data (**9a** < **9c**; **11a** < **10b** < **10d**).

As is observed in the Figure 2.23a, the calculated spin density in the optimized T_1 state of the selected complexes **9** (**9a**,**c**,**d**) is mainly located on one of the HC^N ligands and the platinum. Thus, the luminescence is ascribed to a mixed ^{3}IL/^{3}MLCT (Pt→HC^N) excited state. It is worth to mention that, in the complex with two Hdfppy ligands **9d**, the geometry optimization of the T_1 reveals a notable structural distortion relative to the S_0, causing a remarkable planarization of one of the Hdfppy ligands with a concomitant shortening of the Pt-H(*pseudoaxial*) distance (by 0.31Å) (Figure 2.23b). We think that this strong distortion could be behind the severe quenching of the luminescence for this complex in fluid solution.

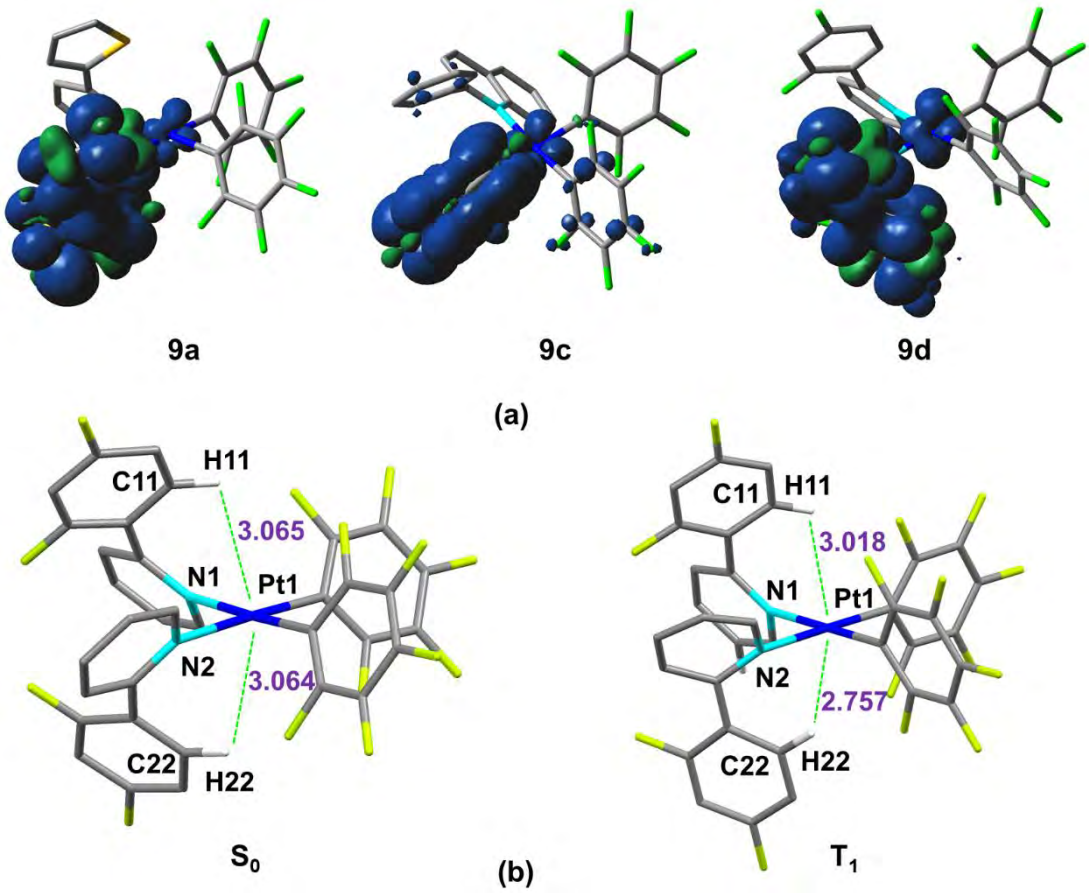

Figure 2.23. (a) Spin density plots of the $[Pt(HC^{\wedge}N)_2(C_6F_5)_2]$ complexes (**9a**, **9c** and **9d**). (b) Optimized structures of S_0 and T_1 states of **9d** derivative.

For the cyclometalated complexes **10b**, **10d** and **11a**, the spin density plots at the optimized T_1 state (Figure 2.24) are similar, being located on the C^N unit and platinum. The calculated spin density over the platinum is higher in complexes **10** (0.186 **10b**, 0.179 **10a**) than in the dmso complex **11a** (0.116). These calculations support a mixed ^{3}IL' (C^N)/^{3}ML'CT origin for their emission, with lower ^{3}ML'CT contribution in **11a**. The lowest contribution of the Pt in **11a**, which could reduce the effective intersystem crossing S_1-T_1, thus explaining the appearance of fluorescence in CH_2Cl_2 at 298 K. The remarkable redshift from **10d** to **10b**, both in the calculated absorption and emission spectra, results from the substantial decrease HOMO-LUMO splitting, associated to the strong electron-withdrawing nature of the benzothiazole group.[108]

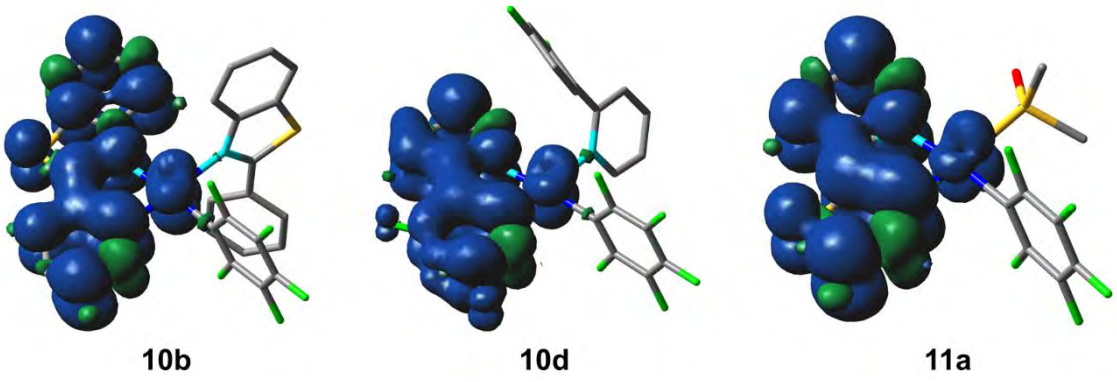

Figure 2.24. Spin density plots of the cyclometalated complexes **10b**, **10d** and **11a**.

2.1.5 Biological assays

Platinum-based complexes are one of the highest success in the study of inorganic complexes with medicinal properties. The discovery of cisplatin, cis-$[Pt(NH_3)_2Cl_2]$ antitumor activity in 1960s by Rosenberg *et al.*,[109] which effectively treats testicular, ovarian, head, neck and lung cancer,[52c] increased the interest in the development of other cytotoxic platinum-based compounds. However, only two platinum compounds besides cisplatin (carboplatin and oxaliplatin, Figure 2.25)[110] are used worldwide for treating cancer and, even being introduced to the medicinal market almost 40 years ago, they are nowadays the most widely used drugs in chemotherapy.[110a]

Their mechanism of action relies on binding DNA (preferentially with the N7 atom of purine nucleobases) forming different Pt-DNA adducts, which causes the inhibition of DNA replication and transcription leading to the cell death process known as apoptosis (Figure 2.26).[111]

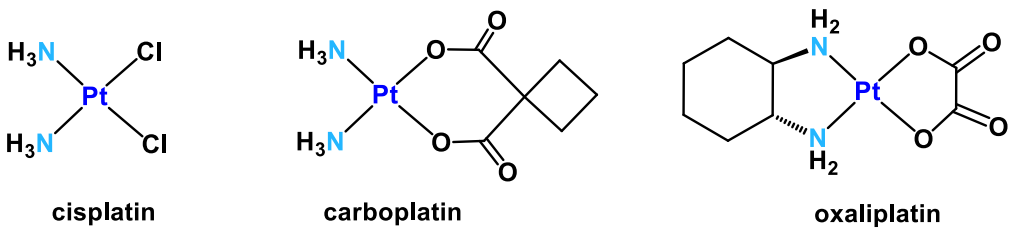

Figure 2.25. Worldwide used anticancer drugs: cisplatin, carboplatin and oxaliplatin.

However, their acquired resistance, unpleasant side effects[112] and the desire of providing broad-spectrum antitumor drugs have inspired the development of other types of platinum-based complexes with different mechanisms of action.[52c, 110a, 111, 113]

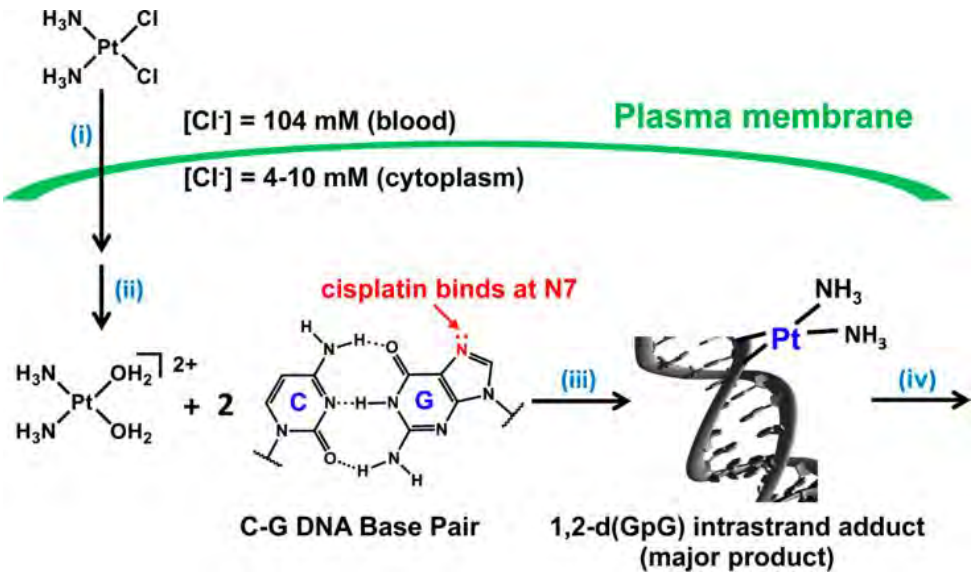

Figure 2.26. Four steps of the mechanism of cisplatin and, by extension, related platinum anticancer drugs. (i) Cellular uptake, (ii) aquation/activation, (iii) DNA binding, and (iv) cellular processing of DNA lesions leading to apoptosis.[110a]

In this context, Pt(II) complexes with cyclometalated ligands have shown promising properties as an antineoplastic agents, exhibiting high cytotoxicity in cisplatin-resistant cancer models and have displayed promising *in vivo* activity. Therefore, they have attracted tremendous research interest in the last years.[8, 30b, 113c, 114] These complexes contain a strong σ(C-Pt) bond, which improve their stability against biological reduction and ligand exchange reactions.[115] Furthermore, the presence of aromatic rings favors their intercalation between base pairs of DNA by non-covalent π···π stacking interactions.[116] Finally, the introduction of auxiliary labile ligands to the platinum sphere could led to a mixed action, through a covalent interaction with DNA (as for cisplatin).[117] All these factors allow tuning the cytotoxic activity and the photophysical properties of these derivatives by changing either the cyclometalated ligands or the ancillary group taking into account that small modifications can induce big changes in the biological effect. The cytotoxicity of several platinum compounds containing bidentate (C^N) or terdentate (C^N^N) and (C^N^S) ligands have been studied.[30b, 114d, 118]

On the other hand, it should be mentioned that angiogenesis is the process through which new blood vessels are formed from pre-existing vessels and that it is a crucial step for the formation, progression and metastasis of numerous types of cancer. Therefore, platinum complexes with antiangiogenic properties are a great alternative to more classic platinum compounds similar to cisplatin for treating cancer. J. Ruiz and V. Marchán have

recently studied a novel series of cyclometalated platinum complexes, which display dual antitumor and antiangiogenic activity.[114b, 114f]

Moreover, cyclometalated Pt(II) complexes of polypyridyl ligands display excellent photophysical properties. In many cases, tunable phosphorescence emission with high luminescence quantum yields, photostability and long excited-state lifetimes have been achieved by varying the electronic nature of the C^N ligand. Consequently, these complexes are also gaining attention as luminescent labels for bioimaging.[13g, 13i, 13l, 30c] These type of complexes provide advantage over currently available imagen agents (organic dyes, fluorophore-conjugated antibodies or fluorescent proteins).[119] Their long lifetimes (μs to ms) permit the discrimination from background fluorescence of biological media through spectral or temporal resolution and their square-planar configuration makes its luminescence highly sensitive to very small environmental changes, which is why they have been used as DNA sensors too.[120] Finally, the photostability of these complexes allows the continuous monitoring of biological events by fluorescence spectroscopy and microscopy.

In this context we considered of interest to establish a collaboration with the research team "Lung Cancer and Respiratory Diseases" led by Jose García Pichel in the CIBIR centre, in order to study the biological properties of selected complexes.

In particular, we decided to evaluate the biological activity of the dmso compounds **11a** and **11b**. The cytotoxicity of complexes **11a** and **11b** described in this Memory, together with the compound **11-ppy**, previously prepared by the group,[49b] were analysed towards human lung cancer (A549) and non-tumorigenic bronchial epithelial (NL20) cells, by the MTS assay. Furthermore, as these complexes are strongly emissive, their cellular localization was investigated by fluorescence microscopy.

First, in order to assess the effect of dmso and cellular medium on the activity of complexes **11a**, **11b** and **11-ppy**, we studied their stability in these media. The stability of the complexes in dmso was monitored by ^{1}H NMR in dmso-d^6 solutions, observing that the compounds show identical spectra after 15 days at 298 K.

On the other hand, the compounds were dissolved in dmso (16 mM **11a**, **11-ppy**; 8 mM **11b**) and their solution behaviour in cellular medium was analysed through UV-vis absorption spectroscopy. The experimental conditions to record adequate absorption

spectra are in the range to those employed for activity investigations (5×10^{-5} M in RPMI 1640 medium as used in MTS assays, see Experimental Section), maintaining very low dmso content (≤ 1%). As illustrated in Figure 2.27, which shows the spectra for **11a**, **11b** and **11-ppy** in the biological medium, the three platinum complexes manifest a remarkable stability with the time with no evidence of changes even over a period of 96 h, time sufficiently long for them to reach their biological target (72 h).

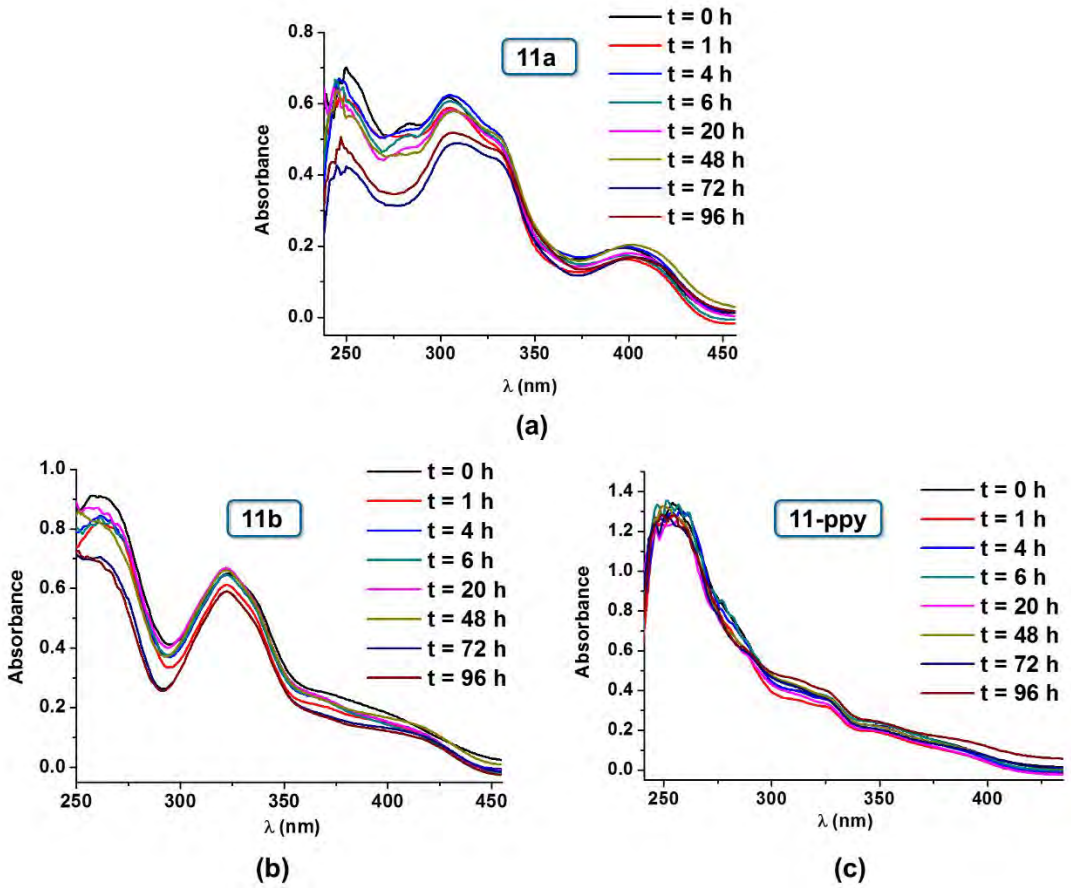

Figure 2.27. UV-vis absorption spectra of (a) **11a**, (b) **11b** and (c) **11-ppy** in a concentration of 5×10^{-5} M recorded in dmso (<1%)-cellular medium after been kept at room temperature since 0 h to 96 h (intervals in legends).

2.1.5.1 Cytotoxicity tests (MTS assay)

The *in vitro* anti-cancer properties of compounds **11a**, **11b** and **11-ppy** towards human lung cell lines A549 (tumoral adenocarcinomic alveolar basal epithelial cells) and NL20 (non-tumorigenic immortalized bronchial epithelial cells) were examined, by means of (3-(4,5-dimethylthiazol-2-yl)-5-(3-carboxymethoxyphenyl)-2-(4-sulfophenyl)-2H-tetrazolium) hydrolysis method (MTS assay). The cytotoxicity of cisplatin was also

examined as a reference. The IC_{50} values were determined after cellular exposure to compounds for 72h (Table 2.7 and Figure 2.28). The cisplatin IC_{50} dose towards A549 cells (6.45 μM) was similar to that recently reported.[121] Complexes **11a**, **11b** and **11-ppy** were found to display similar anti-cancer activity towards these cells, although showing between 3 or 4 times less cytotoxic activity than cisplatin (24.7, 23.5 and 18.9 μM, respectively). When tested in the NL20 non-tumorigenic cells, these complexes showed approximately double cytotoxic activity with IC_{50} values of 10.45, 11.13 and 9.03 μM, respectively. Similarly, cisplatin showed the same ratio of increased cytotoxicity towards this cell line (IC_{50}: 2.83 μM). It is important to notice that **11a**, **11b** and **11-ppy** showed steeper curve falls of cytotoxicity with rising concentrations when compared to cisplatin, an effect observed in both cell lines (Figure 2.28). These results indicate a highly homogeneous response towards these compounds, and may suggest different cytotoxic mechanism of action compared to cisplatin. Shallow concentration-response relationships were previously interpreted as a sign of multiple cellular targets,[122] and therefore, could explain the higher cytotoxic activity of cisplatin in these cells.

Table 2.7. Cytotoxic IC_{50} values (μM) and fluorescence cellular localization of **11a**, **11b**, **11-ppy** and cisplatin in human lung cell lines A549 and NL20.

	A549		NL20	
Complex	**IC_{50} [a]**	**Cellular localization**	**IC_{50} [a]**	**Cellular localization**
11a	24.70 ± 0.38	Cytoplasm (perinuclear), nucleus (condensed DNA) and nucleolus	10.45 ± 0.24	Cytoplasm (perinuclear), and nucleolus
11b	23.46 ± 2.78	Cytoplasm (perinuclear)	11.13 ± 0.09	Cytoplasm (perinuclear)
11-ppy	18.92 ± 0.36	Cytoplasm (perinuclear), nucleus and nucleolus	9.03 ± 0.29	Cytoplasm (perinuclear) and nucleolus
Cisplatin	6.45 ± 0.47	-	2.83 ± 0.36	-

[a] IC_{50} values are presented as mean ± the standard error of the mean of three different experiments

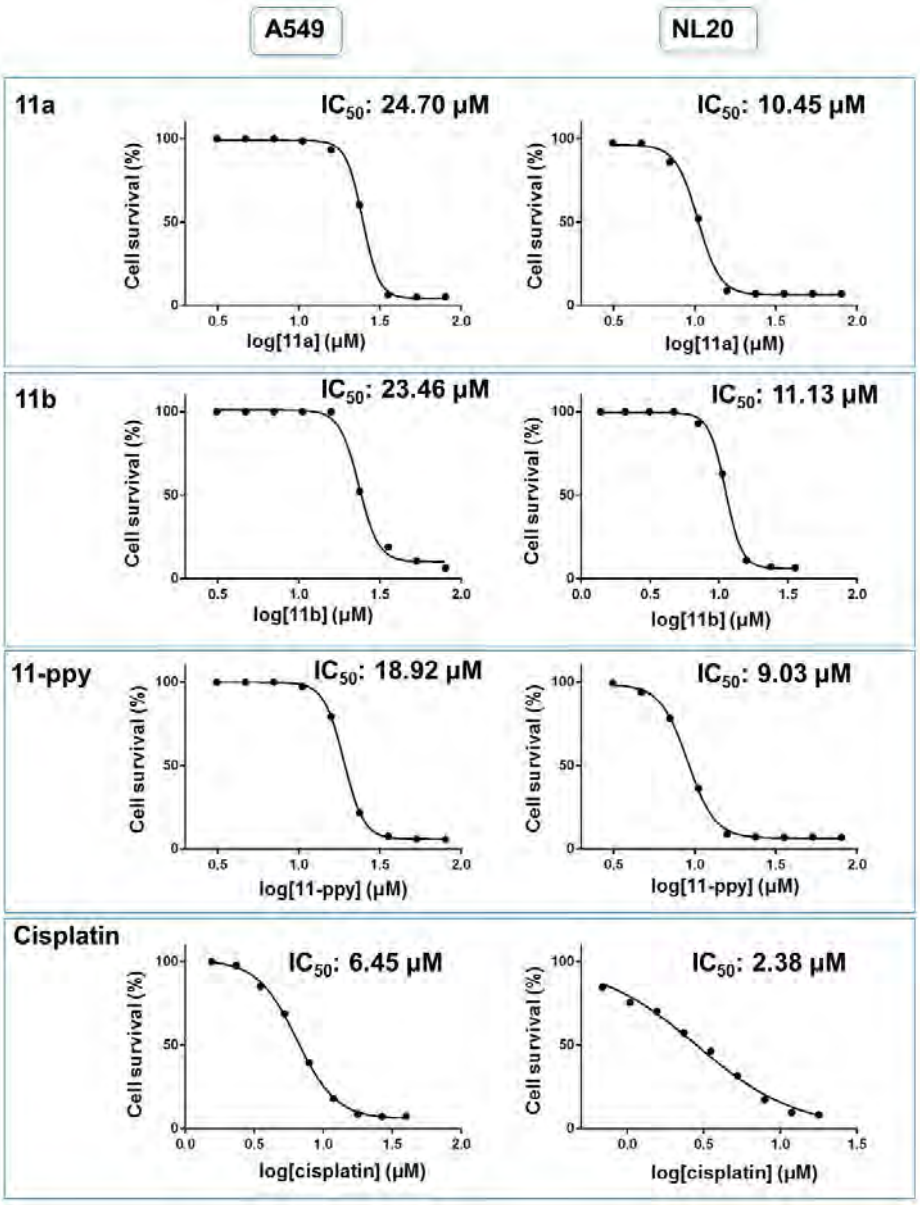

Figure 2.28. Dose-response curves for determination of the IC_{50} cytotoxicity values of **11a**, **11b** and **11-ppy**, and their comparison with cisplatin, in A549 and NL20 cell lines. The IC_{50} values correspond to the dose required to inhibit 50% cellular growth, determined from the dose-dependence of surviving cells after cellular exposure to compounds for 72 h.

2.1.5.2 Fluorescence microscopy cellular localization

Owing to the favourable emission properties of **11a**, **11b** and **11-ppy** complexes, their potential as contrast agents was also assessed. The evaluation of the intracellular localization in living cells, was assessed by fluorescence microscopy. It should be mentioned that for the complex **11a** in dmso solution, the fluorescent band that appeared in CH_2Cl_2 solution at high energy (435 nm) is now very weak (see Figure 2.29). Therefore, no cross talk between the phosphorescence emission of this complex and the fluorophore employed to stain the nuclear DNA (Hoechst 33258), which emits at 461 nm, was expected.

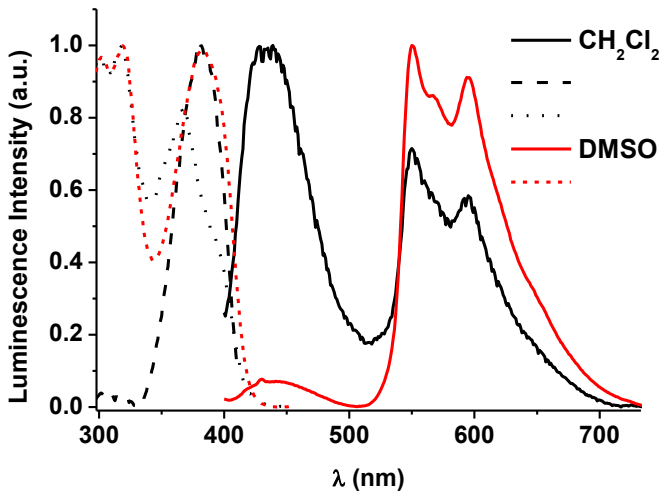

Figure 2.29. Comparative normalized excitation and emission spectra of **11a** in CH_2Cl_2 and dmso (5×10^{-5} M) at 298 K.

To this aim, the compounds were incubated at concentrations of 40 μM, both alone (as control) and in combination with the DNA binder Hoechst 33258 (3.2 μM), with A549 and NL20 human cells and with immortalized mouse embryonic fibroblasts obtained from lungs (LMEFs) for 30 min. Living cell preparations were examined with a fluorescence microscope,[123] suitable for alternate imaging with Nomarski DIC transmitted light, and with green, red and blue fluorescent emitted light. The superimposition of images obtained with Nomarski visualization and Hoechst staining of nuclear DNA helped to ascertain the site of fluorescence at subcellular levels. The results of cellular localization of **11a**, **11b** and **11-ppy** are shown in Figure 2.30 and they are summarized in Table 2.7. None of the complexes showed blue light emission, the spectral

region where Hoechst 33258 bound to DNA is visible (λ_{em} 461 nm)[124] and *vice versa*, Hoechst stain did not show emission bleeding in green and red channels, when their stains were performed separately. However, the three complexes showed the same pattern of cell staining when they were observed in green and red channels, but with a higher intensity in the green region, according to their spectral profiles. Complexes **11a** and **11-ppy** showed brighter cell staining than **11b**, an effect that could be caused by differential fluorescent emission enhancement due to interactions with specific molecular environment.

Staining in different inner cell compartments indicates that cell membranes are permeable to these compounds, and demonstrate that they can be traced in living cells using emission microscopy. It was previously noticed that dmso increases cellular permeability to cisplatin that could be mediated by dmso facilitation of platinum-protein binding.[125] It is possible that the presence of dmso in the structure of complexes **11a**, **11b** and **11-ppy** would help their cellular internalization. It should be noted that, although the three complexes stained the cytoplasm, with brighter emission in the perinuclear area, there were subtle differences among them, and between cell lines. Thus, **11a** and **11-ppy** additionally stained nucleoli in both human cell lines and lung embryonic fibroblasts (LMEFs), and the rest of the nucleus with variable intensity in A549 and LMEFs (Figure A2.11). Interestingly, **11a** strongly marked nuclei with condensed DNA in A549 cells, as revealed its co-localization with the highest levels of Hoechts staining (Figure 2.30). Localization of platinum (II) complexes in perinuclear areas, nuclei and nucleoli was previously described, without further rationalization of their differential binding to specific subcellular compartments.[30c, 123a]

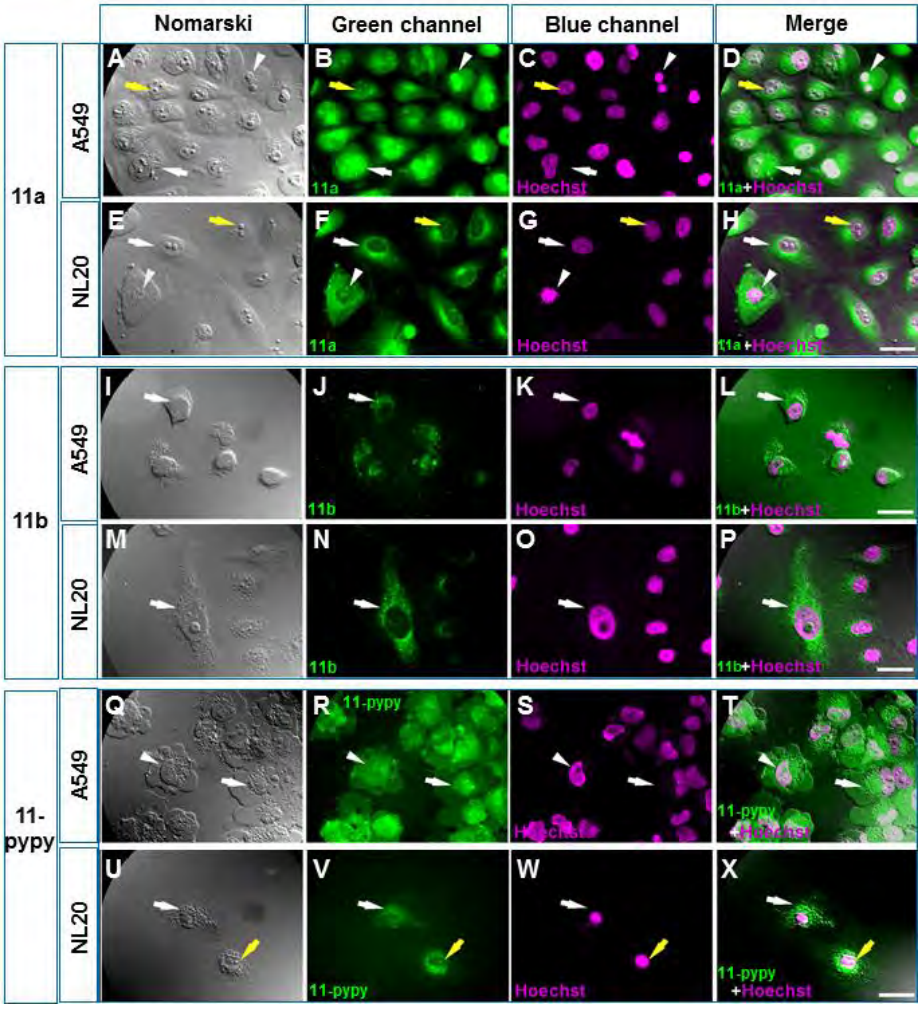

Figure 2.30. Fluorescence images of A549 and NL20 cells treated with complexes **11a**, **11b and 11-ppy**. Living cells were treated with complexes **11a** (A-H), **11b** (I-P) or **11-ppy** (Q-X) (40 μM) mixed with the DNA binder Hoechst 33258 (3.2 μM) for 30 min. Cells were visualized by microscopy either for Nomarski white-light transmission (A, E, I, M, Q, U), or fluorescence emission in green (B, F, J, N, R, V) and blue (C, G, K, O, S, W). Overlay of Nomarski, green and blue images are shown in right panels (D, H, L, P, T, X) (merged). Note that in A549 cells, **11a,** and with less intensity **11b,** stain the cytoplasm in green, with higher intensity in perinuclear areas (white arrows) in both cell lines. **11a,** but not **11b,** strongly stains nuclear condensed DNA (white arrowheads), and nucleoli (yellow arrows). Complex **11-ppy** stains the cytoplasm, stronger in the perinuclear structures (white arrows), and most nuclei (white arrowheads) including nucleoli, both in green and in red (with less intensity). In NL20 cells, **11a** stains the cytoplasm, stronger in perinuclear localization (white arroheads), and nucleoli (yellow arrows), but does not stain condensed DNA in nuclei (white arrowheads); **11b** only stains the cytoplasm with a punctuated pattern (white arrows); **11-ppy** stains the perinuclear cytoplasm (white arrows) and nucleoli (yellow arrows) in green, and in red with less intensity. Scales bar in H, P and X: 30 μm.

2.2 Luminescent homoleptic bis-cyclometalated Pt(IV) compounds

The first part of this Chapter (2.1) collects the synthesis of mono(cyclometalated) Pt(II) complexes [Pt(C^N)(HC^N)(C_6F_5)] (**10a-d**) containing an additional HC^N molecule as auxiliary ligand. X-ray structures of **10b** and **10d** revealed that the aromatic group of the pendant ligand establishes a short Pt···H-C^N bonding interaction, a structural feature that we envisage might facilitate its metalation by electrophilic attack of the platinum center upon oxidation. Thus, we thought that the compounds **10** could behave as excellent precursors for the preparation of luminescent homoleptic bis-cyclometalated Pt(IV) **12** complexes featuring C_6F_5 and Cl as auxiliary ligands. To obtain tuneability of the emission properties, the series of HC^N ligands depicted in Scheme 2.2 were also employed. In this part, we have included the compound [Pt(bzq)(Hbzq)(C_6F_5)] **10e**, with the bzq ligand as precursor, which was previously published by our group.[46]

As it was expected, the presence of two cyclometalated ligands coordinated to the platinum in the new homoleptic Pt(IV) compounds favours their luminescence properties. Besides, with the aim of improving the emissive properties, we have changed the Cl^- ligand by stronger ligand-field auxiliary ligands as cyanide (CN^-), 4-Methylpyridine (Mepy) or 1,2-bi(4-pyridyl)ethylene (bpe), giving rise to compounds **13-15**.

The reactions included in this Chapter 2.2 are summarized in the Scheme 2.4. The optical properties of all complexes are described in detail and interpreted with the aid of DFT and TD-DFT theoretical calculations.

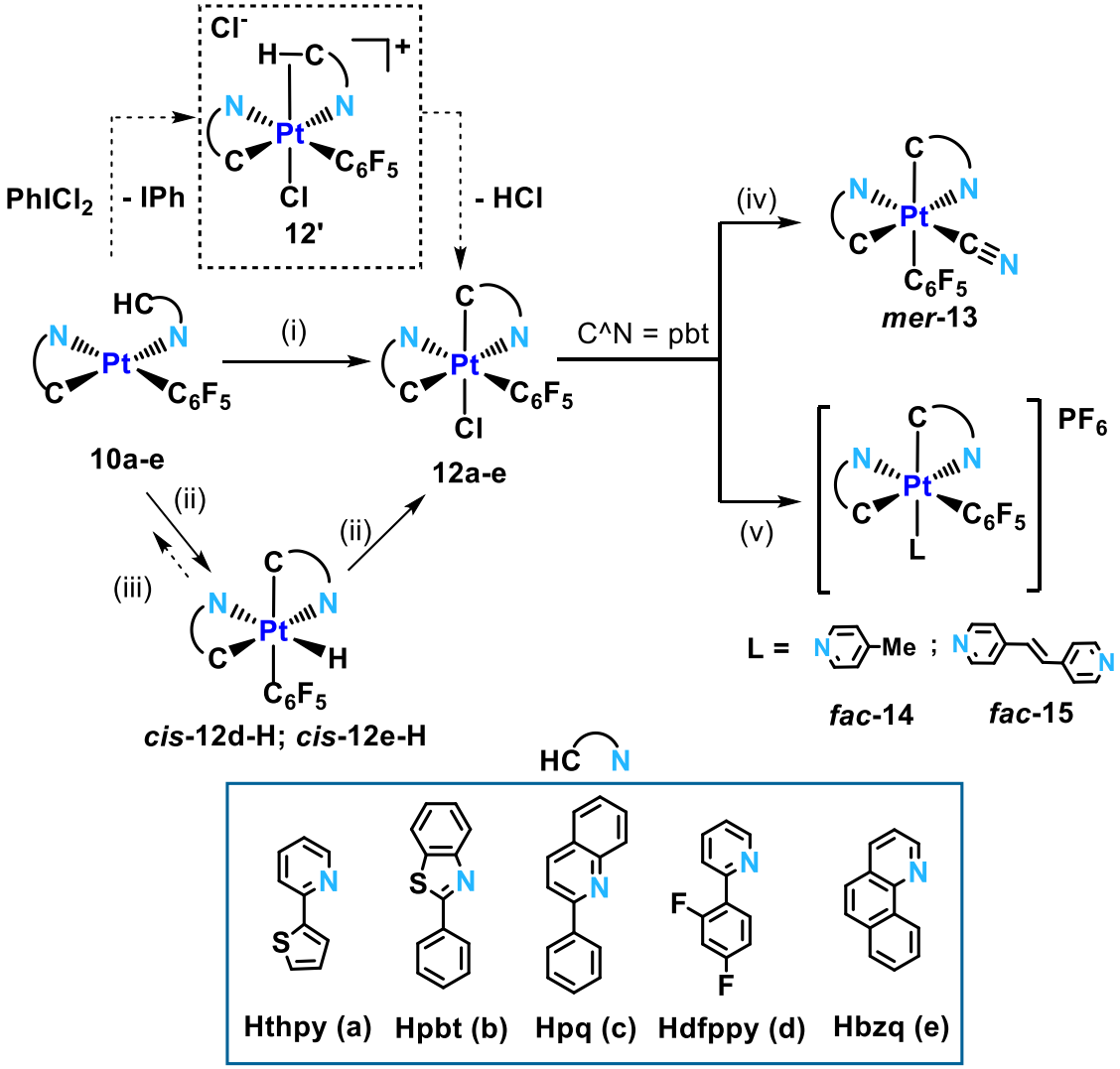

Scheme 2.4. (i) $PhICl_2$ (1.3 equiv), CH_2Cl_2, 0ºC (**12b**,**d**,**e**), -30ºC (**12a**); $PhICl_2$ (1.3 equiv), CH_2Cl_2/acetone, -30ºC, Na_2CO_3 (**12c**) (ii) hν, CD_2Cl_2. (iii) 12h in the dark. (iv) KCN (3 equiv), $KClO_4$ (excess), MeOH/acetone at reflux, 1 day. (v) Mepy (2.5 equiv), $TlPF_6$ (1.5 equiv), $KClO_4$ (excess), MeOH/acetone at reflux, 3 days for **14**; bpe (2 equiv), $TlPF_6$ (1 equiv), $KClO_4$ (excess), MeOH/acetone at reflux, 11 days for **15**.

2.2.1 Synthesis and spectroscopic characterization

2.2.1.1 *fac*-[Pt(C^N)$_2$(C$_6$F$_5$)Cl] 12 complexes

A convenient strategy for the synthesis of a family of stable bis(cyclometalated) pentafluorophenyl Pt(IV) complexes (**12a-e**) has been developed. As is shown in Scheme 2.5, the homoleptic Pt(IV) compounds *fac*-[Pt(C^N)$_2$(C$_6$F$_5$)Cl] (C^N = thpy **12a**, pbt **12b**, pq **12c**, dfppy **12d**, bzq **12e**) were easily synthesized by an oxidation reaction of complexes **10** with PhICl$_2$ in dichloromethane at low temperature (0ºC for **12b**,**d**,**e** and -30ºC for **12a**,**c**). The resulting Pt(IV) intermediate species evolve through a fast C-H activation of the pendant HC^N ligand. The reaction takes place with a high degree of stereoselectivity, with retention of the meridional (C$_6$F$_5$)(C^N)N disposition of the precursor and giving rise only to the facial C,C,C enantiomeric pair (ΛΔ).

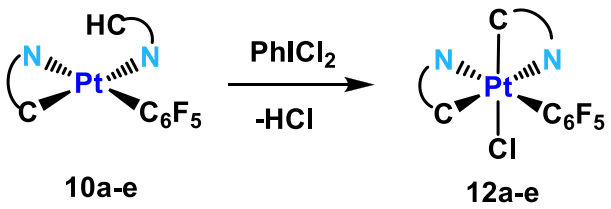

C^N = thpy **a**, pbt **b**, pq **c**, dfppy **d**, bzq **e**

Scheme 2.5. Synthesis of *fac*-**12** complexes: PhICl$_2$ (1.3 equiv), CH$_2$Cl$_2$, 0ºC (**12b**,**d**,**e**), -30ºC (**12a**); PhICl$_2$ (1.3 equiv), CH$_2$Cl$_2$/acetone, -30ºC, Na$_2$CO$_3$ (**12c**).

Based on previous studies on the oxidation of Pt(II) cyclometalated species with the iodine (III) reagent dichloroiodobenzene,[84, 87, 126] we propose that complexes **12** are formed following the mechanism showed in the Scheme 2.6. As the initial step, we propose an electrophilic oxidation of the Pt(II) center with the incorporation of the Cl$^+$ on the less congested face opposite to the pendant HC^N ligand to yield the coordinatively unsaturated pentacoordinate species **12'**. It is suggested that these cationic pentacoordinate **12'** species can be stabilized by a C-H agostic interaction.[73m, 126e, 127] Although rarely detected, five coordinate 16e$^-$ species of Pt(IV) stabilized either by sp^2 or sp^3 C-H agostic interactions,[73f, 126c, 128] are frequently invoked as reaction intermediates and they have been recently confirmed by X-ray crystallography.[128a-c] The final formation of the *fac*-bis(cyclometalated) Pt(IV) complexes **12** could be rapidly driven by subsequent proton transfer of the HC^N pendant ligand to the anion Cl$^-$ producing HCl, which is always detected in the reaction media. The presence of HCl can trigger the displacement

of the HC^N ligand by the chloride,[66] as we have detected in some cases when the reaction was performed at room temperature. For this reason, low temperature and the presence of a base (for the formation of **12c**), is necessary for the correct metalation of the HC^N ligand to give the final monometallic Pt(IV) complexes with two cyclometalated ligands.

In order to confirm the proposed mechanism, the reaction of **10d** with $PhICl_2$ was monitored in CH_2Cl_2 at low temperature by ^1H and ^{19}F NMR spectroscopy. Unluckily, we could not detect the signals of the corresponding **12'd** intermediate. Only the signals due to the precursor **10d** and those attributed to the gradual formation of the final complex **12d** were observed.

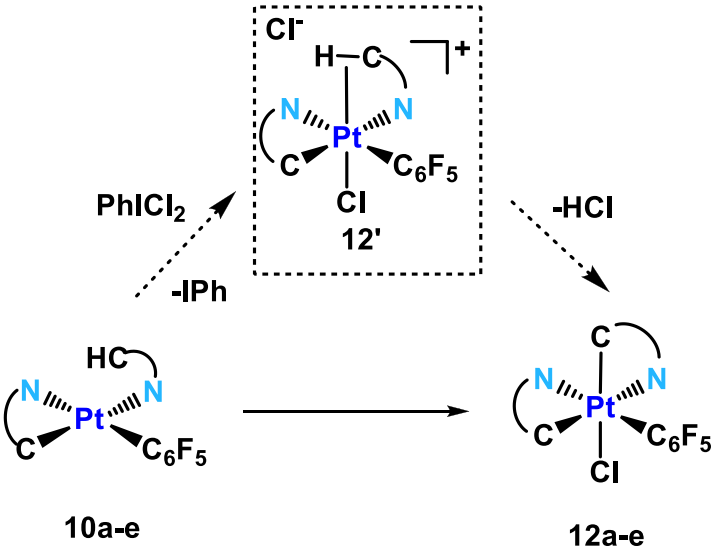

C^N = thpy **a**, pbt **b**, pq **c**, dfppy **d**, bzq **e**

Scheme 2.6

All these homoleptic Pt(IV) complexes were fully characterized by multinuclear NMR spectroscopy, IR, mass spectrometry and elemental analysis. NMR signals were assigned on the basis of ^1H-^1H (COSY, TOCSY), ^1H-^{13}C (HSQC, HMBC), NOE experiments as well as $^1H\{^{19}F\}$ and $^{19}F\{^1H\}$ NMR spectra.

The NMR spectra of *fac*-$[Pt(C^N)_2(C_6F_5)Cl]$ **12** support the double metalation and the formation of the *fac*-C,C,C_{Rf} isomers was also confirmed by X-ray diffraction of **12c**,**d**,**e** (Section 2.2.3). The ^1H and $^{13}C\{^1H\}$ NMR spectra display two sets of signals corresponding to the two non-equivalent cyclometalated ligands and the ^{19}F NMR spectra show the five characteristics resonances of the C_6F_5 ligand (Figure 2.31). In all complexes, the resonance of the proton adjacent to metalated C^N' ring ($H^{10'}$ in **12a**; $H^{11'}$

in **12b**,**d**; $H^{9'}$ in **12e**) is observed slightly downfield shifted (δ 6.51-7.47) in relation to that of Pt(II) precursors **10a-e**, with a significant decrease (*ca.* 1/3) in the value of the $^{3}J_{Pt-H}$ coupling constant (18-54 Hz), which is consistent with the change from Pt^{II} to Pt^{IV}.[71c, 84] The *ortho*-H of the second C^N ligand (H^{10} in **12a**; H^{11} in **12d**,**b**; H^{12} in **12c**; H^{9} in **12e**) appears more deshielded overlapping with other signals, except in **12a**, which is also well resolved (Figure 2.31a).

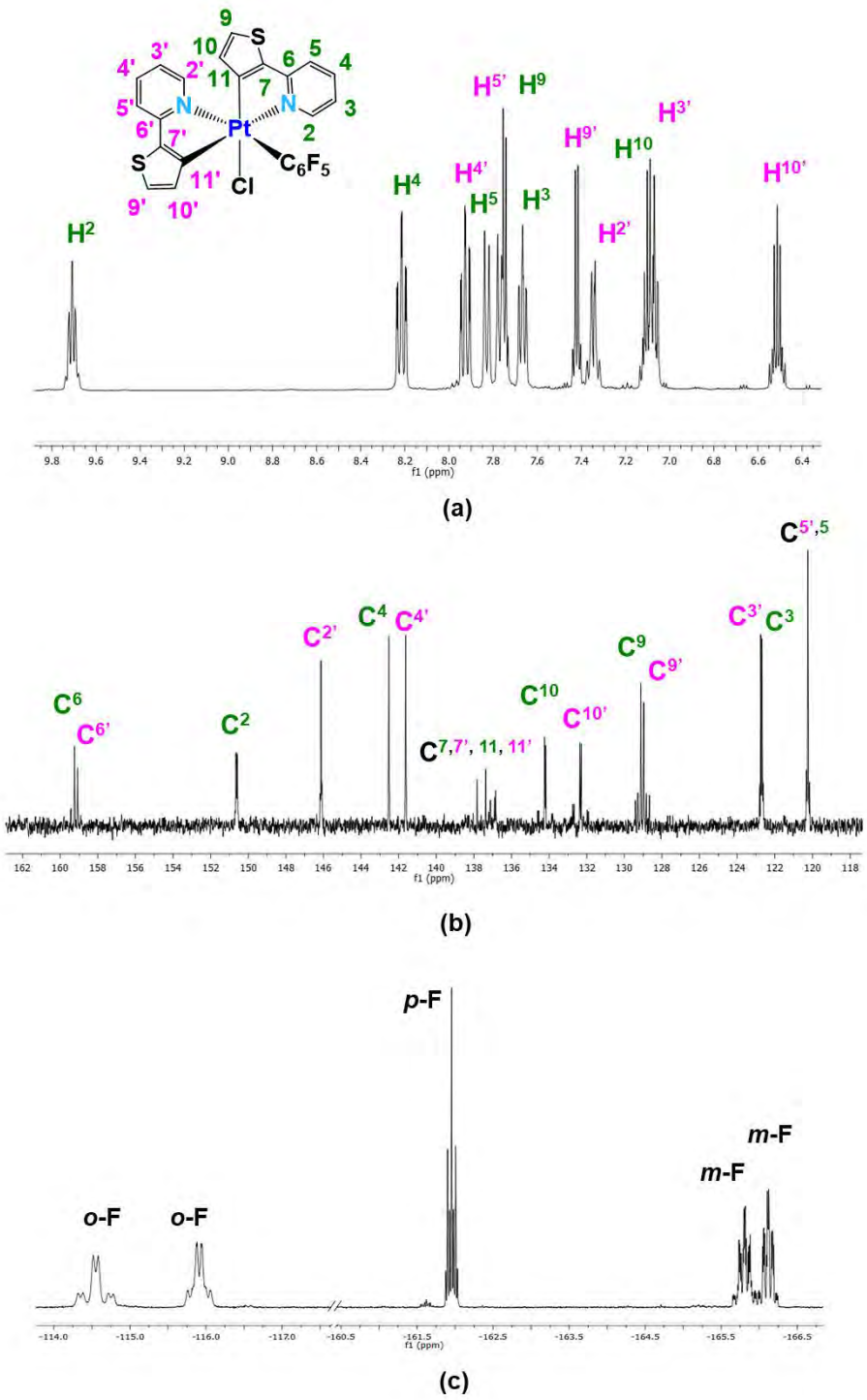

Figure 2.31. (a) ^{1}H, (b) $^{13}C\{^{1}H\}$ and (c) ^{19}F NMR of **12a** in CD_3COCD_3

In these complexes, the closeness of the *ortho*-fluorine atoms of the C_6F_5 ligand to the two protons adjacent to the C-metalated rings ($H^{10,10'}$ **12a**; $H^{11,11'}$ **12b,d**; $H^{12,12'}$ **12c**; $H^{9,9'}$**12e**) and to H^2 (**12a,d,e**) or H^7 (**12b**)/H^8(**12c**) (see Experimental section for labelling and details) is reflected in an additional coupling in the corresponding signals (^1H, ^{13}C, ^{19}F resonances) and confirmed by decoupling $^1H\{^{19}F\}$ and $^{19}F\{^1H\}$ (Figure 2.32) and NOE experiments (Figure 2.33). The most significant evidence of a ^1H-^{19}F coupling is observed in the signal that corresponds to the H^7 proton, either by decoupling $^1H\{^{19}F\}$ or by irradiating at 7.74 ppm (where the H^6 signal appears) with a clear change from a triplet to a doublet.

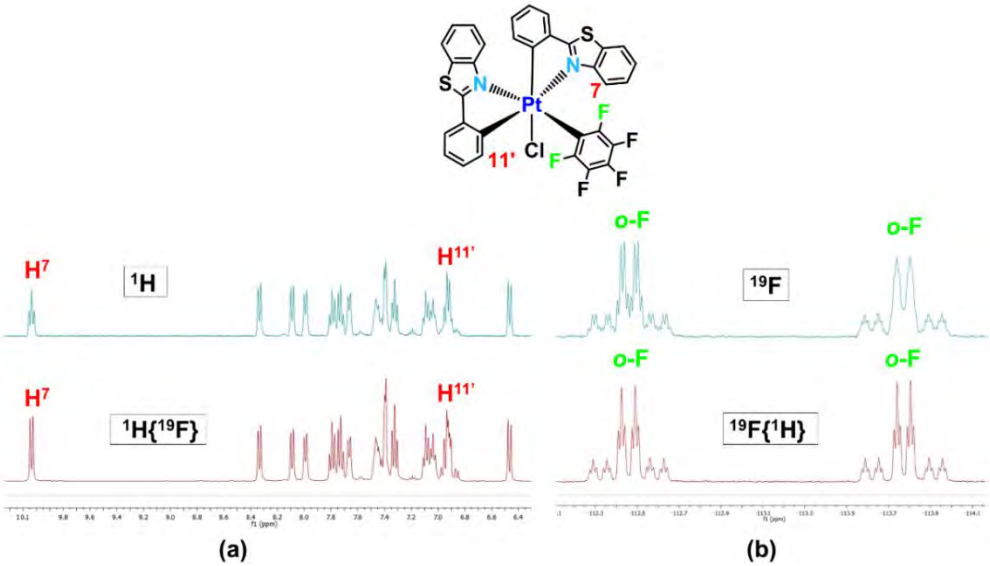

Figure 2.32. (a) ^1H and $^1H\{^{19}F\}$ and (b) ^{19}F and $^{19}F\{^1H\}$ NMR spectra of **12b**.

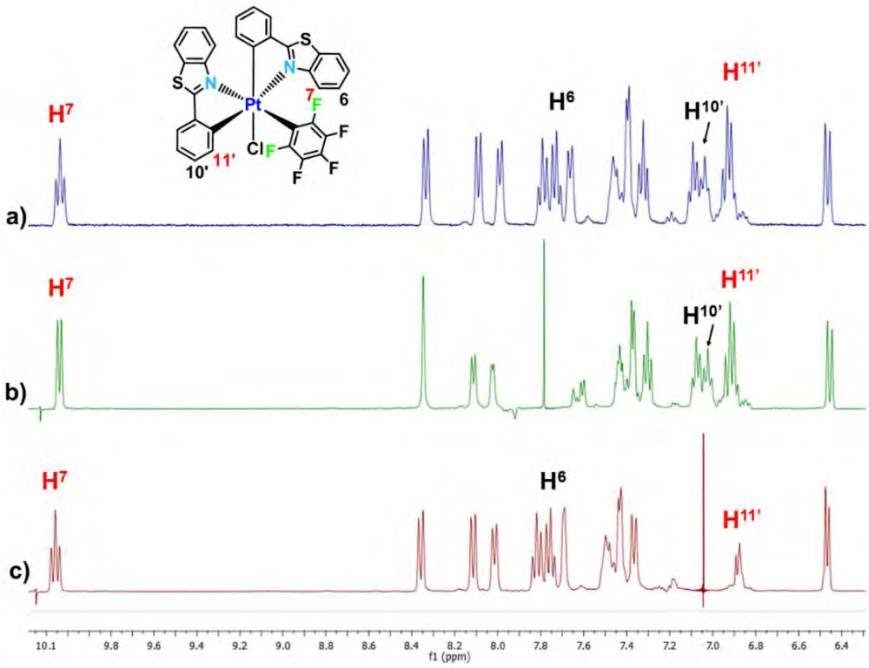

Figure 2.33. NOE experiments of **12b** irradiating at (b) 7.74 ppm and (c) 7.05 ppm.

The coordination of the C_6F_5 ring to Pt^{IV} is also reflected in the $^3J_{Pt-F}$ values (82 - 151 Hz), which show an important decrease with respect to the values found in the mono(cyclometalated) Pt(II) complexes **10a-e** (455-500 Hz).[46, 129] In **12d**, the four *meta*-fluorine resonances of the two non-equivalent *dfppy* groups show the expected platinum satellites (Figure 2.34) with a lower value of the long range four bond $^4J_{Pt-F}$ (29 - 45 Hz) than those observed in the related Pt(II) derivative **10d** (66, 55 Hz).

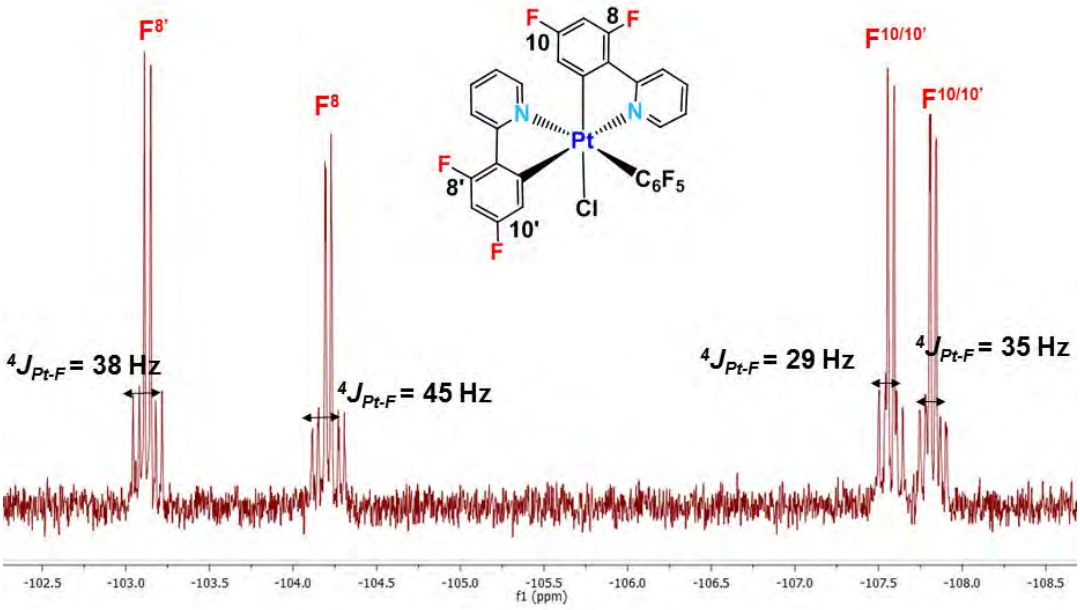

Figure 2.34. Section of the $^{19}F\{^1H\}$ NMR of **12d** complex showing the four *meta*-fluorine resonances of the two *dfppy* groups.

Interestingly, we found that the Pt(II) complex [Pt(bzq)(Hbzq)(C_6F_5)] **10e** was photosensitive. Thus, a solution of **10e** in CH_2Cl_2 was left to stand with daylight in the lab and its progress was monitored by NMR. After 3 days in CH_2Cl_2 solution, around the 35% of the initial derivative had evolved to a mixture of mainly the *cis*-C-H oxidative addition product [the hydride *cis*-[Pt(bzq)$_2$(C_6F_5)H] (***cis*-12e-H**)] and [Pt(bzq)$_2$(C_6F_5)Cl] (**12e**) with a final ratio of **10e**: ***cis*-12e-H**: **12e** ~ 64:26:10 (Figure 2.35a). In the ^1H NMR spectrum, the signal of the hydride appears at -16.9 ppm as a doublet, due to small coupling to the *ortho*-fluorine of the C_6F_5 group, with a high platinum coupling constant (1343 Hz), indicating that the hydride is in a *trans* disposition to the N-donor ligand[130] (Figure 2.35a). In the ^{19}F NMR spectrum (Figure 2.35b) the two *ortho*-fluorine resonances of ***cis*-12e-H** are seen well separated (δ -108.8, -120.5) with $^3J_{Pt-oF}$ values of 279 Hz and ~ 42 Hz respectively. The low-frequency signal at δ -120.5 is tentatively

ascribed to the *ortho*-fluorine close to the hydride and the small coupling to ^{195}Pt (42 Hz) could be due to its simultaneous interaction with the hydride ligand.

It should be pointed out that, although hydride Pt(IV) species are very uncommon, there are some recent examples in the bibliography, in particular alkylhydrides, invoked as transient or short-lived intermediate species in stoichiometric and catalytic systems.[73f, 130-131] Besides, they have been proposed in cyclometalation reactions involving electron-rich platinum(II) substrates,[73f, 126e, 130-131] but their direct evidence has only recently invoked in closely related systems.[95] Indeed, González-Herrero *et al*. have recently reported the first direct detection of a hydride intermediate in a cyclometalation reaction of a Pt(II) complex. They have demonstrated that the visible-light driven cyclometalation of the pendant Hppy ligand in complexes [Pt(ppy)(Hppy)R] (R = Me, C_6F_5), carried out in toluene-d^8, takes place through a photochemical oxidative addition of the C−H bond, which is facilitated by population of the ^{3}MLCT excited state. They found that, in the case of the methyl precursor, the intermediate [Pt(ppy)$_2$HMe] undergoes elimination of methane with final formation of [Pt(ppy)$_2$], whereas for the pentafluorophenyl system, thermal reversion to the precursor complex was observed.[95] In our system, the Pt(IV) hydride derivate, ***cis*-12e-H**, seems to be more stable and able to abstract a chlorine atom from the CH_2Cl_2 solvent to finally form the compound [Pt(bzq)$_2$(C_6F_5)Cl] **12e**.

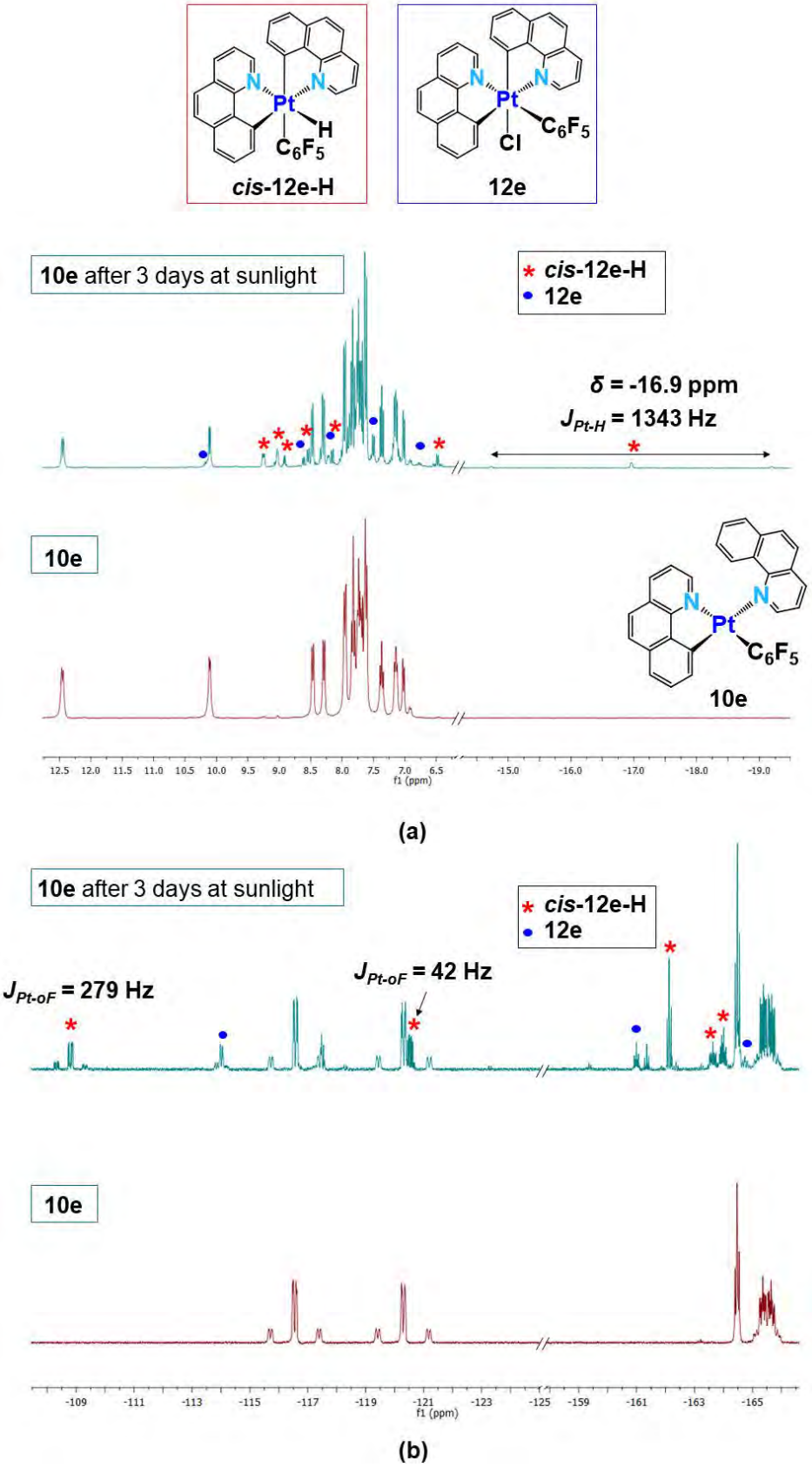

Figure 2.35. Evolution of **10e** on standing 3 days with daylight. (a) Selected region of the ^{1}H NMR spectra (300 MHz) and (b) ^{19}F NMR spectra.

Taking into account these interesting results, the photoreactivity of the Pt(II) complexes [Pt(C^N)(HC^N)(C_6F_5)] **10** in CD_2Cl_2 solutions was also examined (Scheme 2.7). The formation of the Pt(IV) complexes with dfppy **12d** and bzq **12e** was fast and clean when solutions of complexes **10d** and **10e** in CD_2Cl_2 were irradiated with a mercury lamp of 400 W for 2h. Unfortunately, irradiations of the rest of the complexes in CD_2Cl_2 solutions showed only partial conversions, with complexes **12a-c** formed in yields of around 10%, together with a complicated mixture of species. For complexes **10d** and **10e**, monitorization of the reactions by ^{1}H and ^{19}F NMR spectroscopy revealed the initial formation of the corresponding species ***cis*-12d-H** and ***cis*-12e-H** as the only intermediate species in the formation of final complexes **12d** and **12e**, respectively. The characterization of these hydride intermediate species was performed upon irradiation with a 125 W lamp, because the formation of ***cis*-12d-H** and ***cis*-12e-H** was better controlled than with a 400 W lamp.

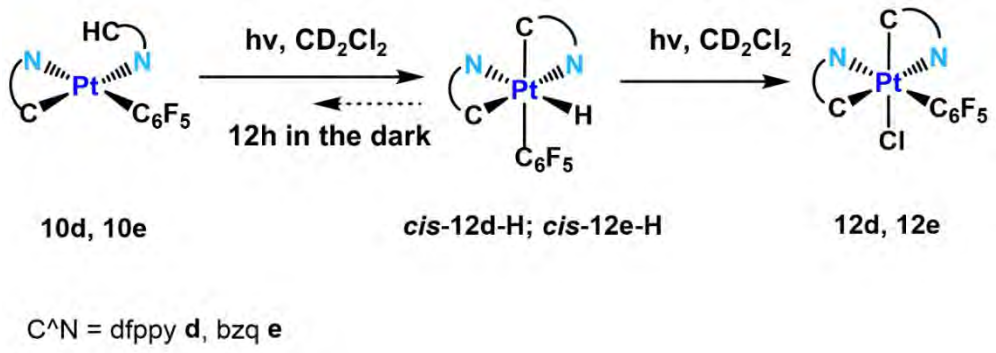

Scheme 2.7

As illustration, the evolution of the irradiation of **10d** with the time, monitored by ^{1}H and ^{19}F NMR spectroscopy, is shown in Figure 2.36. It is worth to mention the role of the solvent in these photochemistry reactions, as the formation of **12d,e** from the initial hydride ***cis*-12d-H** and ***cis*-12e-H** only takes place in CD_2Cl_2. Indeed, when the irradiations of **10d** and **10e** solutions were carried out in toluene-d^8, although the hydrides were also formed as primary intermediate species, these evolved into a complex mixture of unidentified products after further irradiation. Therefore, the solvent must donate chlorine atoms for the next step in the formation of the Pt(IV) [Pt(C^N)$_2$(C_6F_5)Cl] derivatives. It is suggested that, under photolytic conditions, abstraction of hydrogen atom from the hydride complexes (***cis*-12d,e-H**) takes place forming a radical pentacoordinate [Pt^{III}(C^N)$_2$(C_6F_5)]$^\bullet$ species, which can isomerize and quickly react with the CD_2Cl_2 solvent forming the final *fac*-[Pt(C^N)$_2$(C_6F_5)Cl]. In support of this, we found that a

mixture of **10d** and the hydride ***cis*-12d-H**, generated after 30 min of irradiation (~ 65/35 **10d**/***cis*-12d-H**), does not evolve to the chloride complex **12d** in the dark (Scheme 2.7). In fact, without further irradiation, partial reversion of the hydride ***cis*-12d-H** to the precursor **10d** was only observed. Rourke *et al*. noted previously the easy photodecomposition of the phenylpyridine derivative [Pt(ppy)Cl(Hppy)] in $CHCl_3$ either on standing in air or under irradiation conditions to yield the Pt(IV) bis(cyclometalated) complex *cis*-[Pt(ppy)$_2$Cl$_2$] among a mixture of other Pt(IV) species.[132]

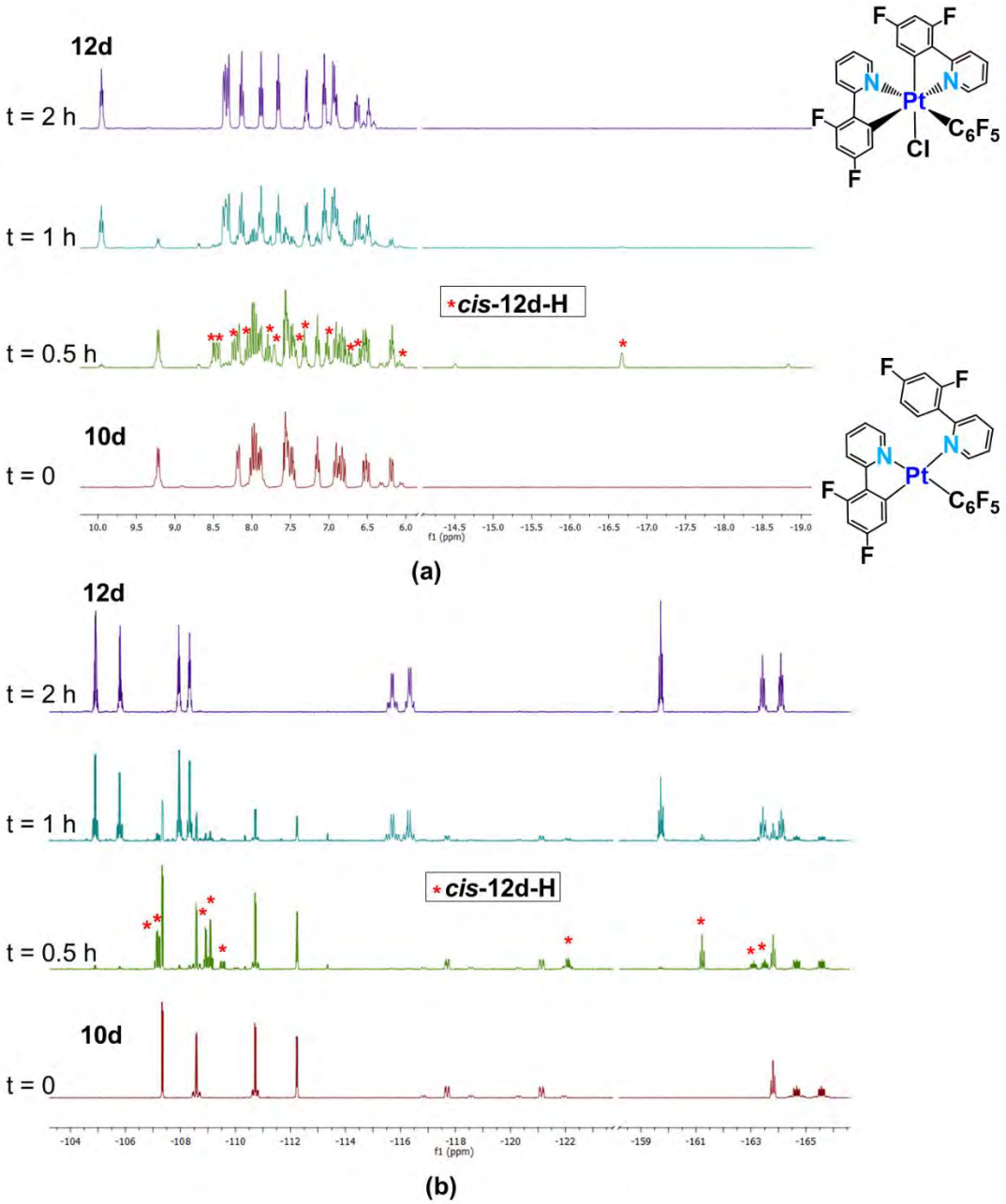

Figure 2.36. Control by NMR spectroscopy of the irradiation of **10d** in CD_2Cl_2 (Hg lamp, 125 W, t = 0.5, 1 and 2h), showing the formation of **12d** and ***cis*-12d-H** as an intermediate. (a) ^{1}H NMR spectra and (b) ^{19}F spectra.

2.2.1.2 $[Pt(C^N)_2(C_6F_5)L]^n$ (n = 0, L = CN 13; n = +1, L = Mepy 14, bpe 15) complexes

With the aim of improving the emissive properties of the Pt(IV) compounds, we decided to perform substitution reactions of the chlorine atom in the selected $[Pt(pbt)_2(C_6F_5)Cl]$ **12b** compound by stronger-field ligands. The coligands chosen were cyanide (CN^-), 4-methylpyridine (Mepy) and 1,2-Di(4-pyridyl)ethylene (bpe) ligands to give rise to the neutral $[Pt(pbt)_2(C_6F_5)(CN)]$ or the cationic $[Pt(pbt)_2(C_6F_5)L][PF_6]$ (L = Mepy **14**, bpe **15**) compounds. The cyanide complex **13** was prepared, as shown in Scheme 2.8i, from *fac*-**12b** and KCN (3 equiv.) in the presence of a large excess of $KClO_4$ to facilitate the abstraction of the chloride in a mixture of MeOH/acetone at reflux (24 h). The derivatives **14** and **15** were prepared from **12b** by adding Mepy (2.5 equiv.) or bpe (2 equiv.), in the same conditions but in presence of $TlPF_6$ at reflux (3 days **14**, 11 days **15**) (Scheme 2.8ii).

Interestingly, it was observed that when the chlorine was substituted with cyanide (CN^-), the reaction took place with isomerization, leading to the *mer*-$[Pt(pbt)_2(C_6F_5)CN]$ **13** compound (Scheme 2.8i), as supported by NMR spectroscopy and confirmed by single-crystal X-ray diffraction. In contrast, the substitution of the Cl^- by Mepy or bpe was carried out with a retention of the *fac*-C,C,C disposition of the **12b** precursor, giving rise to *fac*-$[Pt(pbt)_2(C_6F_5)L]^+$ (L = Mepy **14**, bpe **15**) complexes (Scheme 2.8ii), confirmed also by NMR spectroscopy and X-ray diffraction studies.

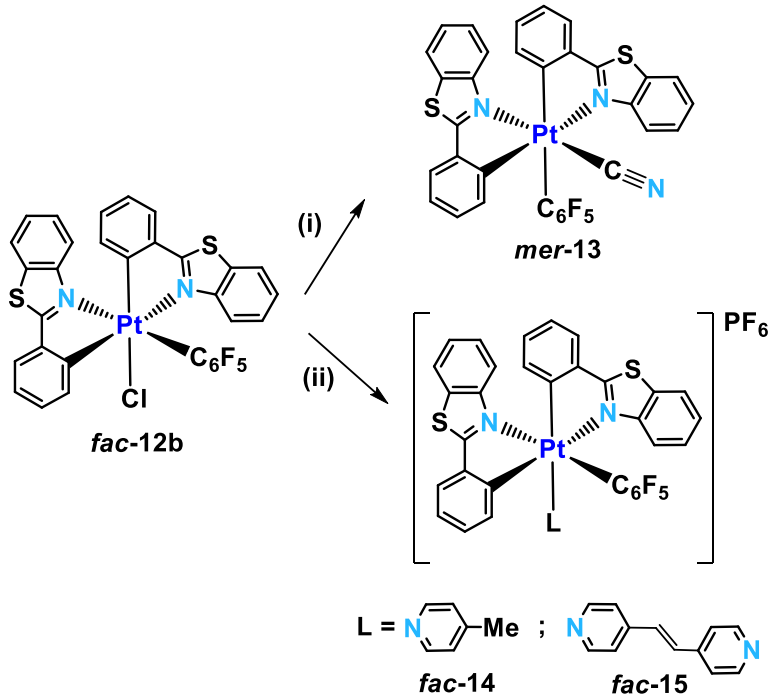

Scheme 2.8. Reagents and conditions: (i) KCN (3 equiv), $KClO_4$ (excess), MeOH/acetone at reflux, 1 day. (ii) Mepy (2.5 equiv), $TlPF_6$ (1.5 equiv), $KClO_4$ (excess), MeOH/acetone at reflux, 3 days for **14**; bpe (2 equiv), $TlPF_6$ (1 equiv), $KClO_4$ (excess), MeOH/acetone at reflux, 11 days for **15**.

It is worth noting that Pt(IV) complexes with cyclometalated ligands and with cyanide or monodentate pyridine ligands are very uncommon. In particular, as far as we know, the diiodide cyanide *trans*-[Pt(C^N^N)(CN)I_2] containing the tridentate 6-phenyl-2,2'-bipyridyl ligand is the only reported example of a Pt(IV) complex containing cyclometalated and cyanide groups.[99d] Interestingly, this complex was generated by reaction of the diamino carbene of Pt(II) [Pt(C^N^N){C(NH^{t}Bu)(NHMe)}] with MeI under UV-visible light. Besides, L. Dutton *et al.*[63] reported a cyclometalated Pt(IV) compound with monodentate pyridine ligands $[Pt(ppy)_2(4\text{-}NMe_2\text{-}py)_2]^{2+}$, prepared by reaction of the bis-cyclometalated Pt(II) compound $[Pt(ppy)_2]$ with the oxidant $[PhI(4\text{-}NMe_2\text{-}py)_2]^{2+}$, and whose structure was confirmed by X-ray.

All these complexes were also fully characterized by multinuclear NMR spectroscopy, IR, mass spectrometry and elemental analysis. NMR signals were assigned on the basis of ^{1}H-^{1}H (COSY, TOCSY), ^{1}H-^{13}C (HSQC, HMBC), NOE experiments as well as ^{1}H{^{19}F} and ^{19}F{^{1}H} NMR spectra.

The substitution of the Cl^- atom in $[Pt(pbt)_2(C_6F_5)Cl]$ **12b** by the CN^- ligand to form $[Pt(pbt)_2(C_6F_5)CN]$ **13** arises with isomerization from *fac*-C,C,C_{Rf} to *mer*-C,C,C_{Rf}. This implicates the migration of the C_6F_5 ring from the initial position *trans* to N-metalated atom to the site *trans* to the C-metalated atom. This change is clearly deduced from the comparison of the ^{1}H NMR spectra of **12b** and **13**, as is illustrated in the Figure 2.37. The most significant difference in the spectra of the two complexes is the proximity of the H^7 proton of the benzothiazole unit to the diamagnetic current of the C_6F_5 ring in **13**, which leads to a remarkable upfield shift in its signal in relation to the precursor **12b** (δ_{H7} = 6.5 in **13** *vs* 10.05 in **12b**). In contrast, the $H^{11'}$ proton of the aryl cyclometalated ligand in **13** is away from the diamagnetic current of the C_6F_5, appearing clearly shifted downfield in relation to that **12b**, where the $H^{11'}$ proton is affected by the shielding current of the C_6F_5 ring ($\delta_{H11'}$ = 8.61 in **13**, 6.93 in **12b**). Besides, this $H^{11'}$ appears in **13** retaining also the coupling to the other *o*-F ($J_{H\text{-}oF}$ = 5 Hz). Finally, the H^{11} proton of the second cyclometalated group (C^N *trans* to C_6F_5) moves upfield and is observed as a doublet in **13** because the H···*o*F coupling through space is lost. The high *trans* influence of the two mutually *trans* carbon atoms ($C_{ipso,C6F5}$ and $C_{metalated}$) is reflected in the reduced values of the *o*-F (C_6F_5 group) and Pt coupling constant ($^3J_{Pt\text{-}oF}$ = 87, 41 Hz **13** *vs* 102, 114 Hz **12b**).

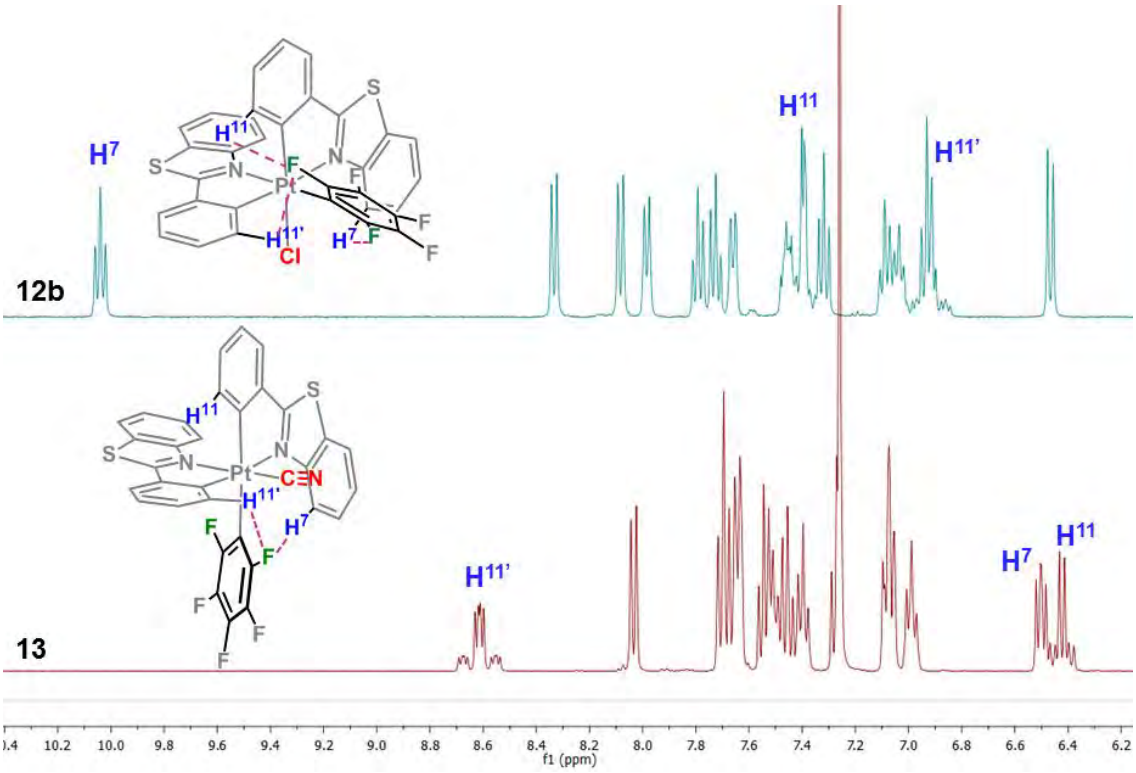

Figure 2.37. ^{1}H NMR spectra of **12b** and **13**.

When the Cl^- is substituted by Mepy or bpe in **12b** to give the cationic compounds **14** or **15** respectively, the reaction occurs with retention of the configuration *fac*-C,C,C_{Rf} of the precursor **12b**, as is reflected in their NMR spectra. In the ^{1}H NMR spectra, the most significant signal corresponds to the $H^{11'}$ proton, which appears as a pseudo triplet ($J_{H11\text{-}H10} \approx J_{H11\text{-}oF} \approx$ 6Hz), with the expected Pt satellites, at similar δ in the three complexes (δ $H^{11'}$: 6.93 **12b**, 6.88 **14**, 6.89 **15**). As illustration, the comparison between the ^{1}H NMR of **12b** and **14** is shown in the Figure 2.38. As shown, the H^{11} appears as a triplet confirming the $H^{11}\cdots o$F coupling through the space, which is possible in the *fac*-C,C,C_{Rf} configuration, but not in a *mer*-C,C,C_{Rf} isomer. In addition, the H^7 proton, which overlaps with other signals, is clearly upfield shifted in relation to **12b** due to the anisotropic effect of the pyridine ring.

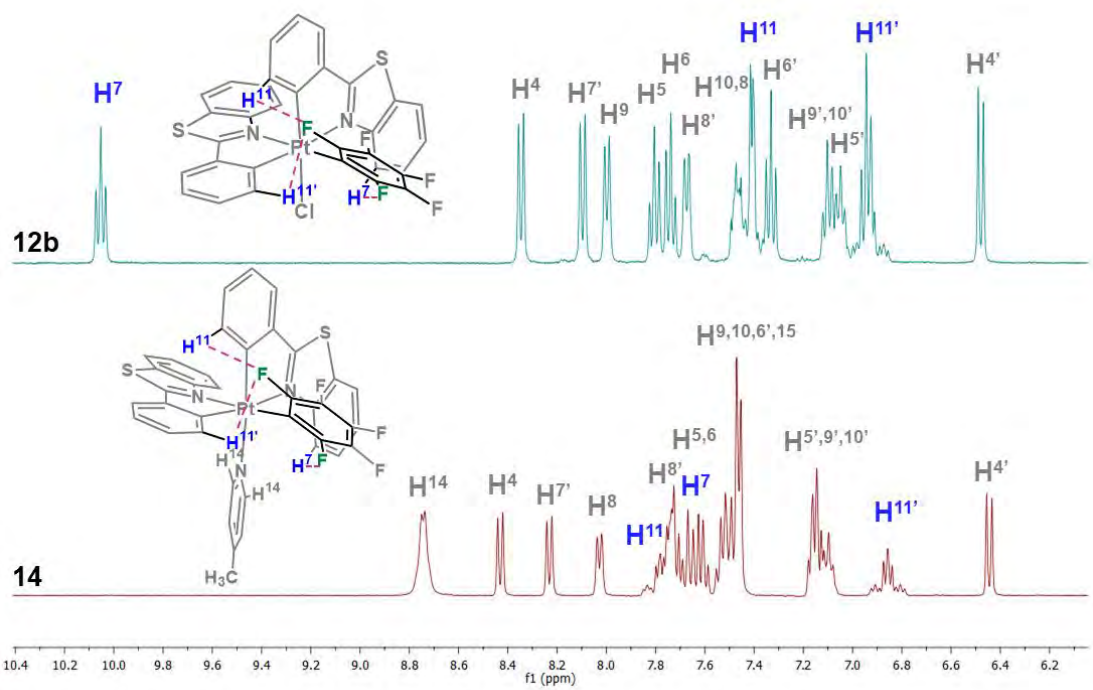

Figure 2.38. ^{1}H NMR spectra of **12b** and **14**.

As expected, the presence of the anion PF_6^- in **14** and **15** is reflected in the $^{19}F\{^1H\}$ and $^{31}P\{^1H\}$ NMR spectra. The $^{19}F\{^1H\}$ NMR spectra (Figure 2.39) confirm the presence of a rigid C_6F_5 group and a doublet (δ -72.6, $^1J_{P\text{-}F}$ = 706 **14**, 709 **15** Hz), corresponding to the PF_6.

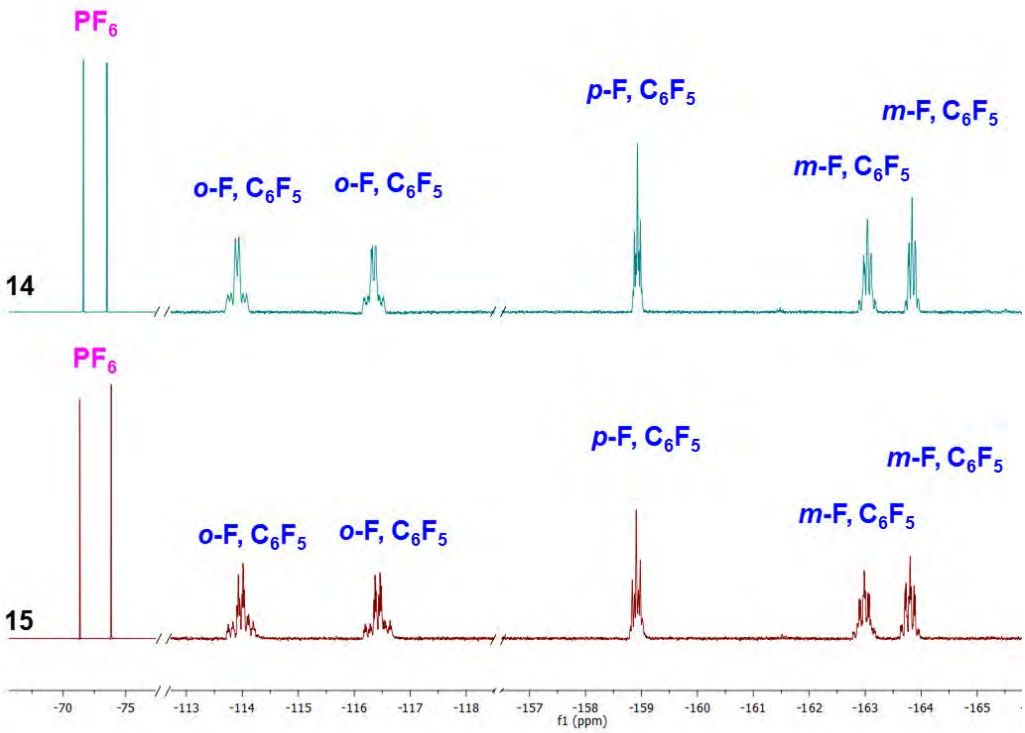

Figure 2.39. $^{19}F\{^{1}H\}$ NMR spectra of **14** and **15**.

The ^{1}H NMR spectra of the cationic complex *fac*-[Pt(pbt)$_2$(C$_6$F$_5$)(bpe)][PF$_6$] **15**, reveals the presence of two isomers in a molar ratio 1:0.15, which are attributed to the two conformations *E* and *Z* of the 1,2-di(4-pyridyl)ethylene (bpe) ligand. The major component is tentatively assigned to the *E*-form around the C=C double bond because this isomer is expected to reduce the steric constraint about the Pt centre. The presence of the *Z*-[Pt(pbt)$_2$(C$_6$F$_5$)(bpe)][PF$_6$] form, in small amount, suggests that the bpe ligand suffers an easy photoisomerization. This isomerization with light has been recently observed in Pt(II) bimetallic compounds with the bpe bridging unit.[133] Indeed, control of the photoisomerization process in an acetone-d^6 solution, with a 125 W lamp, revealed that a final photostationary state between both isomers, with a proportion of 1:1.15 (*E*:*Z*), is reached after 40 min (Figure 2.40). Crystals of complex **15** were obtained by diffusion of *n*-hexane into a solution in acetone and subjected to an X-ray diffraction study (see below). It should be noted that, in the *Z* form, the second pyridine ring of the bpe ligand is oriented towards the equatorial phenylbenzothiazole group, as confirmed this X-ray study. This orientation causes a negligible influence in the chemical shifts of the fluorine resonances of the C$_6$F$_5$, as observed by monitoring the corresponding $^{19}F\{^{1}H\}$ NMR spectra.

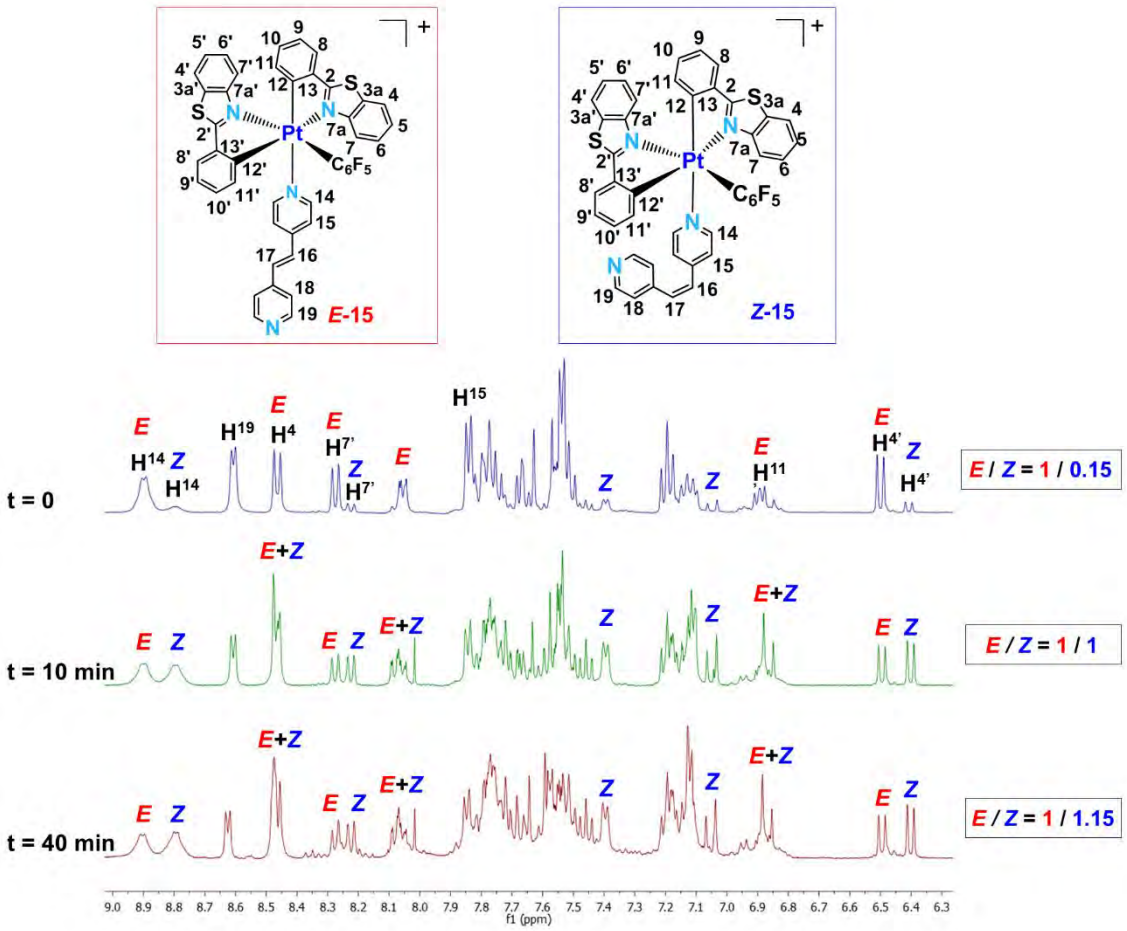

Figure 2.40. Control by ^{1}H NMR spectroscopy of the irradiation of **15** in CD_3COCD_3 (Hg lamp, 125 W, t = 0, 10 min, 40 min), showing the formation of the isomer *Z*.

By comparison, the photostability of **12**, **13** and **14** compounds were examined, remaining unaltered upon irradiation with a 125 W mercury lamp in CH_2Cl_2 solution for 4 h (Figure A2.12 and A2.13). It should be noted that González-Herrero *et al*. have published that some cycloplatinated(IV) complexes of the type *unsym*-$[Pt(ppy)_2X_2]$[65a] were non-stable upon irradition with UV light.

2.2.3 Crystal structures

Crystal structures of the Pt(IV) compounds **12c**,**d**,**e**, **13-15** were solved by X-ray diffraction studies. Crystallographic data are given in the Experimental Section (Tables E5 and E6). It is interesting to point out that the molecules are chiral but, as they crystallized in centrosymmetric space groups, the two enantiomers (Δ and Λ) are present in the unit cell. For all complexes, the Δ enantiomer has been represented.

The molecular structures of **12c**·0.5thf, **12d** and **12e**·5.5thf are shown in the Figure 2.41, selected distances and angles are collected in Table 2.8. In **12c**·0.5thf, two molecules of the same enantiomeric (i.e Δ) complex *fac*-[Pt(pq)$_2$(C$_6$F$_5$)Cl] and one molecule of thf were found in the asymmetric unit, with weak contacts between them. The two molecules (A and B) correspond to the same isomer and display similar metric data, except for the tilt of the C$_6$F$_5$ ring. Hence, only the molecule A is included in the Figure 2.41.

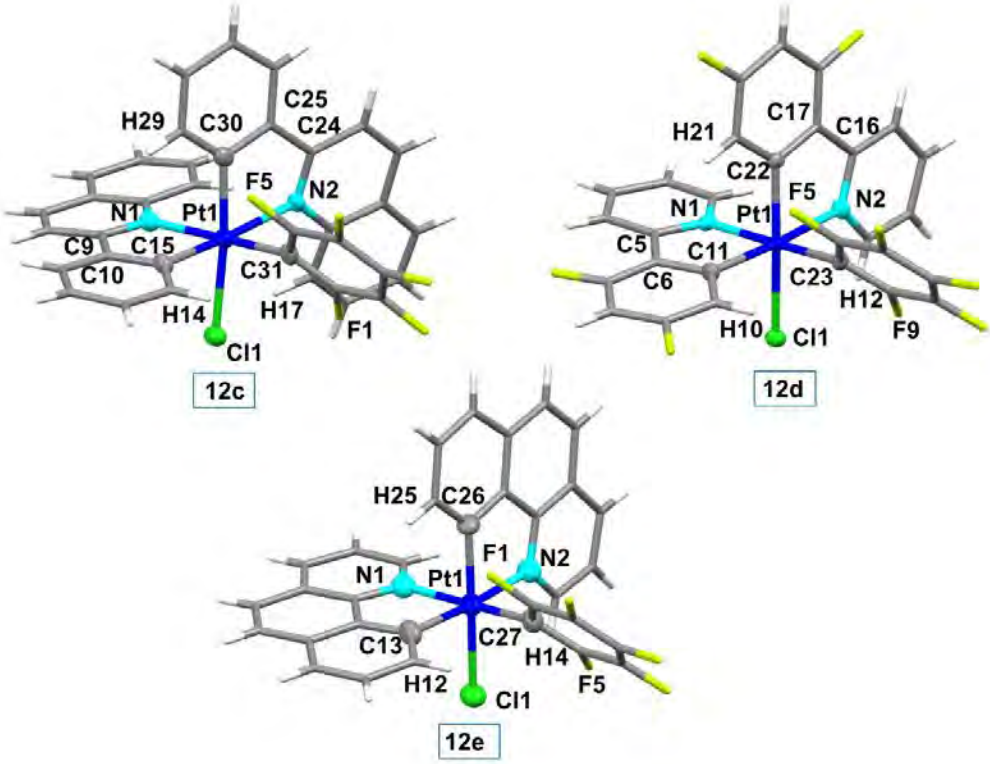

Figure 2.41. Molecular structures of **12c** (molecule A), **12d** and **12e**.

Table 2.8: Selected distances (Å) and angles (°) for complexes **12c** (molecule A), **12d** and **12e**.

12c·0.5thf (molecule A)			
Distances (Å)		**Angles (°)**	
Pt(1)-N(1)	2.164(3)	C(15)-Pt(1)-N(1)	80.20(15)
Pt(1)-N(2)	2.264(3)	N(1)-Pt(1)-N(2)	104.07(13)
Pt(1)-C(15)	2.022(4)	C(31)-Pt(1)-N(2)	81.53(14)
Pt(1)-C(31)	2.062(4)	C(15)-Pt(1)-C(31)	93.90(17)
Pt(1)-C(30)	2.022(4)	C(30)-Pt(1)-N(1)	88.82(14)
Pt(1)-Cl(1)	2.4464(11)	C(30)-Pt(1)-C(15)	95.32(17)
C(9)-C(10)	1.457(6)	C(30)-Pt(1)-C(31)	89.27(16)
C(24)-C(25)	1.458(6)	C(30)-Pt(1)-N(2)	78.87(15)
H(14)···F(5)	2.588	Cl(1)-Pt(1)-N(1)	85.79(10)
H(17)···F(1)	2.900	Cl(1)-Pt(1)-C(15)	82.27(12)
H(29)···F(5)	3.035	Cl(1)-Pt(1)-C(31)	95.92(12)
		Cl(1)-Pt(1)-N(2)	103.92(9)
12d			
Distances (Å)		**Angles (°)**	
Pt(1)-N(1)	2.0943(19)	C(11)-Pt(1)-N(1)	80.20(9)
Pt(1)-N(2)	2.130(2)	N(1)-Pt(1)-N(2)	95.24(8)
Pt(1)-C(11)	2.012(3)	C(23)-Pt(1)-N(2)	88.13(9)
Pt(1)-C(23)	2.070(2)	C(11)-Pt(1)-C(23)	96.31(10)
Pt(1)-C(22)	2.026(2)	C(22)-Pt(1)-N(1)	86.89(8)
Pt(1)-Cl(1)	2.4198(6)	C(22)-Pt(1)-C(11)	97.77(10)
C(5)-C(6)	1.469(3)	C(22)-Pt(1)-C(23)	89.91(9)
C(16)-C(17)	1.470(3)	C(22)-Pt(1)-N(2)	80.07(9)
H(10)···F(5)	2.562	Cl(1)-Pt(1)-N(1)	87.89(6)
H(12)···F(9)	2.533	Cl(1)-Pt(1)-C(11)	85.84(7)
H(21)···F(5)	2.683	Cl(1)-Pt(1)-C(23)	95.61(7)
		Cl(1)-Pt(1)-N(2)	95.85(6)
12e·5.5thf			
Distances (Å)	**Angles (°)**	**Distances (Å)**	**Angles (°)**
Pt(1)-N(1)	2.097(4)	C(13)-Pt(1)-N(1)	80.8(2)
Pt(1)-N(2)	2.144(4)	N(1)-Pt(1)-N(2)	93.47(19)
Pt(1)-C(13)	2.026(5)	C(27)-Pt(1)-N(2)	90.7(2)
Pt(1)-C(27)	2.035(5)	C(13)-Pt(1)-C(27)	94.9(2)
Pt(1)-C(26)	2.037(5)	C(26)-Pt(1)-N(1)	86.17(19)
Pt(1)-Cl(1)	2.4181(13)	C(26)-Pt(1)-C(13)	97.5(2)
H(12)···F(1)	2.518	C(26)-Pt(1)-C(27)	91.2(2)
H(14)···F(5)	2.562	C(26)-Pt(1)-N(2)	80.65(19)
H(25)···F(1)	2.647	Cl(1)-Pt(1)-N(1)	88.97(12)
		Cl(1)-Pt(1)-C(13)	86.56(16)
		Cl(1)-Pt(1)-C(27)	94.05(15)
		Cl(1)-Pt(1)-N(2)	94.81(12)

In accordance with the spectroscopic data, **12c-e** molecules display slightly distorted octahedral geometry around the platinum center and the *fac* disposition of the three carbon atoms C,C,C_{Rf} is confirmed. The bond lengths are in accordance with the *trans* influence of the ligands and compare well with the data of other Pt(IV) complexes found in the bibliography.[65a, 66-67, 84] The Pt-N1 bond distance *trans* to C_6F_5 ligand

[2.0943(19) - 2.164(3) Å] is shorter than the Pt-N2 *trans* to the metalated C atom [2.130(2) - 2.264(3) Å], indicating the larger *trans* influence of the metalated C atom compared to that of the C atom of the C_6F_5 group. The two Pt-$C_{metalated}$ [2.012(3) – 2.037 (5)] lengths are slightly shorter than the Pt-C_6F_5 distances [2.035(5) - 2.070(5) Å] and, as expected, these distances are longer than those seen in similar Pt(II) compounds,[44-46, 49-50, 105, 129] which is characteristic of Pt(IV) compounds. For instance, the Pt-$C_{metalated}$ and the Pt-C_{C6F5} distances of the Pt(IV) compound **12d**, with two metalated dfppy ligands, are longer than in its Pt(II) precursor **10d**, previously described, [Pt-C11,C22 2.012(3), 2.026(2); Pt-C23 2.070(2) Å in **12d** *vs* Pt-C11 1.981(3) and Pt-C23 2.019 (3) Å **10d**]. Besides, the Pt-Cl [2.418(1) - 2.446(1) Å] distances are similar to those found in other related systems with the Cl atom *trans* to metalated carbon atoms.[66, 132]

In **12d** and **12e**, the C_6F_5 ligand is tilted towards the most open angles $C_{metalated}$-Pt-$C_{metalated}$ (97.5, 97.77º) and Cl-Pt-N2 (94.81 – 95.85º), and due to its remarkable steric bulk, the two *ortho*-fluorine atoms establish short *intramolecular* contacts. Thus, the distances of the *o*-F to the two hydrogen atoms *ortho* to $C_{metalated}$ (2.562, 2.683 Å **12d**; 2.518, 2.647 Å **12e**) and to the *ortho* hydrogen to N2 (2.533 - 2.562 Å) are shorter or close to the van der Waals limit (2.67 Å). However, in **12c**, only one short H-*o*F contact is seen for each molecule (F5··H14 2.588 Å in molecule **A**; H50··F10 2.430 Å in molecule **B**), probably due to the simultaneous occurrence of short $F_{(C6F5)}\cdots F_{(C6F5)}$ *intermolecular* interactions between the two molecules present in the asymmetric unit, as is shown in Figure 2.42.

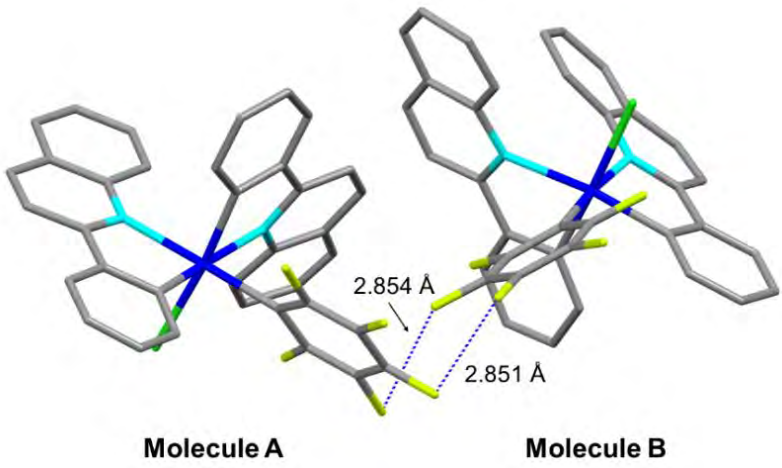

Figure 2.42. View of the two molecules (A and B) found in the asymmetric unit for the compound **12c**, showing the intermolecular F···F interactions between the C_6F_5 groups.

The crystal packing of **12c-e** is displayed in the Figures 2.43, A2.14 and A2.15. For **12c** and **12e**, the packing shows dimers with effective π···π interactions between the cyclometalated ligands, whereas in **12d** the packing is formed by chains supported by non-linear π···π interactions between the dfppy ligands. Besides, for the three complexes the packing is reinforced by H···Cl (2.82 – 2.90 Å) and F_{C6F5}···F_{C6F5} (2.813 Å **12e**) secondary contacts.

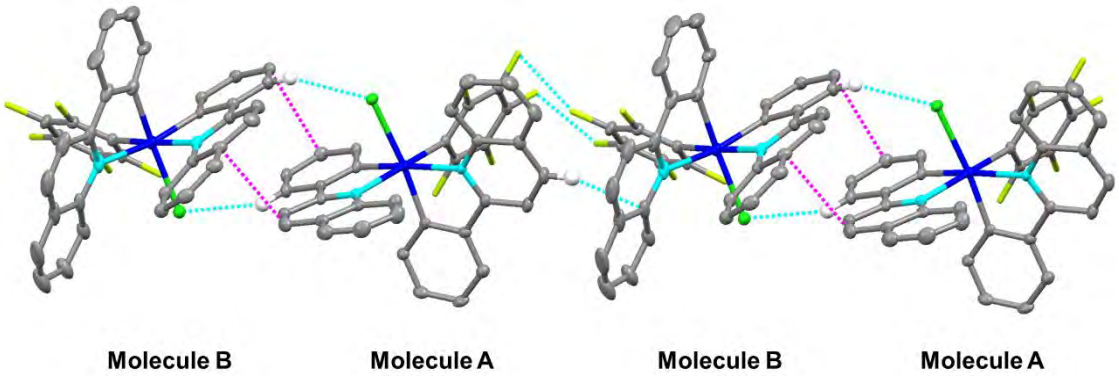

Figure 2.43. Crystal packing of **12c**·0.5 THF showing π···π (3.38 – 3.40 Å) and H···Cl (2.90 Å) interactions between the dimers.

The structure of complex **13** (Figure 2.44a and Table 2.9) confirms that the chloride/cyanide exchange in **12b** takes place with isomerization from *fac* (**12b**) to *mer* (**13**), as was predicted by the NMR studies. The Pt(IV) center displays a slightly distorted geometry retaining the mutually *cis*-(*C,C*) arrangement of the two pbt ligands of the precursor **12b**. The C_6F_5 group is located *trans* to the metalated C, and the cyanide group *cis* to C_6F_5. The Pt-C(C_6F_5) distance [2.147(2) Å] is longer to those seen in complexes **12** [2.035(5) - 2.070(5) Å], according to the higher *trans* influence of metalated C atom compared to the N donor atom. Comparing the Pt-$C_{metalated}$ distances, we found that the Pt-C13 [2.026(2) Å] length is shorter than the Pt-C26 [2.076(2) Å], due to the lower *trans* influence of the N atom in relation to the C_6F_5 group. The Pt-C_{CN} length is very short [1.963 (2) Å] and compares well to that reported for *trans*-[Pt(C^N^N)(CN)I_2] (HC^N^N = 6-phenyl, 2,2'bipyridine) [1.988(9) Å].[99d] Crystal structures of cyanide cyclometalated Pt(IV) derivatives are rare and, as far as we know, this is the first example of a Pt(IV) complex containing two cyclometalated groups and a cyanide ligand.

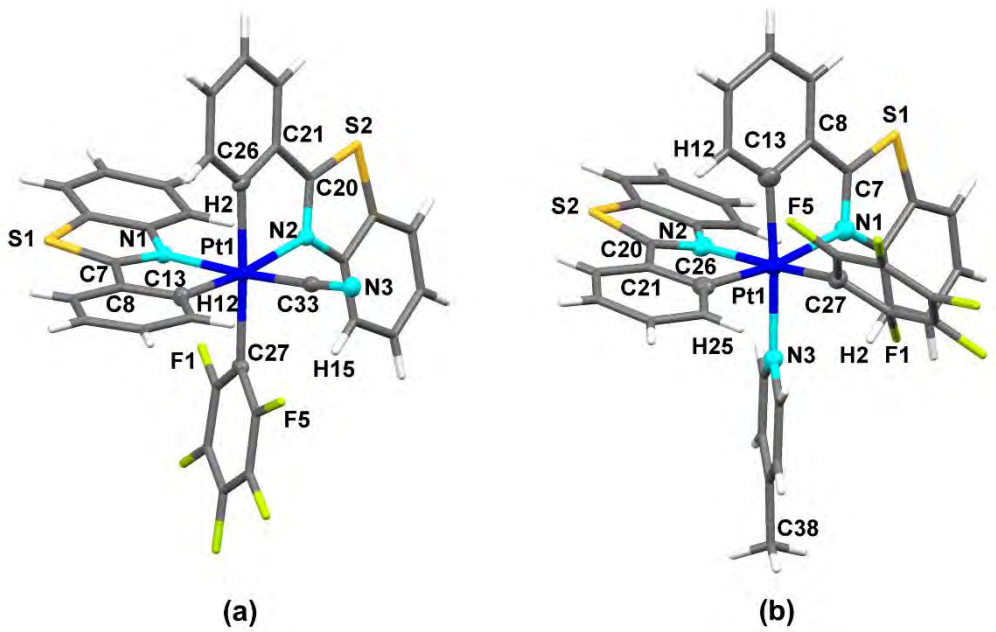

Figure 2.44. Molecular structure of (a) *mer*-[Pt(pbt)$_2$(C$_6$F$_5$)(CN)] **13** and the cation (b) *fac*-[Pt(pbt)$_2$(C$_6$F$_5$)(Mepy)]$^+$ in **14**.

Table 2.9: Selected distances (Å) and angles (°) for complexes **13** and **14**.

13			
Distances (Å)		**Angles (°)**	
Pt(1)-N(1)	2.1075(19)	C(13)-Pt(1)-N(1)	81.04(8)
Pt(1)-N(2)	2.1637(19)	N(1)-Pt(1)-N(2)	97.47(7)
Pt(1)-C(13)	2.026(2)	C(33)-Pt(1)-N(2)	86.93(8)
Pt(1)-C(33)	1.963(2)	C(33)-Pt(1)-C(13)	93.70(9)
Pt(1)-C(26)	2.076(2)	C(26)-Pt(1)-N(1)	85.65(8)
Pt(1)-C(27)	2.147(2)	C(26)-Pt(1)-C(13)	93.32(10)
C(7)-C(8)	1.451(3)	C(26)-Pt(1)-C(33)	88.41(9)
C(20)-C(21)	1.449(3)	C(26)-Pt(1)-N(2)	79.19(9)
H(12)···F(5)	2.542	C(27)-Pt(1)-N(1)	92.17(8)
H(2)···F(1)	2.888	C(27)-Pt(1)-C(13)	85.77(9)
H(15)···F(1)	3.017	C(27)-Pt(1)-C(33)	93.71(9)
		C(27)-Pt(1)-N(2)	101.69(8)
14·CH$_3$COCH$_3$			
Distances (Å)		**Angles (°)**	
Pt(1)-N(1)	2.210(3)	C(27)-Pt(1)-N(1)	88.24(13)
Pt(1)-N(2)	2.127(3)	N(1)-Pt(1)-N(2)	95.03(12)
Pt(1)-C(26)	2.037(4)	C(26)-Pt(1)-N(2)	80.59(14)
Pt(1)-C(27)	2.045(4)	C(26)-Pt(1)-C(27)	95.51(15)
Pt(1)-C(13)	2.041(4)	C(13)-Pt(1)-N(1)	80.15(14)
Pt(1)-N(3)	2.170(3)	C(13)-Pt(1)-N(2)	85.52(13)
C(7)-C(8)	1.449(6)	C(13)-Pt(1)-C(26)	91.91(15)
C(20)-C(21)	1.443(5)	C(13)-Pt(1)-C(27)	90.16(14)
H(12)···F(5)	2.675	N(3)-Pt(1)-N(1)	100.98(11)
H(2)···F(1)	2.422	N(3)-Pt(1)-N(2)	90.86(11)
H(25)···F(5)	2.669	N(3)-Pt(1)-C(26)	86.72(13)
		N(3)-Pt(1)-C(27)	93.39(13)

By contrast, the structure of **14**·CH_3COCH_3 confirms the retention of the *fac*-C,C,C_{Rf} configuration of the precursor **12b** in accordance with the NMR data (Figure 2.44b and Table 2.9). The Pt-C(C_6F_5) distance [2.045(4) Å] is similar to those found in compounds **12**, and the Pt-N1, Pt-N2 and Pt-N3 lenghts [2.127(3) - 2.210(3) Å] are within the range expected for these bonds. As far as we know, examples of X-ray structures of cyclometalated Pt(IV) complexes with monodentate pyridines are very scarce.[63, 134]

The molecular packing of **13**, given in Figure A2.16, shows a chain generated by $\pi_{C6F5}\cdots\pi_{C6F5}$ (3.39 Å **13**) intermolecular interactions, supported by $H_{pbt}\cdots F_{C6F5}$ and $N_{C\equiv N}\cdots S_{pbt}$ secondary interactions. For **14**, the packing shows dimers generated by short $\pi_{pbt}\cdots\pi_{pbt}$ (3.379 Å) interactions, which further engages through $F_{C6F5}\cdots F_{C6F5}$ contacts (Figure 2.45).

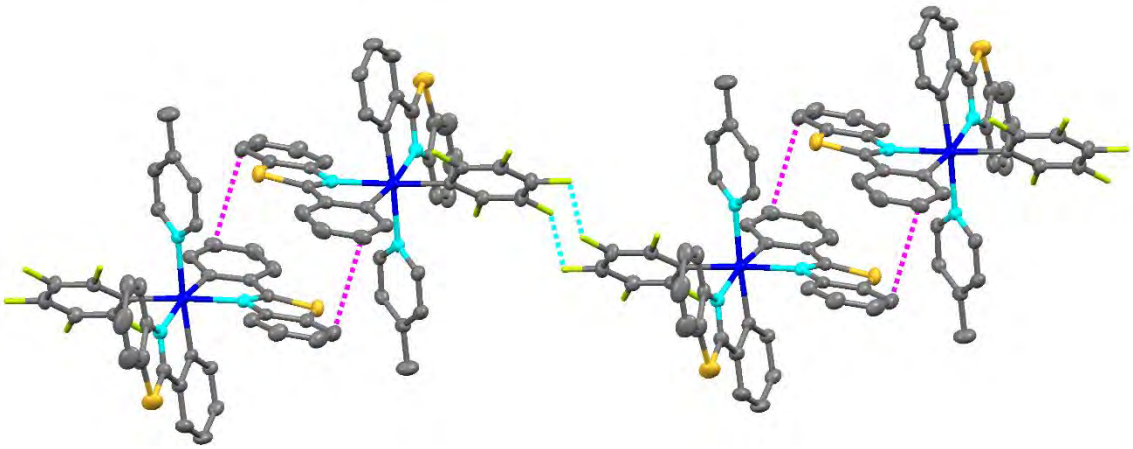

Figure 2.45. Crystal packing of complex **14**. The supramolecular packing is formed by dimers supported by $\pi\cdots\pi$ (3.379 Å) stacking interactions between two pbt groups, which are additionally connected by $F_{C6F5}\cdots F_{C6F5}$ (2.825 Å) interactions.

As it has been commented before, the visible light induces isomerization of the bpe-containing complex **15**. To examine the visible light influence on complex **15**, two sets of conditions were used for growing the crystals: at dark and under ambient light. Unfortunately, the quality of the crystals grown in the presence or absence of light was very poor for a single-crystal X-ray diffraction analysis. The best data were obtained when the crystals were grown by diffusion of *n*-hexane into a solution of complex **15** in acetone under ambient light at room temperature. Although the structure could not be completely refined, the connectivity of the structure was established and reveals a positional disorder of the bpe ligand in two positions, *E* and *Z* in a proportion of 60 and 40%, respectively (Figure 2.46). As it was expected, the structure shows the *fac*-(C,C,C_{Rf})

disposition and the orientation of the bpe group towards the equatorial pbt ligand in its *Z* form, as were predicted by the NMR studies. The Pt-N1, Pt-N2 and Pt-N3 lengths [2.130 (5) – 2.218 (5) Å] are almost identical to those found for **14**. Besides, the Pt-C13 distance (2.036 Å) is similar to that found in **14** (2.041 Å), indicating a similar *trans* influence of the bpe and Mepy ligands. This structure is consistent with previous work reported by N.Wang, T.Peng and S.Wang[133] for triarylboronfunctionalized Pt(II) dinuclear complexes with bpe bridging unit, where the growing of the crystals at either room temperature or at 4ºC in the dark gave only the *E* isomer, whereas the ambient light illumination is the key factor for *Z*-isomer formation.

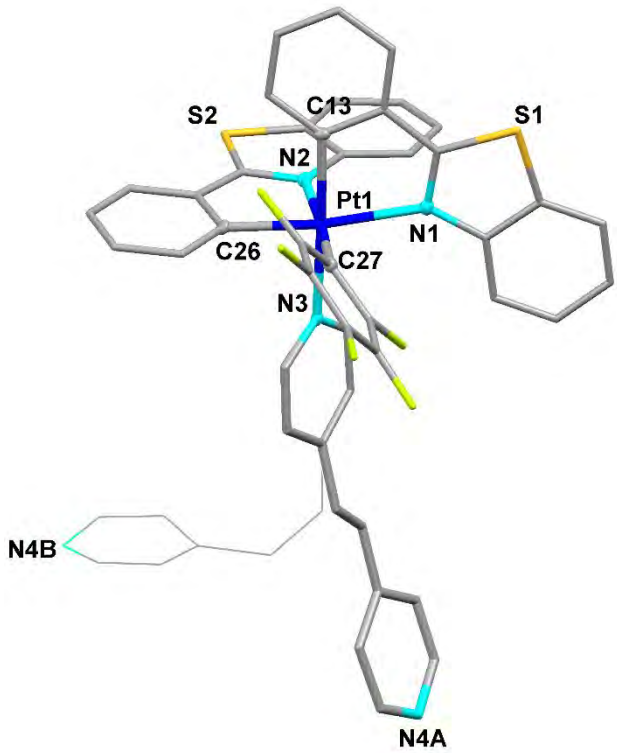

Figure 2.46. Molecular structure of the cation $[Pt(pbt)_2(C_6F_5)(bpe)]^+$ in **15** showing the two disordered positions: *E* (thick line) and *Z* (thin line).

2.2.4 Photophysical properties

2.2.4.1 Absorption spectroscopy

The UV-vis absorption spectra of all of the complexes were measured in CH_2Cl_2 solutions and the data are summarized in Table 2.10. In all compounds, the high-energy intense absorptions are attributed to ligand based π···π* transitions.

Table 2.10. Absorption data for compounds **12-15** in CH_2Cl_2 (5×10^{-5} M) solutions.

Compound	λ_{abs}/nm (10^3 ε/M^{-1} cm^{-1})
fac-[Pt(thpy)$_2$(C_6F_5)Cl] **12a**	231 (26), 289 (30.3), 348 (21), 355_{sh} (20)
fac-[Pt(pbt)$_2$(C_6F_5)Cl] **12b**	231 (47.4), 255 (23.8), 263 (22), 304 (27.9), 318 (32.7), 341 (31.3), 356 (23.1)
fac-[Pt(pq)$_2$(C_6F_5)Cl] **12c**	231 (49.1), 277 (52.4), 320 (16.5), 352 (21.9), 365 (21.3)
fac-[Pt(dfppy)$_2$(C_6F_5)Cl] **12d**	230 (31.3), 255 (22), 266 (18), 311 (18.2), 325 (15.2)
fac-[Pt(bzq)$_2$(C_6F_5)Cl] **12e**	232 (46.7), 284 (29.5), 357 (5.3), 375 (6.6)
mer-[Pt(pbt)$_2$(C_6F_5)(CN)] **13**	232 (41.3), 256 (19.8), 263 (20.3), 303 (27.2), 318 (33.6), 338 (34.4), 353 (24.9)
fac-[Pt(pbt)$_2$(C_6F_5)(Mepy)][PF_6] **14**	207 (37.6), 258 (21.4), 264 (19.0), 306 (24.7), 320 (29.4), 338 (30.8), 354 (21.8)
fac-[Pt(pbt)$_2$(C_6F_5)(bpe)][PF_6] **15**	231 (21.4), 258 (10.5), 265 (11.4), 307 (27.5), 317 (29.4), 332 (23.3), 356 (10.4)

Complexes **12a-e** exhibit, in the low energy region, structured bands (Figure 2.47), notably blue shifted in relation to those of the precursors **10a-e**, in accordance with the loss of colour after the oxidation of Pt(II) to Pt(IV). This effect is illustrated in Figure A2.17 where the spectrum of **12d** is compared with that of **10d** and studied by TD-DFT (see Section 2.2.5). These low energy bands range from 325 to 375 nm and display a strong dependence on the cyclometalated ligand in the order: dfppy (325 **12d**) > pbt (356 **12b**) ~ thpy (355_{sh} **12a**) > pq (365 **12c**) > bzq (375 nm **12e**), which correlates with the energies of the π* orbitals of C^N groups. MO analysis of the complexes **12c**,**d**,**e** (Table A2.5) confirm the expected remarkable decrease of the Pt orbitals in the HOMOs in relation to those found in the Pt(II) precursors (see section 2.1.4). This analysis allowed to assign the low-energy bands to a mixture of intra and interligand character (with variation along the series) involving the cyclometalated groups, which are non-equivalent

(^{1}IL/^{1}LLCT). The observed tendency correlates well with the more intense calculated values (S_3 346 nm **12c**, S_2 310 nm **12d**, S_1 353 nm **12e**) (see below).

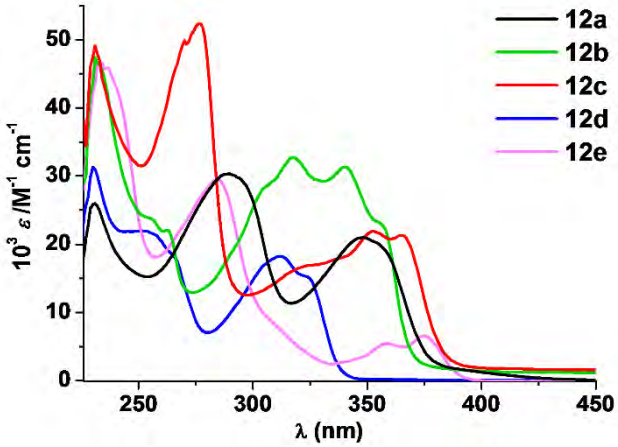

Figure 2.47. Absorption spectra of the Pt(IV) complexes *fac*-[Pt(C^N)$_2$(C$_6$F$_5$)Cl] **12** in CH_2Cl_2 (5 × 10^{-5} M) at 298 K.

The absorption spectra of *mer*-[Pt(pbt)$_2$(C$_6$F$_5$)CN] **13** and *fac*-[Pt(pbt)$_2$(C$_6$F$_5$)(L)][PF$_6$] (L = Mepy **14**) are rather similar to that of the precursor **12b** (dotted line in Figure 2.48) with only minor changes in the low-energy maxima (Table 2.10). TD-DFT calculations on **13** reveal that the isomerization *fac* to *mer* causes a higher contribution of the C$_6$F$_5$ ring to the lower energy transitions (S_2, S_3), which can be attributed to ^{1}IL transitions with some ligand to ligand (C$_6$F$_5$ → C^N) (^{1}L'LCT) parentage (see section 2.2.5). However, TD-DFT calculations on **14** show similar results to that obtained for compounds **12**, according to the retention of the *fac*-C,C,C$_{Rf}$ disposition, with the most intense low-energy bands S_2 (H-1→L) and S_3 (H→L+1) ascribed to ^{1}IL transitions.

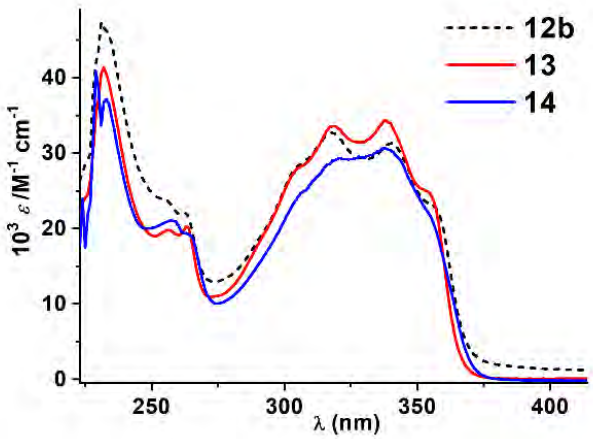

Figure 2.48. Absorption spectra of the Pt(IV) complexes *fac*-[Pt(C^N)$_2$(C$_6$F$_5$)Cl] **12b**, **13** and **14** in CH_2Cl_2 (5 × 10^{-5} M) at 298 K.

Complex **15** absorbs light, which results in its isomerization. Thus, a CH_2Cl_2 solution (5×10^{-5} M) of crystals of the bpe complex **15** isomers (mixture of 60:40, *E:Z* forms; see X-ray diffraction section) were irradiated using a monochromator centered at 320 nm during 1 hour (Figure 2.49). The irradiation process, monitored by UV-Vis spectroscopy, displays a decreased low-energy band centered at ~ 315 nm and an increased high-energy band at ~ 265 nm, reaching the photostationary state after 15 minutes of irradiation. We tentatively assign this change of the absorption to an isomerization process of the C=C bond in the bpe ligand from the *E*-isomer to the *Z*-form. Once the photostationary state was reached, subsequent irradiation at 255 nm with a hand-UV lamp was performed to explore if the process could be reversible but, unfortunately, no changes in the absorption of the mixture were observed under those conditions.

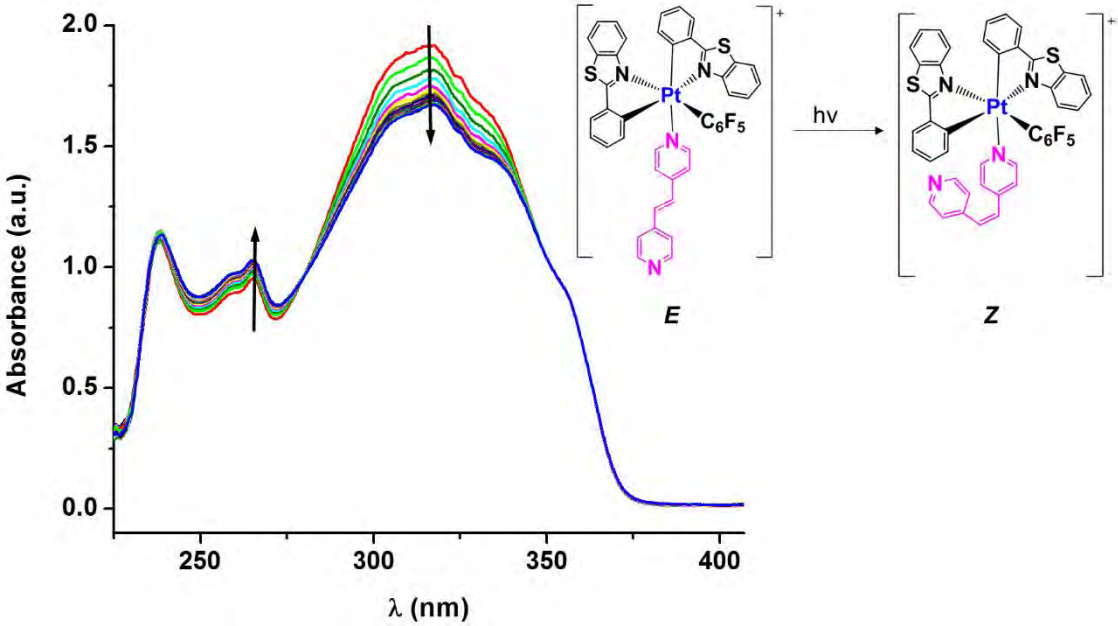

Figure 2.49. Change in the absorption spectra of **15** (crystals, 60:40, *E:Z*) in CH_2Cl_2 (5×10^{-5} M) with 320 nm irradiation.

2.1.4.2 Emission spectroscopy

The emission data of all the complexes in deoxygenated CH_2Cl_2 solutions and PMMA films are listed in Table 2.11 and the corresponding data in the solid state are included in Table 2.12. All the compounds show structured emission bands with large Stokes shifts and long lifetimes (μs) typical of triplet states.

Table 2.11. Photophysical data of complexes **12-15** in CH_2Cl_2/thf (5×10^{-5} M) and PMMA (10% wt.).

		T[a] (K)	λ_{em}/nm [a]	ϕ/% [b]	τ/μs	k_r/s^{-1} [c]	k_{nr}/s^{-1} [d]
12a	CH_2Cl_2	298	515		1.5		
		77	510		415.6		
	PMMA	298	515	8.2	49	1.7×10^3	1.9×10^4
12b	CH_2Cl_2	298	495		1.7		
		77	490		208		
	PMMA	298	500	3.1	56	5.5×10^2	1.7×10^4
12c	CH_2Cl_2	298	512		1.2		
		77	503		432		
	PMMA	298	505	18.1	98	1.8×10^3	8.4×10^4
12d	CH_2Cl_2	298	440		2.0		
		77	436		385		
	PMMA	298	440	8.7	130	6.7×10^2	7.0×10^3
12e	thf	77 [e]	477		3987		
	CH_2Cl_2	77 [e]	487		3658		
	PMMA	298	488	2.4	232	1.0×10^2	4.2×10^3
13	CH_2Cl_2	298	495		1.1		
		77	493		293		
	PMMA	298	495	18.4	56	3.3×10^3	1.5×10^4
14	CH_2Cl_2	298	495		5.0		
		77	492		204		
	PMMA	298	498	30.2	115	2.6×10^3	6.1×10^3
15	CH_2Cl_2	77	494		174		

[a] Highest-energy emission peak. [b] Absolute quantum yields determined by the absolute method using an integrated sphere. In solution at 298 K under Ar the quantum yields are too low to be accurately measured. [c] Radiative rate constant $K_r = \phi / \tau$. [d] Non-radiative rate constant $K_{nr} = (1-\phi) / \tau$. [e] Not emissive at 298 K.

Table 2.12. Photophysical data for complexes **12-15** in the solid state.

	T[a] (K)	λ_{em}/nm (λ_{ex}/nm)	ϕ^a (%)	τ/μs	k_r/s^{-1} [b]	k_{nr}/s^{-1} [c]
12b	77 [d]	520, 540_{max}, 560 (355-370)		106.3 (51%), 43.3 (49%)		
12c	298	580_{max}, 620_{sh} (365-430)	4.6	6.5 (18%), 0.7 (82%)	2.6×10^4	5.5×10^5
	77	530_{max}, 570, 620 (365-440)		141.6 (56%), 38.1 (44%)		
12d	298	505_{sh}, 540_{max}, 580, 625_{sh} (330-380) (Crystals)	8.8	118.3 (57%), 28.1 (43%) (505) 295.4 (72%), 61.7 (28%) (540)	3.7×10^2	4.0×10^3
	77	465, 494, 530_{max}, 570_{sh} (370)		20.7 (65%), 269.5 (35%) (494) 369.5 (66%), 20.2 (34%) (530)		
12e	77 [d]	507, 524, 540_{max}, 570, 620_{sh} (365-420)		1413.2 (54%), 568.6 (46%) (507) 1203.4 (27%), 5102.6 (73%) (524)		
13	298	530_{max}, 574, 620_{sh} (370)	8	21.3 (64%), 42.2 (36%)	2.8×10^3	3.2×10^4
	77	520, 550_{max}, 595_{sh} (370)		196.2 (90%), 37.0 (10%)		
14	298	540_{max}, 583_{max}, 630 (365-440)	22	11.2	2.0×10^4	7.0×10^4
	77	535_{max}, 580, 623 (365-440)		24.3		

[a] Absolute quantum yields determined by the absolute method using an integrated sphere. [b] Radiative rate constant $K_r = \phi / \tau$. [c] Nonradiative rate constant $K_{nr} = (1-\phi) / \tau$. [d] Not emissive at 298 K.

Complexes fac-[Pt(C^N)$_2$(C$_6$F$_5$)Cl] ***12***

With the exception of the bzq derivative **12e**, all Pt(IV) complexes **12** are emissive in fluid CH_2Cl_2 solutions at 298 K. However, all the complexes are emissive in frozen matrices at 77 K and in doped PMMA films at 298 K. The room temperature emission spectra for **12a-e** in doped (10%) PMMA films are shown in Figure 2.50 and the emissions in fluid CH_2Cl_2 solutions for **12a-d** at 298 K, which are essentially identical, are provided in the Figure A2.18. In glassy media (CH_2Cl_2 5×10^{-5} M solution at 77 K), the emissions are sharper with minor variations in their maxima (Figure 2.51).

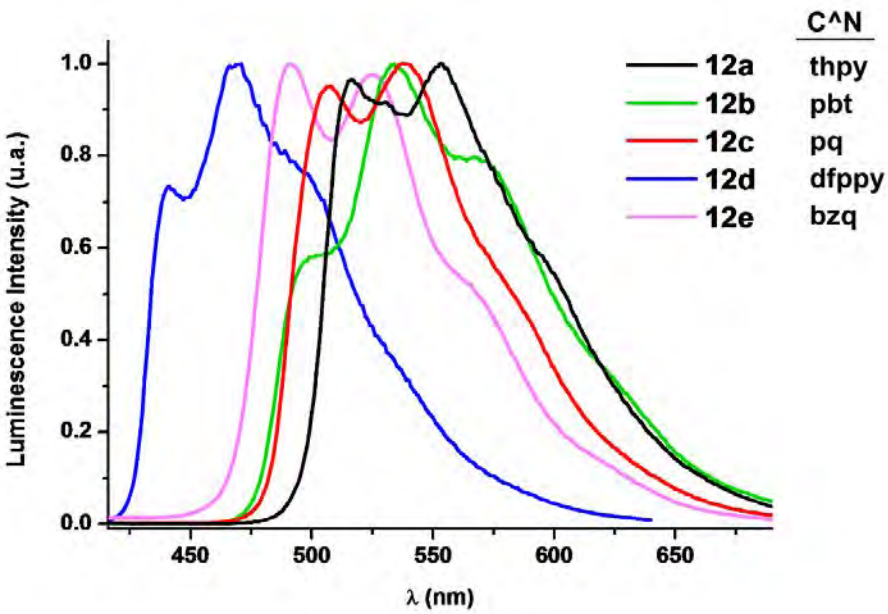

Figure 2.50. Normalized emission spectra of *fac*-[Pt(C^N)$_2$(C$_6$F$_5$)Cl] **12a-e** in PMMA (10 % wt) at 298 K

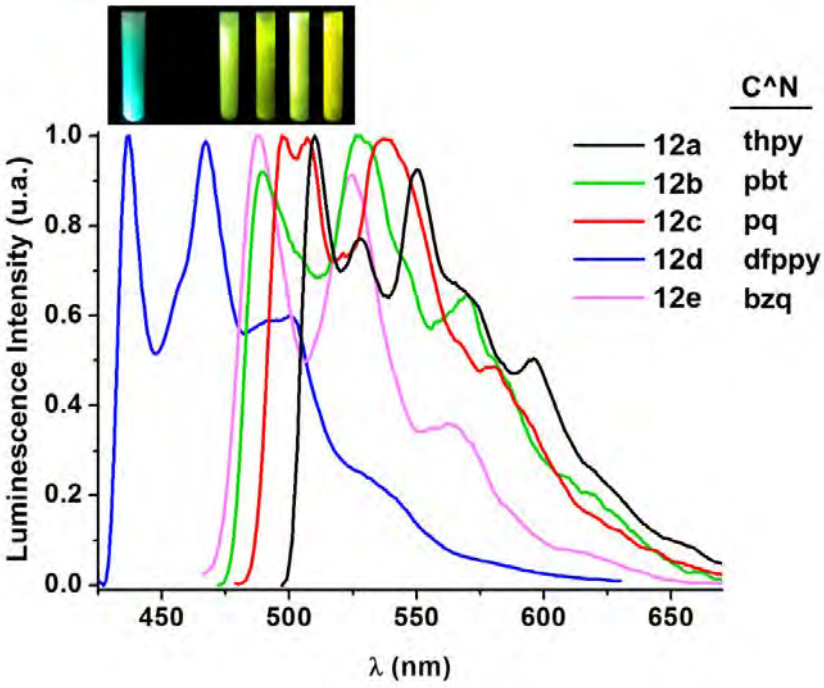

Figure 2.51. Normalized emission spectra of *fac*-[Pt(C^N)$_2$(C$_6$F$_5$)Cl] **12a-e** in CH_2Cl_2 5 × 10^{-5} M solution at 77 K.

In all media, the well-defined vibrational features suggest emissions primarily from a ligand centered ^{3}IL excited state. This assignation is in accordance with other examples of cyclometalated Pt(IV) complexes found in the bibliography.[25, 57-59, 60-62, 65a,

[66-67, 135] To support this assignation, theoretical calculations for **12c**,**d**,**e** were carried out, confirming the predominant ^{3}IL character of the transitions, with minor ^{3}MLCT character (see below, section 2.2.5).

The emission maximum depends on the cyclometalated ligand and it shifts to lower energies along the sequence **12d** (440) > **12e** (477, glass) > **12b** (495) > **12c** (512) > **12a** (515 nm). This tendency correlates well with the values calculated by DFT calculations from optimized T_1 excited states on the selected **12c,d,e** complexes (see below). In support to this assignment, the emissions of Pt(IV) complexes **12** are remarkably blue shifted in comparison with the results obtained for the precursors Pt(II) complexes **10** [Δ(cm^{-1}) CH_2Cl_2, 77 K: 1400 (thpy **a**); 1334 (pbt **b**); 1350 (pq **c**); 1222 (dfppy **d**); 346 (in THF, bzq **e**)]. Besides, the measured lifetimes undergo a considerable increase compared to those found for complexes **10** (CH_2Cl_2, 77 K, 208 for **12b** to 432 μs **12c** *vs* 14.9 for **10c** to 31 μs **10a**).

For the bzq derivative *fac*-[Pt(bzq)$_2$(C_6F_5)Cl] **12e**, the highest energy peak in thf solution at 77 K is only slightly blue shifted in relation to its precursor **10e** (477nm **12e** *vs* 485 nm **10e**,[46] thf at 77 K). However, the lifetime suffers a marked increase from 571 μs for **10e** to the value of 3987 μs observed in **12e**, which could be ascribed to the null ^{3}MLCT character in the emission. To the best of our knowledge, very few cyclometalated complexes display so long lifetime.[58, 65a, 66-67, 136] In the case of **12e**, the observed high value of the lifetime can be attributed to the extended π character of the benzoquinolinyl (bzq) ligand. We note that this characteristic could be of interest, because phosphorescent complexes with so long lifetimes have attracted attention in recent years due to their potential in photocatalysis,[137] photosensitizers,[138] chemosensors or biomaging[13g, 13l, 30] and optical sensors.[12g, 12h, 31]

The quantum yields of complexes **12** were measured in PMMA (10% *wt*) and the obtained values, from low to moderated (2.4 **12e** to 18.1 % **12c**) do not show any clear trend. The highest value was observed for the pq derivative **12c**. The lifetimes in PMMA at 298 K are shorter than in frozen CH_2Cl_2 glasses, by a factor between 3 for **12d** and 17 for **12e**, probably due to an easier access to deactivating excited states at room temperature. Decay rate constants from the experimentally determined quantum yields and lifetimes in PMMA have been estimated by assuming that the excited state is formed with unitary efficiency. The data (Table 2.11) reveal that both, the radiative (K_r) and non-

radiative (K_{nr}) rate constants, for complexes **12** are smaller than for Pt(II) complexes **10** (2 orders of magnitude for K_r), in accordance with a much lower ^{3}MLCT character in the ^{3}IL emission, which gives rise to smaller spin-orbit coupling (SOC).

In the solid state at room temperature, only weak emissions are detected for **12c** and **12d**, with quantum yield values of 4.6 and 8.8 respectively (Table 2.12). Emission spectra of crystals obtained of **12d** showed that the intensities of the first two peaks (505, 540 nm) are dependent upon the λ_{ex} used, and the excitation spectra monitored at both peaks are also slightly different (Figure A2.19), thus suggesting the presence of two close chromophoric environments. All the complexes exhibit strong emission in solid state at 77 K, showing structured profiles, generally red shifted in relation to those found in PMMA or solution (Figure 2.52). This could be related to the formation of some emissive species with excimeric character due to the presence of extensive π···π intermolecular interactions, as found in the X-ray structures. Besides, for these compounds in the solid state, the decays fit to two components and the values of the lifetimes are notably shorter than in CH_2Cl_2 at 77 K, which could be also attributed to triplet-triplet annihilation caused by closer intermolecular interactions in the solid state.[139]

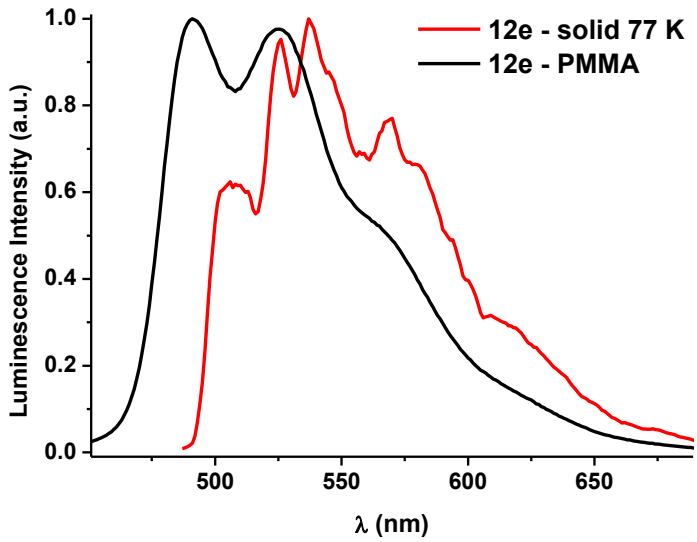

Figure 2.52. Normalized emission spectra of *fac*-[Pt(bzq)$_2$(C$_6$F$_5$)Cl] **12e** in the solid state at 77 K and in PMMA film (wt 10 %).

*Complexes **13**, **14** and **15***

Compounds *mer*-[Pt(pbt)$_2$(C$_6$F$_5$)CN] **13** and *fac*-[Pt(pbt)$_2$(C$_6$F$_5$)Mepy][PF$_6$] **14** are emissive in all media, showing almost identical emission features to that of the precursor **12b** in PMMA, solution or solid state (Figure 2.53). In contrast, complex *fac*-[Pt(pbt)$_2$(C$_6$F$_5$)(bpe)][PF$_6$] **15** only shows a very weak emission in glassy CH_2Cl_2 solution, with similar pattern to those observed for **12b**, **13** and **14** (Figure 2.53b) but it is non-emissive in solid (298 or 77 K), PMMA or solution at room temperature. The quenching of the emission is tentatively attributed to the occurrence of a photo-isomerization process from *E* to *Z* on the bis(4-pyridyl)ethylene (bpe) ligand that we have also observed by ^{1}H NMR monitoring when the complex was irradiated in a CD_3COCD_3 solution, as we have commented before. This process seems to be efficient at 298 K and somewhat reduced in frozen matrix.

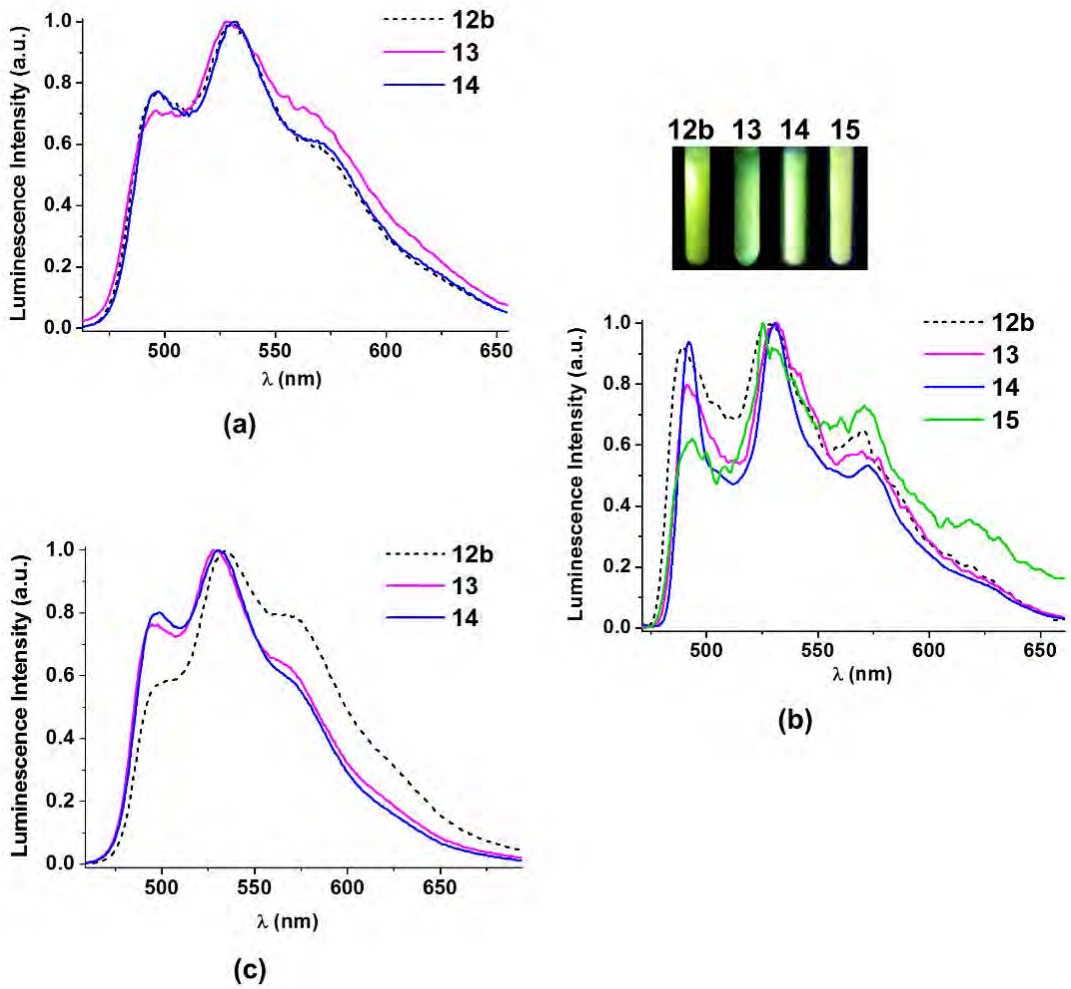

Figure 2.53. Emission spectra of **12b** (dotted lines), **13**, **14** and **15** in (a) CH_2Cl_2 at 298 K, (b) CH_2Cl_2 at 77 K, (c) PMMA (10 % wt) at 298 K.

The similarity of the emissions and the lifetimes values in comparison to **12b** indicates a similar ^{3}IL nature for the excited state as was confirmed by theoretical calculations (section 2.2.5). However, **13** and **14** undergo a substantial increase of the emission quantum yields in PMMA in relation to **12b** [ϕ (%) 18.4 **13**, 30.2 **14** *vs* 3.1 **12b**].

In the same line, while solid **12b** is not emissive at 298 K, **13** and **14** display in the solid state a similar structured emission with moderate quantum yields (8 % **13**, 22 % **14**). At 77 K, the emission of **13** and **14** are redshifted in relation to PMMA (Figure 2.54) due to the presence of π···π intermolecular interactions, as is found in the X-ray structures. Their lifetimes are also shorter than in frozen CH_2Cl_2 glasses, as found for **12**, likely due to easy triplet-triplet annihilation for close molecules in the solid state.

Therefore, it seems reasonable to assume that the Cl/CN and Cl/Mepy exchanges do not change the nature of the emissive state but the stronger ligand field character of the CN^- ligand and, to a lesser extent, the Mepy group, raise the energy of non-emissive MC states, thereby reducing detrimental quenching and thus increasing the quantum yields values. It should be noted that *fac*-**14** displays higher quantum yield than *mer*-**13**, either in PPMA or solid state, which could be attributed to the presence of more-accessible nonradiative states in the *mer* isomers. In this sense, González-Herrero *et al*, have studied the synthesis and photophysical properties of a series of complexes *mer*-[Pt(C^N)$_3$]OTf (C^N = ppy, tpy, dfppy, ppz, flpy)[67a, 67c], *mer*-[Pt(dfppy)$_2$(ppy)]OTf [67b] and *mer*-[Pt(ppy)$_2$(flpy)](OTf)][67c] which display weak emission, and their photoisomerization to their respective *fac* isomers, which show intense luminescence with high quantum yields. Besides, they have studied that this fact could be attributed to a thermally accessible LMCT (ligand-to-metal charge-transfer) excited state in the *mer* isomers, which deactivate the luminescence and provides the photoisomerization.

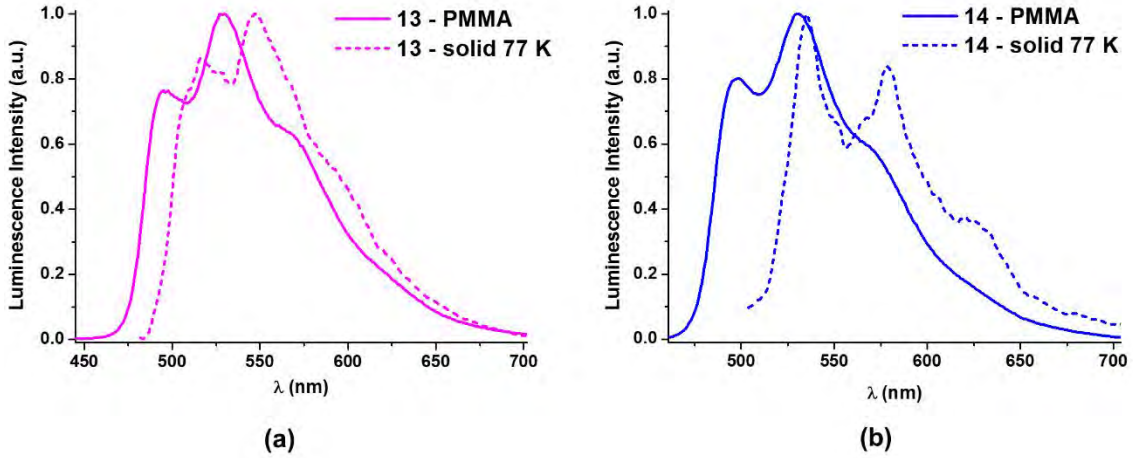

Figure 2.54. Normalized emission spectra of (a) **13** and (b) **14** in PMMA (10 % *wt.*) and solid state at 77 K.

2.2.5 Theoretical calculations

For a better understanding of the photophysical properties of the Pt(IV) compounds, a combined DFT and TD-DFT theoretical calculations study was carried out for selected compounds (**12c**, **12d**, **12e**, **13** and **14**) in the presence of solvent (CH_2Cl_2) at the B3LYP/(6-31G**+LANL2DZ) level. The geometries of the complexes were fully optimized without imposing any symmetry constrains (Figure A2.20). In all the selected compounds, the bond distances and angles of the optimized geometries (S_0 and T_1) are in agreement with the values found in their respective X-ray structures (Table A2.4). Figures A2.21-A2.25 show the frontier orbital plots of the S_0 optimized geometries in CH_2Cl_2 and the molecular orbital compositions are included in the Table A2.5.

A schematic representation of the energy and electron density contours calculated for the highest occupied (HOMO to HOMO-2) and lowest-unoccupied (LUMO to LUMO+2) molecular orbitals for complexes **12c**, **12d**, **12e**, **13** and **14** is depicted in the Figure 2.55. The first unoccupied orbital with a metal contribution higher than 30 % is represented by a red line. For all the complexes, the major contribution to the HOMO and LUMO orbitals arises from the cyclometalated C^N units, with small contribution of the ancillary Cl and C_6F_5 ligands in some compounds (Table A2.5).

Among complexes **12** (see Figure 2.55a), the most significant difference is that in **12e** the HOMO and LUMO are localized on the π and π* orbitals of the bzq group, which is in *trans* to the C_6F_5 ligand (bzq 1), while HOMO-1 and LUMO+1 are localized on the

second bzq (bzq 2). It should be noted that the LUMO, LUMO+1 and HOMO, HOMO-1 are very close in energy between them, indicating that minor changes could cause the inversion of these orbitals. However, in the remaining complexes, the HOMO and LUMO are distributed between both no equivalent C^N units, with a higher contribution of the C^N *trans* to C_6F_5 in **12d** and *trans* to Cl in **12c**, thus anticipating a mixed degree of LLCT character in the low-lying excitations. The contribution of the metal to the HOMO is notably decreased (4 – 6 %) in comparison with the precursors **10** (35 **10b**, 38 % **10d**) with the greatest contribution calculated for the complex with the 2-phenylquinoline (pq) as the cyclometalated ligand **12c** (6 %). The effect of the strong electron-withdrawing character of the difluorophenylpyridine group in **12d** is reflected in the energy of the highest occupied orbitals. Thus, the HOMO-1 and HOMO-2, that have a remarkable contribution from the auxiliary C_6F_5 ligand, are very close in energy not only between them but also with the HOMO (HOMO-1 0.02, HOMO-2 0.14 eV). However, for **12c** and **12e**, the contribution of the C_6F_5 ligand is relevant in the HOMO-2, but in these complexes lies at significantly lower energies than the HOMO (0.28 eV **12c**, 0.45 eV **12e**). Besides, although the influence of the chloride ligand in the HOMOs is generally irrelevant, an increased contribution is found in **12c**. The LUMO is localized on the C^N ligand *trans* to the C_6F_5 ligand in complexes **12e** (88 %) and **12c** (94 %), whereas there is a contribution from both cyclometalated units in **12d** (51 and 39 %), thereby indicating greater delocalization. The first unoccupied orbital with relevant metal contribution (>30 %) is LUMO+2 in **12c**, LUMO+4 in **12d** and LUMO+5 in **12e** (red lines in Figure 2.55a), which are located above the LUMO by 0.89 **12c**, 0.82 **12d** and 0.99 eV **12e**. It should be noted that, whereas high contribution of the metal in the unoccupied orbitals can be the responsible of no radiative processes, the contribution of the metal in the HOMOs orbitals usually favours the phosphorescence properties.[1b, 14g, 140]

In the cyanide compound *mer*-[Pt(pbt)$_2$(C_6F_5)(CN)] **13**, the HOMO is located on the pbt ligand *trans* to C_6F_5, whereas the LUMO is located on the pbt ligand *trans* to CN group, likely due to the change from *fac*-[Pt(CCC_{Rf})] to *mer*-[Pt(CCC_{Rf})] disposition. On the other hand, in the cationic complex *fac*-[Pt(pbt)$_2$(C_6F_5)(Mepy)]$^+$ **14**, the HOMO is mainly formed by π orbitals of the pbt group *trans* to the Mepy ligand and the LUMO is centred on the pbt *trans* to the C_6F_5 (Figure 2.55b). The most remarkable difference between both complexes is that the unoccupied orbital with a significant metal contribution is the LUMO+2 in **13** (0.82 eV above LUMO) and the LUMO+16 (2.99 eV

above LUMO) in **14**. Therefore, the unoccupied orbitals with significant Pt contribution lie at much higher energies in the *fac*-**14** derivative in comparison with the *mer*-**13** complex, revealing that the *fac* geometry favours a larger ligand-field separation. So, in spite of the weaker ligand-field of the Mepy ligand in relation to CN^-, this might be the reason to the stronger emission of **14** compared to **13** in all media.[65a, 67]

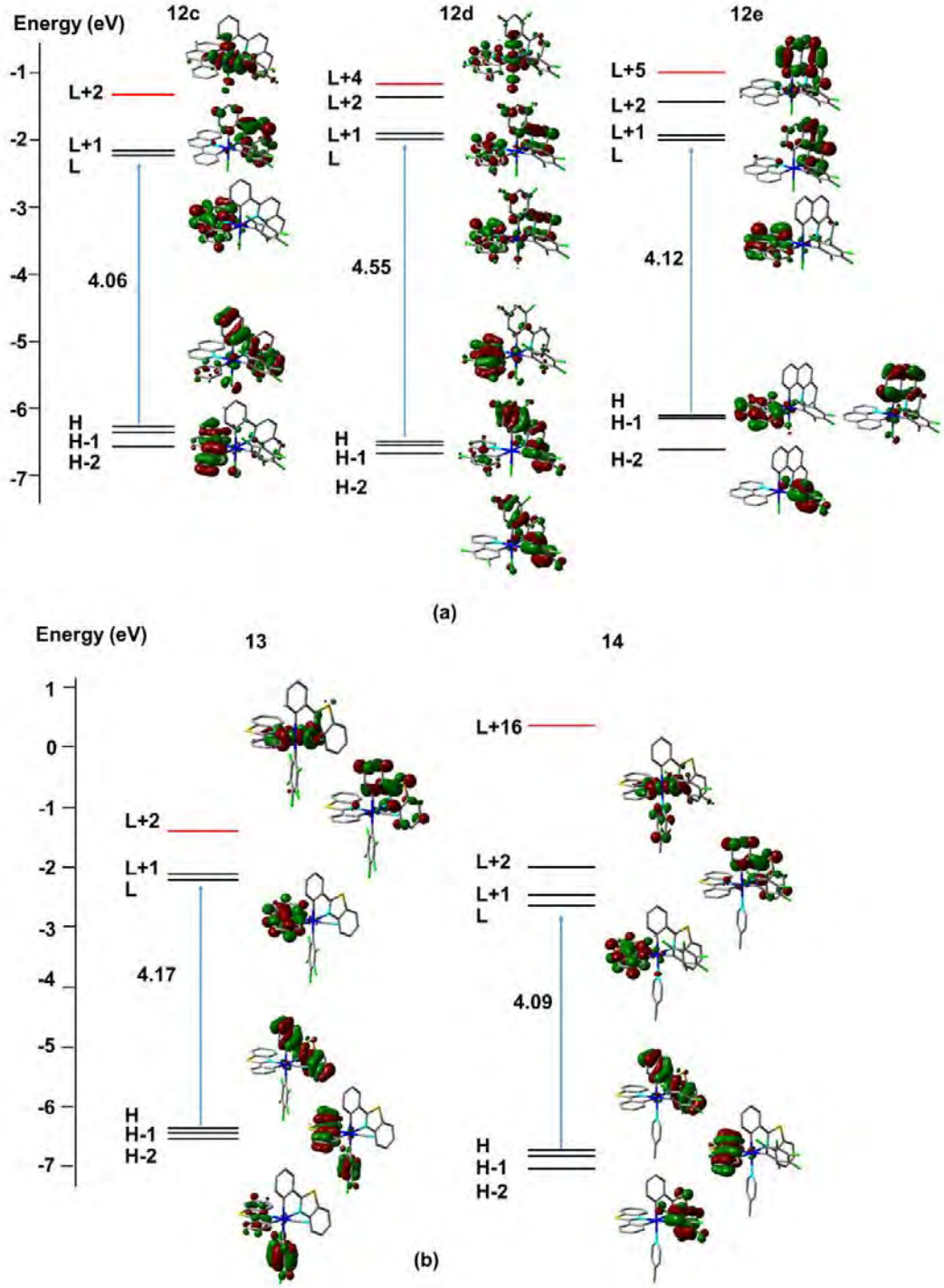

Figure 2.55. Schematic representation of selected frontier orbitals of (a) **12c**, **12d**, **12e** and (b) **13** and **14** complexes. The red lines represent the first unoccupied orbital with > 30 % metal contribution.

To get further inside into the luminescent properties of these compounds, TD-DFT calculations were carried out at the S_0 geometry for compounds **12c**, **12d**, **12e**, **13** and **14**. Relevant energies, oscillator strengths for selected singlets and triplets excitations and transition assignments are collected in Tables A2.6 and A2.7. For the low-lying excitations, the main character and the percentage of MLCT (or LMCT) were estimated taking into account the metal orbital contribution to the involved orbitals and are included in the Tables. The calculated transitions for the selected complexes reproduce well the shape of the corresponding experimental UV spectra (Figure 2.56). Moreover, the oscillator strengths for the most intense low-lying excitations (calcd S_3, 356 **12c**; S_2, 310 **12d**; S_1, 353 nm **12e**) reproduce qualitatively well the intensity of the experimental profiles (exptl 365 **12c**, 325 **12d**, 375 nm **12e**). The observed blue-shift in **12d** might be attributed to the stabilization of the HOMO due to the electron withdrawing nature of the difluoropyridine ligand, while the redshift in **12e** can be ascribed to the good π-accepting character of the benquinolinyl-based LUMO.

For **12e**, the most intense low-lying transition corresponds to ^{1}IL, whereas for **12c** and **12d** it has mainly mixed ^{1}IL/^{1}LLCT character with minor ^{1}L'LCT (C_6F_5→dfppy) contribution in **12d**. In **12c**, the two lowest singlets predicted at lower energies (S_1 358, S_2 349 nm) also have a small contribution from the chlorine ligand and can be described as an admixture of ^{1}LLCT/^{1}(X+L')CT/^{1}IL. These low-energy transitions have negligible ^{1}MLCT (**12c**,**e**) or ^{1}LMCT (**12d**) character (Table A2.6).

In the case of complexes **13** and **14**, the calculated most intense excitations are very similar (S_3 332 **13**, 333 nm **14**) having ^{1}IL character with some ^{1}L'LCT (C_6F_5→C^N) contribution in **13**, whereas the two weak singlets S_1 and S_2 have ^{1}LLCT character in both complexes with some ^{1}L'LCT character in the S_2 of **13**.

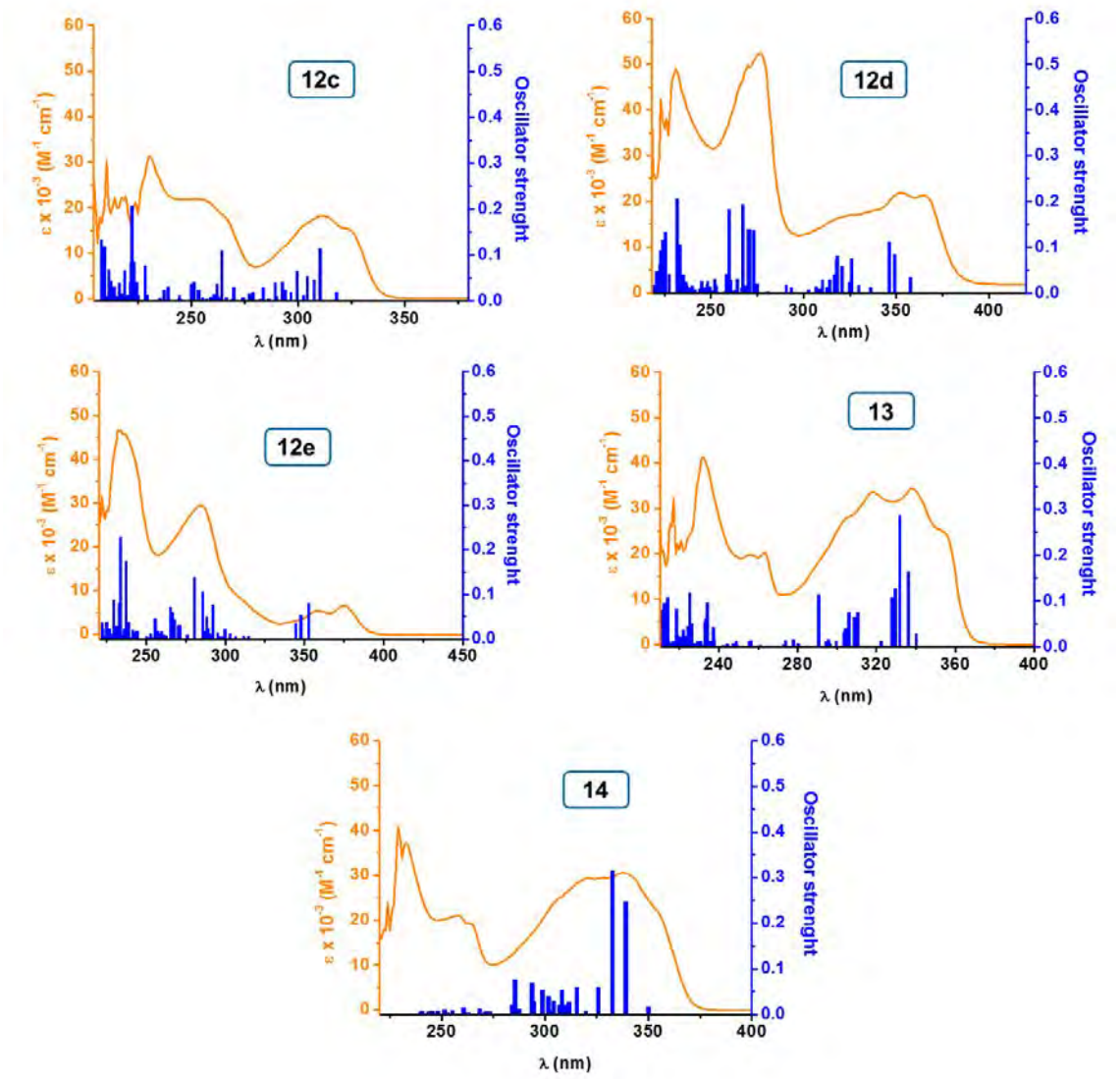

Figure 2.56. Calculated stick absorption spectra of the Pt(IV) complexes **12c**, **12d**, **12e**, **13** and **14** in CH_2Cl_2 compared with the experimental spectra.

The properties of the five lowest-energy triplet states T_1-T_5 for the optimized structures of the ground state S_0 were calculated and the corresponding assignments detailed in Table A2.7. The T_1 and T_2 states are very close in energy (0.0125 – 0.0241 eV) for **12c-e**, **14** and almost degenerated in **13** (0.00118 eV). However, T_3-T_5 are well above for all the complexes and are not considered (T_3-T_2 = 0.394 **12c**, 0.644 **12d**, 0.327 **12e**, 0.671 **13**, 0.622 eV **14**).

For the phenylquinolinyl complex **12c**, the T_1 and T_2 states have complex configuration ^{3}IL/^{3}LLCT/^{3}(X+L')CT, with minor contribution of the auxiliary C_6F_5 (L') and chlorine (X) groups. For **12d**, T_1 and T_2 states have mixed ^{3}LC/^{3}LLCT character for both triplets, thus mimicking the low-energy absorption features, whereas for **12e**, the

results predict states of primarily ^{3}IL nature. Insignificant (< 4.4 %) ^{3}MLCT (**12c**, **12e)** or ^{3}LMCT character (**12d**, **13** and **14**) is calculated for the five low-lying triplets (Table A2.7).

The calculated wavelengths of these T_1 states by TD-DFT at the ground-state S_0 geometry agree with the tendency observed for the experimental phosphorescence data (calcd 413 **12d**, 459 **13** ≈ 464 **14**, 475 nm **12c** *vs* exptl 440 **12d**, 495 **13**, **14**, 512 **12c**). Complex **12e** is not emissive in fluid solution, but the calculated value at 459 nm compares with its emission in rigid media (477 nm, CH_2Cl_2 ,77K).

For further details on the emissive properties, the geometries of the T_1 state in **12c-e**, **13** and **14** complexes were optimized. The calculated electronic energies for the optimized T_1 geometry in the T_1 state relative to the energy in the S_0 state (adiabatic energy differences) are underestimated in relation to the experimental values, but they also follow the tendency observed experimentally (calcd. 499 **12d**, 557 **12e**, 577 **12c**; 606 **13** ≈ 599 nm **14**). The spin density distribution has been studied and is shown in Figure 2.57. As can be observed, the distribution is entirely centered on one of the cyclometalated ligands with negligible metal or auxiliary ligands contribution, thus supporting a primarily ^{3}IL nature of the emission for all the studied Pt(IV) complexes. The topology of the spin density resembles the LUMO for complexes **12c**, **12e** and **14** and the LUMO+1 for **13**.

For complexes **12c**, **12e**, **13** and **14** the compositions of the SOMO and SOMO-1 (Table A2.8 and Figures A2.26-2.27) identify the excitations as HOMO → LUMO for **12e**, HOMO-1 → LUMO for **12c** and **14**, and HOMO → LUMO+1 for **13**, which allows us to deduce the phosphorescence as ^{3}IL. However, in **12d**, analysis of the spin density or the SOMO and SOMO-1 plots reveals a strong localization on one of the C^N ligands in the optimized T_1, which contrasts with the delocalization of the low-lying unoccupied orbitals found in the optimized S_0 geometry, which suggests a higher distortion upon excitation.

Finally, the calculated spin density over the platinum center is very low in all the complexes (0.000314 **13** - 0.0109 **12d**), in agreement with the small metal contribution to the highest-occupied orbitals involved in the excitations.

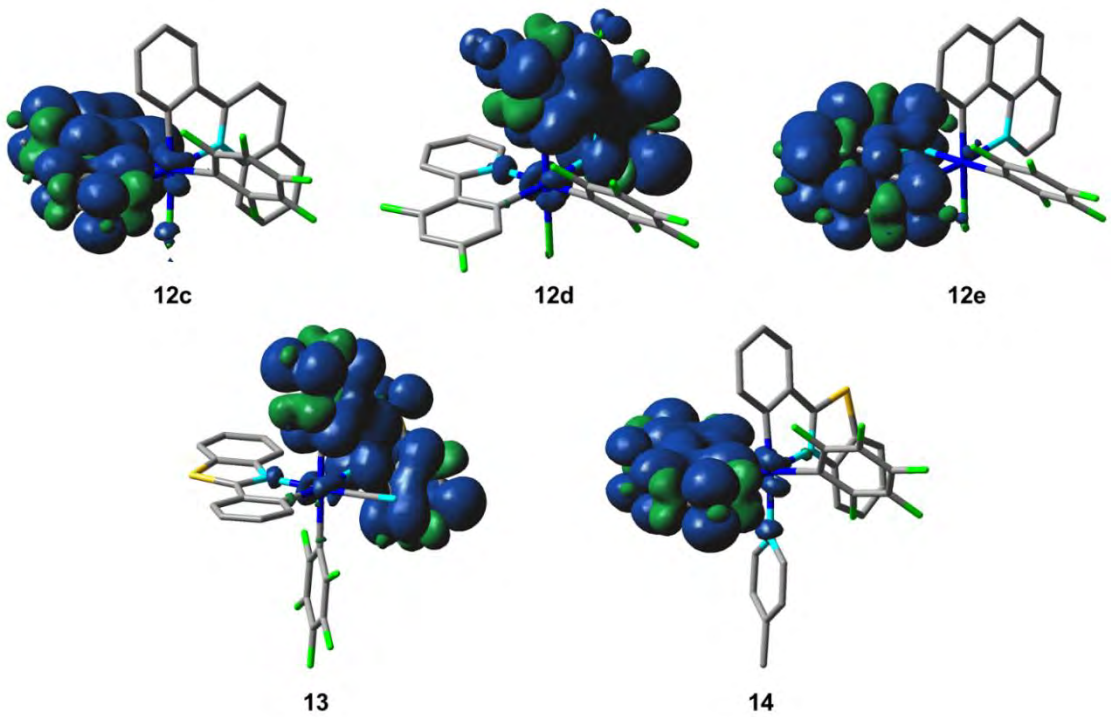

Figure 2.57. Spin density plots of **12c**, **12d**, **12e**, **13** and **14**.

2.3 Appendix

Appendix - Chapter 2.1

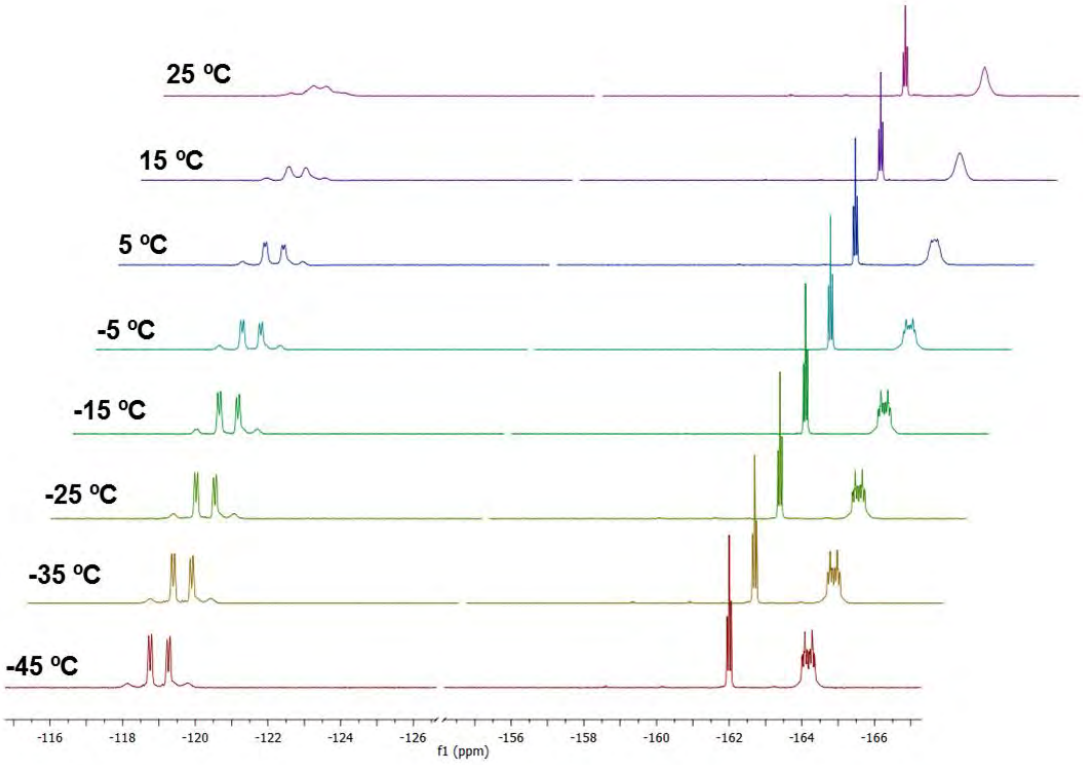

Figure A2.1. Variable temperature ^{19}F NMR spectra of **9a** in $CDCl_3$.

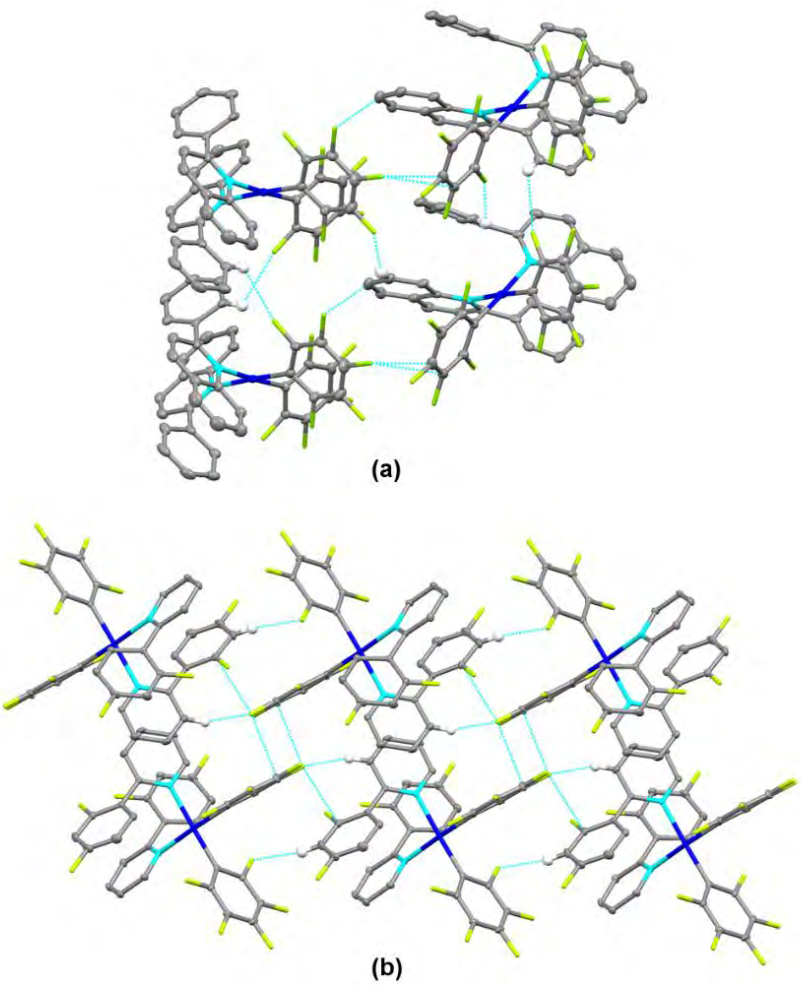

Figure A2.2. (a) View of the secondary interactions in the structure **9c**.0.75CH_2Cl_2: $F_{C6F5}\cdots C_{C6F5}$ (3.04 Å), $F_{C6F5}\cdots C_{Hpq}$ (3.15 Å) and $F_{C6F5}\cdots H_{Hpq}$ (2.59 Å). (b) Crystal packing of **9d** showing the short intermolecular contacts [$C_{C6F5}\cdots F_{C6F5}$ (3.05 Å), $F_{C6F5}\cdots C_{dfppy}$ (3.01 Å) and $H_{dfppy}\cdots F_{C6F5}$ (2.64-2.50 Å)].

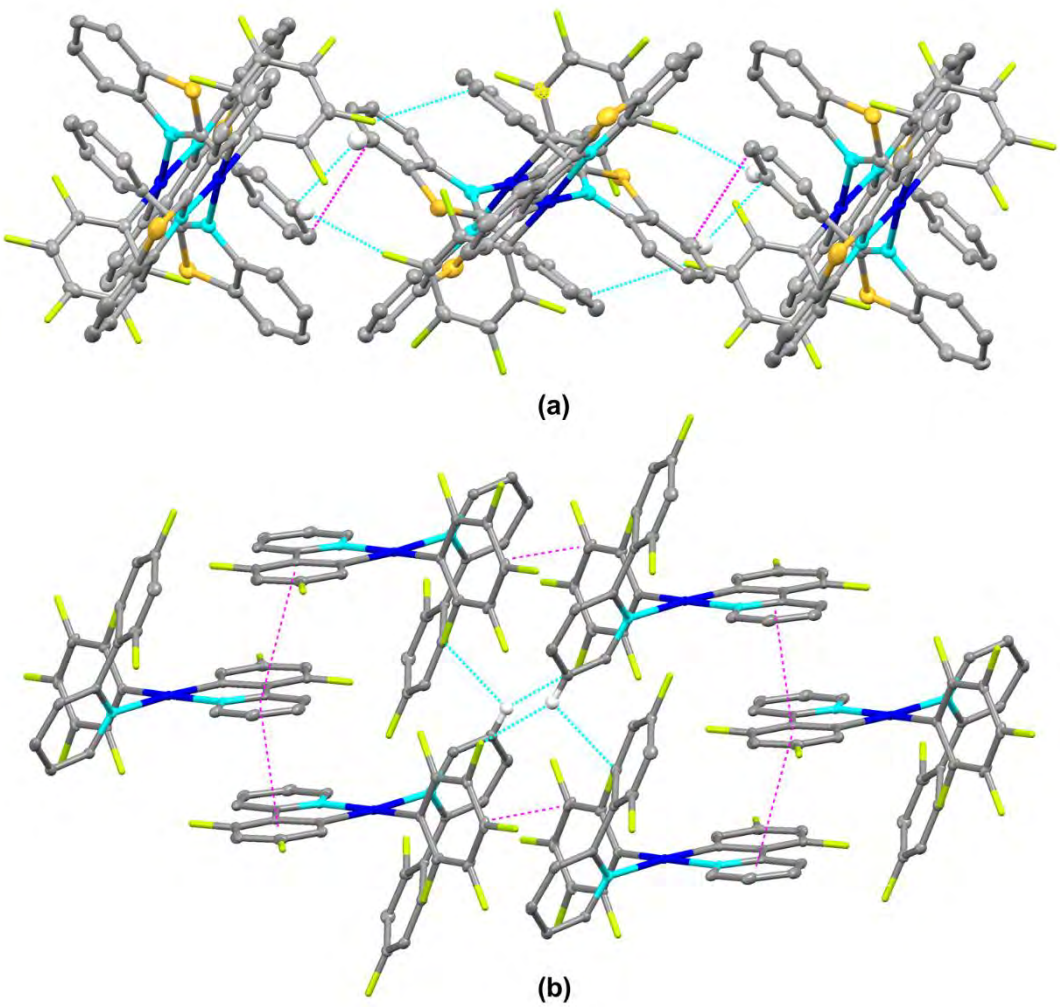

Figure A2.3. Additional contacts of (a) **10b** showing the interactions between dimers supported by π···π interactions ($C_{Hpbt}\cdots C_{Hpbt}$, 3.35, pink lines) and weak interactions (blue) [$H_{Hpbt}\cdots F_{C6F5}$, 2.66 Å; $H_{bt}\cdots C_{Hpbt}$, 2.81 Å; $C_{Hpbt}\cdots F_{C6F5}$, 3.12 Å] and (b) **10d** showing the [$C_6F_5\cdots C_6F_5$ (3.43 Å) (pink lines) and $H_{Hdfppy}\cdots F_{C6F5}$ (3.08 - 3.17 Å) (blue lines)] contacts between the chains.

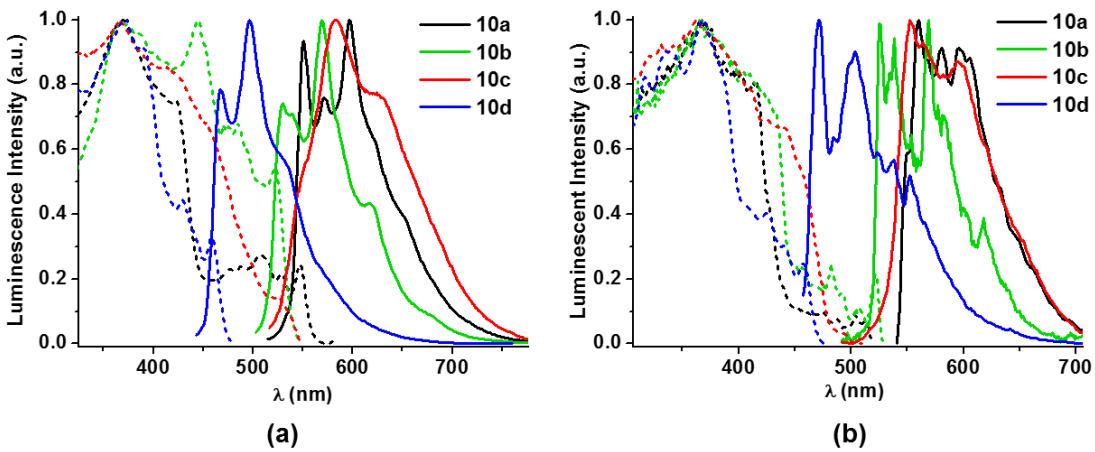

Figure A2.4. Normalized excitation and emission spectra of complexes **10a-d** in solid state at (a) 298 K and (b) 77K.

Table A2.1. DFT optimized geometries for ground state and triplet state of complexes **9a**, **9c**, **9d**, **10b**, **10d** and **3a**.

9a			
	X-ray	S_0	T_1
Pt-N(1)	2.110(3)	2.214	2.220
Pt-N(2)	2.111(3)	2.217	2.195
Pt-C(19)	2.012(4)	2.021	2.023
Pt-C(25)	2.015(4)	2.021	2.029
C(14)-C(15)	1.464(6)	1.469	1.393
H(16)···Pt	3.044	2.895	2.675
N(1)-Pt-N(2)	88.97(12)	89.65	88.62
C(19)-Pt-N(2)	88.80(14)	91.01	92.41
C(25)-Pt-N(1)	89.79(14)	91.88	91.77
C(19)-Pt-C(25)	92.46(16)	87.45	97.20
9c			
	X-ray	S_0	T_1
Pt-N(1)	2.173(6)	2.251	2.163
Pt-N(2)	2.133(5)	2.251	2.254
Pt-C(31)	2.012(8)	2.030	2.047
Pt-C(37)	2.011(6)	2.030	2.023
H(14)···Pt	2.773	2.677	2.665
H(29)···Pt	2.759	2.677	2.710
N(2)-Pt-N(1)	90.1(2)	92.7	92.5
C(31)-Pt-N(2)	91.5(2)	90.9	90.0
C(31)-Pt-C(37)	87.2(3)	85.5	85.9
C(37)-Pt-N(1)	91.4(2)	90.9	91.5
9d			
	X-ray	S_0	T_1
Pt(1)-N(1)	2.117(2)	2.198	2.212
Pt(1)-N(2)	2.117(2)	2.198	2.167
Pt(1)-C(23)	2.012(3)	2.025	2.037
Pt(1)-C(29)	2.013(3)	2.025	2.027
N(1)-Pt(1)-N(2)	90.82(9)	92.48	89.15
C(23)-Pt(1)-N(1)	90.85(10)	89.61	91.01
C(29)-Pt(1)-C(23)	86.63(11)	88.36	87.06
C(29)-Pt(1)-N(2)	91.71(10)	89.61	92.76
H(11)···Pt(1)	2.982	3.065	3.018
H(22)···Pt(1)	2.897	3.064	2.757

C(11)-Pt(1)	3.316	3.406	3.380
C(22)-Pt(1)	3.212	3.406	3.309
		10b	
	X-ray	S_0	T_1
Pt-N(1)	2.101(3)	2.194	2.130
Pt-N(2)	2.152(3)	2.244	2.263
Pt-C(9)	2.007(3)	2.004	1.981
Pt-C(27)	2.005(4)	2.019	2.034
H(22)···Pt	2.587	2.831	2.890
H(15)···Pt	2.786	2.881	2.908
N(1)-Pt-N(2)	96.90(12)	99.14	98.61
C(27)-Pt-N(2)	90.65(12)	87.20	86.00
C(27)-Pt-C(9)	91.20(15)	93.72	93.36
C(9)-Pt-N(1)	81.37(15)	79.95	82.034
		10d	
	X-ray	S_0	T_1
Pt(1)-N(1)	2.072(2)	2.134	2.095
Pt(1)-N(2)	2.153(3)	2.243	2.258
Pt(1)-C(11)	1.981(3)	1.998	1.971
Pt(1)-C(23)	2.019(3)	2.036	2.048
N(1)-Pt(1)-N(2)	96.78(10)	96.16	95.47
C(11)-Pt(1)-N(1)	80.91(12)	80.20	81.61
C(11)-Pt(1)-C(23)	92.46(13)	94.50	94.23
C(23)-Pt(1)-N(2)	89.77(11)	89.10	88.62
H(22)···Pt(1)	3.058	3.186	3.213
C(22)-Pt(1)	3.390	3.492	3.520
		11a	
	X-ray	S_0	T_1
Pt-N(1)	2.009(7)	2.168	2.139
Pt-C(1)	2.049(9)	2.005	1.975
Pt-S(2)	2.296(2)	2.438	2.450
Pt-C(10)	2.007(10)	2.034	2.041
O(1)-S(2)	1.472(6)	1.510	1.510
S(2)-C(16)	1.789(9)	1.819	1.820
S(2)-C(17)	1.795(9)	1.820	1.821
C(10)-Pt(1)-C(1)	91.5(4)	91.9	91.4
C(1)-Pt(1)-N(1)	79.0(3)	79.8	81.1
C(10)-Pt(1)-S(2)	92.0(3)	90.6	90.2

N(1)-Pt-S(2)	98.09(18)	97.8	97.4
O(1)-S(2)-Pt(1)	116.9(3)	120.1	120.4

Table A2.2. Composition (%) of Frontier MOs in the ground state for complexes **9a**, **9c**, **9d**, **10b**, **10d** and **11a** in CH_2Cl_2.

9a							**9c**					
MO	eV	C_6F_5 (1)	C_6F_5 (2)	Pt	Hthpy (1)	Hthpy (2)	eV	C_6F_5 (1)	C_6F_5 (2)	Pt	Hpq (1)	Hpq (2)
L+5	-0.15	1	1	2	75	22	-0.3	2	2	2	49	45
L+4	-0.52	24	25	34	10	8	-0.53	25	25	31	10	10
L+3	-1.03	2	1	2	65	30	-0.81	1	1	1	49	48
L+2	-1.18	0	1	1	31	67	-0.89	0	0	1	49	50
L+1	-1.66	0	0	2	72	26	-1.92	0	0	1	49	49
LUMO	-1.74	0	0	1	27	72	-2.02	0	0	1	49	49
HOMO	-5.82	3	3	73	10	11	-5.86	4	4	82	5	5
H-1	-6.02	34	31	32	2	1	-6.01	28	28	30	7	7
H-2	-6.23	17	19	33	14	17	-6.15	26	26	30	9	9
H-3	-6.39	18	1	16	45	21	-6.37	46	49	3	1	1
H-4	-6.39	41	45	3	4	7	-6.38	6	4	39	26	26
H-5	-6.46	41	52	1	5	1	-6.48	48	47	4	1	1

9d							**10b**				
MO	eV	C_6F_5 (1)	C_6F_5 (2)	Pt	Hdfppy (1)	Hdfppy (2)	eV	pbt	Hpbt	C_6F_5	Pt
L+5	-0.52	0	0	1	49	49	-0.3	21	45	16	13
L+4	-0.66	9	9	16	33	33	-0.43	37	57	2	4
L+3	-1.0	2	2	4	46	46	-0.52	51	47	0	2
L+2	-1.14	1	1	1	49	49	-0.61	15	77	2	5
L+1	-1.58	0	0	2	49	49	-1.91	4	94	0	1
LUMO	-1.64	0	0	1	49	49	-1.94	91	5	0	4
HOMO	-5.97	4	4	82	5	5	-5.82	63	1	0	35
H-1	-6.1	32	32	33	1	1	-5.97	4	5	4	87
H-2	-6.34	29	29	34	4	4	-6.12	3	3	66	28
H-3	-6.44	49	49	1	0	0	-6.32	58	1	3	38
H-4	-6.51	49	49	1	1	1	-6.39	1	1	99	0
H-5	-6.69	2	2	45	26	26	-6.53	69	9	2	20

10d						**11a**				
MO	eV	dfppy	Hdfppy	C_6F_5	Pt	eV	C_6F_5	thpy	dmso	Pt
L+5	-0.27	18	6	42	34	0.1	31	11	27	30
L+4	-0.55	9	87	0	3	0.03	82	5	1	11
L+3	-0.97	76	23	0	1	0.01	65	7	15	13
L+2	-1.13	19	79	1	1	-0.6	33	24	11	32
L+1	-1.59	19	79	0	2	-1.05	0	98	0	1
LUMO	-1.73	74	21	0	5	-1.84	1	89	2	8
HOMO	-5.96	60	2	0	38	-5.74	0	85	1	14
H-1	-6.06	3	5	3	89	-6.33	68	5	3	25
H-2	-6.24	3	2	69	26	-6.41	15	4	0	81
H-3	-6.4	83	1	3	13	-6.46	50	42	0	7
H-4	-6.52	2	0	97	1	-6.51	49	41	0	10
H-5	-6.64	19	1	4	76	-6.92	4	14	0	81

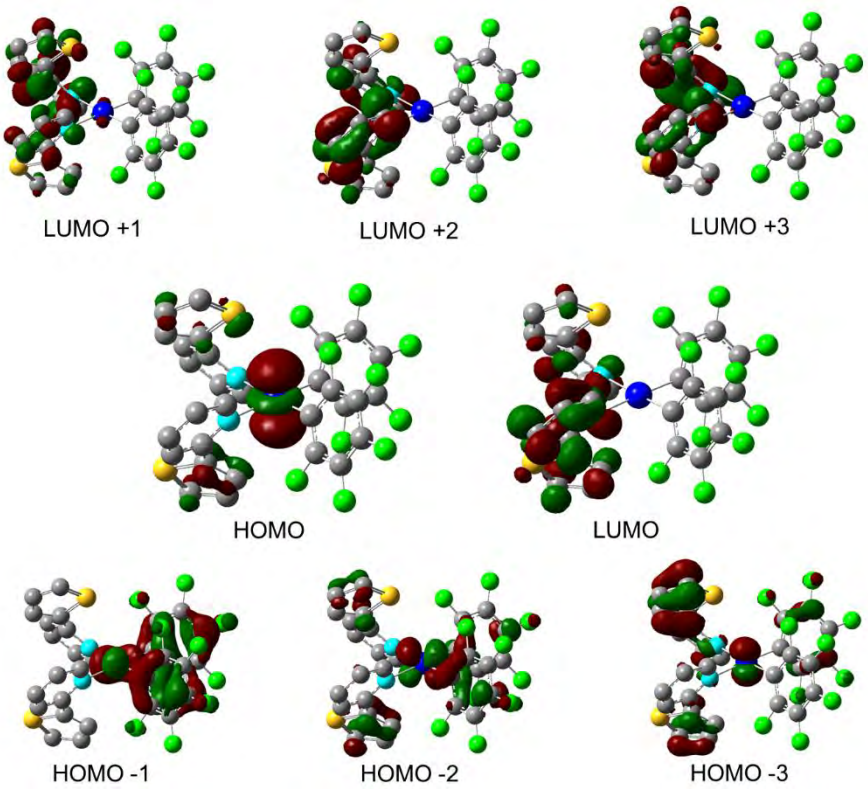

Figure A2.5. Selected frontier Molecular Orbitals for complex **9a**.

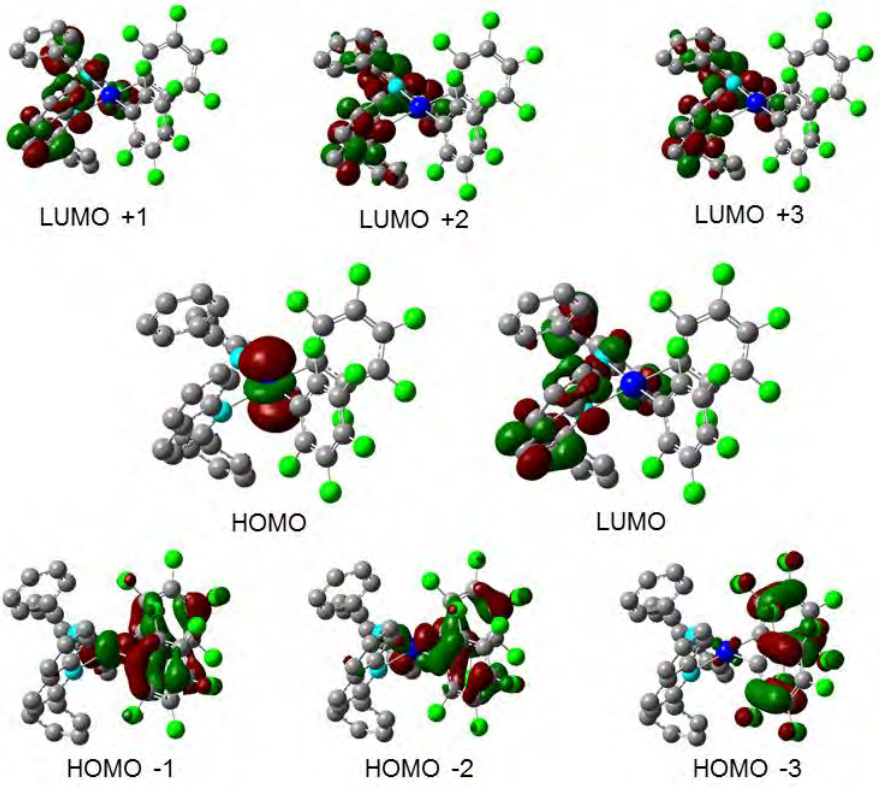

Figure A2.6. Selected frontier Molecular Orbitals for complex **9c**.

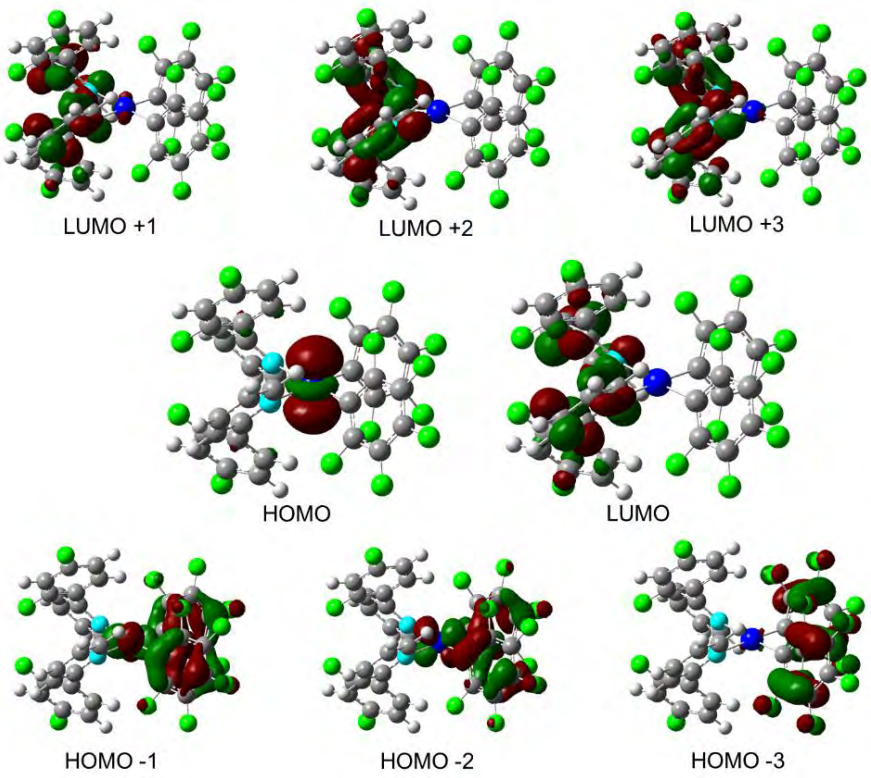

Figure A2.7. Selected frontier Molecular Orbitals for complex **9d**.

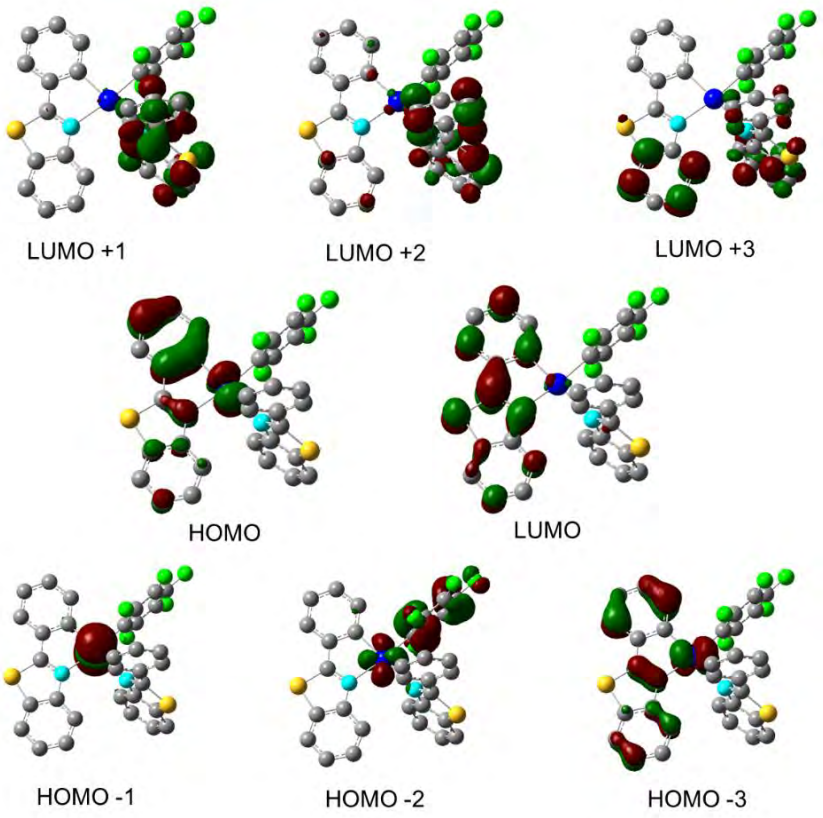

Figure A2.8. Selected frontier Molecular Orbitals for complex **10b**.

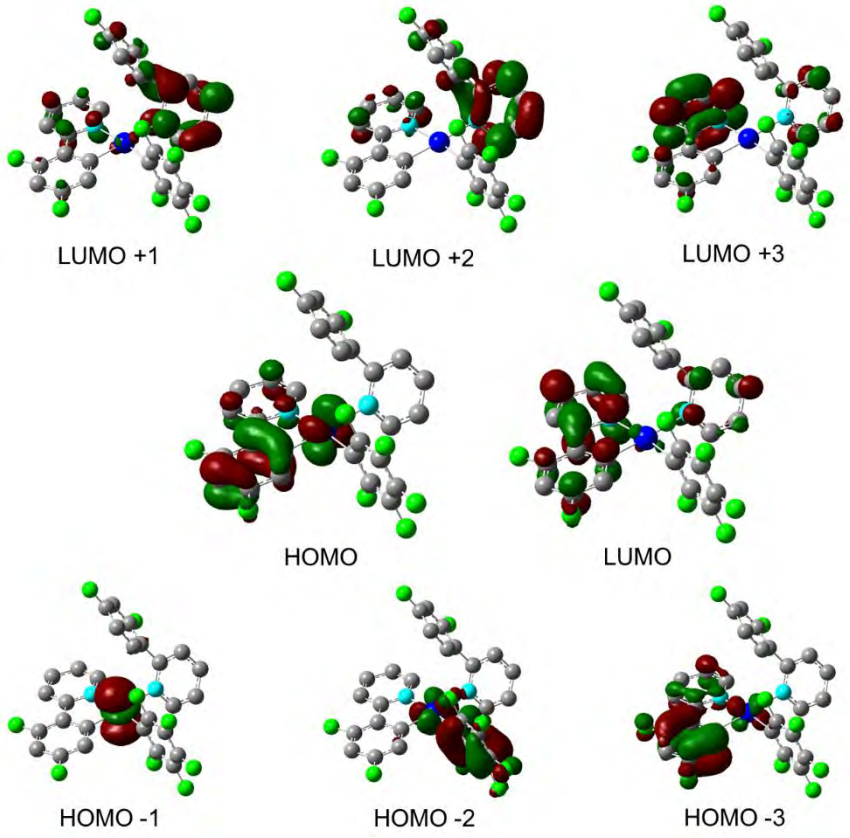

Figure A2.9. Selected frontier Molecular Orbitals for complex **10d**.

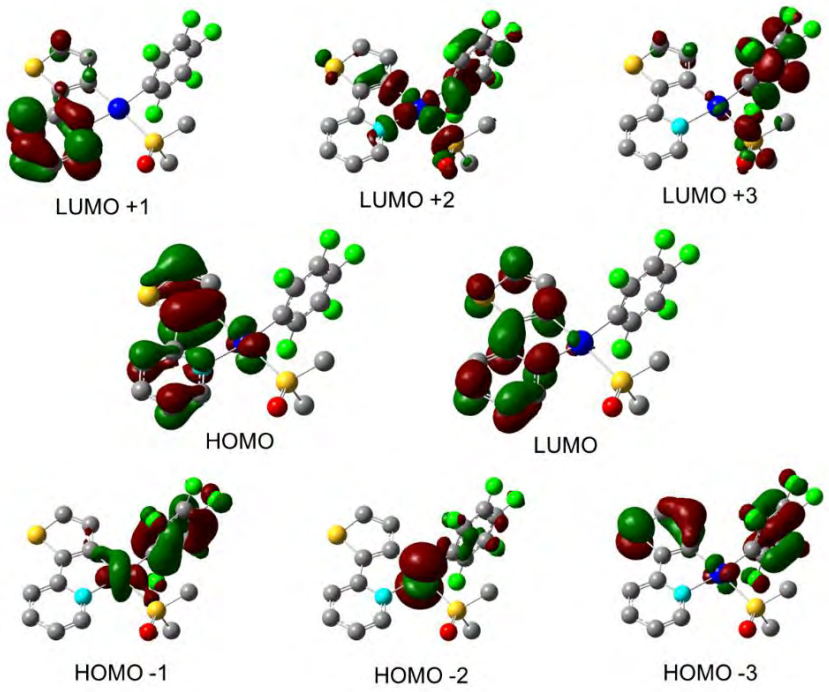

Figure A2.10. Selected frontier Molecular Orbitals for complex **11a**.

Table A2.3. Selected vertical excitation energies singlets and first triplets computed by TD-DFT/ SCRF (CH_2Cl_2) with the orbitals involved for complexes for **9a**, **9c**, **9d**, **10b** and **11a**.

	State	λ_{ex}(calc) (nm)	f^a	Transition (% Contribution)
9a	T_1	435.93	0.0	H-6→L (11%), H-2→L (10%), H→L (27%)
	T_2	416.32	0.0	H-3→L+1 (21%), H→L+1 (13%)
	S_1	374.76	0.0125	H→L (98%)
	S_2	367.86	0.0005	H→L+1 (98%)
	S_3	339.32	0.0043	H-1→L (97%)
	S_4	332.56	0.0105	H-1→L+1 (96%)
	S_5	322.96	0.0102	H-2→L (92%)
	S_6	318.87	0.0256	H-2→L+1 (74%), H→L+2 (13%)
	S_7	316.95	0.0081	H-2→L+1 (15%), H→L+2 (79%)
	S_8	313.46	0.0021	H→L+3 (42%), H→L+4 (41%)
	S_9	308.42	0.1169	H-4→L (11%), H-3→L (74%)
	S_{10}	303.59	0.0496	H-4→L+1 (10%), H-3→L+1 (77%)
	S_{11}	300.08	0.0114	H→L+3 (49%), H→L+4 (38%)
9c	T_1	462.69	0.0	H-6→L+1 (18%), H-4→L (28%), H-2→L+1 (11%), H-1→L (18%)
	T_2	461.09	0.0	H-6→L (20%), H-4→L+1 (25%), H-2→L (14%), H-1→L+1 (16%)
	T_3	405.36	0.0	H→L (94%)
	S_1	400.50	0.0075	H→L (98%)
	S_2	388.44	0.0006	H→L+1 (99%)
	S_3	365.57	0.0164	H-1→L (95%)
	S_4	354.44	0.0414	H-2→L (21%), H-1→L+1 (74%)
	S_5	350.28	0.0035	H-2→L (74%), H-1→L+1 (21%)
	S_6	342.58	0.003	H-2→L+1 (93%)
	S_7	333.91	0.0563	H-4→L (89%)
	S_8	322.70	0.0096	H-4→L+1 (16%), H-3→L (76%)
	S_9	321.28	0.0413	H-4→L+1 (73%), H-3→L (13%)
	S_{10}	318.04	0.0044	H-5→L (47%), H-3→L+1 (50%)
	S_{11}	311.25	0.0152	H→L+4 (85%)
	S_{12}	308.11	0.0058	H-7→L (17%), H-6→L (72%)
	S_{13}	306.96	0.0046	H-5→L (46%), H-3→L+1 (45%)
9d	T_1	369.23	0.0	H-5→L (11%), H→L (47%)
	T_2	366.80	0.0	H-5→L+1 (12%), H→L+1 (39%)
	S_1	352.17	0.0076	H→L (98%)
	S_3	325.61	0.0017	H-1→L (96%)
	S_4	320.24	0.0088	H-1→L+1 (96%)
	S_5	308.23	0.0122	H-2→L+1 (11%), H→L+3 (23%), H→L+4 (25%), H→L+6 (33%)
	S_6	307.40	0.0084	H-2→L (80%), H→L+2 (12%)
	S_8	302.54	0.0082	H-2→L (11%), H→L+2 (85%)
	S_9	290.70	0.0127	H-5→L (33%), H→L+3 (37%)
	S_{11}	288.27	0.0224	H-5→L (19%), H-4→L (22%), H-3→L+1 (10%), H→L+3 (26%)
10b	T_1	491.98	0.0	H-3→L (11%), H→L (76%)
	T_2	419.99	0.0	H-6→L+1 (50%), H-1→L+1 (14%)
	S_1	394.56	0.099	H→L (84%)
	S_2	389.66	0.0208	H-1→L (87%)

	S_3	379.23	0.0077	H-1→L+1 (48%), H→L+1 (45%)
	S_4	374.07	0.0031	H-1→L+1 (46%), H→L+1 (50%)
	S_5	351.52	0.0061	H-2→L (93%)
	S_6	347.42	0.0161	H-2→L+1 (94%)
	S_7	330.68	0.1064	H-3→L (78%)
	S_8	327.82	0.0124	H-3→L+1 (83%)
	S_9	316.70	0.002	H-4→L+1 (91%)
	S_{10}	312.08	0.0185	H-4→L (86%)
	S_{11}	309.79	0.317	H-5→L (76%)
	S_{12}	302.74	0.0264	H-5→L+1 (85%)
10d	T_1	434.37	0.0	H-3→L (12%), H→L (59%)
	T_2	371.20	0.0	H-1→L (87%)
	S_1	358.84	0.0297	H→L (90%)
	S_2	356.98	0.009	H-1→L (95%)
	S_4	333.59	0.0131	H→L+1 (87%)
	S_5	322.25	0.0131	H-2→L (97%)
	S_6	309.35	0.0297	H-2→L+1 (91%)
	S_7	305.69	0.0815	H-5→L (10%), H-3→L (72%)
	S_8	301.23	0.0261	H-5→L (49%), H→L+2 (23%), H→L+3 (16%)
11a	T_1	527.81	0.0	H→L (90%)
	T_2	361.53	0.0	H-3→L (17%), H→L+1 (60%)
	S_1	374.06	0.1164	H→L (94%)
	S_2	337.60	0.0081	H-2→L (11%), H-1→L (89%)
	S_3	314.37	0.0052	H-2→L (84%), H-1→L (10%)
	S_4	304.45	0.0503	H-5→L (21%), H-3→L (21%), H→L+1 (51%)
	S_5	298.41	0.1355	H-5→L (14%), H-3→L (69%), H→L+1 (11%)
	S_6	295.56	0.0014	H→L+2 (89%)
	S_7	290.13	0.0043	H-4→L (94%)
	S_8	285.92	0.1805	H-5→L (38%), H-1→L+2 (20%), H→L+1 (27%)
	S_9	282.45	0.1241	H-5→L (22%), H-2→L+2 (11%), H-1→L+2 (55%)

[a] Oscillator Strength

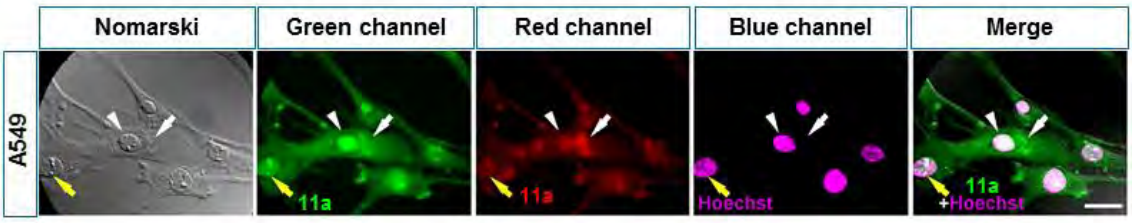

Figure A2.11. Fluorescence images of mouse lung embryonic fibroblasts (LMEFs) treated with **11a.** Living LMEFs were treated with complex **11a** (40 μM), in combination with the DNA binder Hoechst 33258 (3.2 μM) for 30 min. Cells were visualized by microscopy either for Nomarski white-light transmission or for fluorescence emission in green red and blue. Overlay of Nomarski, green, red and blue image is shown in right panel. **11a** stains the cytoplasm, stronger in perinuclear areas (white arrows), nuclei (white arrowheads) and nucleoli (yellow arrows) in green, and in red with less intensity.

Appendix - Chapter 2.2

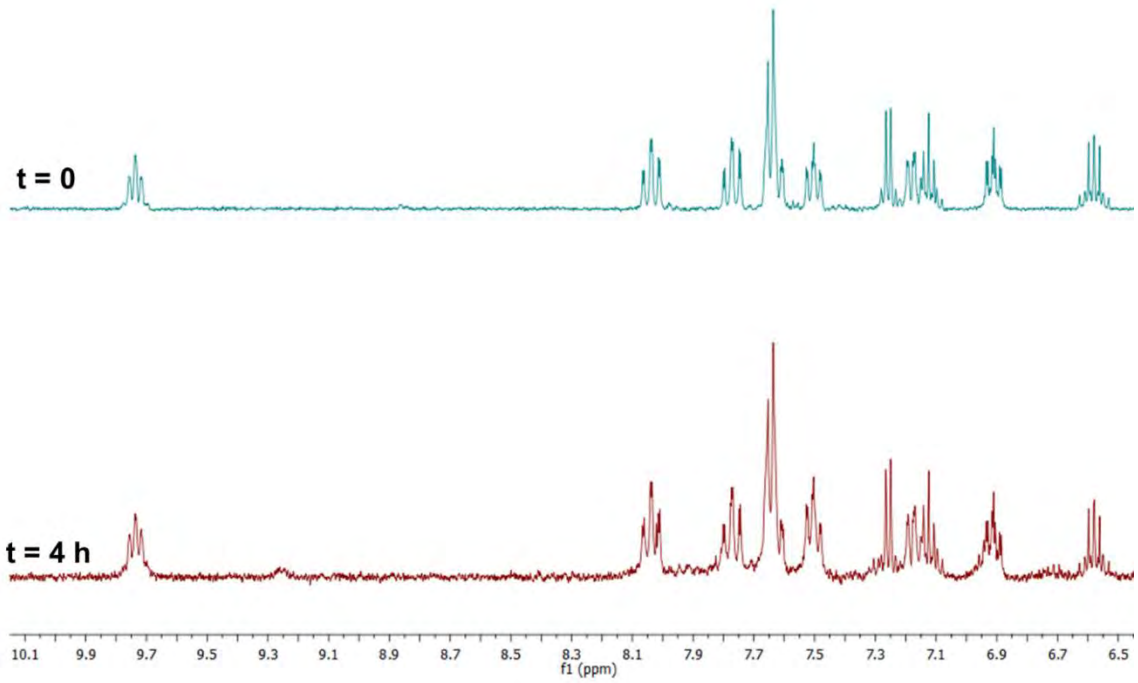

Figure A2.12. ^{1}H NMR spectra of **12a** in CD_2Cl_2 before and after irradiation with a 125 Hg lamp.

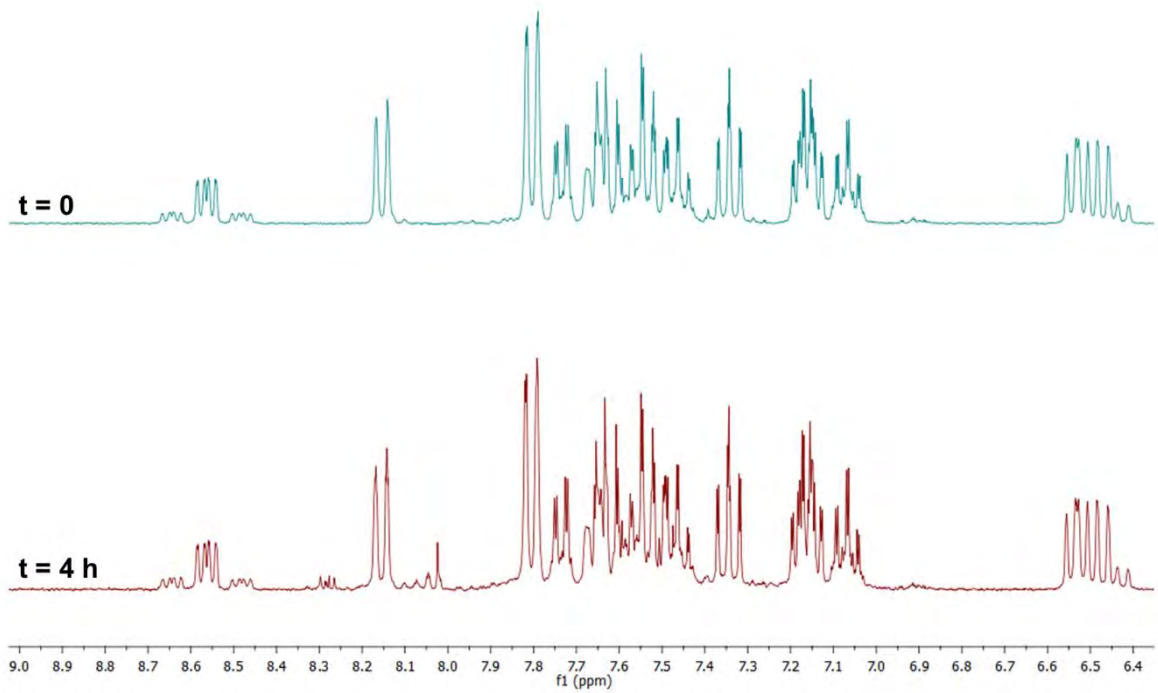

Figure A2.13. ^{1}H NMR spectra of **13** in CD_2Cl_2 before and after irradiation with a 125 Hg lamp.

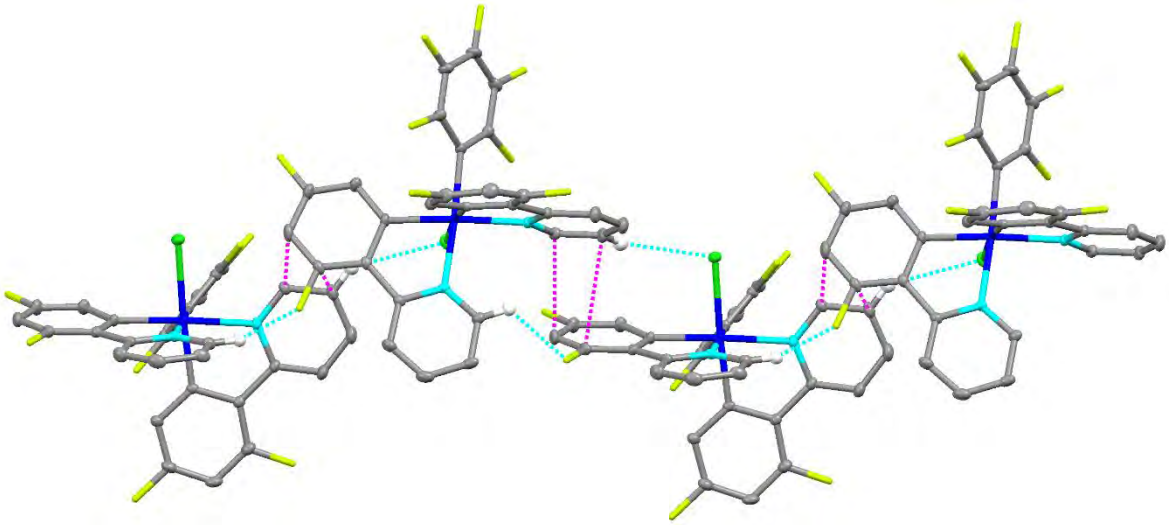

Figure A2.14. Crystal packing of **12d** showing a chain formed by non-linear π···π interactions (3.37 - 3.39 Å), H···Cl (2.87 Å) and H_{dfppy}···F_{dfppy} (2.41 Å).

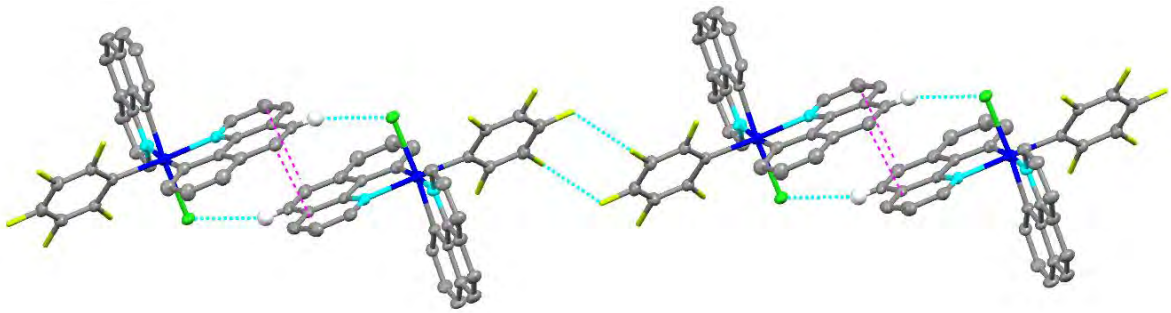

Figure A2.15. Crystal packing of **12e**·5.5thf showing dimers supported by π···π (3.46 – 3.59 Å) and H···Cl (2.82 Å) interactions and C_{C6F5}···C_{C6F5} (2.813 Å) interactions between the dimers.

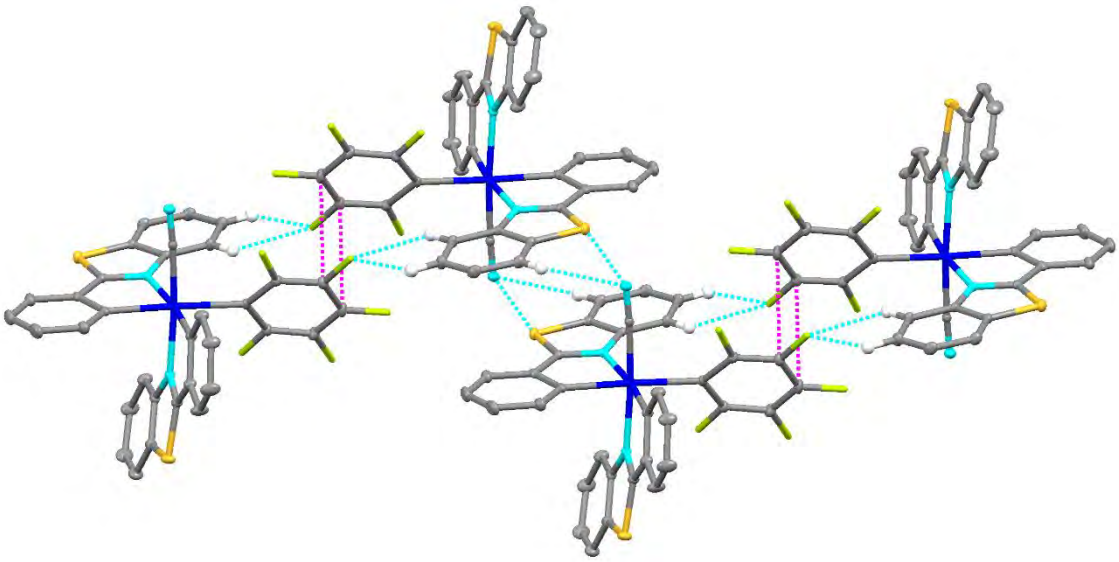

Figure A2.16. Crystal packing of complex **13** showing the π···π intermolecular interactions involving C_6F_5 rings (3.39 Å, pink) and secondary weak interactions (blue) [F_{C6F5}···H_{pbt} 2.47 – 2.53, N_{CN}···S_{pbt} 3.28, N_{CN}···H_{pbt} 2.55 Å].

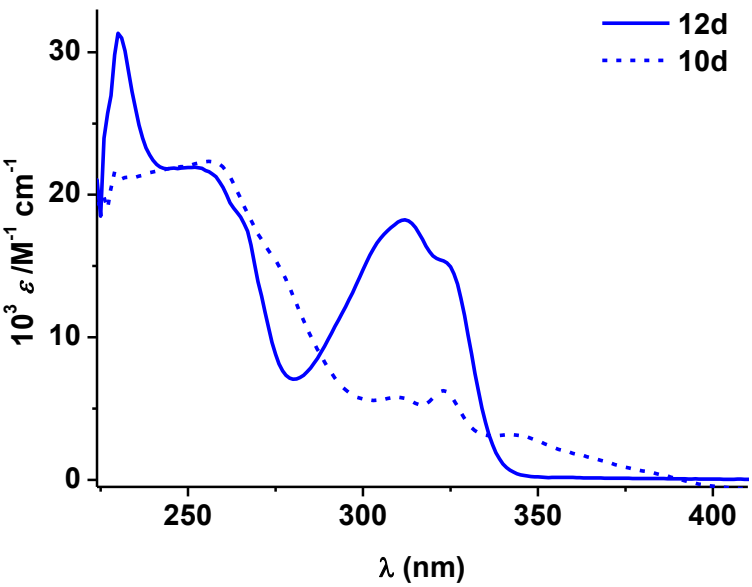

Figure A2.17. Absorption spectra of **12d** *vs* **10d** in CH_2Cl_2 5 × 10^{-5} M at 298 K.

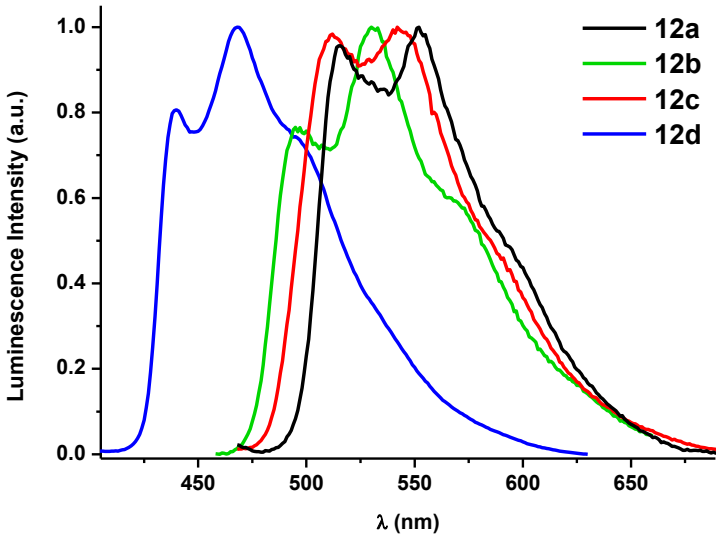

Figure A2.18. Normalized emission spectra of **12a-d** in CH_2Cl_2 5×10^{-5} M at 298 K.

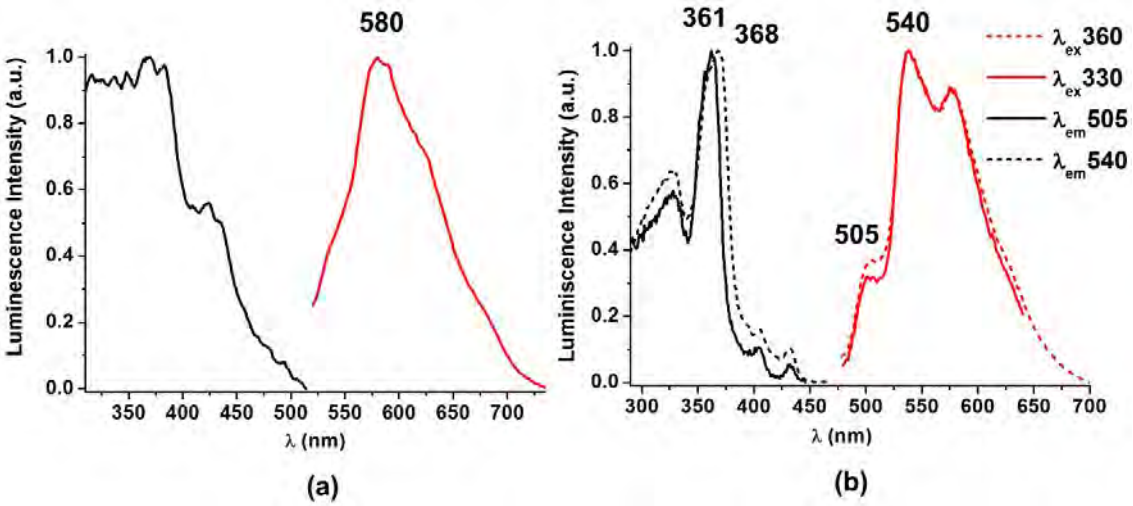

Figure A2.19. Normalized excitation and emission spectra of (a) **12c** and (b) **12d** in the solid state at 298 K.

Table A2.4. DFT optimized geometries for ground state and triplet state of complexes **12c**, **12d**, **12e**, **13** and **14**.

12c-molecule A			
	X-ray	S_0	T_1
Pt(1)-N(1)	2.164(3)	2.244	2.199
Pt(1)-N(2)	2.264(3)	2.362	2.364
Pt(1)-C(15)	2.022(4)	2.026	2.023
Pt(1)-C(31)	2.062(4)	2.068	2.073
Pt(1)-C(30)	2.022(4)	2.039	2.045
Pt(1)-Cl(1)	2.4464(11)	2.571	2.583
H(14)···F(5)	2.588	2.662	2.756
H(17)···F(1)	2.900	2.785	2.598
H(29)···F(5)	3.035	2.986	2.771
C(15)-Pt(1)-N(1)	80.20(15)	79.22	79.59
N(1)-Pt(1)-N(2)	104.07(13)	103.67	100.25
C(31)-Pt(1)-N(2)	81.53(14)	82.62	85.29
C(15)-Pt(1)-C(31)	93.90(17)	94.10	94.33
Cl(1)-Pt(1)-N(1)	85.79(10)	87.14	89.05
Cl(1)-Pt(1)-C(15)	82.27(12)	81.54	81.99
Cl(1)-Pt(1)-C(31)	95.92(12)	95.76	95.15
Cl(1)-Pt(1)-N(2)	103.92(9)	103.96	103.72
12d			
	X-ray	S_0	T_1
Pt(1)-N(1)	2.0943(19)	2.149	2.159
Pt(1)-N(2)	2.130(2)	2.196	2.175
Pt(1)-C(11)	2.012(3)	2.033	2.037
Pt(1)-C(23)	2.070(2)	2.076	2.072
Pt(1)-C(22)	2.026(2)	2.042	2.033
Pt(1)-Cl(1)	2.4198(6)	2.525	2.526
H(10)···F(5)	2.562	2.539	2.533
H(12)···F(9)	2.534	2.509	2.553
H(21)···F(5)	2.683	2.671	2.740
N(1)-Pt(1)-N(2)	95.24(8)	94.27	93.91
C(11)-Pt-(1)-N(1)	80.20(9)	79.86	79.64
C(11)-Pt(1)-C(23)	96.31(10)	96.92	97.21
C(23)-Pt(1)-N(2)	88.13(9)	88.83	89.14
Cl(1)-Pt(1)-N(1)	87.89(6)	87.65	87.62
Cl(1)-Pt(1)-C(11)	85.84(7)	85.86	86.00

Cl(1)-Pt(1)-C(23)	95.61(7)	95.06	95.12
Cl(1)-Pt(1)-N(2)	95.85(6)	96.10	95.57

12e

	X-ray	S_0	T_1
Pt(1)-N(1)	2.097(4)	2.169	2.154
Pt(1)-N(2)	2.144(4)	2.226	2.215
Pt(1)-C(13)	2.026(5)	2.040	2.030
Pt(1)-C(26)	2.037(5)	2.049	2.051
Pt(1)-C(27)	2.035(5)	2.068	2.075
Pt(1)-Cl(1)	2.4181(13)	2.539	2.537
H(12)···F(1)	2.518	2.487	2.517
H(14)···F(5)	2.562	2.519	2.532
H(25)···F(1)	2.647	2.631	2.622
N(1)-Pt-N(2)	93.47(19)	92.73	93.15
C(13)-Pt-N(1)	80.8(2)	80.60	80.16
C(13)-Pt-C(27)	94.9(2)	96.58	96.60
C(27)-Pt-N(2)	90.7(2)	89.98	89.98
Cl(1)-Pt(1)-N(1)	88.97(12)	87.51	88.72
Cl(1)-Pt(1)-C(13)	86.56(16)	87.06	86.34
Cl(1)-Pt(1)-C(27)	94.05(15)	95.10	94.58
Cl(1)-Pt(1)-N(2)	94.81(12)	95.04	95.15

13

	X-ray	S_0	T_1
Pt(1)-N(1)	2.1075(19)	2.173	2.184
Pt(1)-N(2)	2.1637(19)	2.273	2.241
Pt(1)-C(13)	2.026(2)	2.034	2.036
Pt(1)-C(33)	1.963(2)	1.963	1.960
Pt(1)-C(26)	2.076(2)	2.099	2.095
Pt(1)-C(27)	2.147(2)	2.178	2.178
H(12)···F(5)	2.542	2.592	2.623
H(2)···F(1)	2.888	2.751	2.711
H(15)···F(1)	3.017	2.723	2.867
N(1)-Pt(1)-N(2)	97.47(7)	99.86	98.91
C(13)-Pt(1)-N(1)	81.04(8)	79.75	79.67
C(13)-Pt(1)-C(33)	93.70(9)	95.07	95.04
C(33)-Pt-N(2)	86.93(8)	84.66	85.86
C(27)-Pt(1)-N(1)	92.17(8)	91.08	90.71
C(27)-Pt(1)-C(13)	85.77(9)	87.64	88.25

C(27)-Pt(1)-C(33)	93.71(9)	92.84	92.71
C(27)-Pt(1)-N(2)	101.69(8)	100.56	99.29
		14	
	X-ray	S_0	T_1
Pt(1)-N(1)	2.210(3)	2.286	2.294
Pt(1)-N(2)	2.127(3)	2.204	2.181
Pt(1)-C(26)	2.037(4)	2.042	2.036
Pt(1)-C(27)	2.045(4)	2.064	2.068
Pt(1)-C(13)	2.041(4)	2.047	2.045
Pt(1)-N(3)	2.170(3)	2.275	2.293
C(7)-C(8)	1.449(6)	1.450	1.450
C(20)-C(21)	1.443(5)	1.448	1.377
H(12)···F(5)	2.675	2.757	2.809
H(2)···F(1)	2.422	2.555	2.533
H(25)···F(5)	2.669	2.530	2.540
C(27)-Pt(1)-N(1)	88.24(13)	86.48	85.99
N(1)-Pt(1)-N(2)	95.03(12)	97.53	97.52
C(26)-Pt(1)-N(2)	80.59(14)	79.60	80.65
C(26)-Pt(1)-C(27)	95.51(15)	96.03	95.57
N(3)-Pt(1)-N(1)	100.98(11)	101.12	101.41
N(3)-Pt(1)-N(2)	90.86(11)	89.00	87.94
N(3)-Pt(1)-C(26)	86.72(13)	83.80	83.94
N(3)-Pt(1)-C(27)	93.39(13)	94.39	94.48

12c	
S_0	**T_1**
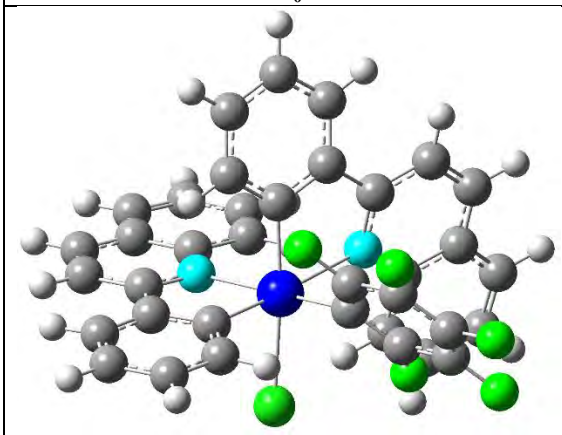	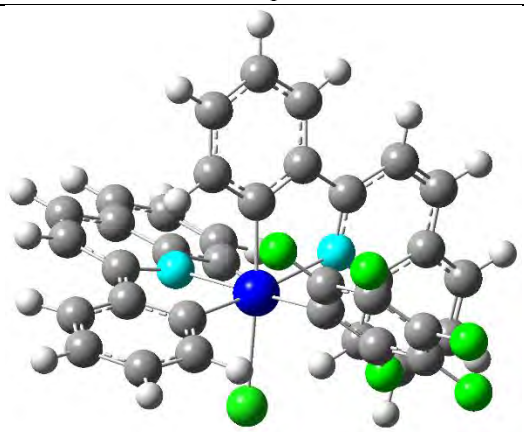

12d	
S_0	T_1
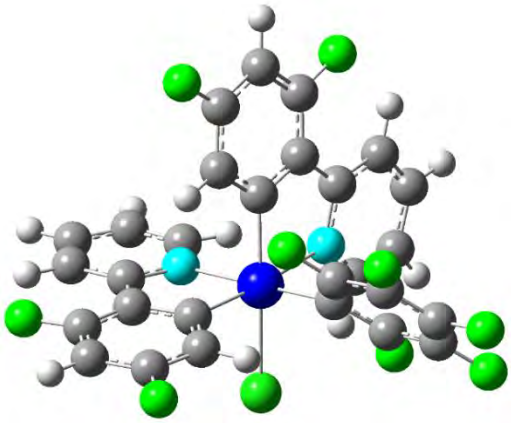	
12e	
S_0	T_1
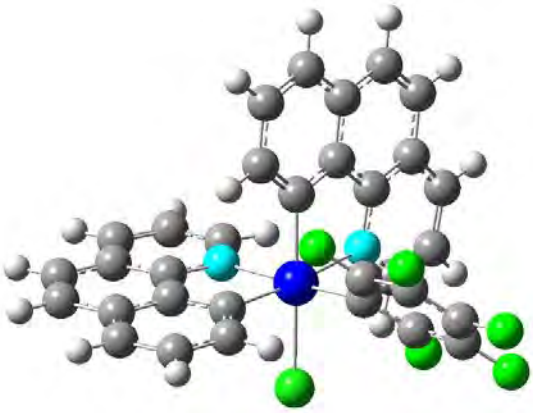	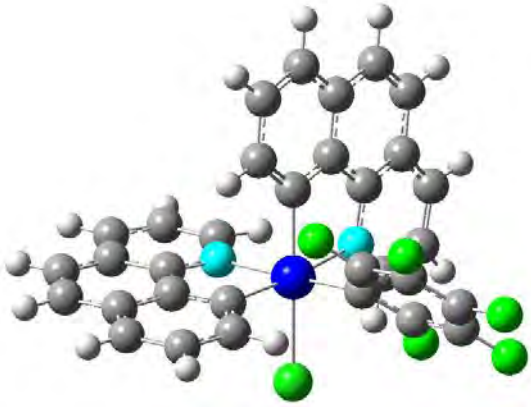
13	
S_0	T_1
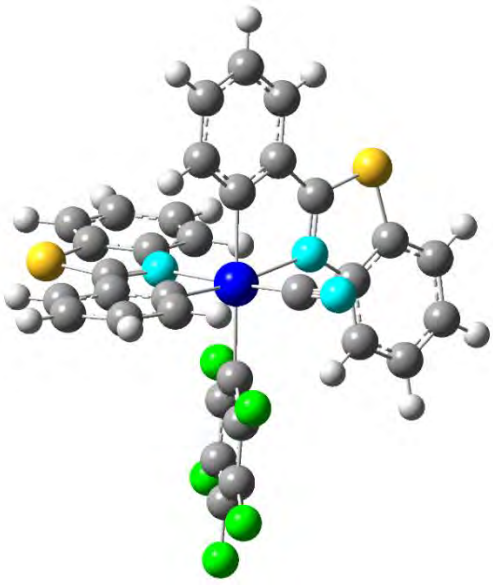	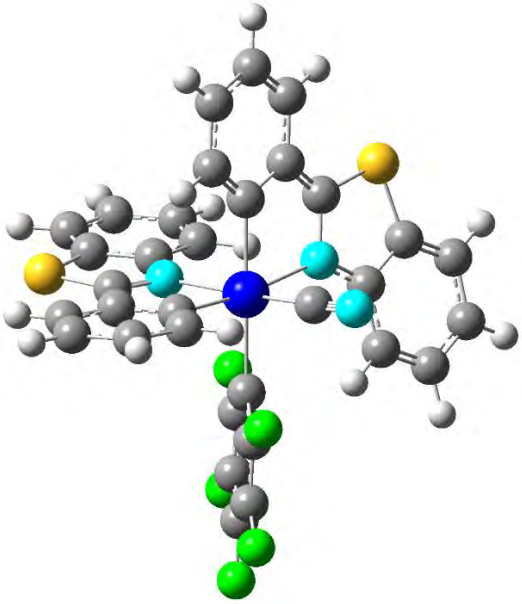

14	
S_0	T_1
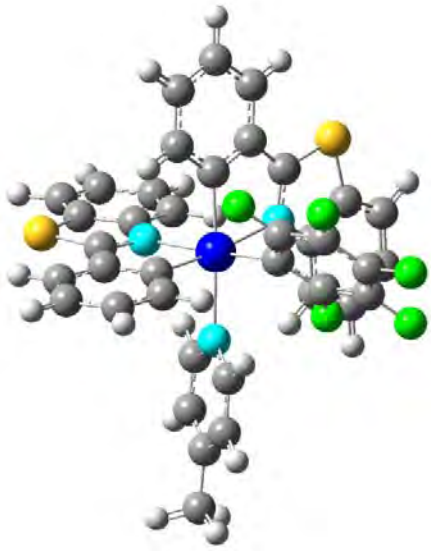	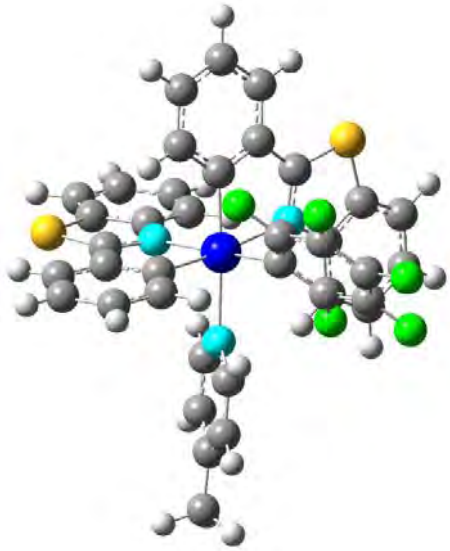

Figure A2.20. Optimized structures of S_0 and T_1 states of **12c**, **12d**, **12e**, **13**, and **14**.

Table A2.5. Composition (%) of Frontier MOs in the ground state for complexes **12c**, **12d**, **12e**, **13** and **14** in dichloromethane.

12c							**12d**					
MO	eV	C_6F_5	pq (1)	pq (2)	Pt	Cl	eV	C_6F_5	dfppy (1)	dfppy (2)	Pt	Cl
L+5	-1.10	1	23	70	5	1	-1.12	2	40	56	2	0
L+4	-1.21	5	33	43	17	3	-1.17	17	33	14	34	1
L+3	-1.24	4	70	9	15	2	-1.29	5	40	42	10	2
L+2	-1.34	28	17	18	34	4	-1.37	11	31	30	21	7
L+1	-2.16	0	4	94	2	0	-1.92	0	40	56	3	1
L	-2.23	1	94	2	2	1	-1.99	2	51	39	6	2
H	-6.29	9	13	66	6	7	-6.54	6	75	12	4	4
H-1	-6.38	1	77	17	1	4	-6.56	33	18	47	1	1
H-2	-6.57	53	6	24	4	13	-6.68	61	2	32	2	3
H-3	-6.62	26	30	23	1	21	-6.74	67	4	14	9	7
H-4	-6.67	41	7	35	8	10	-6.89	3	79	3	4	11
H-5	-6.70	2	36	52	0	9	-6.94	19	2	31	5	43
12e							**13**					
MO	eV	C_6F_5	bzq(1)	bzq(2)	Pt	Cl	eV	C_6F_5	pbt(1)	pbt(2)	Pt	CN
L+5	-1.00	16	30	17	35	2	-0.52	1	15	83	1	0
L+4	-1.13	19	23	26	26	6	-0.59	1	81	16	2	0
L+3	-1.43	2	80	11	5	2	-0.82	23	17	24	31	6
L+2	-1.44	3	9	83	5	0	-1.4	4	30	14	41	11
L+1	-1.96	0	7	91	1	0	-2.13	0	6	91	3	0
L	-1.99	1	88	7	3	1	-2.22	1	93	5	1	0
H	-6.11	1	92	2	4	2	-6.39	2	1	96	2	0
H-1	-6.16	3	1	87	6	4	-6.45	27	69	2	2	0
H-2	-6.56	92	1	5	0	1	-6.55	73	25	0	1	0
H-3	-6.63	49	34	6	6	5	-6.67	84	2	8	6	0
H-4	-6.71	27	57	10	3	2	-6.81	0	2	97	1	0
H-5	-6.74	8	7	72	3	10	-6.83	15	66	16	2	1

14						
MO	eV	C_6F_5	pbt(1)	pbt(2)	Pt	Me-py
L+5	-1.19	1	3	4	1	91
L+4	-1.59	6	16	17	24	37
L+3	-1.84	12	9	13	18	48
L+2	-2.01	19	21	12	29	20
L+1	-2.48	1	6	90	3	0
L	-2.65	2	90	4	4	1
H	-6.74	4	0	94	2	0
H-1	-6.85	0	97	1	2	0
H-2	-7.05	69	1	30	0	0
H-3	-7.12	28	1	71	1	0
H-4	-7.18	31	56	6	6	0
H-5	-7.26	35	44	17	4	1

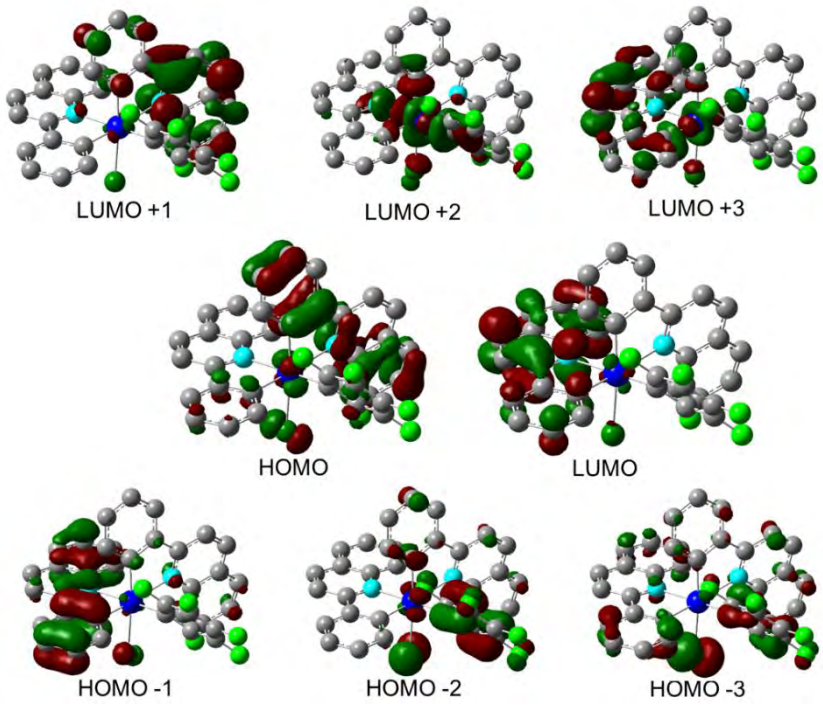

Figure A2.21. Selected frontier Molecular Orbitals for complex **12c** (molecule A).

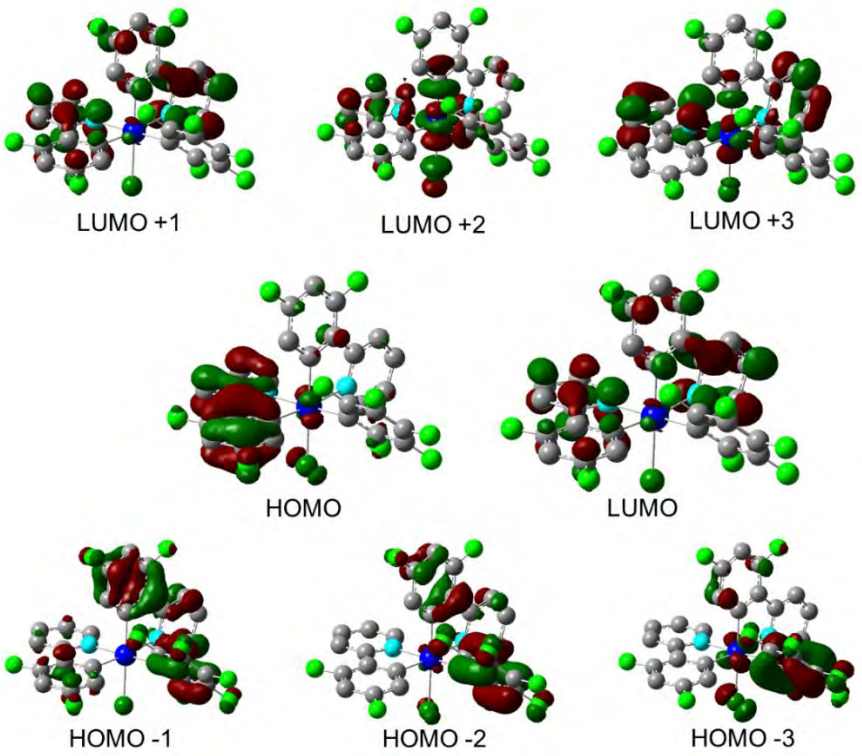

Figure A2.22. Selected frontier Molecular Orbitals for complex **12d**.

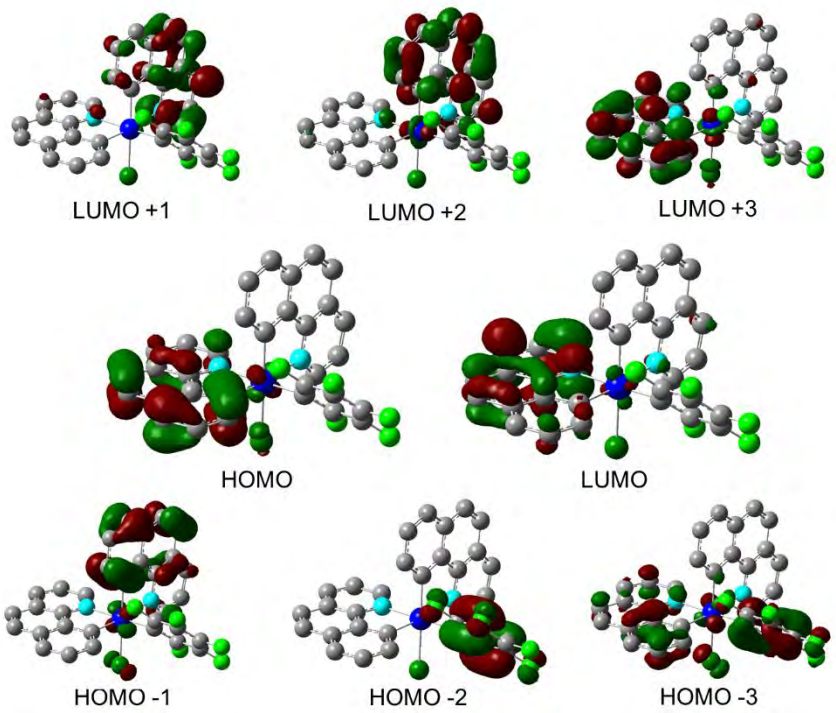

Figure A2.23 Selected frontier Molecular Orbitals for complex **12e**.

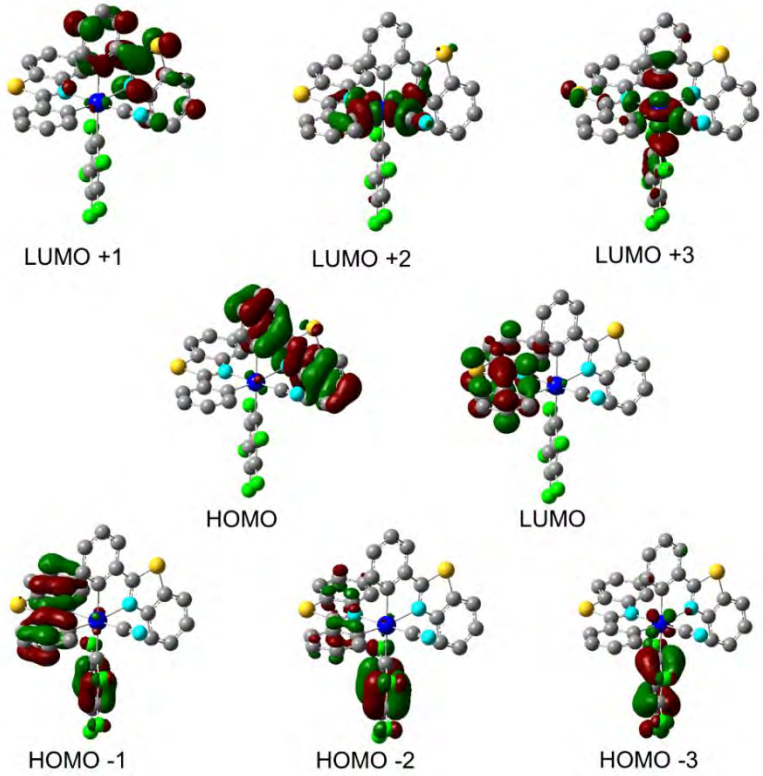

Figure A2.24. Selected frontier Molecular Orbitals for complex **13**.

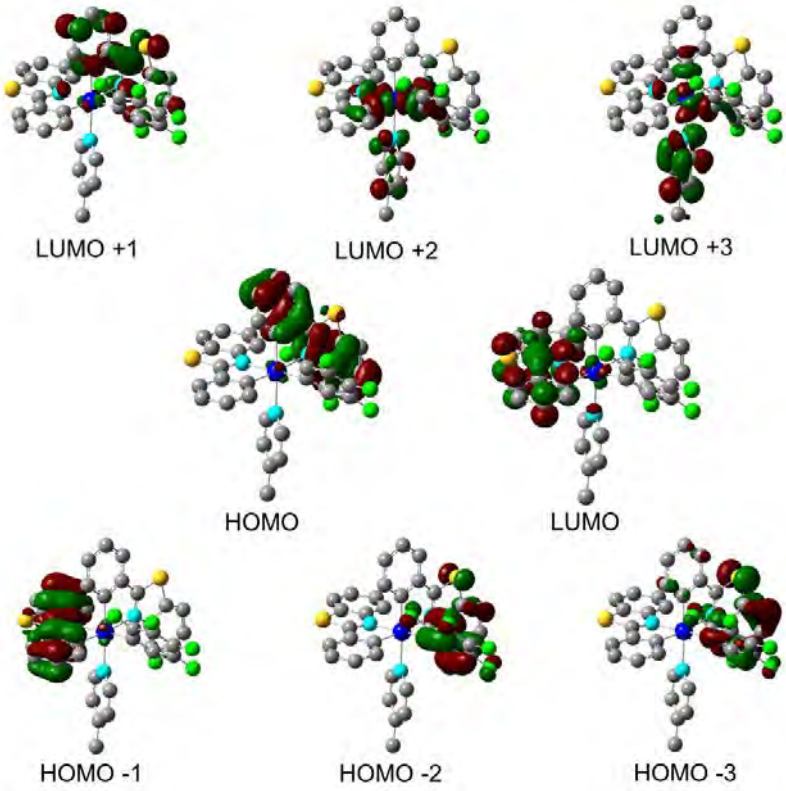

Figure A2.25. Selected frontier Molecular Orbitals for complex **14**.

Table A2.6. Selected vertical excitation energies singlets computed by TD-DFT/ SCRF (CH_2Cl_2) with the orbitals involved for complexes for **12c**, **12d**, **12e**, **13** and **14**.

	State	λ_{ex}(calc) (nm)	f [a]	Transition (% Contribution)	Metal % CT	Main character [b]
12c	S_1	357.63	0.0339	H→L (88%)	3.1	(X+L')LCT
	S_2	349.12	0.0837	H→L+1 (91%)	3.6	(X+L')LCT
	S_3	346.24	0.1124	H-1→L (85%)	-1.0	IL
	S_4	336.44	0.0119	H-1→L+1 (95%)		
	S_5	329.76	0.0165	H-2→L (59%)		
	S_6	325.84	0.0753	H-3→L (16%), H-2→L+1 (71%)		
	S_7	324.83	0.025	H-4→L (33%), H-3→L (26%), H-2→L+1 (16%)		
	S_8	320.64	0.0579	H-3→L+1 (76%)		
	S_9	318.29	0.0803	H-6→L (31%), H-5→L (44%)		
	S_{10}	317.77	0.0732	H-3→L (29%), H-2→L (12%)		
	S_{11}	316.88	0.0397	H-7→L (10%), H-4→L+1 (68%)		
	S_{12}	314.10	0.028	H-8→L+1 (11%), H-5→L+1 (59%), H-3→L+1 (11%)		
	S_{13}	312.49	0.0123	H-8→L (27%), H-6→L (16%), H-4→L (20%), H-2→L (13%)		
	S_{14}	310.20	0.0288	H-7→L (29%), H-6→L (14%), H-6→L+1 (15%), H-4→L+1 (11%)		
12d	S_1	317.99	0.0189	H→L (68%), H-5→L (4%), H-3→L (7%), H→L+2 (4%)	-2.7	IL/LLCT
	S_2	310.26	0.114	H-1→L (80%)	-4.9	IL/L'LCT
	S_3	307.41	0.0458	H-1→L+1 (12%), H→L+1 (64%)	-0.2	IL/LLCT
	S_4	304.33	0.053	H-3→L (34%), H-2→L (23%), H-1→L (10%)	-1.6	L'LCT
	S_5	302.46	0.0115	H-3→L (19%), H-1→L+1 (53%), H→L+1 (12%)		
	S_6	299.45	0.0656	H-3→L (16%), H-2→L (46%), H-1→L+1 (22%)		
	S_7	296.53	0.0195	H-3→L+1 (32%), H-2→L+1 (28%)		
	S_8	293.99	0.024	H-6→L (10%), H-5→L (12%), H-3→L+1 (25%), H-2→L+1 (31%)		
	S_9	292.56	0.0416	H-4→L (55%), H-4→L+1 (12%), H-2→L+1 (14%)		
	S_{10}	289.82	0.01	H-6→L (51%)		
	S_{11}	289.20	0.0395	H-5→L (45%), H-3→L+1 (29%)		
12e	S_1	352.75	0.0796	H→L (87%)	0.9	IL
	S_2	347.73	0.0538	H-1→L (57%), H-1→L+1 (33%)	3.2	IL/LLCT
	S_3	344.35	0.0344	H-1→L (36%), H-1→L+1 (58%)	3.9	IL/LLCT
	S_5	314.53	0.0062	H-4→L (22%), H-3→L (33%), H→L+3 (31%)		
	S_6	311.73	0.0051	H-1→L+2 (23%), H-1→L+3 (14%), H-1→L+4 (25%)		
	S_7	309.50	0.0012	H-5→L+1 (17%), H-2→L+1 (32%), H-1→L+2 (11%), H-1→L+3 (16%)		

	S_8	306.48	0.0049	H-3→L+1 (21%), H-2→L (11%), H-2→L+1 (32%), H-1→L+2 (13%)		
	S_9	303.03	0.0069	H-5→L+1 (15%), H-3→L+1 (42%), H-2→L (17%)		
	S_{10}	302.99	0.0125	H-6→L (16%), H-3→L (14%), H-2→L (18%), H-2→L+1 (14%)		
	S_{11}	302.66	0.0029	H→L+2 (57%), H→L+5 (11%)		
	S_{12}	299.75	0.0216	H-3→L (14%), H-2→L (31%), H→L+3 (11%)		
	S_{13}	297.85	0.0043	H-7→L (29%), H-5→L (37%)		
13	S_1	340.21	0.0292	H→L (94%)	1.0	LLCT
	S_2	336.24	0.1639	H-1→L (82%)	0.7	IL/L'LCT
	S_3	331.82	0.2876	H-2→L (14%), H→L+1 (73%)	-1.2	IL/L'LCT
	S_4	329.59	0.1268	H-2→L (56%), H-1→L+1 (25%), H→L+1 (14%)	-0.8	L'LCT/LLCT
	S_5	327.78	0.1076	H-2→L (25%), H-1→L+1 (61%)	-1.1	LLCT/L'LCT
	S_6	322.22	0.0123	H-3→L (97%)		
	S_8	310.53	0.0744	H-5→L (20%), H-5→L+1 (17%), H-3→L+1 (51%)		
	S_9	308.73	0.0644	H-5→L (31%), H-3→L+1 (41%)		
	S_{10}	305.91	0.0754	H-5→L (20%), H-5→L+1 (54%)		
	S_{11}	304.17	0.0414	H-6→L (69%), H-5→L (18%)		
14	S_1	349.96	0.0163	H→L (95%)	-2.2	LLCT
	S_2	339.12	0.2464	H-1→L (88%)	-2.3	IL
	S_3	332.64	0.3161	H→L+1 (88%)	-1.9	IL
	S_4	325.66	0.06	H-1→L+1 (88%)	-2.2	LLCT
	S_5	319.75	0.0068	H-4→L (10%), H-3→L (21%), H-2→L (48%)	-3.8	LLCT/IL/L'LCT
	S_6	315.46	0.0599	H-4→L (37%), H-2→L (30%)	-2.1	LLCT/IL/L'LCT
	S_7	311.70	0.027	H-5→L (18%), H-4→L (41%), H-3→L (27%)		
	S_8	310.14	0.0211	H-2→L (12%), H-2→L+1 (75%)		
	S_9	308.21	0.0533	H→L+2 (75%)		
	S_{11}	307.00	0.0205	H-6→L (14%), H-3→L+1 (54%)		
	S_{12}	304.15	0.0296	H-6→L (54%), H-3→L (17%), H-3→L+1 (10%)		
	S_{14}	301.74	0.0402	H-7→L (19%), H-4→L+1 (42%), H-3→L+1 (13%)		
	S_{15}	298.83	0.0542	H-7→L (53%), H-4→L+1 (18%)		

[a] Oscillator Strength; [b] L = C^N ligand (pq **12c**, dfppy **12d**, bzq **12e**, pbt **13**, **14**), L' = C_6F_5, X = Cl.

Table A2.7. Selected vertical excitation energies first triplets computed by TDDFT/SCRF (CH_2Cl_2) with the orbitals involved for complexes for **12c**, **12d**, **12e**, **13** and **14**.

	State	λ/nm	F [a]	Transition (% Contribution)	Metal %CT	Main character [b]
12c	T_1	475.41	0.0	H-4→L+1 (10%), H-1→L+1 (13%), H→L+1 (50%)	2.4	IL/LLCT/(X+L') LCT
	T_2	473.15	0.0	H-6→L (10%), H-1→L (51%)	-0.7	IL/(X+L')LCT
	T_3	411.26	0.0	H-7→L (18%), H-6→L (24%), H-1→L (16%), H→L (10%)	0.3	
	T_4	405.06	0.0	H-5→L+1 (32%), H-3→L+1 (14%), H-2→L+1 (13%), H→L+1 (15%)	0.3	
	T_5	363.92	0.0	H-5→L (24%), H-3→L (22%), H→L (24%), H-8→L (7%)	-0.1	
12d	T_1	412.97	0.0	H→L (36%), H→L+1 (25%)	-1.8	IL/LLCT
	T_2	409.97	0.0	H-2→L (11%), H-2→L+1 (12%), H-1→L (20%), H-1→L+1 (21%)	-2.0	IL/L'LCT
	T_3	337.98	0.0	H-3→L (10%), H-3→L+8 (20%), H-2→L+9 (16%), H-1→L+9 (10%), H-5→L+8 (5%), H-3→L+2 (9%)	-0.3	
	T_4	333.02	0.0	H→L (14%), H→L+2 (14%), H→L+5 (10%), H-4→L (9%), H→L+3 (9%)	-4.4	
	T_5	327.95	0.0	H-3→L (12%), H→L+3 (14%), H-5→L (9%), H-1→L (7%)	-2.5	
12e	T_1	459.20	0.0	H→L (35%), H→L+3 (27%)	0.8	IL
	T_2	455.14	0.0	H-5→L+1 (14%), H-1→L+1 (33%), H-1→L+2 (30%)	2.8	IL
	T_3	406.40	0.0	H→L (50%), H→L+3 (24%)	0.3	
	T_4	399.98	0.0	H-1→L (10%), H-1→L+1 (48%), H-1→L+2 (22%)	3.2	
	T_5	363.53	0.0	H-4→L (27%), H-3→L (24%), H→L+3 (27%)	0.6	
13	T_1	458.65	0.0	H→L+1 (82%)	-1.0	IL
	T_2	458.45	0.0	H-2→L (18%), H-1→L (63%)	0.7	IL/L'LCT
	T_3	367.31	0.0	H-6→L (23%), H-5→L (49%)	1.2	
	T_4	364.10	0.0	H-4→L+1 (69%), H-9→L+1 (3%), H-4→L (4%), H-4→L+5 (6%)	-2.2	
	T_5	358.82	0.0	H-6→L (56%), H-5→L (21%), H-8→L (7%)	2.1	
14	T_1	464.04	0.0	H-1→L (86%)	-2.4	IL
	T_2	458.26	0.0	H→L+1 (82%)	-1.3	IL
	T_3	372.55	0.0	H-5→L (27%), H-4→L (49%)	1.2	
	T_4	368.60	0.0	H-3→L+1 (47%), H-2→L+1 (22%)	-2.4	
	T_5	354.56	0.0	H-7→L (43%), H-6→L (13%), H→L (25%)	0.07	

[a] Oscillator Strength; [b] L = C^N ligand (pq **12c**, dfppy **12d**, bzq **12e**, pbt **13**, **14**), L' = C_6F_5, X = Cl

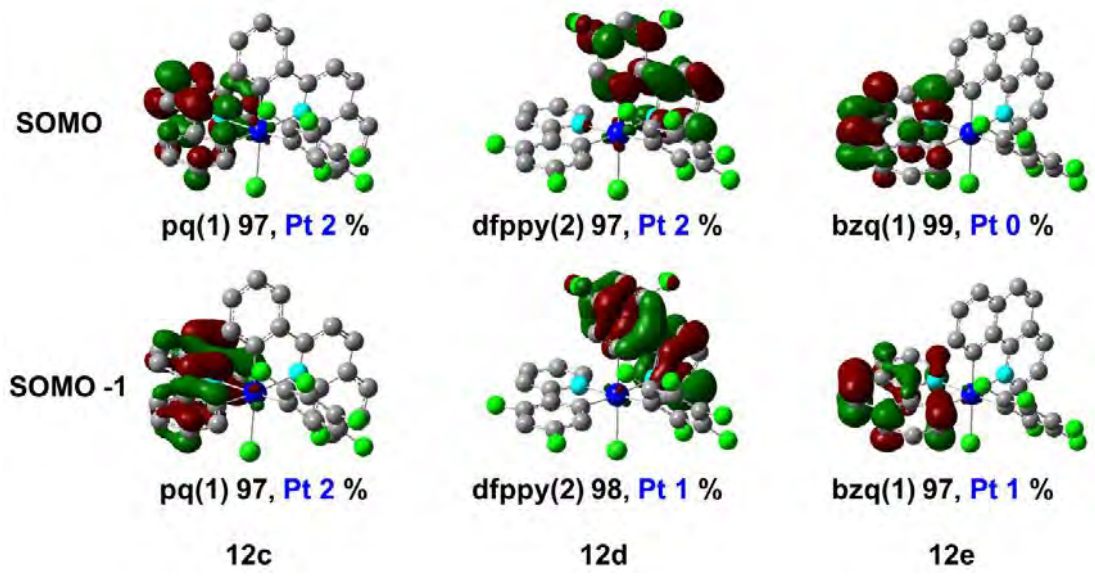

Figure A2.26. SOMO and SOMO-1 of complexes **12c**, **12d** and **12e**.

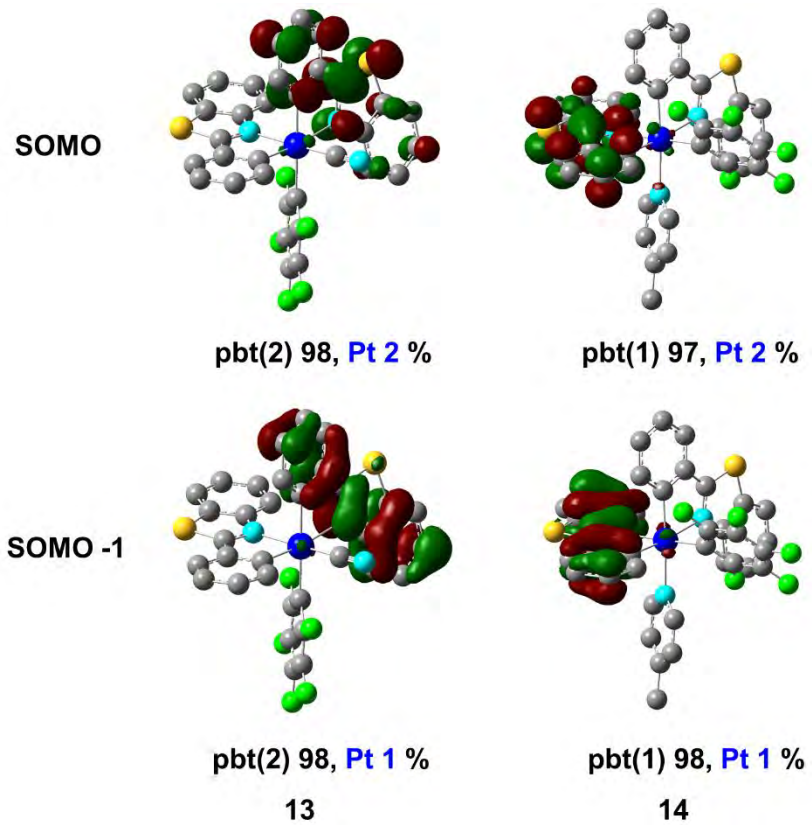

Figure A2.27. SOMO and SOMO-1 of complexes **13** and **14**.

Table A2.8. Composition (%) of frontier molecular orbitals in the first triple-state for **12c**, **12d**, **12e**, **13** and **14**.

12c						
	eV	C_6F_5	pq(1)	pq(2)	Pt	Cl
SOMO	-4.00	1	97	0	2	1
SOMO-1	-4.77	0	97	1	2	0
12d						
	eV	C_6F_5	dfppy(1)	dfppy(2)	Pt	Cl
SOMO	-3.77	0	1	97	2	0
SOMO-1	-4.81	0	0	98	1	0
12e						
	eV	C_6F_5	bzq(1)	bzq(2)	Pt	Cl
SOMO	-3.65	0	99	0	0	0
SOMO-1	-4.45	0	97	0	1	1
13						
	eV	C_6F_5	pbt(1)	pbt(2)	Pt	CN
SOMO	-3.98	0	1	98	2	0
SOMO-1	-4.68	0	0	98	1	0
14						
	eV	C_6F_5	pbt(1)	pbt(2)	Pt	Mepy
SOMO	-4.42	0	97	0	2	1
SOMO-1	5.17	0	98	0	1	0

Capítulo 3

Compuestos luminiscentes heterolépticos bis-ciclometalados de Pt(II) y Pt(IV) con ligandos pentafluorofenilo

Como se ha comentado en el Capítulo anterior, los estudios sobre las propiedades del estado excitado en compuestos de Pt(IV) con ligandos ciclometalados son escasos, probablemente debido a que estos estudios se han centrado principalmente en el Pt(II).

En los derivados de Pt(IV) con ligandos ciclometalados disminuye, de manera importante, la contribución del metal en las transiciones al estado excitado metal-ligando (MLCT), en comparación con sistemas similares de Ir(III) o Pt(II).[56] Esto se debe a la baja energía que presentan los orbitales d ocupados centrados en el metal en estos compuestos de Pt(IV).[56] Sin embargo, el platino juega un papel muy importante en las propiedades emisivas, ya que permite que el cruce intersistémico sea eficiente por el acoplamiento espín-órbita, lo que implica la formación de un estado excitado triplete. No obstante, como se ha explicado en la Introducción, la elección de los ligandos permite modular la eficiencia de la emisión. La coordinación de ligandos con mucha conjugación π puede dar lugar a una disminución de la influencia del metal, generando un menor acoplamiento espín-órbita, favoreciendo la emisión fluorescente del ligando.

En el **Capítulo 2** de esta Memoria se describe la síntesis de compuestos homolépticos de Pt(IV) $[Pt(C^\wedge N)_2(C_6F_5)Cl]$, que contienen dos ligandos ciclometalados iguales y el grupo pentafluorofenilo como coligando. Los compuestos se obtuvieron por la oxidación de los precursores de Pt(II) $[Pt(C^\wedge N)(HC^\wedge N)(C_6F_5)]$ que, al contener un ligando HC^N coordinado a través del nitrógeno, son precursores adecuados para la subsiguiente ciclometalación del ligando HC^N por reacción con el oxidante $PhICl_2$. Además, también se ha sustituido el átomo de Cl^- por otros ligandos de campo más fuerte (CN^-, Mepy y bpe) en el derivado con el ligando ciclometalado fenilbenzotiazol. En general, estos compuestos de Pt(IV) presentan luminiscencias asignadas a transiciones fundamentalmente ^{3}IL, con tiempos de vida más largos que los precursores de Pt(II), que presentan emisiones asignadas fundamentalmente a transiciones ^{3}IL/^{3}MLCT.

Se ha estudiado recientemente, en compuestos de Ir(III), que la incorporación de diferentes ligandos ciclometalados al centro metálico aporta muchas ventajas en las propiedades emisivas de estos compuestos organometálicos como, por ejemplo, la modulación del color de la emisión, la mejora de los rendimientos cuánticos y las eficiencias en electroluminiscencia.[141] Sin embargo, aunque en los últimos años se han estudiado algunos derivados ciclometalados de Pt(IV) luminiscentes,[27, 56, 62, 64-65, 67-68, 70] la síntesis de sistemas emisivos de compuestos ciclometalados de Pt(IV) con dos ligandos ciclometalados diferentes está prácticamente sin explorar.[67b, 67c]

Con el objetivo de continuar con el estudio de sistemas de Pt(IV) luminiscentes y de obtener emisiones más eficientes, nos propusimos abordar la preparación de nuevos compuestos de Pt(IV) que incorporaran dos cromóforos diferentes coordinados al centro de platino. Además, pensamos que el grupo C_6F_5 también sería un coligando adecuado para estos sistemas debido a que forma sistemas estables frente a procesos de reducción y/o eliminación reductora bajo condiciones térmicas y fotoquímicas.[67b] Por lo tanto, consideramos que el producto de partida idóneo sería el compuesto [Pt(bzq)(C_6F_5)(acetona)],[46] ya comentado previamente. Así, el desplazamiento de la molécula lábil de acetona por diferentes ligandos heterocíclicos nos ha permitido la preparación de compuestos de Pt(II) de estequiometría [Pt(bzq)(HC^N)(C_6F_5)], con el ligando 7,8-benzoquinoleína ciclometalado, y otro ligando heterocíclico coordinado a través del nitrógeno. La primera parte de este capítulo (**Capítulo 3.1**) recoge la síntesis, caracterización y un estudio detallado de las propiedades de los compuestos de Pt(II) [Pt(bzq)(HC^N)(C_6F_5)].

En la segunda parte de este capítulo (**Capítulo 3.2**), se aborda la síntesis de los compuestos heterolépticos de Pt(IV) *fac*-[Pt(bzq)(C^N)(C_6F_5)Cl], con los grupos C_6F_5 y Cl^- como ligandos auxiliares, obtenidos por oxidación de los derivados [Pt(bzq)(HC^N)(C_6F_5)].

Todos estos derivados tienen en común el ligando benzoquinoleína (bzq) y se diferencian en el segundo ligando C^N. Para estos sistemas hemos elegido seis ligandos heterocíclicos diferentes [HC^N = 2-(2-tienil)piridina (Hthpy), 2-fenilbenzotiazol (Hpbt), 2-fenilquinoleína (Hpq), 2-(2,4-difluorofenil)piridina (Hdfppy), 2,5-diphenil-1,3,4-oxadiazol (Hoxd) y 1-(2-piridil)pireno (Hpypy)]. Además, en esta parte se estudia con detalle la influencia del segundo ligando ciclometalado en las propiedades fotofísicas de

los derivados finales de Pt(IV), comparándolas con los precursores de Pt(II), con ayuda de cálculos teóricos DFT y TD-DFT.

3.1 Compuestos luminiscentes de Pt(II) [Pt(bzq)(HC^N)(C_6F_5)]

3.1.1 Síntesis y caracterización

Los compuestos de Pt(II) [Pt(bzq)(HC^N)(C_6F_5)] **16** (HC^N = Hthpy **a**, Hpbt **b**, Hpq **c**, Hdfppy **d**, Hoxd **f**, Hpypy **g**) se sintetizan, como se ha adelantado en la Introducción de este Capítulo, a partir del solvato [Pt(bzq)(C_6F_5)(acetona)].[46] El desplazamiento de la molécula de acetona se lleva a cabo de manera eficaz y rápida por la adición de un equivalente del correspondiente ligando heterocíclico HC^N en condiciones suaves de reacción (CH_2Cl_2, 298 K, **16a-f**; acetona, 0º, **16g**) (Esquema 3.1), produciéndose los compuestos **16a-g** con buenos rendimientos (64 % **16c** – 84 % **16a**).

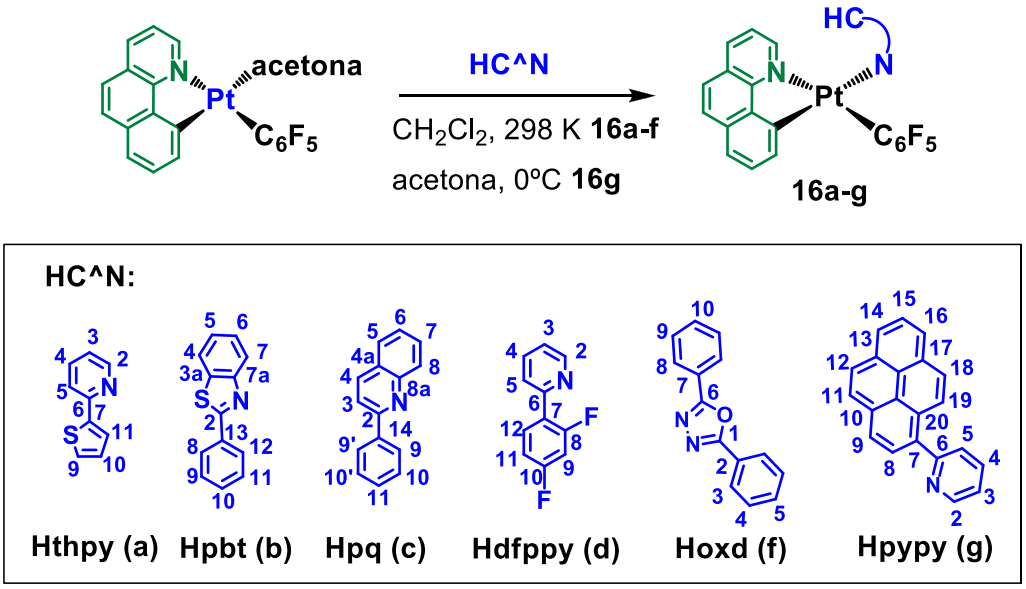

Esquema 3.1. Síntesis de los compuestos de Pt(II) [Pt(bzq)(HC^N)(C_6F_5)] **16a-g**.

La combinación de las técnicas de difracción de Rayos X (**16a**, **16f**), IR, espectrometría ESI (Electrospray Mass spectra) y análisis elemental nos ha permitido confirmar la formulación propuesta para estos compuestos de Pt(II). La presencia de un grupo pentafluorofenilo se confirma por IR, observándose una banda de vibración $\nu_{X\text{-sens}}$ para cada compuesto.

Todos los derivados de Pt(II) han sido caracterizados mediante espectroscopía de RMN monodimensional (^{1}H, ^{13}C{^{1}H} y ^{19}F{^{1}H}) y bidimensional (^{1}H-^{1}H COSY y TOCSY, ^{1}H-^{13}C HSQC y HMBC)]. En los espectros de RMN de ^{1}H y ^{13}C{^{1}H} de estos

compuestos monometalados de Pt(II) se pueden observar dos grupos de señales, uno correspondiente al ligando metalado bzq y otro que corresponde al ligando HC^N coordinado a través del nitrógeno (Figuras 3.1a,b y A3.1).

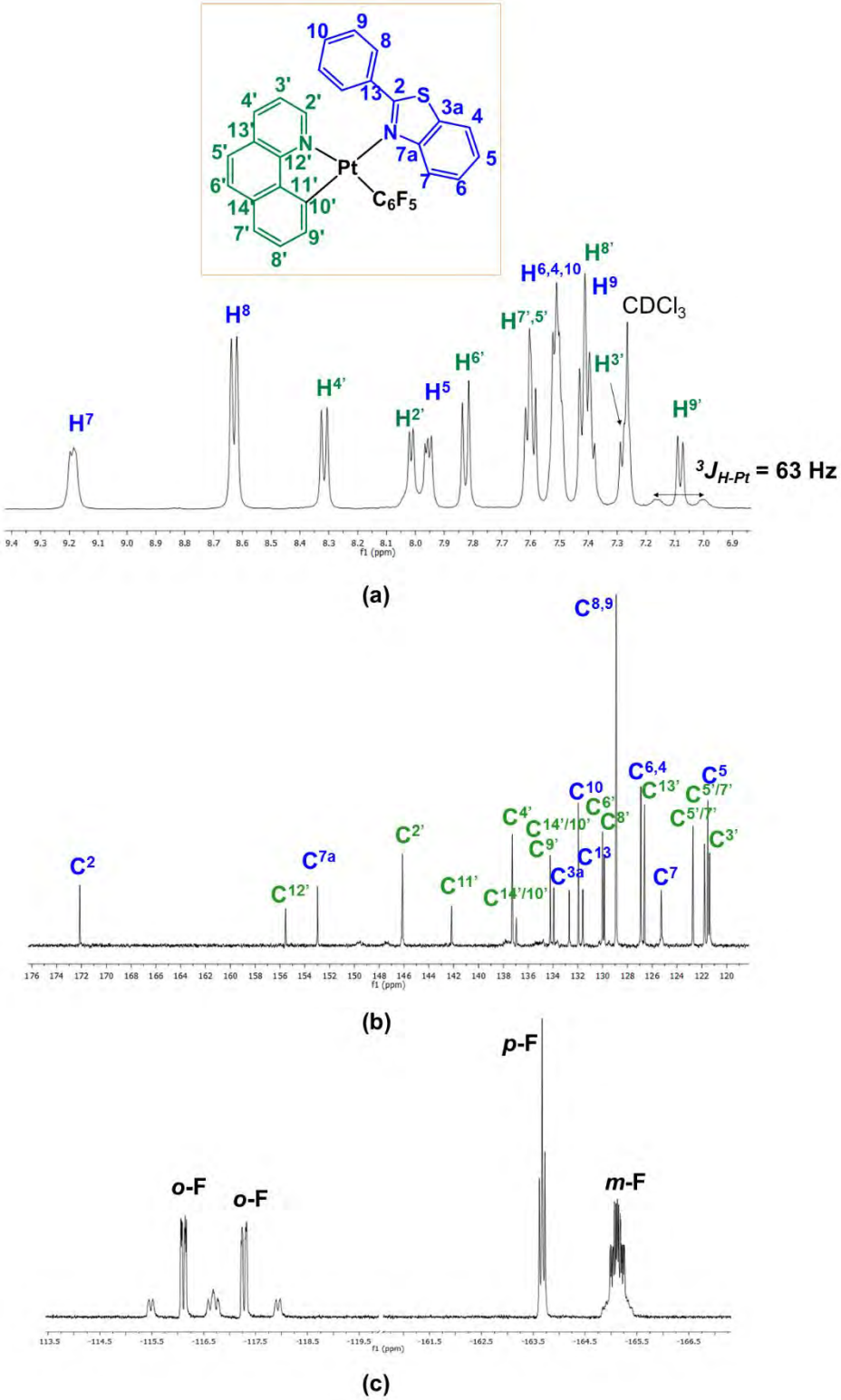

Figura 3.1. Espectros de RMN de (a) ^{1}H, (b) $^{13}C\{^{1}H\}$ y (c) $^{19}F\{^{1}H\}$ del compuesto **16b** en $CDCl_3$.

La señal más característica que presentan estos derivados es la que corresponde al protón que está en posición *orto* con respecto al carbono metalado del ligando bzq ($H^{9'}$). Esta señal aparece a frecuencias relativamente bajas (δ = 7.08 – 6.72) debido a las corrientes diamagnéticas del grupo C_6F_5 y presenta satélites a platino ($^3J_{Pt-H}$ = 59 – 64 Hz) con valores similares a otros compuestos de Pt(II) que presentan el ligando bzq ciclometalado.[46] La sustitución del ligando de acetona por un ligando heterocíclico más voluminoso se refleja en los espectros de $^{19}F\{^1H\}$, ya que se observa un patrón de 5 señales correspondientes al ligando C_6F_5, lo que indica una situación estática durante el tiempo de respuesta de la técnica, debido a las restricciones estéricas que sufre este grupo (Figura 3.1c).

Las estructuras de los compuestos **16a**·0.25CH_2Cl_2 y **16f**·$CHCl_3$ han sido confirmadas por difracción de Rayos X. Se obtuvieron monocristales adecuados por lenta difusión de *n*-hexano sobre una disolución del correspondiente compuesto en diclorometano (**16a**) o cloroformo (**16f**) a -30ºC (Figura 3.2 y Tabla 3.1). En el compuesto **16a** se observan dos moléculas en la unidad asimétrica A y B que forman una interacción F···F entre los grupos C_6F_5 (2.876 Å). Las dos moléculas presentan datos de distancias y ángulos muy similares, por lo que sólo los datos de la molécula A están dados en la Tabla 3.1.

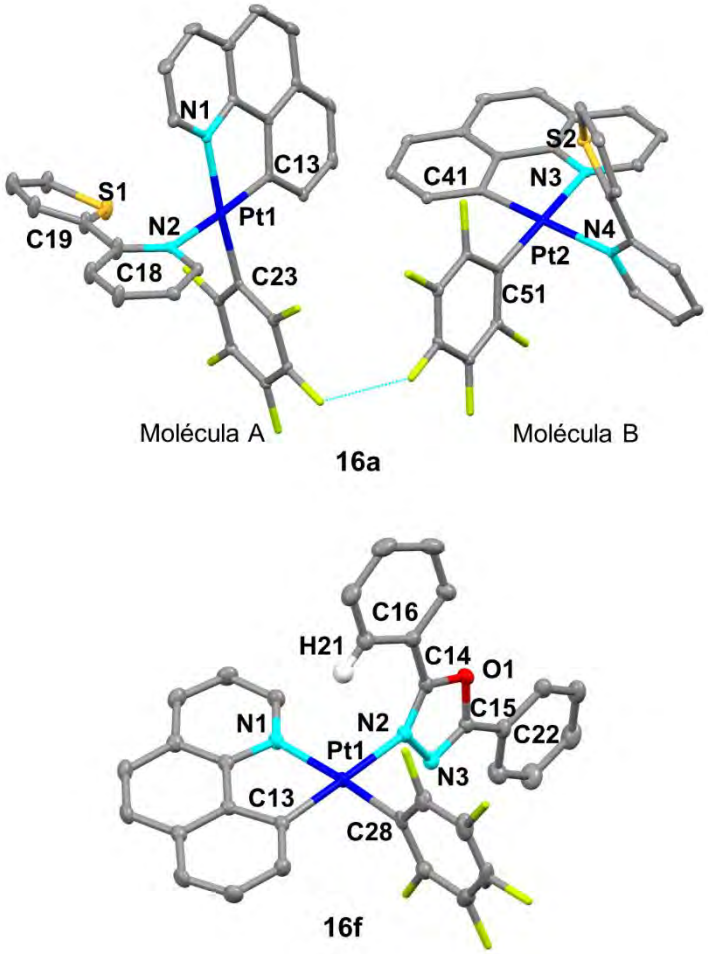

Figura 3.2. Estructuras de Rayos X de los compuestos [Pt(bzq)(Hthpy)(C_6F_5)] **16a** y [Pt(bzq)(Hthpy)(C_6F_5)] **16f**.

Tabla 3.1. Distancias (Å) y ángulos (°) seleccionados para los compuestos **16a**·0.25CH_2Cl_2 (molécula A) y **16f**·$CHCl_3$.

16a·0.25CH_2Cl_2 (molécula A)			
Distancias (Å)		**Ángulos (°)**	
Pt(1)-N(1)	2.081(3)	N(1)-Pt(1)-N(2)	94.11(12)
Pt(1)-N(2)	2.131(3)	C(13)-Pt(1)-N(1)	82.14(13)
Pt(1)-C(13)	1.997(4)	C(13)-Pt(1)-C(23)	94.48(15)
Pt(1)-C(23)	2.004(4)	C(23)-Pt(1)-N(2)	88.93(13)
C(18)-C(19)	1.461(5)		
H(14)···Pt(1)	2.901		
16f·$CHCl_3$			
Distancias (Å)		**Ángulos (°)**	
Pt(1)-N(1)	2.0888(18)	N(1)-Pt(1)-N(2)	94.81(7)
Pt(1)-N(2)	2.1186(18)	C(13)-Pt(1)-N(1)	82.09(8)
Pt(1)-C(13)	1.987(2)	C(13)-Pt(1)-C(28)	92.70(9)
Pt(1)-C(28)	2.005(2)	C(28)-Pt(1)-N(2)	90.46(8)
C(14)-C(16)	1.457(3)		
C(15)-C(22)	1.460(3)		
H(21)···Pt(1)	2.712		

Estos derivados de Pt(II) muestran, como era de esperar, una geometría plano-cuadrada distorsionada en torno al centro de platino, y confirman la retención de la disposición *cis* entre el carbono metalado de la bzq y el grupo pentafluorofenilo, que presenta el precursor [Pt(bzq)(C_6F_5)(acetona)].[46] En los dos casos, la distancia entre el átomo de Pt y el nitrógeno del ligando heterocíclico thpy (**16a**) u oxd (**16f**) [Pt-N2 = 2.131(3) **16a**, 2.1186(18) Å **16f**] es mayor que la distancia entre el platino y el nitrógeno de la bzq [Pt-N1 = 2.081(3) **16a**, 2.0888(18) Å **16f**], lo que indica que el carbono metalado ejerce una mayor influencia *trans* que el carbono del grupo C_6F_5.

En la estructura cristalina del compuesto [Pt(bzq)(Hoxd)(C_6F_5)] **16f**, se observa que uno de los anillos fenílicos del ligando Hoxd está inclinado 11.6º con respecto a la unidad oxadiazol, orientando uno de los protones hacia el centro del platino (Pt-H21 = 2.712 Å), como ocurría en los compuestos de Pt(II) [Pt(C^N)(HC^N)(C_6F_5)] **10** del **Capítulo 2**. Sin embargo, en el compuesto con el ligando Hthpy, [Pt(bzq)(Hthpy)(C_6F_5)] **16a**, es el átomo de azufre el que aparece orientado hacia el átomo de platino en lugar del protón H-C del anillo tienílico. Además, la distancia Pt···S (3.15 Å) es menor que la suma de los radios van der Waals (3.55 Å), como ocurre en otros compuestos similares como *trans*-[Pt(Br-pbt-*κ*C)Cl($PTA)_2$][101b] [3.073 Å; PTA = 1,3,5-triaza-7-fosfatriciclo(3.3.1.1)decano] o [Pt(ppy)(9S3)]$^+$ [2.9518(17) Å, 9S3 = 1,4,7-tritiaciclononano].[142]

En el derivado [Pt(bzq)(Hthpy)(C_6F_5)] **16a** las moléculas forman un apilamiento π···π no lineal entre los ligandos ciclometalados bzq (3.34 Å) y entre los ligandos bzq-Hthpy (3.39 Å) y Hthpy-Hthpy (3.29 Å), reforzado por interacciones secundarias F_{C6F5}···F_{C6F5} y H_{bzq}···C_{C6F5} (Figura A3.2). En [Pt(bzq)(Hoxd)(C_6F_5)] **16f** existe un apilamiento π···π más eficaz que el del compuesto **16a** entre los ligandos ciclometalados bzq (3.39 Å) y bzq-Hoxd (3.26-3.40 Å) (Figura 3.2), reforzado también por interacciones secundarias H_{bzq}···C_{C6F5} y H_{oxd}···F_{C6F5}.

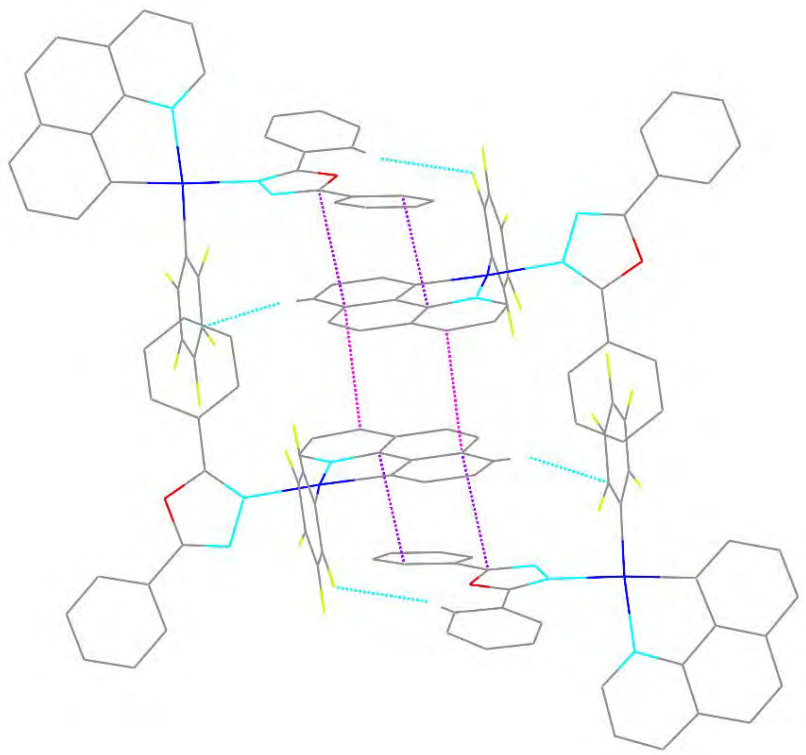

Figura 3.2. Estructura supramolecular del derivado [Pt(bzq)(Hoxd)(C_6F_5)] **16f** mostrando la cadena formado por interacciones π···π entre los ligandos ciclometalados bzq (3.39 Å) (líneas rosas) y entre los ligandos bzq y Hoxd (3.26-3.40 Å) (líneas moradas), reforzadas por interacciones secundarias $H_{bzq}\cdots C_{C6F5}$ (2.82 Å) and $H_{oxd}\cdots F_{C6F5}$ (2.62 Å) (líneas azules).

3.1.2 Propiedades ópticas

Se ha realizado un estudio detallado de los espectros de absorción y emisión de todos los compuestos de Pt(II) **16a-g**. Para comprender mejor la naturaleza de las propiedades ópticas de estos derivados de Pt(II) se ha llevado a cabo un estudio teórico mediante Density Functional Theory (DFT) y Time Dependent-Density Functional Theory (TD-DFT) para los compuestos [Pt(bzq)(HC^N)(C_6F_5)] (HC^N = Hthpy **16a**, Hpq **16c**, Hdfppy **16d** y Hoxd **16f**). El estudio se centró en los derivados caracterizados mediante difracción de Rayos X **16a** y **16f** y, para completar el estudio, se realizaron también cálculos teóricos de los compuestos **16c** y **16d**, usando el método B3LYP con la base LanL2DZ para el átomo de platino y la base 6-31G(d,p) para los átomos de los ligandos. Todos los datos de los cálculos teóricos están recogidos en las Tablas A3.1-A3.5.

3.1.2.1 Espectros de absorción y cálculos teóricos

Se ha realizado un estudio de los espectros de absorción UV-visible de todos los compuestos [Pt(bzq)(HC^N)(C_6F_5)] **16a-g** en disoluciones de CH_2Cl_2 5×10^{-5} M. Todos los datos experimentales se recogen en la Tabla 3.2, y los espectros se recogen en la Figura 3.3.

Tabla 3.2. Datos de absorción UV-visible de los compuestos de Pt(II), [Pt(bzq)(HC^N)(C_6F_5)] **16**, en CH_2Cl_2 5×10^{-5} M.

Compuesto	**λ_{abs}/nm (10^3 ε/M^{-1} cm^{-1})**
[Pt(bzq)(Hthpy-*κN*)(C_6F_5)] (**16a**)	253 (31), 302 (16), 315_h (13.8), 335 (7.2), 366 (2.9), 419 (1.3)
[Pt(bzq)(Hpbt-*κN*)(C_6F_5)] (**16b**)	253 (37), 279 (16), 306 (21), 365 (3.3), 417 (1.5)
[Pt(bzq)(Hpq-*κN*)(C_6F_5)] (**16c**)	233 (50), 253 (43), 312 (14), 327 (12.5), 375 (3.6), 425 (1.8)
[Pt(bzq)(Hdfppy-*κN*)(C_6F_5)] (**16d**)	220 (76), 252 (65), 278 (25), 311 (16), 338 (10), 365 (4), 415 (2.6)
[Pt(bzq)(Hoxd-*κN*)(C_6F_5)] (**16f**)	252 (105), 278 (62), 294 (58), 308 (43), 333 (16), 358 (7), 411 (3.9)
[Pt(bzq)(Hpypy-*κN*)(C_6F_5)] (**16g**)	243 (57), 255_h (47.4), 280 (31.4), 315 (16), 350 (23), 367_h (18), 422 (2.5)

Tomando como referencia las asignaciones dadas en complejos similares de Pt(II) con ligandos ciclometalados, y con el apoyo de los cálculos teóricos, se asignan las bandas intensas de absorción que aparecen en los espectros de absorción de los compuestos **16a-f** en la zona de alta energía (220-330 nm) a transiciones ^{1}IL localizadas en los ligandos bzq, HC^N y el grupo C_6F_5. Sin embargo, en el compuesto **16g**, las bandas que corresponden a transiciones $^1\pi$-π^* centradas en el ligando Hpypy aparecen a energías más bajas (350, 367_{sh} nm) (Figura 3.3).

Como puede apreciarse en la ampliación de la zona de baja energía de la Figura 3.3, aparecen bandas anchas a 411 - 425 nm, con un valor de coeficiente de extinción molar bajo. Estas bandas se han asignado, con el apoyo de cálculos teóricos, a transiciones con mezcla de contribución ^{1}IL' y ^{1}ML'CT (L' = bzq) centradas principalmente en el ligando bzq ciclometalado. Además, también se han encontrado transiciones con cierta contribución de transferencia de carga metal-ligando desde el metal hacia el ligando HC^N coordinado por el nitrógeno. Esto último pone de manifiesto una dependencia del tipo de ligando HC^N en el máximo de las bandas en la región de baja energía, ya que se

observa una ligera variación que sigue el orden: 411 **16f** (Hoxd) < 415 **16d** (Hdfppy) < 417 **16b** (Hpbt) < 419 **16a** (Hthpy) < 422 **16g** (Hpypy) < 425 nm **16c** (Hpq).

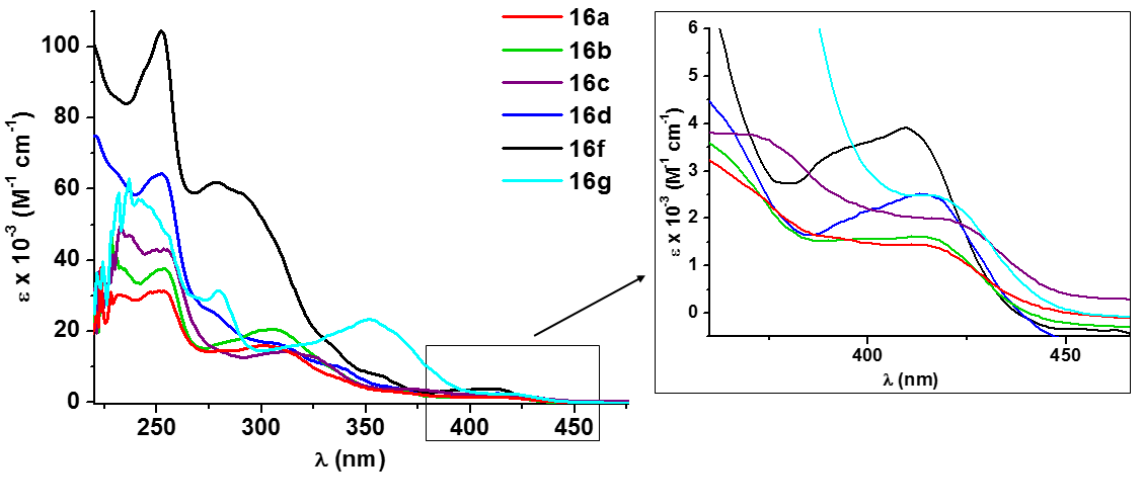

Figura 3.3. Espectro UV-Visible de los compuestos [Pt(bzq)(HC^N)(C_6F_5)] **16a-g** en CH_2Cl_2 5 × 10^{-5} M.

La comparación de los espectros de UV experimentales con los calculados para los compuestos **16a**, **16c**, **16d** y **16f** se muestra en la Figura A3.3. Como se puede observar, los cálculos teóricos representados por barras azules se ajustan razonadamente bien a los datos experimentales. Además, se ha representado de forma esquemática la energía de los orbitales ocupados HOMO y HOMO-1 y los orbitales vacíos LUMO y LUMO+1 implicados en las excitaciones seleccionadas S_1, S_2 y S_3 (Figura 3.4) para los compuestos de Pt(II) [Pt(bzq)(HC^N)(C_6F_5)] (HC^N = Hthpy **16a**, Hdfppy **16d**, Hpq **16c** y Hoxd **16f**). La transición calculada con mayor valor de fuerza del oscilador (f) está señalada con una flecha más gruesa.

Con la toda la información extraída de los cálculos teóricos DFT y TD-DFT, decidimos abordar el estudio de los orbitales implicados en las principales transiciones implicadas en las bandas de baja energía. En los compuestos **16a** y **16d**, la transición calculada más intensa (con mayor fuerza del oscilador) es la S_1, y es una transición HOMO → LUMO (Figura 3.4a). En ambos derivados, el orbital HOMO tiene una importante contribución del ligando ciclometalado bzq (~ 70 %) y del átomo de platino (~ 29 %), mientras que el orbital LUMO está centrado principalmente en el orbital π* de la bzq (Tabla A3.3). El orbital vacío π* centrado en el ligando HC^N Hthpy (**16a**) o Hdffpy (**16d**) contribuye en el orbital desocupado LUMO+1 y participa en la transición S_3.

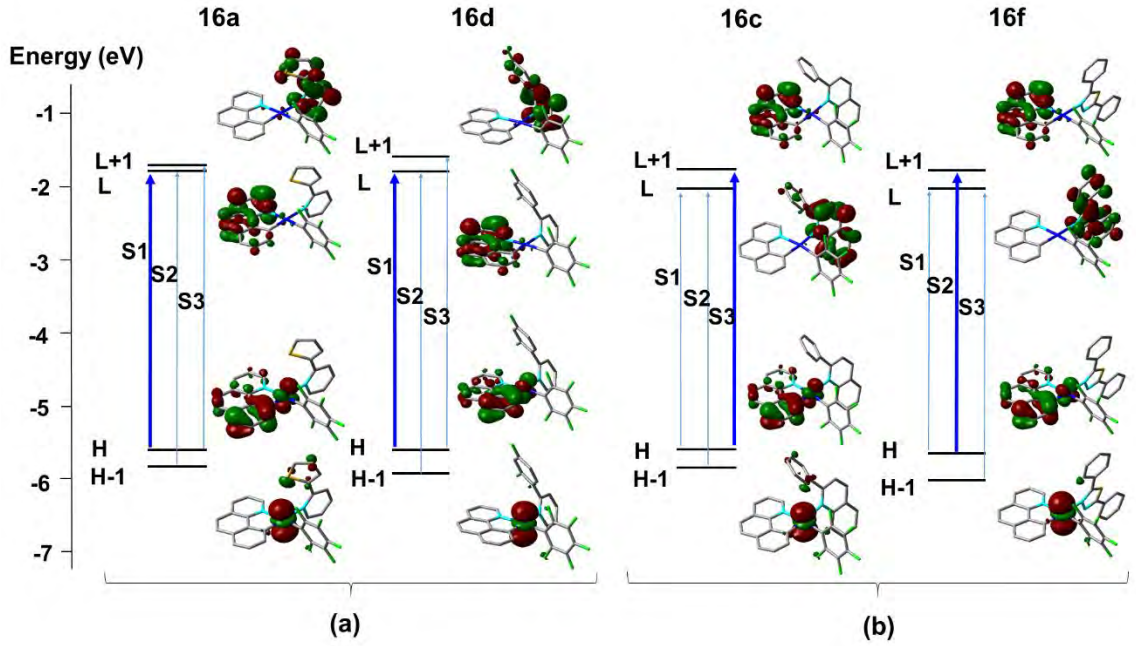

Figura 3.4. Diagrama de energía de los orbitales frontera y excitaciones seleccionadas calculadas mediante cálculos teóricos para **16a**, **16c**, **16d** y **16f**.

Para los derivados con los ligandos Hpq (**16c**) y Hoxd (**16f**) (Figura 3.4b), la composición del HOMO es similar a la de los derivados **16a** y **16d** ya que está centrado en la bzq (~ 70 %) y en el platino (~ 27 %). Sin embargo, la energía de los orbitales π* de los ligandos Hpq y Hoxd es más baja que la de los orbitales π* del ligando ciclometalado bzq y, por lo tanto, el orbital LUMO está centrado en el ligando HC^N y el LUMO+1 en la bzq. Sin embargo, la transición calculada con mayor fuerza del oscilador en estos compuestos (S_3 **16c**, S_2 **16f**) es una transición HOMO → LUMO+1, por lo que se asigna a una transición con mezcla de contribución ^{1}IL'/^{1}ML'CT centrada en el ligando ciclometalado bzq. En estos compuestos, la primera transición calculada S_1 (413 **16c**, 399 nm **16f**) tiene un valor de la fuerza del oscilador muy bajo. Esta transición HOMO → LUMO tiene carácter ligando (bzq) → ligando (HC^N) y metal (Pt) → ligando (HC^N) y podría explicar el desplazamiento hacia el rojo que se observa en la banda de baja energía del espectro de UV del derivado con el ligando Hpq **16c** (425 nm) (Tabla 3.2).

3.1.2.2 Espectros de emisión y cálculos teóricos

Se han medido las propiedades emisivas de los compuestos de Pt(II) en CH_2Cl_2 5 × 10^{-5} M y en estado sólido a temperatura ambiente y a 77 K. Además, también se han medido los espectros de emisión de los compuestos en films de poliestireno (PS) a

temperatura ambiente. En la Tabla 3.3 se recogen los datos extraídos de los estudios de luminiscencia en disolución y en PS y en la Tabla 3.4 se muestran los datos en estado sólido (en algunos casos, sólido cristalino).

Disolución y PS

Todos los compuestos de Pt(II) son emisivos tanto en disolución como en PS. Los compuestos **16a-f** muestran bandas de emisión ligeramente estructuradas a temperatura ambiente con máximos en 490-518 nm. Estas bandas sufren un desplazamiento a energías más altas en disolución a 77 K (λ_{max} = 482-490 nm) y en PS (476-503 nm) (Figura 3.5). Se han medido los rendimientos cuánticos de emisión (ϕ_{em}) en PS, obteniéndose valores entre 13.4 (**16a**) y 16.3 % (**16b**). Además, se han medido los tiempos de vida de todos los compuestos en diferentes picos. En general, el tiempo de vida para los compuestos **16b**,**d** y **f** se ajusta de manera razonable a una componente, mientras que para el resto de compuestos se ajusta a dos componentes o muestran diferentes tiempos de vida en distintos picos de emisión, lo que pone de manifiesto la presencia de estados emisivos cercanos en energía.

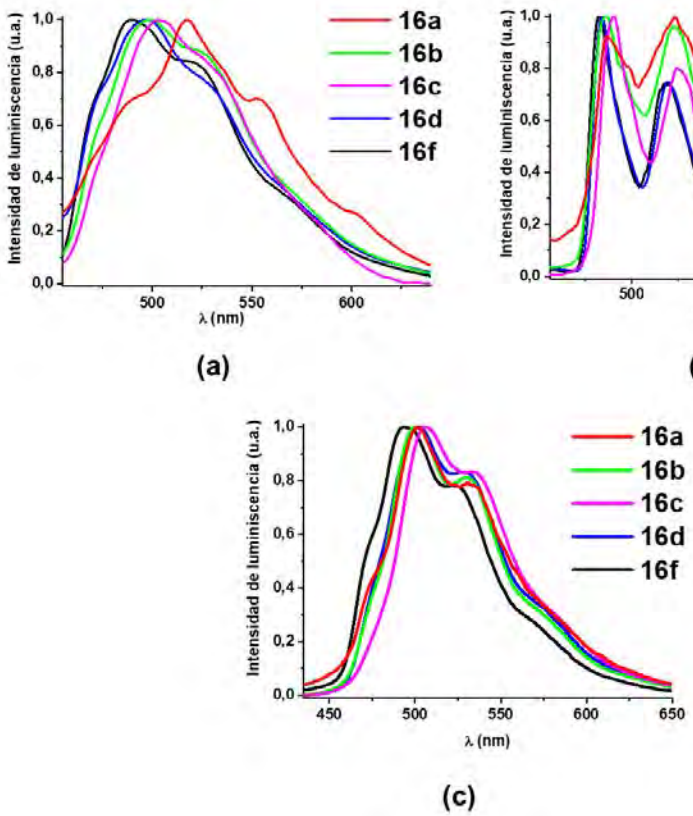

Figura 3.5. Espectros normalizados de emisión en (a) CH_2Cl_2 5 × 10^{-5} M a 298 K (b) CH_2Cl_2 5 × 10^{-5} M a 77 K y (c) PS (10 %) de los compuestos **16a-f**.

Tabla 3.3. Datos fotofísicos de los compuestos **16a-g** en CH_2Cl_2 5 × 10^{-5} M y PS (10 % **16a-f**, 5% **16g**).

Compuesto		Tª (K)	λ_{em}/nm (λ_{ex}/nm)	ϕ (%)ª	τ(μs)
16a	CH_2Cl_2	298	487_h, 518_{max}, 555, 603sh (365)	-	0.5 (81%), 3 (19%) (487); 0.7 (84%), 8.7 (16%) (518)
		77	487, 524_{max}, 552, 586_h (365-410)	-	455 (52%), 104 (48%)
	PS	298	476_{sh}, 502_{max}, 534, 581 (365-420)	13.4	10 (70%), 42 (30%)
16b	CH_2Cl_2	298	471_h, 499_{max}, 526, 570_h (365-415)	-	0.6
		77	485_{max}, 525, 560_h (365-425)	-	390
	PS	298	476_h, 500_{max}, 531, 576_h (320-430)	26.3	41
16c	CH_2Cl_2	298	474_h, 504_{max}, 530, 575_h (330-365)	-	0.7 (474); 1.2 (504)
		77	490_{max}, 527, 570_h (320-420)	-	312
	PS	298	506_{max}, 536, 583_h (365-430)	19	28
16d	CH_2Cl_2	298	472_h, 496_{max}, 528, 570_h (365-410)	-	0.4
		77	483_{max}, 520, 560 (365-415)	-	445
	PS	298	477_h, 502_{max}, 530, 578_h (330-43)	26	38
16f	CH_2Cl_2	298	470_h, 490_{max}, 522, 570sh (330-410)	-	0.3
			350, 470, 490_{max}, 522, 570_h (300-310)		
		77	482_{max}, 520, 560 (310-410)	-	538
	PS	298	473_h, 495_{max}, 526, 572 (320-420)	22.8	39
16g	CH_2Cl_2	298	393_{max}, 410, 625, 682 (350-400) (disolución desoxigenada)	-	0.010 (393)
		77	480, 516, 557, 612_{max}, 673, 740 (415)	-	264 (480); 2309 (612)
	PS (5 %)	298	626_{max}, 684, 757 (380-440)	16.4	0.61

ª Rendimiento cuántico medido con esfera integradora.

En términos generales, y con ayuda de los cálculos teóricos, se asigna la emisión a transiciones con mezcla de contribuciones fundamentalmente ^{3}IL'/^{3}ML'CT (L' = bzq) centradas en el fragmento metal-ligando ciclometalado (Pt-bzq). Además, en los derivados con HC^N = Hpbt **16b**, Hdfppy **16d** y Hoxd **16f**, también participa, con una baja contribución, el ligando coordinado a través del nitrógeno HC^N. Se ha encontrado cierta contribución de transiciones adicionales ^{3}IL/^{3}MLCT/^{3}L'LCT (L' = bzq; L = HC^N) en los derivados con los ligandos Hthpy **16a** y Hpq **16c**.

Con objeto de asignar con mayor precisión la naturaleza de las emisiones en estos compuestos, se han estudiado con detalle los cálculos teóricos DFT y TD-DFT realizados para los derivados **16a**, **16c**, **16d** y **16f**. Para ello, se analizaron la energía y la composición de los tripletes de más baja energía mediante cálculos TD-DFT en CH_2Cl_2 a partir de las geometrías optimizadas en el estado fundamental S_0 (Tabla A3.4 y Figura 3.6). En los compuestos **16a**, **16d** y **16f**, los estados tripletes T_1 y T_2 aparecen a energías muy similares (T_1/T_2 : 467.33/440.70 nm **16a**; 466.63/441.96 nm **16d**; 465.05/438.00 nm **16f**). Estos estados triplete tienen una configuración principalmente bzq→bzq/Pt→bzq (^{3}IL'/^{3}ML'CT) e implican excitaciones electrónicas a orbitales desocupados (**16a, 16d**: LUMO/LUMO+2; **16f**: LUMO+1/LUMO+3) centrados en el ligando L' bzq ciclometalado.

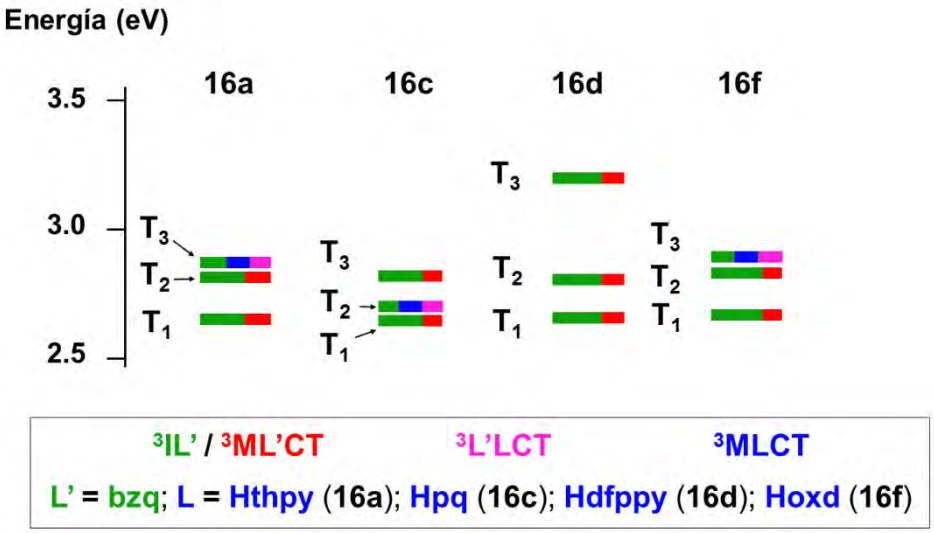

Figura 3.6. Representación esquemática de la contribución del Pt y los grupos bzq y HC^N en los tripletes $T_{1\text{-}3}$ para **16a**, **16c**, **16d** y **16f**.

En el derivado **16c** con HC^N = Hpq la transición triplete T_1 presenta, de manera similar al resto de los derivados, una contribución ^{3}IL'/^{3}ML'CT centrada en la unidad Pt(bzq). Sin embargo, la transición T_2, que aparece tan solo 0.01 eV por encima en energía que T_1, tiene una composición más compleja ^{3}IL'/^{3}L'LCT/^{3}MLCT. En los compuestos **16a** y **16f**, es la transición T_3 la que presenta una composición compleja similar pero, en los dos casos, aparece más lejos de T_1 (T_3-T_1 = 0.22 **16a**, 0.21 eV **16f**). Estos resultados ponen de manifiesto que, a excepción del derivado con el ligando Hdffpy, estos sistemas presentan diferentes estados emisivos cercanos en energía.

Con el objetivo de seguir estudiando el carácter de las emisiones en estos compuestos de Pt(II), se ha realizado también la optimización del primer estado triplete T_1 mediante cálculos teóricos DFT (Figura 3.7 y Figura A3.4) para los compuestos **16a**, **16c**, **16d** en CH_2Cl_2. Para el derivado con el ligando Hoxd **16f**, no se pudo realizar con éxito la optimización del T_1 en CH_2Cl_2, por lo que los resultados de la optimización para este compuesto están dados en fase gas. Los resultados son muy similares a los obtenidos mediante el análisis de los tripletes por TD-DFT desde el estado fundamental comentados anteriormente. El análisis de la distribución de la densidad de espín (Figura 3.7) muestra que, para los derivados **16a**, **16d** y **16f**, la densidad está localizada en el fragmento Pt(bzq), mientras que para **16c**, la densidad está principalmente centrada en el centro metálico y en el ligando Hpq.

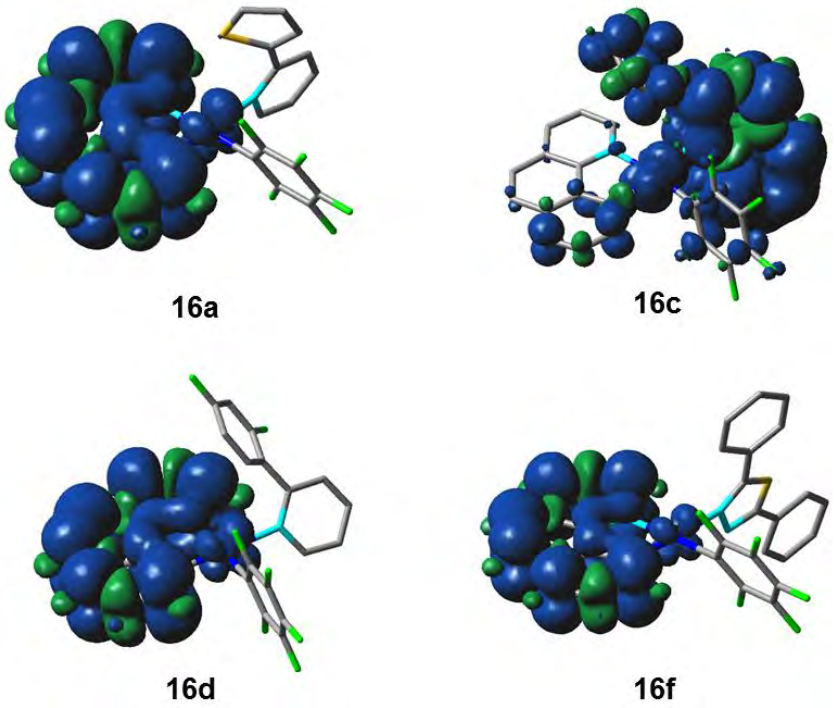

Figura 3.7. Distribución de la densidad de espín para los compuestos **16a**, **16c**, **16d** (CH_2Cl_2) y **16f** (fase gas).

Las longitudes de onda de emisión calculadas mediante la diferencia de energías triplete – singlete de la estructura optimizada en el estado triplete (ΔE_{T1-S0}) en CH_2Cl_2 [ΔE_{T1-S0} calculada: **16d** (556) ≈ **16a** (557) < **16c** (506)] se ajustan de manera razonable a la emisión observada en PS [**16d** (502) = **16a** (502) < **16c** (506 nm)]. Para el compuesto **16f**, sólo se ha podido calcular la longitud de onda de emisión en fase gas, siendo el valor

calculado mucho menos energético que el máximo de emisión observado en PS (λ_{calc} *vs* λ_{em} = 567 *vs* 495 nm).

El derivado que contiene ligando 1-(2-piridil)pireno [Pt(bzq)(Hpypy)(C_6F_5)] **16g** muestra, en disolución desoxigenada de CH_2Cl_2 5×10^{-5} M, una banda de emisión estructurada de tiempo de vida muy corto (10 ns) a 393 nm de color violeta y otra mucho menos intensa a 625 nm (Figura 3.8a, línea azul clara). La banda de emisión de alta energía es prácticamente idéntica a la que muestra el ligando Hpypy libre (línea negra discontinua en la Figura 3.8a) por lo que se asigna a una banda de fluorescencia $^1\pi\pi^*$ centrada en el ligando Hpypy. Sin embargo, la banda que aparece a 625 nm se atribuye a una banda de fosforescencia centrada en el ligando $^3\pi\pi^*_{Hpypy}$. Para comprobar esta asignación, se midió el espectro de emisión de la misma muestra disuelta en CH_2Cl_2 5×10^{-5} sin desoxigenar y, como era de esperar, la banda de fosforescencia $^3\pi\pi^*_{Hpypy}$ (625 nm) desaparece, modificándose el color de emisión de violeta a azul (Figura 3.8a, línea azul oscura).

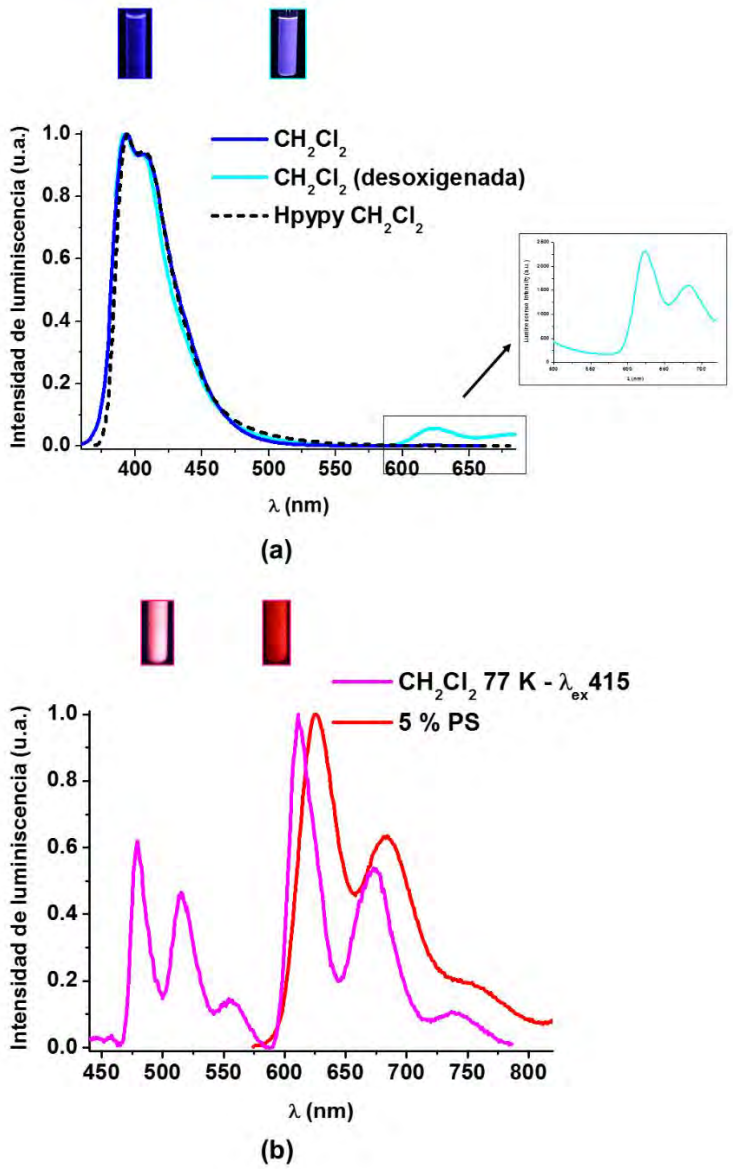

Figura 3.8. Espectros de emisión de (a) **16g** en una disolución de CH_2Cl_2 sin desoxigenar (línea azul) y desoxigenada (línea azul claro) y del ligando Hpypy libre en CH_2Cl_2 a 298 K (línea negra discontínua); (b) **16g** en CH_2Cl_2 a 77 K (línea rosa) y en PS (5 %, línea roja).

Cuando la disolución del compuesto **16g** en CH_2Cl_2 se congela a 77 K, no solo desaparece la banda de fluorescencia centrada en el ligando Hpypy $^1\pi\pi^*_{Hpypy}$ para dar la banda de fosforescencia $^3\pi\pi^*_{Hpypy}$ a 612 nm, sino que también se consigue, en este medio rígido, la banda de fosforescencia centrada en la unidad Pt(bzq) a 480 nm (Figura 3.8b, línea rosa). Por lo tanto, con una longitud de onda de excitación de 415 nm, se consigue una luminiscencia color rosa debida a una emisión dual que da lugar a dos bandas estructuradas con máximos de emisión en 480 y 612 nm.

El tiempo de vida media (264 μs) medido en la banda de emisión a 480 nm es del mismo orden que los tiempos de vida del resto de los derivados en CH_2Cl_2 a 77 K, por lo

que se confirma que, en esa banda, el estado excitado tiene carácter ^{3}IL'(bzq)/^{3}ML'CT (Pt→bzq). Además, el alto valor del tiempo de vida media (2309 μs) que se observa en la banda de baja energía, asignada a fosforescencia centrada en el ligando Hpypy, está de acuerdo con la alta deslocalización electrónica que presenta el ligando.[143] Curiosamente, cuando la emisión de este compuesto se registra en PS a 298 K, la luminiscencia es de color rojo y, en su espectro de emisión, sólo se observa una banda de baja energía a 626 nm asignada a una fosforescencia centrada en el ligando $^3\pi\pi^*_{Hpypy}$ (Figura 3.8b, línea roja).[144] Esto puede ser debido a que el estado excitado de baja energía centrado en el ligando Hpypy es más accesible a temperatura ambiente y, por lo tanto, sólo se observa emisión desde ese estado, eliminándose la emisión desde el estado excitado asignado a la fosforescencia del fragmento Pt(bzq).

Estado sólido

Aunque el compuesto **16g** no es luminiscente en estado sólido, los derivados **16a-f** muestran emisiones estructuradas que dependen de la temperatura (Tabla 3.4 y Figura 3.9). Así, los compuestos **16a-d** exhiben a temperatura ambiente bandas de baja energía (λ_{max} = ~ 560-590 nm), que se asignan tentativamente a la población de un estado emisivo de carácter excimérico (favorecido a 298 K) formado por la presencia de interacciones intermoleculares π···π entre los ligandos heterocíclicos (bzq-bzq y bzq-HC^N). A baja temperatura aparecen nuevas bandas a energías más altas (λ_{max} = 515-550 nm), que se atribuyen fundamentalmente a emisión en los monómeros, o mezclas con excímeros o con estados emisivos próximos.

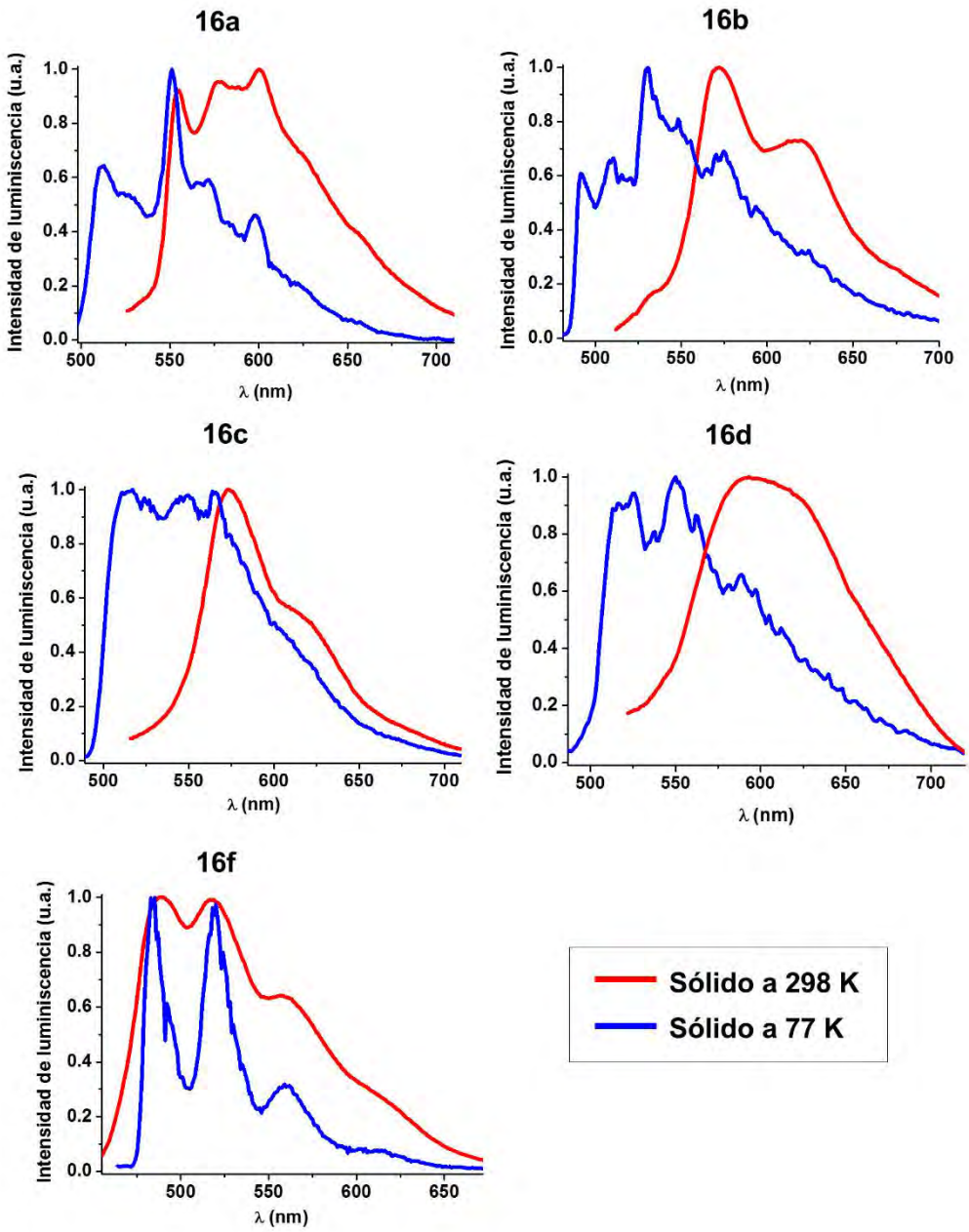

Figura 3.9. Espectros de emisión de los compuestos **16a-f** en estado sólido a 298 K y 77 K.

Tabla 3.4. Datos fotofísicos de los compuestos **16a-f** en estado sólido.

Compuesto	Tª (K)	λ_{em}/nm (λ_{ex}/nm)	τ(μs)
16a	298	554, 578, 600_{max}, 625_{sh}, 659_{sh} (340-430)	21 (83%), 60 (17%) (554); 29 (57%), 62 (43%) (600)
	77	512, 551_{max}, 572, 600, 624_{sh} (365-420)	288 (71%), 71 (29%) (512); 281 (56%), 34 (44%) (551)
16b	298	570_{max}, 620 (365-410)	101 (74%), 13 (26%)
	77	490, 510, 530_{max}, 575, 525 (365-425)	20 (58%), 108 (42%) (490); 128 (69%), 530 (31%) (530)
16c	298	573_{max}, 620 (340-430)	28
	77	515_{max}, 550, 566_{max}, 605_{sh} (365-420)	35 (77%), 94 (23%) (515); 114 (566)
16d	298	590_{max}, 622 (380-430)	117
	77	520, 550_{max}, 590 (340-470)	69 (67%), 271 (33%)
16f	298	488_{max}, 517, 558, 615 (320-430)	10.4 (488); 12 (49%), 41 (51%) (558)
	77	484_{max}, 520, 560, 612_{sh} (365-450)	69 (29%), 303 (71%) (484); 436 (520)

Como se aprecia en la Figura 3.9, el compuesto [Pt(bzq)(Hoxd)(C_6F_5)] **16f** (sólido microcristalino) muestra a temperatura ambiente una emisión estructurada probablemente debido a diferentes estados emisivos próximos en energía. Para comprobarlo, se ha registrado el espectro recogiendo la emisión a diferentes tiempos (Figura 3.10). A 298 K, el espectro muestra dos bandas estructuradas con máximos en 488 nm y 558 nm. El tiempo de vida de la banda a 488 nm es de 10.4 μs, mientras que la banda que sale a 558 nm muestra un tiempo de vida que se ajusta a dos componentes [12 (49 %), 41 μs (51 %)]. Como se observa en la Figura 3.10, la banda de tiempo de vida más corto (488 nm) desaparece a los 100 μs. Por comparación con otros compuestos de Pt(II) que contienen el fragmento Pt(bzq), esta banda se asigna a un estado excitado con carácter ^{3}IL'/^{3}ML'CT centrado en la unidad Pt(bzq). Además, esta banda es similar a la que se observa para este compuesto en CH_2Cl_2, asignada anteriormente a una transición ^{3}IL'/^{3}ML'CT. Sin embargo, la banda estructurada que aparece a baja energía (558 nm) que muestra un tiempo de vida más largo, se asigna tentativamente a una emisión excimérica probablemente con carácter de transferencia de carga *inter*molecular ^{3}L'LCT, bzq→Hoxd. Es interesante comentar que una transición *intra*molecular ^{3}L'LCT bzq→Hoxd centrada en el monómero es menos probable ya que, segú los cálculos realizados en fase gas (Tabla A3.5), esta transición se espera que ocurra a energías más altas (T_2, 461 nm).

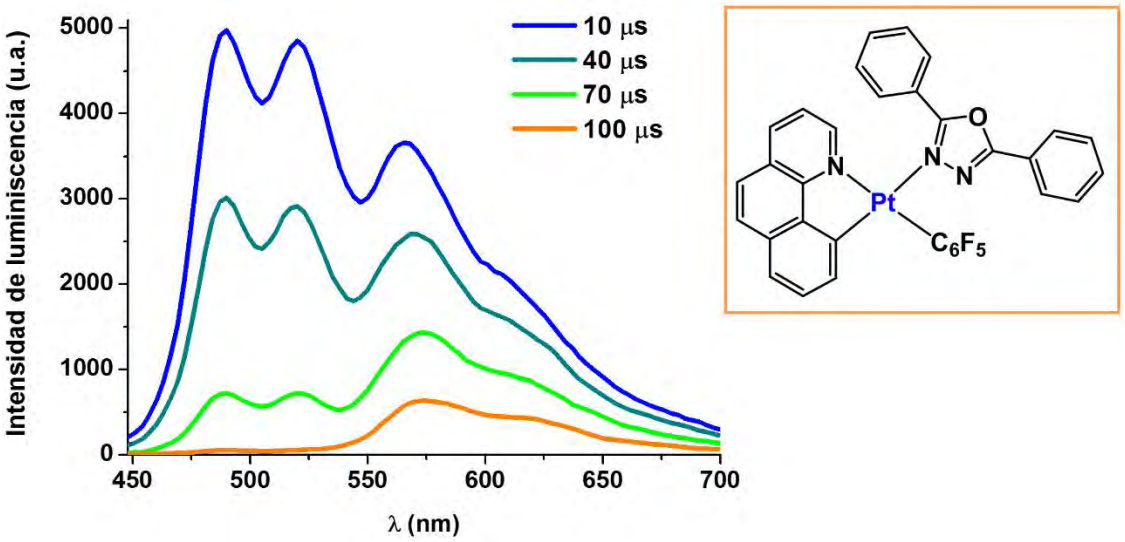

Figura 3.10. Espectros de emisión de **16f** en estado sólido (sólido microcristalino) a 298 K, registrando la emisión a diferentes tiempos.

3.2 Compuestos luminiscentes heterolépticos de Pt(IV) *fac*-[Pt(bzq)(C^N)(C_6F_5)Cl]

En la primera parte de este Capítulo (**Capítulo 3.1**) se describe la síntesis y caracterización de compuestos de Pt(II) [Pt(bzq)(HC^N)(C_6F_5)] **16a-g**, que contienen el ligando benzoquinoleína (bzq) ortometalado, un ligando heterocíclico HC^N coordinado a través del nitrógeno y un grupo pentafluorofenilo.

Debido a la fácil ortometalación del ligando HC^N, los derivados **16a-g** han resultado ser precursores adecuados para la síntesis de compuestos bis-(ciclometalados) de Pt(IV) de estequiometría [Pt(bzq)(C^N)(C_6F_5)Cl] **17**, que muestran propiedades luminiscentes. Los nuevos derivados de Pt(IV) tienen en común el ligando ortometalado bzq así como los grupos auxiliares Cl y C_6F_5, diferenciándose solamente en el segundo ligando ciclometalado C^N. Por lo tanto, un análisis exhaustivo de las propiedades ópticas de estos derivados nos permitirá determinar el rol del segundo ligando C^N en sus propiedades emisivas.

La segunda parte de este Capítulo (**Capítulo 3.2**) se centra en la síntesis, caracterización y estudio de las propiedades ópticas de derivados de Pt(IV) que contienen dos ligandos ciclometalados diferentes coordinados al centro metálico. Además, para una mejor comprensión de las propiedades ópticas de estos compuestos, los estudios de absorción y emisión están apoyados en cálculos teóricos DFT y TD-DFT.

3.2.1 Síntesis y caracterización

Los compuestos de Pt(IV) con dos ligandos ciclometalados diferentes *fac*-[Pt(bzq)(C^N)(C_6F_5)Cl] (C^N = thpy **17a**, pbt **17b**, pq **17c**, dfppy **17d**, pypy **17g**) se sintetizaron de manera directa mediante la reacción de oxidación de los precursores de Pt(II) [Pt(bzq)(HC^N)(C_6F_5)] (HC^N = Hthpy **16a**, Hpbt **16b**, Hpq **16c**, Hdfppy **16d**, Hpypy **16g**) a 0ºC (**17b-d**) o -30 ºC (**17a**, **17g**), utilizando como oxidante el derivado $PhICl_2$ (Esquema 3.2).

Los compuestos finales se obtuvieron con una alta pureza y con buenos rendimientos (70 - 81 %). Además, como se ha visto en los compuestos homolépticos de Pt(IV) [Pt(C^N)$_2$(C_6F_5)Cl] del **Capítulo 2**, estos derivados de Pt(IV) se obtienen de

manera estereoselectiva, con retención de la disposición meridional del fragmento Pt(C_6F_5)(C^N)$_{bzq}$N de los precursores para dar únicamente los compuestos *fac*-C,C,C en el par enantiomérico ΔΛ.

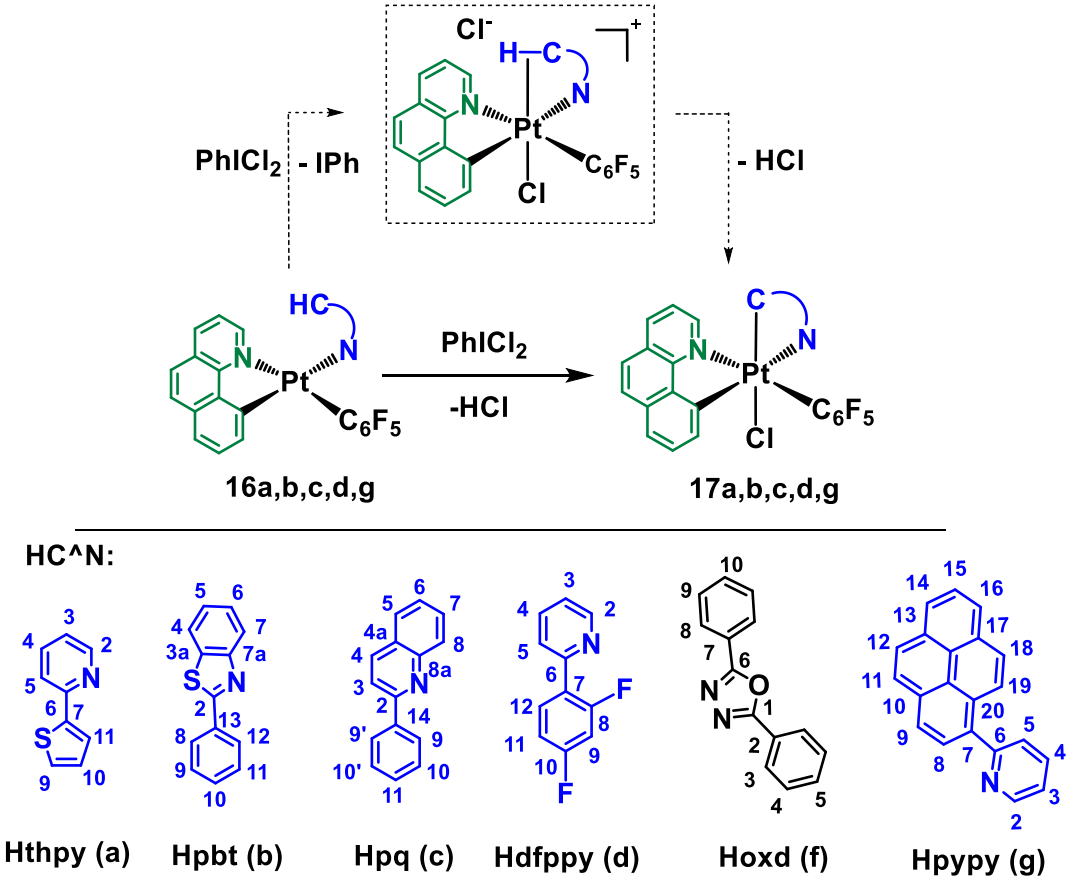

Esquema 3.2. Síntesis de los compuestos heterolépticos bis(ciclometalados) de Pt(IV): $PhICl_2$ (~ 1.3 equiv), CH_2Cl_2, 0ºC (**12b**,**c**,**d**); $PhICl_2$ (1.3 equiv), CH_2Cl_2/acetona, -30ºC, Na_2CO_3 (**17a**, **17g**).

El mecanismo propuesto para la formación de los compuestos heterolépticos es el mismo que se propuso para la formación de los derivados homolépticos de Pt(IV) del **Capítulo 2** y se muestra también en el Esquema 3.2. Se propone un ataque electrófilo del Cl^+ al centro metálico de Pt(II), que da lugar a un intermedio pentacoordinado de Pt(IV) estabilizado por una interacción agóstica entre el platino y el enlace C-H del ligando heterocíclico HC^N. Una transferencia del protón al anión Cl^- da lugar a la ortometalación del ligando heterocíclico con la formación de HCl. Para **17a** y **17g** se requiere, además de baja temperatura, la adición de una base (Na_2CO_3) para neutralizar el HCl generado en la reacción y así evitar el desplazamiento del ligando HC^N por el cloruro antes de que se produzca la ortometalación del mismo.[66]

Desafortunadamente, todos los intentos de ortometalación del ligando 2,5-difenil-1,3,4-oxadiazol (Hoxd) en el precursor de Pt(II) [Pt(bzq)(Hoxd)(C_6F_5)] **16f** para dar el

correspondiente compuesto de Pt(IV) *fac*-[Pt(bzq)(oxd)(C_6F_5)Cl] **17f** fueron infructuosos. Si la reacción se lleva a cabo sin añadir base al medio de reacción, se forma un producto insoluble que se identifica como el derivado [Pt(bzq)(C_6F_5)Cl(μ-Cl)]$_2$ **C**. Como se ha comentado en el **Capítulo 1**, este producto se puede obtener mediante la reacción de oxidación del compuesto [Pt(bzq)(C_6F_5)(acetona)][46] utilizando el oxidante $PhICl_2$. Por lo tanto, resulta lógico pensar que, cuando se lleva a cabo la reacción de oxidación del derivado [Pt(bzq)(Hoxd)(C_6F_5)] **16f** con $PhICl_2$, ocurre un ataque nucleóflilo del anión Cl^-, desplazando el ligando Hoxd e impidiendo así la activación C-H, necesaria para la subsiguiente ortometalación. Sin embargo, si la reacción de oxidación del precursor **16f** se lleva a cabo en CH_2Cl_2/acetona (1:1) (disolventes no-anhidros) a -50ºC en presencia de base (Na_2CO_3, exceso), se forma un nuevo derivado identificado como el compuesto dinulear de Pt(IV) [Pt(bzq)(C_6F_5)Cl(μ-OH)]$_2$ **18**, que contiene los grupos C_6F_5 en disposición *syn*, como se confirma por difracción de Rayos-X (Esquema 3.3). Además, este derivado también se obtiene de manera directa mediante la reacción del solvato [Pt(bzq)(C_6F_5)(acetona)][46] con $PhICl_2$ en las mismas condiciones de reacción. Hay que comentar que no existen muchos ejemplos en la bibliografía donde se utilicen ligandos con el fragmento 1,2,3-oxadiazol en reacciones de ortometalación.[145]

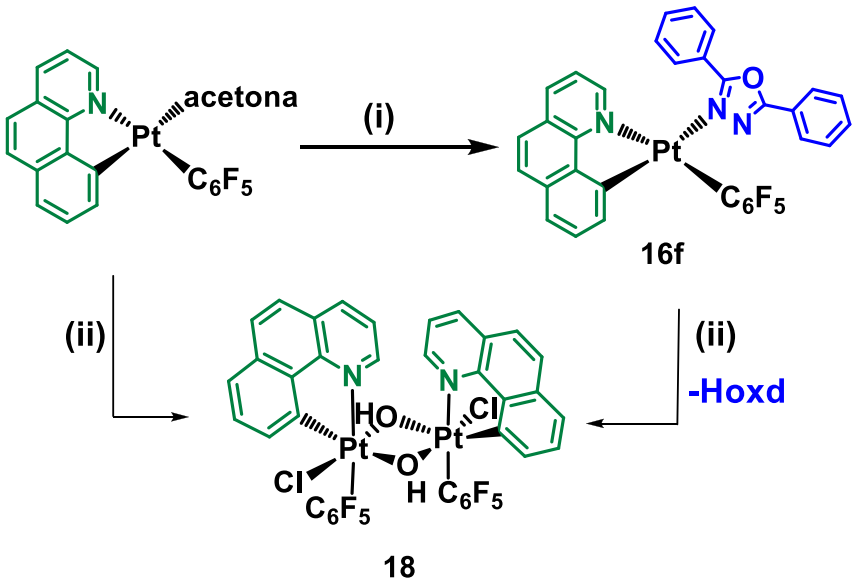

Esquema 3.3. Síntesis del derivado dinuclear [Pt(bzq)(C_6F_5)Cl(μ-OH)]$_2$ **18**. (i) Hoxd, CH_2Cl_2; (ii): $PhICl_2$, Na_2CO_3, -50º C, CH_2Cl_2/acetona (disolventes no-anhidros).

Los derivados *fac*-[Pt(bzq)(C^N)(C_6F_5)Cl] **17** y **18** se han caracterizado completamente mediante las técnicas habituales: RMN, difracción de Rayos X (**17c**, **17d**, **17g** y **18**), IR, espectrometría ESI (Electrospray Mass spectra) y análisis elemental.

Se ha llevado a cabo la asignación de todas las señales de ^{1}H y ^{13}C, y ^{19}F mediante los espectros de RMN monodimensionales [^{1}H, ^{13}C{H} y ^{19}F{^{1}H}] y bidimensionales (^{1}H-^{1}H COSY y TOCSY, ^{1}H-^{13}C HSQC y HMBC) (ver Experimental). Los espectros de RMN de ^{1}H y ^{13}C{^{1}H} de los derivados **17** muestran dos grupos de señales debido a la presencia de los dos ligandos ciclometalados diferentes. Así, un grupo de señales corresponde al ligando bzq (común en todos los compuestos), y el otro grupo al ligando C^N. Además, como se puede observar en las Figuras 3.11 y A3.5, el desplazamiento químico de las señales de ^{1}H y ^{13}C correspondientes al ligando bzq aparecen, en todos los derivados, a un desplazamiento prácticamente idéntico.

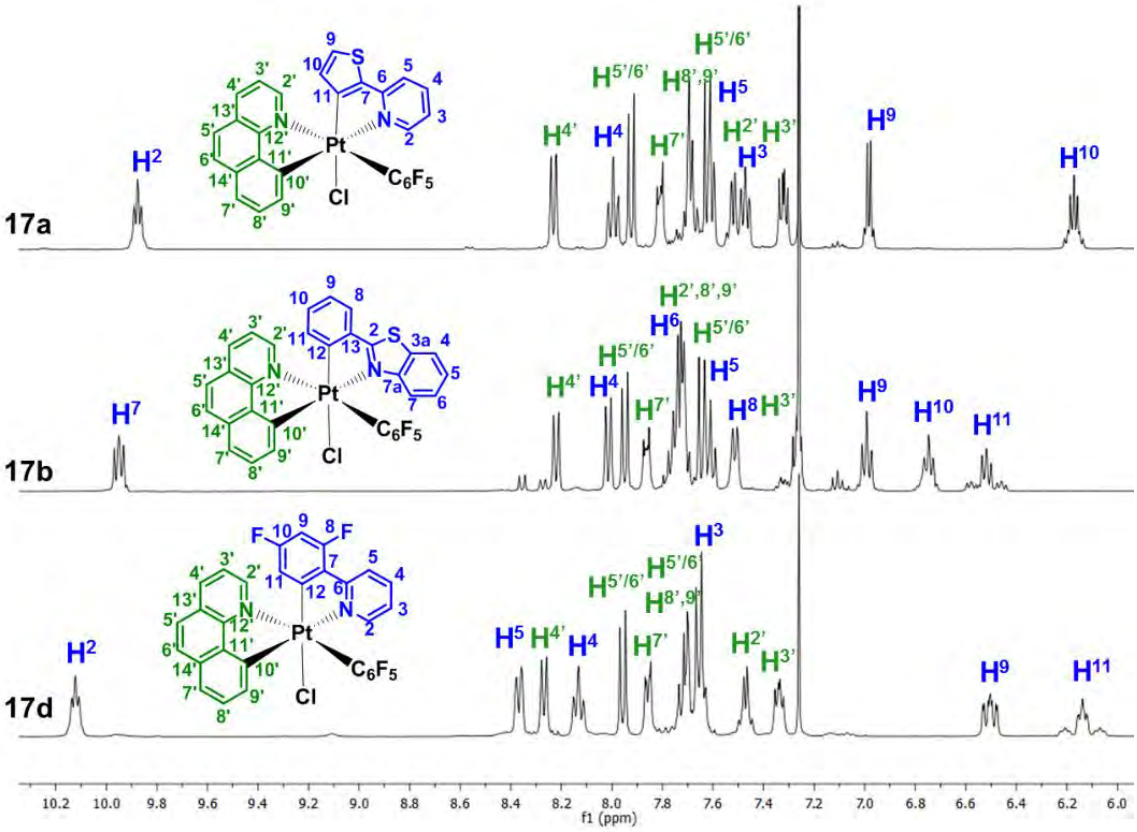

Figura 3.11. Espectros de RMN de ^{1}H de los derivados **17a**, **17b** y **17d** en $CDCl_3$.

La señal que corresponde al protón en posición *orto* del carbono metalado (**17a**: H^{10}, **17b,d**: H^{11}, **17c**: H^{12}) del segundo ligando heterocíclico C^N, aparece notablemente desplazada a la zona de baja frecuencia (δ = 6.14 – 6.52) en comparación con los precursores de Pt(II) y muestran satélites de platino con un valor de la constante de

acoplamiento $J_{Pt\text{-}H}$ ($^3J_{Pt\text{-}H}$ = 18 **17a**; 47 **17b,c**; 55 Hz **17d**), del mismo orden que en los derivados de Pt(IV) homolépticos comentados en el **Capítulo 2**. Estos protones en posición *orto* al carbono metalado y los que están en posición *orto* al átomo de nitrógeno (H^2 **17a**,**d**,**g**; H^7 **17b**; H^8 **17c**) muestran, en los espectros de RMN de ^1H, y en algunos casos en los de $^{13}C\{^1H\}$, acoplamientos adicionales $H_{C^\wedge N}\cdots F_{C6F5}$ o $C_{C^\wedge N}\cdots F_{C6F5}$ debido a la proximidad de estos protones a los átomos de flúor *orto* del grupo pentafluorofenilo (ver Experimental). Esto se ha comprobado mediante la técnica de difracción de Rayos X para los compuestos **17c,d,g**, encontrándose que el valor de las distancias $H\cdots F_{C6F5}$ (2.506 – 2.876 Å) es próximo o menor que el valor de la suma de los radios de van der Waals (2.67 Å). Además, se ha observado también en las estructuras de Rayos X, que la distancia del protón situado en posición *orto* al carbono metalado ($H^{9'}$) presenta interacción $H\cdots F_{C6F5}$ (2.490 – 2.545 Å). Sin embargo, debido a que en los espectros de RMN de ^1H la señal correspondiente a este protón aparece generalmente solapada con otras señales, sólo se observa experimentalmente el acoplamiento $H^{9'}\cdots oF$ en el espectro de ^1H del compuesto **17c** ($J_{H\text{-}oF}$ = 5.3 Hz).

El cambio en el estado de oxidación de Pt(II) a Pt(IV) se refleja también en los espectros de $^{19}F\{^1H\}$ de estos derivados **17**, ya que se observa una importante disminución del valor de la constante de acoplamiento entre el átomo de platino y los átomos de flúor en posición *orto* del grupo C_6F_5, en comparación con los precursores de Pt(II) **16** ($J_{Pt\text{-}oF}$ = 454 – 521 Hz **16a-d,g** *vs* 85 – 127 Hz **17a-d,g**). El complejo dinuclear $[Pt(bzq)(C_6F_5)Cl(\mu\text{-}OH)]_2$ **18** exhibe, en sus espectros de ^1H y $^{13}C\{^1H\}$, únicamente las señales debidas al ligando benzoquinolato, y su espectro de $^{19}F\{^1H\}$ muestra las cinco señales características del anillo rígido C_6F_5 (ver Experimental).

Con el fin de determinar la fotoestabilidad de los compuestos de Pt(IV), se irradiaron durante 4 horas disoluciones de ellos en CD_2Cl_2 utilizando una lámpara de mercurio de 125 W. La monitorización de estas irradiaciones por RMN reveló que estos derivados son estables en ese tiempo, al igual que se observó para los derivados homolépticos de Pt(IV) *fac*-$[Pt(C^\wedge N)_2(C_6F_5)Cl]$ **12**.

3.2.2 Estructuras cristalinas

Se han determinado las estructuras cristalinas de los compuestos *fac*-[Pt(bzq)(pbt)(C_6F_5)Cl] (**17c**·3.25CH_3COCH_3), *fac*-[Pt(bzq)(dfppy)(C_6F_5)Cl] (**17d**), *fac*-[Pt(bzq)(dfppy)(C_6F_5)Cl] (**17g**·0.5 THF) y [Pt(bzq)(C_6F_5)Cl(μ-OH)]$_2$ (**18**·2CH_3COCH_3) (Figuras 3.12 y 3.14; Tablas A3.6, A3.7). Los detalles de la obtención de los monocristales empleados para los correspondientes estudios se detallan en la parte Experimental.

Las moléculas de los compuestos de Pt(IV), **17c**·3.25CH_3COCH_3, **17d** y **17g**·0.5 THF, son quirales. Sin embargo, estos derivados cristalizan en grupos centrosimétricos (ver Experimental), por lo que podemos afirmar que en la celdilla unidad están presentes los dos enantiómeros Δ y Λ. En la Figura 3.12 están representados los enantiómeros Δ.

Las estructuras cristalinas de los tres compuestos muestran geometrías octaédricas y confirman la disposición *fac-C,C,C$_{Rf}$* de los dos carbonos metalados y el carbono *ipso* del grupo C_6F_5. Las distancias Pt-Cl [2.408(2)–2.466(2) Å] son similares a las de otros compuestos relacionados que contienen un átomo de Cl en posición *trans* a un carbono metalado.[66, 132] Las dos distancias Pt-$C_{metalado}$ [2.008(7)-2.038(4) Å] son ligeramente más cortas que las distancias Pt-C_{C6F5} [2.047(7)-2.076(10) Å], lo que está de acuerdo con una mayor influencia *trans* de los carbonos metalados. Por el mismo motivo, la distancia entre el platino y el nitrógeno N1 situado *trans* al grupo C_6F_5 [Pt-N1: 2.092(7)–2.121(3) Å] es más pequeña que la distancia entre el platino y el nitrógeno N2 situado *trans* al carbono metalado de la bzq [Pt-N2: 2.126(6)–2.230(7) Å]. Los valores de los ángulos C-Pt-N del ligando bzq [81.2(2)-81.51(13)º] y del segundo ligando ciclometalado (pq **17c**, dfppy **17d** y pypy **17g**) [79.5(3)-80.8(3)º] son similares a los que se encuentran en compuestos similares de Pt(IV) con ligandos ciclometalados.[65a, 67b, 70]

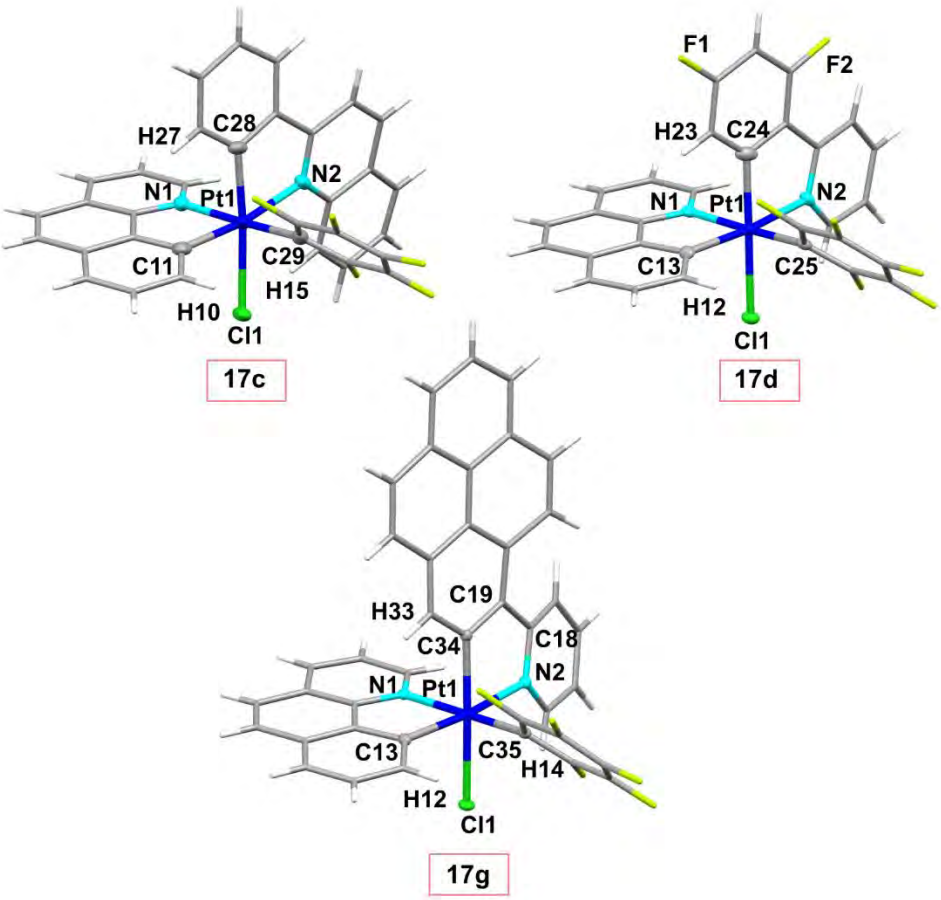

Figura 3.12. Estructuras de Rayos X de los compuestos **17c**, **17d** y **17g**.

El análisis de las interacciones intermoleculares en las estructuras cristalinas revela que las moléculas de los compuestos *fac*-[Pt(bzq)(pq)(C_6F_5)Cl] **17c** y *fac*-[Pt(bzq)(dfppy)(C_6F_5)Cl] **17d** están ordenadas formando cadenas con interacciones π···π entre los ligandos ciclometalados (bzq···bzq y pq···pq en **17c**, Figura 3.13; bzq···dfppy en **17d**, Figura A3.6a). Además, estas cadenas están reforzadas por interacciones secundarias $H_{C^\wedge N}$···Cl y $H_{C^\wedge N}$···F_{C6F5}. En el derivado *fac*-[Pt(bzq)(pypy)(C_6F_5)Cl] **17g** se observan interacciones π···π entre los ligandos pypy···bzq e interacciones adicionales C_{bzq}···H_{bzq} y ⊥(CH···π)$_{pypy}$, además de interacciones secundarias H_{bzq}···C_{C6F5}, H_{bzq}···F_{C6F5} (2.452 Å) y H_{pypy}···F_{C6F5} (Figura A3.6b).

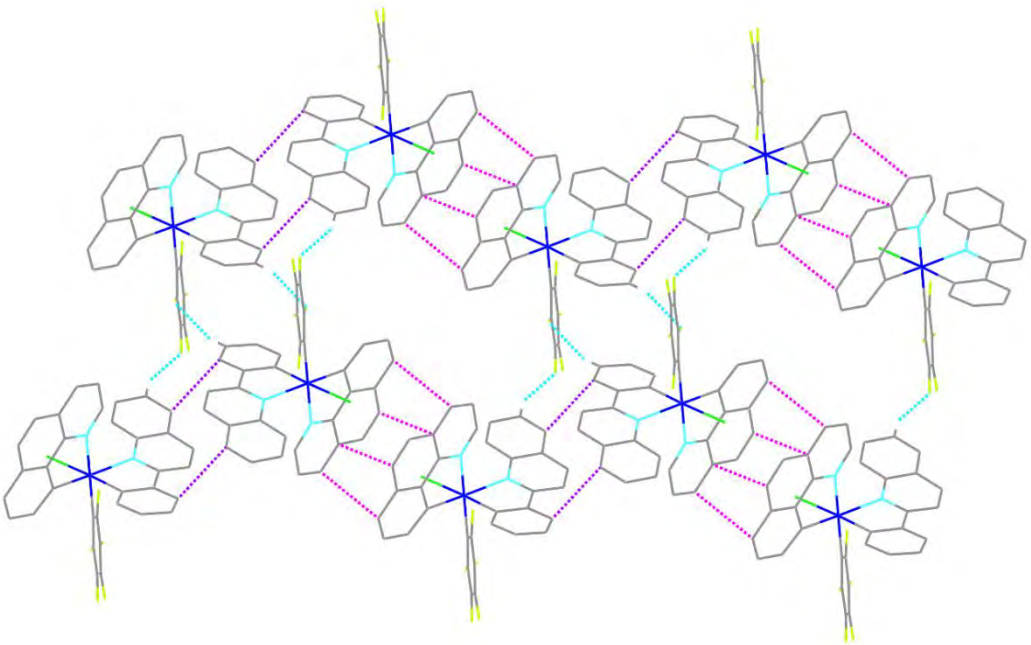

Figura 3.13. Estructura supramolecular del compuesto **17c** formada por cadenas soportadas por interacciones π···π no-lineales entre los ligandos pq (3.40 Å) (líneas moradas), interacciones π···π entre los ligandos bzq (3.29-3.31 Å) (líneas rosas) e interacciones secundarias H_{bzq}···F_{C6F5} (2.44 Å), H_{pq}···F_{C6F5} (2.61 Å) y Hpq···Cl (2.92 Å) (líneas azules).

La estructura cristalina del compuesto [Pt(bzq)(C_6F_5)Cl(μ-OH)]$_2$ (**18**·2CH_3COCH_3) (Tabla A3.7 y Experimental) confirma la estructura molecular de este compuesto (Figura 3.14) y revela la retención de la disposición meridional del ligando bzq y del C_6F_5 en ambos centros metálicos. A pesar de que los anillos pentafluorofenilo podrían situarse en disposición *syn* o *anti* y los átomos de cloro en *trans* o en *cis*, sólo se observa en su estructura la combinación *syn*$_{(C6F5)}$-*trans*$_{(Cl)}$. Como se puede ver en la Figura 3.14, la formación de este isómero podría estar favorecida por las interacciones π···π entre los anillos pentafluorofenilo situados en *syn*. Por otra parte, este isómero permite también la presencia de interacciones π···π entre los ligandos bzq, que sólo son posibles si los ligandos de Cl se sitúan en posición *trans*.

La separación Pt···Pt (3.315 Å) es similar a la que se encuentra en otros compuestos bimetálicos de Pt(IV) que contienen puentes OH.[146] Las distancias Pt-C_{bzq} [2.017(3), 2.019(3) Å] son similares a las que se observan en los compuestos **17c,d,g**. Los puentes OH son asimétricos con las distancias [Pt(1)-O(1) 2.180(2) Å y Pt(2)-O(2) 2.182(2) Å] claramente más largas que las separaciones [Pt(1)-O(2) 2.041(2) Å y Pt(2)-O(1) 2.037(2) Å], debido a la mayor influencia *trans* del carbono situado en posición *tran*s en relación a la del átomo de Cl.

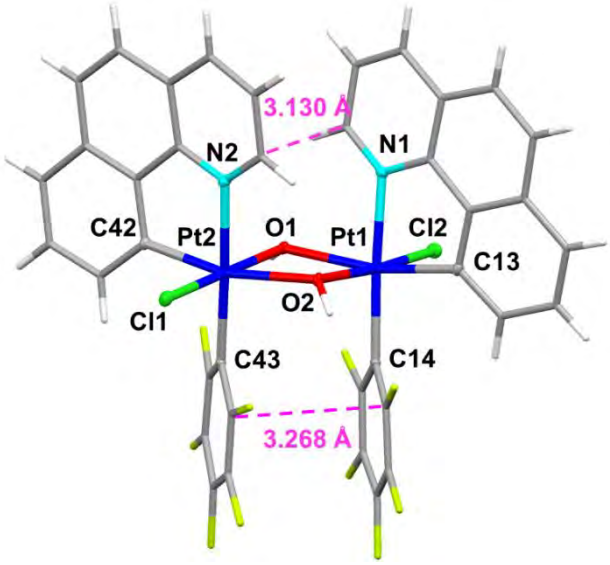

Figura 3.14. Estructura de Rayos X del compuesto $[Pt(bzq)(C_6F_5)Cl(\mu\text{-}OH)]_2$ (**18**)

El análisis de la red extendida de la estructura cristalina para este derivado revela la presencia de dímeros formados mediante interacciones π···π entre los ligandos ciclometalados bzq y contactos Hbzq···Cl. Además, los dímeros establecen contactos adicionales mediante interacciones OH···Cl (Ver Figura 3.15).

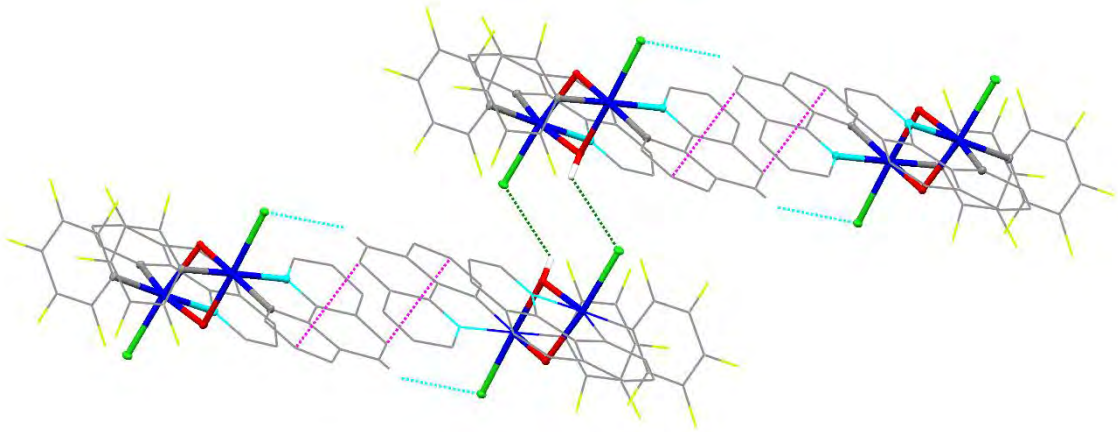

Figura 3.15. Estructura supramolecular del compuesto **18** mostrando dímeros con interacciones π···π entre los ligandos bzq (3.345 Å) (líneas rosas) y Hbzq···Cl (2.866 Å) (líneas azules), e interacciones HOH···Cl (2.889 Å) entre los dímeros (líneas verdes).

Aunque se han encontrado en la bibliografía estructuras cristalinas de compuestos de Pt(IV) con μ-OH,[146-147] ésta es, hasta donde nosotros sabemos, la primera estructura de Rayos-X de un compuesto dinuclear de Pt(IV) que contiene ligandos ciclometalados y grupos OH actuando como puente.

3.2.3 Propiedades ópticas

Se ha realizado un estudio de los espectros de absorción y emisión de todos los compuestos heterolépticos de Pt(IV) **17**. Además, se ha llevado a cabo un estudio de cálculos teóricos DFT y TD-DFT para los compuestos **17a**, **17c**, **17d** y **17g** con el objetivo de asignar con mayor precisión la naturaleza de las propiedades ópticas. En todos los compuestos se ha usado el método B3LYP, con la base LanL2DZ para el átomo de platino y la base 6-31G(d,p) para los átomos de los ligandos. En los compuestos **17c**, **17d** y **17g**, las distancias obtenidas por cálculos teóricos son comparables con las obtenidas por difracción de Rayos-X (Tabla A3.8). Los resultados de los cálculos teóricos están recogidos en las Tablas A3.8-A3.12.

3.2.3.1 Espectros de absorción y cálculos teóricos

Los espectros de absorción UV/Vis de todos los compuestos se han medido en disoluciones de CH_2Cl_2 5×10^{-5} M. Los datos de las absorciones están recogidos en la Tabla 3.5 mientras que los espectros de absorción están representados en la Figura 3.16. Los espectros calculados por cálculos teóricos TD-DFT en CH_2Cl_2 para los derivados **17a**, **17c**, **17d** y **17g** se ajustan bien a los espectros experimentales y están representados en la Figura A3.7, donde se muestra también la asignación de las transiciones calculadas en las bandas de menor energía (Tabla A3.9).

Tabla 3.5. Datos de absorción UV-visible de los compuestos de Pt(IV) *fac*-[Pt(bzq)(C^N)(C_6F_5)Cl] **17a-g** en CH_2Cl_2 5×10^{-5} M.

Compuesto	**λ_{abs}/nm (10^3 ε/M^{-1} cm^{-1})**
[Pt(bzq)(thpy)(C_6F_5)Cl] (**17a**)	231 (28.7), 245_{sh} (19), 286 (21.6), 343 (7.4), 357 (7.9), 378 (3.4)
[Pt(bzq)(pbt)(C_6F_5)Cl] (**17b**)	245 (34), 244_{sh} (35.3), 263 (25), 287 (28), 315 (20.5), 341 (17.3), 357 (13.6), 377 (4.3)
[Pt(bzq)(pq)(C_6F_5)Cl] (**17c**)	235 (52.5), 267 (38), 278 (47), 289_{sh} (26), 315 (12.2), 352 (13.3), 365 (13.7), 379 (5.6)
[Pt(bzq)(dfppy)(C_6F_5)Cl] (**17d**)	234 (41), 241_{sh} (35.4), 265 (20.5), 287 (22.6), 312 (13.4), 360 (3.5), 378 (4.3)
[Pt(bzq)(pypy)(C_6F_5)Cl] (**17g**)	220 (91.6), 246 (92.3), 287 (42.2), 321 (17.2), 365 (19.7), 393 (41.5), 417 (45)

Las bandas de baja energía (335-390 nm) que presentan los compuestos **17a-d** (Figura 3.16) aparecen desplazadas hacia el azul en relación a las de los precursores de Pt(II) **16a-d** (411-425 nm). Este hecho se manifiesta en el cambio en el color cuando los compuestos de Pt(II), de color amarillo, se oxidan a Pt(IV) formando compuestos de color amarillo muy pálido (**17d**) o blanco (**17a-c**) lo que, de acuerdo con los cálculos teóricos, se debe a la estabilización de los orbitales *d* centrados en el metal.

Debido a que estos compuestos contienen dos ligandos ciclometalados diferentes, se asignan las bandas de absorción de baja energía a excitaciones solapadas que se atribuyen fundamentalmente a transiciones a ^{1}IL/ ^{1}IL' (L' = bzq; L = ligando C^N), con algo de contribución de transferencia de carga ligando-ligando (^{1}LL'CT).

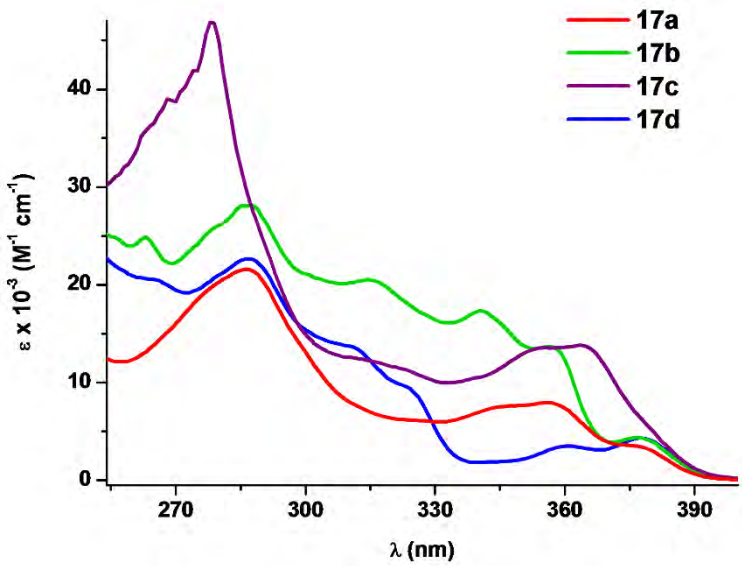

Figura 3.16. Espectros de absorción UV-Visible de (a) compuestos [Pt(bzq)(C^N)(C_6F_5)Cl] (C^N = thpy **17a**, pbt **17b**, pq **17c**, dfppy **17d**).

Con el fin de asignar las bandas de baja energía de estos compuestos **17a-d** con más detalle, se han comparado los espectros de absorción de [Pt(bzq)(thpy)(C_6F_5)Cl] **17a**, [Pt(bzq)(pbt)(C_6F_5)Cl] **17b**, [Pt(bzq)(pq)(C_6F_5)Cl] **17c** y [Pt(bzq)(dfppy)(C_6F_5)Cl] **17d** con los derivados homolépticos de Pt(IV) estudiados en el **Capítulo 2**, [Pt(thpy)$_2$(C_6F_5)Cl] **12a**, [Pt(pbt)$_2$(C_6F_5)Cl] **12b**, [Pt(pq)$_2$(C_6F_5)Cl] **12c**, [Pt(dfppy)$_2$(C_6F_5)Cl] **12d**. De esta manera, podemos identificar y diferenciar las transiciones centradas en la bzq y las que se deben al segundo ligando ciclometalado C^N. Además, también hemos empleado la información que proporcionan los cálculos teóricos, que confirman la muy escasa contribución del platino en los orbitales frontera de estos compuestos. A modo de esquema, se han representado los orbitales calculados que

participan en las transiciones singlete de baja energía para los compuestos **17a**, **17c** y **17d**. La transición con mayor fuerza del oscilador está representada mediante una flecha más gruesa (Figura 3.17).

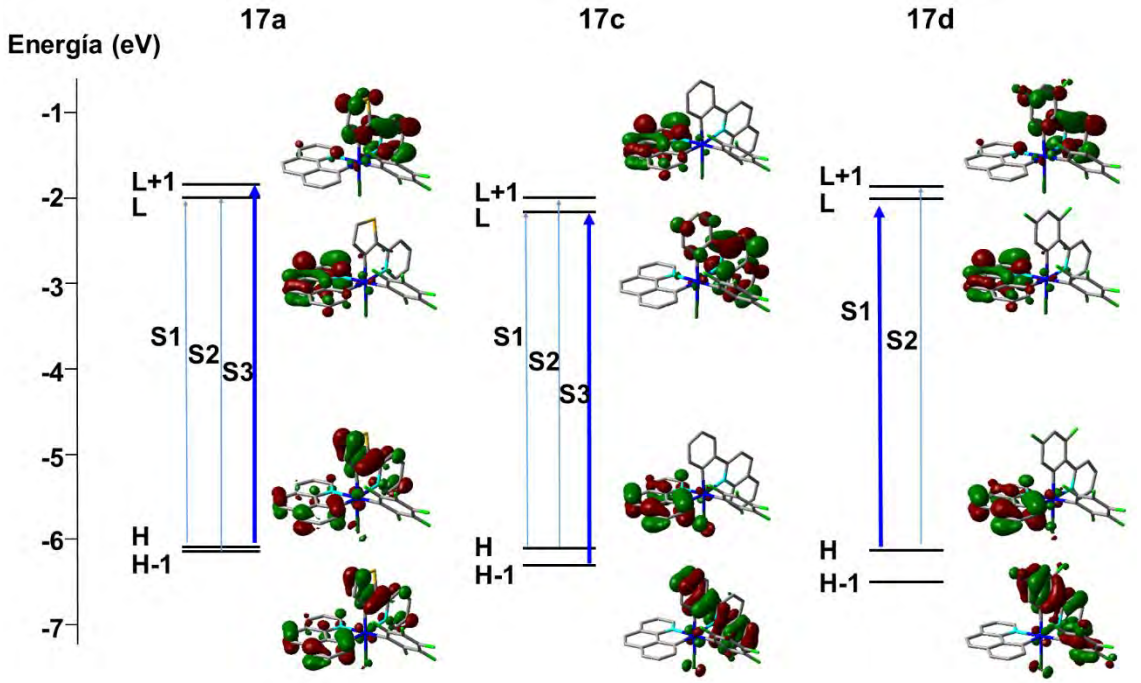

Figura 3.17. Diagrama esquemático de energía de los orbitales frontera y excitaciones seleccionadas calculadas por cálculos teóricos para **17a**, **17c**, **17d**.

Como se aprecia en la Figura 3.16, los compuestos **17a-c** presentan un perfil complejo formado por una banda estructurada intensa (**17a, 17b**: 357, **17c**: 365 nm) similar a la observada en **12a-c**, que se asigna principalmente a una transición (^{1}IL) centrada en el segundo ligando ciclometalado (C^N). Además, presentan otra banda menos intensa (hombro en **17c**) a más baja energía (377-379 nm), que no se observa en los espectros de los correspondientes derivados homolépticos *fac*-[Pt(C^N)$_2$(C_6F_5)Cl] **12a-c**, que se atribuye a una transición centrada en la bzq (^{1}IL'), con algo de contribución ^{1}L'LCT.

Así, para el derivado **17a** con el ligando thpy como segundo ligando ciclometalado, los orbitales vacíos LUMO y LUMO+1 están centrados en la bzq y en ligando thpy respectivamente, mientras que los orbitales ocupados HOMO y HOMO-1 están distribuidos entre los dos ligandos (Figura 3.17), lo que origina transiciones más deslocalizadas. En este derivado, las primeras transiciones calculadas S_{1-3} tienen una fuerza del oscilador media, siendo algo más intensa la S_3, y corresponden a excitaciones

HOMO→LUMO (S_1), HOMO→LUMO +1 (S_3) y HOMO-1→LUMO (S_2) asignadas a transiciones ^{1}IL'/^{1}LL'CT ($S_{1,2}$) y IL/L'LCT (S_3) (L' = bzq, L= thpy). Para el derivado [Pt(bzq)(pq)C_6F_5)Cl] **17c**, la transición calculada más intensa es la S_3 y corresponde a una excitación HOMO-1→LUMO centrada en el ligando pq (Figura 3.17). Además, en este derivado la transición S_2 tiene menor frecuencia del oscilador que la S_3 y corresponde a una transición HOMO→LUMO+1 localizada en el ligando bzq, mientras que la transición S_1 (HOMO→LUMO), con una fuerza del oscilador prácticamente nula, es una transición de transferencia de carga bzq→pq.

El perfil de absorción del derivado con el ligando dfppy *fac*-[Pt(bzq)(dfppy)(C_6F_5)Cl] **17d** es similar al del complejo homoléptico [Pt(bzq)$_2$(C_6F_5)Cl] **12e**. Su espectro de absorción en CH_2Cl_2 presenta dos bandas a 360 y 378 nm, que coinciden con las bandas de absorción que muestra el derivado homoléptico [Pt(bzq)$_2$(C_6F_5)Cl] **12e** en el mismo disolvente. Por lo tanto, estas bandas se asignan a transiciones ^{1}IL' localizadas en el ligando bzq, siendo insignificante la contribución del ligando dfppy en estas transiciones. Los cálculos teóricos realizados para este derivado **17d** revelan que la transición calculada de menor energía S_1 corresponde a una excitación HOMO→LUMO (353 nm) localizada en la bzq. El ligando dfppy contribuye en la transición S_2 de más alta energía (332 nm), asignada a una excitación HOMO→LUMO+1, con menor fuerza del oscilador y carácter de transferencia de carga L'LCT bzq→dfppy.

El espectro de absorción del derivado con el ligando pypy *fac*-[Pt(bzq)(pypy)(C_6F_5)Cl] **17g** se representa en la Figura 3.18a. Este derivado muestra, en la zona de baja energía, una banda de absorción intensa y estructurada con dos máximos en 393 y 417 nm, que se atribuyen a transiciones ^{1}IL centradas en el ligando pypy. Los cálculos teóricos revelan que la transición calculada S_1 (425 nm) corresponde a una excitación HOMO→LUMO centrada en el ligando pypy (Figura 3.18b). Además, la comparación del espectro de absorción de este derivado **17g** con el de su precursor de Pt(II), [Pt(bzq)(Hpypy)(C_6F_5)] **16g** (línea discontinua en la Figura 3.8a), nos revela que la banda de absorción del derivado de Pt(IV) está notablemente desplazada hacia el rojo. Este batocromismo se ha observado previamente en otros compuestos de Pt(II)[148] e Ir(III)[144] con ligandos ciclometalados que contienen la unidad pireno y se atribuye a la ciclometalación del ligando pirenilpireno, ya que la formación del enlace Pt-C_{pypy} incrementa la planaridad y la deslocalización π del ligando pireno.

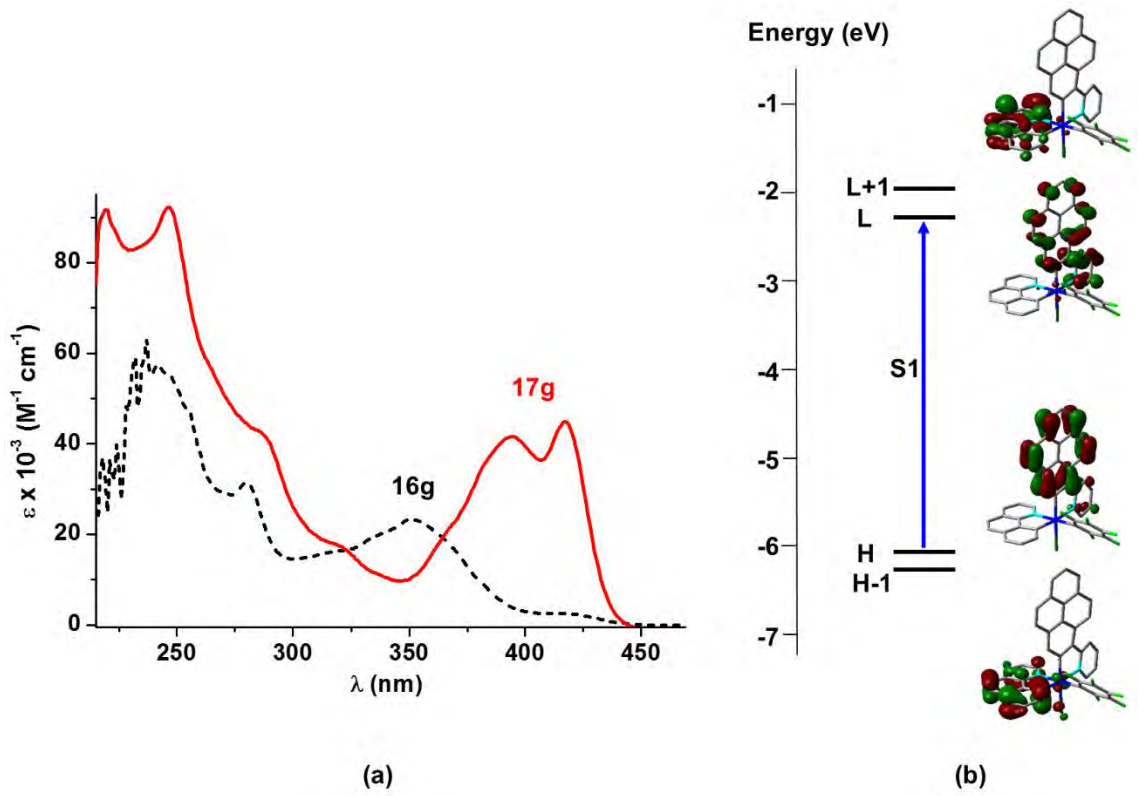

Figura 3.18. (a) Espectro de absorción UV-Vis del derivado [Pt(bzq)(pypy)(C_6F_5)(Cl)] **17g** (línea roja) y del precursor [Pt(bzq)(Hpypy)(C_6F_5)] **16g** (línea negra discontínua). (b) Diagrama esquemático de energía de los orbitales frontera y excitaciones seleccionadas calculadas por cálculos teóricos para **17g**.

3.2.3.2 Espectros de emisión y cálculos teóricos

Se han medido los espectros de emisión de los derivados *fac*-[Pt(bzq)(C^N)(C_6F_5)Cl] **17** en disoluciones de CH_2Cl_2 5 × 10^{-5} M y en estado sólido a temperatura ambiente y a baja temperatura (77 K) así como en films de los compuestos en PS. Los datos en disolución para los derivados **17a-d** se recogen en la Tabla 3.6 y los del estado sólido en la Tabla 3.7, mientras que las emisiones del derivado **17g** se muestran en la Tabla 3.8.

*Derivados **17a-d** – Disolución y PS*

Los derivados **17a-d** muestran bandas de emisión estructuradas en films de PS y en disoluciones desoxigenadas de CH_2Cl_2 5 × 10^{-5} M (a temperatura ambiente o baja temperatura), con tiempos de vida en el rango de los µs (Tabla 3.6 y Figuras 3.19, 3.20 y A3.8). El valor de los tiempos de vida media en disolución es significativamente mayor

cuando la medida se realiza a baja temperatura (1.3 – 3.2 µs CH_2Cl_2 298 K *vs* 210 - 4313 µs CH_2Cl_2 77 K), debido a una disminución de los procesos no radiativos.

Tabla 3.6. Datos fotofísicos de los compuestos **17a-g** en CH_2Cl_2 5×10^{-5} M y PS (10 % **17b,c**; 5% **17a,d,g**).

Compuesto		T[a] (K)	λ_{em}/nm (λ_{ex}/nm)	ϕ (%)[a]	τ (µs)
17a	CH_2Cl_2	298	522, 550_{max}, 595_{sh} (340-380)	-	1.5
		77	506_{max}, 548, 597 (365-375)	-	499
	PS (5%)	298	512, 550_{max}, 592_{sh} (365-380)	11	48 (67%), 171 (33%) (550)
17b	CH_2Cl_2	298	497, 533_{max}, 574, 630_{sh} (350-365)	-	3.2
		77	493_{max}, 531_{max}, 575_{sh}, 622 (340-375)	-	210
	PS	298	498, 533_{max}, 574_{sh} (365-380)	22	44.2
17c	CH_2Cl_2	298	512_{max}, 545, 589_{sh} (325-395)	-	2.2
		77	499_{max}, 538, 580 (365)	-	417
	PS	298	508, 542_{max}, 585 (325-395)	85	61
17d	CH_2Cl_2	298	492, 526_{max}, 568_{sh} (365-380)	-	1.3
		77	483, 520_{max}, 560, 611_{sh} (355-375)	-	4313
	PS (5%)	298	490, 528_{max}, 566, 615_{sh} (365-380)	<1	197

[a] Rendimiento cuántico medido con esfera integradora.

Como se aprecia en la Figura 3.19, las emisiones en CH_2Cl_2 experimentan un ligero desplazamiento hacia energías más altas (más notable en **17a** y **17c**) y una mayor estructuración en vidrio congelado a 77 K, con respecto a temperatura ambiente. Estas características son coherentes con un estado excitado de carácter fundamentalmente intraligando ^{3}IL en el que la contribución ^{3}MLCT es prácticamente nula.[57-58, 59b, 60-62, 65a, 66-67, 95, 135a] En el derivado [Pt(bzq)(thpy)(C_6F_5)Cl] **17a** se observa un mayor rigidocromismo (522 → 506 nm, 16 nm) que en el resto de los derivados, lo que sugiere una cierta contribución adicional de transferencia de carga ligando-ligando ^{3}LLCT, que también se apoya mediante cálculos teóricos.

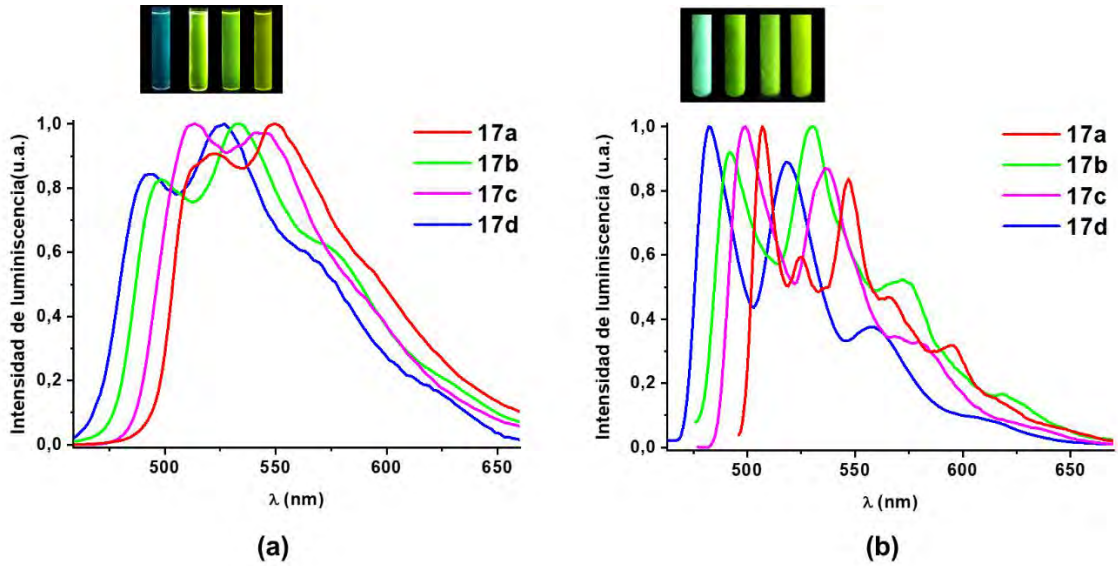

Figura 3.19. Espectros normalizados de emisión en (a) CH_2Cl_2 5 × 10^{-5} M a 298 K (b) CH_2Cl_2 5 × 10^{-5} M a 77 K de los compuestos **17a-d**.

Los máximos de emisión de los derivados *fac*-[Pt(bzq)(C^N)(C_6F_5)Cl] (C^N = thpy **17a**, pbt **17b**, pq **17c**, dfppy **17d**) en CH_2Cl_2 a 298 K siguen el orden 492 **17d** < 497 **17b** < 512 **17c** < 522 nm **17a**. Con fines comparativos, se ha calculado por TD-DFT la primera transición triplete (T_1) para los ligandos heterocíclicos libres (thpy **a**, pbt **b**, pq **c**, dfppy **d**, bzq) a partir de la geometría optimizada S_0 (Tabla A3.11), observándose la misma tendencia que en los derivados **17a-d**: 392 dffpy **d** < 444 bzq < 449 pbt **b** < 460 pq **c** < 466 thpy **a**. De acuerdo con ello, parece razonable sugerir que, de los dos ligandos ciclometalados (bzq y C^N) la emisión se localiza fundamentalmente en el ligando que presenta menor energía de la transición π···π*. Esta hipótesis se ve apoyada al comparar los espectros de emisión de estos derivados heterolépticos [Pt(bzq)(C^N)(C_6F_5)Cl] **17a-d** con los derivados homolépticos [Pt(C^N)$_2$(C_6F_5)Cl] **12** estudiados en el **Capítulo 2**.

Así, los espectros de emisión de los derivados [Pt(bzq)(C^N)(C_6F_5)Cl] (C^N = thpy **17a**, pbt **17b**, pq **17c**) son similares a los correspondientes derivados homolépticos [Pt(C^N)$_2$(C_6F_5)Cl] (C^N = thpy **12a**, pbt **12b**, pq **12c**) lo que indica que, en estos derivados (**17a-c**), la emisión se centra en el segundo ligando ciclometalado C^N, siendo una transición fundamentalmente ^{3}IL.

En la misma línea, la emisión en CH_2Cl_2 a 77 K del derivado [Pt(bzq)(dfppy)(C_6F_5)Cl] **17d** (483 nm) aparece notablemente desplazada hacia el rojo en relación a la emisión que muestra el derivado homoléptico [Pt(dfppy)$_2$(C_6F_5)Cl] **12d** (436 nm) en las mismas condiciones. En este caso, la emisión de **17d** es similar a la que

presenta el derivado homoléptico con el ligando bzq, [Pt(bzq)$_2$(C$_6$F$_5$)Cl] **12e** (487 nm) (Figura 3.20), lo que indica que, para la combinación bzq/dfppy (en **17d**), la emisión intraligando está centrada en la bzq (^{3}IL', L' = bzq). El tiempo de vida en CH_2Cl_2 (77 K) para **17d** es mucho más largo (4313 μs) que los valores encontrados en el resto de derivados (Tabla 3.6), lo que está de acuerdo con la mayor deslocalización electrónica que presenta el ligando bzq. También hay que destacar que, mientras que el derivado homoléptico *fac*-[Pt(bzq)$_2$(C$_6$F$_5$)Cl] **12e** no es emisivo en disolución a temperatura ambiente, el derivado heteroléptico [Pt(bzq)(dfppy)(C$_6$F$_5$)Cl] **17d** muestra una emisión débil centrada en 492 nm.

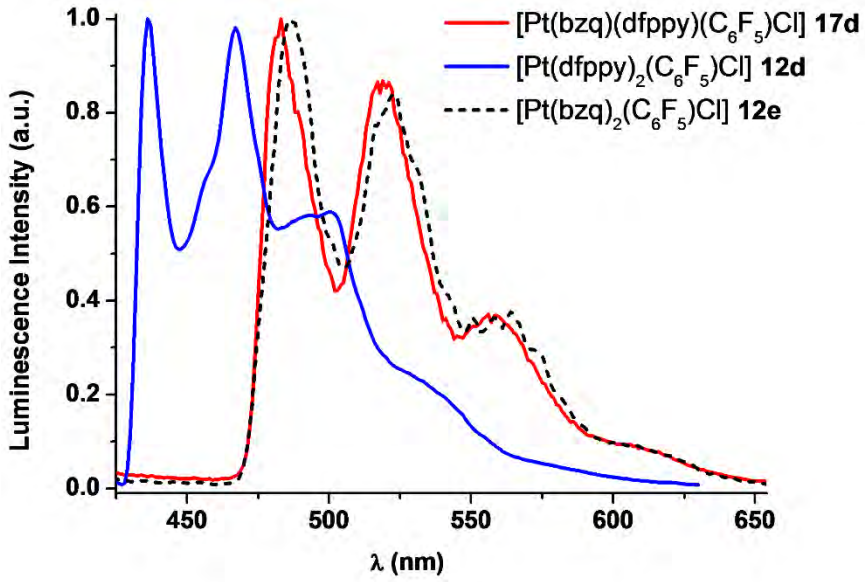

Figura 3.20. Comparación de los espectros de emisión de los derivados **17d**, **12d** y **12e** en CH_2Cl_2 a 77 K.

Los rendimientos cuánticos de **17a-d** medidos en PS (Tabla 3.6) revelan que mientras el derivado con el ligando dfppy muestra un valor del rendimiento cuántico bajo **17d** (<1 %), los valores son relativamente altos para el resto de los derivados (11 % **17a**, 22 % **17b**, 85 % **17c**). Es destacable que los rendimientos cuánticos son más altos que los de los derivados homolépticos *fac*-[Pt(C^N)$_2$(C$_6$F$_5$)Cl] (C^N = thpy 8.2 %, pbt 3.1 %, pq 18.2 %), lo que confirma que la coordinación de dos ligandos ciclometalados diferentes al centro metálico aumenta la eficiencia de las emisiones.[141a, 149]

*Derivados **17a-d** – Estado sólido*

Aunque los compuestos **17a-d** no muestran emisión en estado sólido a temperatura ambiente, todos los derivados presentan una emisión intensa a 77 K (Tabla 3.7 y Figura 3.21).

Tabla 3.7. Datos fotofísicos de los compuestos **17a-d** en estado sólido.

Compuesto	T[a] (K)	λ_{em}/nm (λ_{ex}/nm)	τ/μs
17a	298	-	-
	77	514, 533, 554_{max}, 573, 600, 625_{sh} (365-390)	74 (58%), 178 (42%) (514); 123 (81%), 322 (65%) (554)
17b	298	-	-
	77	495, 535_{max}, 580 (350-380)	95
17c	298	-	-
	77	526_{max}, 565_{max}, 611_{sh} (365-395)	186
17d	298	-	-
	77	495_{max}, 435, 580_{sh} (365-390)	2220

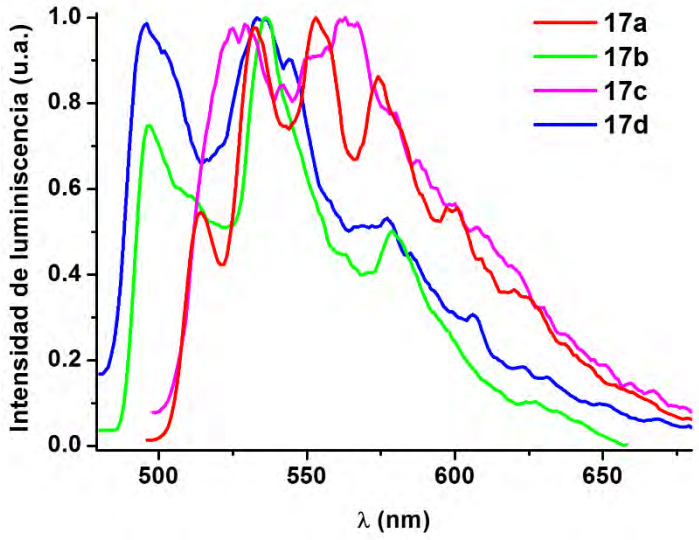

Figura 3.21. Espectros normalizados de emisión en estado sólido a 77 K de los compuestos **17a-d**.

En los derivados **17b-d**, los espectros de emisión en estado sólido a 77 K son similares a los que se observan en disolución y en PS sugiriendo, por tanto, un estado excitado de carácter similar centrado en el segundo ligando ciclometalado para **17b,c** y en la bzq para **17d** [^{3}IL (L = pbt **17b**, pq **17c**); ^{3}IL' (L' = bzq **17d**)]. Para estos compuestos, los tiempos de vida media ajustan a una componente y los valores son más

cortos (**17b**: 95, **17c**: 186, **17d**: 2220 µs) que los que se observan en CH_2Cl_2 a 77 K (**17b**: 210, **17c**: 417, **17d**: 4313 µs). Este hecho tiene precedentes y puede atribuirse a que la presencia de interacciones intermoleculares, más favorecidas en estado sólido, facilitan la desactivación por fácil aniquilación triplete-triplete.[139]

Sin embargo, el compuesto [Pt(bzq)(thpy)(C_6F_5)Cl] **17a** muestra en estado sólido a 77 K (Figura 3.21) un perfil de emisión más complejo, con un tiempo de vida que ajusta a dos componentes. Esto sugiere la presencia de dos emisiones cercanas, atribuidas probablemente a transiciones ^{3}IL'/^{3}IL/^{3}LLCT, como se confirma por cálculos teóricos.

*Derivados **17a-d** – Cálculos teóricos*

Para confirmar la naturaleza del estado excitado de estos compuestos de Pt(IV) heterolépticos, se han analizado las propiedades de los primeros estados excitados triplete T_1-T_5, calculados por TD-DFT a partir de la geometría optimizada en el estado fundamental (S_0). Los resultados se recogen en la Tabla A3.12 y se esquematizan en la Figura 3.22.

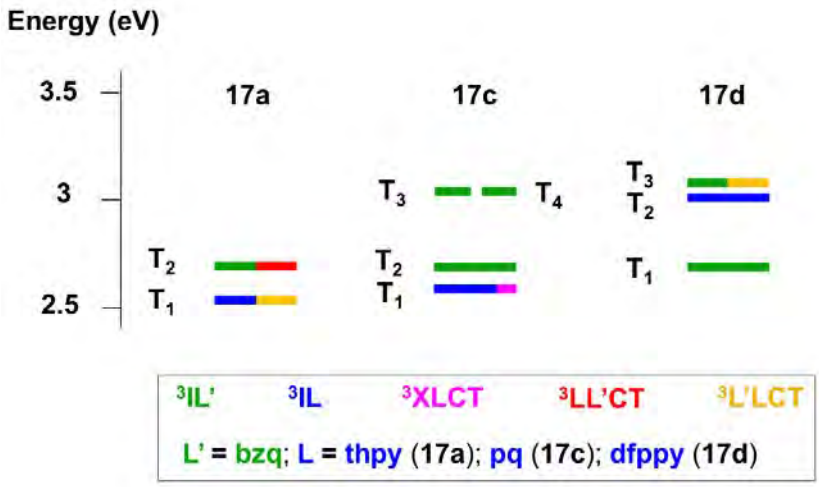

Figura 3.22. Representación esquemática de la contribución de los grupos ciclometalados en los primeros tripletes para **17a**, **17c** y **17d**.

En coherencia con los espectros observados, el primer estado excitado calculado triplete T_1 (459 nm) para el derivado [Pt(bzq)(dfppy)(C_6F_5)Cl] **17d**, tiene un carácter intraligando centrado en la bzq (^{3}IL'). El T_2 está centrado en el ligando dfppy, pero está muy separado en energía del T_1 (0.33 eV), por lo que se descarta su participación en la emisión.

Sin embargo, para el compuesto [Pt(bzq)(thpy)(C_6F_5)Cl] **17a**, el estudio del primer triplete calculado (485.4 nm) revela una mezcla de contribución intraligando centrada en el thpy (^{3}IL) y ligando (bzq) → ligando (thpy). El segundo triplete T_2 tiene también una naturaleza compleja, formado principalmente por transiciones ^{3}IL' (L' = bzq) y de transferencia de carga ligando (thpy) → ligando (bzq) (^{3}LL'CT). El primer triplete calculado (T_1 = 476.6 nm) para [Pt(bzq)(pq)(C_6F_5)Cl] **17c** está formado mayoritariamente por una transición centrada en el ligando pq (^{3}IL), con una pequeña contribución ligando-ligando (Cl→pq, ^{3}XLCT), ya que el átomo de Cl contribuye con un 20% en el orbital HOMO-4 de este derivado. Además, es importante señalar que el triplete T_2 se encuentra energéticamente cerca del T_1 (0.08 eV) y está compuesto principalmente por transiciones $\pi\cdots\pi^*$ centradas en la bzq.

Se ha realizado también la optimización del primer estado triplete T_1 para **17a**,**c**,**d**. En la Figura A3.9 se representa la composición de los orbitales SOMO y SOMO-1 y la Figura 3.23 muestra la densidad de spin para estos derivados. Podemos observar que, con excepción del derivado **17c**, los resultados son similares a los comentados anteriormente, ya que para el derivado **17a** la densidad de espín (o los orbitales SOMO y SOMO-1) se centra en el ligando ciclometalado thpy, mientras que en el derivado **17d** la densidad electrónica está localizada en la bzq.

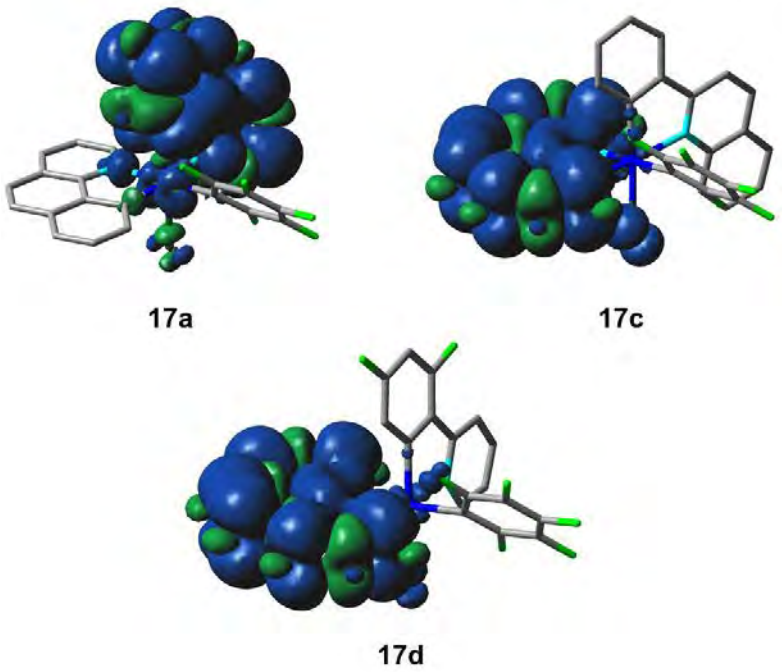

Figura 3.23. Distribución de la densidad de espín para los compuestos **17a**, **17c** y **17d** en fase gas.

Es importante comentar que los resultados obtenidos en estos cálculos teóricos para **17a-c** ponen de manifiesto que estos derivados presentan estados excitados tripletes cercanos con configuraciones complejas, por lo que pequeños cambios en el entorno puede provocar que la emisión sea asignada a transiciones con mezcla de contribuciones ^{3}IL'/^{3}IL/^{3}LLCT.

Derivado [Pt(bzq)(pypy)(C_6F_5)Cl] ***17g*** *– Emisión y cálculos teóricos*

Los datos de emisión en disolución, PS y estado sólido para el derivado con el ligando ciclometalado pypy **17g**, se recogen en la Tabla 3.8 y los espectros de emisión se muestran en las Figuras 3.24 y 3.25. Los resultados obtenidos por cálculos teóricos (DFT y TD-DFT) se recogen en las Tablas A3.8-3.12 y en las Figuras 3.24 y 3.25.

Tabla 3.8. Datos fotofísicos del compuesto **17g**.

	T[a] (K)	**λ_{em}/nm (λ_{ex}/nm)**	**Φ (%)[a]**	**τ/μs**
CH_2Cl_2 (5×10^{-5} M)	298	444_{max}, 465_{sh}	-	0.08
	77	444_{max}, 468, 683	-	75.9 (683)
PS (5 %)	298	476_{max}, 514_{sh}, 684	[b]	0.5 (82%), 6 (18%) (476)
Sólido	298	480_{max}, 512_{sh} (327-422)	0.35 (480); 0.44 (512)	298
	77	466_{max}, 486, 508_{sh} (365-420)	-	77

[a] Rendimiento cuántico medido con esfera integradora; [b] Señal demasiado débil

Este compuesto solo presenta emisión desde el estado triplete (fosforescencia) en medios rígidos [disolución a 77 K y en PS (5 %)]. En el espectro de emisión en disolución de CH_2Cl_2 a temperatura ambiente se observa una banda a 444 nm con un tiempo de vida media corto de 80 ns (Figura 3.24a). Su espectro de excitación coincide con la banda de absorción asignada previamente a una transición intraligando centrada en el ligando pireno, lo que indica que se trata de una emisión de fluorescencia localizada en el ligando pypy ($^1\pi\pi^*$). Esta banda de fluorescencia aparece desplazada hacia menores energías con respecto a la banda de fluorescencia del derivado de Pt(II) [Pt(bzq)(Hpypy)(C_6F_5)] **16g** (393 nm), que tiene el Hpypy coordinado a través del nitrógeno. Por lo tanto, la ciclometalación del ligando provoca el desplazamiento batocrómico de la banda de fluorescencia, como se ha observado para otros derivados.[57] A 77 K, además de la emisión de fluorescencia $^1\pi\cdots\pi^*_{pypy}$ (444 nm) aparece, con una menor contribución, una banda a

683 nm con un tiempo de vida largo (76 µs) que se atribuye, con apoyo de cálculos teóricos (Figura 3.24b), a fosforescencia centrada en el ligando pypy (Figura 3.24a).

Este derivado muestra, en films de PS (5%), una emisión dual 476/684 nm (Figura 3.24a). La banda de baja energía (684 nm) se atribuye, como en CH_2Cl_2 a 77 K, a fosforescencia localizada en el cromóforo pirenilpireno ($^3\pi\pi^*_{pypy}$). Sin embargo, la banda de alta energía (476 nm) está desplazada hacia el rojo con respecto a la banda de fluorescencia $^1\pi\pi^*_{pypy}$ observada en disolución (444 nm) y, además, el tiempo de vida medido en el máximo de esta banda es relativamente largo [(0.5 (82 %), 6 µs (18%)]. En este derivado los cálculos teóricos realizados revelan que el estado excitado $^1\pi\pi^*_{pypy}$ está relativamente próximo al ^{3}IL' centrado en la bzq (Figura 3.24b). De acuerdo con ello, nosotros atribuimos tentativamente esta emisión a una mezcla de estados excitados ($^1\pi\pi^*_{pypy}/^3IL'_{bzq}$).

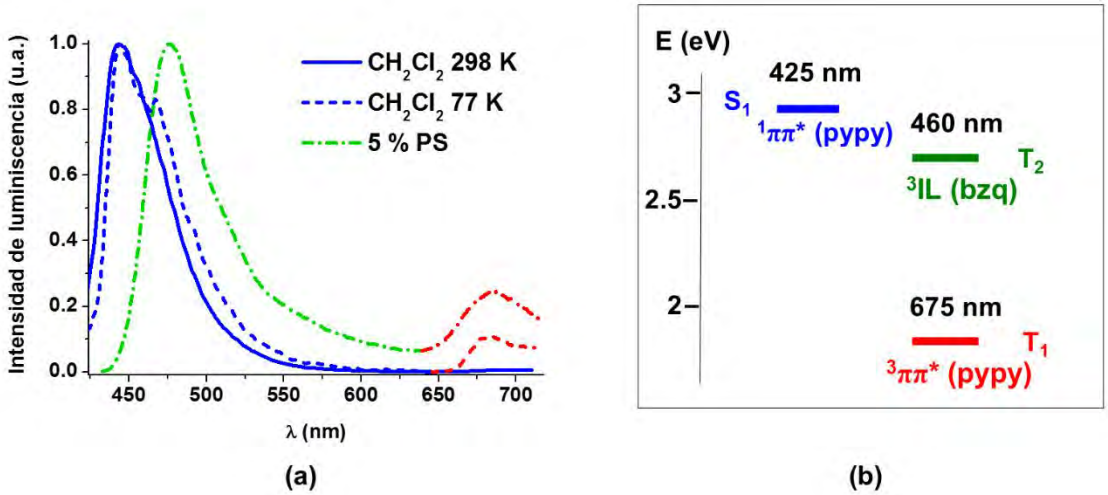

Figura 3.24.(a) Espectros de emisión normalizados del derivado **17g** en CH_2Cl_2 5×10^{-5} M a 298 K y 77 K y en PS (5 %). (b) Energía calculada de estados excitados seleccionados para **17g**.

Se ha realizado también la optimización del primer estado triplete T_1 por cálculos teóricos DFT. En la Figura 3.25a se representa la composición de los orbitales SOMO y SOMO-1, mientras que la densidad de spin se muestra en la Figura 3.25b. Se observa, tanto para la optimización en fase gas o en CH_2Cl_2, que el T_1 está localizado en el ligando pypy confirmándose, por lo tanto, que la banda de fosforescencia observada a menor energía se debe a un estado triplete localizado en el pypy.

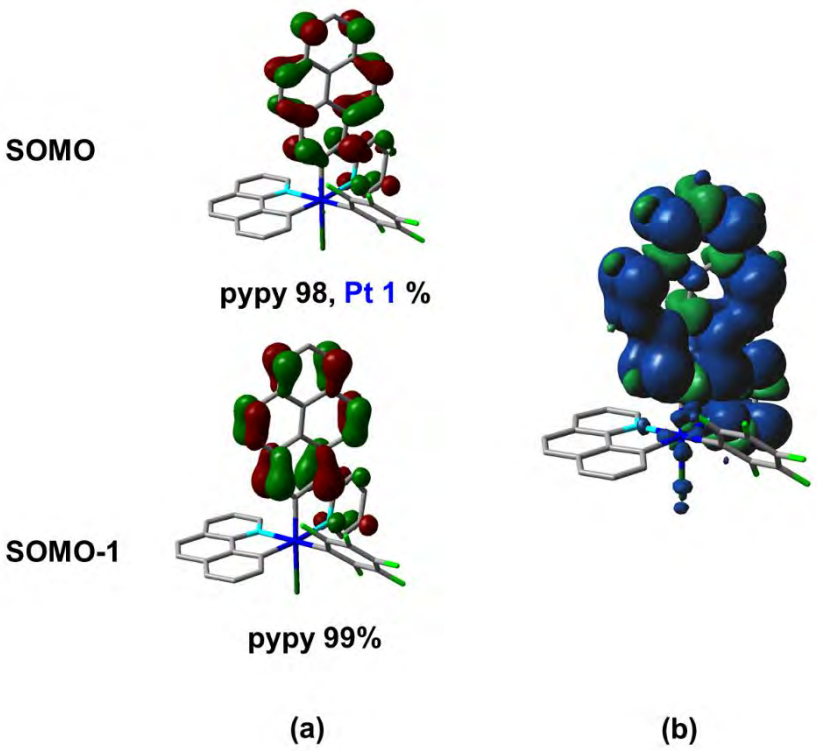

Figura 3.25. (a) Dibujo de los orbitales SOMO y SOMO-1 en el estado triplete y (b) distribución de la densidad de spin para el derivado **17g** en CH_2Cl_2.

En estado sólido, el derivado [Pt(bzq)(pypy)(C_6F_5)Cl] **17g** muestra una banda ligeramente estructurada en la zona verde del espectro (480 nm) a temperatura ambiente, que se desplaza hacia el azul (466 nm) al bajar la temperatura (Figura 3.26). En base al perfil estructurado de las bandas y el tiempo de vida media (0.35 μs), se propone un estado excitado con mezcla de contribución $^1\pi\pi^*_{pypy}/^3IL'_{bzq}$.

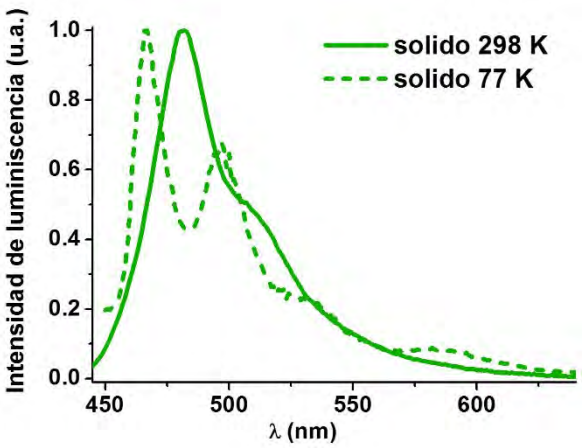

Figura 3.26. Espectros de emisión normalizados del derivado **17g** en estado sólido a 298 K y 77 K.

Conviene mencionar que es difícil obtener fosforescencia a temperatura ambiente en compuestos con fluoróforos aromáticos, debido a que este tipo de ligandos suelen provocar que los derivados presenten acoplamientos espín-órbita débiles y mucha diferencia energética entre los estados singlete y triplete de más baja energía, lo que hace que el cruce intersistémico $S_1 \rightarrow T_1$ sea más difícil. Sin embargo, se han publicado algunos ejemplos donde se ha observado emisión desde el estado excitado triplete centrado en el pireno (^{3}pyr*) dando lugar a emisiones duales fluorescencia/fosforescencia en derivados ciclometalados d^8 de Pt(II) y d^6 de Ir(III).[143, 150]

3.3 Apéndice

Apéndice – Capítulo 3.1

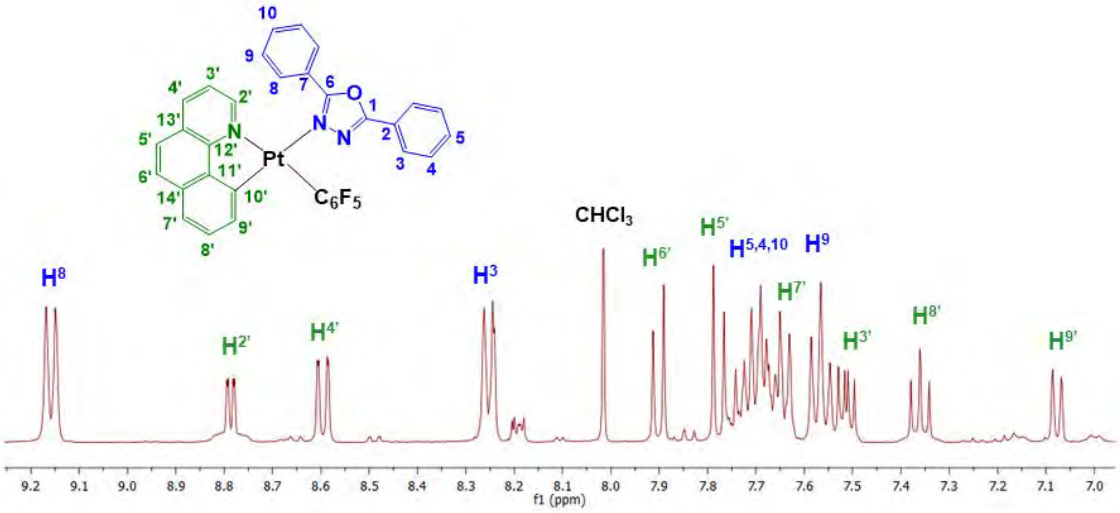

Figura A3.1. Espectro de RMN de ^{1}H en CD_3COCD_3 del compuesto **16f**.

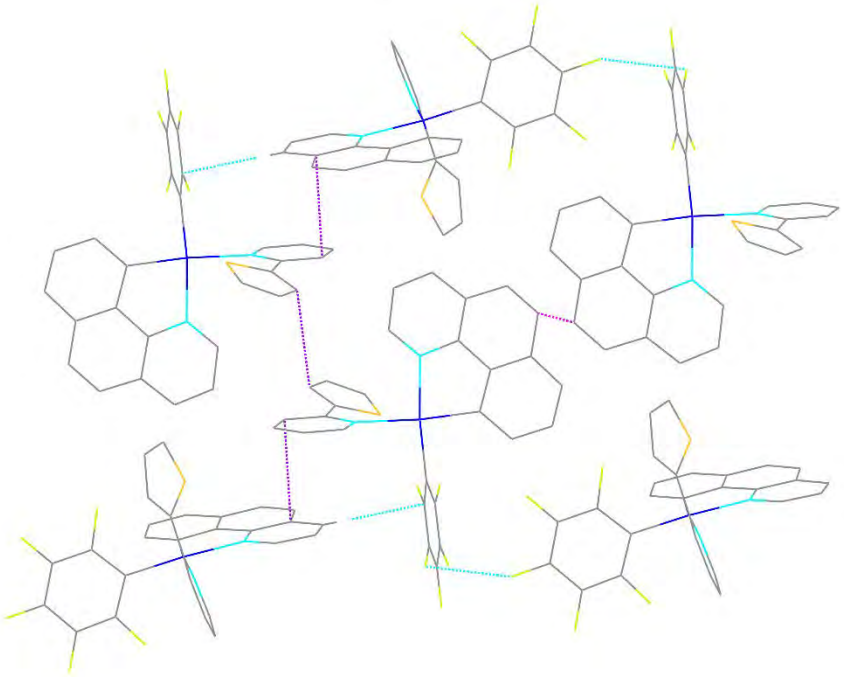

Figura A3.2. Estructura supramolecular del derivado [Pt(bzq)(Hthpy)(C_6F_5)] **16a** formado por interacciones π···π no lineales entre los grupos bzq ciclometalados (3.34 Å) (líneas rosas) y entre los grupos bzq-thpy (3.39 Å) ythpy-thpy (3.29 Å) (líneas moradas), reforzadas con interacciones secundarias H_{bzq}···C_{C6F5} (2.78 Å) y F_{C6F5}···F_{C6F5} (2.88 Å) (líneas azules).

Tabla A3.1. Comparación de las distancias y ángulos de enlace de las estructuras experimentales y las estructuras optimizadas (S_0 y T_1) mediante cálculos DFT de **16a**, **16c**, **16d** en CH_2Cl_2 y de **16f** en fase gas.

16a – molécula A				**16c**			
	Rayos X	S_0	T_1		Rayos X	S_0	T_1
Pt-N(1)	2.081(3)	2.151	2.146	Pt-N(1)	-	2.151	2.162
Pt-N(2)	2.131(3)	2.239	2.233	Pt-N(2)	-	2.280	2.178
Pt-C(13)	1.997(4)	2.006	1.986	Pt(1)-C(10')	-	2.008	2.019
Pt-C(23)	2.004(4)	2.027	2.036	Pt(1)-C_{C6F5}	-	2.038	2.030
N(1)-Pt-N(2)	94.11(12)	95.42	95.19	N(1)-Pt-N(2)	-	94.47	94.72
C(13)-Pt-N(1)	82.14(13)	80.97	80.55	C(10')-Pt-N(1)	-	80.84	80.69
C(13)-Pt-C(23)	94.48(15)	94.73	95.33	C(10')-Pt-C_{C6F5}	-	93.02	92.96
C(23)-Pt-N(2)	88.93(13)	88.85	88.92	C_{C6F5}-Pt-N(2)	-	91.90	91.90
S(1)···Pt	3.150	3.428	3.423	H(9)···Pt	-	2.884	2.740
16d				**16f**			
	Rayos X	S_0	T_1		Rayos X	S_0	T_1
Pt-N(1)	-	2.158	2.152	Pt-N(1)	2.0888 (18)	2.121	2.145
Pt-N(2)	-	2.253	2.245	Pt-N(2)	2.1186 (18)	2.209	2.201
Pt-C(10')	-	2.006	1.987	Pt-C(13)	1.987(2)	2.003	1.985
Pt-C_{C6F5}	-	2.028	2.037	Pt-C(28)	2.005(2)	2.028	2.036
N(1)-Pt-N(2)	-	95.15	95.18	N(1)-Pt-N(2)	94.81(7)	94.48	94.51
C(10')-Pt-N(1)	-	80.86	81.42	C(13)-Pt-N(1)	82.09(8)	81.02	80.58
C(10')-Pt-C_{C6F5}	-	93.67	94.31	C(13)-Pt-C(28)	92.70(9)	94.36	95.11
C_{C6F5}-Pt-N(2)	-	90.25	90.05	C(28)-Pt-N(2)	90.46(8)	90.134	89.81
H(12)···Pt	-	3.224	3.195	H(21)···Pt	2.712	2.677	2.645

Tabla A3.2. Estados seleccionados singlete (S_0) de más baja energía calculados mediante TDDFT/SCRF (CH_2Cl_2) con las energías de excitación verticales y los orbitales implicados para **16a**, **16c**, **16d**, y **16f**.

	Estado	**λ/nm**	**f** [a]	**Transición (% Contribución)**
16a	S_1	394.78	0.046	H→L (93%)
	S_2	381.06	0.0047	H-1→L (86%)
	S_3	377.37	0.0059	H-1→L (10%), H-1→L+1 (18%), H→L+1 (69%)
	S_4	368.98	0.0097	H-1→L+1 (77%), H→L+1 (19%)
	S_5	343.34	0.023	H-2→L (79%), H-2→L+1 (15%)
	S_6	338.96	0.0197	H-2→L (12%), H-2→L+1 (81%)
	S_7	333.01	0.0296	H-3→L (21%), H→L+2 (60%)
	S_8	321.48	0.0147	H-1→L+2 (84%)
	S_9	315.22	0.0602	H-3→L (15%), H→L+2 (15%), H→L+3 (43%)
	S_{10}	314.55	0.0468	H-6→L+1 (13%), H-3→L+1 (72%)
	S_{11}	310.61	0.1123	H-3→L (33%), H→L+3 (43%)
	S_{13}	305.87	0.0411	H-4→L (39%), H-4→L+1 (36%)

	S_{15}	301.65	0.0821	H-5→L+1 (32%), H-4→L (12%), H-4→L+1 (11%), H-2→L+2 (10%)
	S_{16}	300.76	0.0535	H-6→L (25%), H-5→L+1 (43%)
	S_{17}	299.52	0.0302	H-5→L (25%), H-4→L (11%), H-3→L+2 (11%), H-2→L+2 (28%)
16c	S_1	413.08	0.0076	H→L (91%)
	S_2	400.78	0.0068	H-1→L (93%)
	S_3	392.43	0.0412	H→L+1 (92%)
	S_5	365.84	0.0178	H-2→L (97%)
	S_6	340.41	0.0295	H-3→L (82%)
	S_7	338.74	0.0231	H-2→L+1 (85%)
	S_8	330.79	0.0359	H-3→L+1 (31%), H→L+2 (56%)
	S_{10}	316.42	0.0109	H-1→L+2 (86%)
	S_{11}	312.77	0.1591	H-5→L (23%), H-3→L+1 (36%), H→L+2 (18%)
	S_{13}	305.83	0.0695	H-7→L (16%), H-6→L (19%), H→L+3 (46%)
	S_{15}	301.50	0.0786	H-6→L (11%), H-5→L+1 (38%), H→L+3 (27%)
	S_{16}	297.87	0.0681	H-7→L (39%), H-2→L+2 (10%)
16d	S_1	395.52	0.0409	H→L (95%)
	S_2	372.56	0.0045	H-1→L (99%)
	S_3	359.24	0.0237	H→L+1 (96%)
	S_5	334.12	0.0106	H-3→L (13%), H-2→L (55%), H→L+2 (26%)
	S_6	330.90	0.0179	H-3→L (23%), H-2→L (41%), H→L+2 (31%)
	S_7	316.90	0.0799	H-3→L (14%), H-2→L+1 (71%)
	S_9	311.67	0.0793	H-3→L (28%), H-2→L+1 (23%), H→L+2 (23%), H→L+3 (13%)
	S_{10}	309.16	0.045	H→L+3 (83%)
	S_{11}	304.76	0.0133	H-5→L+1 (13%), H-3→L+1 (76%)
	S_{13}	298.39	0.0102	H-1→L+3 (83%)
	S_{14}	294.78	0.0372	H-7→L (21%), H-6→L (12%), H-4→L (23%), H-3→L+2 (26%)
16f	S_1	398.70	0.013	H→L (89%)
	S_2	387.33	0.0418	H→L+1 (86%)
	S_3	376.55	0.0011	H-1→L (95%)
	S_5	359.88	0.0227	H-2→L (94%)
	S_6	339.43	0.029	H-2→L+1 (88%)
	S_7	332.02	0.0315	H-3→L (21%), H-3→L+1 (13%), H→L+2 (39%), H→L+3 (13%)
	S_8	328.09	0.0516	H-3→L (64%), H→L+2 (17%)
	S_9	323.98	0.003	H-4→L (15%), H-3→L+1 (16%), H→L+2 (33%), H→L+3 (29%)
	S_{12}	308.75	0.21	H-3→L+1 (47%), H→L+3 (33%)
	S_{13}	307.00	0.4548	H-5→L (82%)
	S_{14}	304.36	0.0713	H-1→L+3 (78%)

[a] Fuerza del oscilador

Tabla A3.3. Composición (%) de los orbitales moleculares frontera en el estado fundamental para **16a**, **16c**, **16d** y **16f** en CH_2Cl_2.

	16a					**16c**				
OM	eV	C_6F_5	bzq	Hthpy	Pt	eV	C_6F_5	bzq	Hpq	Pt
L+5	-0.1	36	18	18	27	-0.27	22	9	48	21
L+4	-0.26	2	75	16	7	-0.36	2	38	55	5
L+3	-1.07	0	12	86	2	-0.98	1	1	98	1
L+2	-1.21	0	84	13	3	-1.17	0	95	1	4
L+1	-1.7	0	3	95	1	-1.76	0	94	2	3
L	-1.78	0	94	3	3	-2.03	0	1	98	1
H	-5.6	0	68	3	29	-5.59	0	69	2	28
H-1	-5.83	4	5	11	81	-5.86	3	5	10	82
H-2	-6.02	60	4	5	31	-6.04	58	5	6	31
H-3	-6.28	17	43	16	24	-6.27	9	57	4	30
H-4	-6.34	41	22	30	8	-6.41	94	3	1	2
H-5	-6.38	50	2	44	4	-6.56	3	29	39	30
	16d					**16f**				
OM	eV	C_6F_5	bzq	Hdfppy	Pt	eV	C_6F_5	bzq	Hoxd	Pt
L+5	-0.2	25	49	8	18	-0.45	0	0	100	0
L+4	-0.57	0	10	86	3	-0.46	2	0	95	3
L+3	-1.05	1	4	94	1	-1.18	0	86	10	4
L+2	-1.19	0	90	6	4	-1.36	0	10	89	1
L+1	-1.58	0	4	95	1	-1.78	0	95	1	3
L	-1.8	0	94	2	3	-2.03	0	1	98	1
H	-5.61	0	70	2	28	-5.65	0	73	1	26
H-1	-5.93	3	3	4	90	-6.02	5	3	2	90
H-2	-6.14	65	4	2	29	-6.05	59	6	4	32
H-3	-6.3	5	63	0	31	-6.32	16	60	2	21
H-4	-6.48	97	1	0	2	-6.38	88	8	0	4
H-5	-6.67	3	42	1	54	-6.58	5	8	79	8

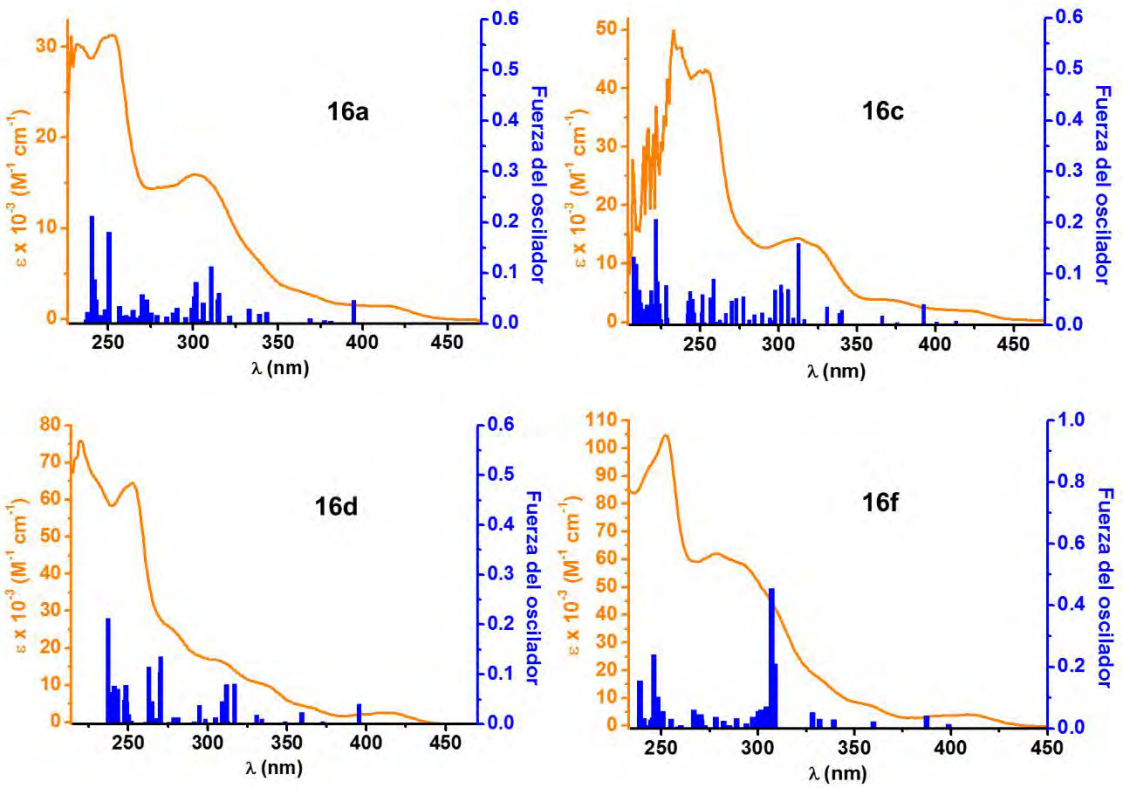

Figura A3.3. Espectros de absorción calculados (barras azules) en CH_2Cl_2 y espectros experimentales de UV-vis en CH_2Cl_2 para los compuestos de Pt(II) **16a**, **16c**, **16d** y **16f**.

Tabla A3.4. Estados seleccionados triplete (T_1) de más baja energía calculados mediante TDDFT/SCRF (CH_2Cl_2) con las energías de excitación verticales y los orbitales implicados para **16a**, **16c**, **16d**, y **16f**.

		λ/nm	f [a]	Transición (% Contribución)
16a	T_1	467.33	0.0	H-3→L (17%), H→L (24%), H→L+2 (26%)
	T_2	440.70	0.0	H→L (67%), H→L+2 (16%)
	T_3	431.86	0.0	H-5→L+1 (25%), H-4→L+1 (18%), H-3→L+1 (11%)
	T_4	390.42	0.0	H-1→L (83%)
	T_5	387.73	0.0	H-3→L (31%), H→L+2 (27%)
16c	T_1	466.31	0.0	H-3→L+1 (23%), H→L+1 (23%), H→L+2 (30%)
	T_2	463.14	0.0	H-6→L (11%), H-5→L (28%), H-2→L (14%), H→L (14%)
	T_3	439.91	0.0	H→L+1 (66%), H→L+2 (17%)
	T_4	411.41	0.0	H-1→L (17%), H→L (57%)
	T_5	405.18	0.0	H-1→L (75%), H→L (21%)
16d	T_1	466.63	0.0	H-3→L (26%), H→L (22%), H→L+2 (29%)
	T_2	441.96	0.0	H→L (71%), H→L+2 (16%)
	T_3	387.86	0.0	H-3→L (43%), H-1→L (10%), H→L+2 (26%)
	T_4	381.53	0.0	H-1→L (85%)
	T_5	370.86	0.0	H-6→L+1 (12%), H-1→L+1 (10%), H→L+1 (47%)
16f	T_1	465.05	0.0	H-3→L+1 (23%), H→L+1 (18%), H→L+3 (31%)
	T_2	438.00	0.0	H→L+1 (68%), H→L+3 (12%)
	T_3	430.89	0.0	H-5→L (56%), H-2→L (11%)
	T_4	396.44	0.0	H→L (81%)
	T_5	385.89	0.0	H-3→L+1 (35%), H-2→L+1 (11%), H→L+3 (30%)

[a] fuerza del oscilador

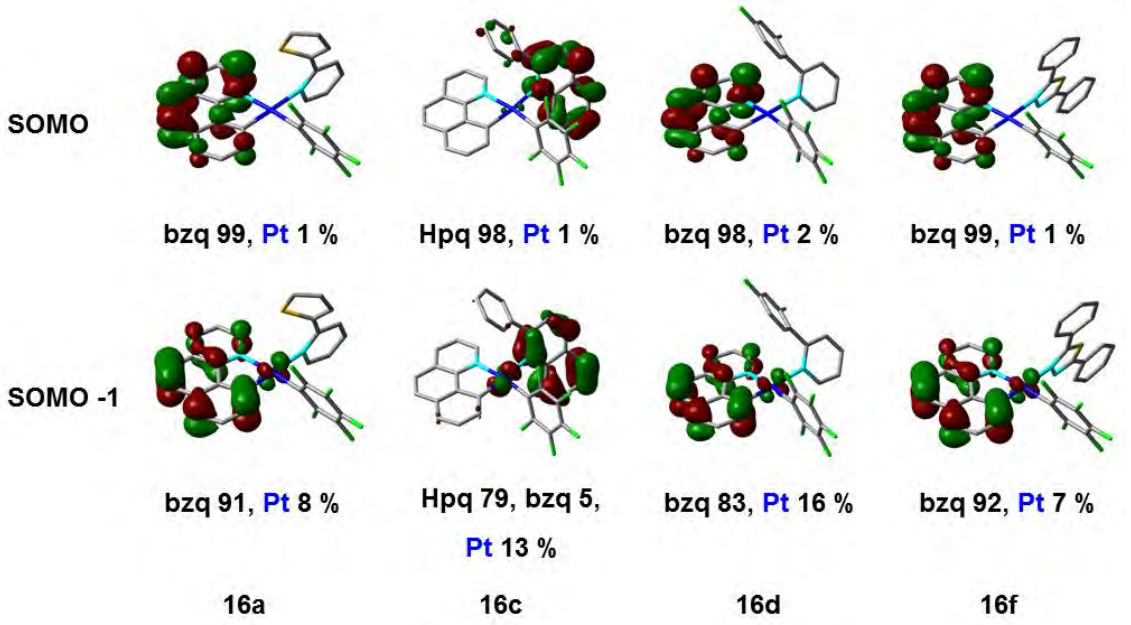

Figura A3.4. Dibujo de los orbitales SOMO y SOMO-1 en el estado triplete obtenidos por DFT para **16a**, **16c**, **16d** (en CH_2Cl_2) y **16f** (en fase gas).

Tabla A3.5

(a) Estados seleccionados triplete (T_1) de más baja energía calculados en fase gas para **16f**.

		λ/nm	f	Transición (% Contribución)
16f	T_1	478.00	0.0	H-4→L+1 (18%), H→L+1 (45%), H→L+3 (19%)
	T_2	461.80	0.0	H→L (56%), H→L+1 (12%)
	T_3	449.88	0.0	H-4→L+1 (11%), H→L (10%), H→L+1 (36%), H→L+3 (19%)
	T_4	433.28	0.0	H-1→L (42%), H→L (26%)
	T_5	423.90	0.0	H-2→L (89%)

(b) Composición (%) de los orbitales moleculares frontera en el estado fundamental para **16f** en fase gas.

OM	eV	C_6F_5	bzq	Hoxd	Pt
LUMO+5	-0.5	1	0	97	1
LUMO+4	-0.66	0	0	100	0
LUMO+3	-1.03	0	94	3	3
LUMO+2	-1.43	0	3	96	1
LUMO+1	-1.68	0	96	1	3
LUMO	-2.12	0	1	98	1
HOMO	-5.39	0	71	1	28
HOMO-1	-5.65	67	4	2	27
HOMO-2	-5.74	7	4	2	87
HOMO-3	-5.89	97	0	0	3
HOMO-4	-6.13	6	67	1	27
HOMO-5	-6.45	2	34	9	55

Apéndice Capítulo 3.2

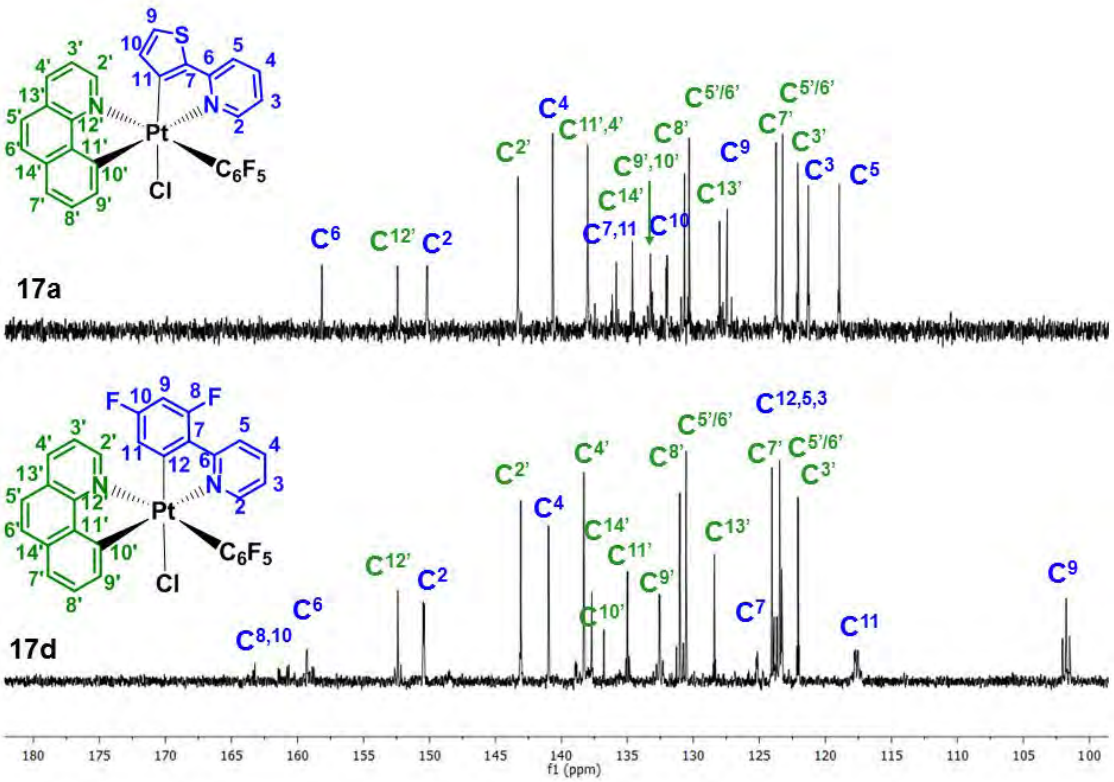

Figura A3.5. Espectro de RMN de $^{13}C\{^{1}H\}$ de los derivados **17a** y **17d** en $CDCl_3$.

Tabla A3.6. Distancias (Å) y ángulos (°) seleccionados para los compuestos **17c**·3.25CH_3COCH_3, **17d** y **17g**·0.5THF.

17c·3.25CH_3COCH_3			
Distancias (Å)		**Ángulos (°)**	
N(1)-Pt(1)	2.092(7)	N(1)-Pt(1)-N(2)	92.8(3)
N(2)-Pt(1)	2.230(7)	C(11)-Pt(1)-N(1)	81.3(3)
C(11)-Pt(1)	2.023(9)	C(11)-Pt(1)-C(29)	95.8(4)
C(29)-Pt(1)	2.076(10)	C(29)-Pt(1)-N(2)	89.6(3)
C(28)-Pt(1)	2.024(7)	C(28)-Pt(1)-N(1)	87.9(3)
Cl(1)-Pt(1)	2.4655(19)	C(28)-Pt(1)-C(11)	94.0(3)
C(22)-C(23)	1.469(14)	C(28)-Pt(1)-C(29)	88.4(3)
H(10)···F(5)	2.545	C(28)-Pt(1)-N(2)	79.5(3)
H(15)···F(1)	2.876	Cl(1)-Pt(1)-N(1)	90.65(18)
H(27)···F(5)	2.788	Cl(1)-Pt(1)-N(2)	105.01(19)
		Cl(1)-Pt(1)-C(11)	81.4(2)
		Cl(1)-Pt(1)-C(29)	92.8(3)
17d			
Distancias (Å)		**Ángulos (°)**	
N(1)-Pt(1)	2.112(5)	N(1)-Pt(1)-N(2)	92.2(2)
N(2)-Pt(1)	2.126(6)	C(13)-Pt(1)-N(1)	81.2(2)
C(13)-Pt(1)	2.008(7)	C(13)-Pt(1)-C(25)	97.1(3)
C(25)-Pt(1)	2.047(7)	C(25)-Pt(1)-N(2)	89.3(2)
C(24)-Pt(1)	2.026(7)	C(24)-Pt(1)-N(1)	87.6(3)
Cl(1)-Pt(1)	2.4084(17)	C(24)-Pt(1)-C(13)	95.9(3)
C(18)-C(19)	1.465(11)	C(24)-Pt(1)-C(25)	89.7(3)
H(12)···F(7)	2.490	C(24)-Pt(1)-N(2)	80.8(3)
H(14)···F(3)	2.578	Cl(1)-Pt(1)-N(1)	89.62(15)
H(23)···F(7)	2.698	Cl(1)-Pt(1)-N(2)	97.02(16)
		Cl(1)-Pt(1)-C(13)	85.94(19)
		Cl(1)-Pt(1)-C(25)	93.15(18)
17g·0.5THF			
Distancias (Å)		**Ángulos (°)**	
N(1)-Pt(1)	2.121(3)	N(1)-Pt(1)-N(2)	91.08(11)
N(2)-Pt(1)	2.147(3)	C(13)-Pt(1)-N(1)	81.51(13)
C(13)-Pt(1)	2.038(4)	C(13)-Pt(1)-C(35)	94.75(14)
C(35)-Pt(1)	2.061(3)	C(35)-Pt(1)-N(2)	92.57(13)
C(34)-Pt(1)	2.044(3)	C(34)-Pt(1)-N(1)	86.11(12)
Cl(1)-Pt(1)	2.4293(12)	C(34)-Pt(1)-C(13)	97.76(14)
C(18)-C(19)	1.485(5)	C(34)-Pt(1)-C(35)	92.27(13)
H(12)···F(5)	2.499	C(34)-Pt(1)-N(2)	79.51(12)
H(14)···F(1)	2.506	Cl(1)-Pt(1)-N(1)	89.09(8)
H(33)···F(5)	2.627	Cl(1)-Pt(1)-N(2)	96.91(8)
		Cl(1)-Pt(1)-C(13)	85.16(10)
		Cl(1)-Pt(1)-C(35)	92.78(10)

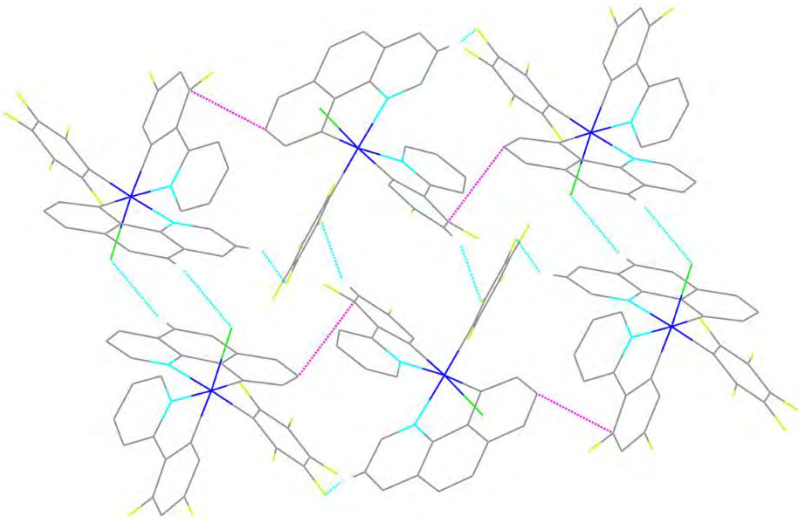

(a)

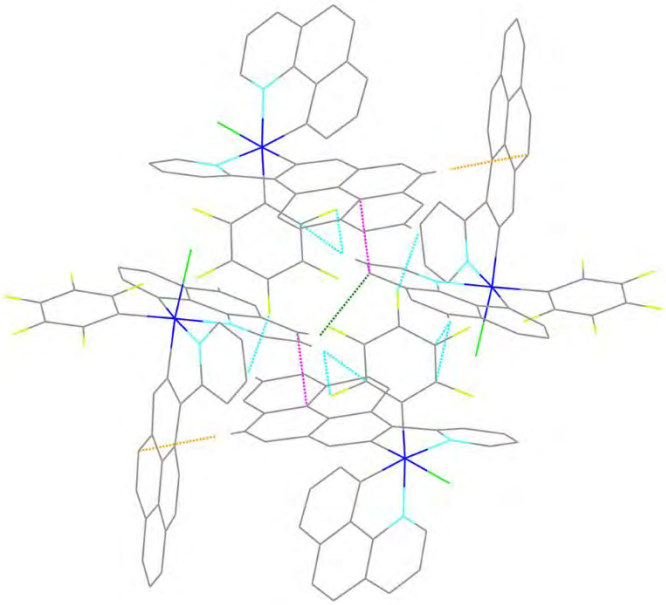

(b)

Figura A3.6. (a) Estructura supramolecular de [Pt(bzq)(dfppy)(C_6F_5)Cl] **17d** formada por cadenas con interacciones no-lineales π···π entre los ligandos bzq y dfppy (3.29 Å) (líneas rosas), conectadas por interacciones secundarias H_{bzq}···Cl (2.64 Å), H_{bzq}···F_{C6F5} (2.64 Å) y H_{dfppy}···F_{C6F5} (2.40 Å) (líneas azules). (b) Estructura supramolecular de [Pt(bzq)(pypy)(C_6F_5)Cl] **17g** mostrando interacciones π···π entre los ligandos pypy y bzq (3.311 Å) (líneas rosas), interacciones C_{bzq}···H_{bzq} (2.709 Å) (líneas verdes) y ⊥ C_{pypy}···H_{pypy} (2.768 Å) (líneas naranjas) e interacciones secundarias H_{bzq}···C_{C6F5} (2.785-2.887 Å); H_{bzq}···F_{C6F5} (2.452 Å); H_{pypy}···F_{C6F5} (2.619 Å) (líneas azules).

Tabla A3.7. Distancias (Å) y ángulos (°) seleccionados para el derivado $[Pt(bzq)(C_6F_5)Cl(\mu\text{-}OH)]_2$ (**18**·$2CH_3COCH_3$)

18·$2CH_3COCH_3$			
Distancias (Å)		**Ángulos (°)**	
N(1)-Pt(1)	2.108(3)	Pt(1)-O(1)-Pt(2)	103.58(10)
C(13)-Pt(1)	2.017(3)	Pt(1)-O(2)-Pt(2)	103.39(9)
Cl(2)-Pt(1)	2.2940(8)	O(1)-Pt(1)-O(2)	75.80(9)
C(14)-Pt(1)	2.029(3)	O(1)-Pt(2)-O(2)	75.85(9)
O(1)-Pt(1)	2.180(2)	N(1)-Pt(1)-C(13)	81.62(12)
O(2)-Pt(1)	2.041(2)	N(2)-Pt(2)-C(42)	177.84(11)
O(1)-Pt(2)	2.037(2)	C(14)-Pt(1)-C(13)	94.84(13)
O(2)-Pt(2)	2.182(2)	Cl(2)-Pt(1)-O(1)	98.90(6)
N(2)-Pt(2)	2.104(3)	C(13)-Pt(1)-O(2)	97.95(11)
C(42)-Pt(2)	2.019(3)	C(42)-Pt(2)-O(1)	96.18(11)
C(43)-Pt(2)	2.039(3)	Cl(1)-Pt(2)-O(2)	98.84(6)
Cl(1)-Pt(2)	2.3025(8)	C(42)-Pt(2)-C(43)	95.96(12)
Pt(1)···Pt(2)	3.3147 (4)		

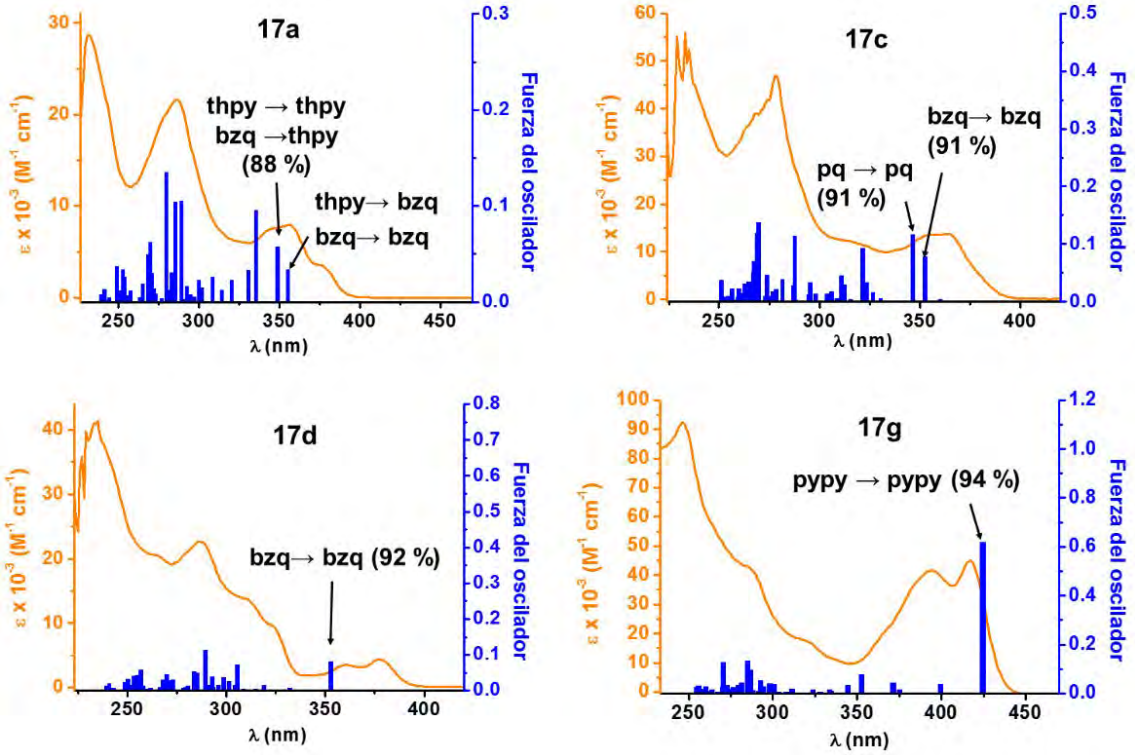

Figura A3.7. Espectros de absorción calculados (dibujados en barras azules) en CH_2Cl_2 y espectros experimentales de UV-vis en CH_2Cl_2 para los compuestos de Pt(II) **17a**, **17c**, **17d** y **17g**.

Tabla A3.8. Comparación de las distancias y ángulos de enlace de las estructuras experimentales y las estructuras optimizadas (S_0 y T_1) mediante cálculos DFT de **17a**, **17c**, **17d** y **17g**.

17a			
	Rayos X	**S_0**	**T_1**
N(1)-Pt(1)	-	2.170	2.155
N(2)-Pt(1)	-	2.243	2.230
C(10')-Pt(1)	-	2.039	2.029
C_{C6F5}-Pt(1)	-	2.066	2.073
C(11)-Pt(1)	-	2.031	2.032
Cl(1)-Pt(1)	-	2.527	2.524
H(10)···F_{C6F5}	-	2.704	2.697
H(9')···F_{C6F5}	-	2.526	2.550
H(2)··· F_{C6F5}	-	2.523	2.528
N(1)-Pt(1)-N(2)	-	93.11	93.47
C(10')-Pt(1)-N(1)	-	80.62	80.20
C(10')-Pt(1)-C_{C6F5}	-	96.34	96.40
C_{C6F5}-Pt(1)-N(2)	-	89.74	89.74
Cl(1)-Pt(1)-N(1)	-	87.08	88.15
Cl(1)-Pt(1)-N(2)	-	95.79	95.81
Cl(1)-Pt(1)-C(10')	-	87.40	86.83
Cl(1)-Pt(1)-C_{C6F5}	-	96.76	95.31
17c			
	Rayos X	**S_0**	**T_1**
N(1)-Pt(1)	2.092(7)	2.163	2.149
N(2)-Pt(1)	2.230(7)	2.322	2.304
C(11)-Pt(1)	2.023(9)	2.039	2.029
C(29)-Pt(1)	2.076(10)	2.066	2.072
C(28)-Pt(1)	2.024(7)	2.039	2.039
Cl(1)-Pt(1)	2.4655(19)	2.576	2.579
H(10)···F(5)	2.545	2.456	2.491
H(15)···F(1)	2.876	2.820	2.846
H(27)···F(5)	2.788	2.811	2.806
N(1)-Pt(1)-N(2)	92.8(3)	93.17	93.70
C(11)-Pt(1)-N(1)	81.3(3)	80.74	80.26
C(11)-Pt(1)-C(29)	95.8(4)	97.15	97.19
C(29)-Pt(1)-N(2)	89.6(3)	88.76	88.65
Cl(1)-Pt(1)-N(1)	90.65(18)	88.27	89.73
Cl(1)-Pt(1)-N(2)	105.01(19)	104.62	105.24
Cl(1)-Pt(1)-C(11)	81.4(2)	80.93	79.49
Cl(1)-Pt(1)-C(29)	92.8(3)	90.03	92.08
17d			
	Rayos X	**S_0**	**T_1**
N(1)-Pt(1)	2.112(5)	2.169	2.154
N(2)-Pt(1)	2.126(6)	2.205	2.194
C(13)-Pt(1)	2.008(7)	2.042	2.034
C(25)-Pt(1)	2.047(7)	2.071	2.078
C(24)-Pt(1)	2.026(7)	2.041	2.041
Cl(1)-Pt(1)	2.4084(17)	2.528	2.527
H(12)···F(7)	2.490	2.497	2.521
H(14)···F(3)	2.578	2.528	2.538
H(23)···F(7)	2.698	2.663	2.649
N(1)-Pt(1)-N(2)	92.2(2)	93.25	93.45

C(13)-Pt(1)-N(1)	81.2(2)	80.60	80.14
C(13)-Pt(1)-C(25)	97.1(3)	96.19	96.38
C(25)-Pt(1)-N(2)	89.3(2)	89.86	89.91
Cl(1)-Pt(1)-N(1)	89.62(15)	87.03	88.65
Cl(1)-Pt(1)-N(2)	97.02(16)	95.97	96.16
Cl(1)-Pt(1)-C(13)	85.94(19)	86.20	85.43
Cl(1)-Pt(1)-C(25)	93.15(18)	95.22	94.37

17g

	Rayos X	**S_0**	**T_1**
N(1)-Pt(1)	2.121(3)	2.173	2.173
N(2)-Pt(1)	2.147(3)	2.191	2.190
C(13)-Pt(1)	2.038(4)	2.044	2.044
C(35)-Pt(1)	2.061(3)	2.067	2.064
C(34)-Pt(1)	2.044(3)	2.045	2.044
Cl(1)-Pt(1)	2.4293(12)	2.543	2.546
H(12)···F(5)	2.499	2.477	2.498
H(14)···F(1)	2.627	2.523	2.599
H(33)···F(5)	2.627	2.729	2.895
N(1)-Pt(1)-N(2)	91.08(11)	92.38	92.89
C(13)-Pt(1)-N(1)	81.51(13)	80.45	80.48
C(13)-Pt(1)-C(35)	94.75(14)	96.86	96.53
C(35)-Pt(1)-N(2)	92.57(13)	90.22	89.99
Cl(1)-Pt(1)-N(1)	89.09(8)	87.63	87.15
Cl(1)-Pt(1)-N(2)	96.91(8)	96.29	96.09
Cl(1)-Pt(1)-C(13)	85.16(10)	85.77	86.12
Cl(1)-Pt(1)-C(35)	92.78(10)	94.53	95.17

Tabla A3.9. Estados seleccionados singlete (S_0) de más baja energía calculados mediante TDDFT/SCRF (CH_2Cl_2) con las energías de excitación verticales y los orbitales implicados para **17a**, **17c**, **17d**, y **17g**.

	Estado	λ/nm	f [a]	Transición (% Contribución)
17a	S_1	355.23	0.0341	H→L (94%)
	S_2	348.83	0.0575	H-1→L (93%)
	S_3	335.48	0.0954	H→L+1 (88%)
	S_4	330.85	0.0327	H-1→L+1 (88%)
	S_5	320.37	0.0228	H→L+2 (36%), H→L+3 (20%)
	S_6	314.22	0.0125	H-4→>L (23%), H-3→L (27%), H-1→L+2 (29%)
	S_7	308.28	0.0258	H-4→L (18%), H-3→L (36%), H→L+2 (17%)
	S_9	301.86	0.015	H-3→L+1 (31%), H-1→L+2 (12%), H-1→L+3 (13%), H→L+3 (12%)
	S_{10}	299.96	0.0224	H-5→L (15%), H-3→L+1 (33%), H-1→L+3 (10%)
	S_{15}	292.27	0.0165	H-5→L (48%), H-4→L (11%)
	S_{17}	288.83	0.1046	H-4→L (16%), H-4→L+1 (30%), H-1→L+2 (12%), H-1→L+3 (15%)
	S_{18}	285.07	0.1045	H-7→L (11%), H-5→L+1 (30%), H-4→L+1 (25%)
17c	S_1	360.11	0.005	H→L (97%)
	S_2	352.68	0.0783	H→L+1 (91%)
	S_3	346.53	0.116	H-1→L (91%)
	S_5	326.62	0.0164	H-2→L (89%)
	S_6	323.37	0.0334	H-3→L (85%)
	S_7	321.58	0.0924	H-4→L (82%)
	S_9	312.42	0.03	H-7→L (63%), H-6→L (28%)
	S_{10}	310.89	0.0454	H-6→L (26%), H-5→L (56%)
	S_{12}	306.08	0.0174	H-7→L+1 (25%), H-3→L+1 (21%), H→L+2 (14%)
	S_{14}	303.65	0.014	H→L+4 (53%)
	S_{17}	295.50	0.0334	H-8→L (83%)
	S_{22}	287.69	0.1133	H-6→L+1 (18%), H→L+2 (24%), H→L+3 (13%)
17d	S_1	352.86	0.0816	H→L (92%)
	S_2	331.95	0.0056	H→L+1 (96%)
	S_3	319.11	0.0141	H-2→L (28%), H-1→L (46%)
	S_5	308.74	0.0051	H-3→L (11%), H-2→L+1 (13%), H-1→L (15%), H-1→L+1 (28%)
	S_6	305.58	0.0715	H-4→L (13%), H-2→L (19%), H-1→L+1 (43%)
	S_7	304.22	0.0144	H→L+2 (12%), H→L+3 (53%)
	S_8	301.30	0.0269	H-3→L (49%), H-2→L (11%), H-2→L+1 (21%)
	S_9	298.51	0.0366	H-5→L (10%), H-3→L+1 (11%), H-2→L+1 (37%), H-1→L+1 (18%)
	S_{10}	295.75	0.0144	H-6→L (21%), H-5→L (12%), H-3→L+1 (32%), H-2→L+1 (11%)
	S_{12}	292.94	0.0384	H-3→L+1 (12%), H-1→L+3 (11%), H→L+5 (12%)
	S_{13}	292.09	0.0125	H-6→L (20%), H-5→L (11%), H-3→L+1 (12%), H→L+5 (35%)
	S_{14}	291.23	0.0153	H-6→L (20%), H-5→L (37%)
	S_{15}	289.28	0.1134	H-4→L (17%), H-4→L+1 (22%), H→L+2 (19%), H→L+3 (17%)
17g	S_1	424.55	0.6173	H→L (94%)
	S_2	399.75	0.038	H→L+1 (98%)

	S_3	375.35	0.015	H-2→L (25%), H-1→L (68%)
	S_4	371.37	0.0429	H-2→L (59%), H-1→L (30%)
	S_5	352.60	0.0786	H-1→L+1 (91%)
	S_6	344.64	0.035	H→L+2 (90%)
	S_8	333.78	0.0161	H-2→L+1 (25%), H→L+3 (59%), H→L+4 (11%)
	S_{11}	323.65	0.016	H→L+3 (13%), H→L+4 (76%)
	S_{14}	311.34	0.02	H-6→L (15%), H→L+5 (55%)
	S_{18}	300.86	0.0367	H-4→L+1 (21%), H-3→L+1 (37%)
	S_{19}	300.68	0.0163	H-7→L (20%), H-1→L+2 (17%), H-1→L+4 (20%)
	S_{21}	298.24	0.0397	H-1→L+4 (18%), H→L+6 (16%)
	S_{28}	286.70	0.0955	H-5→L+1 (17%), H-1→L+3 (37%)
	S_{29}	284.93	0.1334	H-2→L+2 (37%), H-2→L+4 (27%)

[a] Fuerza del oscilador

Tabla A3.10. Composición (%) de los orbitales moleculares frontera en el estado fundamental para **17a**, **17c**, **17d** y **17g** en CH_2Cl_2.

	17a						**17c**					
MO	eV	C_6F_5	bzq	thpy	Pt	Cl	eV	C_6F_5	bzq	pq	Pt	Cl
L+5	-1.07	19	30	14	35	1	-1.08	7	16	54	18	5
L+4	-1.14	2	7	87	3	1	-1.19	11	25	34	28	2
L+3	-1.22	14	27	34	21	5	-1.2	16	14	49	19	2
L+2	-1.47	4	75	7	10	4	-1.45	2	88	3	5	2
L+1	-1.86	1	9	86	4	0	-2.01	1	96	1	2	1
L	-2.01	1	88	7	3	1	-2.18	0	2	96	2	0
H	-6.11	1	40	51	4	3	-6.12	1	89	2	2	6
H-1	-6.16	0	53	41	4	2	-6.33	8	1	83	4	4
H-2	-6.59	92	3	3	1	1	-6.55	76	6	9	4	5
H-3	-6.62	51	19	11	9	9	-6.6	55	15	19	6	5
H-4	-6.74	16	78	2	2	2	-6.67	2	5	71	3	20
H-5	-6.84	24	1	36	4	35	-6.73	36	49	6	2	7
	17d						**17g**					
MO	eV	C_6F_5	bzq	dfppy	Pt	Cl	eV	C_6F_5	bzq	pypy	Pt	Cl
L+5	-1.05	18	28	19	34	2	-0.97	10	23	34	29	4
L+4	-1.14	2	7	87	4	0	-1.15	22	24	23	27	4
L+3	-1.27	14	30	29	22	6	-1.33	1	25	72	2	0
L+2	-1.48	4	74	8	10	3	-1.46	2	61	28	7	2
L+1	-1.88	0	8	88	3	0	-1.98	1	95	2	2	1
L	-2.03	1	89	6	3	1	-2.3	0	1	96	2	0
H	-6.15	1	92	1	3	2	-5.53	0	0	99	0	0
H-1	-6.52	27	1	65	3	4	-6.09	1	91	2	4	3
H-2	-6.63	60	16	10	7	7	-6.25	2	2	84	7	5
H-3	-6.66	54	14	27	3	3	-6.56	97	1	1	0	1
H-4	-6.75	24	69	3	3	2	-6.62	47	39	6	5	4
H-5	-6.88	21	2	29	5	43	-6.71	35	59	2	3	2

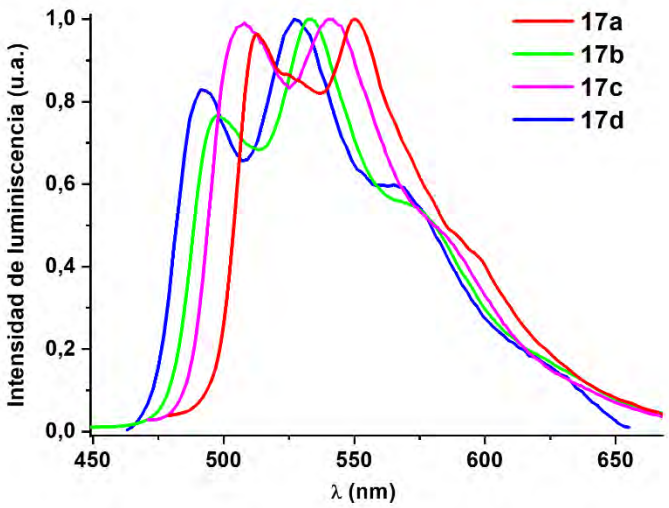

Figura 3.8. Espectros normalizados de emisión en films de PS de los derivados **17a**, **17d** (5 %) y **17b**, **17c** (10 %).

Tabla A3.11. Estados seleccionados triplete calculados por TD-DFT a partir de la geometría del estado fundamental (S_0) para los ligandos heterocíclicos libres.

	T_1 CH_2Cl_2 (nm)	**T_1 fase gas (nm)**
bzq	444	447
thpy (a)	466	464
pbt (b)	449	450
pq (c)	460	463
dfppy (d)	392	393
pypy (g)	610	613

Tabla A3.12. Estados seleccionados triplete calculados mediante TDDFT/SCRF (CH_2Cl_2) a partir de la geometría optimizada en el estado fundamental (S_0), con las energías de excitación verticales y los orbitales implicados para **17a**, **17c**, **17d**, y **17g**.

	Estado	λ/nm	f [a]	Transición (% Contribución)
17a	T_1	485.43	0.0	H-1→L+1 (32%), H→L+1 (45%)
	T_2	458.69	0.0	H-4→L (11%), H-1→L (18%), H-1→L+2 (16%), H→L (16%), H→L+2 (13%)
	T_3	405.37	0.0	H-1→L (26%), H-1→L+2 (12%), H→L (26%), H→L+2 (11%)
	T_4	362.80	0.0	H-4→L (40%), H-3→L (16%), H-1→L+2 (15%), H→L+2 (12%)
	T_5	355.45	0.0	H-1→L (33%), H→L (34%)
17c	T_1	476.58	0.0	H-4→L (11%), H-1→L (63%)
	T_2	458.98	0.0	H→L+1 (35%), H→L+2 (31%)
	T_3	407.18	0.0	H→L+1 (52%), H→L+2 (22%)
	T_4	364.33	0.0	H-4→L (47%), H-1→L (15%)
	T_5	361.16	0.0	H-5→L+1 (23%), H-3→L+1 (11%), H→L (15%), H→L+2 (23%)
17d	T_1	459.01	0.0	H→L (36%), H→L+2 (28%)
	T_2	409.56	0.0	H-3→L+1 (14%), H-1→L+1 (52%)
	T_3	406.34	0.0	H→L (51%), H→L+2 (22%)
	T_4	363.31	0.0	H-4→L (35%), H-3→L (10%), H-2→L (13%), H→L+2 (27%)
	T_5	338.10	0.0	H-3→L+9 (10%)
17g	T_1	675.07	0.0	H→L (89%)
	T_2	459.91	0.0	H-1→L+1 (37%), H-1→L+2 (22%)
	T_3	433.34	0.0	H-2→L (83%)
	T_4	408.11	0.0	H-1→L+1 (44%), H-1→L+2 (17%), H→L+1 (11%)
	T_5	401.75	0.0	H→L+1 (76%)

[a] Fuerza del oscilador

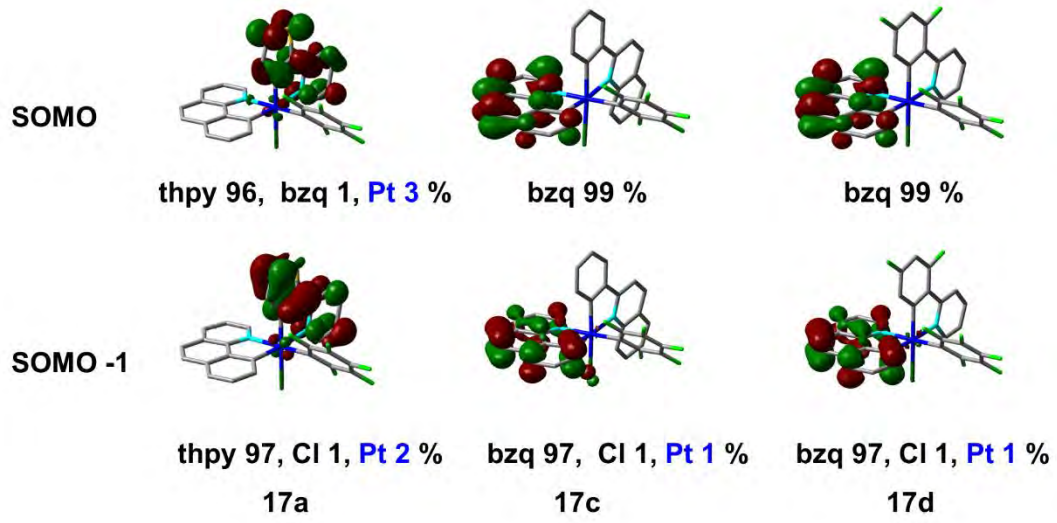

Figura A3.9. Dibujo de los orbitales SOMO y SOMO-1 en el estado triplete obtenidos por DFT para **17a**, **17c** y **17d** en fase gas

Chapter 4

Heterobimetallic Pt(II)-Au(I) complexes

Heterometallic complexes (with two or more different metal centers in their structure) have been widely studied for many research groups and nowadays they continue captivating chemists because of their interesting structural features, reactivity and potential applications. These systems not only have displayed fascinating photochemical and photophysical properties,[18a, 27] but have also showed promising potential as catalytic systems[151] and anticancer drugs.[152]

In cancer therapy, the monometallic platinum compound *cis*-$[Pt(NH_3)_2Cl_2]$ (cisplatin),[109] was discovered as the most powerful chemotherapeutic agent against ovarian, testicular head, neck and small-cell lung cancer. As we have commented in **Chapter 2**, cisplatin and its analogues (carboplatin and oxaliplatin),[110] whose mechanism consists in forming different Pt-DNA adducts by DNA binding,[111a] are nowadays the most widely used drugs for cancer treatment.[110a] However, their severe toxic and side effects (nephrotoxicity, neurotoxicity, etc), the development of acquired resistance and their limited spectrum of action has triggered the interest on the study of alternative metal-based anticancer drugs.[153] Thus, a great number of non-platinum monometallic complexes have been developed and some of them have been approved in clinical trials.[14h, 154] For example, Ru(III) complexes NAMI-A and KP1019 have shown promising results from phase I clinical test and the phosphine-gold(I)-thiolate complex (auranofin), which has been used for over 30 years for the treatment of rheumatoid arthritis, has also shown promising potential as anticancer agent recently (Figure 4.1).[155] Gold compounds - either gold(III) or gold(I) - have also gained attention as promising cancer chemotherapeutic agents.[156] Indeed, several gold complexes have demonstrated potent tumour cell grown inhibitory properties with lower cytotoxicity and fewer side effects.[152b, 157] Their mechanism of action generally relies on the reaction with protein targets and many of them inhibit the enzyme thioredoxin reductase (TrxR) with high potency and specificity.[157b, 158]

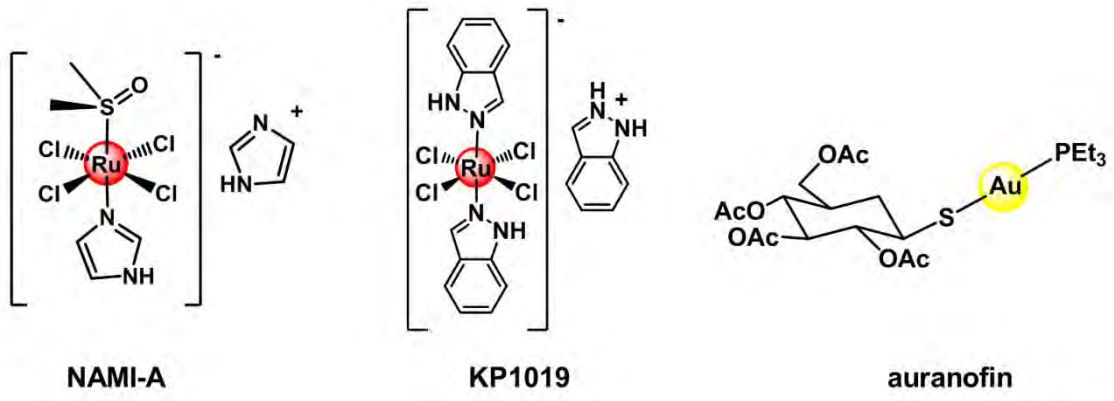

Figure 4.1. Some metallic drugs approved and in clinical trials.

On the other hand, polynuclear complexes, *i.e.*, two or more metal centers connected through an appropriate linker, appeared as a new approach to introduce new modes of action to overcome chemoresistant cancers.[159] In this context, a growing number of multinuclear complexes have been reported,[152b, 159-160] including polynuclear derivatives containing platinum.[161] Heterometallic compounds have also been developed to improve the anticancer properties of single metallodrugs.[158, 162] The principal hypothesis was established by A. Casini and co-workers and supports the idea of that the presence of two different metal-based compounds into one system may enhance their anticancer properties thanks to the multiplication of the potential biological targets and to the new synergic and/or cooperative physicochemical properties of the bimetallic species (Figure 4.2).[163]

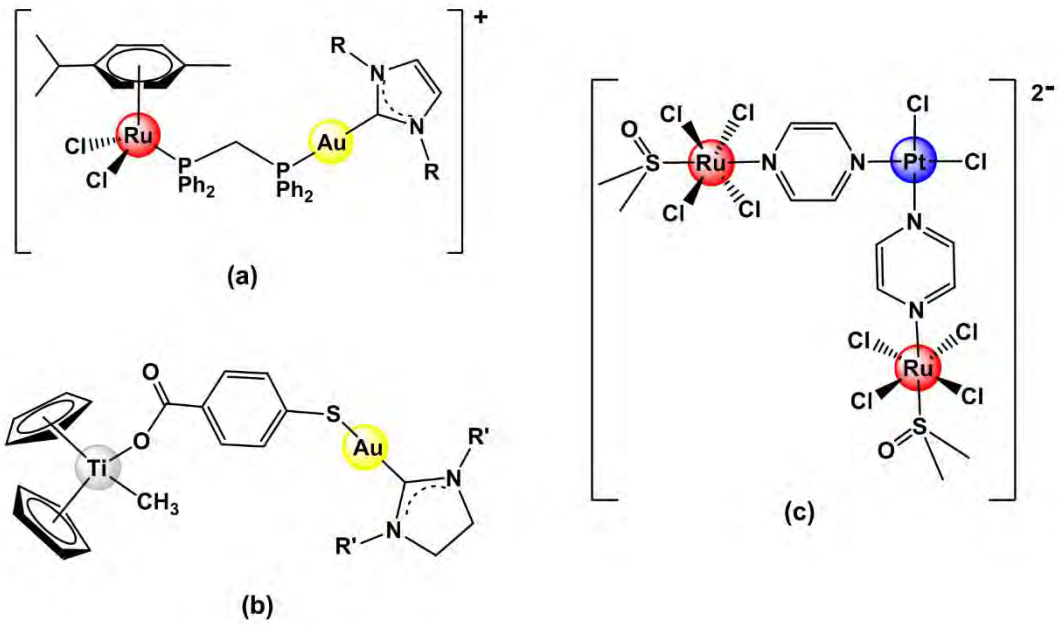

Figure 4.2. Some heterobimetallic complexes with anticancer properties.

Within this area, gold and platinum derivatives have revealed to be two of the most cytotoxic metallodrugs and they seem to have different mechanisms of action. Therefore, it is reasonable to think that the combination of both fragments could give rise to interesting bimetallic complexes with biomedical and/or photophysical properties. Based on this idea, some Pt(II)-Au(I) complexes have been recently reported displaying remarkable cytotoxic properties (Figure 4.3).[158, 164]

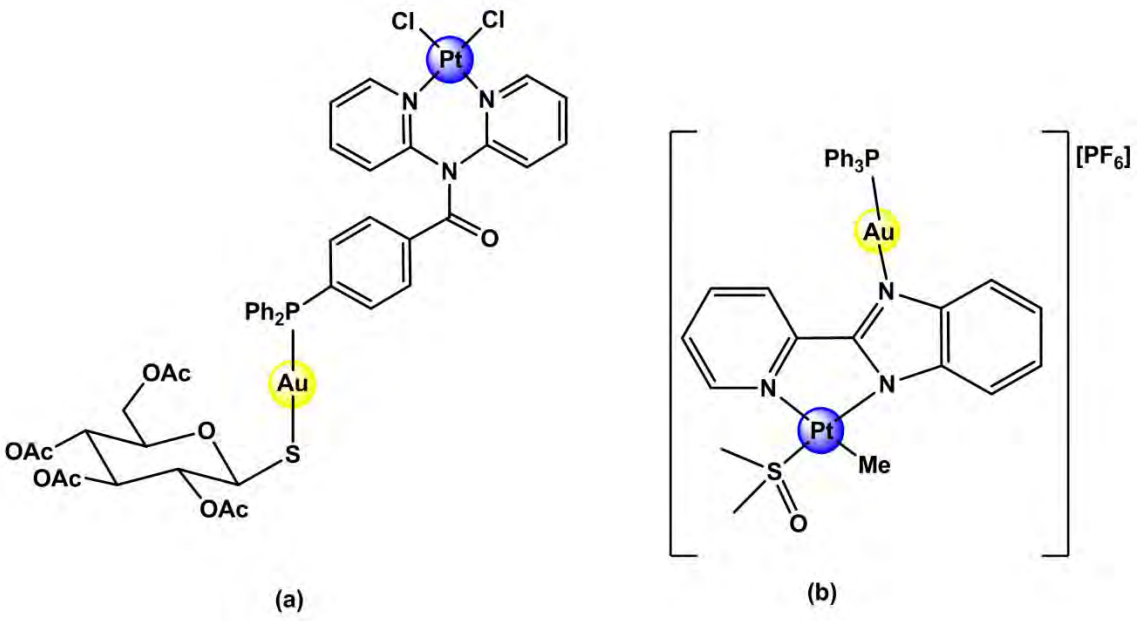

Figure 4.3. Highly cytotoxic Pt(II)-Au(I) compounds.

In ocassions, the reported metallodrugs display also luminescent properties due to the presence of organic luminophores in their structure, which allow their visualization by fluorescence or confocal microscopy. Indeed, these techniques are one of the most explored strategies to achieve metal-compounds imaging due to their sensitive detection, which reveals information about the mechanism of action of multiple drugs.[152b] In this area, several interesting luminescent heterometallic compounds displaying not only cytotoxic activity but also providing information about their internalization, mechanism, localization, bio-distribution and biological targets have been developed.[162e, 165]

In the goal of bimetallic complexes, the choice of the appropriate binding ligands to link the metal centers is important in order to ensure their stability and also to prevent the formation of undesirable products. Within this frame, the 1,1-bis(diphenylphosphanyl)methane (dppm) ligand has special interest for its use as binding ligand. In mononuclear complexes, the dppm is under strain when acts as a chelated

ligand caused by the formation of a four-membered ring. Thus, its monodentated coordination is favoured and permits the binding coordination to a second heterometal by the other free phosphane atom. On the other hand, the presence of a short chain between the phosphane heads holds the metal centers close allowing the interaction to each other, which may lead to changes in their properties.[166] The bonding of the monodentate κ^1-dppm ligand to a metal center and the subsequent coordination to a second metal complex unit is a reasonable strategy for the synthesis of heterobimetallic systems, which has been successfully employed (Scheme 4.1).[162f]

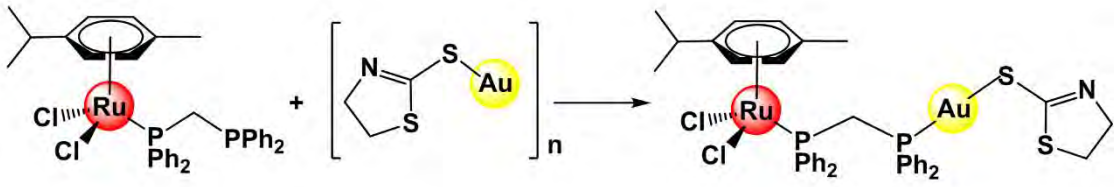

Scheme 4.1. Synthesis strategy of a binuclear complex with a dppm linker.[162f]

Following our interest in cyclometalated platinum systems with the "Pt(bzq)(C_6F_5)" fragment, we decided to prepare appropriate cyclometalated Pt(II) precursors for the subsequent synthesis of Pt(II)-Au(I) heterobimetallic complexes containing the dppm binding ligand.

In this Chapter, we describe the synthesis of the monometallic complex [Pt(bzq)(C_6F_5)(dppm)] **19** and its subsequent use as a precursor to give the new bimetallic derivative [Pt(bzq)(C_6F_5)(μ-dppm)AuCl] **20**. We also present their characterization, optical properties and theoretical calculations. This study was carried out in collaboration with the research group of Dr. Hamid R. Shahsavari, that prepared the bimetallic analogues [Pt(C^N)(*p*-MeC_6H_4)(μ-dpppm)AuCl] (C^N = bzq **20b***, ppy **20c***), featuring the *p*-MeC_6H_4 group as auxiliary ligand, using the monometallic derivatives [Pt(C^N)(*p*-MeC_6H_4)(κ^1-dppm)] (C^N = bzq **19b***, ppy **19c***)[167] as precursors. The biological properties of **19** and **20** have been evaluated and compared with those of the analogues **19b*,c*** and **20b*,c***.

4.1 Synthesis and Characterization

The synthesis of the monometallic Pt(II) complexes [Pt(bzq)(C_6F_5)(dppm)] **19**, [Pt(bzq)(C_6F_5)(κ^1-dppmO)] **19-O**, and the bimetallic Pt(II)-Au(I) derivative [Pt(bzq)(μ-dppm)(C_6F_5)AuCl] **20** are displayed in the Schemes 4.2-4.4.

Monometallic complexes [Pt(bzq)(C_6F_5)(dppm)(C_6F_5)] ***19*** *and [Pt(bzq)(C_6F_5)(κ^1-dppmO)]* ***19-O***

The synthesis of the monometallic derivative [Pt(bzq)(C_6F_5)(dppm)] **19** was initially attempted by treatment of the solvate [Pt(bzq)(C_6F_5)(acetone)] with one equiv. of 1,1-bis(diphenylphosphanyl)metane (dppm) in acetone. Unfortunately, this reaction did not allow to obtain **19** as a pure product, because a complex mixture of products was formed, as observed by ^{1}H, ^{19}F{^{1}H} and ^{31}P{^{1}H} NMR spectroscopy, including the desired product **19**, the oxidized [Pt(bzq)(C_6F_5)(κ^1-dppmO)] **19-O** and also the bimetallic [Pt(bzq)(C_6F_5)(μ-dppm)]$_2$ complex.

In view of these results, we used the solvate [Pt(bzq)(C_6F_5)(dmso)], prepared by addition of dmso to a solution of [Pt(bzq)(C_6F_5)(acetone)] in Et_2O/acetone (2.5:1) (see Experimental Section), as starting product. Thus, the reaction of the solvate [Pt(bzq)(C_6F_5)(dmso)] with 1,1-bis(diphenylphosphanyl)metane (dppm) in acetone, in a 1:1 molar ratio for 30 min, gave rise to [Pt(bzq)(C_6F_5)(dppm)] **19** as a pure solid (Scheme 4.2). It should be mentioned that, when the reaction was carried out in CH_2Cl_2, a mixture of **19** and side products was also detected by NMR spectroscopy.

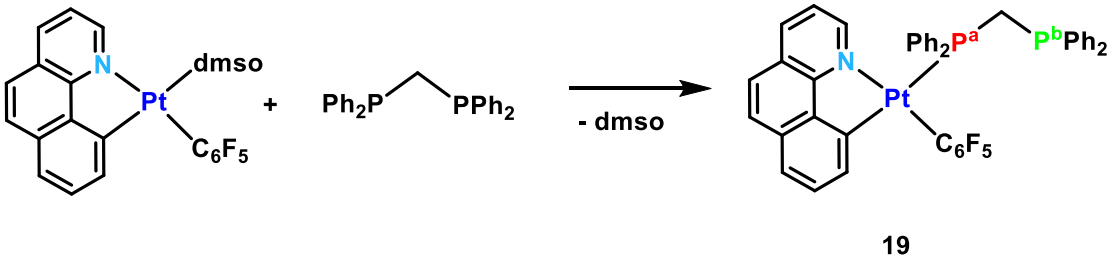

Scheme 4.2

Attempts to obtain appropriate monocrystals for X-ray diffraction studies (see below) by slow diffusion of Et_2O into a solution of **19** in CH_2Cl_2, lead to the complex [Pt(bzq)(C_6F_5)(κ^1-dppmO)] **19-O** by the oxidation of the free phosphane head, as is shown in the Scheme 4.3.

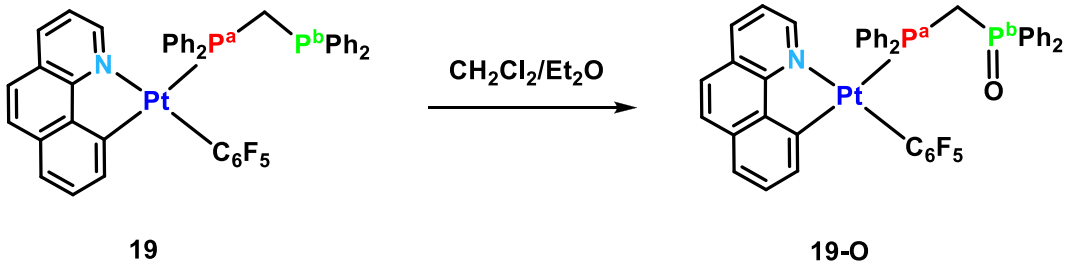

19 **19-O**

Scheme 4.3

Pt(II) **19** and **19-O** derivatives were characterized by multinuclear [^{1}H, ^{31}P{^{1}H} and ^{19}F{^{1}H}] NMR and mass spectrometry. In the ^{1}H NMR, the signal of CH_2P_2 of the dppm ligand appears at δ 3.65 in **19** and at δ 3.34 in **19-O**, with a platinum coupling constant ($^{3}J_{Pt\text{-}H}$) of 26 and 33 Hz, respectively. The complexity of the system in the aromatic region precludes a detailed and complete assignment of the signals corresponding to the bzq ligand on the basis of bidimensional ^{1}H-^{1}H (COSY, TOCSY) spectra (see Experimental Section for details). As illustration, the ^{31}P{^{1}H} NMR spectra of the complexes [Pt(bzq)(C_6F_5)(dppm)] **19** and [Pt(bzq)(C_6F_5)(κ^1-dppmO)] **19-O** are compared in the Figure 4.4. The ^{31}P{^{1}H} NMR spectrum of **19** displays the expected two different signals due to the coordinated (δ P^a 12.62) and free (δ P^b -25.3) P atoms of the dppm ligand. The most deshielded signal (P^a) appears as a doublet ($^{2}J_{P^aP^b}$ = 85 Hz) with the expected platinum satellites ($^{1}J_{PtP^a}$ = 1963 Hz), whereas the signal of P^b is resolved as a doublet ($^{2}J_{P^aP^b}$ = 85 Hz) of pseudo-triplets, due to the additional coupling to a close *o*-F of the C_6F_5 group. The oxidation of the terminal phosphorous atom in the compound **19a-O** is clearly reflected in the ^{31}P{^{1}H} NMR spectrum by a remarkable downfield shift of the P^b signal (δ 25.30), which appears as a doublet exhibiting a three-bond coupling constant to ^{195}Pt center ($^{3}J_{PtP^b}$) of 46 Hz. The signal of the P^a atom appears at similar shift with comparable $^{1}J_{PtP^a}$ coupling constant (1950 Hz) to that found for **19**, although with a decrease of the $^{2}J_{P^aP^b}$ value from 85 to 13 Hz.

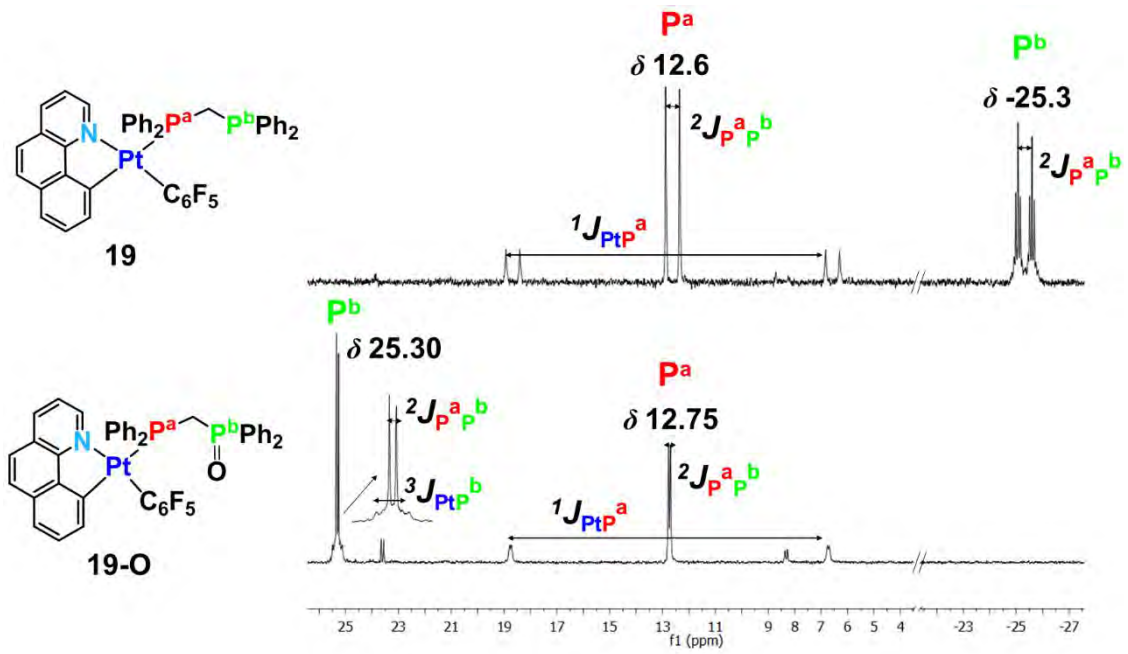

Figure 4.4. $^{31}P\{^1H\}$ NMR spectra of the complexes [Pt(bzq)(C_6F_5)(dppm)] **19** and [Pt(bzq)(C_6F_5)(κ^1-dppmO)] **19-O**.

The $^{19}F\{^1H\}$ NMR spectra of **19** and **19-O** exhibit the typical AA'MXX' pattern for two *o*-F, one *p*-F and two *m*-F of the C_6F_5 ring, indicating a free rotation of the ring. A relatively high $^3J_{Pt\text{-}oF}$ (496 **19**, 490 Hz **19-O**) coupling constant is observed, thus supporting the *trans* disposition of the C_6F_5 group relative to the N-atom of the bzq cyclometalated ligand (Figure 4.5).

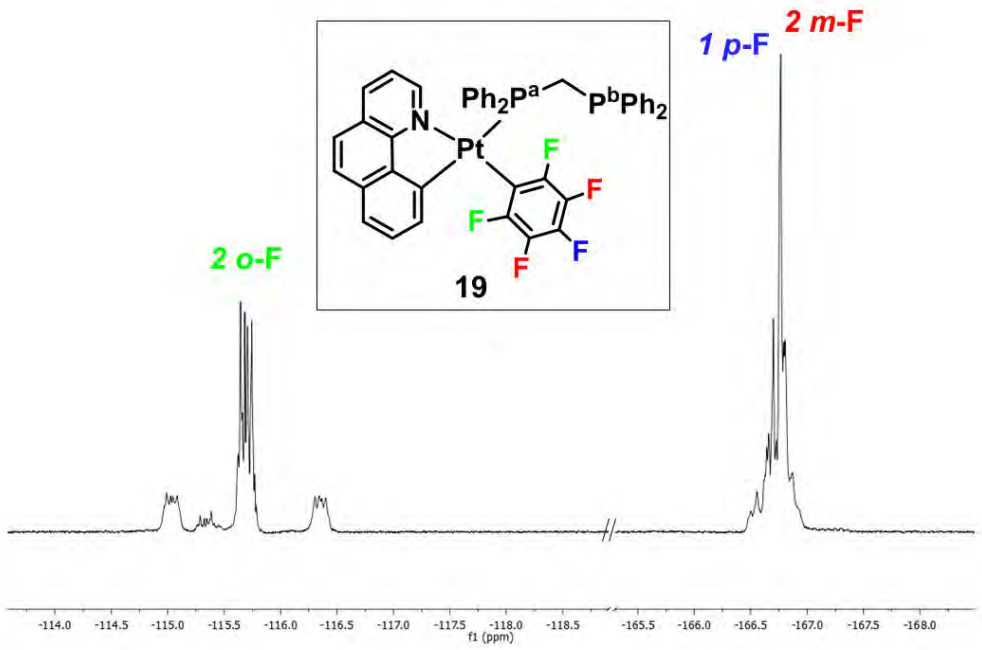

Figure 4.5. $^{19}F\{^1H\}$ NMR spectrum of [Pt(bzq)(C_6F_5)(dppm)] **19** in CD_3COCD_3.

Bimetallic complex [Pt(bzq)(C_6F_5)(μ-dppm)AuCl] ***20***

The treatment of the monometallic [Pt(bzq)(C_6F_5)(dppm)] **19** with one equiv. of the Au precursor complex [AuCl(SMe_2)],[168] at -50ºC in CH_2Cl_2 for 10 min yielded the bimetallic complex [Pt(bzq)(C_6F_5)(μ-dppm)AuCl] (**20**) (Scheme 4.4) as a pure yellow solid. However, when the reaction was performed at room temperature, a mixture of products were detected by NMR spectroscopy.

Scheme 4.4

The heterometallic [Pt(bzq)(C_6F_5)(μ-dppm)AuCl] **20** derivative was characterized by ESI(+), elemental analysis and NMR spectroscopy. The molecular peak for **20** is related to $[M+Na]^+$ fragment. The NMR signals were assigned on the basis of ^1H, $^{19}F\{^1H\}$, $^{31}P\{^1H\}$, ^1H-^1H (COSY, TOCSY) NMR spectra. The signal of the CH_2 of the dppm group was undoubtedly detected, appearing at 3.63 ppm with slightly higher platinum satellites ($^3J_{Pt\text{-}H}$ = 34 Hz) in relation to the precursor (26 Hz). The ^1H and $^{31}P\{^1H\}$ NMR spectra are shown in the Figure 4.6. Due to the complexity of the proton spectra in the aromatic zone, only some signals of the bzq ligand could be assigned (Figure 4.6a). The most significant feature in their $^{31}P\{^1H\}$ NMR spectrum is observed in the P^b resonance, which shifts downfield in relation to the precursor **19** (δ P^b 19.07 **20** *vs* -25.3 **19**) due to the coordination to Au(I), whereas the one-bond coupling constant P^a-Pt is slightly reduced ($^1J_{PtP^a}$ 1890 **20** *vs* 1963 Hz **19**) (Figure 4.6b). Its $^{19}F\{^1H\}$ NMR spectrum shows the three-signals pattern for the C_6F_5 group, with a $^3J_{Pt\text{-}oF}$ of 475 Hz indicating, as for **19** and **19-O**, the *trans* disposition of the C_6F_5 group relative to the N atom of the bzq ligand.

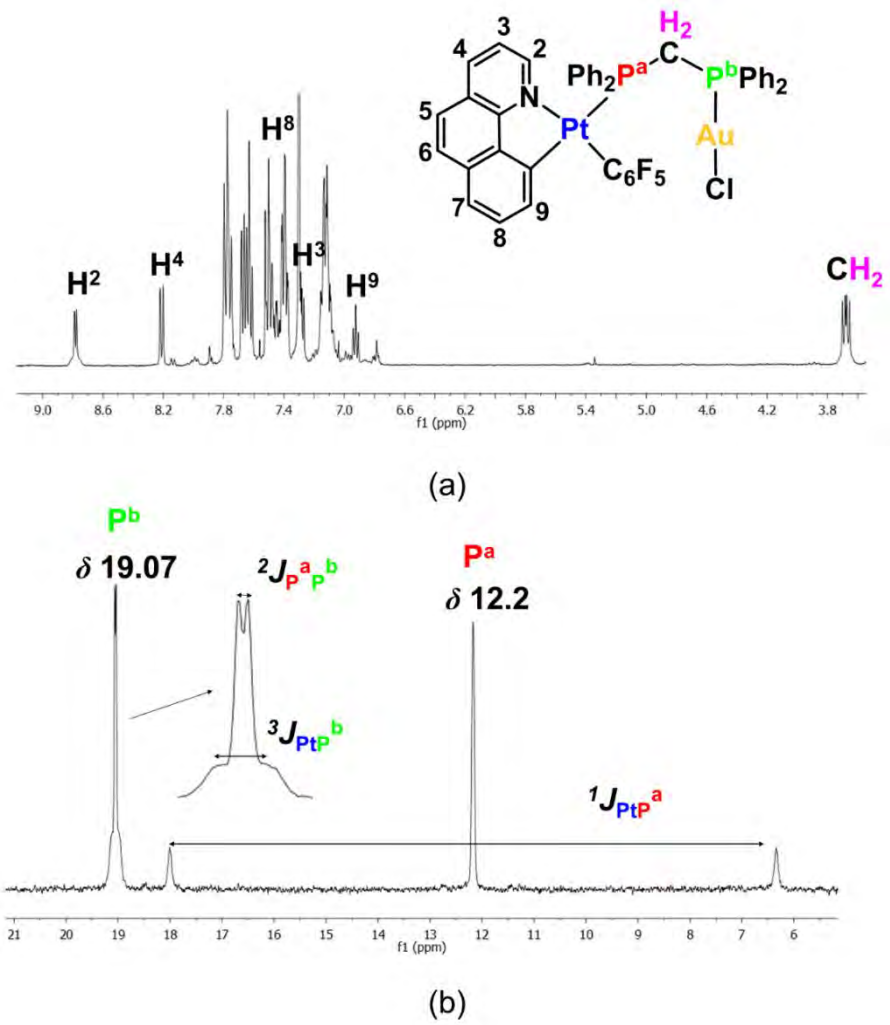

Figure 4.6. (a) ^{1}H and (b) ^{31}P{^{1}H} NMR spectra in $CDCl_3$ of the complex [Pt(bzq)(C_6F_5)(μ-dppm)AuCl] **20**.

4.2 Crystal structures

The structures of complexes **19-O**·Et_2O and **20**·2.5CH_2Cl_2 were stablished by X-ray crystallography (Figures 4.7- 4.9 and Tables 4.1 and 4.2). Even though the compound **19** is stable in the solid state, crystals of **19-O**, in which the free P head of the dppm group is oxidized, were separated during attempts to obtain suitable crystals for X-ray diffraction study of **19** in CH_2Cl_2/Et_2O.

The structure of [Pt(bzq)(C_6F_5)(κ^1-dppmO)] **19a-O** (Figure 4.7) confirms the square-planar coordination environment for the Pt(II) center and the presence of the pendant free phosphane. The bonds and angles are in accordance to those of the related cyclometalated Pt(II) compounds.[48, 169] As we have observed in other compounds described in this Thesis, the C-*ipso* atom (C14) of the C_6F_5 group and the N atom (N1) of

the bzq ligand show a mutually *trans* disposition. The P2-O1 bond length [1.484(2) Å] and the O1-P2-C angles [112.7(1)-113.5(1)º] of the terminal dppm-O ligand are in the range of those observed for terminal phosphane oxides.[170] The dppm group is inclined forming an angle of 63.13º between the Pt coordination plane and the P1-C44-P2 plane, locating the O1 atom in a long distance to the platinum center [O1···Pt1 4.858(2) Å]. It should be pointed out that one phenyl ring coordinated to the P2 atom of the dppm group lies above the cycloplatinaned bzq ligand, close to the Pt atom, with a Pt-C43 distance [3.472(4) Å] close to the Van der Waals limit (3.42 Å),[97] suggesting some degree of Pt···π_{phenyl} interaction.

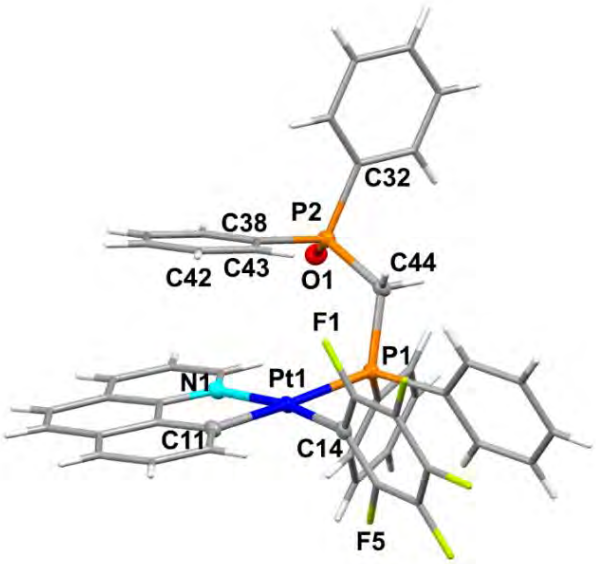

Figure 4.7. Molecular structure of [Pt(bzq)(C_6F_5)(κ^1-dppmO)] **19a-O**.

Table 4.1. Selected distances (Å) and angles (°) for **19-O**·Et_2O

19-O·Et_2O			
Distances (Å)		**Angles (°)**	
Pt(1)-N(1)	2.113(3)	N(1)-Pt(1)-C(11)	80.6(1)
Pt(1)-C(11)	2.055(3)	C(11)-Pt(1)-C(14)	90.5(1)
Pt(1)-P(1)	2.3238(8)	C(14)-Pt(1)-P(1)	88.93(9)
Pt(1)-C(14)	2.008(3)	P(1)-Pt(1)-N(1)	100.32(8)
P(2)-O(1)	1.484(2)	P(1)-C(44)-P(2)	121.1(2)
P(2)···Pt(1)	4.2684(9)	O(1)-P(2)-C(44)	113.5(1)
O(1)···Pt(1)	4.858(2)	O(1)-P(2)-C(32)	112.7(1)
O(1)···F(1)	6.652 (3)	O(1)-P(2)-C(38)	113.0(1)
C(38)···Pt(1)	3.811(3)		
C(43)···Pt(1)	3.472(4)		
C(42)···Pt(1)	3.980(4)		

The supramolecular packing of the complex **19-O** (Figure 4.8) shows the formation of dimers with intermolecular π···π interactions between the cyclometalated groups (3.398-3.445 Å) (pink lines), supported by secondary O···H_{Ph} (2.618 Å) and F_{C6F5}···H (2.564 Å) secondary contacts (blue lines).

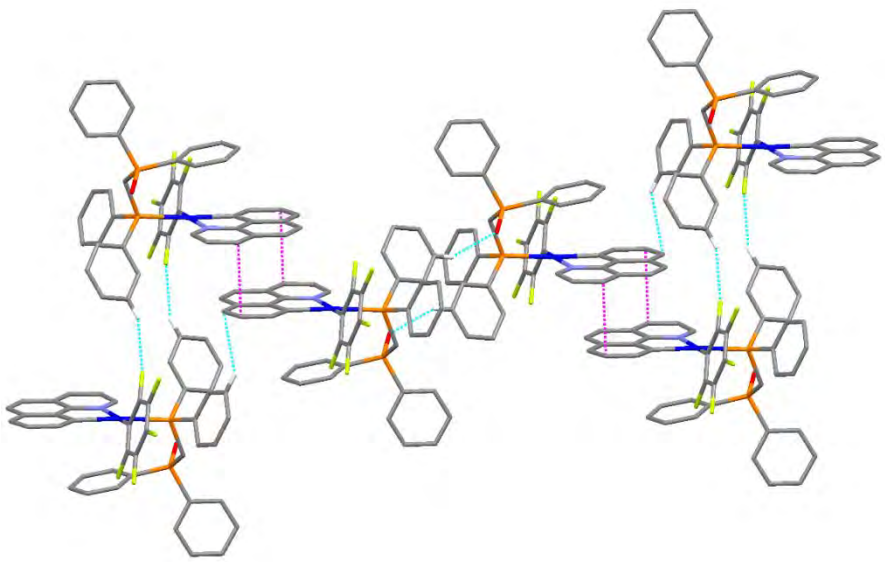

Figure 4.8. Crystal packing of [Pt(bzq)(C_6F_5)(κ^1-dppmO)] **19-O**·Et_2O.

The X-ray structure of the heterobimetallic complex [Pt(bzq)(C_6F_5)(μ-dppm)AuCl] **20**·2.5CH_2Cl_2 confirms the coordination of the AuCl unit to the P2 of the dppm ligand of the precursor **19**, which is acting as a bridging group between the Pt and Au metal centers (Figure 4.9). The steric hindrance of the bulky C_6F_5 group likely affects to the orientation of the P-Au-Cl in relation to the planar Pt(II) moiety, being situated in opposite side, with a long Pt-Au distance (5.375 Å), excluding any metallophilic interaction.

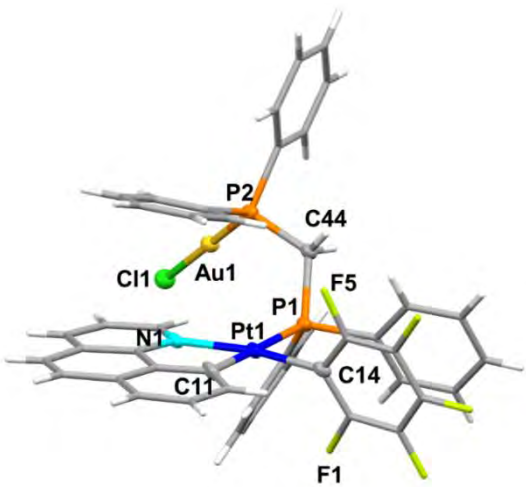

Figure 4.9. Molecular structure of [Pt(bzq)(C_6F_5)(μ-dppm)AuCl] **20**.

Table 4.2. Selected distances (Å) and angles (°) for **20**·2.5CH_2Cl_2.

20·2.5CH_2Cl_2			
Distances (Å)		**Distances (Å)**	
Pt(1)-N(1)	2.117(7)	N(1)-Pt(1)-C(11)	80.0(3)
Pt(1)-C(11)	2.035(8)	C(11)-Pt(1)-C(14)	90.7(4)
Pt(1)-C(14)	1.997(9)	C(14)-Pt(1)-P(1)	88.7(2)
Pt(1)-P(1)	2.3405(19)	P(1)-Pt(1)-N(1)	100.80(19)
Au(1)···Pt(1)	5.3752(5)	P(1)-C(44)-P(2)	122.1(5)
Cl(1)···Pt(1)	6.931(2)		

The molecular packing of **20** (Figure 4.10) is similar to that found for the monometallic derivative **19-O**, showing dimers supported by intermolecular π···π contacts between the bzq cyclometalated groups (3.268-3.333 Å) (pink lines), reinforced by H_{Ph}···Cl (2.744-2.882 Å), H_{Ph}···F_{C6F5} (2.550 Å), H_{Ph}···CPh and H_{Ph}···C_{bzq} (2.784-2.875 Å) secondary interactions (blue lines).

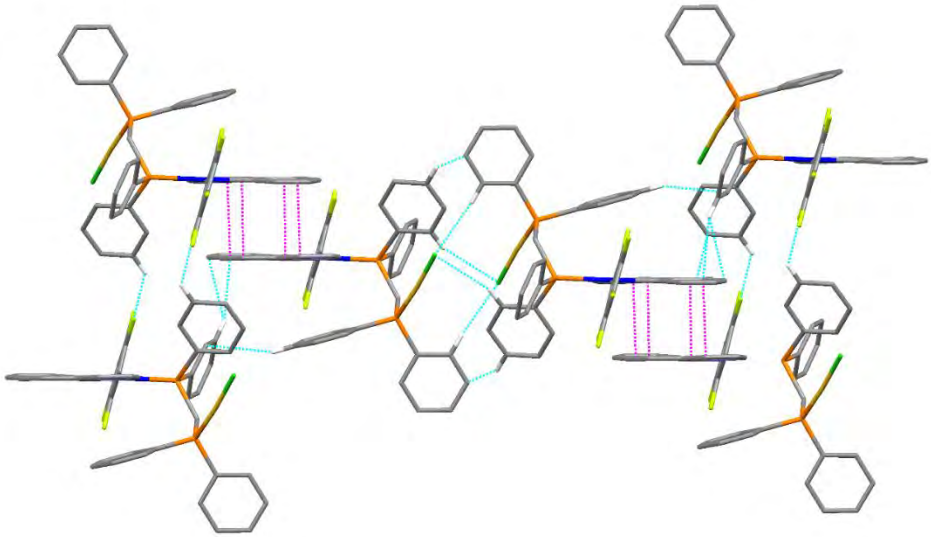

Figure 4.10. Crystal packing of [Pt(bzq)(C_6F_5)(μ-dppm)AuCl] **20**·2.5CH_2Cl_2

4.3 Photophysical properties

4.3.1 Absorption spectroscopy

The electronic absorption spectra of **19** and **20** were recorded in CH_2Cl_2 5×10^{-5} M solutions and in solid state (Table 4.3, Figures 4.11 in solution and A4.1 in the solid state).

Table 4.3. Absorption data for compounds **19** and **20** in CH_2Cl_2 (5×10^{-5} M) solutions and in the solid state.

Compound	λ_{abs}/nm (10^3 ε/M^{-1} cm^{-1})
[Pt(bzq)(C_6F_5)(dppm)] **19**	257 (37), 302 (17), 352 (4.5), 407 (3.7); **CH_2Cl_2** 309, 352 401; **Solid**
[Pt(bzq)(C_6F_5)(μ-dppm)AuCl] **20**	268 (21), 299 (13), 355 (3), 404 (1.8); **CH_2Cl_2** 302, 357, 406; **Solid**

The UV-Vis spectra in solution for the monometallic **19** and bimetallic **20** complexes show high energy intense bands with wavelengths below 325 nm, which are attributed to π-π* intra-ligand ^{1}IL or ^{I}IL' transitions (L = bzq, L' = C_6F_5). These bands have also contributions from intra-ligand charge transfer in the phenyl rings of the dppm group (ML''CT + L''LCT, L'' = dppm), as has been confirmed by theoretical calculations (see below). Furthermore, both complexes **19** and **20** show bands in the low energy region (352, 407 nm for **19**; 355, 404 nm for **20**), which are attributed, with the aid of theoretical calculations and by comparison to related complexes,[27] to mixed ^{1}MLCT/^{1}IL transitions. As is shown in the Figures 4.11 and A4.1, the absorption spectra remain almost unaltered after the addition of the Au-Cl moiety, either in solution or in the solid state.

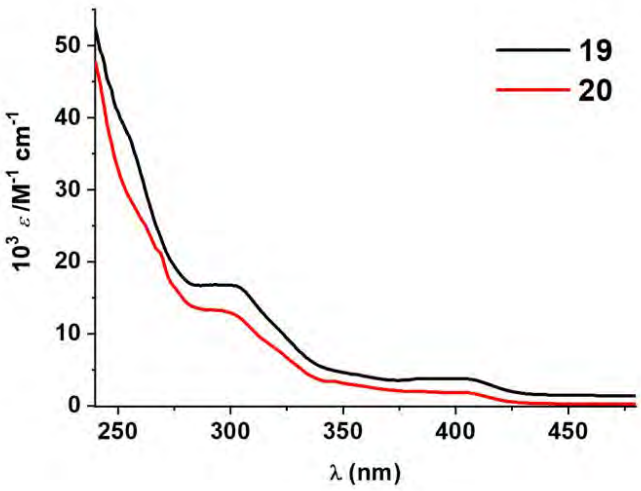

Figure 4.11. UV/Vis absorbance spectra in CH_2Cl_2 solution (5×10^{-5} M) of **19** and **20**.

4.3.2 Emission spectroscopy

The emission data of complexes [Pt(bzq)(C_6F_5)(dppm)] **19** and [Pt(bzq)(C_6F_5)(μ-dppm)AuCl] **20** in deoxygenated CH_2Cl_2 solutions and solid state are included in Table 4.4. Both compounds show structured emission bands in the green region, with large Stokes shifts and long lifetimes (μs) typical of triplet states.

The emission and excitation spectra obtained in solid are displayed in Figure 4.12 and those obtained in CH_2Cl_2 in Figure 4.13, showing essentially similar patterns for the mononuclear and heteronuclear complexes. For both derivatives, the emission band shapes and wavelengths remain unaltered by changing the excitation wavelength either at room or low temperature. In rigid media (solid and CH_2Cl_2 at 77 K), the complexes show long lifetimes, as has been previously observed in platinum complexes containing the cyclometalated bzq ligand,[46] indicating excited states of mixed ^{3}IL/^{3}MLCT nature.

Table 4.4. Photophysical data of [Pt(bzq)(C_6F_5)(dppm)] **19** and [Pt(bzq)(C_6F_5)(μ-dppm)AuCl] **20** in the solid state and CH_2Cl_2 5 × 10^{-5} M solutions.

Complex		T[a] (K)	λ_{em}/nm [a]	τ/μs	ϕ/% [b]
19	Solid	298	492_{max}, 519, 558_{sh}	8.4 (89%), 24.1 (11%)	3
		77	494_{max}, 530, 570_{sh}	532 (53%), 311 (47%)	
	CH_2Cl_2	77	478_{max}, 514, 553_{sh}	1115 (26 %), 680 (74 %)	
20	Solid	298	494_{max}, 524	10.44	2
		77	494_{max}, 533, 571_{sh}	380	
	CH_2Cl_2	298	465_{max}, 496, 520_{sh}	0.3	
		77	478_{max}, 513, 553_{sh}	1306 (8 %), 525 (92 %)	

[a] λ_{ex} 365-380 nm. [b] Absolute quantum yields determined by the absolute method using an integrated sphere.

Complexes **19** and **20** display similar structured emission in the solid state, with broader shape emission bands at room temperature (Figure 4.12). The measured quantum yields in the solid state show similar low values for both complexes (3 % **19**, 2 % **20**), which is likely attributed to a significant quenching due to the presence of *inter*molecular π···π interactions, as has been observed in the supramolecular packing of **20**. At low temperature, the emission bands become more intensified and more structured, and a remarkable increase in the luminescence lifetime is observed (Table 4.4), thus suggesting an increase of the ^{3}IL character.

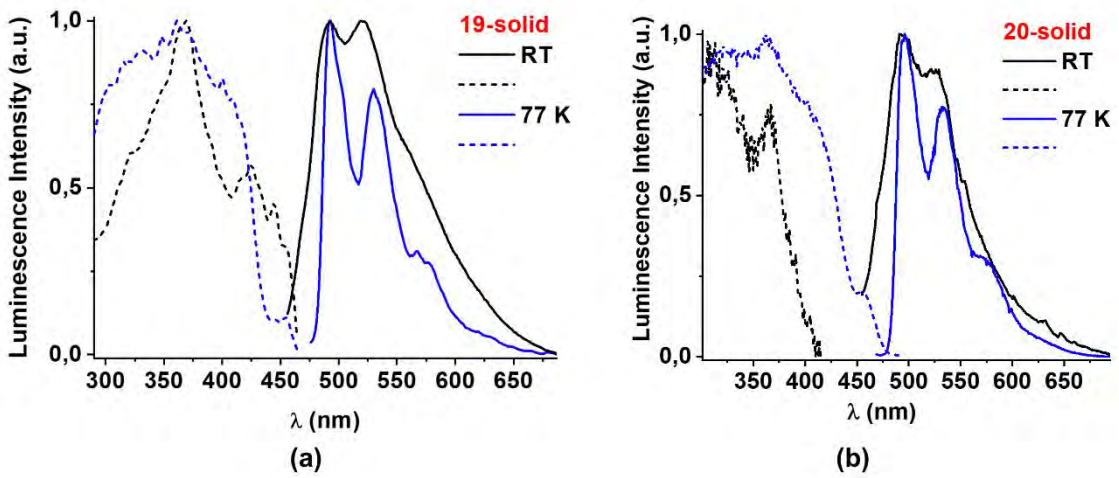

Figure 4.12. Normalized emission and excitation spectra in the solid state at 298 and 77 K of (a) [Pt(bzq)(C_6F_5)(dppm)] **19** and (b) [Pt(bzq)(C_6F_5)(μ-dppm)AuCl] **20**.

In CH_2Cl_2 solution, only the derivative [Pt(bzq)(C_6F_5)(μ-dppm)AuCl] **20** exhibits a weak emission at room temperature. However, by decreasing the temperature to 77 K, both complexes are strongly emissive showing well resolved structured phosphorescence emission bands (Figure 4.13). The lack of the luminescence in the mononuclear complex [Pt(bzq)(C_6F_5)(dppm)] **19** in relation to previously reported [Pt(bzq)(C_6F_5)L][48] complexes could be attributed to easier thermal access to non-radiative deactivation through molecular motions and non-covalent intermolecular interactions due to the presence of pendant free phosphine. It should be noted that the emission bands are slightly blue shifted in relation to those observed in the solid state [λ_{max} (77 K): 494 solid *vs* 478 nm solution in **19** and **20**].

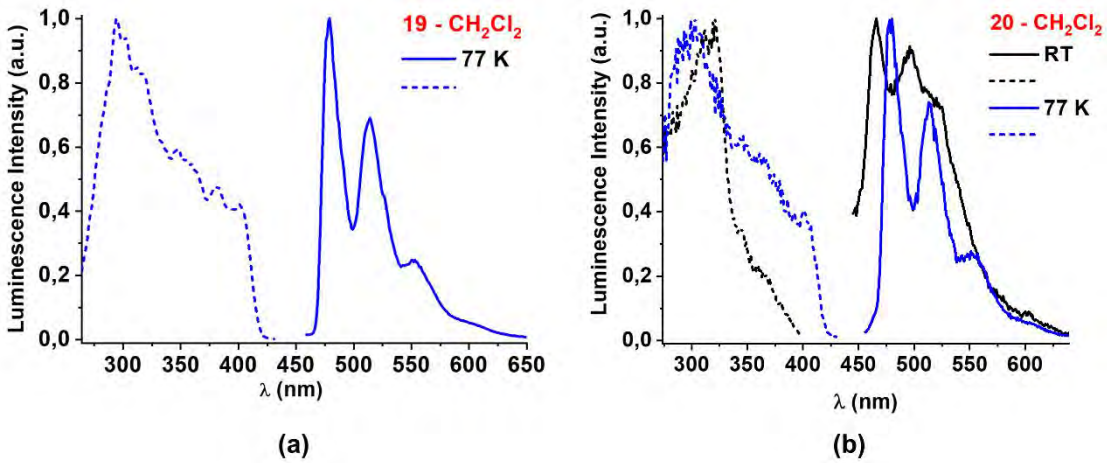

Figure 4.13. Normalized emission and excitation spectra in CH_2Cl_2 5 × 10^{-5} M of (a) [Pt(bzq)(C_6F_5)(dppm)] **19** at 77 K and (b) [Pt(bzq)(C_6F_5)(μ-dppm)AuCl] **20** at 298 K and 77 K.

4.4 Theoretical calculations

Density functional theory (DFT) and time-dependent DFT (TD-DFT) calculations have been performed for complexes **19** and **20**. The effect of the solvent (CH_2Cl_2) was taken into account using the polarized continuum model (PCM) approach. The geometries of the complexes were fully optimized without imposing any symmetry constraints. For the optimization, the available crystal structures were used directly (**20**) or indirectly (**19**) to make input files for the software. The bond distances and angles, detailed in Table A4.1, are consistent with those obtained by X-ray for **20** and the optimized structures are displayed in the Figure 4.14. Contour plots of frontier orbitals (S_0) CH_2Cl_2 are displayed in Figures A4.2, A4.3 and the molecular orbital compositions given in Tables A4.2, A4.3.

Plots of the highest occupied orbital (HOMO) and lowest unoccupied molecular orbital (LUMO) are shown in Figure 4.15.

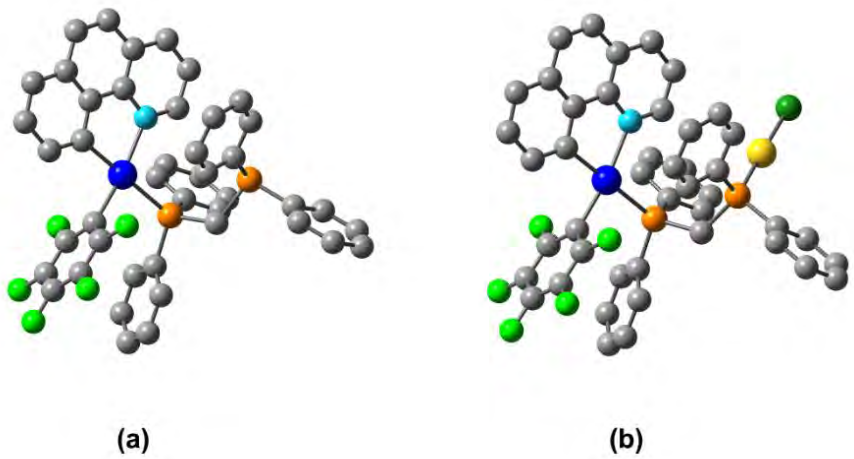

Figure 4.14. DFT-optimized geometries of (a) **19** and (b) **20** in CH_2Cl_2. Hydrogen atoms were eliminated for clarity.

As is shown for **19**, the HOMO is located mainly on the bzq (71 %) and Pt (26 %), while the LUMO and L+1 are almost completely localized on the bzq cyclometalated ligand. In the heterobimetallic complex **20**, the composition of the orbital frontiers is rather similar to its precursor **19**, being the HOMO located on the bzq (72 %) and Pt (25 %) and the LUMO on the bzq fragment. The dppm ligand has an important contribution in the L+2 orbital (84 %) and from L+4 to L+9 (82 to 65 %) in **19**, while in **20** this group has a 59 to 87 % of contribution in the L+1 to L+8 orbitals. However, the Au-Cl fragment has almost negligible contribution in most of the MOs in the heterometallic complex **20**.

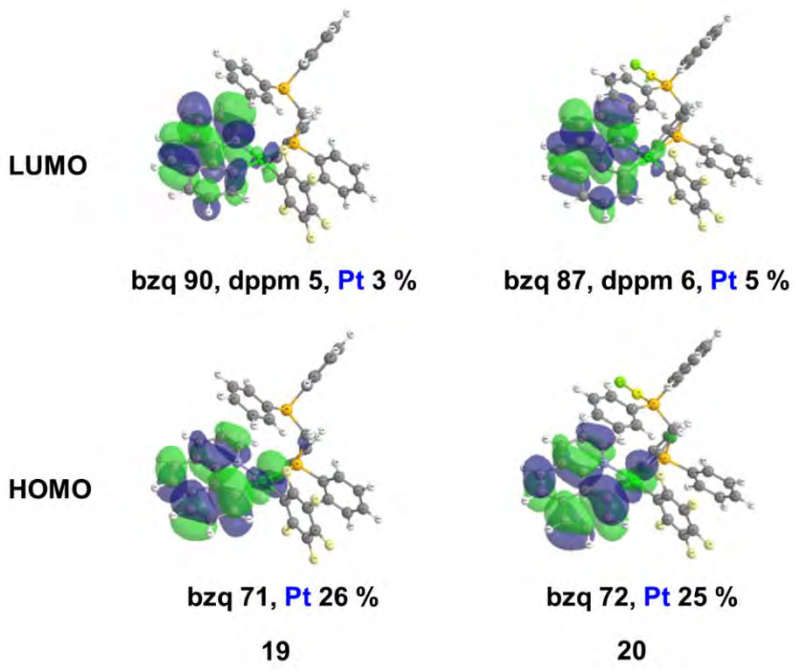

Figure 4.15. Plots of HOMO and LUMO for **19** and **20**.

Selected singlets excitations calculated by TD-DFT at their optimized S_0 geometry in CH_2Cl_2 with detailed descriptions of absorption wavelength, oscillator strength and transition assignments are collected in Table A4.4. For comparison, the calculated singlet excitations and the corresponding experimental absorption spectra are shown in Figure 4.16. In both complexes, the first calculated excitation $S_0 \rightarrow S_1$ is mainly an HOMO to LUMO transition (λ_{calcd} = 379 nm), having similar oscillator strength (0.054). Thus, this transition can be ascribed as a mixed ^{1}ILCT/^{1}MLCT (L = bzq, M = Pt) transition. As expected, the dppm ligand participates in electronic transitions at higher energies in ML''CT and L''LCT transitions (L'' = dppm) (see Table A4.4), but the ^{1}ILCT character still has an outstanding presence. However, the Au-Cl fragment does not participate in any electronic transitions and the C_6F_5 group has a negligible contribution in the electronic transitions of both complexes.

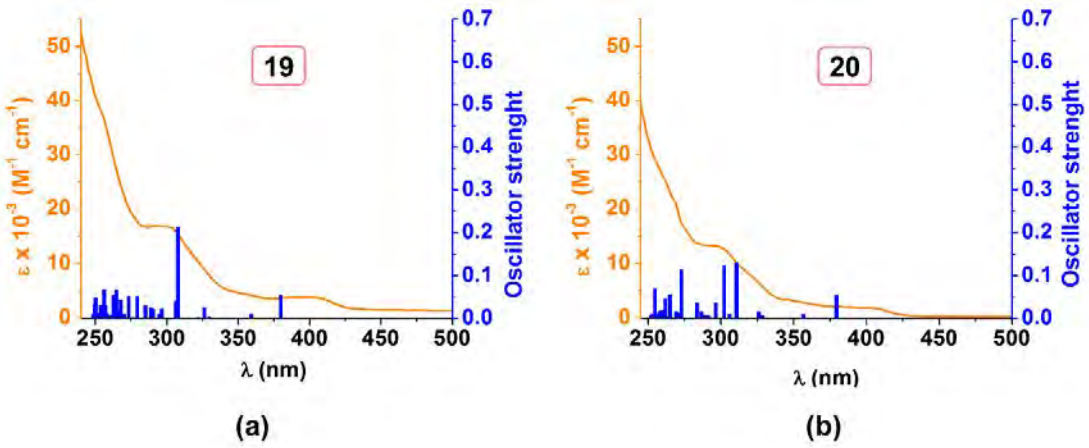

Figure 4.16. Calculated stick absorption spectra of (a) [Pt(bzq)(C_6F_5)(dppm)] **19** and (b) [Pt(bzq)(C_6F_5)(μ-dppm)AuCl] **20**.

4.5 Biological Activity Studies

As we have commented in the Introduction of this Chapter, the synthesis and characterization of both complexes **19** and **20** was carried out as a part of a collaboration with Dr. Shahsavari's lab, in which the series of analogues monometallic [Pt(C^N)(*p*-MeC_6H_4)(κ^1-dppm)] (C^N = bzq **19b***, ppy **19c***)[167] and bimetallic [Pt(C^N)(*p*-MeC_6H_4)(μ-dppm)Au(Cl)] (C^N = bzq **20b***, ppy **20c***) complexes were also studied (Figure 4.17).

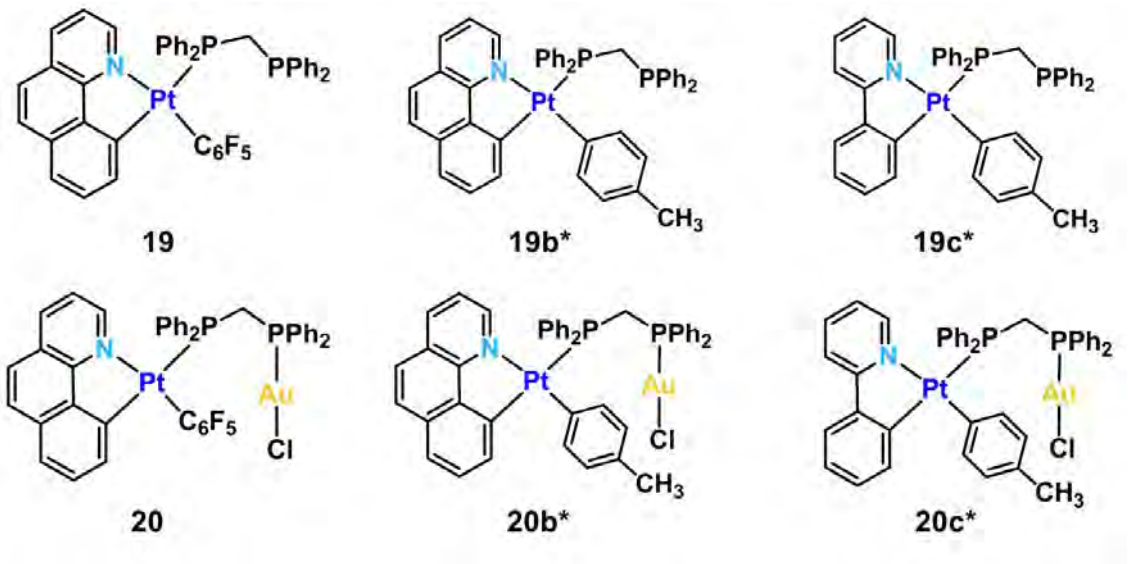

Figure 4.17

In this collaboration, the *in vitro* cyctotoxic activity of **19**, **19b*,c*** and **20**, **20b*,c*** complexes were evaluated on three human cancer cell lines, MCF-7 (breast

cancer), SKOV3 (ovarian cancer), and A549 (non-small cell lung cancer). Besides, non-tumorigenic epithelial breast cell line (MCF-10A) was used to investigate the selectivity between cancer and normal cell lines. For comparison, the cytotoxic activity of cisplatin, Auranofin and [ClAu(μ-dppm)AuCl],[168] as a model complex for "AuClP" unit, were also evaluated against those cell lines (Table 4.5).

As shown in Table 4.5, the series of mononuclear platinum complexes **19**, **19b***,**c***, as well as the compound [ClAu(μ-dppm)AuCl], exhibit low potency in inhibiting cell proliferation. However, in all cases, the heterobimetallic Pt(II)-Au(I) **20**, **20b*,c*** derivatives show an improvement of the IC_{50} (drug concentrations required to inhibit cell growth by 50%) values in comparison to their monometallic precursors, suggesting a cooperative effect of both metal fragments.

The bimetallic compound [Pt(bzq)(*p*-MeC_6H_4)(μ-dppm)Au(Cl)] **20b*** display the best anti-proliferative activity, showing lower IC_{50} values than cisplatin (5.47 μM, 10.73 μM, 2.27 μM **20b*** *vs* 9.63 μM, 15.66 μM, 11.34 μM cisplatin) against the three cancer cell lines A549, SKOV3 and MCF-7, respectively. Besides, its cytotoxicity improves with respect to Auranofin for A549 and MCF-7 cell lines.

Table 4.5. *In vitro* cytotoxic activity against non-small cell lung cancer (A549), ovarian cancer (SKOV3), breast cancer (MCF-7) and non-tumorigenic epithelial breast cell line (MCF-10A).

	IC_{50} (μM ± SD)			
Complex	**A549**	**SKOV3**	**MCF-7**	**MCF-10A**
19	>100	>100		>100
19b*	>100	>100	>100	>100
19c*	>100	>100	>100	>100
20	86.32 ± 2.17	95.16 ± 2.71	78.52 ± 1.38	>100
20b*	5.47 ± 1.32	10.73 ± 1.72	2.27 ± 0.16	>100
20c*	8.51 ± 1.82	18.92 ± 0.28	3.89 ± 0.29	>100
cisplatin	9.63 ± 1.39	15.66 ± 1.34	11.34 ± 1.52	>100
Auranofin	6.14 ± 1.06	6.28 ± 0.67	5.17 ± 0.34	-
[ClAu(μ-dppm)AuCl]	>100	>100	85.31 ± 1.27	-

Although [Pt(ppy)(*p*-MeC_6H_4)(μ-dppm)Au(Cl)] **20c*** also exhibits a higher anti-proliferative activity than cisplatin (against A549, MCF-7) and Auranofin (against MCF-7), it shows, in all cases, higher IC_{50} values than **20b*** (**20c*/20b***: 8.51/5.47 A549; 18.92/10.73 SKOV3; 3.89/2.27 MCF-7). This indicates that the presence of the bzq ligand (in **20b***) has a greater effect on the cytotoxicity than the ppy ligand (in **20c***). On the other hand, it is clearly observed that the presence of the *p*-MeC_6H_4 coordinated to the

Pt(II) center in **20b*** and **20c*** improves notably the cytotoxic properties in comparison to the C_6F_5 ligand in **20** (Table 4.5).

All the compounds show higher anti-proliferative activity on the cancer cell lines in comparison to those found on the non-tumorigenic epithelial breast cell line (MCF-10S), suggesting good selectivity of the compounds between the tumorigenic and non-tumorigenic cell lines. The selectivity is undoubtedly observed for the compounds **20b*** and **20c***, which show very cytotoxic values in the breast cancer cell lines MCF-7 (IC_{50} = 2.27 μM **20b***, 3.89 **20c***), while the IC_{50} value found for the non-tumorigenic epithelial breast cell line (MCF-10A) is >100 μM in both cases. These data suggest that **20b*** and **20c*** show greater specifity toward human breast cancer cells with less damage to normal epithelial breast cells.

On the other hand, intracelular localization by fluorescence microscopy experiments were assesed for the bimetallic complex [Pt(bzq)(C_6F_5)(μ-dppm)AuCl] **20** containing the C_6F_5 ligand, which is the only compound emissive in solution at 298 K. As illustrated in Figure 4.18 and A4.4, the MCF-7 cells treated with 1000 μM of **20** for 4 hours show greenish light emission. As can be observed, compound **20** efficiently penetrates into the cells, mostly localized in the nucleus with less dispersion in the cytoplasm of MCF-7 cells.

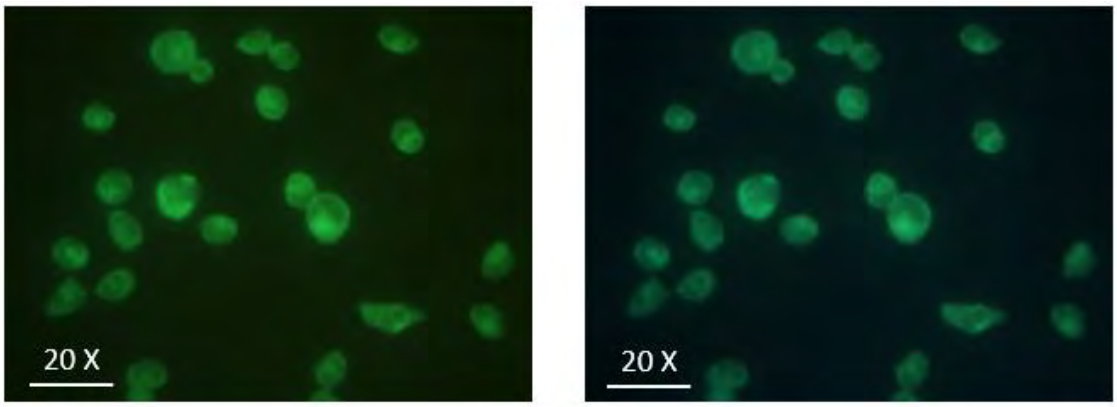

Figure 4.18. Selected fluorescence images of MCF-7 cells treated with complex **20**. Images were taken at 20 X magnification.

4.6 Appendix

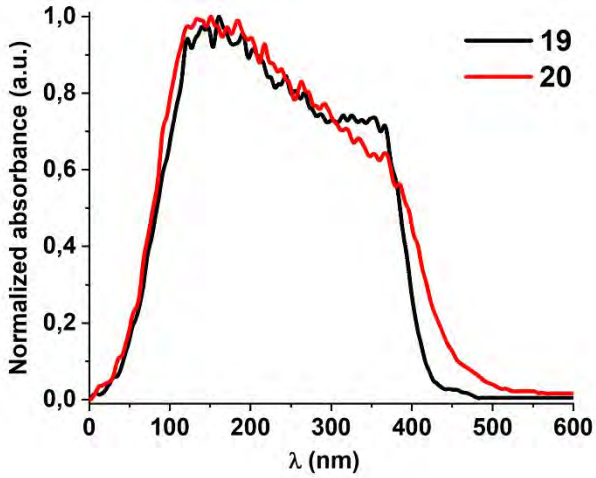

Figure A4.1. DRUV (diffuse reflectance UV/Vis) spectra of **19** and **20** complexes in the solid state.

Table A4.1. Bond distances and angles for the optimized geometries of [Pt(bzq)(C_6F_5)(dppm)] **19** and [Pt(bzq)(C_6F_5)(μ-dppm)AuCl] **20** in CH_2Cl_2.

19			
Distances (Å)		**Angles (°)**	
Pt(1)-N(1)	2.18432	C(11)-Pt(1)-N(1)	79.85228
Pt(1)-C(11)	2.04865	N(1)-Pt(1)-P(1)	99.89494
Pt(1)-P(1)	2.44068	P(1)-Pt(1)-C(14)	88.98576
Pt(1)-C(14)	2.02665	C(14)-Pt(1)-C(11)	91.26777
P(1)-C(44)	1.86690	N(1)-Pt(1)-C(14)	171.1182
C(44)-P(82)	1.88493	P(1)-Pt(1)-C(11)	179.6331
		Pt(1)-P(1)-C(44)	115.8086
		P(1)-C(44)-P(2)	117.7904
20			
Distances (Å)		**Distances (Å)**	
Pt(1)-N(1)	2.18456	N(1)-Pt(1)-C(11)	79.79776
Pt(1)-C(11)	2.04798	C(11)-Pt(1)-C(14)	90.66314
Pt(1)-C(14)	2.02828	C(22)-Pt(1)-P(1)	89.31184
Pt(1)-P(1)	2.44909	P(1)-Pt(1)-N(1)	100.2118
P(1)-C(44)	1.88049	C(11)-Pt(1)-P(1)	179.0859
C(44)-P(2)	1.85920	C(22)-Pt(1)-N(1)	170.4198
P(2)-Au(1)	2.31265	Pt(1)-P(1)-C(44)	117.8495
Au(1)-Cl(1)	2.39637	P(1)-C(44)-P(2)	123.8110
		C(44)-P(2)-Au(1)	115.5315
		P(2)-Au(1)-Cl(1)	177.2288

Table A4.2. Composition (%) of Frontier MOs in the ground state for complex **19** in CH_2Cl_2.

MO	eV	Pt	bzq	dppm	C_6F_5
LUMO+10	-0.127	25	15	31	29
LUMO +9	-0.204	2	31	65	2
LUMO +8	-0.249	10	10	72	8
LUMO +7	-0.308	3	8	88	1
LUMO +6	-0.458	6	9	81	4
LUMO +5	-0.524	2	14	82	2
LUMO +4	-0.682	9	6	82	2
LUMO +3	-0.756	8	86	3	3
LUMO +2	-0.924	4	11	84	1
LUMO +1	-1.254	3	80	16	1
LUMO	-1.811	3	90	5	2
HOMO	-5.750	26	71	0	3
HOMO -1	-6.055	70	9	8	12
HOMO -2	-6.162	29	3	18	50
HOMO -3	-6.225	12	3	80	5
HOMO -4	-6.345	23	60	2	15
HOMO -5	-6.422	4	8	2	86
HOMO -6	-6.604	10	32	55	2
HOMO -7	-6.779	68	23	4	6
HOMO -8	-6.917	36	22	41	1
HOMO -9	-6.971	11	9	80	0
HOMO -10	-6.991	13	11	74	1

Table A4.3. Composition (%) of Frontier MOs in the ground state for complex **20** in CH_2Cl_2.

MO	eV	Pt	bzq	dppm	C_6F_5	Au-Cl
LUMO+10	-0.288	1	6	74	2	17
LUMO +9	-0.379	13	15	46	8	18
LUMO +8	-0.510	3	1	87	0	9
LUMO +7	-0.576	10	11	71	4	3
LUMO +6	-0.678	1	4	73	0	22
LUMO +5	-0.827	13	7	72	5	3
LUMO +4	-1.023	2	10	82	0	6
LUMO +3	-1.124	1	2	66	0	31
LUMO +2	-1.223	2	33	62	0	3
LUMO +1	-1.361	1	37	59	1	2
LUMO	-1.876	5	87	6	0	2
HOMO	-5.813	25	72	3	0	0
HOMO -1	-6.144	71	9	6	14	0
HOMO -2	-6.247	40	2	6	51	0
HOMO -3	-6.397	22	64	1	13	0
HOMO -4	-6.488	3	7	9	81	0
HOMO -5	-6.757	11	31	56	2	0
HOMO -6	-6.854	66	21	5	6	2
HOMO -7	-6.956	2	8	67	0	23
HOMO -8	-7.024	49	35	14	2	0
HOMO -9	-7.092	8	4	80	2	6
HOMO -10	-7.190	1	2	70	0	27

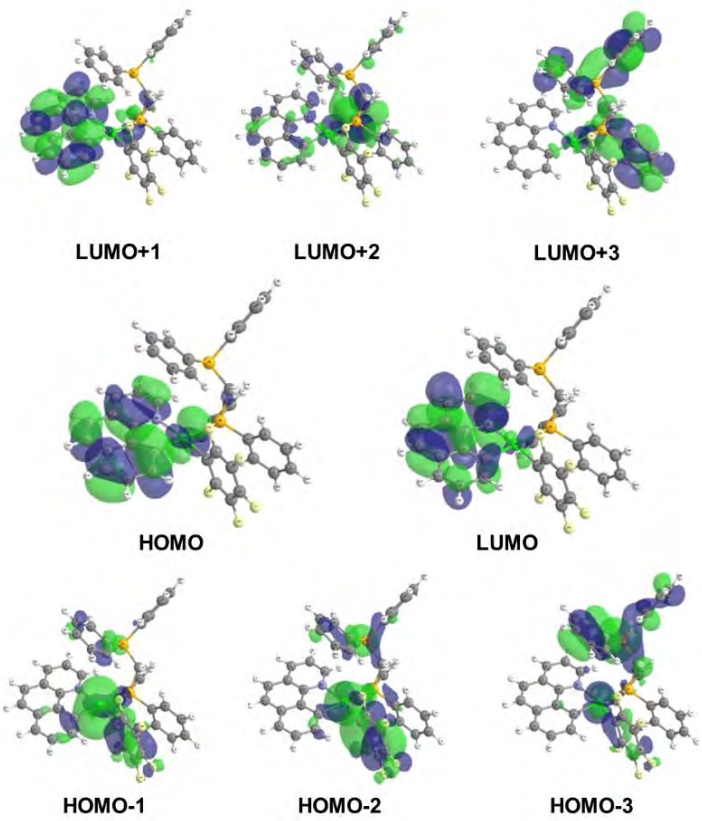

Figure A4.2. Selected frontier Molecular Orbitals for complex **19**.

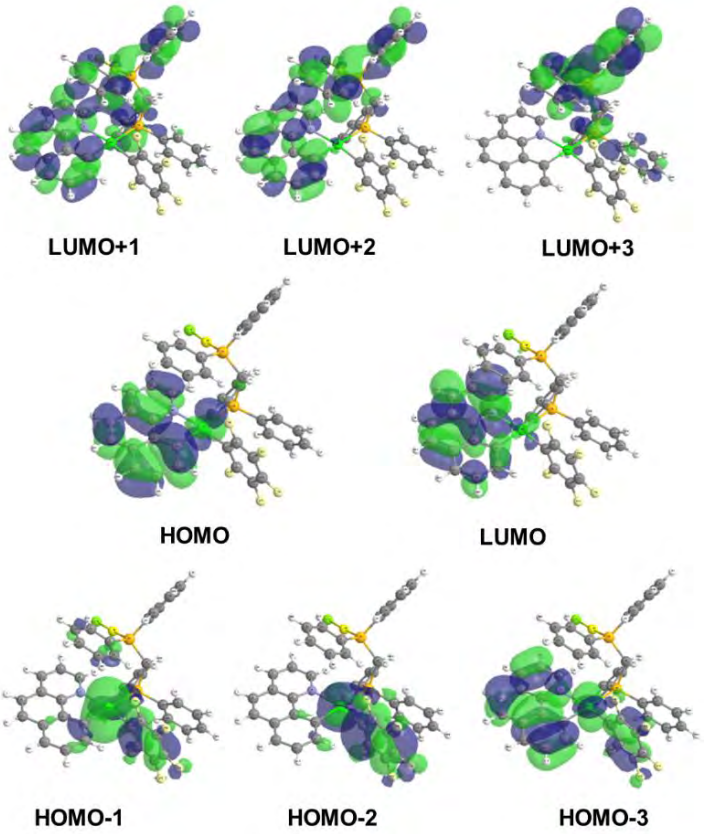

Figure A4.3. Selected frontier Molecular Orbitals for complex **20**.

Table A4.4. Wavelengths and nature of transitions for **19** and **20**.

	State	λ_{ex}(calc) (nm)	f [a]	Transition (% Contribution)	Main character [b]
19	S_1	379	0.053	HOMO→LUMO (95%)	ILCT/MLCT
	S_4	326	0.026	H-4→LUMO (44%) HOMO→L+1 (38%)	ILCT/MLCT ILCT/MLCT/ML″CT
	S_6	307	0.213	H-4→LUMO (33%) HOMO→L+1 (44%)	ILCT/MLCT ILCT/MLCT/ML″CT
	S_{15}	279	0.052	H-3→L+1 (81%)	MLCT/L″LCT
	S_{17}	273	0.053	H-8→LUMO (33%) H-4→L+1(10%) HOMO→L+3(11%) HOMO→L+5 (11%)	ILCT/MLCT/L″LCT ILCT/MLCT/ML″CT ILCT/MLCT LL″CT/ML″CT
	S_{24}	264	0.067	H-7→L+1 (42%) H-3→L+2 (15%)	ILCT/MLCT/ML″CT IL″CT/MLCT
20	S_1	379	0.054	HOMO→LUMO (95%)	ILCT/MLCT
	S_4	326	0.015	H-3→LUMO (42%) H-2→LUMO (16%) HOMO→L+1 (27%)	ILCT/MLCT MLCT/L′LCT ILCT/ML″CT/LL″CT
	S_5	310	0.130	H-3→LUMO (26%) HOMO→L+1 (59%)	ILCT/MLCT ILCT/ML″CT/LL″CT
	S_7	302	0.124	H-3→LUMO (10%) HOMO→L+2 (77%)	ILCT/MLCT ILCT/ML″CT/LL″CT
	S_9	296	0.036	H-6→LUMO (35%) H-4→LUMO (11%) H-3→L+1 (19%)	MLCT/ILCT L′LCT ILCT/ML″CT/LL″CT
	S_{20}	272	0.113	H-8→LUMO (32%) H-6→LUMO (10%) H-3→L+1 (16%)	ILCT/MLCT MLCT/ILCT ILCT/ML″CT/LL″CT
	S_{27}	264	0.056	H-6→L+1 (13%) H-3→L+2 (27%)	MLCT/ML″CT/ILCT ILCT/ML″CT/LL″CT
	S_{39}	254	0.071	H-3→L+3 (34%) H-3→L+4 (13%) HOMO→L+8 (14%)	ML″CT/LL″CT/L′L″CT ML″CT/LL″CT/ILCT/ L′L″CT ML″CT/LL″CT

[a] Oscillator Strength; [b] M = Pt, L = bzq, L' = C_6F_5, L'' = dppm, M' = Au, X = Cl.

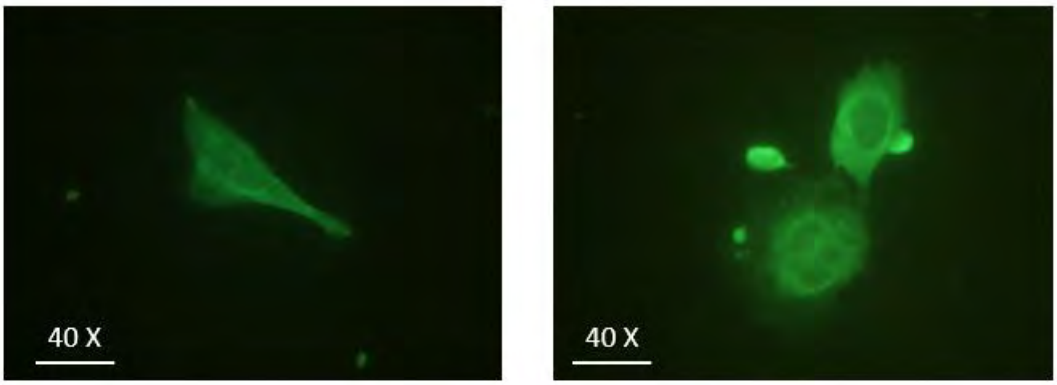

Figure A4.4. Selected fluorescence images of MCF-7 cells treated with complex **20**, taken at 40 X magnification.

Summary and Conclusions

Summary and conclusions

Summary

Chapter 1. Oxidation reactions of derivatives [Pt(bzq)(C_6F_5)L] (L = HC≡CFc, CH_3COCH_3, tht)

The chemical oxidation of the complex [Pt(bzq)(C_6F_5)(η^2-HC≡CFc)] with $PhICl_2$ and I_2 was previously studied by Sergio Sánchez in our research group. These reactions were found to evolve with formation of the unusual halideferrocenyl(vinyl)benzoquinoline Pt(II) compounds [Pt{bzq-κN-η^2-CH=C(X)Fc}(C_6F_5)X] (X = Cl **A**, I **B**), arising from C-X and C-C coupling processes, together with small amounts of the corresponding Pt(IV) species [Pt(bzq)(C_6F_5)X(μ-X)]$_2$ (X = Cl **C**, I **D**). In the context of these results, our first goal was to obtain the new formed ligands.

Thus, **in the first part of in this Chapter**, we describe the displacement reactions of **A** and **B** with PPh_3 to yield the complexes *trans*-[Pt(C_6F_5)X(PPh_3)$_2$] and the new functionalized (vinyl)-benzoquinoline ligands [(*Z*)-bzq-CH=C(X)Fc] (X = Cl **1**, I **2**). X-ray diffraction study of **1** confirms the geminal disposition of the Fc group and chlorine.

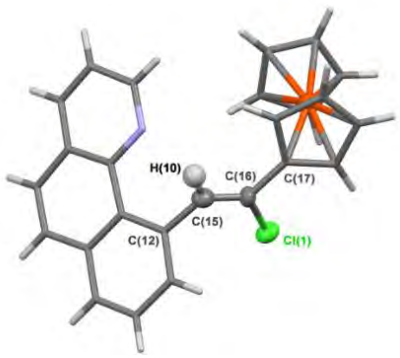

The **second part of this Chapter** is focused on the preparation of mononuclear Pt(IV) derivatives [Pt(bzq)(C_6F_5)X_2(L)] (L = dmso **3**-**5**, tht **6**-**8**). To this end, the reactions of Pt(IV) dinuclear species [Pt(bzq)(C_6F_5)X(μ-X)]$_2$ (X = Cl **C**, I **D**, Br **E**) (straightforward obtained by oxidation of [Pt(bzq)(C_6F_5)(acetone)] with $PhICl_2$, I_2 and Br_2, respectively) with dmso, were initially studied. These reactions provided the mononuclear complexes [Pt(bzq)(C_6F_5)X_2(dmso)] (X = Cl **3**, I **4**, Br **5**) as a mixture of *cis*-[Pt(bzq)(C_6F_5)X_2(dmso-κS)] and *trans*-[Pt(bzq)(C_6F_5)X_2(dmso-κO)] isomers (*cis/trans*: 1/1 **3**, 1/1 **4**, 2/1 **5**), as confirmed

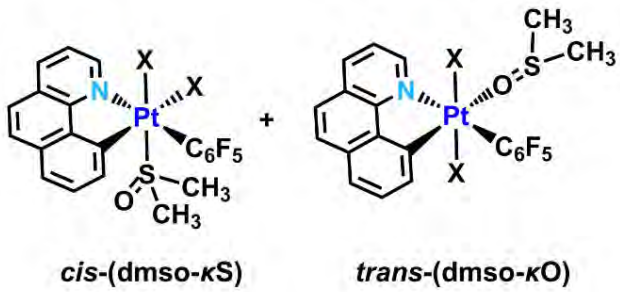

by the combination of exhaustive NMR studies, X-ray diffraction studies and DFT theoretical calculations.

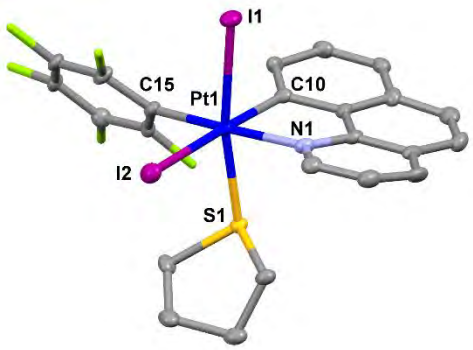

For comparative purposes, the synthesis of the tetrahydrothiophene derivatives was attempted by direct oxidation of [Pt(bzq)(C_6F_5)(tht)] with $PhICl_2$, I_2 and Br_2. These reactions evolved with formation of the Pt(IV) complexes [Pt(bzq)(C_6F_5)X_2(tht)] (X = Cl **6**, I **7**, Br **8**), identified also as a mixture of *cis:trans* isomers for **6** and **7** (*cis/trans*: 7/1 **6**, 5/1 **7**), from which the *cis* isomer of **7** can be separated by crystallization and studied by X-ray crystallography. However, [Pt(bzq)(C_6F_5)Br_2(tht)] **8** was purely obtained as the *cis* isomer and its structure was confirmed by single-crystal analysis. Unfortunately, none of the complexes **3-8** displayed emissive properties.

Chapter 2. Luminescent pentafluorophenyl homoleptic cyclometalated Pt(II) and Pt(IV) compounds

This Chapter is focused on the synthesis, characterization and study of the photophysical properties, supported by DFT/TD-DFT calculations, of luminescent pentafluorophenyl cyclometalated Pt(II) and Pt(IV) complexes.

In the first section of this Chapter (2.1), a series of luminescent mono-pentafluorophenyl Pt(II) derivatives [Pt(C^N)(HC^N-*κN*)(C_6F_5)] (C^N = thpy **10a**, pbt **10b**, pq **10c**, dfppy **10d**), containing a cyclometalated ligand and a N-coordinated heteroaryl HC^N ligand, have been prepared by C-H activation of one of the HC^N pendant ligand in the corresponding *cis*-[Pt(HC^N-*κN*)$_2$(C_6F_5)$_2$] (HC^N = Hthpy **9a**, Hpbt **9b**, Hpq **9c**, Hdfppy **9d**) complexes.

Complexes **10** evolve in dmso solution into solvate complexes [Pt(C^N)(C_6F_5)(dmso)] (C^N = thpy **11a**, pbt **11b**), whose synthesis and properties are also described. Unfortunately, all attemps to prepare the corresponfing solvate complex **11c**, bearing the pq ligand, were unfructuous. A combination of X-ray crystallography (**9a**, **9c**, **9d**, **10b**, **10d**, **11a, 11b**) and mainly multinuclear NMR spectroscopy support

their formulation. The absorption spectra of complexes **9** follow the tendency of the corresponding free ligands, with aditional weak low-energy tails ascribed to ^{1}MLCT with some ^{1}IL contribution (L = HC^N). The presence of a cyclometalated group is reflected in complexes **10** and **11** in a more intense low-energy feature, attributed mainly to ^{1}IL'/^{1}ML'CT (L' = C^N) transitions. All Pt(II) complexes show long-lived emission in degassed fluid solutions and in the solid state at 298 and at 77 K. On the basis of theoretical calculations, the emission of complexes **9** has been assigned to a ^{3}MLCT (Pt→HC^N) with some ^{3}IL (HC^N) character, whereas for the cyclometalated complexes **10** and **11** to a mixed ^{3}IL'/^{3}ML'CT (L' = C^N) excited state with lower contribution of the metal in the solvate complexes **11**.

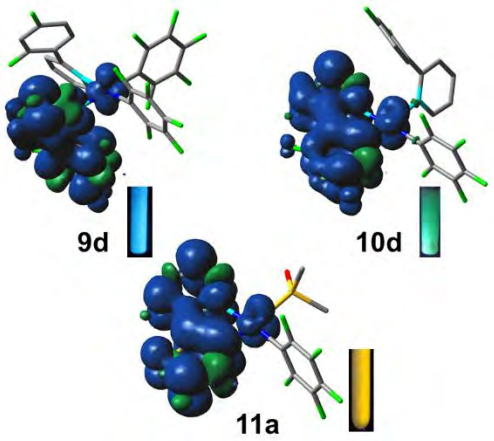

The stability in biological media and the biological properties (cytotoxicity and fluorescence microscocopy cellular localization) of **11a** and **11b** were evaluated. These complexes display low cytotoxicity towards the human lung cancer (A549) (between three or four times less cytotoxicity than cispatin) and low selectivity when compared to the cytotoxicity towards the non-tumorigenic NL20 cells. Fluorescence microscopy revealed their efficient cellular internalization and their localization in the cytoplasm, with brighter emission in the perinuclear area.

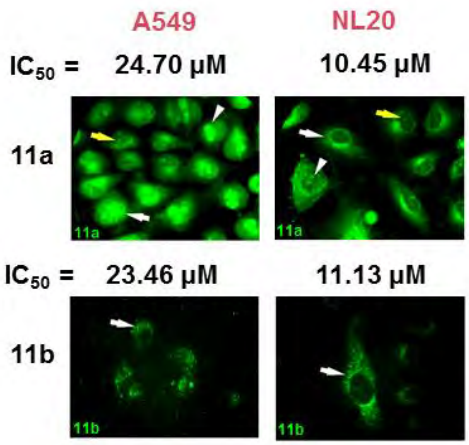

In the second part of this Chapter (2.2), we report the synthesis, characterization, photophysics and computational studies of stable bis(cyclometalated) pentafluorophenyl Pt(IV) complexes $[Pt(C^N)_2(C_6F_5)X]^n$ (n = 0, X = Cl **12a-e**, CN^- **13**; n = +1, X = Mepy **14**, bpe **15**).

Complexes *fac*-$[Pt(C^N)_2(C_6F_5)Cl]$ (C^N = thpy **12a**, pbt **12b**, pq **12c**, dfppy **12d**, bzq **12e**) were prepared by chemical oxidation at low temperature with $PhICl_2$ of the cyclometalated Pt(II) complexes $[Pt(C^N)(HC^N\text{-}\kappa N)(C_6F_5)]$ **10a-d** or **10e**. The

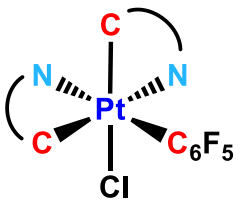

stereoselectivity of the reaction suggests the formation of cationic five-coordinate $[Pt(C^N)(HC^N)(C_6F_5)Cl]^+$ intermediates, stabilized by an aryl agostic C-H interaction, with subsequent metalation and formation of *fac*-**12a-e** and HCl. Complexes **12d** and **12e** were also generated by irradiation of solutions of complexes **10d** and **10e** in CH_2Cl_2 with a 400 W lamp for 2 h. Monitorization of this reaction by NMR revealed the formation of the hydride *cis*-$[Pt(C^N)_2(C_6F_5)H]$ complexes as the only detected intermediate species.

All complexes were fully characterized and the structures of **12c**, **12d** and **12e** confirmed by X-ray diffraction studies. The substitution of Cl^- in the phenylbenzothiazol complex *fac*-$[Pt(pbt)_2(C_6F_5)Cl]$ **12b** by CN^- , Mepy or bpe was carried out. Whereas the substitution with CN^- arises with isomerization from *fac* to *mer* conformation to form the isomer *mer*-$[Pt(pbt)_2(C_6F_5)(CN)]$ **13**, the Cl^-/Mepy or Cl^-/bpe exchanges do not induce isomerization, giving rise to the cationic complexes *fac*-$[Pt(pbt)_2(C_6F_5)(Mepy)][PF_6]$ **14** and *fac*-$[Pt(pbt)_2(C_6F_5)(bpe)][PF_6]$ **15**, respectively. Irradiation studies, monitored by NMR and UV-Vis for complex **15** in acetone-d^6, revealed an easy isomerization process *E*/*Z* on the bpe ligand, which affects on its photoemission. X-ray diffraction and NMR studies for **13**, **14** and **15** confirmed their *mer* (**13**) or *fac* (**14**, **15**) disposition and the *E*/*Z* isomerization for **15**.

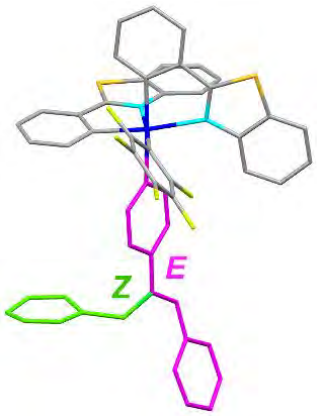

The absorption spectra of all the Pt(IV) complexes show blue-shifted low-energy features in comparison to those of the Pt(II) precursors, reflecting the stabilization of high occupied orbitals upon oxidation of the Pt center. Theoretical calculations revealed these bands as having mainly a mixture of ^{1}IL/^{1}LLCT character involving the cyclometalated groups.

The emission properties of all complexes were evaluated in solution, solid state and PMMA films. In general, the complexes *fac*-[Pt(C^N)$_2$(C$_6$F$_5$)Cl] **12a-e** show structured bands, that are blue-shifted and have longer lifetimes [τ = 208 – 3658 μs, CH_2Cl_2 (77 K)] than those of their Pt(II) precursors **10a-e**. Computational studies support an emission ascribed to a ^{3}IL (L = C^N) excited state, with a negligible participation of the metal. The highest-energy emission peak varies in function of the cyclometalated ligand, following the tendency dfppy (**12d**) > bzq (**12e**) > pbt (**12b**) > pq (**12c**) > thpy (**12a**), a tendency that correlates with the values calculated for optimized T_1 excited states in selected molecules. Complexes **13** and **14** are emissive in all media, whereas **15** only shows a weak emission in glassy CH_2Cl_2, likely due to the *E*/*Z* isomerization process on the bpe ligand. Complexes **13-15** display similar ^{3}IL emission to that found for their precursor **12b**, revealing that the Cl^-/CN^-, Cl^-/Mepy or Cl^-/bpe exchanges do not have a remarkable influence on the nature of the emissive state. However, the substitution of the Cl^- atom for CN^- (**13**) and Mepy (**14**) increases the efficiency of the emission by raising the energy of the deactivating MC states (more notably in **14**), as was confirmed by theoretical calculations.

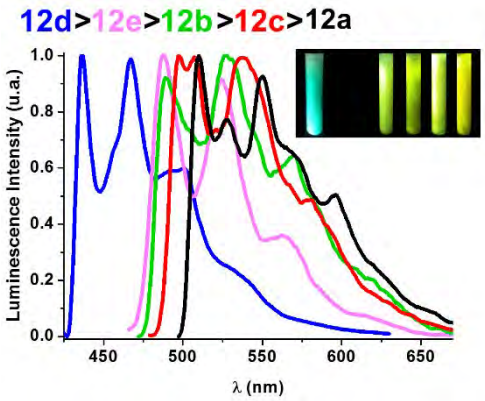

Chapter 3. Luminescent pentafluorophenyl heteroleptic cyclometalated Pt(II) and Pt(IV) compounds

In this Chapter, a series of neutral pentafluorophenyl benzoquinolinyl Pt(II) complexes [Pt(bzq)(HC^N-*κN*)(C$_6$F$_5$)] (HC^N = Hthpy **16a**, Hpbt **16b**, Hpq **16c**, Hdfppy **16d**, Hoxd **16f**, Hpypy **16g**), bearing non-metalated N-heterocyclic HC^N ligands and heteroleptic bis(cyclometalated) Pt(IV) *fac*-[Pt(bzq)(C^N)(C$_6$F$_5$)Cl] (**17a-g**), generated by oxidation of **16a-g**, are presented. The impact on the photophysical behaviour of the different electronic nature of the auxiliary HC^N ligand [in Pt(II) complexes] or C^N cyclometalating groups [in Pt(IV) derivatives] was assesed with the aid of DFT and TD-DFT theoretical calculations.

In the first section of this Chapter (3.1), the synthesis, characterization and photophysical properties of Pt(II) complexes [Pt(bzq)(HC^N-*κN*)(C_6F_5)] **16a-g**, obtained from the solvate [Pt(bzq)(C_6F_5)(acetone)] are described. The structures of **16a** and **16f** were confirmed by X-ray diffraction studies and the complete ^{1}H and ^{13}C assignment was performed on the basis of 1D and 2D NMR experiments. For all complexes, the low-lying absorption bands are assigned to an admixture of ^{1}IL'/^{1}ML'CT located on the cyclometalated Pt(bzq) unit, with minor ^{1}MLCT or ^{1}L'LCT for **16c** and **16f** (L' = bzq, L = HC^N) character, supported by TD-DFT calculations. Complexes **16a-f** exhibit long-lived phosphorescent emission in solution and in PS films, attributed to an admixture ^{3}IL'/^{3}ML'CT centered on the bzq ligand, with minor ^{3}IL/^{3}MLCT/^{3}L'LCT (L' = bzq, L = HC^N) contribution in **16a** and **16c**. In **16g**, the presence of the strongly delocalized pyrene ligand (Hpypy), promotes fluorescence/phosphorescence dual emission ($^1\pi\pi^*_{Hpypy}$/$^3\pi\pi^*_{Hpypy}$) in CH_2Cl_2 at 298 K and dual phosphorescence [^{3}IL'$_{bzq}$/^{3}ML'CT$_{Pt\rightarrow bzq}$ and $^3\pi\pi^*_{Hpypy}$] at 77 K. In the solid state, **16a-f** show emissions coming from excimeric excited states due to π···π interactions, ^{3}IL'/^{3}ML'CT monomeric or close-emissive excited states.

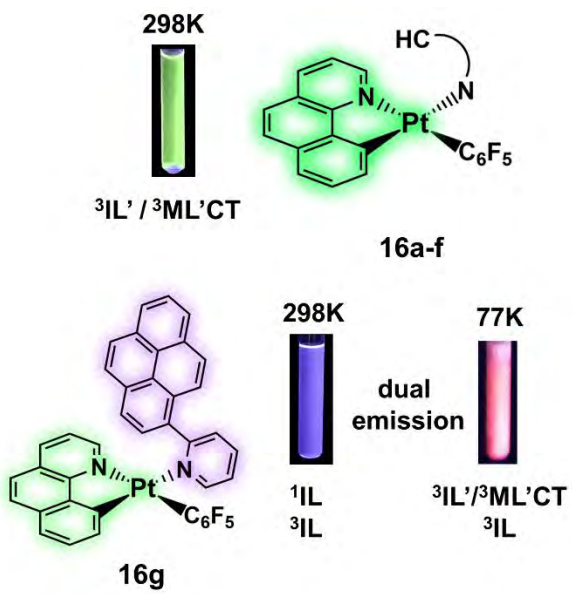

The second section of this Chapter describes the synthesis, characterization and optical properties of Pt(IV) complexes *fac*-[Pt(bzq)(C^N)(C_6F_5)Cl] (**17a,b,c,d,g**), featuring bzq and a second different cyclometalated C^N ligand, selectively obtained by oxidation of Pt(II) **16** derivatives with $PhICl_2$, with concomitant second metalation of the HC^N pendant ligand. All attempts to obtain complex **17f** bearing the oxd cyclometalated ligand failed, as the oxidation of **16f** occurs with the displacement of Hoxd ligand and the formation of bimetallic Pt(IV) complex *syn*-[Pt(bzq)(C_6F_5)Cl(μ-OH)]$_2$ **18**. Structures of **17c**, **17d**, **17g** and **18** were confirmed by X-ray diffraction studies and the

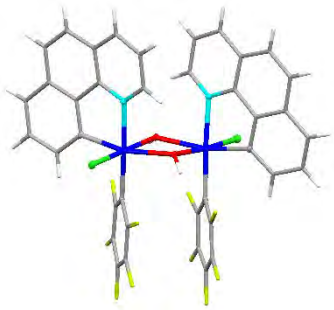

complete ^{1}H and ^{13}C assignment of all compounds were performed by analysis of 1D and 2D NMR experiments.

Complexes **17a-d** showed structured long-lived phosphorescence emission. Theoretical calculations suggested that the emission arises from the cyclometalated ligand having the lowest energy. Thus, in complexes **17a-c** the emission arises mainly from the second C^N ligand (with some ^{3}L'LCT in **17a**) and from the bzq in **17d**, as was confirmed by comparison to the homoleptic complexes **12**. The observed emissions in **17a-c** are more efficient than those of their homoleptic analogues [ϕ (%), 11/8.2 (**17a**/**12a**), 22/3.1 (**17b**/**12b**), 85/18.1 (**17c**/**12c**)], indicating that the coordination of two different cyclometalated ligands improves the emission efficiency.

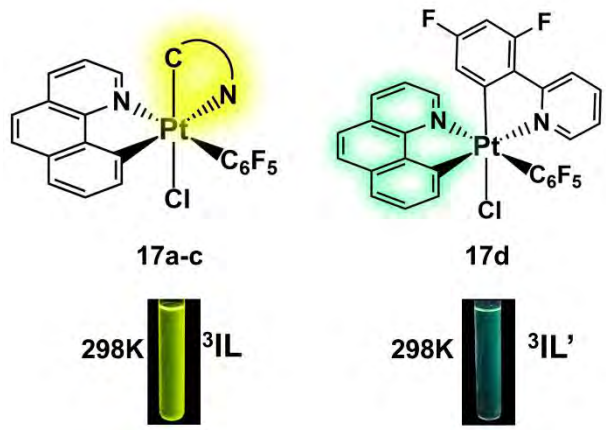

Complex **17g**, bearing the cyclometalated pypy ligand, shows pyrene-localized fluorescence ($^{1}\pi\pi^{*}_{pypy}$) in fluid CH_2Cl_2 solution and dual fluorescence ($^{1}\pi\pi^{*}_{pypy}$)/phosphorescence ($^{3}\pi\pi^{*}_{pypy}$) at 77 K. In PS and in the solid state the emission of **17g** is ascribed to mixed $^{1}\pi\pi^{*}_{pypy}/^{3}IL_{bzq}$ (close emissive states, theoretical calculations), together with a low-energy band due to $^{3}\pi\pi^{*}_{pypy}$ (in PS). The dominant $^{1}\pi\pi^{*}_{pypy}$ fluorescence is presumably due to the low contribution of the Pt orbitals in the transitions, which causes inefficient singlet-triplet intersystem crossing.

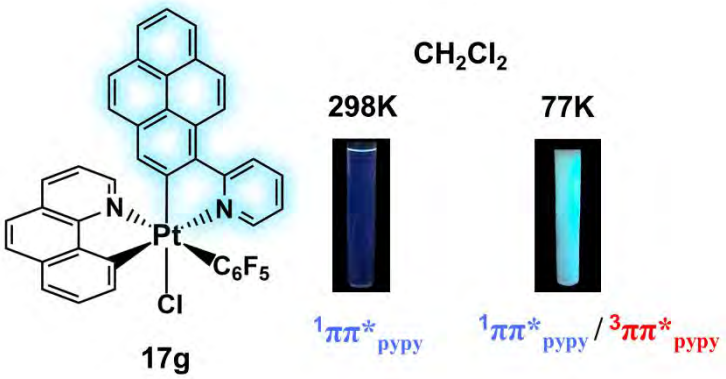

Chapter 4. Heterobimetallic Pt(II)-Au(I) complexes

In this chapter, the synthesis and properties of [Pt(bzq)(C_6F_5)(κ^1-dppm)] **19**, and the bimetallic complex [Pt(bzq)(C_6F_5)(μ-dppm)AuCl] **20,** bearing the dppm as bridging ligand, are described. Both complexes were characterized by means of NMR spectroscopy and by X-ray diffraction. The crystallization process of **19** produced the oxidation of the free phosphine head, giving rise to [Pt(bzq)(C_6F_5)(κ^1-dppmO)] **19-O**. The crystal structure of **20** showed no Pt(II)-Au(I) bonding interaction. The lack of Pt(II)-Au(I) bond caused that the heterometallic complex **20** shows similar electronic structure and optical properties than the precursor **19**. They exhibit similar long-lived phosphorescence emissions, assigned to excited states of ^{3}IL(bzq)/^{3}MLCT(Pt→bzq) character, with a negligible contribution of the Au-Cl moiety in **20**.

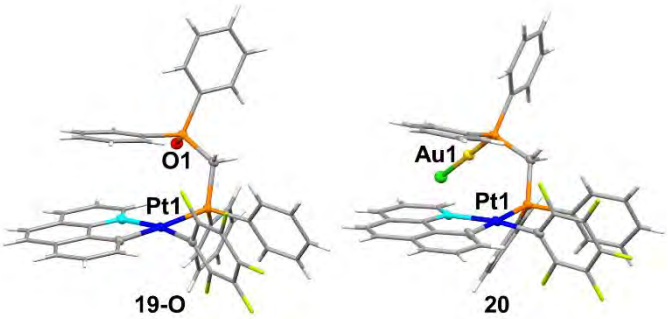

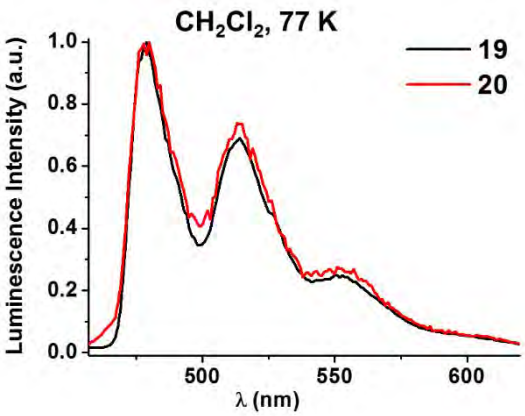

The cytotoxic activities of both compounds were evaluated and compared to the monometallic [Pt(C^N)(*p*-MeC_6H_4)(κ^1-dppm)] (C^N = bzq **19b***, ppy **19c***) and bimetallic [Pt(C^N)(*p*-MeC_6H_4)(μ-dppm)AuCl] (C^N = bzq **20b***, ppy **20c***) analogues, in collaboration with Dr. H. R. Shahsavari's research group. The heterometallic Pt-Au **20** complex displayed an improvement of the *in vitro* cytotoxic activity against MCF-7 (breast), SKOV3 (ovarian), and A549 (lung) cancer cell lines in comparison to the platinum precursor **19** and to [ClAu(μ-dppm)AuCl], suggesting a cooperative effect of both metallic fragments. Also, the presence of the bzq cyclometalated ligand and the *p*-MeC_6H_4 group improves the anti-proliferative activity in comparison to the ppy and C_6F_5 ligands. Due to the emissive properties of **20** in solution at 298 K, fluorescence microscopy imaging experiments were

performed. This compound internalizes into the MCF-7 cells, revealing its effective localization in the nucleus with less dispersion in the cytoplasm.

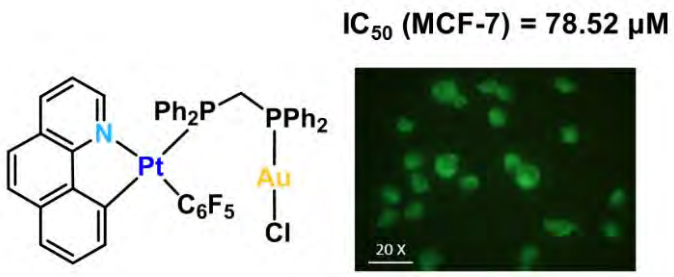

Conclusions

- ✓ Unusual functionalized (vinyl)-benzoquinoline free ligands [(*Z*)-bzq-CH=C(X)Fc] (X = Cl, I), with ferrocenyl/halide geminal disposition (X = Cl, X-ray), have been obtained.

- ✓ Oxidation reactions using as precursors the labile substrates [Pt(bzq)(C_6F_5)(S)] (S = CH_3COCH_3, tht) has allowed to prepare a family of mononuclear non-luminescent Pt(IV) derivatives [Pt(bzq)(C_6F_5)X_2(L)] (L = dmso, tht) as a mixture of *cis*/*trans* isomers.

- ✓ Pentafluorophenyl luminescent Pt(II) complexes [Pt(C^N)(HC^N-κN)(C_6F_5)] (HC^N = thpy, pbt, pq, dfppy), with one cyclometalated and one pendant *N*-coordinated heteroaryl ligand, have been prepared by induced C-H metalation on *cis*-[Pt(HC^N-κN)$_2$(C_6F_5)$_2$]. These complexes exhibit long-lived emission in all media, with excited states assigned to ^{3}MLCT/^{3}IL (L = HC^N) in the (κ-*N*)$_2$ derivatives and to ^{3}IL'/^{3}ML'CT (L' = C^N) in the cyclometalated complexes. The cycloplatinated systems evolve in dmso to [Pt(C^N)(C_6F_5)(dmso)] and the emissive and biological properties of [Pt(C^N)(C_6F_5)(dmso)] (C^N = thpy, pbt) have been evaluated.

- ✓ Oxidation reactions of Pt(II) complexes [Pt(C^N)(HC^N-κN)(C_6F_5)] with subsequent metalation of the pendant HC^N ligand give rise to luminescent homoleptic Pt(IV) *fac*-[Pt(C^N)$_2$(C_6F_5)Cl] (C^N = thpy, pbt, pq, dfppy, bzq) derivatives. Some of the Pt(IV) complexes were alternatively obtained by light-irradiation in chlorine solvents, through hydride species *cis*-[Pt(C^N)$_2$(C_6F_5)H] as intermediates. Substitution of Cl^- by CN^- in the pbt derivative evolves with isomerization from *fac* to *mer* conformation, whereas the change by Mepy or bpe does not produce isomerization, giving rise to cationic *fac*-[Pt(pbt)$_2$(C_6F_5)L]$^+$ (L = Mepy, bpe) complexes. These Pt(IV) complexes exhibit structured emissions arising from ^{3}IL states, as supported by calculations, blue-shifted and with longer lifetimes than those of their Pt(II) precursors. The substitution of the chloride by CN^- or Mepy does not affect to the nature of the emissive state, although increases the efficiency of the emission, whereas an easy *E*/*Z* isomerization on the bpe ligand deactivates the photoemission.

- ✓ Following a similar strategy, a new family of heteroleptic benzoquinolinyl Pt(II) complexes [Pt(bzq)(HC^N-κN)(C_6F_5)] (HC^N = Hthpy, Hpbt, Hpq, Hdfppy, Hoxd, Hpypy), bearing *N*-heterocyclic HC^N ligands of diverse electronic properties, have been prepared as precursors to synthetize heteroleptic Pt(IV) complexes *fac*-[Pt(bzq)(C^N)(C_6F_5)Cl] (C^N = thpy, pbt, pq, dfppy, pypy). Pt(II) complexes [Pt(bzq)(HC^N-κN)(C_6F_5)] display phosphorescence centered on the Pt(bzq) moiety (^{3}IL'/^{3}ML'CT) with minor contributions involving the non-metalated ligands. However, the complex [Pt(bzq)(Hpypy)(C_6F_5)] shows dual fluorescence/phosphorescence ($^1\pi\pi^*/^3\pi\pi^*)_{Hpypy}$ emission located in the pyridyl pyrene or dual phosphorescence located on the Pt(bzq) unit (^{3}IL'/^{3}ML'CT) and on the Hpypy ($^3\pi\pi^*$) respectively, depending on the temperature. Upon oxidation, the Pt(IV) complexes display ligand-based phosphorescence, arising mainly from the C^N group having the lowest-lying $\pi^*_{(C^N)}$ orbital. The emissions are more efficient than those found in the related homoleptic complexes, indicating that the coordination of two different cyclometalated ligands improves the emission efficiency.

- ✓ Finally, the mononuclear Pt(II) [Pt(bzq)(C_6F_5)(κ^1-dppm)] and the bimetallic Pt(II)-Au(I) [Pt(bzq)(C_6F_5)(μ-dppm)AuCl] derivatives have been prepared and their optical and biological properties have been compared. Both complexes display similar long-lived ^{3}IL(bzq)/^{3}MLCT(Pt-bzq) emission, likely due to the absence of Pt-Au bond. The heterobimetallic complex shows an improvement of the *in vitro* cytotoxic activity in comparison to the Pt(II) monometallic and to [ClAu(μ-dppm)AuCl] derivative, suggesting a cooperative effect of the metal fragments. Fluorescence microscopy revealed that the Pt(II)-Au(I) complex internalized into MCF7 cells and localized mostly in the nucleus.

Resumen y Conclusiones

Resumen y conclusiones

Resumen

Capítulo 1. Reacciones de oxidación de compuestos [Pt(bzq)(C_6F_5)L] (L = HC≡CFc, CH_3COCH_3, tht)

Los primeros estudios sobre la oxidación del sustrato [Pt(bzq)(C_6F_5)(η^2-HC≡CFc)] con $PhICl_2$ o I_2 se llevaron a cabo en nuestro grupo de investigación por Sergio Sánchez. Se observó que las reacciones evolucionaban hacia la formación de derivados de Pt(II) [Pt{bzq-κN-η^2-CH=C(X)Fc}(C_6F_5)X] (X = Cl **A**, I **B**), que contienen los ligandos funcionalizados (*Z*)-10-[1-X,1-ferrocenilvinilo]benzoquinoleína, generados a través de procesos de acoplamiento C-X y C-C, junto con pequeñas cantidades de los derivados de Pt(IV) [Pt(bzq)(C_6F_5)X(μ-X)]$_2$ (X = Cl **C**, I **D**). En este contexto, nuestro primer objetivo fue la obtención de los nuevos ligandos funcionalizados.

Así, en **la primera parte este Capítulo** se describe las reacciones de desplazamiento de **A** y **B** con PPh_3, que dan lugar a la formación de los derivados *trans*-[Pt(C_6F_5)X(PPh_3)$_2$] y los nuevos ligandos funcionalizados (*Z*)-10-[1-X,1-ferrocenilvinilo]benzoquinoleína (X = Cl **1**, I **2**). La estructura cristalina del derivado **1** confirma que el átomo de Cl y el grupo Fc se encuentran en disposición geminal.

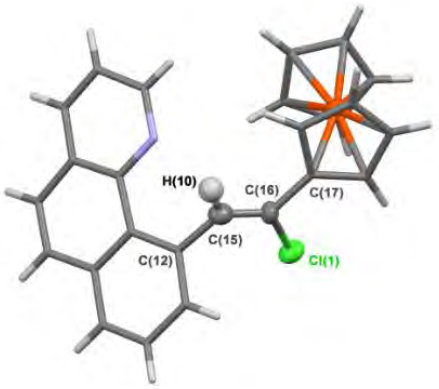

La **segunda parte del Capítulo** se centra en la preparación de derivados de Pt(IV) mononucleares del tipo [Pt(bzq)(C_6F_5)X_2(L)] (L = dmso **3-5**; tht **6-8**). Con este fin, se estudian inicialmente las reacciones de los derivados dinucleares [Pt(bzq)(C_6F_5)X(μ-X)]$_2$ (X = Cl **C**, I **D**, Br **E**) (obtenidos por oxidación del solvato [Pt(bzq)(C_6F_5)(acetona)] con $PhICl_2$, I_2 and Br_2, respectivamente) con dmso. Estas reacciones permiten obtener los compuestos

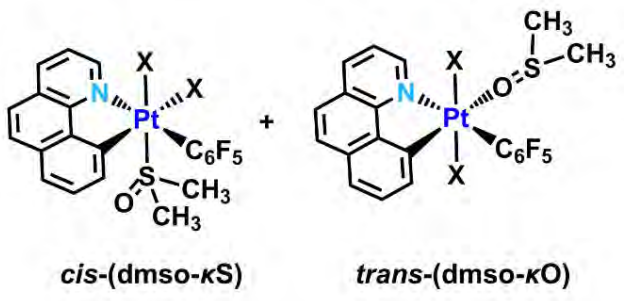

mononucleares [Pt(bzq)(C_6F_5)X_2(dmso)] (X = Cl **3**, I **4**, Br **5**), identificados como una mezcla de isómeros *cis*-[Pt(bzq)(C_6F_5)X_2(dmso-*κS*)] y *trans*-[Pt(bzq)(C_6F_5)X_2(dmso-*κO*)] (*cis/trans*: 1/1 **3**, 1/1 **4**, 2/1 **5**), como se ha confirmado por estudios de RMN, Rayos X [**trans-5 (dmso-*κO*)**] y cálculos teóricos DFT.

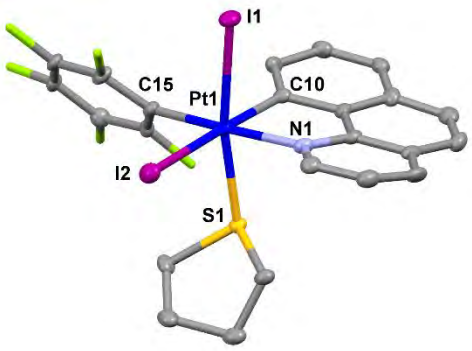

Con fines comparativos, se estudia la oxidación del precursor [Pt(bzq)(C_6F_5)(tht)] con $PhICl_2$, I_2 o Br_2. Estas reacciones dan lugar a la formación de los derivados de Pt(IV) [Pt(bzq)(C_6F_5)X_2(tht)] (X = Cl **6**, I **7**, Br **8**), identificados también como una mezcla de isómeros *cis*:*trans* en **6** y **7** (*cis*/*trans*: 7/1 **6**, 5/1 **7**), de la que es posible separar por cristalización, el isómero *cis* del derivado **7** para su estudio por difracción de Rayos X. Sin embargo, el compuesto [Pt(bzq)(C_6F_5)Br_2(tht)] **8** se obtiene puro como el iómero *cis*, y su estructura se ha confirmado mediante Rayos X. Desafortunadamente, ninguno de los derivados **3-8** son emisivos.

Capítulo 2. Derivados luminiscentes homolépticos pentafluorofenil-ciclometalados de Pt(II) and Pt(IV)

Este Capítulo se centra en la síntesis, caracterización y estudio de las propiedades fotofísicas, con el apoyo de cálculos teóricos DFT/TD-DFT, de compuestos luminiscentes pentafluorofenil-ciclometalados de Pt(II) y Pt(IV).

En la primera parte del Capítulo 2 (2.1), se describe una serie de compuestos de Pt(II) [Pt(C^N)(HC^N-*κN*)(C_6F_5)] (C^N = thpy **10a**, pbt **10b**, pq **10c**, dfppy **10d**), que contienen un ligando ciclometalado, un ligando HC^N heterocíclico N-coordinado y el grupo C_6F_5. Estos derivados se preparan por la activación C-H de uno de los ligandos HC^N en los correspondientes precursores *cis*-[Pt(HC^N-*κN*)$_2$(C_6F_5)$_2$] (HC^N = Hthpy **9a**, Hpbt **9b**, Hpq **9c**, Hdfppy **9d**).

Los compuestos **10** evolucionan en disolución de dmso hacia los derivados [Pt(C^N)(C_6F_5)(dmso)] (C^N = thpy **11a**, pbt **11b**), incluyéndose su síntesis y propiedades. Desafortunadamente, no se consiguió preparar el derivado análogo **11c** con el ligando pq. El estudio combinado de RMN multinuclear y difracción de Rayos X (**9a**,

9c, **9d**, **10b**, **10d**, **11a, 11b**) confirmó la formulación de estos compuestos. Los espectros de absorción de los compuestos **9** siguen la tendencia de los correspondientes ligandos libres, con bandas adicionales débiles en la zona de baja energía, asignadas a transiciones principalmente ^{1}MLCT con alguna contribución ^{1}IL (L = HC^N). Los derivados **10** y **11**, que contienen un ligando ciclometalado muestran, en la zona de baja energía, bandas más intensas asignadas a transiciones ^{1}IL'/^{1}ML'CT (L' = C^N). Todos los derivados de Pt(II) muestran emisiones con tiempos de vida largos tanto en disoluciones desoxigenadas como en estado sólido, a 298 K y a 77 K. Con apoyo de cálculos teóricos, la emisión de los derivados **9** se asigna a transiciones ^{3}MLCT (Pt→HC^N) con cierto carácter ^{3}IL (HC^N), mientras que para los derivados ciclometalados **10** y **11** se atribuye a un estado excitado de carácter ^{3}IL'/^{3}ML'CT (L' = C^N) con una menor contribución del metal en los derivados **11**.

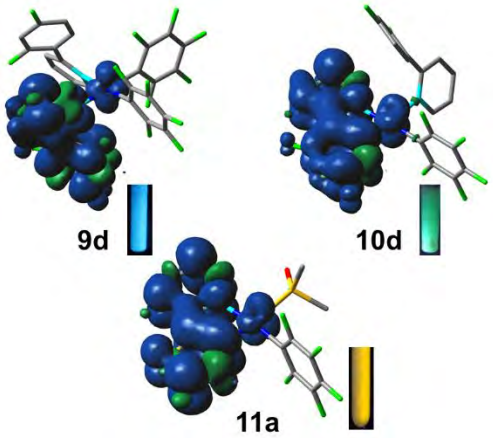

Se han evaluado tanto la estabilidad en medio biológico como las propiedades biológicas (citotoxicidad y localización celular por microscopía de fluorescencia) de los derivados **11a** y **11b**. Ambos compuestos muestran una citotoxicidad entre 3 y 4 veces menor que el *cis*-platino frente a células tumorales de pulmón humano (A549) y una baja selectividad comparada a la citotoxicidad frente a la línea de células no tumorales NL20. Los estudios por microscopía de fluorescencia revelan la internalización celular de ambos compuestos, así como su lozalización principalmente en el citoplasma, con una emisión más intensa en el área perinuclear.

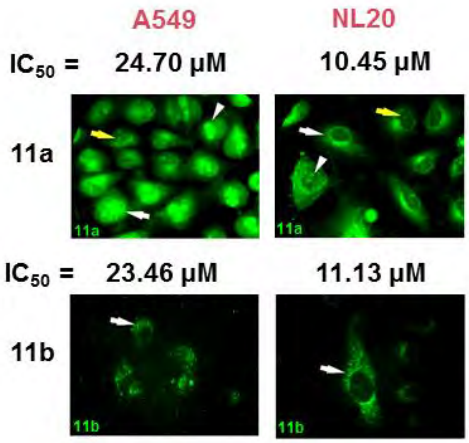

La segunda parte del Capítulo (2.2) se centra en la síntesis, caracterización, fotofísica y estudios computacionales de compuestos estables bis-ciclometalados de Pt(IV) que contienen el grupo pentafluorofenilo $[Pt(C^N)_2(C_6F_5)X]^n$ (n = 0, X = Cl **12a-e**, CN^- **13**; n = +1, X = Mepy **14**, bpe **15**).

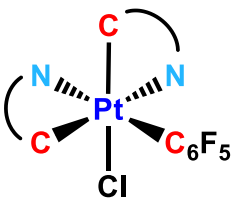

Se han preparado los derivados *fac*-[Pt(C^N)$_2$(C$_6$F$_5$)Cl] (C^N = thpy **12a**, pbt **12b**, pq **12c**, dfppy **12d**, bzq **12e**) mediante la reacción de oxidación con PhICl$_2$ a baja temperatura de los derivados ciclometalados de Pt(II) [Pt(C^N)(HC^N-*κN*)(C$_6$F$_5$)] **10a-d** ó **10e**. La estereoselectividad de la reacción sugiere la formación inicial de un intermedio catiónico pentacoordinado [Pt(C^N)(HC^N)(C$_6$F$_5$)Cl]$^+$, estabilizado por una interacción agóstica C-H, seguido de metalación del ligando HC^N para dar los derivados *fac*-**12a-e** y HCl. Los compuestos **12d** y **12e** se han preparado alternativamente por irradiación con una lámpara de 400 W durante 2 horas de disoluciones de los derivados **10d** y **10e** en CH$_2$Cl$_2$. El seguimiento de la irradiación por RMN reveló la formación del hidruro *cis*-[Pt(C^N)$_2$(C$_6$F$_5$)H] como único intermedio.

Se han caracterizado todos los compuestos, y las estructuras de los derivados **12c**, **12d** y **12e** se han confirmado por difracción de Rayos X. Se ha llevado a cabo la sustitución del Cl$^-$ por CN$^-$, Mepy ó bpe en el complejo con el ligando fenilbenzotiazol, *fac*-[Pt(pbt)$_2$(C$_6$F$_5$)Cl] **12b**. Mientras que la sustitución con CN$^-$ provoca isomerización de *fac* a *mer*, obteniéndose el isómero *mer*-[Pt(pbt)$_2$(C$_6$F$_5$)(CN)] **13**, el intercambio Cl$^-$/Mepy ó Cl$^-$/bpe se produce con retención de la disposición *fac* del precursor, formando los compuestos catiónicos *fac*-[Pt(pbt)$_2$(C$_6$F$_5$)(Mepy)][PF$_6$] **14** y *fac*-[Pt(pbt)$_2$(C$_6$F$_5$)(bpe)][PF$_6$] **15**, respectivamente. El seguimiento por RMN y UV-Vis de la irradiación del derivado **15** disuelto en acetona-d^6, muestra que el ligando bpe sufre un proceso de isomerización *E/Z* en el ligando bpe, que contribuye a la desactivación de su emisión a temperatura ambiente. Los estudios de difracción de Rayos X y de RMN en los compuestos **13**, **14** y **15** confirmaron la disposición *mer* (**13**) o *fac* (**14**, **15**) y la isomerización *E/Z* en el derivado **15**.

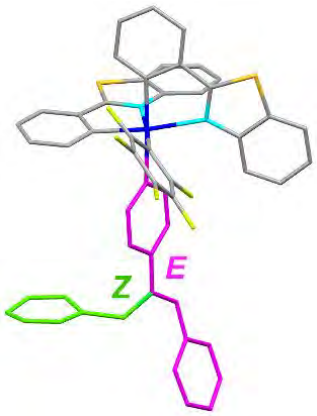

Los espectros de absorción de todos los compuestos de Pt(IV) muestran, en la zona de baja energía, bandas desplazadas hacia el azul en comparación con los precursores de Pt(II), debido a la estabilización del HOMO tras el proceso de oxidación del centro de Pt. Estas bandas se atribuyen, con el apoyo de cálculos teóricos, a transiciones de carácter ^{1}IL/^{1}LLCT centradas en los grupos ciclometalados.

Se han evaluado las propiedades emisivas de todos los derivados en disolución, estado sólido y en films de PMMA. En general, los compuestos *fac*-[Pt(C^N)$_2$(C_6F_5)Cl] **12a-e** muestran bandas estructuradas desplazadas hacia el azul y con tiempos de vida mayores [τ = 208 – 3658 μs, CH_2Cl_2 (77 K)] que los precursores de Pt(II) **10a-e**. Los cálculos teóricos indican que la emisión en los compuestos de Pt(IV) proviene de un estado excitado de carácter principalmente ^{3}IL (L = C^N). Los máximos de emisión varían en función del ligando ciclometalado de acuerdo con la siguiente serie: dfppy (**12d**) > bzq (**12e**) > pbt (**12b**) > pq (**12c**) > thpy (**12a**), de acuerdo con la emisión calculada mediante la optimización del T_1. Mientras que los derivados **13** y **14** son emisivos en todos los medios, el compuesto **15** solo es emisivo en CH_2Cl_2 a 77 K, seguramente debido al proceso de isomerización *E/Z* que sufre el ligando bpe. Los derivados **13-15** muestran una emisión ^{3}IL similar a la del precursor **12b**, indicando que la sustitución del Cl^- por CN^-, Mepy o bpe no afecta a la naturaleza del estado emisivo. Sin embargo, la sustitución del Cl^- por CN^- (**13**) y Mepy (**14**) aumenta la eficiencia de las emisiones (sobre todo en el derivado **14**), debido a la desestabilización de estados desactivantes centrados en el metal (^{3}MC), como se confirma por cálculos teóricos.

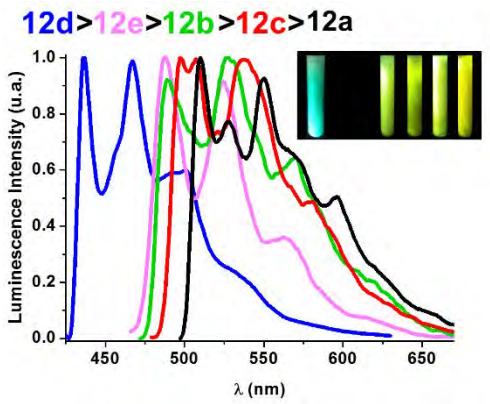

Capítulo 3. Compuestos luminiscentes heterolépticos bis-ciclometalados de Pt(II) y Pt(IV) con ligandos pentafluorofenilo

En este Capítulo, se estudian una serie de derivados de Pt(II) [Pt(bzq)(HC^N-*κN*)(C_6F_5)] (HC^N = Hthpy **16a**, Hpbt **16b**, Hpq **16c**, Hdfppy **16d**, Hoxd **16f**, Hpypy **16g**), que contienen el ligando ciclometalado bzq y otro ligando HC^N, y sus reacciones de oxidación para formar derivados heterolépticos de Pt(IV) *fac*-[Pt(bzq)(C^N)(C_6F_5)Cl] (**17a-g**). Se ha estudiado la influencia de la naturaleza electrónica de los diferentes ligandos auxiliares HC^N [en los compuestos de Pt(II)] o de los grupos ciclometalados C^N [en los derivados de Pt(IV)] en las propiedades fotofísicas, con el apoyo de cálculos teóricos DFT y TD-DFT.

En la primera parte de este Capítulo (3.1), se describe la síntesis, caracterización y estudio de las propiedades fotofísicas de los compuestos de Pt(II) [Pt(bzq)(HC^N-*κN*)(C_6F_5)] **16a-g** que se obtienen a partir del solvato [Pt(bzq)(C_6F_5)(acetona)]. Se ha realizado una asignación completa de las señales de ^{1}H and ^{13}C mediante experimentos de RMN 1D y 2D y se han confirmado las estructuras de los derivados **16a** y **16f** por difracción de Rayos X.

Los espectros de absorción de todos los derivados muestran, en la zona de baja energía, bandas que se atribuyen (con el apoyo de cálculos TD-DFT) a mezcla de transiciones ^{1}IL'/^{1}ML'CT, centradas en la unidad Pt(bzq), con contribuciones adicionales ^{1}MLCT o ^{1}L'LCT en **16c** y **16f** (L' = bzq, L = HC^N). Los derivados **16a-f** muestran emisiones fosforescentes en disolución y en films de PS, que se asignan a estados excitados de carácter ^{3}IL'/^{3}ML'CT centrados en el ligando bzq, con menor contribución de ^{3}IL/^{3}MLCT/^{3}L'LCT (L' = bzq, L = HC^N) en **16a** y **16c**. En el derivado **16g**, la presencia del ligando pireno (Hpypy), muy conjugado, provoca una emisión dual fluorescencia/fosforescencia ($^1\pi\pi^*_{Hpypy}$/$^3\pi\pi^*_{Hpypy}$) en CH_2Cl_2 a 298 K y una fosforescencia dual (^{3}IL'$_{bzq}$ / ^{3}ML'CT$_{Pt\rightarrow bzq}$ y $^3\pi\pi^*_{Hpypy}$) a 77K. En estado sólido, los derivados **16a-f** muestran emisiones que provienen de estados excitados de carácter excimérico debido a interacciones π···π, estados excitados ^{3}IL'/^{3}ML'CT o estados emisivos próximos.

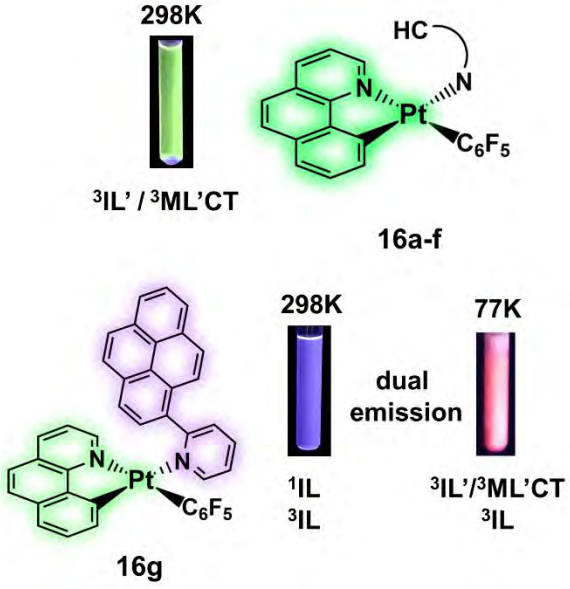

En la segunda parte del Capítulo (3.2) se describe la síntesis, caracterización y estudio de las propiedades ópticas de los compuestos de Pt(IV), *fac*-[Pt(bzq)(C^N)(C_6F_5)Cl] (**17a,b,c,d,g**), que contienen el ligando bzq y un segundo ligando ciclometalado C^N. Estos se obtienen por oxidación de los derivados de Pt(II) **16** con $PhICl_2$, y segunda metalación del ligando N-heterocíclico HC^N. Sin embargo, todos los intentos de obtener el compuesto **17f** con el ligando oxd ciclometalado fueron

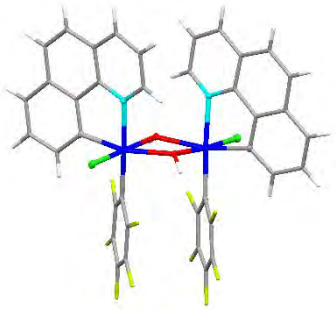

infructuosos, ya se produce el desplazamiento del ligando Hoxd y la formación del compuesto bimetálico de Pt(IV) *syn*-[Pt(bzq)(C_6F_5)Cl(μ-OH)]$_2$ **18**. Las estructuras de los derivados **17c**, **17d**, **17g** and **18** se han confirmado por difracción de Rayos X, y se ha llevado a cabo la asignación completa de las señales de ^{1}H and ^{13}C en todos los compuestos, mediante experimentos de RMN 1D y 2D.

Los compuestos **17a-d** muestran emisiones fosforescentes con bandas estructuradas y tiempos de vida largos, centradas en el ligando ciclometalado de menor energía, en coherencia también con cálculos teóricos. Así, en los derivados **17a-c**, la emisión se localiza en el segundo ligando ciclometalado C^N (con algo de contribución ^{3}L'LCT en **17a**), y en el ligando bzq en **17d**. Esta asignación se confirmó por comparación con los espectros de emisión de los derivados homolépticos de Pt(IV) **12**. Las emisiones de los derivados **17a-c** son más eficientes que las que se observan en los respectivos análogos homolépticos [ϕ (%), 11/8.2 (**17a**/**12a**), 22/3.1 (**17b**/**12b**), 85/18.1 (**17c**/**12c**)], indicando que la coordinación de dos ligandos diferentes mejora las propiedades emisivas.

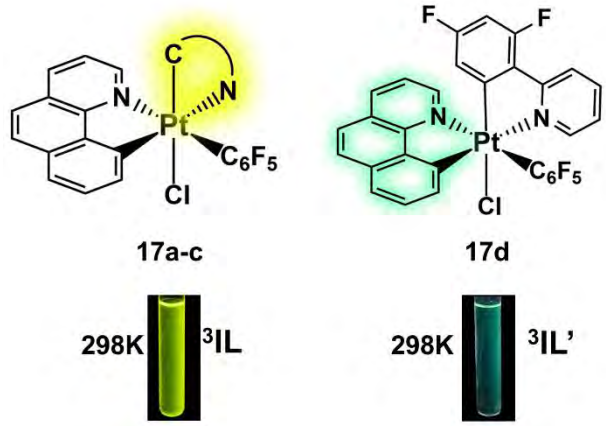

El derivado **17g**, que contiene el ligando pypy ciclometalado, muestra en disolución a temperatura ambiente una emisión de fluorescencia localizada en el pireno ($^1\pi\pi^*_{pypy}$) y una emisión dual fluorescencia($^1\pi\pi^*_{pypy}$)/fosforescencia ($^3\pi\pi^*_{pypy}$) cuando la disolución se congela a 77 K. Este compuesto muestra, en PS y en estado sólido, una emisión que se asigna a una mezcla de estados emisivos próximos $^1\pi\pi^*_{pypy}/^3$IL'$_{bzq}$, junto con una banda adicional en la zona de baja energía atribuida a $^3\pi\pi^*_{pypy}$ (en PS). El hecho de que en este derivado **17g** se observe mayoritariamente fluorescencia, se debe probablemente a la baja contribución de los orbitales del Pt en las transiciones, lo que provoca que el cruce intersistémico singlete-triplete sea poco eficiente.

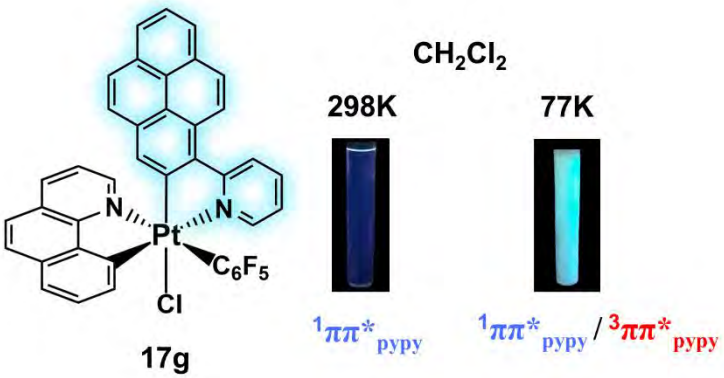

Capítulo 4. Derivados heterobimetálicos Pt(II)-Au(I)

En este Capítulo se describe la síntesis y propiedades de [Pt(bzq)(C_6F_5)(κ^1-dppm)] **19** y del derivado bimetálico Pt(II)-Au(I) [Pt(bzq)(C_6F_5)(μ-dppm)AuCl] **20**, con el ligando dppm actuando de puente entre los centros metálicos. Ambos compuestos se han caracterizado por RMN y sus estructuras se han confirmado por difracción de Rayos X. Durante el proceso de cristalización del derivado **19** se produce la oxidación de fósfororo libre del grupo dppm, dando lugar la especie [Pt(bzq)(C_6F_5)(κ^1-dppmO)] **19-O**. La estructura cristalina de **20** revela que no existe enlace entre los centros de Pt(II)-Au(I) lo que se refleja en sus propiedades ópticas. Ambos derivados muestran emisiones fosforescentes con tiempos de vida largos, que se asignan a estados excitados de carácter ^{3}IL(bzq)/^{3}MLCT(Pt→bzq), siendo prácticamente nula la contribución del fragmento Au-Cl en **20**.

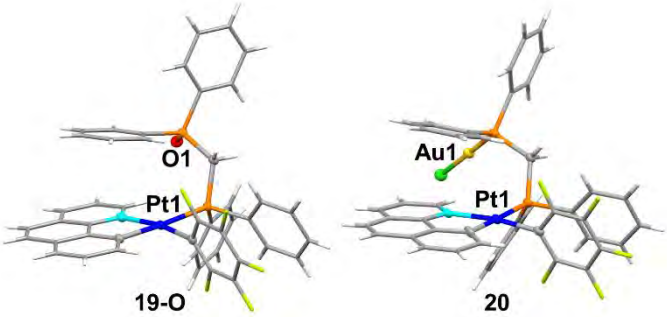

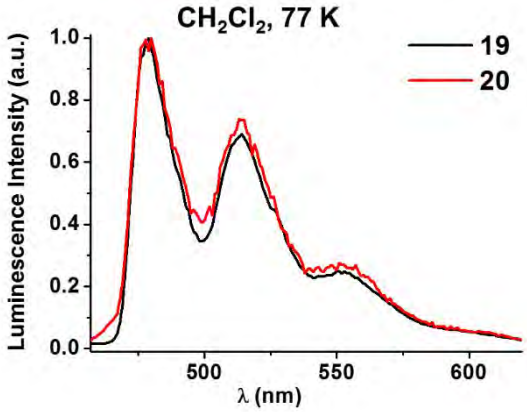

Se ha evaluado la actividad citotóxica de ambos derivados, y se ha comparado con la de derivados análogos monometálicos [Pt(C^N)(*p*-MeC_6H_4)(κ^1-dppm)] (C^N = bzq **19b***, ppy **19c***) y bimetálicos [Pt(C^N)(*p*-MeC_6H_4)(μ-dppm)AuCl] (C^N = bzq **20b***, ppy **20c***), en colaboración con el grupo de investigación del Dr. H. R. Shahsavari. El derivado heterobimetálico Pt-Au **20** muestra una mejora en la actividad citotóxica evaluada *in vitro* frente a las líneas tumorales MCF-7 (cáncer de mama), SKOV3 (cáncer de ovario)y A549 (cáncer de pulmón), en comparación con las del precursor de platino **19** y con [ClAu(μ-dppm)AuCl], lo que sugiere un efecto cooperativo de los dos centros metálicos. Además, se observado que la

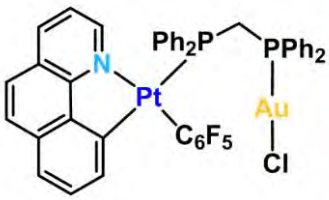

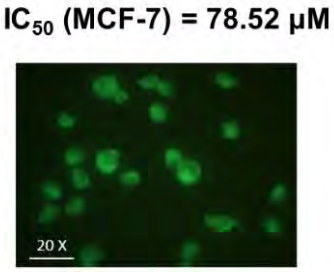

presencia del ligando ciclometalado bzq y del grupo *p*-MeC_6H_4 mejora la actividad citotóxica respecto a los grupos pypy y C_6F_5. Debido a que el derivado **20** es emisivo en disolución a temperatura ambiente, se han llevado a cabo experimentos de microscopía de fluorescencia observándose que este derivado internaliza de manera eficiente en las células MCF-7, localizándose principalmente en el núcleo, con menos dispersión en el citoplasma.

Conclusiones

- ✓ Se han obtenido los ligandos libres funcionalizados vinil benzoquinoleína [(*Z*)-bzq-CH=C(X)Fc] (X = Cl, I), con los grupos ferrocenilo/haluro en posición geminal (X = Cl, Rayos X).

- ✓ Las reacciones de oxidación de los solvatos [Pt(bzq)(C_6F_5)(S)] (S = CH_3COCH_3, tht) han permitido preparar una familia de derivados mononucleares no emisivos de Pt(IV) [Pt(bzq)(C_6F_5)X_2(L)] (L = dmso, tht), identificados como una mezcla de isómeros *cis* y *trans*.

- ✓ Se han preparado pentafluorofenil derivados luminiscentes de Pt(II) [Pt(C^N)(HC^N-κN)(C_6F_5)] (HC^N = thpy, pbt, pq, dfppy), que contienen un ligando ciclometalado y un ligando heterocíclico coordinado a través del nitrógeno, mediante la metalación de uno de los ligandos HC^N en los precursores *cis*-[Pt(HC^N-κN)$_2$(C_6F_5)$_2$]. Todos los derivados muestran emisiones fosforescentes con tiempos de vida largos, asignadas a estados excitados de carácter ^{3}MLCT/^{3}IL (L = HC^N) en los derivados (κ-*N*)$_2$ y a ^{3}IL'/^{3}ML'CT (L' = C^N) en los derivados ciclometalados. Los sistemas ciclometalados evolucionan en dmso a los derivados [Pt(C^N)(C_6F_5)(dmso)], y se han evaluado las propiedades emisivas y las propiedades biológicas de los solvatos de dmso con C^N = thpy, pbt.

- ✓ Las reacciones de oxidación con $PhICl_2$ de los compuestos de Pt(II) [Pt(C^N)(HC^N-κN)(C_6F_5)] produce una fácil metalación del ligando HC^N, y genera los derivados luminiscentes de Pt(IV) *fac*-[Pt(C^N)$_2$(C_6F_5)Cl] (C^N = thpy, pbt, pq, dfppy, bzq). Algunos de los derivados de Pt(IV) se han obtenido también por irradiación en disolventes clorados a través de especies hidruro *cis*-[Pt(C^N)$_2$(C_6F_5)H], detectados como intermedios. La sustitución del Cl^- por CN^- en el derivado de pbt provoca la isomerización de *fac* a *mer*, mientras que la sustitución por Mepy o bpe no produce isomerización, formándose los derivados catiónicos *fac*-[Pt(pbt)$_2$(C_6F_5)L]$^+$ (L = Mepy, bpe). Los compuestos de Pt(IV) presentan emisiones estructuradas que provienen de estados excitados ^{3}IL, como se confirma por cálculos teóricos, desplazadas hacia el azul y con tiempos de vida más largos que los precursores de Pt(II). La sustitución del Cl^- por CN^- o Mepy

no afecta a la naturaleza del estado emisivo, pero sí incrementa la eficiencia de las emisiones. Sin embargo, la sustitución por bpe desactiva la emisión debido a un proceso de isomerización *E/Z* en este ligando.

- ✓ Siguiendo una estrategia similar, se ha preparado una familia de compuestos de Pt(II) [Pt(bzq)(HC^N-*κN*)(C_6F_5)] (HC^N = Hthpy, Hpbt, Hpq, Hdfppy, Hoxd, Hpypy), con el ligando bzq y ligandos N-heterocíclicos HC^N, con propiedades electrónicas diferentes, como precursores para la preparación de derivados heterolépticos de Pt(IV) *fac*-[Pt(bzq)(C^N)(C_6F_5)Cl] (C^N = thpy, pbt, pq, dfppy, pypy). Los compuestos [Pt(bzq)(HC^N-*κN*)(C_6F_5)] muestran emisiones fosforescentes centradas en el fragmento Pt(bzq) (^{3}IL'/^{3}ML'CT), con una menor contribución de los ligandos no ciclometalados. Sin embargo, el compuesto [Pt(bzq)(Hpypy)(C_6F_5)] muestra una emisión dual fluorescencia/fosforescencia ($^1\pi\pi^*/^3\pi\pi^*$)$_{Hpypy}$ localizada en el ligando pireno, o una fosforescencia dual localizada en la unidad Pt(bzq) (^{3}IL'/^{3}ML'CT) y en el ligando Hpypy ($^3\pi\pi^*$), dependiendo de la temperatura. Tras la oxidación, los derivados de Pt(IV) muestran emisiones fosforescentes localizadas en el grupo C^N con el orbital π* más bajo en energía. Estos derivados presentan emisiones más eficientes que los derivados homolépticos, indicando que la coordinación de dos ligandos ciclometalados diferentes mejora las propiedades emisivas.

- ✓ Para finalizar, se ha preparado el derivado mononuclear de Pt(II) [Pt(bzq)(C_6F_5)(κ^1-dppm)] y el derivado bimetálico Pt(II)-Au(I) [Pt(bzq)(C_6F_5)(μ-dppm)AuCl] y se han estudiado y comparado sus propiedades ópticas y biológicas. Ambos compuestos muestran una emisión similar con tiempo de vida largo, que se asigna a estados excitados de carácter ^{3}IL(bzq)/^{3}MLCT(Pt-bzq), probablemente debido a que no existe enlace entre los centros metálicos. Se ha observado una mejora en las propiedades citotóxicas *in vitro* para el derivado heterobimetálico, en comparación con el derivado monometálico de Pt(II) y con [ClAu(μ-dppm)AuCl], sugiriendo un posible efecto cooperativo de los centros metálicos. Los experimentos de microscopía de fluorescencia revelan la internalización del compuesto bimetálico Pt(II)-Au(I) en las células MCF7 y su localización principalmente en el núcleo.

Experimental

A. Instrumental and spectroscopic techniques

Elemental analyses

Elemental analyses have been carried out with a Carlo Erba EA1110 CHNS/O microanalyzer.

Mass spectra

The Electrospray Mass spectra were performed using a VG Autospec double-focusing mass spectrometer operating in the negative FAB mode or a HP5989B mass spectrometer with interphase API-ES HP 59987A. MALDI-TOF spectra have been recorded in a Microflex MALDI-TOF Bruker spectrometer operating in the linear and reflector modes using dithranol as matrix in those cases that it was needed.

Infrared spectra

IR spectra were obtained from Nujol mulls between polyethylene sheets (Nujol absorptions: 2900, 1452, 1377, 1362 cm^{-1}), using a Nicolet Nexus FT-IR spectrometer between 4000 and 200 cm^{-1}.

Nuclear Magnetic Resonance spectra

The ^{1}H, ^{19}F, $^{19}F\{^{1}H\}$, $^{31}P\{^{1}H\}$, $^{13}C\{^{1}H\}$, and $^{195}Pt\{^{1}H\}$ NMR experiments described in this memory were recorded on a Bruker AVANCE 400 and/or a Bruker ARX300 spectrometer. Chemical shifts are reported in parts per million (ppm) relative to external standards ($SiMe_4$ for ^{1}H and $^{13}C\{^{1}H\}$, $CFCl_3$ for ^{19}F and $^{19}F\{^{1}H\}$ and 85% H_3PO_4 for $^{31}P\{^{1}H\}$) and all coupling constants are given in hertz (Hz).

UV-Vis spectroscopy

UV-Vis spectra were recorded on a Hewlet Packard 8453 spectrometer. The DRUV (diffuse reflectance ultraviolet) in the solid state have been using a Shimadzu UV-3600 spectrometer with a Harrick Praying Mantis accessory coupled to it. Samples were prepared mixing the complex with KBr, and the reflectance information transformed following the Kubelka-Munk function.

Emission spectroscopy, quantum yields and lifetime measurements

Excitation and emission spectra were obtained on a Jobin-Yvon Horiba Fluorolog 3-11, Tau-3 spectrofluorimeter. The lifetime measurements were performed operating in the phosphorimeter mode (with a F1-1029 lifetime emission PMT assembly, using a 450 W Xe lamp) or with a Data station HUB-B with a nanoLED controller and software DAS6. The nanoLEDs employed for lifetime measurements were of 450, 390, 370, 350 or 320 nm with pulse lengths of 0.8-1.4 ns. Quantum yields in the solid state or PMMA and PS films were measured using a F-3018 Integrating Sphere mounted on a Fluorolog 3-11 Tau-3 spectrofluorimeter. Data have been fittered using the Jobin-Yvon software package and Origin 8.0.

Theoretical calculations

Calculations of all complexes were carried out with the Gaussian 09 package[171] using Becke's three-parameter functional combined with Lee–Yang–Parr's correlation functional (B3LYP) in the singlet state (S_0) and the unrestricted U-B3LYP in the triplet state (T_1).[172] The basis set used was the LanL2DZ effective core potential for Pt and 6-31G (d,p) for the ligand atoms.[173]

In **Chapter 1**, all isomers were optimized without considering solvent effects and no negative values were found in the results of the vibrational frequency analysis. In **Chapters 2 and 3**, DFT and the time-dependent density-functional theory (TD-DFT) calculations were carried out using the polarizable continuum model approach (PCM)[174] implemented in the Gaussian 09 software or in gas phase for complexes **17**. No negative frequency was found in the vibrational frequency analysis of the final equilibrium geometries, with the exception of **16f** when the optimization was carried out in the triplet state including solvent effects (CH_2Cl_2) at the PCM level. For this reason, the data related to the triplet state in **16f** are reported in gas phase. Percentage compositions of molecular orbitals were calculated using the Gauss-Sum program.[175] The emission energy was calculated as the difference of the DFT-optimized T_1 geometry for both states (adiabatic electronic transition). The charge-transfer character between the metal and the ligands, denoted as "metal %CT" (**Chapter 2.2**),[67b and references therein] has been estimated for selected singlet and triplet vertical excitations obtained from TD-DFT calculations by using the following equation: metal %CT = $\Sigma[C(i\rightarrow j)]^2(\%Mi-\%Mj)$, where $C(i\rightarrow j)$ are the

coefficients of each of the participating monoexcitations and %Mi and %Mj are the percentages of the metal orbital contribution to the involved molecular orbitals. Positive metal %CT indicate a net metal-to-ligand charge-transfer character (MLCT), while negative values indicate a net ligand-to-metal charge transfer character (LMCT).

In **Chapter 4**, the theoretical calculations were performed by Dr. Shahsavari's research group, with the program suite Gaussian 09[171] using the B3LYP level of theory.[172] The LANL2DZ basis set was chosen to describe Pt and the 6-31G(d) basis set was chosen for other atoms.[173] The geometries of complexes were fully optimized by employing the density functional theory without imposing any symmetry constraints. In order to ensure the optimized geometries, frequency calculation were performed employing analytical second derivatives. Solvent effects was considered by the conductor-like polarizable continuum model (CPCM).[176] The calculations for the electronic absorption spectra by time-dependent DFT (TD-DFT) were performed at the same level of theory. The compositions of molecular orbitals and theoretical absorption spectra were plotted using "Chemissian" software.[177]

Crystal structures

The diffraction data were collected using graphite monochromatic Mo-Kα radiation with a Nonius-κCCD diffractometer at a temperature of 173 K with an Oxford Cryosystem temperature controller, and images processed using the DENZO and SCALEPACK suite of programs[178] or with a Bruker APEX-II diffractometer at a temperature of 120 K using the APEX-II software. Details concerning structural resolution, including special methodology, are included in section D.

Cell culture

Chapter 2 – Collaboration with CIBIR

Human lung cell lines A549 (adenocarcinomic alveolar basal epithelial cells) and NL20 (immortalized bronchial epithelial cells), and immortalized mouse embryonic fibroblasts (3T3) obtained from lungs (LMEFs), were cultured following the American Type Culture Collection (http://www.atcc.org) recommendations and standard methods. A549 and LMEF cells were maintained in RPMI 1640 and DMEM (Dulbecco's Modified Eagle's Medium), respectively, supplemented with 10 % fetal bovine serum (FBS) and

2.0 mM L-glutamine. The NL20 cell line was grown in Ham's F-12 medium supplemented with 1.5 g/L sodium bicarbonate, 2.7 g/L glucose, 2.0 mM L-glutamine, 0.1 mM non-essential aminoacids, 0.005 mg/mL insulin, 10 ng/mL epidermal growth factor, 0.001 mg/mL transferrin, 500 ng/mL hydrocortisone and 4% FBS. Penicillin (100 U/mL) and streptomycin (100 µg/mL) were added to all media. Cultures were maintained under a humidified atmosphere of 95% air/5% CO_2 at 37 °C, and were sub-cultured before they get confluent using a 0.25% trypsin-EDTA solution.

Chapter 4 – Collaboration with Dr. Shahsavari's research group.

Human cancer cell lines, MCF-7 (breast cancer), SKOV3 (ovarian cancer), and A549 (non-small cell lung cancer) were purchased from National Cell Bank of Iran (NCBI, Pasteur Institute, Tehran, Iran). The cells were grown in complete culture media containing RPMI 1640 (Biosera, France), 10 % fetal bovine serum (FBS; Gibco, USA) and 1 % penicillin–streptomycin (Biosera, France) and kept at 37 °C in a humidified CO_2 incubator. MCF10A cells (human breast epithelial cell line) were cultured in DMEM/ Ham′s F-12 (GIBCO-Invitrogen, Carlsbad, CA) supplemented with 100 ng/mL cholera toxin, 20 ng/mL epidermal growth factor (EGF), 0.01 mg/mL insulin, 500 ng/mL hydrocortisone, and 5 % chelextreated horse serum.

Cytotoxicity assay

Chapter 2 – Collaboration with CIBIR

The MTS (3-(4,5-dimethylthiazol-2-yl)-5-(3-carboxymethoxyphenyl)-2-(4sulfophenyl)-2H-tetrazolium) hydrolysis method (MTS-based CellTiter® 96. AQueous Assay; Promega Corp., Madison, WI) was used to determine cell viability as an indicator for A549 and NL20 cell sensitivity to the complexes. 50 µL of exponentially growing cells were seeded at a density of 1.5×10^3 (A549) or 7.0×10^3 (NL20) cells per well, in a 96-well flat-bottomed microplate in their respective cell culture growing media with reduced concentrations of FBS, 5% in the case of A549 and 2% for NL20. 24 h later, they were incubated for 72 h with the compounds. The complexes were dissolved at their maximal solubility in DMSO (**11a** and **11-ppy*** at 16 mM, and **11b** at 8 mM) and cisplatin (Alfa Aesar; Karlsruhe, Germany), as a reference, was dissolved at 6.4 mM in saline solution (0.15 M NaCl).[179] These stock solutions were kept frozen until they were dissolved in a test medium as nine 2 × serial dilutions (1 : 1.5). 50 µL of each compound

dilution or the medium alone was added to the growing cells in the 96-well plate designed as previously recommended.[180] Final concentrations in sextuplicates ranged from: 3.12 to 80 μM (**11a**, **11b** and **11-ppy***), and 1.56 to 40 μM (cisplatin) for A549 cells; 3.12 to 80 μM (**11a** and **11-ppy***), 1.38 to 35.5 μM (**11b**) and 0.69 to 17.77 μM (cisplatin) for NL20 cells. After 72 h at 37 °C, 20 μl of MTS was added and the plates were incubated for 1–2 h at 37 °C. Finally, the optical density was measured at 590 nm using a 96-well multiscanner autoreader (POLARstar Omega, BMG Labtech, Germany). Each experiment was repeated three times. Appropriate solvent controls were run along with samples to discard the DMSO cytotoxic effect at concentrations ≤ 1%. The IC_{50} value (drug concentration that produced 50% inhibition of cell proliferation) was calculated by plotting the percentage of growing inhibition versus log of the drug concentration using the GraphPad Prism 6 (La Jolla, CA) software.

Chapter 4 – Collaboration with Dr. Shahsavari's research group.

Cytotoxic activities of the synthesized compounds were investigated using a standard 3-(4,5-dimethylthiazol-yl)-2,5-diphenyltetrazolium bromide (MTT) assay, as described previously.[181] To do this, the cells with a density of 0.8×10^4 cells per well were seeded in 96-well microplates and kept for 24 h to recover. The cells were then treated with the synthesized compounds in different concentrations from 1 to 100 μM in a triplicate manner and incubated for more 72 hours at 37 °C in humidified CO_2 incubator. Following incubation, the media were completely discarded and replaced with 150 μL of RPMI 1640 containing 0.5 mg/mL MTT solution and incubated at room temperature for 3 h. To dissolve the formazan crystals, the media containing MTT was discarded again and 150 μL of dmso was added to each well and incubated for more 30 min at 37 °C in the dark. The absorbance of individual well was then read at 490 nm with an ELISA reader. The 50 % inhibitory concentration of each compound, representing IC_{50}, was calculated using Curve- Expert 1.4. Data are presented as mean ±SD.

Localization in cells

Chapter 2 – Collaboration with CIBIR

A549 and NL20 cells were cultured over one cm diameter poly-L-lysine coated coverslips into a 24-well plate with 1 mL per well of supplemented culture medium for 48 h. After incubation at 37 °C for 30 min in 1 mL of a new cell line specific medium

containing 40 μM of each compound and 3.2 μM of Hoechst 33258 (Sigma), the cells were finally washed twice in phosphate buffer saline (PBS, pH 7.2). Hoechst 33258 was added as a fluorescent stain for chromosomes suitable for nuclei staining in living cells due to its non-toxic effect and permeability through cell membranes.[124] As a control to discard emission bleeding between light channels, the incubation of cells was also performed separately with each compound (**11a**, **11b** and **11-ppy***) and also with Hoechst alone. The cells were finally washed twice in phosphate buffer saline (PBS, pH 7.2). Coverslips were removed, mounted on glass slides and sealed with vaseline before being immediately examined under a fluorescence microscope (Leica DM600B). The microscope was equipped with a Nomarski differential interference contrast for transmitted light, and with an incident light fluorescence illuminator accommodating three filter cubes (N2.1: λ_{ex} filter BP 515-60, dichromatic mirror 580, suppression filter λ_{em} LP 590; Y5: λ_{ex} filter BP 620/60, dichromatic mirror 660, suppression filter λ_{em} BP 700/75; and A4: λ_{ex} filter BP 360/40, dichromatic mirror 400, suppression filter λ_{em} BP 470/40) (Leica), suitable for imaging switching between Nomarski DIC transmitted light, and green, red and blue fluorescent light channels. The images were documented using a 100 × objective (Leica PLAN APO) and a B&W digital camera (Hamamatsu ORCA R2, mod. C10600) with the help of Micro-Manager Open Source Microscopy Software and Fiji/ImageJ free software.[182]

Chapter 4 – Collaboration with Dr. Shahsavari's research group.

The MCF-7 cells were cultured over coverslips in a 6-well plate in complete culture media for 24 h. The cells were then incubated with 1000 μM of **20** at 37 °C for 4 h. The cells were then washed twice in 1 × Phosphate Buffer Saline (PBS, pH = 7.2) and fixed with cold absolute methanol for 15 min (Merck, Germany). Following drying in room temperature, the cell covered by glycerol, mounted on glass slides and were immediately observed under a fluorescence microscope (BX61, Olympus, Japan). The images were taken at 20 × and 40 × magnification and analyzed by the Olympus micro imaging software cellSens (Olympus, Japan). The emission of compound could be detected at two channels (Excitation = 365/10, Emission = 420LP and Excitation = 535/30, Emission = 580LP).

B. Synthesis of the starting materials

The starting materials are prepared following reported procedures

[Pt(bzq)(C_6F_5)(acetone)][46]

[Pt(bzq)(Hbzq-*kN*)(C_6F_5)][46]

[Pt{κ*N*:η^2-bzq-CH=C(Cl)Fc}(C_6F_5)Cl] (**A**)[72]

[Pt{κ*N*:η^2-bzq-CH=C(I)Fc}(C_6F_5)I] (**B**)[72]

[Pt(bzq)(C_6F_5)Cl(μ-Cl)]$_2$ (**C**)[72]

[Pt(bzq)(C_6F_5)I(μ-I)]$_2$ (**D**)[72]

[Pt(bzq)(C_6F_5)Br(μ-Br)]$_2$ (**E**)[72]

[Pt(bzq)(C_6F_5)(tht)][48]

cis-[Pt(C_6F_5)$_2$(thf)$_2$][183]

cis-[Pt(C_6F_5)$_2$(dmso)$_2$][86]

$PhICl_2$[184]

[AuCl(SMe)$_2$][168]

2-phenyl-benzo[*d*]thiazole (Hpbt)[185]

1-(2-pyridyl)pyrene (Hpypy)[186]

Preparation of [Pt(bzq)(C_6F_5)(dmso)]

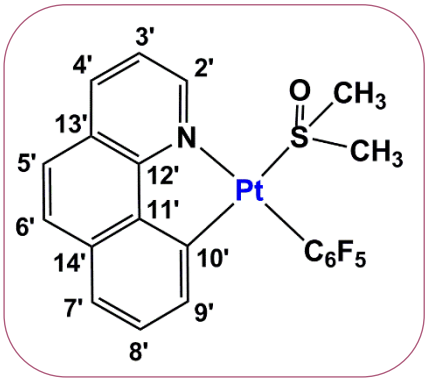

To a yellow solution of [Pt(bzq)(C_6F_5)(acetone)] (0.25 g, 0.47 mmol) in 8 mL of Et_2O/acetone (3:1) was added 0.1 mL of dmso. After 30 min. of stirring, the residue was evaporated to dryness and treated with 1 mL of isopropanol and 5 mL of *n*-hexane. The obtained pallid-yellow solid was filtered and washed with hexane affording [Pt(bzq)(C_6F_5)(dmso)] (0.225 g, 77 %).

ESI (+): *m/z* (%) 718 [M-dmso]+Na^+ (37).

Elemental Analysis (%): Calc. for $C_{21}H_{14}F5NOPtS$: C, 40.78; H, 2.28; N, 2.26; S, 5.18. Found: C, 41.09; H, 2.44; N, 2.01; 5.06.

^{1}H NMR (400.1 MHz, $CDCl_3$, 20ºC, δ): 9.93 (dd, 1H, J= 5.4, J = 1, $^3J_{Pt\text{-}H}$= 20.5, $H^{2'}$), 7.40 (dd, 1H, J= 8.1, J = 1, 1H, $H^{4'}$), 7.78 (d, 1H, J= 8.7, 1H, $H^{5'/6'}$), 7.65-7.60 (m, 3H, $H^{7',5'/6',3'}$), 7.39 (t, 1H, J= 7.6, $H^{8'}$), 6.61 (d, 1H, J= 7.2, $^3J_{Pt\text{-}H}$= 60, $H^{9'}$), 3.12 (s, 6H, $^3J_{Pt\text{-}H}$= 15.1, dmso).

^{13}C{^{1}H} NMR (100.6 MHz, $CDCl_3$, 20ºC, δ): 155.7 (s, $C^{12'}$, bzq), 149.9 (s, $C^{2'}$, bzq), 144.0 (s, $C^{10'}$, bzq), 141.6 (s, $C^{11'}$, bzq), 138.4 (s, $C^{4'}$, bzq), 133.9 (s, $C^{9'}$, bzq), 133.7 (s, $C^{14'}$, bzq), 129.5 (s, $C^{5'/6'}$, bzq), 129.4 (s, $C^{8'}$, bzq), 127.2 (s, $C^{13'}$, bzq), 124.3 (s, $C^{7'}$, bzq), 123.3 (s, $C^{5'/6'}$, bzq), 121.9 (s, $C^{3'}$, bzq), 45.3 (s, $^2J_{Pt\text{-}C}$ = 37, dmso).

^{19}F{^{1}H} (376.5 MHz, $CDCl_3$, 20ºC, δ): -116.7 (dm, $^3J_{Pt\text{-}oF}$ = 484, 2*o*-F, C_6F_5), -159.4 (t, 1*p*-F, C_6F_5), -161.7 (m, 2*m*-F, C_6F_5).

C. Synthesis of new compounds

Preparation of **[bzq-CH=C(Cl)Fc] (1)**

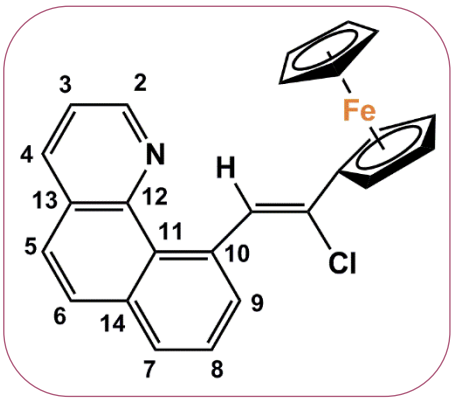

To a cooled (0 ºC) solution of [Pt{κ*N*:η^2-bzq-CH=C(Cl)Fc}(C_6F_5)Cl] (0.129 g, 0.157 mmol) in CH_2Cl_2 (20 mL) was added 2 equiv. of triphenylphosphine (0.082 g, 0.314 mmol). After 1 h of stirring, the solvent was removed and the residue treated with Et_2O (20 mL), giving a solid which was filtered and identified as *trans*-[Pt(C_6F_5)Cl(PPh_3)$_2$] (0.040 g, 28%). The orange filtrate was concentrated to a small volume (2 mL) and purified by column chromatography (SiO_2, *n*-hexane/CH_2Cl_2 8/2) to give **1** as an orange solid (21 mg, 32%).

IR (cm^{-1}): ν(C=C) 1374 (s).

MALDI-TOF(+): *m/z* (%) 423 [M]$^+$ (100).

Elemental Analysis (%): Calc. for $C_{25}H_{18}ClFeN$: C, 70.87; H, 4.28; N, 3.31. Found: C, 70.41; H, 3.89; N, 3.52.

^{1}H NMR (400.1 MHz, $CDCl_3$, 20ºC, *δ*): δ 9.12 (dd, 1H, *J* = 4.2, *J* = 1.6, H^2, bzq), 8.31 (s, 1H, bzq-C*H*=CFcCl), 8.19 (d, 1H, *J* = 8, H^4, bzq), 7.96 (d, 1H, *J* = 7.9, H$^{7/9}$, bzq), 7.92 (d, 1H, *J* = 7.9, H$^{7/9}$, bzq), 7.85 (d, 1H, *J* = 8.8, H$^{5/6}$, bzq), 7.73 (t, 1H, *J* = 7.9, H^8, bzq), 7.70 (d, 1H, *J* = 8.8, H$^{5/6}$, bzq), 7.53 (dd, 1H, *J* = 4.2, *J* = 8.1, H^3, bzq), 4.83 (s, 2H, C_5H_4), 4.36 (s, 2H, C_5H_4), 4.30 (s, 5H, Cp).

^{13}C{^{1}H} NMR (100.6 MHz, $CDCl_3$, 20ºC, *δ*): δ 148.0 (s, C^{12}, bzq), 147.5 (s, C^2, bzq), 135.5 (s, C^4, bzq), 134.8 (s, =*C*(Cl)Fc), 131.2 (s, C$^{7/9}$, bzq), 129.2 (s, bzq), 128.7 (s, C$^{5/6}$, bzq), 128.0 (s, C$^{7/9}$, bzq), 127.7 (s, bzq), 127.3 (s, C^8, bzq), 127.1 (s, *C*H=C(Cl)Fc), 126.7 (s, bzq), 125.6 (s, C$^{5/6}$, bzq), 121.1 (s, C^3, bzq), 69.7 (s, 5C, Cp), 69.1 (s, 2C, C_5H_4), 67.3 (s, 2C, C_5H_4).

$E_{1/2}$ = 0.55 V (*vs* Ag/AgCl) (more waves due to electrogenerated by products are seen at higher potentials).

Preparation of **[bzq-CH=C(I)Fc] (2)**

Following the same procedure as that for **1**, starting from [Pt{κ*N*:η^2-bzq-CH=C(I)Fc}(C_6F_5)I] (0.093 g, 0.093 mmol) and PPh_3 (0.049 g, 0.186 mmol), **2** was obtained as an orange solid after purification by column chromatography (SiO_2, *n*-hexane/CH_2Cl_2 8/2) (0.014 g, 29 %).

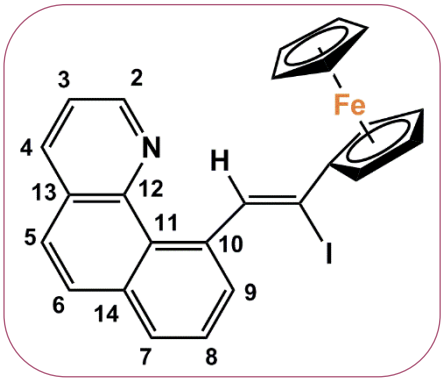

IR (cm^{-1}): ν(C=C) 1374 (s).

MALDI-TOF(+): *m/z* (%) 515 [M]$^+$ (82), 388 [M-I]$^+$ (100).

Elemental Analysis (%): Calc. for $C_{25}H_{18}IFeN$: C, 58.29; H, 3.52; N, 2.72. Found: C, 57.91; H, 3.29; N, 2.51.

^{1}H NMR (400.1 MHz, CD_3COCD_3, 20ºC, *δ*): δ 9.16 (dd, 1H, *J* = 4.3, *J* = 1.4, H^2, bzq), 8.39 (d, 1H, *J* = 8.1, H^4, bzq), 8.19 (s, 1H, bzq-C*H*=CFcI), 8.05 (m, 1H, H^8, bzq), 7.98 (d, 1H, *J* = 8.7, H$^{5/6}$, bzq), 7.86 (d, 1H, *J* = 8.7, H$^{5/6}$, bzq), 7.78-7.73 (m, 2H, H^7, H^9, bzq), 7.67 (m, 1H, H^3, bzq), 4.86 (s, 2H, C_5H_4), 4.44 (s, 2H, C_5H_4), 4.31 (s, 5H, Cp).

^{13}C{^{1}H} NMR (100.6 MHz, CD_3COCD_3, 20ºC, *δ*): δ 148.5 (s, C^{12}, bzq), 147.9 (s, C^2, bzq), 137.3 (s, *C*H=C(I)Fc), 135.8 (s, C^4, bzq), 131.2 (s, C$^{7/9}$, bzq), 130.5 (s, bzq), 128.4 (s, C$^{5/6}$, bzq), 128.3 (s, C^8, bzq), 127.1 (s, C$^{7/9}$, bzq), 126.8 (s, bzq), 126.0 (s, =*C*(I)Fc), 125.8 (s, C$^{5/6}$, bzq), 123.5 (s, bzq), 121.5 (s, C^3, bzq), 69.7 (s, 5C, Cp, Fc), 69.3 (s, 2C, C_5H_4, Fc), 68.9 (s, 2C, C_5H_4, Fc).

$E_{1/2}$ = 0.57 V (*vs* Ag/AgCl) (more waves due to electrogenerated by products are seen at higher potentials).

Preparation of **[Pt(bzq)(C_6F_5)Cl_2(dmso)] (3)**

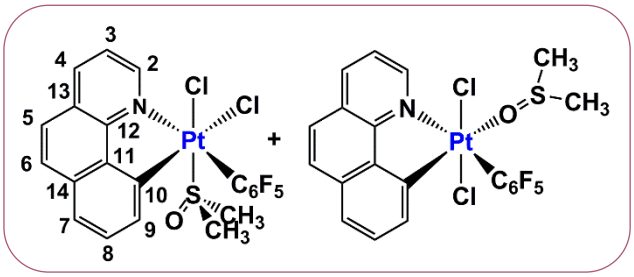

A suspension of [Pt(bzq)(C_6F_5)Cl(μ-Cl)]$_2$ (0.050 g, 0.041 mmol) in 2 mL of dmso was heated to 50ºC for 5 min and stirred until complete dissolution of the corresponding complex. The solution was poured into 400 mL of H_2O and the obtained pale-yellow precipitate was filtered to give **3** (0.046 g, 82%).

IR (cm^{-1}): ν(C-F) 1073 (s), 970 (s); ν(C_6F_5)$_{X\text{-sens}}$ 798 (m); ν(Pt-Cl) 349 (m), 325 (w).

MALDI-TOF (-): *m/z* (%) 646 [M-dmso+Cl]$^-$ (100), 610 [M-dmso]$^-$ (35), 576 [Pt(bzq)(C_6F_5)Cl]$^-$ (62).

Elemental Analysis (%): Calc. for $C_{21}H_{14}Cl_2F_5NOPtS$: C, 36.59; H, 2.05; N 2.03; S 4.65. Found: C, 36.10; H, 2.19; N, 2.26; S, 3.97.

^{1}H NMR (400.1 MHz, CD_3COCD_3, -30º C, *cis*:*trans* isomers ~ 1:1.5, *δ*): *cis*-3(dmso-κ*S*) 9.42 (d, 1H, *J* = 5.0, H^2, bzq), 8.81 (d, 1H, *J* = 8.6, H^4, bzq), 8.10 (m, 3H, H^5, H^6, H^3, bzq), 7.82 (t, 1H, *J* = 8.0, H^8, bzq), 7.59 (d, 1H, *J* = 7.3, H^7, bzq), 7.32 (t, 1H, *J* = 8.4, $J_{Pt\text{-}H}$ = 39, H^9, bzq), 3.08 (s, 3H, CH_3, dmso), 3.03 (s, 3H, CH_3, dmso); ***trans*-3(dmso-κ*O*)** 9.40 (d, 1H, *J* = 5.1, H^2, bzq), 8.85 (d, 1H, *J* = 8.1, H^4, bzq), 8.15-8.04 (m, 3H, H^5, H^6, H^3, bzq), 7.82 (t, 1H, *J* = 8.0, H^8, bzq), 7.59 (d, 1H, *J* = 7.3, H^7, bzq), 7.32 (t, 1H, *J* = 8.4, $J_{Pt\text{-}H}$ = 39, H^9, bzq), 2.54 (s, 6H, dmso). When the temperature was increased, the two Me signals of the *cis* isomer broadened and averaged into one at 3.05 ppm.

^{19}F NMR (376.5 MHz, CD_3COCD_3, -50ºC, *δ*): *cis*-3(dmso-κ*S*) -112.2 (d, $J_{Pt\text{-}oF}$ = 102, 1*o*-F), -119.0 (d, $J_{Pt\text{-}oF}$ = 105, 1*o*-F), -160.8 (t, 1*p*-F), -164.1 (m, 1*m*-F), -165.1 (m, 1*m*-F); ***trans*-3(dmso-κ*O*)** -112.6 (d, $J_{Pt\text{-}oF}$ = 104, 1*o*-F), -117.6 (d, $J_{Pt\text{-}oF}$ = 116, 1*o*-F), -161.0 (t, 1*p*-F), -164.4 (m, 1*m*-F), -166.0 (m, 1*m*-F).

^{19}F NMR (376.5 MHz, CD_3COCD_3, 25ºC, *δ*): -115.0 (br), -161.6 (t, *p*-F, ***trans***), -161.9 (t, *p*-F, ***cis***), -165.5 (m, br, *m*-F, ***trans***), -165.9 (m, br, *m*-F, ***cis***).

Preparation of **[Pt(bzq)(C_6F_5)I_2(dmso)] (4)**

Following the same procedure as that for **3**, starting from [Pt(bzq)(C_6F_5)I(μ-I)]$_2$, (0.040 g, 0.025 mmol), **4** was obtained as an orange solid (0.039 g, 88%).

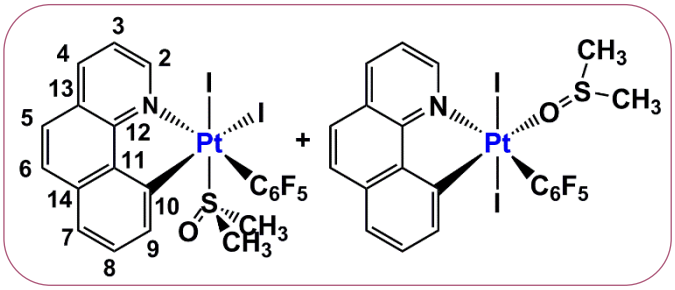

IR (cm^{-1}): ν(C-F) 1066 (m), 967 (m); ν(C_6F_5)$_{X\text{-sens}}$ 791 (m); ν(Pt-I) 247 (w), 224 (w).

MALDI-TOF (-): *m/z* (%) 667 [Pt(bzq)(C_6F_5)I]$^-$ (100). **MALDI-TOF** (+): *m/z* (%) 744 [M-I]$^+$ (17).

Elemental Analysis (%): Calc. for $C_{21}H_{14}I_2F_5NOPtS$: C, 28.92; H, 1.62; N, 1.61; S 3.68. Found C, 28.39; H, 0.97; N, 1.71; S, 3.08.

^{1}H NMR (400.1 MHz, CD_3COCD_3, -50º C, *cis*:*trans* isomers ~ 1:1, *δ*): *cis*-4(dmso-*κS*) 9.47 (d, 1H, *J* = 6.0, H^2, bzq), 8.75 (d, 1H, *J* = 8.1, H^4, bzq), 8.15-8.05 (m, 3H, H^5, H^6, H^3, bzq), 7.66-7.57 (m, 2H, H^7, H^8, bzq), 7.23 (d, 1H, *J* = 7.5, $J_{Pt\text{-}H}$ = 37, H^9, bzq), 3.16 (s, 3H, CH_3, dmso), 2.99 (s, 3H, CH_3, dmso); ***trans*-4(dmso-*κO*)** 9.44 (d, 1H, *J* = 5.1, H^2, bzq), 8.78 (d, 1H, *J* = 8.0, H^4, bzq), 8.15-8.05 (m, 3H, H^5, H^6, H^3, bzq), 7.66-7.57 (m, 2H, H^7, H^8, bzq), 7.29 (d, 1H, *J* = 7.2, H^9, bzq), 2.53 (s, 6H, CH_3, dmso). When the temperature was increased, the two Me signals of the *cis* isomer broadened and averaged into one at 3.06 ppm.

^{19}F NMR (376.5 MHz, CD_3COCD_3, -50ºC, *δ*): *cis*-4(dmso-*κS*) -100.2 (d, $J_{Pt\text{-}oF}$ = 111, 1*o*-F), -106.4 (d, $J_{Pt\text{-}oF}$ = 122, 1*o*-F), -160.9 (t, 1*p*-F), -163.7 (m, 1*m*-F), -165.1 (m, 1*m*-F); ***trans*-4(dmso-κ*O*)** -101.1 (d, $J_{Pt\text{-}oF}$ = 107, 1*o*-F), -105.1 (d, $J_{Pt\text{-}oF}$ = 126, 1*o*-F), -161.2 (t, 1*p*-F), -164.1 (m, 1*m*-F), -165.9 (m, 1*m*-F).

^{19}F NMR (376.5 MHz, CD_3COCD_3, 25ºC, *δ*): -99.5 (s, br, *o*-F, *cis*), -100.7 (s, br, *o*-F, *trans*), -161.9 (t, *p*-F, ***cis* + *trans***), -164.8 (m, br, *m*-F, ***cis* + *trans***), -166.0, -166.4 (m, br, *m*-F, ***cis* + *trans***).

Preparation of **[Pt(bzq)(C_6F_5) Br_2(dmso)] (5)**

Following the same procedure as that for **3**, starting from [Pt(bzq)(C_6F_5)Br(μ-Br)]$_2$, (0.050 g, 0.036 mmol), **5** was obtained as a pale yellow solid (0.044 g, 79%).

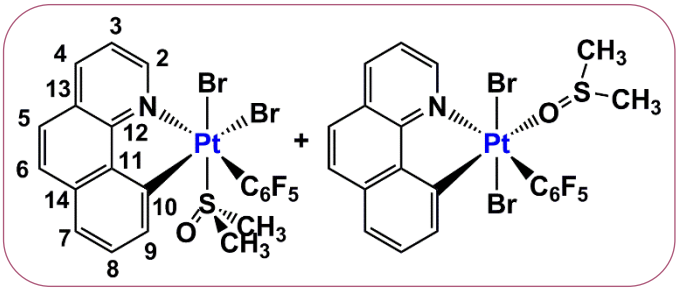

IR ν(cm^{-1}): ν(C-F) 1077 (m), 971 (m); ν(C_6F_5)$_{X\text{-}sens}$ 793 (m); ν(Pt-Br) 268 (w), 232 (w).

MALDI-TOF (-): *m/z* (%) 779 [M]$^-$ (25), 770 [M-dmso]$^-$ (10), 620 [M-dmso-Br]$^-$ (100).

Elemental Analysis (%): Calc. for $C_{21}H_{14}Br_2F_5NOPtS$: C, 32.41; H, 1.81; N, 1.80; S, 4.12. Found: C, 32.13; H, 1.51; N, 2.32; S, 3.75.

^{1}H NMR (400.1 MHz, CD_3COCD_3, -50º C, *cis*:*trans* isomers ~ 2:1, *δ*): *cis*-5(dmso-*κS*) 9.46 (d, 1H, J = 5.2, $J_{Pt\text{-}H}$ = 18, H^2, bzq), 8.82 (d, 1H, J = 7.8, H^4, bzq), 8.08 (m, 3H, H^3, H^5, H^6, bzq), 7.76 (d, 1H, J = 8.0, H^7, bzq), 7.59 (t, 1H, J = 8.0, H^8, bzq), 7.29 (d, 1H, J = 7.1, $J_{Pt\text{-}H}$ = 35, H^9, bzq), 3.15 (s, 3H, CH_3, dmso), 3.01 (s, 3H, CH_3, dmso); ***trans*-5(dmso-*κO*)** 9.42 (d, 1H, J = 5.2, $J_{Pt\text{-}H}$ = 17, H^2, bzq), 8.85 (d, 1H, J = 7.9, H^4, bzq), 8.17 (t, 1H, J = 5.5, H^3, bzq), 8.16 (m, 2H, H^5, H^6, bzq), 7.77 (d, 1H, J = 7.9, H^7, bzq), 7.60 (m, 1H, H^8, bzq), 7.31 (d, 1H, J = 7.9, $J_{Pt\text{-}H}$ = 36, H^9, bzq), 2.55 (s, 6H, CH_3, dmso). When the temperature was increased, the two Me signals of the *cis* isomer broadened and averaged into one at 3.07 ppm.

^{19}F NMR (376.5 MHz, CD_3COCD_3, -50ºC, *δ*): *cis*-5(dmso-*κS*) -107.8 (d, $J_{Pt\text{-}oF}$ = 108, 1*o*-F), -114.4 (d, $J_{Pt\text{-}oF}$ = 114, 1*o*-F), -160.7 (t, 1*p*-F), -163.9 (m, 1*m*-F), -165.1 (m, 1*m*-F); ***trans*-5(dmso-κ*O*)** -108.3 (d, $J_{Pt\text{-}oF}$ = 108, 1*o*-F), -112.9 (d, $J_{Pt\text{-}oF}$ = 113, 1*o*-F), -160.9 (t, 1*p*-F), -164.2 (m, 1*m*-F), -165.9 (m, 1*m*-F).

^{19}F NMR (376.5 MHz, CD_3COCD_3, 25ºC, *δ*): -108.0 (br, *o*-F), -112.6 (br, *o*-F), -161.8 (t, *p*-F, ***cis* + *trans***), -165.6 (m, br, *m*-F, ***cis* + *trans***).

Preparation of **[Pt(bzq)(C_6F_5)Cl_2(tht)] (6)**

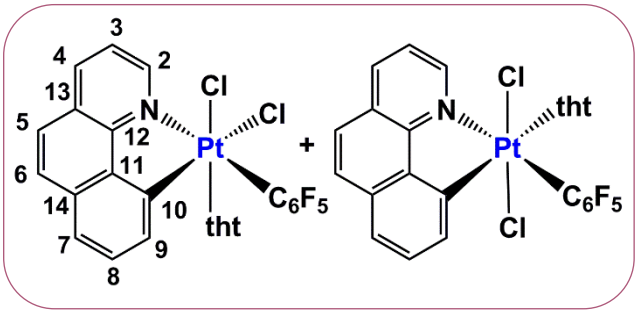

To a solution of [Pt(bzq)(C_6F_5)tht] (0.140 g, 0.223 mmol) in CH_2Cl_2 (20 mL) 1 equiv of $PhICl_2$ (0.061 g, 0.223 mmol) was added. After 1h of reaction, the solvent was evaporated to dryness and the residue was treated with Et_2O (5 mL), obtaining **6** as a pale yellow solid (0.120 g, 77%).

IR (cm^{-1}): ν(C-F) 1079 (s), 967 (s); ν(C_6F_5)$_{X\text{-sens}}$ 796 (s); ν(Pt-Cl) 348 (s), 345 (w).

MALDI-TOF (+): *m/z* (%) 664 $[M- Cl]^+$ (100), 631 $[M-2Cl]^-$ (16).

Elemental Analysis (%): Calc. for $C_{23}H_{16}Cl_2F_5NPtS$: C, 39.50; H, 2.31; N 2.00; S, 4.58. Found: C, 39.23; H, 2.29; N, 2.47; S, 4.62.

^{1}H NMR (400.1 MHz, $CDCl_3$, -30º C, *cis*:*trans* isomers ~ 7:1, *δ*): *cis*-6 10.00 (d, 1H, J = 7.0, $J_{Pt\text{-}H}$ = 20, H^2, bzq), 8.54 (d, 1H, J = 8.0, H^4, bzq), 7.96 (d, 1H, J = 8.4, $H^{5/6}$, bzq), 7.90 (t, 1H, H^3, bzq), 7.80 (m, 2H, $H^{5/6}$, H^7, bzq), 7.66 (t, 1H, J = 7.8, H^8, bzq), 7.45 (t, 1H, J = 7.5, $J_{Pt\text{-}H}$ = 35, H^9, bzq), 3.16 (m, 1H, α-CH_2, tht), 2.96 (m, 1H, α-CH_2, tht), 2.30 (m, 1H, α-CH_2, tht), 2.07 (m, 1H, α-CH_2, tht), 1.81 (m, 1H, β-CH_2, tht), 1.48 (m, 2H, β-CH_2, tht), 1.15 (m, 1H, β-CH_2, tht); ***trans*-6** 9.08 (d, 1H, J = 4, H^2, bzq), 8.45 (d, 1H, J = 10, H^4, bzq), 8.00-7.46 (the rest of the bzq and tht signals are overlapped with signals corresponding to ***cis*-6**).

^{19}F NMR (376.5 MHz, $CDCl_3$, -30ºC, *δ*): *cis*-6 -110.4 (d, $J_{Pt\text{-}oF}$ = 72, 1*o*-F), -117.2 (d, $J_{Pt\text{-}oF}$ = 85, 1*o*-F), -156.8 (t, 1*p*-F), -159.7 (m, 1*m*-F), -161.8 (m, 1*m*-F); ***trans*-6** -113.0 (m, $J_{Pt\text{-}oF}$ ~ 80, 1*o*-F), -119.5 (d, $J_{Pt\text{-}oF}$ ~ 85, 1*o*-F), -157.4 (t, 1*p*-F), -160.5 (m, 1*m*-F), -162.5 (m, 1*m*-F).

A sample was crystallized from CH_2Cl_2/Et_2O giving rise pure ***cis*-6**. **^{1}H NMR (400.1 MHz, CD_3COCD_3, -30º C, *δ*):** 10.03 (d, J = 8.0, $J_{Pt\text{-}H}$ = 20, H^2, bzq), 8.94 (d, J = 8.0, H^4, bzq), 8.18 (m, $H^{5/6}$, H^3, bzq), 8.11 (d, J = 12.0, $H^{5/6}$, bzq), 7.95 (d, J = 8.0, H^7, bzq), 7.71 (t, J = 7.5, H^8, bzq), 7.42 (t, J = 7.5, $J_{Pt\text{-}H}$ = 35, H^9, bzq), 3.08 (m, 2H, *α*-CH_2, tht), 2.25

(m, 1H, α-CH_2, tht), 1.74 (m, 2H, tht), 1.53 (m, 1H, β-CH_2, tht), 1.02 (m, 1H, β-CH_2, tht), 0.66 (m, 1H, β-CH_2, tht).

Preparation of **[Pt(bzq)(C_6F_5)I_2(tht)] (7)**

To a solution of [Pt(bzq)(C_6F_5)tht] (0.150 g, 0.238 mmol) in CH_2Cl_2 (20 mL) 1 equiv of I_2 (0.061 g, 0.238 mmol) was added. After 1h of reaction, the solvent was evaporated to dryness and the residue was treated with Et_2O (5 mL), obtaining **7** as an orange solid (0.126 g, 63 %).

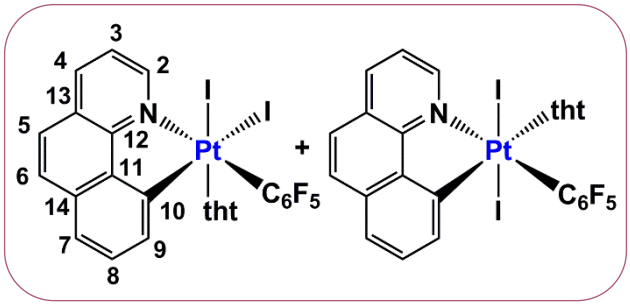

IR (cm^{-1}): ν(C-F) 1078 (s), 970 (s); ν(C_6F_5)$_{X\text{-sens}}$ 795 (s); ν(Pt-I) 224 (w).

MALDI-TOF (+): *m/z* (%) 755 $[M\text{-}I+2H]^+$ (100), 670 $[Pt(bzq)(C_6F_5)I]^+$ (33).

Elemental Analysis (%): Calc. for $C_{23}H_{16}I_2F_5NPtS$: C, 31.31; H, 1.83; N 1.59; S 3.63. Found: C, 30.89; H, 1.97; N, 1.67; S 3.46.

^{1}H NMR (400.1 MHz, CD_3COCD_3, 25º C, *cis*:*trans* isomers ~ 5:1, *δ*): ***cis*-7** 10.44 (d, 1H, J = 8.0, $J_{Pt\text{-}H}$ = 16, H^2, bzq), 8.46 (d, 1H, J = 8.0, H^4, bzq), 7.97 (d, 1H, J = 8.0, $H^{5/6}$, bzq), 7.78 (m, 2H, $H^{5/6}$, H^7, bzq), 7.73 (t, 1H, J = 7.5, H^3, bzq), 7.67 (t, 1H, J = 7.5, H^8, bzq), 7.31 (t, 1H, J = 6.5, $J_{Pt\text{-}H}$ = 38, H^9, bzq), 2.86 (m, 2H, α-CH_2, tht), 2.75 (m, 1H, α-CH_2, tht), 1.78 (m, 1H, α-CH_2, tht), 1.55 (m, 2H, β-CH_2, tht), 0.92 (m, 2H, β-CH_2, tht); ***trans*-7** 9.33 (d, 1H, J = 5.0, $J_{Pt\text{-}H}$ = 20, H^2, bzq), 8.39 (d, 1H, J = 8.0, H^4, bzq), 7.93-7.38 (the rest of the bzq and tht signals appear overlapped with other corresponding to ***cis*-7**).

^{19}F NMR (376.5 MHz, CD_3COCD_3, -30ºC, *δ*): ***cis*-7** -92.2 (d, $J_{Pt\text{-}oF}$ = 109, 1*o*-F), -113.1 (d, $J_{Pt\text{-}oF}$ = 113, 1*o*-F), -159.6 (t, 1*p*-F), -162.9 (m, 1*m*-F), -164.3 (m, 1*m*-F); ***trans*-7** -101.4 (m, 1*o*-F), -105.2 (d, 1*o*-F), -160.8 (t, 1*p*-F), -163.7 (m, 1*m*-F), -165.5 (m, 1*m*-F).

A sample was crystallized from $CHCl_3$/*n*-hexane to give mainly **cis-7**. **^{1}H NMR (400.1 MHz, CD_3COCD_3, 25º C, *δ*):** 10.36 (d, J = 8.0, $J_{Pt\text{-}H}$ = 20, H^2, bzq), 8.83 (d, J = 8.0, H^4, bzq), 8.11 (m, $H^{5/6}$, H^3, bzq), 8.03 (d, J = 12.0, $H^{5/6}$, bzq), 7.86 (d, J = 8.0, H^7, bzq), 7.71 (t, J = 8.0, H^8, bzq), 7.30 (t, J = 7.5, $J_{Pt\text{-}H}$ = 40, H^9, bzq), 2.95 (m, 2H, *α*-CH_2, tht), 1.87 (m, 1H, *α*-CH_2, tht), 1.66 (m, 1H, *α*-CH_2, tht), 1.59 (m, 1H, *β*-CH_2, tht), 1.40 (m, 1H, *β*-CH_2, tht), 0.80 (m, 2H, *β*-CH_2, tht).

Preparation of **[Pt(bzq)(C_6F_5)Br_2(tht)] (8)**

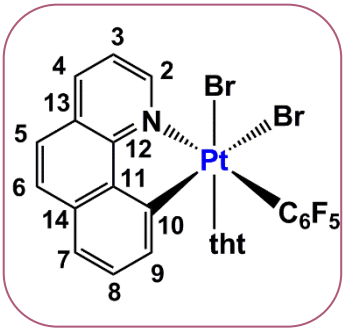

To a solution of [Pt(bzq)(C_6F_5)tht] (0.136 g, 0.216 mmol) in CH_2Cl_2 (20 mL) 1 equiv of Br_2 (11 µL, 0.216 mmol) was added. After 1h of reaction, the solvent was evaporated to dryness and the residue was treated with Et_2O (5 mL), obtaining ***cis*-8** as a white solid (0.080 g, 47%).

IR (cm^{-1}): ν(C-F) 1074 (s), 974 (s); ν(C_6F_5)$_{X\text{-sens}}$ 791 (s); ν(Pt-Br) 234 (w).

MALDI-TOF (+): *m/z* (%) 790 $[M]^+$ (30), 710 $[M\text{-}Br]^+$ (100).

Elemental Analysis (%): Calc. for $C_{23}H_{16}Br_2F_5NPtS$: C, 35.04; H, 2.05; N 1.78; S, 4.07. Found: C, 34.84; H, 2.26; N, 2.18; S, 4.35.

^{1}H NMR (400.1 MHz, CD_3COCD_3, 25º C, *δ*): *cis*-8 10.00 (d, 1H, J = 8, $J_{Pt\text{-}H}$ = 18, H^2, bzq), 8.87 (d, 1H, J = 8.1, H^4, bzq), 8.13 (m, 2H, H^3, $H^{5/6}$, bzq), 8.05 (d, 1H, J = 8.0, $H^{5/6}$, bzq), 7.90 (d, 1H, J = 7.8, H^7, bzq), 7.69 (t, 1H, J = 7.8, H^8, bzq), 7.42 (t, J = 7.8, $J_{Pt\text{-}H}$ = 40, H^9, bzq), 3.13 (m, 1H, α-CH_2, tht), 3.06 (m, 1H, α-CH_2, tht), 2.20 (m, 1H, α-CH_2, tht), 1.80 (m, 1H, α-CH_2, tht), 1.77 (m, 1H, β-CH_2, tht), 1.57 (m, 1H, β-CH_2, tht), 1.04 (m, 1H, β-CH_2, tht), 0.97 (m, 1H, β-CH_2, tht).

^{19}F NMR (282.4 MHz, CD_3COCD_3, -50ºC, *δ*): *cis*-8 -103.3 (d, $J_{Pt\text{-}oF}$ = 87, 1*o*-F), -115.5 (d, $J_{Pt\text{-}oF}$ = 90, 1*o*-F), -160.3 (t, 1*p*-F), -164.0 (m, 1*m*-F), -164.7 (m, 1*m*-F).

Preparation of ***cis*-[Pt(Hthpy-*κN*)$_2$(C$_6$F$_5$)$_2$] (9a)**

To a colourless solution of *cis*-[Pt(C$_6$F$_5$)$_2$(thf)$_2$] (0.250 g, 0.371 mmol) in CH_2Cl_2 (20 mL), two equiv. of 2-(2'-thienyl)pyridine (Hthpy) (0.120 g, 0.742 mmol) were added. After 5 h of stirring, the pale yellow solution obtained was evaporated to dryness and treated with *n*-hexane (5 mL) to afford **9a** as a white solid with orange luminescence (0.278 g, 89 %). Slow crystallization from CH_2Cl_2/*n*-hexane at 298 K gives white crystals with yellow luminescence.

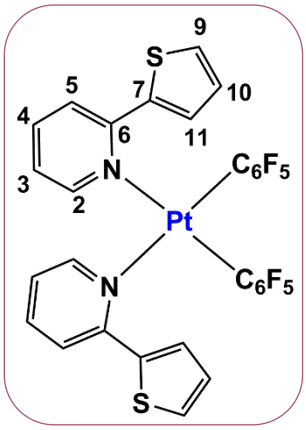

IR (cm^{-1}): ν(C-F) 1060 (m), 952 (m); ν(C$_6$F$_5$)$_{X\text{-sens}}$ 805 (s), 796 (s).

MALDI-TOF (+): *m/z* (%) 683 [M-C$_6$F$_5$ + H]$^+$ (10); **MALDI-TOF (-):** *m/z* (%) 696 [Pt(C$_6$F$_5$)$_3$]$^-$ (20).

Elemental Analysis (%): Calc. for $C_{31}H_{16}F_{10}N_2PtS_2$: C, 43.01; H, 1.86; N, 3.24; S, 7.41. Found: C, 42.93; H, 1.95; N, 3.65; S, 7.01.

^{1}H NMR (400.1 MHz, CDCl$_3$, 20ºC, *δ*): 8.50 (d, 2H, *J*= 3.2, H^{11}), 7.90 (d, 2H, *J*= 5.4, $^3J_{Pt\text{-}H}$= 28.0, H^2), 7.54 (td, 2H, *J*= 7.9, *J*= 1.4, H^4), 7.38 (d, 2H, *J*= 6.9, H^9), 7.23 (d, 2H, *J*= 7.8, H^5), 7.12 (t, 2H, *J*= 4.3, H^{10}), 6.69 (t, 2H, *J*= 6.7, H^3).

^{13}C{^{1}H} NMR (100.6 MHz, CDCl$_3$, 20ºC, *δ*): 153.8 (s, C^6), 153.0 (s, C^2), 140.9 (s, C^7), 136.7 (s, C^4), 130.3 (s, C^{11}), 128.6 (s, C^9), 127.9 (s, C^{10}), 126.3 (s, C^5), 123.5 (s, C^3).

^{19}F (376.5 MHz, CDCl$_3$, 20ºC, *δ*): -118.9 (m, br, 2*o*-F, C$_6$F$_5$), -119.3 (m, br, 2*o*-F, C$_6$F$_5$), -162.5 (t, 2*p*-F, C$_6$F$_5$), -164.7 (m, br, 4*m*-F, C$_6$F$_5$).

^{19}F (376.5 MHz, CDCl$_3$, -45ºC, *δ*): -118.8 (d, $^3J_{Pt\text{-}oF}$ = 462, 2*o*-F, C$_6$F$_5$), -119.3 (d, $^3J_{Pt\text{-}oF}$ = 412, 2*o*-F, C$_6$F$_5$), -162.0 (t, 2*p*-F, C$_6$F$_5$), -164.1 (m, 2*m*-F, C$_6$F$_5$), -164.3 (m, 2*m*-F, C$_6$F$_5$).

Preparation of ***cis*-[Pt(Hpbt-*κ*N)$_2$(C$_6$F$_5$)$_2$] (9b)**

This compound was obtained as a white solid (0.252g, 90%) following a procedure similar to **9a** but stirring for 2 hours, using as starting materials *cis*-[Pt(C$_6$F$_5$)$_2$(thf)$_2$] (0.200 g, 0.297 mmol), and 2-phenylbenzo[d]thiazole (Hpbt) (0.125 g, 0.594 mmol).

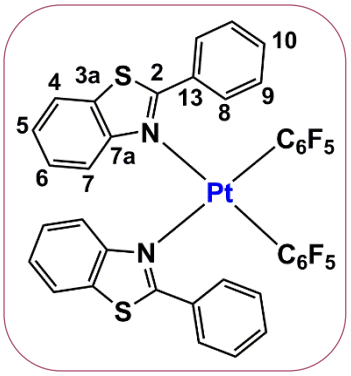

IR (cm^{-1}): ν(C-F) 1066 (m), 961 (m); ν(C$_6$F$_5$)$_{X\text{-sens}}$ 806 (s), 796 (s).

ESI(+): *m/z* (%) 952 [M]$^+$ (3).

Elemental Analysis (%): Calc. for C$_{38}$H$_{18}$F$_{10}$N$_2$PtS$_2$: C, 47.95; H, 1.91; N, 2.94; S, 6.74. Found: C, 47.65; H, 2.19; N, 3.19; S, 6.38.

^{1}H NMR (400.1 MHz, CDCl$_3$, 20ºC, *δ*): 8.13 (d, 4H, *J* = 7.5, H^8), 7.84 (d, 2H, *J* = 8.1, H^7), 7.52 (d, 2H, *J* = 7.8, H^4), 7.23 (t, 2H, *J* = 7.2, H^5), 7.15 (t, 2H, *J* = 7.6, H^6), 7.03 (t, 4H, *J* = 7.5, H^9), 6.84 (t, 2H, *J* = 7.4, H^{10}).

^{13}C{^{1}H} NMR (100.6 MHz, CDCl$_3$, 20ºC, *δ*): 171.5 (s, C^2), 150.9 (s, C^{3a}), 132.0 (s, C^{7a}), 131.6 (s, C^{13}), 130.2 (m, C^{10}), 128.6 (s, C^9), 127.5 (m, C^8), 125.9 (s, C^6), 125.7 (s, C^5), 124.6 (m, C^7), 120.7 (s, C^4).

^{19}F (376.5 MHz, CDCl$_3$, 20ºC, *δ*): -118.8 (d, $^3J_{Pt\text{-}oF}$ = 512, 2*o*-F, C$_6$F$_5$), -121.3 (d, $^3J_{Pt\text{-}oF}$ = 390, 2*o*-F, C$_6$F$_5$), -162.3 (t, 2*p*-F, C$_6$F$_5$), -164.7 (m, 2*m*-F, C$_6$F$_5$), -164.9 (m, 2*m*-F, C$_6$F$_5$).

Preparation of ***cis*-[Pt(Hpq-κN)$_2$(C$_6$F$_5$)$_2$] (9c)**

This compound was obtained as a white solid (0.200 g, 54%) with an orange emission, following a procedure similar to **9a** but stirring for 2 hours, using as starting materials *cis*-[Pt(C$_6$F$_5$)$_2$(thf)$_2$] (0.250 g, 0.397 mmol) and 2-phenylquinoline (Hpq) (0.163 g, 0.795 mmol). Slow crystallization from CH$_2$Cl$_2$/*n*-hexane at 298 K gives white crystals with yellow luminescence.

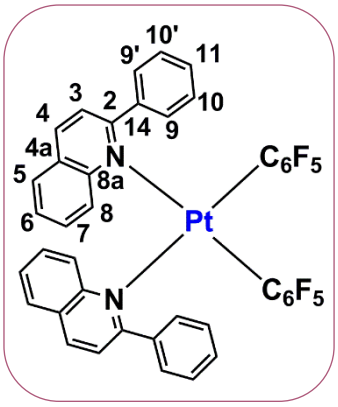

IR (cm^{-1}): ν(C-F) 1064 (m), 957 (m); ν(C$_6$F$_5$)$_{X\text{-sens}}$ 803 (s), 791 (s).

ESI (+): *m/z* (%) 774 [M-C$_6$F$_5$]$^+$ (3); **MALDI-TOF (-):** *m/z* (%) 696 [Pt(C$_6$F$_5$)$_3$]$^-$ (30).

Elemental Analysis (%): Calc. for C$_{42}$H$_{22}$F$_{10}$N$_2$Pt: C, 53.68; H, 2.36; N, 2.98. Found: C, 53.44; H, 2.69; N, 2.68.

^{1}H NMR (400.1 MHz, CDCl$_3$, 20ºC, *δ*): 8.62 (d, 2H, *J*= 8.7, H^8), 8.12 (d, 2H, *J*= 8.3, H^3), 7.57 (d, 2H, *J*= 7.8, H^5), 7.47 (m, br, 4H, H$^{9,9'}$), 7.30 (t, 2H, *J*= 7.0, H^6), 7.19 (t, 2H, *J*= 7.7, H^7), 7.12 (d, 2H, *J*= 8.3, H^4), 6.81 (m, br, 4H, H$^{10,10'}$), 6.71 (t, 2H, *J*= 7.0, H^{11}).

^{1}H NMR (400.1 MHz, CDCl$_3$, -50ºC, *δ*): 8.68 (s, 2H, br, H^9), 8.48 (d, 2H, *J*= 8.9, H^8), 8.16 (d, 2H, *J*= 8.2, H^3), 7.59 (d, 2H, *J*= 7.9, H^5), 7.40 (t, 2H, *J*= 7.5, H^{10}), 7.31 (t, 2H, *J*= 7.2, H^6), 7.17 (t, 2H, *J*= 8.1, H^7), 7.12 (d, 2H, *J*= 8.2, H^4), 6.64 (t, 2H, *J*= 7.2, H^{11}), 6.17 (m, 4H, H$^{10',9'}$).

^{13}C{^{1}H} NMR (100.6 MHz, CDCl$_3$, 20ºC , *δ*): 163.7 (s, C^2), 146.8 (s, C^{4a}), 140.8 (s, C^{8a}), 138.1 (s, C^3), 131.3 (s, C^8), 129.3 (s, C^7), 128.4 (s, C^{11}), 127.8-127.4 (m, C$^{9, 9', 10, 10', 14}$), 126.8 (s, C^6), 126.7 (s, C^5), 125.1 (s, C^4).

^{19}F (376.5 MHz, CDCl$_3$, 20ºC, *δ*): -118.0 (d, $^3J_{Pt\text{-}oF}$ = 500, 2*o*-F, C$_6$F$_5$), -121.6 (d, $^3J_{Pt\text{-}oF}$ = 389, 2*o*-F, C$_6$F$_5$), -163.4 (t, 2*p*-F, C$_6$F$_5$), -165.7 (m, 4*m*-F, C$_6$F$_5$).

Preparation of ***cis*-[Pt(Hdfppy-*κN*)$_2$(C$_6$F$_5$)$_2$] (9d)**

To a colourless solution of *cis*-[Pt(C$_6$F$_5$)$_2$(thf)$_2$] (0.400g, 0.594 mmol) in CH_2Cl_2 (20 mL), two equivalents of 2-(2,4-difluorophenyl)pyridine (Hdfppy) (181 µL, 1.188 mmol) were added. After 2 h of stirring, the solution obtained was evaporated to dryness and treated with Et_2O (5 mL) to afford **9d** as a white solid (0.368 g, 70 %).

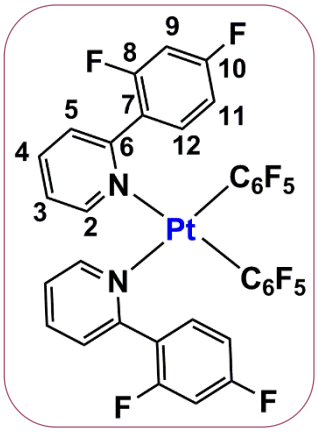

IR (cm^{-1}): ν(C-F, C$_6$F$_5$) 1068 (m), 957 (m); ν(C$_6$F$_5$)$_{X\text{-sens}}$ 807 (s), 797 (s).

ESI (+): *m/z* (%) 934 [M+Na]$^+$ (81)

Elemental Analysis (%): Calc. for $C_{34}H_{14}F_{14}N_2Pt$: C, 44.80; H, 1.55; N, 3.07. Found: C, 44.76; H, 1.69; N, 3.50.

^{1}H NMR (400.1 MHz, CDCl$_3$, 20ºC, *δ*): 9.28 (m, 2H, H^{12}), 7.82 (d, 2H, J = 5.3, $^3J_{Pt\text{-}H}$ = 33, H^2), 7.69 (t, 2H, J = 7.5, H^4), 7.31 (m, 4H, H^{11,5}), 6.86 (t, 2H, J = 6.4, H^3), 6.50 (m, 2H, H^9).

^{13}C{^{1}H} NMR (100.6 MHz, CDCl$_3$, 20ºC, *δ*): 163.5 (dm, $^1J_{C\text{-}F}$ = 253, C$^{8/10}$), 159.0 (dm, $^1J_{C\text{-}F}$ = 255, C$^{8/10}$), 153.5 (s, C^6), 152.1 (s, C^2), 136.5 (s, C^4), 134.2 (m, C^{12}), 128.5 (s, C^5), 124.2 (s, C^3), 122.8 (m, C^7), 111.7 (d, $^2J_{C\text{-}F}$ = 21, C^{11}), 103.8 (t, $^2J_{C\text{-}F}$ = 26, C^9).

^{19}F{^{1}H} NMR (282.4 MHz, CDCl$_3$, 20ºC, *δ*): -106.1 (m, 2F^8, Hdfppy), -112.8 (m, 2F^{10}, Hdfppy), -119.2 (d, $J_{Pt\text{-}oF}$ = 457, 2*o*-F, C$_6$F$_5$), -120.4 (d, $J_{Pt\text{-}oF}$ = 406, 2*o*-F, C$_6$F$_5$), -161.8 (t, 2*p*-F, C$_6$F$_5$), -163.8 (m, 2*m*-F, C$_6$F$_5$), -164.2 (m, 2*m*-F, C$_6$F$_5$).

Preparation of **[Pt(thpy)(Hthpy-*kN*)(C_6F_5)] (10a)**

A white suspension of *cis*-[Pt(Hthpy-*kN*)$_2$(C_6F_5)$_2$] (**9a**) (0.150 g, 0.176 mmol) in xylene (5 mL) was refluxed for 2 h. The orange solution obtained was evaporated to dryness and the residue was treated with *n*-hexane (5 mL) affording **10a** as an orange solid (0.084 g, 70%).

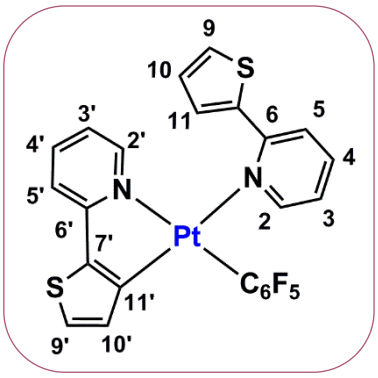

IR (cm^{-1}): ν(C-F) 1063 (m), 954 (m); ν(C_6F_5)$_{X\text{-}sens}$ 800 (vs).

MALDI-TOF(+): *m/z* (%) 516 [M-C_6F_5]$^+$ (31).

Elemental Analysis (%): Calc. for $C_{24}H_{13}F_5N_2PtS_2$: C, 42.17; H, 1.92; N, 4.10; S, 9.38. Found C, 42.53; H, 2.32; N, 4.35; S, 9.66 %.

^{1}H NMR (400.1 MHz, $CDCl_3$, 20ºC, *δ*): 9.19 (d, 1H, *J*= 5.5, $^3J_{Pt\text{-}H}$= 25, H$^{2'}$), 8.10 (d, 1H, *J*= 3.5, H^{11}), 7.87 (t, 1H, *J*= 7.5, H$^{4'}$), 7.77 (d, 1H, *J*= 7.9, H$^{5'}$), 7.70 (t, 1H, *J*= 7.7, H^4), 7.58 (d, *J*= 5.5, $^3J_{Pt\text{-}H}$= 27, H^2), 7.42-7.40 (m, 2H, H^{9,5}), 7.32-7.28 (m, 2H, H$^{9',3'}$), 7.00 (t, 1H, *J* = 4.0, H^{10}), 6.80 (t, 1H, *J*= 6.3, H^3), 6.46 (d, 1H, *J*= 4.7, $^3J_{Pt\text{-}H}$= 26, H$^{10'}$).

^{13}C{^{1}H} NMR (100.6 MHz, $CDCl_3$, 20ºC, *δ*): 161.6 (s, C^6), 154.8 (s, C$^{6'}$), 153.4 (d, *J* = 2.6, $^2J_{Pt\text{-}C}$= 12, C$^{2'}$), 146.9 (s, $^2J_{Pt\text{-}C}$= 12.4, C^2), 142.9 (s, C$^{11'}$), 140.2 (s, C$^{7'}$), 140.0 (s, C^7), 138.8 (s, C^4), 138.1 (s, C$^{4'}$), 135.2 (s, C$^{10'}$), 129.5 (s, C^{11}), 129.2 (s, C$^{9/5}$), 128.1 (s, C$^{3'/9'}$), 127.6 (s, C^{10}), 125.7 (s, $^3J_{Pt\text{-}C}$= 11.2, C$^{5'}$), 123.2 (s, C$^{3'/9'}$), 119.9 (s, C^3), 117.8 (s, C$^{9/5}$).

^{19}F (376.5 MHz, $CDCl_3$, 20ºC, *δ*): -116.8 (dm, $^3J_{Pt\text{-}oF}$ = 455, 1*o*-F, C_6F_5), -119.5 (dm, $^3J_{Pt\text{-}oF}$ = 495, 1*o*-F, C_6F_5), -163.2 (t, 1*p*-F, C_6F_5), -164.8 (m, 1*m*-F, C_6F_5), -165.1 (m, 1*m*-F, C_6F_5).

Preparation of **[Pt(pbt)(Hpbt-κN)(C_6F_5)](10b)**

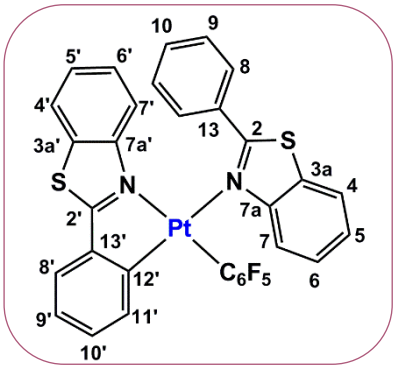

A suspension of *cis*-[Pt(Hpbt-κN)$_2$(C_6F_5)$_2$] (**9b**) (0.200 g, 0.210 mmol) in xylene (5 mL) was refluxed for 2 h. The solvent was evaporated to dryness, CH_2Cl_2 (20 mL) and activated charcoal were added and the suspension was filtered through celite. The yellow filtrate was evaporated to dryness and the residue was treated with *n*-hexane (5 mL) affording **10b** as a yellow solid (0.102 g, 60 %).

IR (cm^{-1}): ν(C-F) 1060 (m), 957 (m); ν(C_6F_5)$_{X\text{-sens}}$ 801 (m).

MALDI-TOF (-): *m/z* (%) 822 $[M+K]^+$ (33)

Elemental Analysis (%): Calc. for $C_{32}H_{17}F_5N_2PtS_2$: C, 49.04; H, 2.19; N, 3.57; S, 8.18. Found: C, 49.33; H, 2.51; N, 3.97; S, 7.93.

^{1}H NMR (400 MHz, $CDCl_3$, 20ºC, δ): 9.12 (m, 1H, $H^{7'}$), 8.43 (d, 2H, *J*= 7.6, H^8, Ph), 7.93 (m, 1H, $H^{4'}$), 7.84 (d, 1H, *J*= 8.0, H^7), 7.63 (d, 1H, *J*= 7.5, $H^{8'}$), 7.54 (t, 1H, *J*= 7.4, H^{10}), 7.48-7.45 (m, 2H, $H^{6',5'}$), 7.43 (t, 2H, *J*= 7.7, H^9, Ph), 7.22 (t, 1H, *J*= 7.6, H^6), 7.10 (t, 1H, *J*= 7.2, $H^{9'}$), 7.00 (t, 1H, *J*= 7.4, $H^{10'}$), 6.95 (t, 1H, *J*= 7.8, H^5), 6.75 (d, 1H, *J*= 7.6, $^3J_{Pt\text{-}H}$= 68, $H^{11'}$), 6.60 (d, 1H, *J*= 8.4, H^4).

^{13}C{^{1}H} NMR (100.6 MHz, $CDCl_3$, 20ºC, δ): 182.5 (s, $C^{2'}$), 172.1 (s, C^2), 153.3 (s, $C^{3a'}$), 150.67 (s, C^{7a}), 141.1 (s, $C^{12'}$), 139.5 (s, $C^{13'}$), 136.7 (s, $C^{11'}$), 132.3-132.0 (s, $C^{3a,\ 13,\ 10',\ 7a',\ 10}$), 129.02 (s, C^9, Ph), 128.6 (s, C^8, Ph), 127.4 (s, C^5), 127.1 (s, $C^{6'/5'}$), 126.7 (s, $C^{6'/5'}$), 125.7 (s, $C^{8'}$), 125.4 (s, $C^{7'}$), 125.0 (s, C^6), 123.8 (s, $C^{9'}$), 122.8 (s, C^7), 121.5 (s, $C^{4'}$), 118.6 (s, C^4).

^{19}F (376.5 MHz, $CDCl_3$, 20ºC, δ): -116.4 (dm, $^3J_{Pt\text{-}oF}$ = 496, 1*o*-F, C_6F_5), -118.2 (dm, $^3J_{Pt\text{-}oF}$ = 500, 1*o*-F, C_6F_5), -163.4 (t, 1*p*-F, C_6F_5), -164.9 (m, 2*m*-F, C_6F_5).

Preparation of **[Pt(pq)(Hpq-κ*N*)(C_6F_5)] (10c)**

This derivative was prepared as an orange solid (0.077 g, 41 %) in a similar way to **10a** starting from *cis*-[Pt(Hpq-κ*N*)$_2$(C_6F_5)$_2$] (**9c**) (0.150 g, 0.238 mmol).

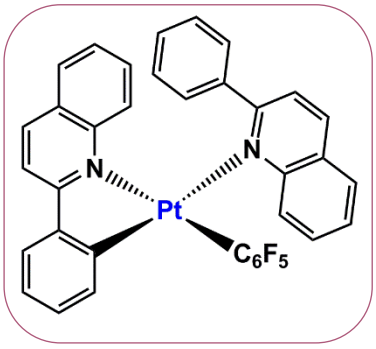

IR (cm^{-1}): ν(C-F) 1059 (m), 958 (m); ν(C_6F_5)$_{X\text{-}sens}$ 798 (s).

MALDI-TOF (+): *m/z* (%) 604 [M-C_6F_5]$^+$ (89).

Elemental Analysis (%): Calc. for $C_{36}H_{21}F_5N_2Pt$: C, 56.03; H, 2.74; N, 3.63. Found: C, 56.41; H, 3.08; N, 3.97.

^{1}H NMR (400.1 MHz, $CDCl_3$, 20ºC, δ): 9.86 (d, 1H, *J* = 8.7), 8.35 (d, 1H, *J* = 8.4), 8.19 (d, 1H, *J* = 8.7), 7.71-7.79 (m, 5H), 7.69-7.64 (m, 3 H), 7.55-7.49 (m, 3H), 7.21 (m, 1H), 7.09 (t, 3H), 6.97 (t, 1H), 6.87-6.80 (m, 2H).

^{13}C{^{1}H} NMR (100.6 MHz, $CDCl_3$, 20ºC, δ): 167.3 (s), 162.7 (s), 147.9 (s), 147.7 (s), 146.3 (s), 141.0 (s), 139.7 (s), 138.9 (s), 138.4 (s), 137.1 (s), 130.7 (s), 130.5 (s), 130.2 (s), 129.6 (s), 129.3 (s), 128.9 (s), 128.5-128.4 (m, 3 C), 128.0 (s), 127.9 (s), 127.7-127.6 (s, 3 C), 125.7 (s), 125.6 (s), 125.5 (s), 124.6 (s), 123.2 (s), 117.1 (s).

^{19}F (376.5 MHz, $CDCl_3$, 20ºC, δ): -116.8 (dm, $^3J_{Pt\text{-}oF}$ = 503, 1*o*-F, C_6F_5), -118.0 (d, $^3J_{Pt\text{-}oF}$ = 461, 1*o*-F, C_6F_5), -163.9 (t, 1*p*-F, C_6F_5), -165.1 (m, 1*m*-F, C_6F_5), -165.1 (m, 1*m*-F, C_6F_5).

Preparation of **[Pt(dfppy)(Hdfppy-*κN*)(C_6F_5)]** (**10d**)

A suspension of *cis*-[Pt(Hdfppy-*κN*)$_2$(C_6F_5)$_2$] (**9d**) (0.164 g, 0.180 mmol) in xylene (5 mL) was refluxed for 5 h to obtain a yellow solution. The solvent was evaporated to dryness and residue was treated with Et_2O (~5 mL) to obtain **10d** as a yellow solid (0.101 g, 75 %).

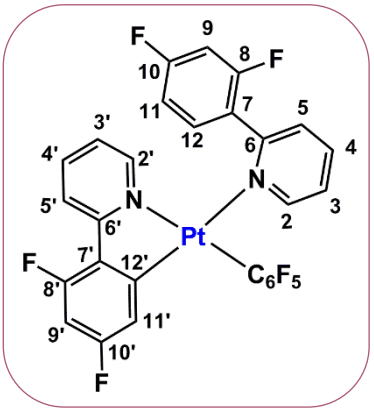

IR (cm^{-1}): ν(C-F, C_6F_5) 1058 (m), 955 (m); ν(C_6F_5)$_{X\text{-sens}}$ 796 (s).

MALDI-TOF(+): *m/z* (%) 742 [M]$^+$ (22).

Elemental Analysis (%): Calc. for $C_{28}H_{13}F_9N_2Pt$: C, 45.23; H, 1.76; N, 3.77. Found: C, 45.71; H, 1.72; N, 4.01.

^{1}H NMR (400 MHz, $CDCl_3$, 20ºC, *δ*): 9.23 (d, 1H, J = 5, $^3J_{Pt\text{-}H}$ = 17, H$^{2'}$), 8.15 (d, 1H, J = 7.7, H^2), 7.97 (t, 1H, J = 7, H$^{4'}$), 7.88 (t, 1H, J = 7, H^3), 7.82 (d, 1H, J = 5, H^5), 7.53 (m, 3H, H$^{3',5',12}$), 7.08 (t, 1H, J = 5, H^4), 6.88 (m, 1H, H^{11}), 6.77 (m, 1H, H^9), 6.48 (m, 1H, H$^{9'}$), 6.22 (d, 1H, $^3J_{Pt\text{-}H}$ = 77, H$^{11'}$).

^{13}C{^{1}H} NMR (100.6 MHz, $CDCl_3$, 20ºC, *δ*): 165.3-158.1 (several multiplets, C$^{8,10,8',10'}$), 155.8 (s, C$^{6'}$), 153.2 (s, C$^{2'}$), 146.9 (s, C^5), 142.8 (m, C$^{7/7'}$), 139.0 (s, C^3), 138.2 (s, C$^{4'}$), 132.0 (m, C^{12}), 128.7 (s, C$^{3'/5',12'}$), 124.7 (s, C$^{3'/5'}$), 122.8 (s, C$^{2,7/7',6}$), 122.1 (s, C^4), 119.4 (dd, $^2J_{C\text{-}F}$ = 18, C$^{11'}$), 111.7 (dd, $^2J_{C\text{-}F}$ = 22, C^{11}), 104.3 (t, $^2J_{C\text{-}F}$ = 26, C^9), 99.5 (m, C$^{9'}$, $^2J_{C\text{-}F}$ = 27).

^{19}F{^{1}H} NMR (282.4 MHz, $CDCl_3$, 20º C, *δ*): -106.0 (d, 1F, $^4J_{F\text{-}F}$ = 9, F^8, Hdfppy), -107.3 (d, 1F, $^4J_{F\text{-}F}$ = 10, $^4J_{Pt\text{-}F}$ = 66, F$^{10'}$, dfppy), -110.4 (d, 1F, $^4J_{F\text{-}F}$ = 10, $^4J_{Pt\text{-}F}$ = 55, F$^{8'}$, dfppy), -112.2 (d, 1F, $^4J_{F\text{-}F}$ = 9, F^{10}, Hdfppy), -117.1 (dm, $J_{Pt\text{-}oF}$ = 482, *o*-F, C_6F_5), -120.4 (dm, $J_{Pt\text{-}oF}$ = 466, *o*-F, C_6F_5), -162.4 (t, *p*-F, C_6F_5), -163.7 (m, *m*-F, C_6F_5), -164.4 (m, *m*-F, C_6F_5).

Preparation of **[Pt(thpy)(C_6F_5)(dmso)] (11a)**

To a white suspension of *cis*-[Pt(C_6F_5)$_2$(dmso)$_2$] (0.181 g, 0.260 mmol) in xylene (5 mL), 2-(2'-thienyl)pyridine (Hthpy) (0.042 g, 0.260 mmol) was added. After 3h of stirring at reflux, the orange solution was cooled at 0º, obtaining **11a** as an orange solid (0.108 g, 70%).

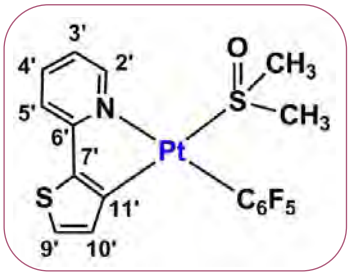

IR (cm^{-1}): ν(C-F) 1060 (m), 956 (m); ν(C_6F_5)$_{X\text{-}sens}$ 801 (m).

ESI (+): *m/z* (%) 523 [M-dmso]$^+$ (17), 601 [M]$^+$ (6).

Elemental Analysis (%): Calc. for $C_{17}H_{12}F_5NOPtS_2$: C, 34.00; H, 2.01; N, 2.33; S, 10.68. Found: C, 34.33; H, 2.28; N, 2.70; S, 11.06.

^{1}H NMR (400.1 MHz, $CDCl_3$, 20ºC, *δ*): 9.46 (d, 1H, *J* = 5.6, $^3J_{Pt\text{-}H}$ = 28.4, H$^{2'}$), 7.81 (t, 1H, *J* = 7.5, H$^{4'}$), 7.43 (d, 1H, *J* = 7.8, H$^{5'}$), 7.23 (d, 1H, *J* = 4.7, H$^{9'}$), 7.13 (t, 1H, *J* = 6.4, H$^{3'}$), 6.04 (d, 1H, *J* = 4.7, $^3J_{Pt\text{-}H}$ = 27, H$^{10'}$), 3.07 (s, 6H, $^3J_{Pt\text{-}H}$ = 16, dmso).

^{13}C{^{1}H} NMR (100.6 MHz, $CDCl_3$, 20ºC, *δ*): 161.2 (s, $^2J_{Pt\text{-}C}$ = 61, C$^{6'}$), 150.6 (s, C$^{2'}$), 149.9 (s, $^1J_{Pt\text{-}C}$ = 1002, C$^{11'}$), 144.4 (s, $^2J_{Pt\text{-}C}$ = 66.4, C$^{7'}$), 139.9 (s, C$^{4'}$), 133.7 (s, $^2J_{Pt\text{-}C}$ = 146, C$^{10'}$), 127.8 (s, $^3J_{Pt\text{-}C}$ = 81.4, C$^{9'}$), 121.1 (s, $^3J_{Pt\text{-}C}$ = 14.6 C$^{3'}$), 118.0 (s, $^3J_{Pt\text{-}C}$ = 26.1, C$^{5'}$), 45.2 (s, $^2J_{Pt\text{-}C}$ = 42.4, dmso).

^{19}F (376.5 MHz, $CDCl_3$, 20ºC, *δ*): -116.9 (dm, $^3J_{Pt\text{-}oF}$ = 477, 2*o*-F, C_6F_5), -159.2 (t, 1*p*-F, C_6F_5), -161.9 (m, 2*m*-F, C_6F_5).

Preparation of **[Pt(pbt)(C_6F_5)(dmso)] (11b)**

A yellow suspension of [Pt(pbt)(Hpbt-κN)(C_6F_5)] (**10b**) (0.150 g, 0.192 mmol) in dimethyl sulfoxide (3 mL) was stirred at reflux for 4 h. The orange solution was evaporated to dryness and treated with *n*-hexane (20 mL). In order to remove the Hpbt generated in the reaction, the solvent was decanted and the white solid residue was treated with cold isopropanol (5 mL) obtaining **11b** (0.060g, 40%).

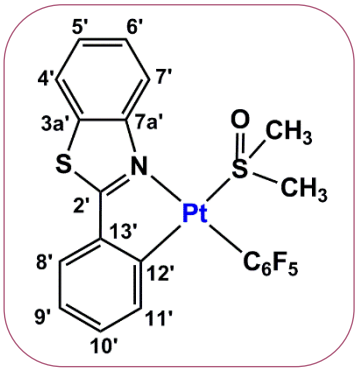

IR (cm^{-1}): ν(C-F) 1066 (m), 957 (m); ν(C_6F_5)$_{X\text{-}sens}$ 805 (m).

ESI (+): *m/z* (%) 651 $[M+H]^+$ (65), 484 $[M-C_6F_5]^+$ (50).

Elemental Analysis (%): Calc. for $C_{21}H_{14}F_5NOPtS_2$: C, 38.77; H, 2.17; N, 2.15; S, 9.86. Found: C, 38.40; H, 2.34; N, 2.41; S, 10.18.

^{1}H NMR (400.1 MHz, $CDCl_3$, 20ºC, δ): 9.05 (d, 1H, J= 8.5, $H^{7'}$), 7.89 (d, 1H, J= 8.0, $H^{4'}$), 7.63 (d, 1H, J= 7.5, $H^{8'}$), 7.59 (t, 1H, J= 8.0, $H^{6'}$), 7.46 (t, 1H, J= 7.5, $H^{5'}$), 7.14 (t, 1H, J= 7.6, $H^{9'}$), 7.04 (t, 1H, J= 7.5, $H^{10'}$), 6.35 (d, 1H, J= 7.8, $^3J_{Pt\text{-}H}$= 63, $H^{11'}$), 3.04 (s, 6H, $^3J_{Pt\text{-}H}$= 13, dmso).

^{13}C{^{1}H} NMR (100.6 MHz, $CDCl_3$, 20ºC, δ): 183.5 (s, $C^{2'}$), 150.6 (s, $C^{3a'}$), 145.2 (s, $C^{13'}$), 141.7 (s, $C^{12'}$), 135.7 (s, $C^{11'}$), 131.8 (s, $C^{10'}$), 131.4 (s, $C^{7a'}$), 127.9 (s, $C^{6'}$), 126.1 (s, $C^{9'}$), 126.0 (s, $C^{5'}$), 125.8 (s, $C^{8'}$), 122.5 (s, $C^{4'}$), 121.7 (s, $C^{7'}$), 46.3 (s, $^2J_{Pt\text{-}C}$ = 40.0, dmso).

^{19}F (376.5 MHz, $CDCl_3$, 20ºC, δ): -116.9 (dm, $^3J_{Pt\text{-}oF}$ = 503, 2*o*-F, C_6F_5), -159.0 (t, 1*p*-F, C_6F_5), -161.4 (m, 2*m*-F, C_6F_5).

Preparation of ***fac*-[Pt(thpy)$_2$(C$_6$F$_5$)Cl] (12a)**

To an orange solution of [Pt(thpy)(Hthpy-*κN*)(C$_6$F$_5$)] (**10a**) (0.164 g, 0.240 mmol) at -30ºC in 20 mL of CH_2Cl_2, $PhICl_2$ (0.085 g, 0.312 mmol) was added. The mixture was stirred at -30ºC for 1/2 h and then allowed to warm to room temperature. After 12 h, the solution was evaporated to dryness and treated with Et_2O (~5 ml) to give **12a** as a white solid (0.12 g, 70%).

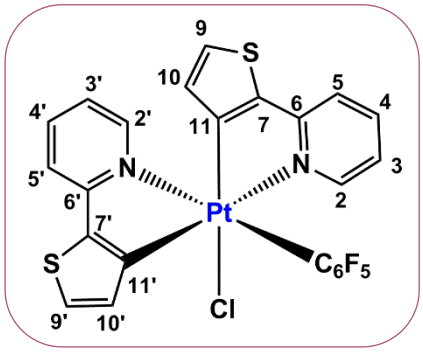

IR (cm^{-1}): ν(C-F, C$_6$F$_5$) 1074 (s), 970 (s); ν(C$_6$F$_5$)$_{X\text{-sens}}$ 796 (s); ν(Pt-Cl) 310 (w).

ESI (+): *m/z* (%) 682 [M-Cl]$^+$ (100).

Elemental Analysis (%): Calc. for $C_{24}H_{12}ClF_5N_2PtS_2$: C, 40.15; H, 1.68; N, 3.90; S, 8.93. Found: C, 40.03; H, 1.86; N, 4.24; S, 8.91.

^{1}H NMR (400.1 MHz, CD$_3$COCD$_3$, 20º C, *δ*): 9.71 (t, 1H, $J_{H\text{-}H} \approx J_{H\text{-}oF} = 6$, $^3J_{H\text{-}Pt} = 12$, H^2), 8.21 (td, 1H, $J = 8$, $J = 2$, H^4), 7.93 (td, 1H, $J = 8$, $J = 2$, H$^{4'}$), 7.83 (d, 1H, $J = 8$, H^5), 7.77 (d, 1H, $J = 8$, H$^{5'}$), 7.75 (d, 1H, $J = 5$, $^4J_{Pt\text{-}H} = 9$, H^9), 7.67 (td, 1H, $J = 6$, $J = 1$, H^3), 7.42 (d, 1H, $J = 5$, $^4J_{H\text{-}Pt} = 10$, H$^{9'}$), 7.35 (dd, 1H, $J = 6$, $J = 1$, $^3J_{H\text{-}Pt} = 16$, H$^{2'}$), 7.11 (d, 1H, $J = 5$, $^3J_{H\text{-}Pt} = 16$, H^{10}), 7.06 (td, 1H, $J = 7$, $J = 1$, H$^{3'}$), 6.51 (t, 1H, $J_{H\text{-}H} \approx J_{H\text{-}oF} = 6$, $^3J_{H\text{-}Pt} = 18$, H$^{10'}$).

^{13}C{^{1}H} NMR (100.6 MHz, CD$_3$COCD$_3$, 20º C, *δ*): 159.2 (s, C^6), 159.1 (s, C$^{6'}$), 150.6 (d, $J_{C\text{-}F} = 7$, $^3J_{C\text{-}Pt} = 10$, C^2), 146.1 (s, $^3J_{C\text{-}Pt} = 8$, C$^{2'}$), 142.5 (s, C^4), 141.6 (s, C$^{4'}$), 137.8, 137.4 (C$^{7,7'}$), 137.1 (d, $J_{C\text{-}F} = 3$, C$^{11/11'}$), 136.9 (d , $J_{C\text{-}F} = 5$, C$^{11/11'}$), 134.2 (d, $J_{C\text{-}F} = 6$, $^2J_{C\text{-}Pt} = 74$, C^{10}), 132.3 (d, $J_{C\text{-}F} = 7$, $^2J_{C\text{-}Pt} = 76$, C$^{10'}$), 129.1 (s, $^3J_{C\text{-}Pt} = 58$, C^9), 129.0 (s, $^3J_{C\text{-}Pt} = 61$, C$^{9'}$), 122.8 (s, $^3J_{C\text{-}Pt} = 13$, C$^{3'}$), 122.7 (s, $^3J_{C\text{-}Pt} = 11$, C^3), 120.2 (s, C$^{5',5}$).

^{19}F NMR (376.5 MHz, CD$_3$COCD$_3$, 20º C, *δ*): -114.5 (d, $J_{Pt\text{-}oF} = 151$, *o*-F, C$_6$F$_5$), -115.9 (dm, $J_{Pt\text{-}oF} = 90$, *o*-F, C$_6$F$_5$), -161.9 (t, *p*-F, C$_6$F$_5$), -165.8 (m, *m*-F, C$_6$F$_5$), -166 (m, *m*-F, C$_6$F$_5$).

Preparation of ***fac*-[Pt(pbt)$_2$(C$_6$F$_5$)Cl] (12b)**.

A yellow solution of [Pt(pbt)(Hpbt-*kN*)(C$_6$F$_5$)] (**10b**) (0.317 g, 0.405 mmol) in CH_2Cl_2 (20 mL) at 0ºC was treated with 0.144 g (0.527 mmol) of $PhICl_2$. After 2 h of stirring, the solvent was removed from the resulting colourless solution and the residue treated with Et_2O (5 ml) to give **12b** as a white solid (0.273 g, 82%).

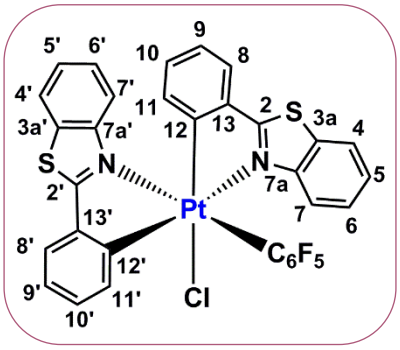

IR (cm^{-1}): ν(C-F, C$_6$F$_5$) 1074 (s), 972 (s); ν(C$_6$F$_5$)$_{X\text{-sens}}$ 794 (s); ν(Pt-Cl) 287 (w).

MALDI-TOF(+): *m/z* (%) 782 [M-Cl]$^+$ (100).

Elemental Analysis (%): Calc. for $C_{32}H_{16}ClF_5N_2PtS_2$: C, 46.98; H, 1.97; N, 3.42; S, 7.84. Found: C, 46.59; H, 2.23; N, 3.75; S, 8.05.

^{1}H NMR (400.1 MHz, CD$_3$COCD$_3$, 20º C, *δ*): 10.05 (m, 1H, H^7), 8.35 (d, 1H, *J* = 8, H^4), 8.10 (d, 1H, *J* = 8, H$^{7'}$), 8.00 (d, 1H, *J* = 8, H^9), 7.81 (t, 1H, *J* = 8, H^5), 7.74 (t, 1H, *J* = 8, H^6), 7.67 (d, 1H, *J* = 8, H$^{8'}$), 7.45-7.39 (m, 3H, H^{10,11,8}), 7.33 (t, 1H, *J* = 7.6, H$^{6'}$), 7.10 (t, 1H, *J* = 7.4, H$^{9'}$), 7.05 (t, 1H, *J* = 7.2, H$^{10'}$), 6.94 (m, 1H, H$^{5'}$), 6.93 (m, 1H, $^3J_{Pt\text{-}H}$ = 43, H$^{11'}$), 6.48 (d, 1H, *J* = 8.6, H$^{4'}$).

^{13}C{^{1}H} NMR (100.6 MHz, CD$_3$COCD$_3$, 20º C, *δ*): 179.3 (s, C$^{2'}$), 178.6 (s, C^2), 152.6 (s, $^3J_{Pt\text{-}C}$ = 14, C^{3a}), 147.6 (s, $^2J_{Pt\text{-}C}$ = 21, C$^{7a'}$), 138.9 (s, C^{13}), 137.0 (s, C$^{13'}$), 136.6-136.5 (C$^{12,12'}$), 134.6 (d, $J_{C\text{-}F}$ = 3, $^2J_{Pt\text{-}C}$ = 46, C^{11}), 133.6 (d, $J_{C\text{-}F}$ = 8, $^2J_{Pt\text{-}C}$ = 47, C$^{11'}$), 132.7 (s, $^3J_{Pt\text{-}C}$ = 52, C^{10}), 132.1 (s, C^{7a}), 131.9 (s, $^2J_{Pt\text{-}C}$ = 52, C$^{10'}$), 131.4 (s, $^3J_{Pt\text{-}C}$ = 13, C$^{3a'}$), 127.8 (s, C^5), 127.7 (s, C$^{5'}$), 126.9-126.7 (C$^{6,8',9}$), 126.24 (s, C$^{6'}$), 126.17 (s, C$^{9'}$), 125.8 (s, $^3J_{Pt\text{-}C}$ = 6, C^8), 124.8 (d, $J_{C\text{-}F}$ = 8, C^7), 123.9 (s, C$^{7'}$), 122.9 (s, C^4), 117.8 (s, C$^{4'}$).

^{19}F NMR (376.5 MHz, CD$_3$COCD$_3$, 20º C, *δ*): -112.4 (dm, $J_{Pt\text{-}oF}$ = 102, *o*-F, C$_6$F$_5$), -113.8 (dm, $J_{Pt\text{-}oF}$ = 114, *o*-F, C$_6$F$_5$), -161.5 (t, *p*-F, C$_6$F$_5$), -165.2 (m, *m*-F, C$_6$F$_5$), -166.0 (m, *m*-F, C$_6$F$_5$).

Preparation of ***fac*-[Pt(pq)$_2$(C$_6$F$_5$)Cl] (12c)**

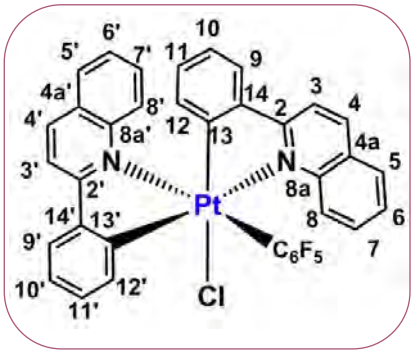

To an orange solution of [Pt(pq)(Hpq-κN)(C$_6$F$_5$)] (**10c**) (0.110 g, 0.143 mmol) in CH_2Cl_2/acetone (1:1, 20 mL) at -30ºC, $PhICl_2$ (0.043 g, 0.157 mmol) and Na_2CO_3 (0.302 g, 2.853 mmol) were added. The mixture was stirred at -30ºC for 30 min and then allowed to warm to room temperature. After 4 h, the yellow suspension was evaporated to dryness, CH_2Cl_2 (40 mL) was added and filtered through celite. The filtrate was evaporated to small volume, and treated with Et_2O (5 ml) to give **12c** as a pale-yellow solid (0.08 g, 70%).

IR (cm^{-1}): ν(C-F, C$_6$F$_5$) 1080 (s), 970 (s); ν(C$_6$F$_5$)$_{X\text{-sens}}$ 787 (m); ν(Pt-Cl) 273 (m).

MALDI-TOF(+): *m/z* (%) 770 [M-Cl]$^+$ (100).

Elemental Analysis (%): Calc. for $C_{36}H_{20}ClF_5N_2Pt$: C, 53.64; H, 2.50; N, 3.48. Found: C, 53.23; H, 2.48; N, 3.45.

^{1}H NMR (400.1 MHz, CD$_3$COCD$_3$, 20º C, δ): 10.55 (dd, 1H, $J_{H\text{-}H}$ = 8, $J_{H\text{-}F}$ = 4, H^8), 8.69 (d, 1H, J = 9, H$^{3'}$), 8.58 (d, 1H, J = 9, H^3), 8.51 (d, 1H, J = 9, H^4), 8.24 (t, 1H, J = 9, H^{10}), 8.22 (d, 1H, J = 8, H$^{4'}$), 8.15-8.13 (m, 2H, H$^{5',5}$), 7.91 (d, 1H, J = 8, H$^{8'}$), 7.87 (t, 1H, J = 8, H^7), 7.80-7.76 (m, 2H, H$^{9',6}$), 7.43 (t, 1H, J = 7, H^{11}), 7.36 (t, 1H, J = 7, H$^{7'}$), 7.32-7.29 (m, 2H, H^{9,12}), 7.02 (t, 1H, J = 8, H$^{10'}$), 6.87 (t, 1H, J = 8, H$^{11'}$), 7.41 (t, 2H, $^3J_{Pt\text{-}H}$ = 42, H$^{12',6'}$).

^{13}C{^{1}H} NMR (100.6 MHz, CD$_3$COCD$_3$, 20º C, δ): 164.6 (s, C$^{2'}$), 164.4 (s, C^2), 148.6 (s, C$^{4a'}$), 148.5 (s, C, pq/pq'), 145.3 (s, C$^{8a'}$), 142.9 (s, C$^{14'}$), 142.2 (s, C^{14}), 142.0 (s, C, pq/pq'), 141.4 (s, C$^{3'}$), 141.1 (s, C^3), 133.9 (s, $^2J_{Pt\text{-}C}$ = 53, C^{12}), 132.1 (d, C$^{12'}$), 131.7 (s, C^9), 130.8 (s, C^7), 130.4 (s, C$^{9'}$), 130.3 (s, C$^{11'}$), 130.2 (s, C^8), 128.9 (s, C$^{8'}$), 128.7 (s, C, pq/pq'), 128.3 (s, C, pq/pq'), 128.1 (s, C$^{5/5'}$), 127.4 (s, C$^{6/9'}$), 127.3 (s, C^{10}), 127.0 (s, C$^{6'/9'}$), 126.9 (s, C$^{7'}$), 125.5 (s, C$^{10'}$), 125.4 (s, C$^{5/5'}$), 125.3 (s, C^{11}), 118.7 (s, C$^{4'}$), 117.9 (s, C^4).

^{19}F NMR (376.5 MHz, CD$_3$COCD$_3$, 20º C, δ): -111.4 (dm, $J_{Pt\text{-}oF}$ = 93, *o*-F, C$_6$F$_5$), -115.7 (dm, $J_{Pt\text{-}oF}$ = 127, *o*-F, C$_6$F$_5$), -162.1 (t, *p*-F, C$_6$F$_5$), -165.5 (m, *m*-F, C$_6$F$_5$), -166 (m, *m*-F, C$_6$F$_5$).

Preparation of ***fac*-[Pt(dfppy)$_2$(C$_6$F$_5$)Cl] (12d)**

This complex was prepared as a white solid (0.070 g, 60%) in a similar way to **12b** but stirring for 5 h, starting from [Pt(dfppy)(Hdfppy-*kN*)(C$_6$F$_5$)] (**10d**) (0.116 g, 0.156 mmol) in CH_2Cl_2 (20 mL) and 0.055 g (0.203 mmol) of $PhICl_2$.

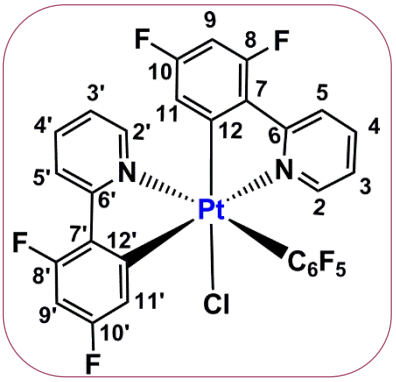

IR (cm^{-1}): ν(C-F, C$_6$F$_5$) 1074 (m), 976 (m); ν(C$_6$F$_5$)$_{X\text{-sens}}$ 797 (s); ν(Pt-Cl) 315 (m).

ESI (+): *m/z* (%) 742 [M-Cl]$^+$ (100).

Elemental Analysis (%): Calc. for $C_{28}H_{12}ClF_9N_2Pt$: C, 43.23; H, 1.55; N, 3.60. Found: C, 42.98; H, 1.72; N, 3.93.

^{1}H NMR (400 MHz, CD$_2$Cl$_2$, 20º C, *δ*): 9.99 (t, 1H, $J_{H\text{-}H} \approx J_{H\text{-}oF} = 6$, H^2), 8.39 (d, 1H, $J = 8$, H$^{2'}$), 8.35 (d, 1H, $J = 8$, H^5), 8.17 (t, 1H, $J = 7.8$, H^4), 7.92 (t, 1H, $J = 8$, H$^{3'}$), 7.69 (t, 1H, $J = 6.5$, H^3), 7.35 (d, 1H, $J = 6.5$, H$^{5'}$), 7.10 (t, 1H, H$^{4'}$), 6.99-6.93 (m, 2H, H$^{9,\,11}$), 6.67 (m, 1H, H$^{9'}$), 6.52 (m, 1H, $J_{Pt\text{-}H} = 54$, H$^{11'}$).

^{19}F{^{1}H} NMR (282.4 MHz, CDCl$_3$, 20º C, *δ*): -103.2 (d, 1F, $^4J_{F\text{-}F} = 11$, $^4J_{Pt\text{-}F} = 38$, F^8, dfppy), -104.2 (dd, 1F, $^4J_{F\text{-}F} = 10$, $^4J_{Pt\text{-}F} = 45$, F^8, dfppy), -107.9 (d, 1F, $^4J_{F\text{-}F} = 11$, $^4J_{Pt\text{-}F} = 29$, F$^{10/10'}$, dfppy/dfppy'), -107.6 (dd, 1F, $^4J_{F\text{-}F} = 10$, $^4J_{Pt\text{-}F} = 35$, F$^{10/10'}$, dfppy/dfppy'), -115.4 (dm, $J_{Pt\text{-}oF} = 103$, *o*-F, C$_6$F$_5$), -116.0 (dm, $J_{Pt\text{-}oF} = 82$, *o*-F, C$_6$F$_5$), -158.1 (t, *p*-F, C$_6$F$_5$), -162.2 (m, *m*-F, C$_6$F$_5$), -162.7 (m, *m*-F, C$_6$F$_5$).

The low solubility precludes its characterization by ^{13}C{^{1}H} NMR.

Photochemical reaction of **10d**.

Alternatively, clean formation of **12d** was observed by irradiation of a degassed solution of **10d** in CD_2Cl_2 in an NMR tube with a Hg lamp of 400 W for 2h. The evolution of the reaction was monitored by ^{1}H and ^{19}F NMR at different reaction times, revealing the formation of the hydride [Pt(dfppy)$_2$(C$_6$F$_5$)H] (***cis*-12d-H**) as the only intermediate species. This reaction took place slower using a Hg lamp of 125W.

Data for ***cis*-12d-H** extracted from the mixture after 30 minutes of irradiation:

^{1}H NMR (400 MHz, CD_2Cl_2, 20º C, δ): 8.49 (d, 1H, J = 6, J_{Pt-H} = 14), 8.43 (d, 1H, J = 8), 8.24 (d, 1H, J = 8), 8.06 (t, 1H, J = 8), 7.79 (t, 1H, J = 8), 7.70 (m, 1H), 7.43 (m), 7.32 (t, 1H, J = 7), 7.00 (t, 1H, J = 7), 6.74 (m), 6.56 (m), 6.16 (d, J = 8, J_{Pt-H} = 42), -16.6 (dm, 1H, J_{Pt-H} = 1300) .

^{19}F{^{1}H} NMR (282.4 MHz, CD_2Cl_2, 20º C, δ): -107.1 (m, 1F, dfppy), -107.2 (m, 1F, dfppy), -108.9 (m, 1F, dfppy), -109.1 (m, 1F, dfppy), -109.6 (dm, J_{Pt-oF} = 278, 1*o*-F, C_6F_5), -122.1 (dm, J_{Pt-oF} = 45, 1*o*-F, C_6F_5), -161.2 (t, 1*p*-F, C_6F_5), -163.1 (m, 1*m*-F, C_6F_5), -163.5 (m, 1*m*-F, C_6F_5).

Preparation of ***fac*-[Pt(bzq)$_2$(C$_6$F$_5$)Cl] (12e)**

This complex was prepared as a white solid (0.165 g, 78 %) in a similar way to **12b** but stirring for 2 h, starting from [Pt(bzq)(Hbzq-*kN*)(C$_6$F$_5$)] (0.203 g, 0.282 mmol) and 0.1 g (0.366 mmol) of PhICl$_2$.

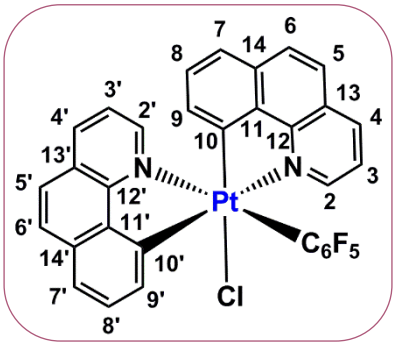

IR (cm^{-1}): ν(C-F, C$_6$F$_5$) 1076 (s), 973 (s); ν(C$_6$F$_5$)$_{X\text{-sens}}$ 795 (s); ν(Pt-Cl) 287 (w).

ESI (+): *m/z* (%) 718 [M-Cl]$^+$ (53).

Elemental Analysis (%): Calc. for C$_{32}$H$_{16}$ClF$_5$N$_2$Pt: C, 50.97; H, 2.14, N, 3.72. Found: C, 50.52; H, 2.16; N, 3.70.

^{1}H NMR (400.1 MHz, CDCl$_3$, 20º C, *δ*): 10.24 (m, 1H, H^2), 8.55 (d, 1H, *J* = 7, H^4), 8.10 (d, 1H, *J* = 6.8, H$^{4'}$), 7.95 (t, 1H, *J* = 6.5, H^3), 7.91 (d, 1H, *J* = 8.6, H$^{5/6}$), 7.86-7.71 (m, 5H, H$^{5',6',7,8,9}$), 7.56 (d, 1H, *J* = 8.7, H$^{5/6}$), 8.69 (d, 1H, *J* = 8.0, H$^{7'}$), 7.15-7.05 (m, 3H, H$^{2',3',8'}$), 6.78 (t, 1H, $J_{H\text{-}H} \approx J_{H\text{-}oF}$ = 7, $J_{Pt\text{-}H}$ = 45, H$^{9'}$).

^{13}C{^{1}H} NMR (100.6 MHz, CDCl$_3$, 20º C, *δ*): 152.5, 151.9 (s, $^2J_{Pt\text{-}C}$ = 50, $^2J_{Pt\text{-}C}$ = 46, C$^{12,12'}$), 149.3 (d, $J_{Pt\text{-}F}$ = 8, C^2), 143.1 (s, $^2J_{Pt\text{-}C}$ = 10, C$^{2'}$), 138.9 (s, C^4), 138.0 (s, $^4J_{Pt\text{-}C}$ = 10, C$^{4'}$), 137.9 (s, C), 136.6 (s, C), 136.2 (s, C), 134.8 (s, $J_{Pt\text{-}C}$ = 27, C), 134.1 (s, $J_{Pt\text{-}C}$ = 29, C,), 133.6 (d, $J_{C\text{-}F}$ = 5, C), 132.7 (d, $J_{C\text{-}F}$ = 4, $J_{Pt\text{-}C}$ = 49, C), 132.2 (d, $J_{C\text{-}F}$ = 4, C$^{9'}$), 130.8 (s, $J_{Pt\text{-}C}$ = 53, C^9), 130.3 (s, C$^{5/6}$), 129.6 (s, C$^{8'/3'}$), 129.5 (s, $^1J_{Pt\text{-}C}$ = 60, C$^{10'}$), 128.1 (s, $J_{Pt\text{-}C}$ = 18, C), 127.6 (s, $J_{Pt\text{-}C}$ = 12, C), 123.8-123.6 (s, 3C), 123.3 (s, C$^{5/6}$), 122.4 (s, $^3J_{Pt\text{-}C}$ = 11, C^3), 121.9 (s, $^3J_{Pt\text{-}C}$ = 16, C$^{8'/3'}$).

^{19}F NMR (376.5 MHz, CDCl$_3$, 20º C, *δ*): -113.6 (dm, $J_{Pt\text{-}oF}$ = 107, *o*-F, C$_6$F$_5$), -113.7 (dm, $J_{Pt\text{-}oF}$ = 117, *o*-F, C$_6$F$_5$), -159.7 (t, *p*-F, C$_6$F$_5$), -163.4 (m, 2*m*-F, C$_6$F$_5$).

Photochemical reaction of [Pt(bzq)(Hbzq-*kN*)(C$_6$F$_5$)]

Alternatively, clean formation of **12e** was observed by irradiation of a degassed solution of [Pt(bzq)(Hbzq-*kN*)(C$_6$F$_5$)][46] in CD$_2$Cl$_2$ in an NMR tube with a Hg lamp of 400 W for 2h. The evolution of the reaction was monitored by ^{1}H and ^{19}F NMR at different reaction times, revealing the formation of the hydride [Pt(bzq)$_2$(C$_6$F$_5$)H] (***cis*-12e-H**) as the only

intermediate species. This reaction took place slower using a Hg lamp of 125 W. Data for ***cis*-12e-H** extracted from the mixture after 10 minutes of irradiation with a Hg lamp of 400 W.

^{1}H NMR (400 MHz, CD_2Cl_2, 20º C, *δ*): 9.33 (m, 1H, bzq), 9.03 (m, 1H, bzq), 8.96 (m, 1H, $J_{Pt\text{-}H}$ = 12, bzq), 8.57 (dd, 1H, *J* = 8, bzq), 8.18 (dd, 1H, *J* = 8, bzq), 6.52 (d, 1H, *J* = 7, $J_{Pt\text{-}H}$ = 34, bzq), -16.9 (dm, 1H, $J_{Pt\text{-}H}$ = 1343).

^{19}F NMR (376.5 MHz, $CDCl_3$, 20º C, *δ*): -108.8 (dm, $J_{Pt\text{-}oF}$ = 279, 1*o*-F, C_6F_5), -120.5 (dm, $J_{Pt\text{-}oF}$ ~ 42, 1*o*-F, C_6F_5), -162.1 (t, 1*p*-F, C_6F_5), -163.6 (m, 1*m*-F, C_6F_5), -164.0 (m, 1*m*-F, C_6F_5).

Preparation of ***mer*-[Pt(pbt)$_2$(C$_6$F$_5$)(CN)] (13)**

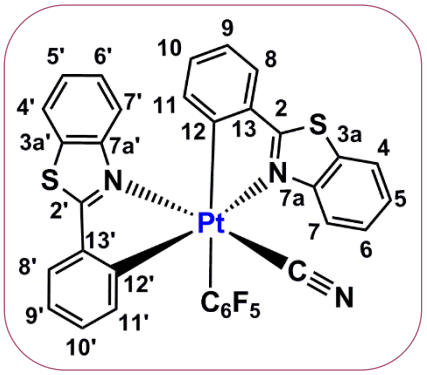

KCN (0.024 g, 0.367 mmol) and $KClO_4$ (0.339 g, 2.440 mmol) were added to a suspension of *fac*-[Pt(pbt)$_2$(C$_6$F$_5$)Cl] (**12b**) (0.100 g, 0.122 mmol) in 50 mL of acetone/MeOH (1:1). The mixture was refluxed for 24 h and evaporated to dryness. 200 mL of CH_2Cl_2 were added to the solid residue and it was washed with H_2O (~4x100 mL). The organic phase was dried with anhydrous $MgSO_4$ and filtered through celite. The solution was evaporated to ~3 mL and treated with Et_2O (~10 mL) to obtain **13** as a white solid (0.055 g, 56 %).

IR (cm^{-1}): ν(CN) 2171 (m); ν(C-F, C$_6$F$_5$) 1071 (m), 965 (m); ν(C$_6$F$_5$)$_{X\text{-sens}}$ 773 (m).

ESI (+): *m/z* (%) 641 [M-C$_6$F$_5$]$^+$ (78), 809 [M+H$^+$]$^+$ (100).

Elemental Analysis (%): Calc. for $C_{33}H_{16}ClF_5N_3PtS_2$: C, 49.01; H, 1.99; N, 5.20; S, 7.93. Found: C, 48.64; H, 2.12; N, 5.40; S, 7.89.

^{1}H NMR (400 MHz, CDCl$_3$, 20º C, *δ*): 8.61 (dd, 1H, $J_{H\text{-}H}$ = 8.0, $J_{H\text{-}oF}$ = 5, $^3J_{H\text{-}Pt}$ = 49, H$^{11'}$), 8.03 (d, 1H, *J* = 8, H$^{4'}$), 7.70 (m, 2H, H^{4,8}), 7.64 (d, 2H, *J* = 8, H$^{8',7'}$), 7.54 (t, 1H, *J* = 8, H$^{5'}$), 7.51 (t, 1H, *J* = 8, H$^{10'}$), 7.45 (t, 1H, *J* = 8, H$^{6'}$), 7.40 (t, 1H, *J* = 8, H$^{9'}$), 7.28 (t, 1H, *J* = 7, H^5), 7.07 (m, 2H, H^{9,6}), 6.99 (t, 1H, *J* = 8, H^{10}), 6.5 (dd, 1H, $J_{H\text{-}H}$ = 8, $J_{H\text{-}oF}$ = 6, 1H, H^7), 6.42 (d, 1H, *J* = 8, $^3J_{H\text{-}Pt}$ = 28, H^{11}).

^{13}C{^{1}H} NMR (100.6 MHz, CDCl$_3$, 20º C, *δ*): 182.8 (s, C^2), 177.1 (s, C$^{2'}$), 150.3 (s, $^3J_{Pt\text{-}C}$ = 13, C$^{3a'}$), 148.35, 148.32 (C^{3a,13}), 139.3 (s, $^1J_{Pt\text{-}C}$ = 95, C^{12}), 137.6 (s, C$^{12'}$), 136.1 (d, $J_{H\text{-}oF}$ = 7, $^2J_{C\text{-}Pt}$ = 53, C$^{11'}$), 135.1 (s, C$^{13'}$), 134.0 (s, $^3J_{C\text{-}Pt}$ = 57.0, C$^{10'}$), 133.1 (s, C^{10}, $^3J_{C\text{-}Pt}$ = 33), 131.9 (s, C^{11}, $^3J_{C\text{-}Pt}$ = 41), 131.4 (s, C$^{7a'}$), 129.9 (s, $^2J_{C\text{-}Pt}$ = 18, C^{7a}), 128.4 (s, C$^{6'}$), 127.8 (s, C$^{9/6}$), 126.8 (s, C$^{5'}$), 126.7 (s, C^8), 126.3 (m, C$^{9/6,8'/7'}$), 125.93 (s, C^5), 125.88 (s, C$^{9'}$), 122.8 (s, C^4), 122.7 (s, C$^{4'}$), 121.8 (s, C$^{8'/7'}$), 119.5 (d, $J_{H\text{-}oF}$ = 8, C^7).

***mer*-[Pt(pbt)$_2$(C$_6$F$_5$)(^{13}CN)], ^{13}C{^{1}H} NMR (100.6 MHz, CDCl$_3$, 20º C, *δ*):** 120.1 (d, $J_{H\text{-}oF}$ = 12, $^1J_{C\text{-}Pt}$ = 728, ^{13}CN).

^{19}F NMR (376.5 MHz, CDCl$_3$, 20º C, *δ*): -111.7 (dm, $J_{o\text{-}F\text{-}Pt}$ = 87, *o*-F, C$_6$F$_5$), -113.3 (dm, $J_{o\text{-}F\text{-}Pt}$ = 41, *o*-F, C$_6$F$_5$), -158.3 (t, *p*-F, C$_6$F$_5$), -161.2 (m, *m*-F, C$_6$F$_5$), -163.2 (m, *m*-F, C$_6$F$_5$).

Preparation of ***fac*-[Pt(pbt)$_2$(C$_6$F$_5$)(Mepy)][PF$_6$] (14)**

4-Methylpyridine (63µL, 0.646 mmol), $TlPF_6$ (0.057g, 0.386 mmol) and $KClO_4$ (excess) were added to a suspension of *fac*-[Pt(pbt)$_2$(C$_6$F$_5$)Cl] (**12b**) (0.211 g, 0.258 mmol) in 50 mL of acetone/MeOH (1:1). The white suspension was refluxed for 3 days and evaporated to dryness. Then, 80 mL of CH_2Cl_2 were added and the mixture was filtered through celite. The filtrate was evaporated to dryness and treated with Et_2O (~5 mL) and MeOH (~5 mL) to obtain **14** as a pale yellow solid (0.205 g, 78 %).

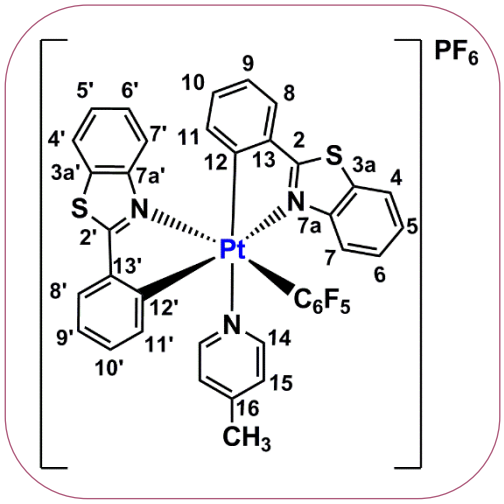

IR (cm^{-1}): ν(C-F, C$_6$F$_5$) 1074 (m), 968 (m); ν(C$_6$F$_5$)$_{X\text{-sens}}$ 758 (m).

ESI (+): *m/z* (%) 875 [M-PF$_6$]$^+$ (100), 782 [(M-Mepy)-PF$_6$]$^+$ (95).

Elemental Analysis (%): Calc. for $C_{38}H_{23}F_{11}N_3PPtS_2$: C, 44.71; H, 2.27; N, 4.12; S, 6.28. Found: C, 45.00; H, 2.68; N, 4.31; S, 6.09.

^{1}H NMR (400.1 MHz, CD$_3$COCD$_3$, 20º C, *δ*): 8.77 (d, 2H, J = 5, $^3J_{Pt\text{-}H}$ = 16, H^{14}, Mepy), 8.45 (d, 1H, J = 8, H^4), 8.26 (d, 1H, J = 8, H$^{7'}$), 8.05 (d, 1H, J = 7.5, H^8), 7.80 (m, 1H, $J_{H\text{-}H} \approx J_{H\text{-}oF}$ = 6, $^3J_{Pt\text{-}H}$ = 40, H^{11}), 7.78-7.71 (m, 2H, J = 8, H$^{8',5}$), 7.69-7.61 (m, 2H, H^{6,7}), 7.58-7.52 (m, 2H, H^{9,10}), 7.49-7.48 (m, 3H, H$^{6',15}$, pbt', Mepy), 7.20-7.09 (m, 3H, H$^{5',9',10'}$), 6.88 (t, 1H, $J_{H\text{-}H} \approx J_{H\text{-}oF}$ = 6, $^3J_{Pt\text{-}H}$ = 40, H$^{11'}$), 6.47 (d, 1H, J = 8.5, H$^{4'}$), 2.45 (s, 3H, CH$_3$, Mepy).

^{13}C{^{1}H} NMR (100.6 MHz, CD$_3$COCD$_3$, 20º C, *δ*): 181.5 (s, $^2J_{Pt\text{-}C}$ = 71, C$^{2/2'}$), 181.2 (s, $^2J_{Pt\text{-}C}$ = 58, C$^{2/2'}$), 155.17 (s, C^{16}, Mepy), 152.30 (C^{14}, Mepy), 151.2 (d, $J_{H\text{-}oF}$ = 2, $^2J_{Pt\text{-}C}$ = 13, C^{7a}), 146.7 (s, $^3J_{Pt\text{-}C}$ = 21, C$^{3a'}$), 138.2 (d, $J_{H\text{-}oF}$ = 1.5, C^{12}), 137.6 (s, C$^{13'}$), 137.4 (s, C^{13}), 135.3 (m, C$^{11'}$), 135.0 (s, C$^{9/10}$), 134.4 (d, $J_{H\text{-}oF}$ = 3, $^2J_{Pt\text{-}C}$ = 45, C^{11}), 133.4 (s, C$^{10'}$), 133.1 (s, C, pbt), 133.1 (s, C, pbt), 130.0 (s, C$^{9'/5'}$), 129.3 (s, C^6), 129.2 (s, C^8), 129.1 (s, C$^{5/8'}$), 129.0 (s, C$^{6'}$), 128.9 (s, C$^{5/8'}$), 128.5 (s, C$^{9/10}$), 128.3 (s, C$^{9'/5'}$), 128.2 (s, C, pbt), 128.1 (s, C^{15}, Mepy), 125.8 (s, C$^{7'}$), 125.1 (s, C^4), 122.3 (d, $J_{H\text{-}oF}$ = 14, C^7), 117.6 (s, C$^{4'}$), 21.3 (s, CH$_3$, Mepy).

$^{19}F\{^1H\}$ NMR (376.5 MHz, CD_3COCD_3, 20º C, δ): -72.6 (d, $^1J_{F\text{-}P}$ = 707, PF_6), -113.9 (dm, $J_{Pt\text{-}oF}$ = 113.5, *o*-F, C_6F_5), -116.4 (dm, $J_{Pt\text{-}oF}$ = 100.6, *o*-F, C_6F_5), -158.9 (t, *p*-F, C_6F_5), -163.0 (m, *m*-F, C_6F_5), -163.8 (m, *m*-F, C_6F_5).

$^{31}P\{^1H\}$ NMR (161.9 MHz, CD_3COCD_3, 20º C, δ): -144.1 (sept, PF_6).

Preparation of ***fac*-[Pt(pbt)$_2$(C$_6$F$_5$)(bpe)][PF$_6$] (15)**

1,2-bi(4-pyridyl)ethylene (bpe) (0.060g, 0.328 mmol), $TlPF_6$ (0.057g, 0.164 mmol) and $KClO_4$ (excess) were added to a suspension of *fac*-[Pt(pbt)$_2$(C$_6$F$_5$)Cl] (**12b**) (0.134 g, 0.164 mmol) in 50 mL of acetone/MeOH (1:1). The white suspension was refluxed for 11 days and evaporated to dryness. Then, 60 mL of CH_2Cl_2 were added and filtered through celite. The filtrate was evaporated to dryness and treated with Et_2O (~5 mL) and MeOH (~5 mL) to obtain **15** as a white solid (0.110 g, 60 %).

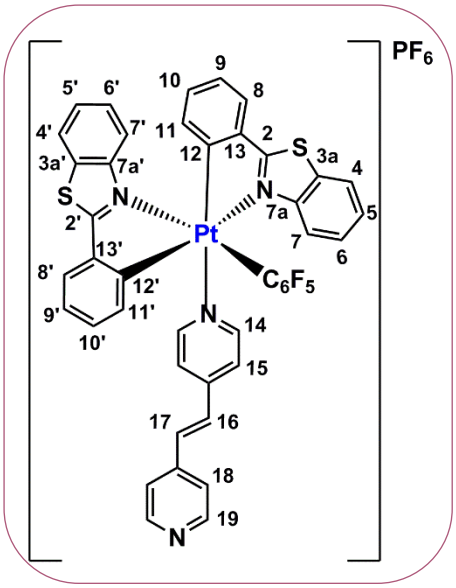

IR (cm^{-1}): ν(C-F, C$_6$F$_5$) 1077 (m), 972 (m); ν(C$_6$F$_5$)$_{X\text{-sens}}$ 757 (m).

ESI (+): *m/z* (%) 782 [(M-bipy)-PF$_6$]$^+$ (100), 964 [M-PF$_6$]$^+$ (82)

Elemental Analysis (%): Calc. for $C_{44}H_{26}F_{11}N_4PPtS_2$: C, 47.62; H, 2.36; N, 5.05; S, 5.78. Found: C, 47.39; H, 2.45; N, 5.04; S, 5.55.

^{1}H NMR (400.1 MHz, CD$_3$COCD$_3$, 20º C, *δ*): 8.90 (d, 2H, J = 5, $^3J_{Pt\text{-}H}$ = 15, H^{14}, bpe), 8.61 (d, 2H, J = 5, H^{19}, bpe), 8.46 (d, 1H, J = 8, H^4), 8.27 (d, 1H, J = 8, H$^{7'}$), 8.06 (d, 1H, J = 7, H^8), 7.84 (d, 2H, J = 6, H^{15}, bpe), 7.80-7.63 (m, 5H, H$^{6,5,10,11,8'}$), 7.57-7.49 (m, 6H, H$^{6',9}$, H^{16,17,18}, bpe), 7.21-7.10 (m, 4H, H$^{5',10',9',7}$), 6.89 (t, 1H, $J_{H\text{-}H} \approx J_{H\text{-}oF}$ = 7, $^3J_{Pt\text{-}H}$ = 40, H$^{11'}$), 6.50 (d, 1H, J = 8, H$^{4'}$).

^{19}F{^{1}H} NMR (282.4 MHz, CD$_3$COCD$_3$, 20º C, *δ*): -72.6 (d, $^1J_{F\text{-}P}$ = 708, PF$_6$), -114.0 (dm, $J_{Pt\text{-}oF}$ = 103, *o*-F, C$_6$F$_5$), -116.4 (dm, $J_{Pt\text{-}oF}$ = 101.8, *o*-F, C$_6$F$_5$), -158.9 (t, *p*-F, C$_6$F$_5$), -163.0 (m, *m*-F, C$_6$F$_5$), -163.8 (m, *m*-F, C$_6$F$_5$).

^{31}P{^{1}H} NMR (121 MHz, CD$_3$COCD$_3$, 20º C, *δ*): -144.3 (sept, PF$_6$).

Preparation of **[Pt(bzq)(Hthpy-*κN*)(C_6F_5)] (16a)**

[Pt(bzq)(C_6F_5)(acetone)] (0.200 g, 0.334 mmol) was added to a solution of 2-(2-thienyl)pyridine (Hthpy) (0.054 g, 0.334 mmol) in CH_2Cl_2 (20 mL). After 30 min of stirring, the solution was evaporated to dryness and treated with Et_2O (5 mL) to afford **16a** as a yellow solid (0.196 g, 84%).

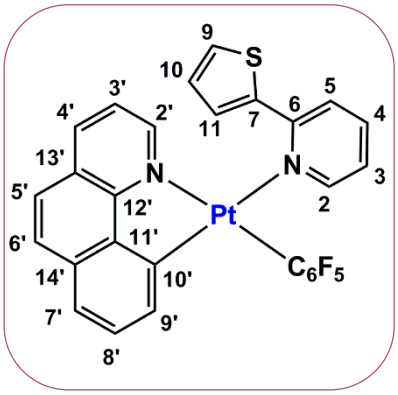

IR (cm^{-1}): ν(C-F, C_6F_5) 1060 (s), 955 (s); ν(C_6F_5)$_{X\text{-sens}}$ 799 (s)

ESI (+): *m/z* calcd. for $C_{28}H_{16}F_5N_2PtS$ $[M + H]^+$ 702.0599; found 702.0594.

Elemental Analysis (%): Calc. for $C_{28}H_{15}F_5N_2SPt$: C, 47.94; H, 2.16; N, 3.99; S, 4.57. Found: C, 48.06; H, 2.42; N, 4.26; S, 4.46.

^{1}H NMR (400.1 MHz, $CDCl_3$, 20º C, *δ*): 9.31 (d, 1H, J = 5.4, $^3J_{H\text{-}Pt}$ = 17, H^2, Hthpy), 8.29 (d, 1H, J = 7.9, $H^{4'}$, bzq), 8.18 (d, 1H, J = 3.5, H^{11}, Hthpy), 8.00 (d, 1H, J = 5.4, $^3J_{H\text{-}Pt}$ = 16, $H^{2'}$, bzq), 7.90 (t, 1H, J = 7.7, H^4, Hthpy), 7.82 (d, 1H, J = 8.0, H^5, Hthpy), 7.78 (d, 1H, J = 8.7, $H^{5'/6'}$, bzq), 7.57-7.54 (m, 2H, $H^{5'/6',7'}$, bzq), 7.38-7.30 (m, 4H, $H^{8',3'}$, bzq, $H^{3,9}$, Hthpy), 7.04 (d, 1H, J = 7.4, $H^{9'}$, bzq), 6.95 (t, 1H, J = 4.2, H^{10}, Hthpy).

^{13}C{^{1}H} NMR (100.6 MHz, CDCl3, 20º C, *δ*): 155.4 (s, $C^{12'}$, bzq), 154.8 (s, C^6, Hthpy), 153.4 (d, $J_{C\text{-}F}$ = 2.6, C^2, Hthpy), 145.6 (s, $^2J_{C\text{-}Pt}$ = 16, $C^{2'}$, bzq), 142.1 (s, $C^{11'}$, bzq), 141.0 (s, C^7, Hthpy), 138.0 (s, C^4, Hthpy), 137.1 (s, $C^{4'}$, bzq), 136.0 (s, $C^{14'}$, bzq), 134.5 (s, $^2J_{C\text{-}Pt}$ = 115, $C^{9'}$, bzq), 133.9 (s, $C^{10'}$, bzq), 130.0 (s, $C^{5'/6'}$, bzq), 129.7 (s, $C^{8'}$, bzq), 129.6 (s, C^{11}, Hthpy), 129.0 (s, C^9, Hthpy), 127.5 (s, C^{10}, Hthpy), 126.9 (s, $C^{13'}$, bzq), 125.7 (s, C^5, Hthpy), 123.4 (s, $^3J_{C\text{-}Pt}$ = 23, C^3, Hthpy), 122.7 (s, $C^{5'/6'}$, bzq), 121.8 (s, $C^{7'}$, bzq), 121.1 (s, $^3J_{C\text{-}Pt}$ = 20, $C^{3'}$, bzq).

^{19}F{^{1}H} NMR (376.5 MHz, $CDCl_3$, 20º C, *δ*): -116.8 (dm, $J_{Pt\text{-}oF}$ = 454, 1*o*-F, C_6F_5), -117.3 (dm, $J_{Pt\text{-}oF}$ = 513, 1*o*-F, C_6F_5), -163.4 (t, 1*p*-F, C_6F_5), -164.5 (m, 1*m*-F, C_6F_5), -164.9 (m, 1*m*-F, C_6F_5).

Preparation of **[Pt(bzq)(Hpbt-κN)(C_6F_5)]** (**16b**)

This compound was prepared as a yellow solid (0.130 g, 70%) in a similar procedure to **16a**, using as starting precursors [Pt(bzq)(C_6F_5)(acetone)] (0.150 g, 0.250 mmol) and 2-phenylbenzothiazole (Hbt) (0.053g, 0.250 mmol) and stirring for 30 min.

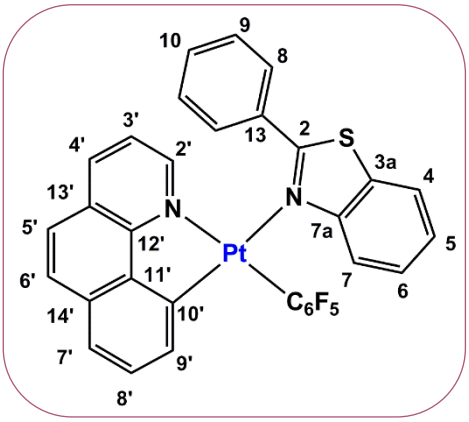

IR (cm^{-1}): ν(C-F, C_6F_5) 1060 (s), 954 (s); ν(C_6F_5)$_{X\text{-sens}}$ 801 (s)

ESI (+): *m/z* calcd. for $C_{32}H_{17}F_5N_2NaPtS$ $[M + Na]^+$ 774.0575; found 774.0570.

Elemental Analysis (%): Calc. for $C_{32}H_{17}F_5N_2SPt$: C, 51.13; H, 2.28; N, 3.73; S, 4.27. Found: C, 51.32; H, 2.53; N, 3.99; S, 3.89.

^{1}H NMR (400.1 MHz, $CDCl_3$, 20º C, *δ*): 9.18 (m, 1H, H^7, Hpbt), 8.62 (d, 2H, J = 7.6, H^8, Hpbt), 8.31 (d, 1H, J = 7.9, $H^{4'}$, bzq), 8.01 (d, 1H, J = 5, $^3J_{H\text{-}Pt}$ = 16, $H^{2'}$, bzq), 7.95 (m, 1H, H^5, Hpbt), 7.82 (d, 1H, J = 8.7, $H^{6'}$, bzq), 7.61-7.58 (m, 2H, $H^{7',5'}$, bzq), 7.52-7.49 (m, 3H, $H^{6,4,10}$, Hpbt), 7.43-7.37 (m, 3H, $H^{8'}$, bzq, H^9, Hpbt), 7.27 (m, 1H, $H^{3'}$, bzq), 7.07 (d, 1H, J = 7.4, $^3J_{H\text{-}Pt}$ = 63, $H^{9'}$, bzq).

^{13}C{^{1}H} NMR (100.6 MHz, $CDCl_3$, 20º C, *δ*): 172.1 (s, C^2, Hpbt), 155.6 (s, $C^{12'}$, bzq), 153.0 (s, C^{7a}, Hpbt), 146.1 (s, $^2J_{C\text{-}Pt}$ = 17, $C^{2'}$, bzq), 142.2 (s, $C^{11'}$, bzq), 137.3 (s, $C^{4'}$, bzq), 137.0 (s, $C^{10'/14'}$, bzq), 134.2 (s, $C^{9'}$, bzq), 133.9 (s, $C^{10'/14'}$, bzq), 132.7 (s, C^{3a}, Hpbt), 131.9 (s, C^{10}, Hpbt), 131.6 (s, C^{13}, Hpbt), 130.0 (s, $C^{6'}$, bzq), 129.9 (s, $C^{8'}$, bzq), 128.9 (s, $C^{8,9}$, Hpbt), 126.9, 126.3 (s, $C^{6,4,13'}$, Hpbt, bzq), 125.3 (d, $J_{C\text{-}F}$ = 2, $^3J_{C\text{-}Pt}$ = 20, C^7, Hpbt), 122.7 (s, $C^{5'/7'}$, bzq), 121.8 (s, $C^{5'/7'}$, bzq), 121.5 (s, C^5, Hpbt), 121.4 (s, $C^{3'}$, bzq).

^{19}F{^{1}H} NMR (376.5 MHz, $CDCl_3$, 20º C, *δ*): -116.1 (dm, $J_{Pt\text{-}oF}$ = 472, 1*o*-F, C_6F_5), -117.3 (dm, $J_{Pt\text{-}oF}$ = 493, 1*o*-F, C_6F_5), -163.7 (t, 1*p*-F, C_6F_5), -165.1 (m, 2*m*-F, C_6F_5).

Preparation of **[Pt(bzq)(Hpq-*κN*)(C_6F_5)]** (**16c**).

This compound was obtained as a yellow solid (0.120 g, 64%) in a similar way to **16a**, using as starting precursors [Pt(bzq)(C_6F_5)(acetone)] (0.150 g, 0.250 mmol) and 2-phenylquinoline (Hpq) (0.051 g, 0.250 mmol) and stirring for 1 h.

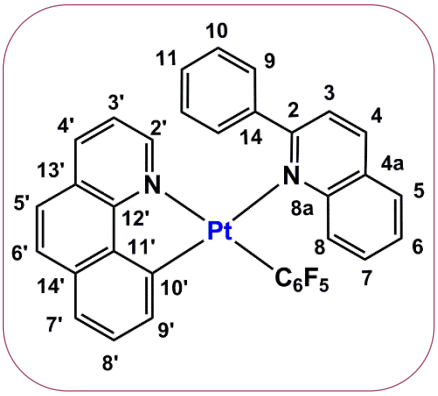

IR (cm^{-1}): ν(C-F, C_6F_5) 1058 (s), 954 (s); ν(C_6F_5)$_{X\text{-}sens}$ 798 (s)

ESI (+): *m/z* calcd. for $C_{34}H_{19}F_5N_2NaPt$ $[M + Na]^+$ 768.1011; found 768.0978.

Elemental Analysis (%): Calc. for $C_{34}H_{19}F_5N_2Pt$: C, 54.77; H, 2.57; N, 3.76. Found: C, 54.48; H, 2.79; N, 4.13.

^{1}H NMR (400.1 MHz, $CDCl_3$, 20º C, *δ*): 10.11 (d, 1H, *J* = 8, H^8, Hpq), 8.44 (d, 1H, *J* = 8.5, H^4, Hpq), 8.34 (d, 1H, *J* = 7.9, $H^{4'}$, bzq), 8.13 (d, 1H, *J* = 5.0, $^3J_{H\text{-}Pt} \approx 20$, $H^{2'}$, bzq), 7.97 (d, 1H, *J* = 7.6, H^5, Hpq), 7.81 (d, 1H, *J* = 8.6, $H^{6'}$, bzq), 7.71 (t, 1H, *J* = 7.0, H^7, Hpq), 7.63-7.54 (m, 6H, $H^{6,3,9/10}$ pq, $H^{7',5'}$ bzq), 7.41 (t, 1H, *J* = 7.4, H^{11}, Hpq), 7.34-7.28 (m, 4H, $H^{9/10}$, Hpq, $H^{3',8'}$, bzq), 7.01 (d, 1H, *J* = 7.0, $^3J_{H\text{-}Pt} = 63$, $H^{9'}$, bzq).

^{13}C{^{1}H} NMR (100.6 MHz, $CDCl_3$, 20º C, *δ*): 163.5 (s, C^2, Hpq), 155.9 (s, $^2J_{C\text{-}Pt} = 86$, $C^{12'}$, bzq), 148.1 (s, C^{8a}, Hpq), 146.3 (s, $^2J_{C\text{-}Pt} = 13$, $C^{2'}$, bzq), 142.1 (s, $C^{11'}$, bzq), 139.8 (s, C^{14}, Hpq), 138.6 (s, C^4, Hpq), 137.4 (s, $C^{14'}$, bzq), 137.1 (s, $C^{4'}$, bzq), 134.4 (s, $^2J_{C\text{-}Pt} = 117$, $C^{9'}$, bzq), 133.9 (s, $C^{10'}$, bzq), 130.5 (s, C^7, Hpq), 130.1 (s, $C^{8,4a}$, Hpq), 129.8 (s, $C^{6'}$, bzq), 129.6 (s, $C^{8',11}$, bzq, Hpq), 128.4 (s, $C^{9/10}$, Hpq), 128.3 (s, $C^{9/10}$, Hpq), 127.8 (s,br, $C^{5,6}$, Hpq), 126.9 (s, $C^{13'}$, bzq), 124.4 (s, $^3J_{C\text{-}Pt} = 10$, C^3, Hpq), 122.6 (s, $C^{5'/7'}$, bzq), 121.3 (s,br, $C^{3',5'/7'}$, bzq).

^{19}F{^{1}H} NMR (376.5 MHz, $CDCl_3$, 20º C, *δ*): -114.7 (dm, $J_{Pt\text{-}oF} = 495$, 1*o*-F, C_6F_5), -118.7 (dm, $J_{Pt\text{-}oF} = 457$, 1*o*-F, C_6F_5), -164.4 (t, 1*p*-F, C_6F_5), -165.4 (m, 1*m*-F, C_6F_5), -166.2 (m, 1*m*-F, C_6F_5).

Preparation of **[Pt(bzq)(Hdfppy-*κN*)(C_6F_5)]** (**16d**).

This compound was obtained as a yellow solid (0.138 g, 75 %) following a procedure similar to **16a**, using as starting precursors [Pt(bzq)(C_6F_5)(acetone)] (0.150 g, 0.250 mmol) and 2-(2,4-difluorophenyl)pyridine (Hdfppy) (38 µL, 0.250 mmol) and stirring for 3 h.

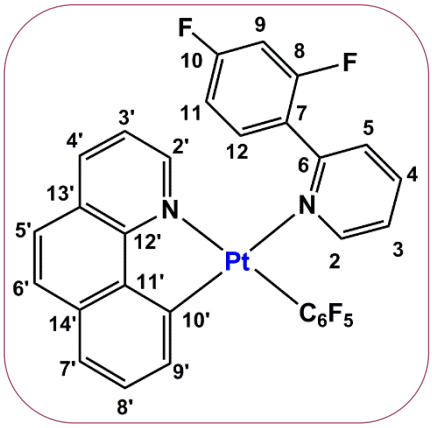

IR (cm^{-1}): ν(C-F, C_6F_5) 1056 (s), 950 (s); ν(C_6F_5)$_{X\text{-}sens}$ 799 (s)

ESI (+): *m/z* calcd. for $C_{30}H_{15}F_7N_2NaPt$ $[M + Na]^+$ 754.0666; found 754.0634.

Elemental Analysis (%): Calc. for $C_{30}H_{15}F_7N_2Pt$: C, 49.26; H, 2.07; N, 3.83. Found: C, 48.93; H, 2.33; N, 4.19.

^{1}H NMR (400.1 MHz, CD_3COCD_3, 20º C, *δ*): 9.46 (d, 1H, *J* = 5.4, $^3J_{H\text{-}Pt}$ = 17, H^2, Hdfppy), 8.64 (d, 1H, *J* = 8.0, $H^{4'}$, bzq), 8.43 (d, 1H, *J* = 5.0, $^3J_{H\text{-}Pt}$ = 21, $H^{2'}$, bzq), 8.23 (t, 1H, *J* = 7.6, H^4, Hdfppy), 7.85 (d, 1H, *J* = 8.7, $H^{6'}$, bzq), 7.81 (t, 1H, *J* = 6.7, H^3, Hdfppy), 7.77-7.74 (m, 2H, $H^{5'}$, bzq, H^5, Hdfppy), 7.71-7.68 (m, 2H, $H^{3'}$, bzq, H^{12}, Hdfppy), 7.54 (d, 1H, *J* = 7.8, $H^{7'}$, bzq), 7.24 (t, 1H, *J* = 7.5, $H^{8'}$, bzq), 7.00-6.92 (m, 2H, $H^{9,11}$, Hdfppy), 6.91 (d, 1H, *J* = 7.9, $^3J_{H\text{-}Pt}$ = 64, $H^{9'}$, bzq).

^{13}C{^{1}H} NMR (100.6 MHz, CD_3COCD_3, 20º C, *δ*): 164.6 (dd, $^1J_{C\text{-}F}$ = 250, $^3J_{C\text{-}F}$ = 12, $C^{8/10}$, Hdfppy), 160.5 (dd, $^1J_{C\text{-}F}$ = 250, $^3J_{C\text{-}F}$ = 12, $C^{8/10}$, Hdfppy), 156.5 (s, C^6, Hdfppy), 155.9 (s, $C^{12'}$, bzq), 154.4 (m, C^2, Hdfppy), 147.8 (m, $^2J_{C\text{-}Pt}$ = 18, $C^{2'}$, bzq), 142.7 (s, $C^{11'}$, bzq), 139.5 (s, C^4, Hdfppy), 138.7 (s, $C^{4'}$, bzq), 138.6 (s, $C^{14'}$, bzq), 135.0 (s, $C^{9'}$, bzq), 134.5 (s, $C^{10'}$, bzq), 133.5 (m, C^{12}, Hdfppy), 130.4 (s, $C^{6'}$, bzq), 129.9 (s, $C^{8'}$, bzq), 129.4 (d, $^4J_{C\text{-}F}$ = 2, C^5, Hdfppy), 127.7 (s, $^3J_{C\text{-}Pt}$ = 18, $C^{13'}$, bzq), 125.9 (s, C^3, Hdfppy), 124.7 (m, $^2J_{C\text{-}F}$ = 14, $^2J_{C\text{-}F}$ = 4, C^7, Hdfppy), 124.0 (s, $C^{5'}$, bzq), 123.0 (s, $^3J_{C\text{-}Pt}$ = 18, $C^{3'}$, bzq), 122.0 (s, $C^{7'}$, bzq), 112.1 (m, $^2J_{C\text{-}F}$ = 21, $^4J_{C\text{-}F}$ = 4, C^{11}, Hdfppy), 104.6 (t, $^2J_{C\text{-}F}$ = 26, C^9, Hdfppy).

^{19}F{^{1}H} NMR (376.5 MHz, CD_3COCD_3, 20º C, *δ*): -109.5 (d, $^4J_{F\text{-}F}$ = 8.6, $F^{8/10}$, Hdfppy), -113.2 (d, $^4J_{F\text{-}F}$ = 8.6, $F^{8/10}$, Hdfppy), -115.6 (dm, $J_{Pt\text{-}oF}$ = 521, 1*o*-F, C_6F_5), -120.9 (dm, $J_{Pt\text{-}oF}$ = 494, 1*o*-F, C_6F_5), -166.3 (t, 1*p*-F, C_6F_5), -166.5 (m, 1*m*-F, C_6F_5), -167.5 (m, 1*m*-F, C_6F_5).

Preparation of **[Pt(bzq)(Hoxd-*κN*)(C_6F_5)]** (**16f**).

This compound was prepared as a yellow solid (0.097 g, 76 %) following a procedure similar to **16a**, using as starting precursors [Pt(bzq)(C_6F_5)(acetone)] (0.110 g, 0.167 mmol) and 2,5-diphenyl-1,3,4-oxadiazole (Hoxd) (0.041, 0.167 mmol) in CH_2Cl_2 (20 mL) and stirring for 4h.

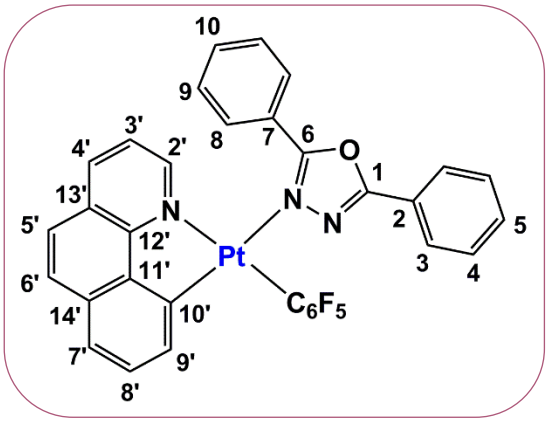

IR (cm^{-1}): ν(C-F, C_6F_5) 1059 (s), 955 (s); ν(C_6F_5)$_{X\text{-sens}}$ 799 (s).

ESI (+): *m/z* calcd. for $C_{33}H_{18}F_5N_3NaOPt$ $[M + Na]^+$ 785.0913; found 785.0900.

Elemental Analysis (%): Calc. for $C_{33}H_{18}F_5N_3OPt$: C, 51.97; H, 2.38; N, 5.51. Found: C, 51.64; H, 2.73; N, 5.69.

^{1}H NMR (400.1 MHz, CD_3COCD_3, 20º C, *δ*): 9.16 (d, 2H, *J* = 8, H^8, Hoxd), 8.77 (d, 1H, *J* = 5.0, $^3J_{H\text{-}Pt}$ = 19, $H^{2'}$, bzq), 8.58 (d, 1H, *J* = 8, $H^{4'}$, bzq), 8.25 (d, 2H, *J* = 7, H^3, Hoxd), 7.89 (d, 1H, *J* = 9, $H^{6'}$, bzq), 7.77 (d, 1H, *J* = 9, $H^{5'}$, bzq), 7.74-7.66 (m, 4H, $H^{4,5,10}$, Hoxd), 7.63 (d, 1H, *J* = 7.5, $H^{7'}$, bzq), 7.56 (t, 2H, *J* = 7.5, H^9, Hoxd), 7.50 (dd, 1H, *J* = 7.5, *J* = 5.4, $H^{3'}$, bzq), 7.36 (t, 1H, *J* = 7.5, $H^{8'}$, bzq), 7.08 (d, 1H, *J* = 7.4, $^3J_{H\text{-}Pt}$ = 63, $H^{9'}$, bzq).

^{13}C{^{1}H} NMR (100.6 MHz, CD_3COCD_3, 20º C, *δ*): 166.6 (s, C^6, Hoxd), 165.5 (s, C^1, Hoxd), 155.7 (s, $C^{12'}$, bzq), 148.7 (s, $C^{2'}$, bzq), 143.1 (s, $C^{11'}$, bzq), 138.9 (s, $C^{14'}$, bzq), 138.8 (s, $C^{4'}$, bzq), 134.9 (s, $C^{9'}$, bzq), 134.6 (s, $C^{10'}$, bzq), 134.2 (s, C^{10}, Hoxd), 133.7 (s, C^5, Hoxd), 130.4 (s, C^4, Hoxd), 130.3 (s, $C^{6'}$, bzq), 130.0 (s, $C^{8'}$, bzq), 129.7 (s, C^9, Hoxd), 129.7 (s, C^8, Hoxd), 128.1 (s, C^3, Hoxd), 127.7 (s, $C^{13'}$, bzq), 124.1 (s, $C^{5'}$, bzq), 123.7 (s, C^2, Hoxd), 122.8 (s, $C^{3'}$, bzq), 122.6 (s, C^7, Hoxd), 122.5 (s, $C^{7'}$, bzq).

^{19}F{^{1}H} NMR (376.5 MHz, CD_3COCD_3, 20º C, *δ*): -117.0 (dm, $J_{Pt\text{-}oF}$ = 495, 2*o*-F, C_6F_5), -166.2 (t, 1*p*-F, C_6F_5), -167.0 (m, 2*m*-F, C_6F_5).

Preparation of **[Pt(bzq)(Hpypy-*κN*)(C_6F_5)] (16g)**

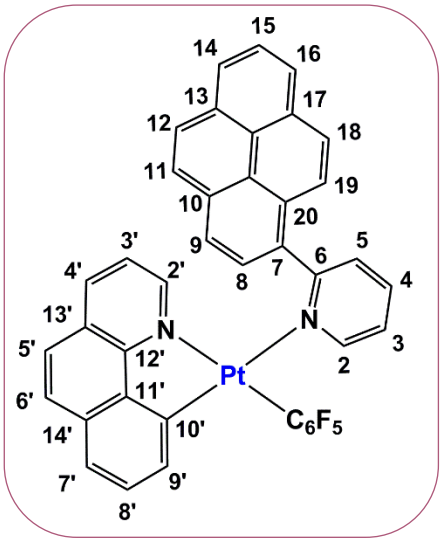

[Pt(bzq)(C_6F_5)(acetone)] (0.150 g, 0.250 mmol) was added to a yellow solution of 1-(2-pyridyl)pyrene (0.070 g, 0.250 mmol) in 20 mL of acetone at 0ºC. After 10 min, a yellow solid precipitated and the cold bath was removed. After 1 h of stirring at room temperature, the solvent was evaporated to 10 mL and the yellow solid was filtered affording **16g** (0.162 g, 79%). NMR data reveals the presence of a majority conformer [~85 (**A**):15(**B**)]

IR (cm^{-1}): ν(C-F, C_6F_5) 1059 (s), 954 (s); ν(C_6F_5)$_{X-sens}$ 803 (s)

ESI (+): *m/z* calcd. for $C_{40}H_{22}F_5N_2Pt$ $[M + H]^+$ 820.1349; found 820.1327.

Elemental Analysis (%): Calc. for $C_{40}H_{21}F_5N_2Pt$: C, 58.61; H, 2.58; N, 3.42. Found: C, 58.43; H, 2.87; N, 3.87.

^{1}H NMR (400.1 MHz, $CDCl_3$, 20º C, *δ*): **Major conformer A** 9.53 (d, 1H, *J* = 5.5, $^3J_{H-Pt}$ = 13, H^2, Hpypy), 8.43 (d, 1H, *J* = 8, Ar), 8.41-8.38 (m, 1H, Ar), 8.26-8.16 (m, 3H, Ar), 8.12-8.04 (m, 4H, H^4, Hpy, Ar), 7.97 (d, 1H, *J* = 8.9, Ar), 7.81 (d, 1H, *J* = 9, Ar), 7.77-7.74 (m, 2H, H^5, Hpypy, Ar), 7.69 (t, 1H, *J* = 7.3, H^3, Hpypy), 7.60-7.56 (m, 2H, Ar), 7.42 (d, 1H, *J* = 10, $H^{7'}$, bzq), 7.14-7.10 (m, 2H, $H^{8'}$, bzq, Ar), 6.72 (d, 1H, *J* = 7.3, $^3J_{H-Pt}$ = 59, $H^{9'}$, bzq). **Minor conformer B** 9.61 (d, 1H, *J* = 5.7, $^3J_{H-Pt}$ = 17, H^2, Hpypy), 6.84 (d, 1H, *J* = 7.1, $^3J_{H-Pt}$ = 60, $H^{9'}$, bzq). The rest of the signals are overlapped with the signals of the major conformer **A**.

^{19}F{^{1}H} NMR (376.5 MHz, $CDCl_3$, 20º C, *δ*): **Major conformer A** -116.3 (dm, J_{Pt-oF} = 517, 1*o*-F, C_6F_5), -122.3 (dm, J_{Pt-oF} = 482, 1*o*-F, C_6F_5), -164.9 (t, 1*p*-F, C_6F_5), -165.6 (m, 1*m*-F, C_6F_5), -166.7 (m, 1*m*-F, C_6F_5); **Minor conformer B** -114.7 (dm, J_{Pt-oF} = 483, 1*o*-F, C_6F_5), -119.6 (dm, J_{Pt-oF} = 497, 1*o*-F, C_6F_5), -163.3 (t, 1*p*-F, C_6F_5), -164.0 (m, 1*m*-F, C_6F_5), -164.8 (m, 1*m*-F, C_6F_5).

Preparation of ***fac*-[Pt(bzq)(thpy)(C_6F_5)Cl] (17a)**.

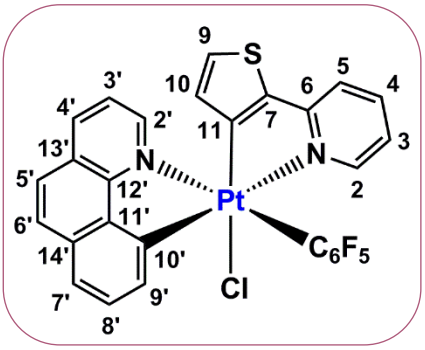

To a yellow solution of [Pt(bzq)(Hthpy-κN)(C_6F_5)] (**16a**) (0.144 g, 0.205 mmol) in CH_2Cl_2/acetone (2:1, 30 mL) at -30ºC, $PhICl_2$ (0.062 g, 0.225 mmol) and Na_2CO_3 (0.435 g, 4.1 mmol) were added. The mixture was stirred at -30ºC for 10 min and then warmed to room temperature. After 3 h, the solvents were evaporated to dryness, and the residue was treated with Et_2O (10 ml) and washed with water obtaining **17a** as a white solid (0.09 g, 70%).

IR (cm^{-1}): ν(C-F, C_6F_5) 1073 (m), 967 (m); ν(C_6F_5)$_{X\text{-sens}}$ 794 (m); ν(Pt-Cl) 305 (m)

ESI (+): *m/z* calcd. for $C_{28}H_{14}F_5N_2PtS$ $[M - Cl]^+$ 700.0442; found 700.0446.

Elemental Analysis (%): Calcd for $C_{28}H_{14}ClF_5N_2SPt$: C, 45.69; H, 1.92; N, 3.81; S, 4.36. Found: C, 45.64; H, 2.12; N, 4.06; S, 4.41.

^{1}H NMR (400.1 MHz, $CDCl_3$, 20º C, δ): 9.88 (t, 1H, $J_{H\text{-}H} \approx J_{H\text{-}oF} = 5.5$, $^3J_{Pt\text{-}H} = 10$, H^2, thpy), 8.23 (d, 1H, $J = 8$, $H^{4'}$, bzq), 8.00 (td, 1H, $J = 7.9$, $J = 1.3$, H^4, thpy), 7.92 (d, 1H, $J = 8.6$, $H^{5'/6'}$, bzq), 7.81 (m, 1H, $H^{7'}$, bzq), 7.71-7.66 (m, 2H, $H^{8',9'}$, bzq), 7.63-7.60 (m, 2H, $H^{5'/6'}$, bzq, H^5, thpy), 7.52 (dd, 1H, $J = 5.3$, $J = 1$, $^3J_{Pt\text{-}H} = 10$, $H^{2'}$, bzq), 7.47 (t, 1H, $J = 6.9$, H^3, thpy), 7.32 (dd, 1H, $J = 7.9$, $J = 5.3$, $H^{3'}$, bzq), 6.99 (d, 1H, $J = 5.0$, $^3J_{Pt\text{-}H} = 9.8$, H^9, thpy), 6.17 (t, 1H, $J_{H\text{-}H} \approx J_{H\text{-}oF} = 5.8$, $^3J_{Pt\text{-}H} = 18$, H^{10}, thpy).

^{13}C{^{1}H} NMR (100.6 MHz, $CDCl_3$, 20º C, δ): 158.2 (s, C^6, thpy), 152.4 (s, $^2J_{Pt\text{-}C} = 36$, $C^{12'}$, bzq), 150.2 (d, $J_{C\text{-}F} = 8$, C^2, thpy), 143.3 (s, $^2J_{Pt\text{-}C} = 11$, $C^{2'}$, bzq), 140.6 (s, C^4, thpy), 138.03-138.00 ($C^{4',11'}$, bzq), 136.2 (s, $C^{7/11}$, thpy), 135.9 (s, $C^{7/11}$, thpy), 134.6 (s, $^3J_{Pt\text{-}C} = 27$, $C^{14'}$, bzq), 133.2 (d, $J_{C\text{-}F} = 4$, $C^{9'}$, bzq), 133.1 (d, $J_{C\text{-}F} = 2.5$, $C^{10'}$, bzq), 132.0 (d, $J_{C\text{-}F} = 8$, $^2J_{Pt\text{-}C} = 80$, C^{10}, thpy), 130.7 (s, $^3J_{Pt\text{-}C} = 52$, $C^{8'}$, bzq), 130.3 (s, $C^{5'/6'}$, bzq), 128.0 (s, $^3J_{Pt\text{-}C} = 18$, $C^{13'}$, bzq), 127.4 (s, $^3J_{Pt\text{-}C} = 66$, C^9, thpy), 123.7 (s, $C^{7'}$, bzq), 123.3 (s, $C^{5'/6'}$, bzq), 122.1 (s, $^3J_{Pt\text{-}C} = 16$, $C^{3'}$, bzq), 121.3 (s, $^3J_{Pt\text{-}C} = 9.5$, C^3, thpy), 119.0 (s, $^3J_{Pt\text{-}C} = 10.5$, C^5, thpy).

^{19}F{^{1}H} NMR (376.5 MHz, $CDCl_3$, 20º C, δ): -113.1 (dm, $J_{Pt\text{-}oF} = 127$, *o*-F, C_6F_5), -115.8 (dm, $J_{Pt\text{-}oF} = 90$, *o*-F, C_6F_5), -159.5 (t, *p*-F, C_6F_5), -163.3 (m, 1*m*-F, C_6F_5), -163.5 (m, 1*m*-F, C_6F_5).

Preparation of ***fac*-[Pt(bzq)(pbt)(C_6F_5)Cl] (17b)**.

A yellow solution of [Pt(bzq)(Hdfppy-κN)(C_6F_5)] (**16b**) (0.123 g, 0.163 mmol) in CH_2Cl_2 (20 mL) at 0ºC was treated with $PhICl_2$ (0.058 g, 0.212 mmol). After 4 h of stirring at room temperature, a pale-yellow solution was obtained and the solvent was evaporated to dryness. The residue was treated with Et_2O (5 mL) to give **17b** as white solid (0.095 g, 74%).

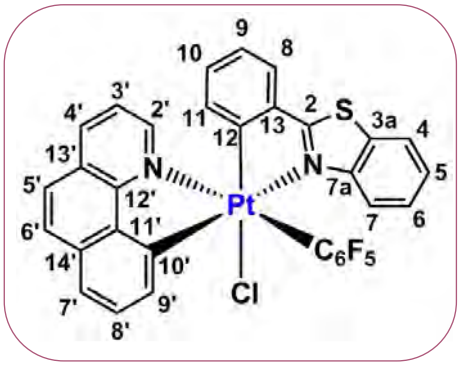

IR (cm^{-1}): ν(C-F, C_6F_5) 1077 (m), 971 (m); ν(C_6F_5)$_{X\text{-sens}}$ 795 (m); ν(Pt-Cl) 285 (w)

ESI (+): *m/z* calcd. for $C_{32}H_{16}F_5N_2PtS$ $[M - Cl]^+$ 750.0599; found 750.0595.

Elemental Analysis (%): Calc. for $C_{32}H_{16}ClF_5N_2SPt$: C, 48.89; H, 2.05; N, 3.56; S, 4.08. Found: C, 48.76; H, 2.29; N, 3.90; S, 3.69.

^{1}H NMR (400.1 MHz, $CDCl_3$, 20º C, δ): 9.95 (t, 1H, $J_{H\text{-}H} \approx J_{H\text{-}oF} = 7$, H^7, pbt), 8.22 (d, 1H, $J = 8$, $H^{4'}$, bzq), 8.01 (d, 1H, $J = 8$, H^4, pbt), 7.95 (d, 1H, $J = 8.6$, $H^{5'/6'}$, bzq), 7.86 (m, 1H, $H^{7'}$, bzq), 7.78-7.69 (m, 4H, $H^{2',8',9'}$, bzq, H^6, pbt), 7.66-7.59 (m, 2H, $H^{5'/6'}$, bzq, H^5, pbt), 7.51 (d, 1H, $J = 7.2$, H^8, pbt), 7.27 (m, 1H, $H^{3'}$, bzq), 6.99 (t, 1H, $J = 7$, H^9, pbt), 6.75 (t, 1H, $J = 7.3$, H^{10}, pbt), 6.52 (t, 1H, $J_{H\text{-}H} \approx J_{H\text{-}oF} = 7.1$, $^3J_{Pt\text{-}H} = 47$, H^{11}, pbt).

^{13}C{^{1}H} NMR (100.6 MHz, $CDCl_3$, 20º C, δ): 178.2 (s, C^2, pbt), 152.0 (s, $C^{12'}$, bzq), 151.4 (m, C^{7a}, pbt), 144.3 (s, $^2J_{Pt\text{-}C} = 10$, $C^{2'}$, bzq), 138.0 (s, $C^{4'}$, bzq), 137.5, 137.2 (s, $C^{11',14'}$, bzq), 136.4 (m, C^{13}, pbt), 136.1 (m, C^{12}, pbt), 134.9-134.8 ($C^{10'}$, bzq, C^{11}, pbt), 132.0-131.7 ($C^{8'/9'}$, bzq, $C^{10,3a}$, pbt), 131.1 (s, $C^{8'/9'}$, bzq), 130.2 (s, $C^{5'/6'}$, bzq), 128.4 (s, C^6, pbt), 128.3 (s, $C^{13'}$, bzq), 126.7 (s, C^5, pbt), 126.5 (s, C^8, pbt), 125.8 (C^9, pbt), 124.9 (d, $J_{C\text{-}F} = 7$, C^7, pbt), 123.9 (s, $C^{7'}$, bzq), 123.5 (s, $C^{5'/6'}$, bzq), 122.4 (s, $^3J_{Pt\text{-}C} = 16.7$, $C^{3'}$, bzq), 121.9 (s, C^4, pbt).

^{19}F{^{1}H} NMR (376.5 MHz, $CDCl_3$, 20º C, δ): -111.3 (dm, $J_{Pt\text{-}oF} = 98$, *o*-F, C_6F_5), -115.2 (dm, $J_{Pt\text{-}oF} = 99$, *o*-F, C_6F_5), -159.5 (t, *p*-F, C_6F_5), -163.3 (m, 1*m*-F, C_6F_5), -163.5 (m, 1*m*-F, C_6F_5).

Preparation of ***fac*-[Pt(bzq)(pq)(C_6F_5)Cl] (17c)**

This complex was obtained as a white solid (0.150 g, 75%) following a similar procedure to **17b**, using as starting materials [Pt(bzq)(Hpq-κ*N*)(C_6F_5)] (**16c**) (0.192 g, 0.257 mmol) and $PhICl_2$ (0.091 g, 0.334 mmol).

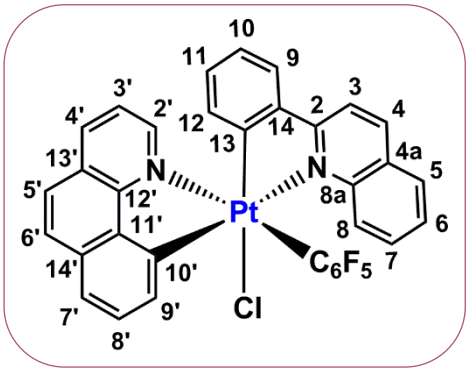

IR (cm^{-1}): ν(C-F, C_6F_5) 1075 (s), 971 (s); ν(C_6F_5)$_{X\text{-}sens}$ 794 (s); ν(Pt-Cl) 271 (m)

ESI (+): *m/z* calcd. for $C_{34}H_{18}F_5N_2Pt$ $[M - Cl]^+$ 744.1035; found 744.1030.

Elemental Analysis (%): Calc. for $C_{34}H_{18}ClF_5N_2Pt$: C, 52.35; H, 2.33; N, 3.59. Found: C, 52.51; H, 2.60; N, 3.88.

^{1}H NMR (400.1 MHz, CD_3COCD_3, 20º C, δ): 10.72 (dd, 1H, $J_{H\text{-}H}$ = 8.9, $J_{H\text{-}oF}$ = 2.5, H^8, pq), 8.77 (d, 1H, *J* = 8.8, H^4, pq), 8.59 (d, 1H, *J* = 8.0, $H^{4'}$, bzq), 8.40 (d, 1H, *J* = 8.5, H^3, pq), 8.30 (d, 1H, *J* = 5.4, $H^{2'}$, bzq), 8.16 (d, 1H, *J* = 8.0, H^5, pq), 8.11 (d, 1H, *J* = 9.0, $H^{5'/6'}$, bzq), 7.96 (d, 1H, *J* = 7.8, $H^{7'}$, bzq), 7.93-7.91 (m, 2H, $H^{5'/6'}$, bzq, H^9, pq), 7.86 (t, 1H, *J* = 7.6, H^7, pq), 7.78 (t, 1H, *J* = 7.6, H^6, pq), 7.72 (t, 1H, *J* = 7.6, $H^{8'}$, bzq), 7.60 (dd, 1H, $J_{H\text{-}H}$ = 7.6, $J_{H\text{-}oF}$ = 5.3, $^3J_{Pt\text{-}C}$ = 41, $H^{9'}$, bzq), 7.51 (dd, 1H, *J* = 8, *J* = 5.5, $H^{3'}$, bzq), 7.05 (t, 1H, *J* = 7.4, H^{10}, pq), 6.74 (t, 1H, *J* = 7.4, H^{11}, pq), 6.47 (dd, 1H, $J_{H\text{-}H}$ = 7.8, $J_{H\text{-}oF}$ = 3.4, $^3J_{Pt\text{-}H}$ = 47, H^{12}, pq).

^{13}C{^{1}H} NMR (100.6 MHz, CD_3COCD_3, 20º C, δ): 164.5 (s, $^2J_{Pt\text{-}C}$ = 48.8, C^2, pq), 151.8 (s, $^2J_{Pt\text{-}C}$ = 53, $C^{12'}$, bzq), 148.9 (d, $J_{F\text{-}C}$ = 2.8, C^{8a}, pq), 146.3 (s, $^2J_{Pt\text{-}C}$ = 12, $C^{2'}$, bzq), 142.6 (s, C^{14}, pq), 141.7 (s, C^4, pq), 138.8 (s, $C^{4'}$, bzq), 138.5 (s, $C^{10'}$, bzq), 137.7 (d, $J_{F\text{-}C}$ = 5.5, C^{13}, pq), 137.2 (s, $C^{11'}$, bzq), 134.7 (s, $^3J_{Pt\text{-}C}$ = 29.7, $C^{14'}$, bzq), 133.4 (d, $J_{C\text{-}F}$ = 5.6, $^2J_{Pt\text{-}C}$ = 52.9, C^{12}, pq), 131.2 (s, C^7, pq), 131.1 (d, $J_{F\text{-}C}$ = 4.5, $C^{9'}$, bzq), 130.5 (s, $^3J_{Pt\text{-}C}$ = 56.4, $C^{8'}$, bzq), 130.3 (s, C^{11}, pq), 129.7 (s, $C^{5'/6'}$, bzq), 129.6 (m, C^8, pq), 128.8 (s, C^{4a}, pq), 128.5 (s, $^3J_{Pt\text{-}C}$ = 18.4, $C^{13'}$, bzq), 128.2 (s, C^5, pq), 127.4 (s, C^6, pq), 127.0 (s, $^3J_{Pt\text{-}C}$ = 30, C^9, pq), 125.5 (s, $^4J_{Pt\text{-}C}$ = 6.7, C^{10}, pq), 124.1 (s, $C^{5'/6'}$, bzq), 123.4 (s, $^4J_{Pt\text{-}C}$ = 7, $C^{7'}$, bzq), 123.0 (s, $^3J_{Pt\text{-}C}$ = 17, $C^{3'}$, bzq), 117.9 (s, $^3J_{Pt\text{-}C}$ = 14, C^3, pq).

$^{19}F\{^1H\}$ NMR (376.5 MHz, CD_3COCD_3, 20º C, *δ*): -111.6 (dm, $J_{Pt\text{-}oF}$ = 95, *o*-F, C_6F_5), -116.4 (dm, $J_{Pt\text{-}oF}$ = 107, *o*-F, C_6F_5), -162.4 (t, *p*-F, C_6F_5), -165.8 (m, 1*m*-F, C_6F_5), -166.5 (m, 1*m*-F, C_6F_5).

Preparation of ***fac*-[Pt(bzq)(dfppy)(C_6F_5)Cl] (17d)**.

This complex was obtained as a pale-yellow solid (0.073 g, 70%) following a similar procedure to **17b**, using as starting materials [Pt(bzq)(Hdfppy-*κN*)(C_6F_5)] (**16d**) (0.100 g, 0.137 mmol) and $PhICl_2$ (0.048 g, 0.203 mmol).

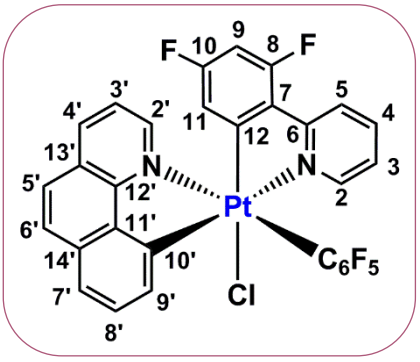

IR (cm^{-1}): ν(C-F, C_6F_5) 1077 (m), 972 (m); ν(C_6F_5)$_{X\text{-}sens}$ 793 (m); ν(Pt-Cl) 301 (m)

ESI (+): *m/z* calcd. for $C_{30}H_{14}F_7N_2Pt$ [M - Cl]$^+$ 730.0690; found 730.0681.

Elemental Analysis (%): Calcd for $C_{30}H_{14}ClF_7N_2Pt$: C, 47.04; H, 1.84; N, 3.66. Found: C, 47.50; H, 2.08; N, 3.81.

^{1}H NMR (400.1 MHz, $CDCl_3$, 20º C, *δ*): 10.12 (t, 1H, $J_{H\text{-}H} \approx J_{H\text{-}oF}$ = 6, $^3J_{Pt\text{-}H}$ = 11, H^2, dfppy), 8.37 (d, 1H, *J* = 8, H^5, dfppy), 8.27 (d, 1H, *J* = 8, H$^{4'}$, bzq), 8.13 (t, 1H, *J* = 7.7, H^4, dfppy), 7.95 (d, 1H, *J* = 8.5, H$^{5'/6'}$, bzq), 7.86 (dd, 1H, *J* = 6.6, *J* = 1.9, H$^{7'}$, bzq), 7.73-7.70 (m, 2H, H$^{8',9'}$, bzq), 7.67-7.63 (m, 2H, H$^{5'/6'}$, bzq, H^3, dfppy), 7.47 (d, 1H, *J* = 5.3, $^3J_{Pt\text{-}H}$ = 17, H$^{2'}$, bzq), 7.33 (dd, 1H, *J* = 7.8, J = 5.5, H$^{3'}$, bzq), 6.50 (ddd, 1H, $^3J_{H\text{-}F}$ = 12.6, $^3J_{H\text{-}F}$ = 8.4, *J* = 2 , H^9, dfppy), 6.14 (m, 1H, $^3J_{Pt\text{-}H}$ = 55, H^{11}, dfppy).

^{13}C{^{1}H} NMR (100.6 MHz, $CDCl_3$, 20º C, *δ*): 162.3 (dd, $^1J_{C\text{-}F}$ = 190, $^3J_{C\text{-}F}$ = 12, C$^{8/10}$, dfppy), 160.0 (dd, $^1J_{C\text{-}F}$ = 192, $^3J_{C\text{-}F}$ = 12, C$^{8/10}$, dfppy), 159.3 (d, $^3J_{C\text{-}F}$ = 6, C^6, dfppy), 152.4 (s, $^2J_{Pt\text{-}C}$ = 48, C$^{12'}$, bzq), 150.4 (d, $J_{C\text{-}F}$ = 7.7, C^2, dfppy), 143.1 (s, $^2J_{Pt\text{-}C}$ = 12, C$^{2'}$, bzq), 141.0 (s, C^4, dfppy), 138.3 (s, C$^{4'}$, bzq), 137.7 (s, $^3J_{Pt\text{-}C}$ = 8.4, C$^{14'}$, bzq), 136.8 (d, $J_{C\text{-}F}$ = 1.4, C$^{10'}$, bzq), 135.0 (s, $^2J_{Pt\text{-}C}$ = 26.5, C$^{11'}$, bzq), 132.6 (d, $J_{C\text{-}F}$ = 4, $^2J_{Pt\text{-}C}$ = 46, C$^{9'}$, bzq), 131.0 (s, $^3J_{Pt\text{-}C}$ = 51, C$^{8'}$, bzq), 130.6 (s, C$^{5'/6'}$, bzq), 128.4 (s, $^3J_{Pt\text{-}C}$ = 18, C$^{13'}$, bzq), 125.2 (m, C^7, dfppy), 124.1 (s, C$^{7'}$, bzq), 123.9-123.3 (C^{12,5,3}, dfppy, C$^{5'/6'}$, bzq), 122.1 (s, $^3J_{Pt\text{-}C}$ = 16, C$^{3'}$, bzq), 117.6 (dm, $J_{C\text{-}F}$ = 21, $^2J_{Pt\text{-}C}$ = 43, C^{11}, dfppy), 101.8 (t, $^2J_{C\text{-}F}$ = 27, C^9, dfppy).

^{19}F{^{1}H} NMR (376.5 MHz, $CDCl_3$, 20º C, *δ*): -105.7 (d, 1F, $^4J_{F\text{-}F}$ = 10, $^4J_{Pt\text{-}F}$ = 46, F$^{8/10}$, dfppy), -108.3 (d, 1F, $^4J_{F\text{-}F}$ = 10, $J_{Pt\text{-}F}$ = 35, F$^{8/10}$, dfppy), -114.8 (dm, $J_{Pt\text{-}oF}$ = 103, *o*-F, C_6F_5), -115.2 (dm, $J_{Pt\text{-}oF}$ = 85, *o*-F, C_6F_5), -159.1 (t, *p*-F, C_6F_5), -163.0 (m, 2*m*-F, C_6F_5).

Preparation of ***fac*-[Pt(bzq)(pypy)(C_6F_5)Cl] (17g)**.

To a yellow solution of [Pt(bzq)(Hpypy-κN)(C_6F_5)] (**16g**) (0.100 g, 0.122 mmol) in CH_2Cl_2/acetone (2:1, 30 mL) at -30ºC, $PhICl_2$ (0.037 g, 0.134 mmol) and Na_2CO_3 (0.129 g, 1.2 mmol) were added. The mixture was stirred at -30ºC for 10 min and then warmed to room temperature. After 1 h, the solvents were evaporated to dryness, and the residue was treated with Et_2O (10 mL) and washed with water obtaining **17g** as a yellow solid (0.084g, 81%).

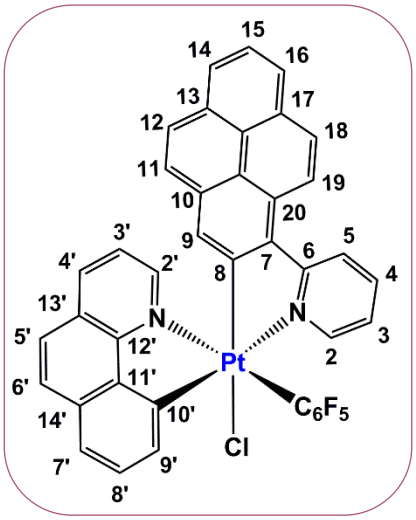

IR (cm^{-1}): ν(C-F, C_6F_5) 1070 (m), 972 (m); ν(C_6F_5)$_{X\text{-}sens}$ 791 (m); ν(Pt-Cl) 270 (w).

ESI (+): *m/z* calcd. for $C_{40}H_{20}F_5N_2Pt$ $[M - Cl]^+$ 818.1192; found 818.1183.

Elemental Analysis (%): Calcd for $C_{40}H_{20}ClF_5N_2Pt$: C, 56.25; H, 2.36; N, 3.28. Found: C, 56.09; H, 2.58; N, 3.52.

^{1}H NMR (400.1 MHz, $CDCl_3$, 20º C, δ): 10.37 (t, 1H, $J_{H\text{-}H} \approx J_{H\text{-}oF} = 5$, H^2, pypy), 8.72 (d, 2H, H^5, pypy, Ar), 8.23 (t, 1H, $J = 8$, H^4, pypy), 8.17-8.14 (m, 3H, Ar), 8.08 (d, 1H, $J = 7.4$, Ar), 8.01 (d, 1H, $J = 8.7$, Ar), 7.95-7.91 (m, 2H, Ar), 7.86-7.77 (m, 3H, Ar), 7.69 (t, 1H, $J = 6.5$, H^3, pypy), 7.64 (d, 1H, $J = 8.7$, Ar), 7.41 (d, 1H, $J = 9$, Ar), 7.32 (d, 1H, H^9, pypy, Ar), 7.22-7.16 (m, 2H, Ar).

^{19}F{^{1}H} NMR (376.5 MHz, $CDCl_3$, 20º C, δ): -114.9 (dm, $J_{Pt\text{-}oF} = 88$, *o*-F, C_6F_5), -115.3 (dm, $J_{Pt\text{-}oF} = 101$, *o*-F, C_6F_5), -159.8 (t, *p*-F, C_6F_5), -163.3 (m, 1*m*-F, C_6F_5), -163.5 (m, 1*m*-F, C_6F_5).

[Pt(bzq)(C_6F_5)Cl(μ-OH)$_2$] (18)

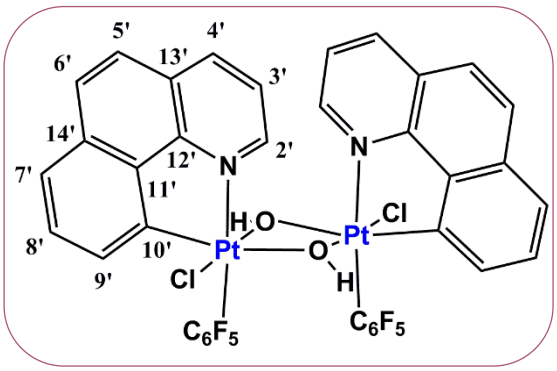

To a mixture of [Pt(bzq)(C_6F_5)(acetone)] (0.143 g, 0.238 mmol) and Na_2CO_3 (0.504 g, 4.76 mmol) in 40 mL of CH_2Cl_2/acetone (1:1) at -50ºC, $PhICl_2$ (0.071 g, 0.262 mmol) was added. After 15 min of stirring, the mixture was warmed to room temperature. After 2 h, the solvents were removed and 60 mL of CH_2Cl_2 were added. Then, the mixture were filtered through celite and the filtered was evaporated to dryness. The residue was treated with 2 mL of acetone and 10 mL of hexane and the solid was filtered and washed with water (20 mL), hexane (10 mL) and Et_2O (10 mL) obtaining **3** (0.08 g, 57 %) as a pale-yellow solid.

IR (cm^{-1}): ν(μOH) 3596 (s), 3585 (s); ν(C-F, C_6F_5) 1078 (s), 970 (s); ν(C_6F_5)$_{X\text{-}sens}$ 803(m); ν(Pt-Cl) 343 (m).

ESI (+): *m/z* calcd. for $C_{38}H_{17}F_{10}Cl_2N_2OPt_2$ $[M - OH]^+$ 1166.9829; found 1166.9786.

Elemental Analysis (%): Calcd for $C_{38}H_{18}Cl_2F_{10}N_2O_2Pt_2$: C, 38.50; H, 1.53; N, 2.36. C, 38.39; H, 1.77; N, 2.69.

^{1}H NMR (400.1 MHz, CD_3COCD_3, 20º C, *δ*): 8.75 (dd, 1H, J = 8.1, J = 1.1, H$^{4'}$), 8.44 (d, 1H, J = 5.4, $^2J_{Pt\text{-}H}$ = 11, H$^{2'}$), 8.13 (d, 1H, J = 8.8, H$^{5'/6'}$), 8.10 (d, 1H, J = 8.8, H$^{5'/6'}$), 7.89 (d, 1H, J = 7.9, H$^{7'}$), 7.57 (t, 1H, J = 7.8, H$^{8'}$), 7.31 (dd, 1H, J = 7.9, J = 5.3, H$^{3'}$), 7.15 (t, 1H, $J_{H\text{-}H} \approx J_{H\text{-}oF}$ = 6.7, $^3J_{Pt\text{-}C}$ = 33, H$^{9'}$).

^{13}C{^{1}H} NMR (100.6 MHz, CD_3COCD_3, 20º C, *δ*): 151.3 (s, C$^{12'}$), 146.2 (s, C$^{2'}$), 140.6 (s, C$^{4'}$), 137.6 (s, C$^{11'}$), 135.4 (s, C$^{14'}$) 133.4 (d, $J_{C\text{-}F}$ = 5, C$^{9'}$), 130.3, 130.2 (C$^{8',5'/6'}$), 129.3 (s, C$^{13'}$), 126.3 (s, C$^{7'}$), 125.5 (s, C$^{5'/6'}$), 124.3 (s, C$^{3'}$), 121.9 (m, C$^{10'}$).

^{19}F{^{1}H} NMR (282.4 MHz, CD_3COCD_3, 20º C, *δ*): -117.5 (dm, $J_{Pt\text{-}oF}$ = 100, *o*-F, C_6F_5), -120.1 (dm, $J_{Pt\text{-}oF}$ = 95, *o*-F, C_6F_5), -159.7 (t, *p*-F, C_6F_5), -163.2 (m, 1*m*-F, C_6F_5), -164.5 (m, 1*m*-F, C_6F_5).

[Pt(bzq)(C_6F_5)(κ^1-dppm)] (19)

To a yellow suspension of [Pt(bzq)(C_6F_5)(dmso)] (0.150 g, 0.243 mmol) in acetone (25 mL), dppm (0.093 g, 0.2425 mmol) was added. After 30 min of stirring, the solution obtained was evaporated to dryness and treated with hexane (5 mL) and cold 2-propanol (2 mL) to afford **19** as a yellow solid. (0.131 g, 58 %).

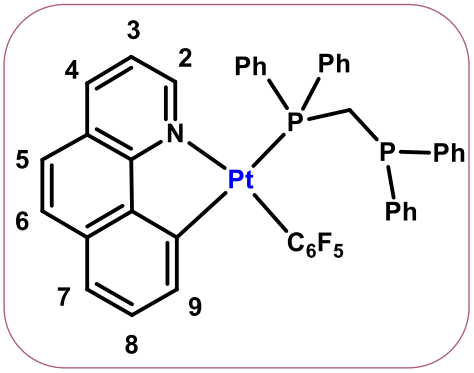

Elemental Analysis (%): Calcd for $C_{44}H_{30}F_5NP_2Pt$: C, 57.15; H, 3.27; N, 1.51%. Found: C, 56.89; H, 3.53; N, 1.78%.

ESI (+): *m/z* (%) 757 $[M-C_6F_5]^+$ (100).

^{1}H NMR (400.1 MHz, CD_3COCD_3, 20º C, δ): 8.39 (d, 1H, J = 8, H^4, bzq), 8.25 (d, 1H, J = 5, $^3J_{Pt-H}$ = 24, H^2, bzq), 7.88 (m, 5H), 7.66 (t, 2H, J = 8), 7.53 (m, 4H), 7.44-7.39 (m, 3H), 7.36-7.33 (m, 4H), 7.14 (dd, 1H, J = 8, J = 5, H^3, bzq), 6.96 (t, 1H, $^3J_{H-H} \approx {}^4J_{P-H}$ = 6, H^9, bzq), 6.92-6.88 (m, 6H), 3.65 (d, 2H, J = 9, $^3J_{Pt-H}$ = 26, CH_2P_2).

^{19}F{^{1}H} NMR (376.5 MHz, CD_3COCD_3, 20º C, δ): -115.7 (dm, J_{Pt-oF} = 496, 2*o*-F, C_6F_5), from -166.5 to -166.9 (m, 1*p*-F, 2*m*-F, C_6F_5).

^{31}P{^{1}H} NMR (161.9 MHz, CD_3COCD_3, 20º C, δ): 12.62 (d, $^2J_{PP}$ = 86, $^1J_{P-Pt}$ = 1963, P^a), -25.3 (dm, $^2J_{PP}$ = 85, $^3J_{PtP}$ = not resolved, P^b).

[Pt(bzq)(C_6F_5)(κ^1-dppmO)] (19-O)

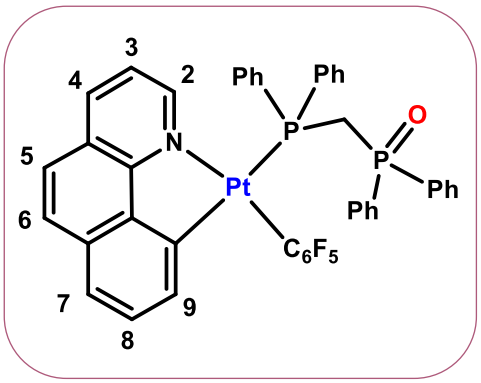

^{1}H NMR (400.1 MHz, $CDCl_3$, 20º C, δ): 8.20 (d, 1H, J = 5, $^3J_{Pt\text{-}H}$ = 23, H^2, bzq), 8.12 (dd, 1H, J = 8, $^4J_{H\text{-}H}$ = 1, H^4, bzq), 8.00-7.95 (m, 4H), 7.75 (d, J = 8, 1H), 7.61-7.54 (m, 5H), 7.47 (d, 1H, J = 8), 7.44 (td, 1H, J = 7, $^5J_{H\text{-}P}$ = 2, H^8, bzq), 7.36-7.32 (m, 2H), 7.27-7.23 (m, 4H), 7.14-7.12 (m, 6H), 6.99-6.93 (m, 2H, $H^{3,9}$, bzq), 3.34 (dd, 2H, J = 12, J = 8, $^3J_{Pt\text{-}H}$ = 33, CH_2P_2).

^{19}F{^{1}H} NMR (376.5 MHz, $CDCl_3$, 20º C, δ): -116.2 (dm, $J_{Pt\text{-}oF}$ = 490, 2*o*-F, C_6F_5), -163.3 (t, 1*p*-F, C_6F_5), -163.8 (m, 2*m*-F, C_6F_5).

^{31}P{^{1}H} NMR (161.9 MHz, $CDCl_3$, 20º C, δ): 25.30 (d, $^2J_{P\text{-}P}$ = 13, $^3J_{P\text{-}Pt}$ = 46, P^b), 12.75 (d, $^2J_{PP}$ = 13, $^1J_{P\text{-}Pt}$ = 1950, P^a).

[Pt(bzq)(C_6F_5)(μ-dppm)AuCl] (20)

[AuCl(SMe_2)] (0.027 gr, 0.093 mmol) was added to a solution of **19** (0.086 gr, 0.093 mmol) in CH_2Cl_2 (20 mL) at -50 ºC**.** After 10 min of stirring, the yellow solution was evaporated until 5 mL and a yellow solid was precipitated with hexane (~10 mL) to obtain **20** as a yellow solid (0.047 g, 44 %)

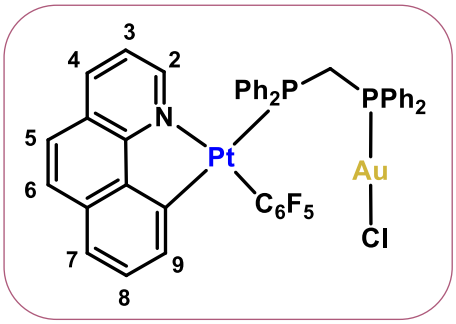

Elemental Analysis (%): Calcd for $C_{44}H_{30}F_5NP_2ClPtAu$ (1157.15): C, 45.67; H, 2.61; N, 1.21%. Found: C, 45.28; H, 2.87; N, 1.49%.

ESI (+): *m/z* (%) 1180 $[M + Na]^+$ (12).

^{1}H NMR (400.1 MHz, $CDCl_3$, 20º C, *δ*): 8.74 (d, 1H, J = 5, $^3J_{Pt\text{-}H}$ = 25, H^2, bzq), 8.17 (dd, 1H, J = 8, $^4J_{H\text{-}H}$ = 1, H^4, bzq), 7.75-7.71 (m, 5H), 7.64-7.57 (m, 5H), 7.48-7.44 (m, 3H), 7.40 (td, 1H, J = 7, $^5J_{H\text{-}P}$ = 2, H^8, bzq), 7.37-7.33 (m, 4H), 7.24 (d, 1H, J = 5, H^3, bzq), 7.12-7.04 (m, 6H), 6.88 (t, 1H, $^3J_{H\text{-}H} \approx {}^4J_{P\text{-}H}$ = 6, H^9, bzq), 3.63 (dd, 2H, J = 11, J = 7, $^3J_{Pt\text{-}H}$ = 34, CH_2P_2).

^{19}F{^{1}H} NMR (376.5 MHz, $CDCl_3$, 20º C, *δ*): -116.6 (dm, $J_{Pt\text{-}oF}$ = 475, 2*o*-F, C_6F_5), -163.2 (t, 1*p*-F, C_6F_5), -163.8 (m, 2*m*-F, C_6F_5).

^{31}P{^{1}H} NMR (161.9 MHz, $CDCl_3$, 20º C, *δ*): 19.07 (d, $^2J_{PP}$ = 4, $^3J_{P\text{-}Pt}$ = 23, P^b), 12.2 (s br, $^2J_{PP}$ = not resolved, $^1J_{P\text{-}Pt}$ = 1890, P^a)

D. X-Ray crystallography

X-RAY CHRYSTALLOGRAPHY EXPERIMENTAL DETAILS: CHAPTER 1

Yellow [***trans*-5(dmso-*κO*)**, ***cis*-8**] and orange (***cis*-7**) crystals were obtained by slow diffusion of hexane into saturated solutions of the corresponding compounds in acetone [***trans*-5(dmso-*κO*)**, ***cis*-8**, -30ºC] and CH_2Cl_2 (***cis*-7**, room temperature).

X-ray intensity data has been collected with a NONIUS-*κ*CCD area-detector diffractometer, using graphite-monochromated Mo K_α radiation ($\lambda(MoK_\alpha)$ 0.71071 Å) and the images were processed using the DENZO and SCALEPACK suite of programs.[178] The structures were solved by Patterson and Fourier methods using SHELXS-97[187] and refined by full-matrix least squares on F^2 with SHELXL-97.[187] The absorption corrections were performed using MULTI-SCAN,[188] with the WINGX program suite.[189] All non-hydrogen atoms were assigned anisotropic displacement parameters. The hydrogen atoms were constrained to idealized geometries fixing isotropic displacement parameters of 1.2 times the U_{iso} value of their attached carbons for aromatic and methylene hydrogens and 1.5 times for the methyl groups. The structure of complex ***trans*-5(dmso-*κO*)** crystallizes with half a molecule of hexane [***trans*-5(dmso-*κO*)**·0.5hexane]. However, we have been not able to model the crystallization solvent present in the structure of complex ***cis*-8**. Examination with PLATON[190] and SQUEEZE[190-191] revealed the presence of two voids of 116 $Å^3$ containing a total of 40 e^-, which fits well for the presence in the unit cell of one molecule of acetone and water (***cis*-8**·0.25acetone·0.25H_2O). The structures present some residual peaks greater than 1 e^- A^{-3} in the vicinity of the metal atoms or solvent molecules, but with no chemical meaning.

Table E.1: Crystallographic data for ***trans*-5(dmso-*κO*)**, ***cis*-7** and ***cis*-8**.

	***trans*-5(dmso-*κO*)**·0.5 hexane	***cis*-7**	***cis*-8**·0.25(acetone)·0.25H_20
Empirical formula	$C_{24}H_{21}Br_2F_5NOPtS$	$C_{23}H_{16}F_5I_2NPtS$	$C_{23}H_{16}$ Br_2F_5NPtS
F_w	821.39	882.32	788.34
T (K)	173(1)	193(1)	173(1)
crystal system, space group	Triclinic, P-1	Monoclinic, P21/n	Monoclinic, P21/n
a(Å)	9.2191(8)	8.4155(4)	8.0406(2)
b(Å)	10.9141(6)	14.3312(7)	25.3286(7)
c(Å)	13.7454(11)	19.5012(11)	12.4714(3)
α(deg)	112.557(4)	90	90
β(deg)	95.355(4)	95.981(2)	104.642(1)
γ(deg)	98.071(5)	90	90
volume (A^3)	1248.1(2)	2339.1(2)	2457.4(1)
Z	2	4	4
D_{calcd} (Mg/m^3)	2.186	2.505	2.131
absorption coefficient (mm^{-1})	8.963	8.780	9.096
F(000)	778	1624	1480
θ range for data collection (deg)	3.77 to 27.48	2.92 to 26.37	1.87 to 27.10
no of data // restraints // params	5676 // 0 // 319	4726 // 0 // 298	5398 // 0 // 298
goodness-of-fit on F^2 [a]	1.037	1.050	1.110
final R indexes [I>2σ(I)] [a]	R_1 = 0.0426, wR_2 = 0.0874	R_1 = 0.0480, wR_2 = 0.1101	R_1 = 0.0340, wR_2 = 0.0910
R indexes (all data) [a]	R_1 = 0.0651, wR_2 = 0.0950	R_1 = 0.0655, wR_2 = 0.1178	R_1 = 0.0376, wR_2 = 0.0928
largest diff peak and hole ($e.Å^{-3}$)	1.430 and -1.650	1.812 and -2.772	2.721 and -3.068

[a] $R1 = \Sigma(|F_o| - |F_c|)/\Sigma|F_o|$; $wR2 = [\Sigma w(F_o^2 - F_c^2)^2/\Sigma wF_o^2]^{1/2}$; goodness of fit = $\{\Sigma[w(F_o^2 - F_c^2)^2]/(N_{obs} - N_{param})\}^{1/2}$; $w = [\sigma^2(F_o) + (g_1P)^2 + g_2P]^{-1}$; $P = [\max(F_o^2;0 + 2F_c^2]/3$.

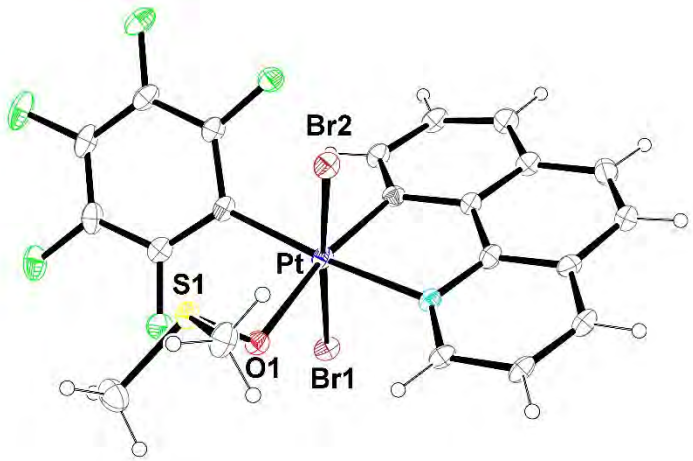

Figure E1. Thermal ellipsoid representation (30 % probability) of the crystal structure of ***trans*-5(dmso-*κO*)**·0.5 hexane.

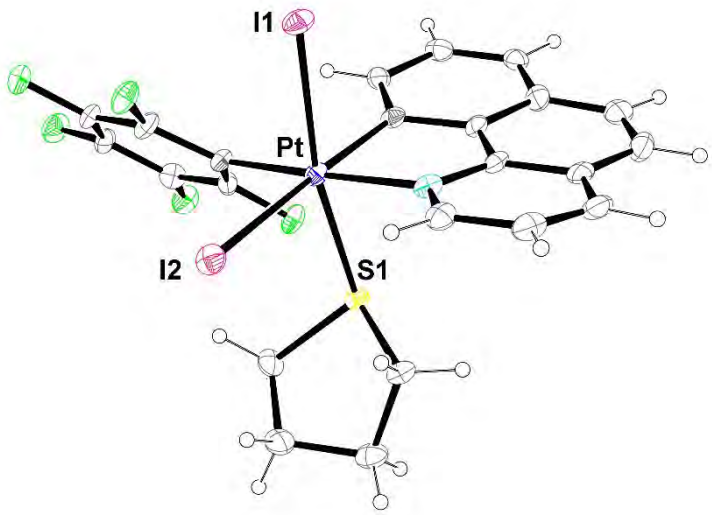

Figure E2. Thermal ellipsoid representation (30 % probability) of the crystal structure of ***cis*-7**.

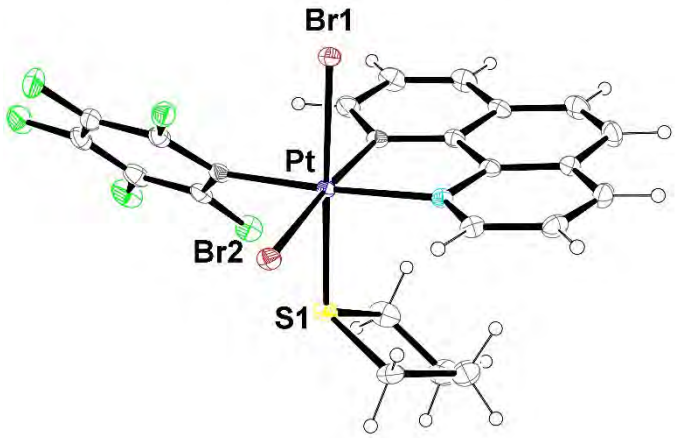

Figure E3. Thermal ellipsoid representation (30 % probability) of the crystal structure of ***cis*-8**.

X-RAY CHRYSTALLOGRAPHY EXPERIMENTAL DETAILS: CHAPTER 2

Chapter 2.1

Yellow (**9a**, **9c** and **11b**), colourless (**9d**, **10d**) and orange (**10b** and **11a**) crystals were obtained by slow diffusion of *n*-hexane into solutions of the complexes in CH_2Cl_2 (**9a**, **9c**, **11a** and **11b**; -30ºC) or $CHCl_3$ (**10b**; room temperature), respectively. Crystals of **9d** were obtained by evaporation of the complex in $CHCl_3$ and solution of **10d** CH_2Cl_2 with Et_2O gave crystals of that derivative. X-ray intensity data were collected with a NONIUS-κCCD area-detector diffractometer, using graphite-monochromatic Mo-K_α radiation, and images processed using the DENZO and SCALEPACK suite of programs,[178] carrying out the absorption correction at this point for complex **9a**. For the rest of the structures, the absorption correction was performed using MULTI-SCAN [188] (**9c**, **9d**, **10b**, **10d** and **11a**) or XABS2 [192] (**11b**), with the WINGX program suite.[189] The structures were solved by Patterson and Fourier methods using DIRDIF2008 (**9a**) and SIR-2004 (**9c**, **10b** and **11a**) or by intrinsic phasing using SHELXT [193] (**9d**, **10d**, **11b**) and refined by full-matrix least squares on F^2 with SHELXL.[193] All non-hydrogen atoms were assigned anisotropic displacement parameters. All the hydrogen atoms were constrained to idealized geometries fixing isotropic displacement parameters 1.2 times the U_{iso} value of their attached carbon for the aromatic carbons and 1.5 times for the methyl groups. For **9a**, positional disorder (70/30) was observed with respect to the position of the sulphur atom in the thienyl rings of both of the pyridine ligands. For **9c**, disordered crystallization molecules of CH_2Cl_2 were observed, but could not be properly modelled. Examination with PLATON[190] and SQUEEZE[190-191] revealed the presence of two voids of 160 $Å^3$ in the unit cell, containing each of them 73 e^-, which fits well with the presence of 3 molecules of CH_2Cl_2 in the unit cell (**9c**·0.75CH_2Cl_2). Finally, the structures show some residual peaks greater than 1 eA^{-3}, but with no chemical meaning.

Table E.2: Crystallographic data for **9a**, **9c·0.75CH$_2$Cl$_2$** and **9d**.

	9a	**9c·0.75CH$_2$Cl$_2$**	**9d**
Empirical formula	$C_{30}H_{14}F_{10}N_2PtS_2$	$C_{42}H_{22}F_{10}N_2Pt$	$C_{34}H_{14}F_{14}N_2Pt$
F_w	851.64	939.70	911.56
T (K)	120(1)	173(1)	173(1)
crystal system, space group	Orthorhombic, P bca	Monoclinic, P 21/n	Triclinic, P -1
a(Å)	12.6350(2)	8.2453(2)	10.51980(10)
b(Å)	18.4730(3)	26.5307(7)	10.7015(2)
c(Å)	23.9410(3)	16.6300(4)	14.6371(3)
α(deg)	90	90	92.6660(10)
β(deg)	90	94.703(2)	109.3410
γ(deg)	90	90	103.6060
volume (A^3)	5587.98(14)	3625.62(16)	1497.21(5)
Z	8	4	2
D_{calcd} (Mg/m^3)	2.025 Mg/m^3	1.722	2.022
absorption coefficient (mm^{-1})	5.264	3.955	4.804
F(000)	3264	1824	872
θ range for data collection (deg)	3.37 to 25.68	1.449 to 25.026	2.128 to 25.680
no of data // restraints // params	5299 / 0 / 358	6376 / 0 / 496	5598 / 0 / 460
goodness-of-fit on F^2 [a]	1.037	1.128	1.047
final R indexes [I>2σ(I)] [a]	R1 = 0.0260, wR2 = 0.0543	R1 = 0.0445, wR2 = 0.1169	R1 = 0.0195, wR2 = 0.0489
R indexes (all data) [a]	R1 = 0.0340, wR2 = 0.0583	R1 = 0.0551, wR2 = 0.1250	R1 = 0.0209, wR2 = 0.0495
largest diff peak and hole (e.Å^{-3})	2.328 and -1.255	2.131 and -2.136	1.137 and -1.136

[a] $R1 = \Sigma(|F_o| - |F_c|)/\Sigma|F_o|$; $wR2 = [\Sigma w(F_o^2 - F_c^2)^2/\Sigma wF_o^2]^{1/2}$; goodness of fit = $\{\Sigma[w(F_o^2 - F_c^2)^2]/(N_{obs} - N_{param})\}^{1/2}$; $w = [\sigma^2(F_o) + (g_1P)^2 + g_2P]^{-1}$; $P = [\max(F_o^2;0 + 2F_c^2]/3$.

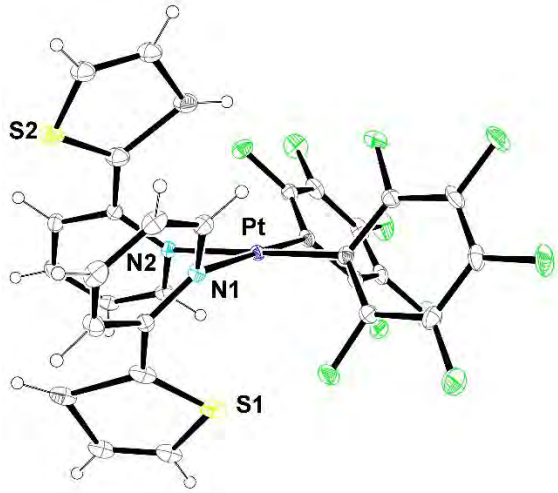

Figure E4. Thermal ellipsoid representation (30 % probability) of the crystal structure of **9a**.

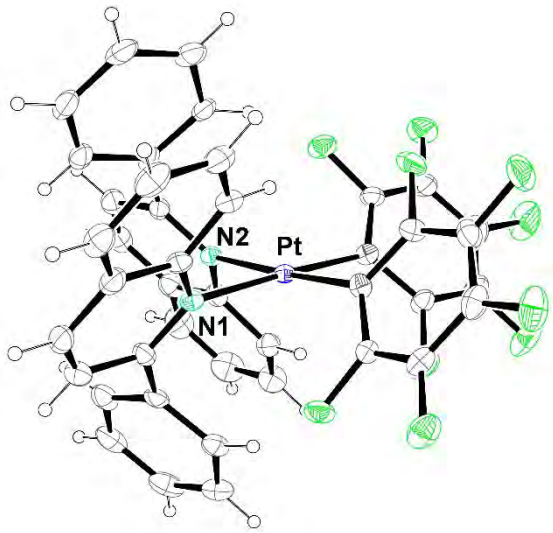

Figure E5. Thermal ellipsoid representation (30 % probability) of the crystal structure of **9c**.

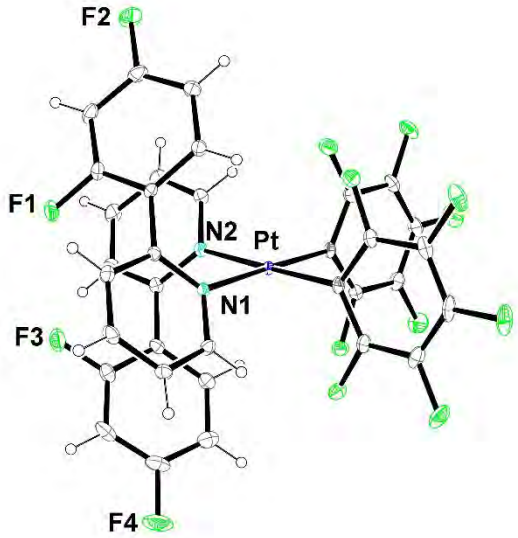

Figure E6. Thermal ellipsoid representation (30 % probability) of the crystal structure of **9d**.

Table E.3: Crystallographic data for **10b** and **10d**.

	10b	**10d**
Empirical formula	$C_{32}H_{17}F_5N_2PtS_2$	$C_{28}H_{13}F_9N_2Pt$
F_w	783.68	743.49
T (K)	173(1)	120(1)
crystal system, space group	Monoclinic, P 21/a	Triclinic, P -1
a(Å)	14.9033(5)	7.7207(3)
b(Å)	12.3384(4)	10.6478(5)
c(Å)	15.0986(4)	15.2717(7)
α(deg)	90.	100.7630(10)
β(deg)	105.414(2)	100.524(3)
γ(deg)	90.	103.732(3)
volume (A^3)	1129.94(9)	1163.74(9)
Z	4	2
D_{calcd} (Mg/m^3)	1.945	2.122
absorption coefficient (mm^{-1})	5.461	6.124
F(000)	1512	708
θ range for data collection (deg)	3.258 to 27.476	2.796 to 27.491
no of data // restraints // params	6068 / 0 / 379	5278 / 0 / 361
goodness-of-fit on F^2 [a]	1.096	0.896
final R indexes [I>2σ(I)] [a]	R1 = 0.0262, wR2 = 0.0551	R1 = 0.0208, wR2 = 0.0574
R indexes (all data) [a]	R1 = 0.0317, wR2 = 0.0571	R1 = 0.0223, wR2 = 0.0585
largest diff peak and hole ($e.Å^{-3}$)	1.417 and -0.779	1.204 and -1.400

[a] $R1 = \Sigma(|F_o| - |F_c|)/\Sigma|F_o|$; $wR2 = [\Sigma w(F_o^2 - F_c^2)^2/\Sigma wF_o^2]^{1/2}$; goodness of fit = $\{\Sigma[w(F_o^2 - F_c^2)^2]/(N_{obs} - N_{param})\}^{1/2}$; $w = [\sigma^2(F_o) + (g_1P)^2 + g_2P]^{-1}$; $P = [\max(F_o^2;0 + 2F_c^2]/3$.

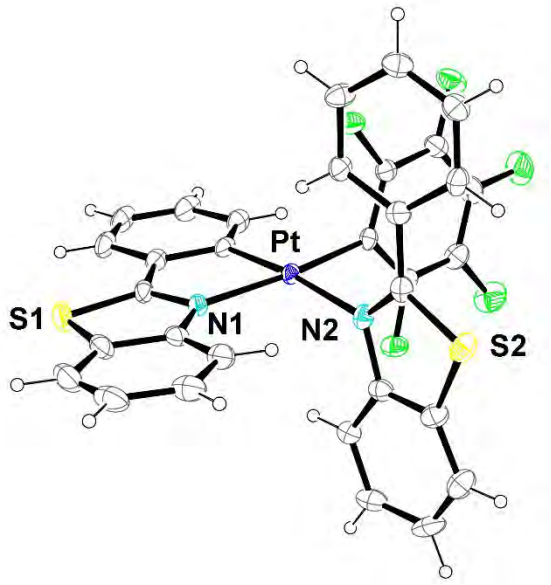

Figure E7. Thermal ellipsoid representation (30 % probability) of the crystal structure of **10b**.

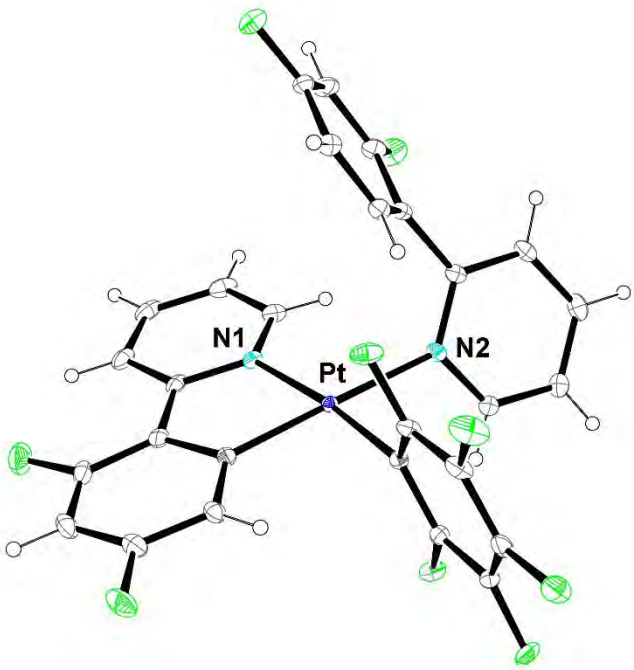

Figure E8. Thermal ellipsoid representation (30 % probability) of the crystal structure of **10d**.

Table E.4: Crystallographic data for **11a** and **11b**.

	11a	**11b**
Empirical formula	$C_{17}H_{12}F_5NOPtS_2$	$C_{21}H_{14}F_5NOPtS_2$
F_w	600.49	650.54
T (K)	173(1)	173 (1)
crystal system, space group	Triclinic, P -1	Triclinic, P -1
a(Å)	6.7971(2)	7.5475(2)
b(Å)	10.3253(5)	11.4335(5)
c(Å)	12.4185(6)	11.8516(5)
α(deg)	84.911(2)	99.861(2)
β(deg)	85.894(3)	98.362(2)
γ(deg)	88.980(3)	91.328(3)
volume (A^3)	865.84(6)	995.69(7)
Z	2	2
D_{calcd} (Mg/m^3)	2.303	2.170
absorption coefficient (mm^{-1})	8.403	7.316
F(000)	568	620
θ range for data collection (deg)	1.650 to 24.711	3.470 to 24.707
no of data // restraints // params	2795 / 0 / 215	3284 / 0 / 280
goodness-of-fit on F^2 [a]	1.197	0.938
final R indexes [I>2σ(I)] [a]	R1 = 0.0547, wR2 = 0.1467	R1 = 0.0345, wR2 = 0.0932
R indexes (all data) [a]	R1 = 0.0556, wR2 = 0.1501	R1 = 0.0349, wR2 = 0.0939
largest diff peak and hole (e.$Å^{-3}$)	2.834 and -3.185	1.768 and -2.827

[a] $R1 = \Sigma(|F_o| - |F_c|)/\Sigma|F_o|$; $wR2 = [\Sigma w(F_o^2 - F_c^2)^2/\Sigma wF_o^2]^{1/2}$; goodness of fit = $\{\Sigma[w(F_o^2 - F_c^2)^2]/(N_{obs} - N_{param})\}^{1/2}$; $w = [\sigma^2(F_o) + (g_1P)^2 + g_2P]^{-1}$; $P = [\max(F_o^2;0 + 2F_c^2]/3$.

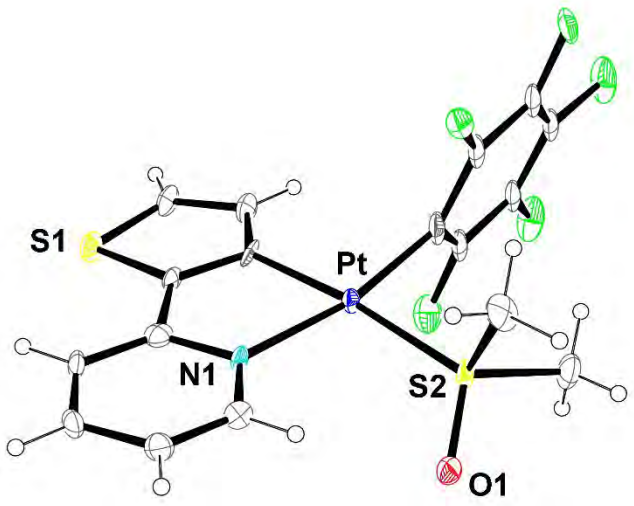

Figure E9. Thermal ellipsoid representation (30 % probability) of the crystal structure of **11a**.

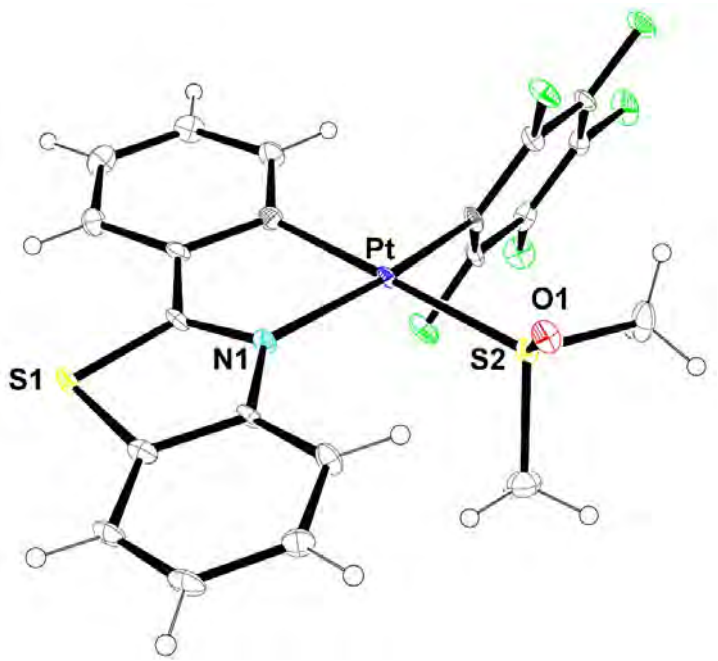

Figure E10. Thermal ellipsoid representation (30 % probability) of the crystal structure of **11b**.

Chapter 2.2

Yellow crystals were obtained by slow diffusion of *n*-hexane into a solution of the complex in THF (**12c**, 298 K; **12e**, -30 ºC) or acetone (**14**, 298 K). Yellow crystals of **12d** were obtained by evaporation of the complex in $CHCl_3$. Solution of **13** in CH_2Cl_2 with MeOH at room temperature gave colourless crystals. X-ray intensity data were collected with a NONIUS-κCCD area-detector diffractometer, using graphite-monochromatic Mo-K_α radiation, and images processed using the DENZO and SCALEPACK suite of programs.[178] Structures were solved by Intrinsic Phasing using SHELXT[193] and refined by full-matrix least squares on F^2 with SHELXL.[193] The absorption correction was performed using MULTISCAN with the WINGX program suite.[189] All non-hydrogen atoms were assigned anisotropic displacement parameters. The hydrogen atoms were constrained to idealized geometries fixing isotropic displacement parameters 1.2 times the U_{iso} value of their attached carbon for the aromatic and methylene hydrogens and 1.5 times for the methyl groups. All complexes crystallized in centrosymmetric groups, so all crystals must be aquiral. Thus, for **12c**, **12d**, **12e**, **13** and **14**, both configurations (ΛΛ and ΔΔ) in a 50:50 ratio were found in unit cell. For complex **12e**, disordered crystallization molecules of THF were observed but could not be adequately modelled and were removed from the model. Examination with [190] and SQUEEZE[190-191] revealed the presence of one void of 785 $Å^3$ in the unit cell was revealed containing 457 e^-, which fits with the presence of 11 molecules of THF in the unit cell giving rise to the stoichiometry (**12e**·5.5THF). For **12c**, two molecules for the complex and one for THF were found in the asymmetric unit, so that the stoichiometry is **12c**·0.5THF. Finally, the structures of **12e** and **14** show some residual peaks greater than 1 e $Å^{-3}$ in the vicinity of the platinum atoms but with no chemical meaning.

Table E.5: Crystallographic data for **12c**·0.5THF, **12d** and **12e**·5.5THF.

	2x(**12c**·0.5THF)	**12d**	**12e**·5.5THF
Empirical formula	$C_{80}H_{56}Cl_2F_{10}N_4OPt_2$	$C_{28}H_{12}ClF_9N_2Pt$	$C_{32}H_{16}ClF_5N_2Pt$
F_w	1684.26	777.94	754.01
T (K)	173(1)	220(2)	173(1)
crystal system, space group	Monoclinic, P 21/n	Monoclinic, P 21/n	Triclinic, P -1
a(Å)	18.0033(4)	10.0675(2)	11.7208(9)
b(Å)	19.6067(5)	18.9691(5)	12.4680(7)
c(Å)	18.3707(3)	12.9358(3)	13.1478(9)
α(deg)	90	90	90.512(4)
β(deg)	110.3950(10)	96.0810(10)	92.285(3)
γ(deg)	90	90	94.474(5)
volume (A^3)	6078.1(2)	2456.47(10)	1913.8(2)
Z	4	4	2
D_{calcd} (Mg/m^3)	1.841	2.103	1.308
absorption coefficient (mm^{-1})	4.770	5.913	3.778
F(000)	3280	1480	724
θ range for data collection (deg)	3.656 to 25.680	2.913 to 27.462	1.638 to 27.650
no of data // restraints // params	11481 / 0 / 856	5562 / 0 / 370	8580 / 0 / 370
goodness-of-fit on F^2 [a]	1.033	1.054	1.051
final R indexes [I>2σ(I)] [a]	R1 = 0.0301, wR2 = 0.0682	R1 = 0.0179, wR2 = 0.0455	R1 = 0.0429, wR2 = 0.1238
R indexes (all data) [a]	R1 = 0.0435, wR2 = 0.0728	R1 = 0.0197, wR2 = 0.0464	R1 = 0.0475, wR2 = 0.1284
largest diff peak and hole ($e.Å^{-3}$)	0.749 and -1.047	0.502 and -1.083	1.652 and -1.620

[a] $R1 = \Sigma(|F_o| - |F_c|)/\Sigma|F_o|$; $wR2 = [\Sigma w(F_o^2 - F_c^2)^2/\Sigma wF_o^2]^{1/2}$; goodness of fit = $\{\Sigma[w(F_o^2 - F_c^2)^2]/(N_{obs} - N_{param})\}^{1/2}$; $w = [\sigma^2(F_o) + (g_1P)^2 + g_2P]^{-1}$; $P = [\max(F_o^2;0 + 2F_c^2]/3$.

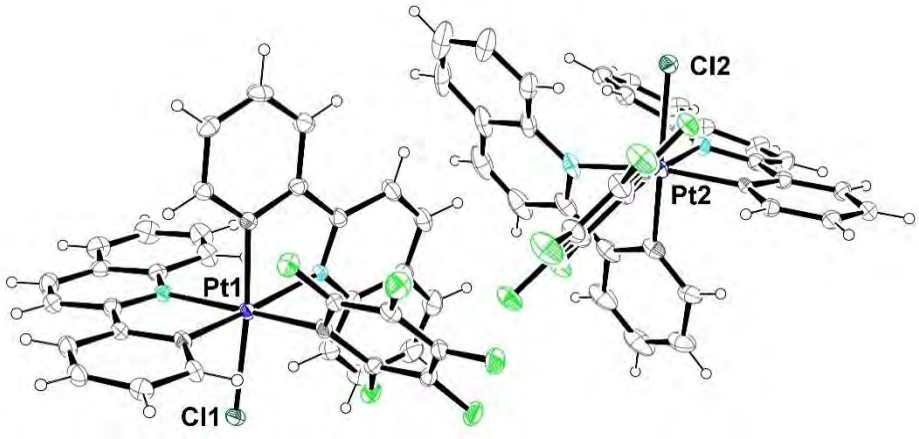

Figure E11. Thermal ellipsoid representation (30 % probability) of the crystal structure of 2x(**12c**·0.5THF) showing A and B molecules.

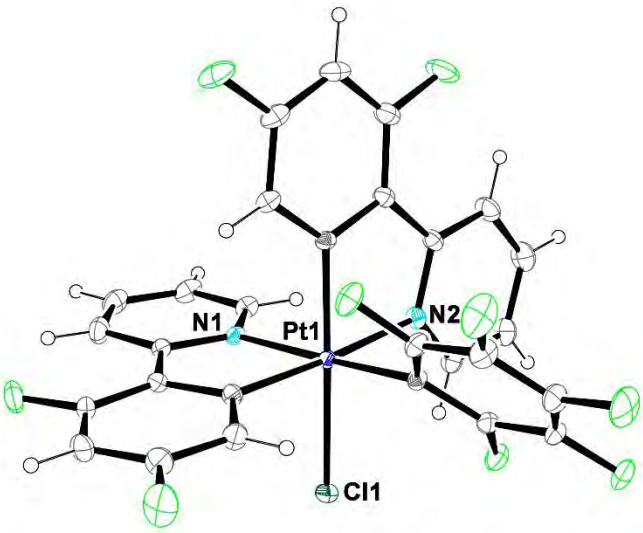

Figure E12. Thermal ellipsoid representation (30 % probability) of the crystal structure of **12d**.

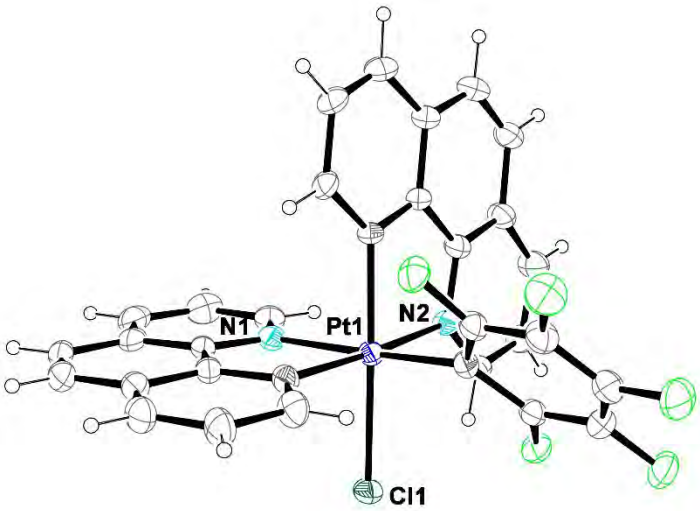

Figure E13. Thermal ellipsoid representation (30 % probability) of the crystal structure of **12e**·5.5THF.

Table E.6: Crystallographic data for **13** and **14**·acetone.

	13	**14**·acetone
Empirical formula	$C_{33}H_{16}F_5N_3PtS_2$	$C_{41}H_{29}F_{11}N_3OPPtS_2$
Fw	808.70	1078.85
T (K)	173(1)	173(1)
crystal system, space group	Monoclinic, P 21/n	Triclinic, P-1
a(Å)	9.89920(10)	10.8839(3)
b(Å)	20.6681(5)	13.1414(4)
c(Å)	13.9256(3)	14.5947(5)
α(deg)	90	79.0260(10)
β(deg)	91.2750(10)	85.881(2)
γ(deg)	90	75.335(2)
volume (A3)	2848.44(10)	1981.93(11)
Z	4	2
Dcalcd (Mg/m3)	1.886	1.808
absorption coefficient (mm-1)	5.135	3.776
F(000)	1560	1056
θ range for data collection (deg)	3.088 to 27.488	2.817 to 25.680
no of data // restraints // params	6485 / 0 / 397	7471 / 0 / 541
goodness-of-fit on F2 a	1.092	1.054
final R indexes [I>2σ(I)] a	R1 = 0.0188, wR2 = 0.0461	R1 = 0.0279, wR2 = 0.0735
R indexes (all data) a	R1 = 0.0204, wR2 = 0.0467	R1 = 0.0296, wR2 = 0.0748
largest diff peak and hole (e.Å –3)	0.878 and -1.148	1.369 and -1.752

[a] $R1 = \Sigma(|F_o| - |F_c|)/\Sigma|F_o|$; $wR2 = [\Sigma w(F_o^2 - F_c^2)^2/\Sigma wF_o^2]^{1/2}$; goodness of fit = $\{\Sigma[w(F_o^2 - F_c^2)^2]/(N_{obs} - N_{param})\}^{1/2}$; $w = [\sigma^2(F_o) + (g_1P)^2 + g_2P]^{-1}$; $P = [\max(F_o^2;0 + 2F_c^2]/3$.

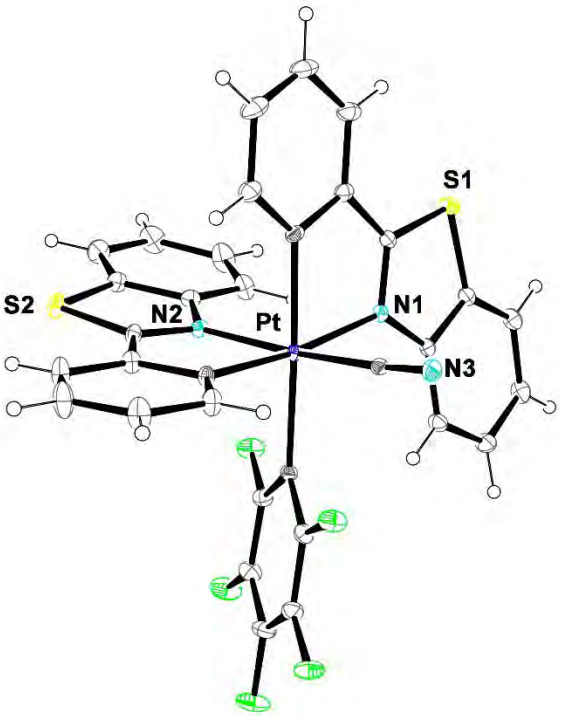

Figure E14. Thermal ellipsoid representation (30 % probability) of the crystal structure of **13**.

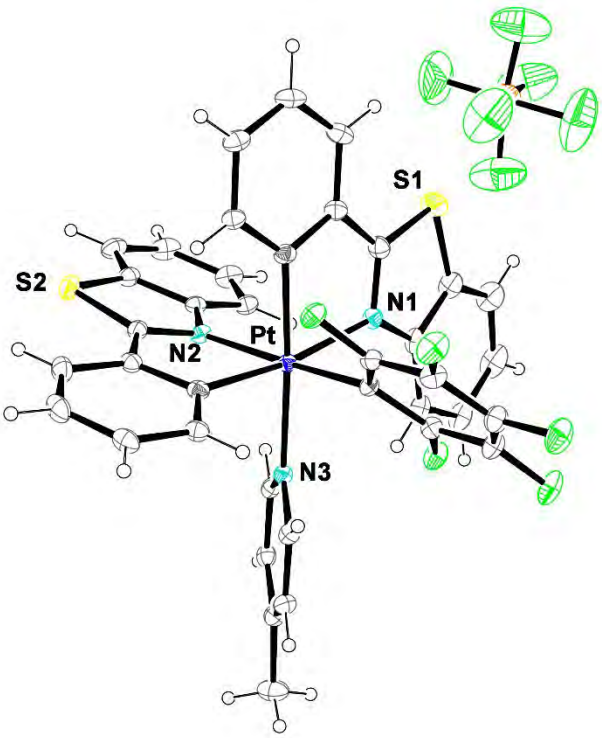

Figure E15. Thermal ellipsoid representation (30 % probability) of the crystal structure of **14**·acetone.

X-RAY CHRYSTALLOGRAPHY EXPERIMENTAL DETAILS: CHAPTER 3

Chapter 3.1

Yellow (**16a**) or colourless (**16f**) crystals were obtained by slow diffusion of n-hexane into a solution of the complex in dichloromethane (**16a**, -30 ºC) or chloroform (**16f**, -30 ºC). The diffraction data were collected using graphite monochromatic Mo-Kα radiation with a Bruker APEX-II diffractometer at a temperature of 130 K using the APEX-II software. The structures were solved by Intrinsic Phasing using SHELXT program[193] and refined by full-matrix least squares on F^2 with SHELXL.[194] The absorption correction was performed using MULTISCAN[188] with the WINGX program suite.[189] All non-hydrogen atoms were assigned anisotropic displacement parameters. The hydrogen atoms were constrained to idealized geometries fixing isotropic displacement parameters 1.2 times the Uiso value of their attached carbon for the aromatic and methylene hydrogens and 1.5 times for the methyl groups. For **16a** the disordered crystallization molecules of solvent were observed but could not be adequately modelled and were removed from the model. Examination with PLATON[190] and SQUEEZE[190-191] revealed one void of 91 $Å^3$ in the unit cell containing 31 e^-, which fits with one molecule of CH_2Cl_2 in the unit cell. Given that two molecules of **16a** were found in the asymmetric unit, the final stoichiometry is **16a**·0.25CH_2Cl_2. Finally, the structure of **16a** shows some residual peaks greater than 1 eA^{-3} in the vicinity of the platinum atoms, but with no chemical meaning.

Table E.7: Crystallographic data for 2x(**16a**·0.25CH_2Cl_2) and **16f**·$CHCl_3$.

	2x(**16a**·0.25CH_2Cl_2)	**16f**·$CHCl_3$
Empirical formula	$C_{56}H_{30}F_{10}N_4Pt_2S_2$	$C_{34}H_{19}Cl_3F_5N_3OPt$
F_w	1403.14	881.96
T (K)	125(2)	130(2)
crystal system, space group	Triclinic, P -1	Monoclinic, P 21/n
a(Å)	13.184(5)	12.580(3)
b(Å)	13.556(4)	19.461(4)
c(Å)	14.915(5)	12.675(3)
α(deg)	108.632(12)	90
β(deg)	110.805(13)	94.722(7)
γ(deg)	90.938(14)	90
volume (A^3)	2335.8(13)	3092.6(12)
Z	2	4
D_{calcd} (Mg/m^3)	1.995	1.894
absorption coefficient (mm^{-1})	6.158	4.861
F(000)	1344	1704
θ range for data collection (deg)	2.968 to 25.682	3.032 to 26.374
no of data // restraints // params	8859 / 0 / 625	6314 / 0 / 424
goodness-of-fit on F^2 [a]	1.285	1.123
final R indexes [I>2σ(I)] [a]	R1 = 0.0214, wR2 = 0.0520	R1 = 0.0157, wR2 = 0.0336
R indexes (all data) [a]	R1 = 0.0250, wR2 = 0.0535	R1 = 0.0199, wR2 = 0.0356
largest diff peak and hole ($e.Å^{-3}$)	1.641 and -2.129	0.527 and -0.685

[a] $R1 = \Sigma(|F_o| - |F_c|)/\Sigma|F_o|$; $wR2 = [\Sigma w(F_o^2 - F_c^2)^2/\Sigma wF_o^2]^{1/2}$; goodness of fit = $\{\Sigma[w(F_o^2 - F_c^2)^2]/(N_{obs} - N_{param})\}^{1/2}$; $w = [\sigma^2(F_o) + (g_1P)^2 + g_2P]^{-1}$; $P = [\max(F_o^2;0 + 2F_c^2]/3$.

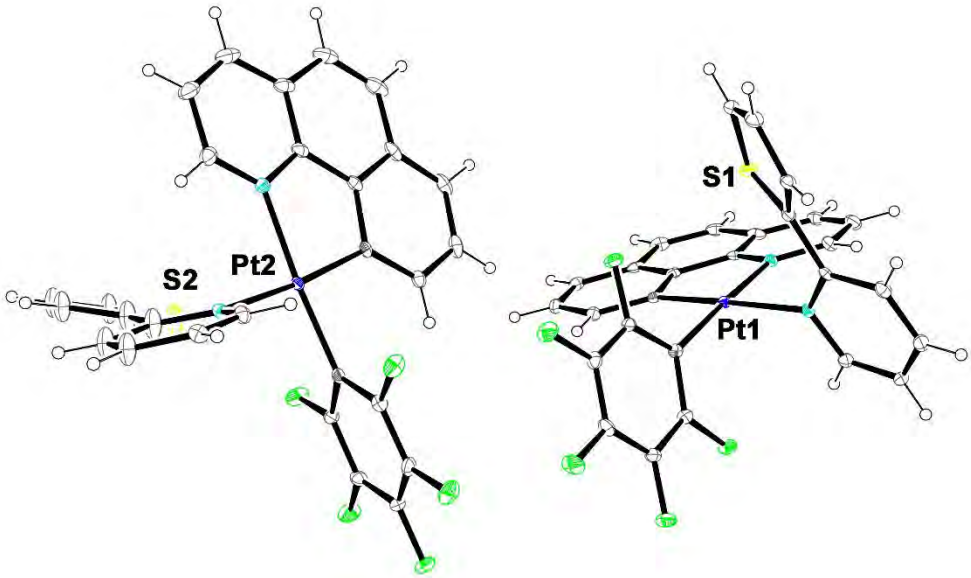

Figure E16. Thermal ellipsoid representation (30 % probability) of the crystal structure of 2x(**16a**·0.25CH_2Cl_2) showing A and B molecules.

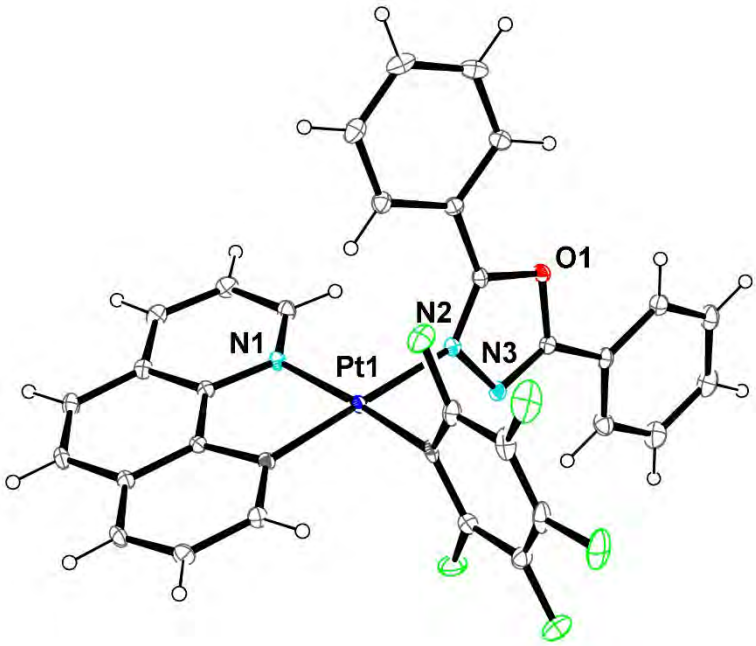

Figure E17. Thermal ellipsoid representation (30 % probability) of the crystal structure of **16f**·$CHCl_3$

Chapter 3.2

Yellow (**17c** and **18**) or colourless crystals (**17d**) were obtained by slow diffusion of *n*-hexane into a solution of the dichloromethane (**17d**, 25 ºC) or acetone (**17c**, **18**, -30 ºC). Slow diffusion of Et_2O into a solution of **17g** in THF gave yellow crystals. The diffraction data were collected using graphite monochromatic Mo-Kα radiation with a Nonius-*κ*CCD diffractometer at a temperature of 173 K with an Oxford Cryosystem temperature controller (**17c**) using the DENZO and SCALEPACK suite of programs[178] or with a Bruker APEX-II diffractometer at a temperature of 130 K (**17d**, **17g**, **18**) using the APEX-II software. The structures were solved by Intrinsic Phasing using SHELXT program[193] and refined by full-matrix least squares on F^2 with SHELXL.[194] The absorption correction was performed using MULTISCAN[188] with the WINGX program suite.[189] All non-hydrogen atoms were assigned anisotropic displacement parameters. The hydrogen atoms were constrained to idealized geometries fixing isotropic displacement parameters 1.2 times the Uiso value of their attached carbon for the aromatic and methylene hydrogens and 1.5 times for the methyl groups. The exception is the hydrogen atoms of the μ-OH groups in **18**, found in the density maps and refined with no positional constraints and a common thermal isotropic parameter. For **17g**, the disordered crystallization molecules of solvent were observed but could not be adequately modelled and were removed from the model. Both structures were examined with PLATON[190] and SQUEEZE[190-191]. For **17g**, the presence of 378 e^- in the unit cell was revealed, which fits with 9 molecules of THF in the unit cell, giving rise to the stoichiometry **17g**·0.5 THF. For **17c**, one molecule of acetone was properly resolved from the difference density map. Further examination of the structure with PLATON and SQUEEZE revealed the presence of four voids of 290 $Å^3$ in the unit cell, containing 600 e^-, which fits well with the presence of additional 2.25 molecules of acetone in the asymmetric unit, so that the final stoichiometry is **17c**·3.25 acetone. Finally, the structure of **17d** and **17g** shows some residual peaks greater than 1 eA^{-3} in the vicinity of the platinum atoms, but with no chemical meaning.

Table E.8: Crystallographic data for **17c**·3.25acetone, **17d**, **17g**·0.5THF and **18**·2acetone.

	17c·3.25acetone	**17d**	**17g**·0.5THF	**18**·2acetone
Empirical formula	$C_{37}H_{24}ClF_5N_2OPt$	$C_{30}H_{14}ClF_7N_2Pt$	$C_{40}H_{20}ClF_5N_2Pt$	$C_{44}H_{30}Cl_2F_{10}N_2O_4Pt_2$
F_w	838.12	765.97	854.12	1301.78
T (K)	173(1)	130(2)	130(2)	132(2) K
crystal system, space group	Monoclinic, C 2/c	Monoclinic, P 21/c	Trigonal, R -3 :H	Triclinic, P-1
a(Å)	31.2671(6)	9.013(2)	25.376(11)	12.7364(13)
b(Å)	12.7818(5)	17.295(5)	25.376	13.0415(15)
c(Å)	20.2983(7)	16.318(4)	27.207(14)	13.8687(16)
α(deg)	90	90	90	76.942(4)
β(deg)	119.952(2)	97.258(9)	90	85.779(4)
γ(deg)	90	90	120	65.314(3)
volume (A^3)	7028.8(4)	2523.3(11)	15173(16)	2038.4(4)
Z	8	4	18	2
D_{calcd} (Mg/m^3)	1.584	2.016	1.683	2.121
absorption coefficient (mm^{-1})	4.126	5.743	4.300	7.081
F(000)	3264	1464	7452	1240
θ range for data collection (deg)	1.503 to 25.025	2.981 to 25.023	3.135 to 25.681	3.125 to 27.959
no of data // restraints // params	6188 / 0 / 424	4445 / 0 / 340	6390 / 0 / 442	9743 / 0 / 585
goodness-of-fit on F^2 [a]	0.989	1.073	1.094	1.280
final R indexes [I>2σ(I)] [a]	R1 = 0.0479, wR2 = 0.1569	R1 = 0.0363, wR2 = 0.0833	R1 = 0.0215, wR2 = 0.0525	R1 = 0.0221, wR2 = 0.0519
R indexes (all data) [a]	R1 = 0.0701, wR2 = 0.1859	R1 = 0.0597, wR2 = 0.0922	R1 = 0.0309, wR2 = 0.0583	R1 = 0.0255, wR2 = 0.0547
largest diff peak and hole ($e.Å^{-3}$)	0.935 and -2.337	1.765 and -1.541	1.339 and -0.721	0.977 and -1.447

[a] $R1 = \Sigma(|F_o| - |F_c|)/\Sigma|F_o|$; $wR2 = [\Sigma w(F_o^2 - F_c^2)^2/\Sigma wF_o^2]^{1/2}$; goodness of fit = $\{\Sigma[w(F_o^2 - F_c^2)^2]/(N_{obs} - N_{param})\}^{1/2}$; $w = [\sigma^2(F_o) + (g_1P)^2 + g_2P]^{-1}$; $P = [\max(F_o^2;0 + 2F_c^2]/3$.

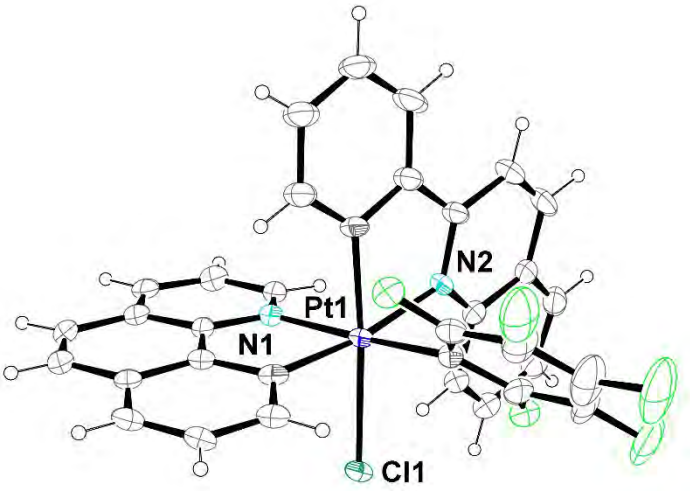

Figure E18. Thermal ellipsoid representation (30 % probability) of the crystal structure of **17c**·3.25acetone.

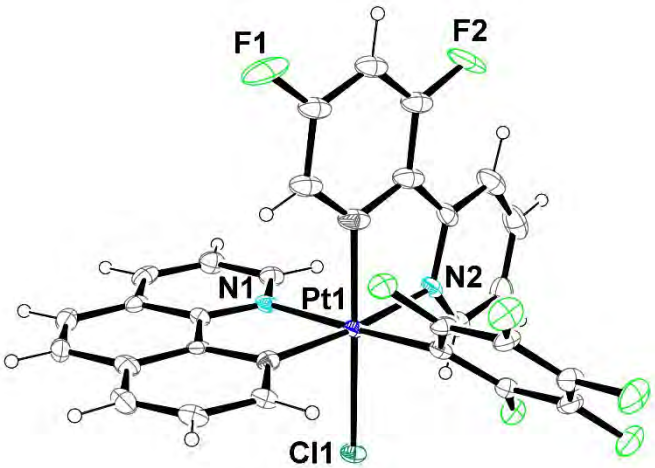

Figure E19. Thermal ellipsoid representation (30 % probability) of the crystal structure of **17d**.

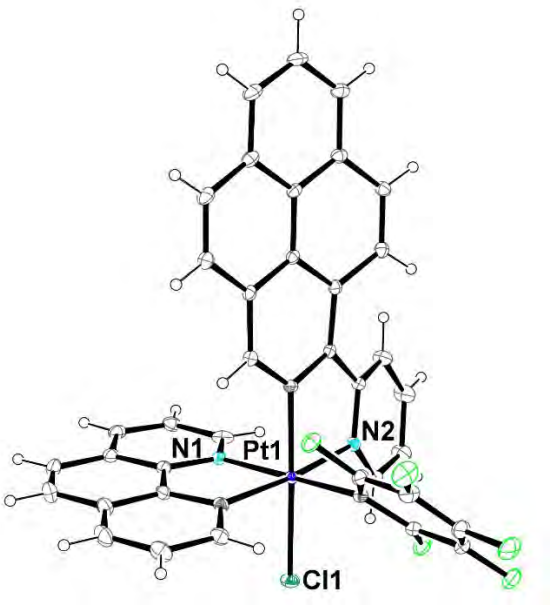

Figure E20. Thermal ellipsoid representation (30 % probability) of the crystal structure of **17g**·0.5THF.

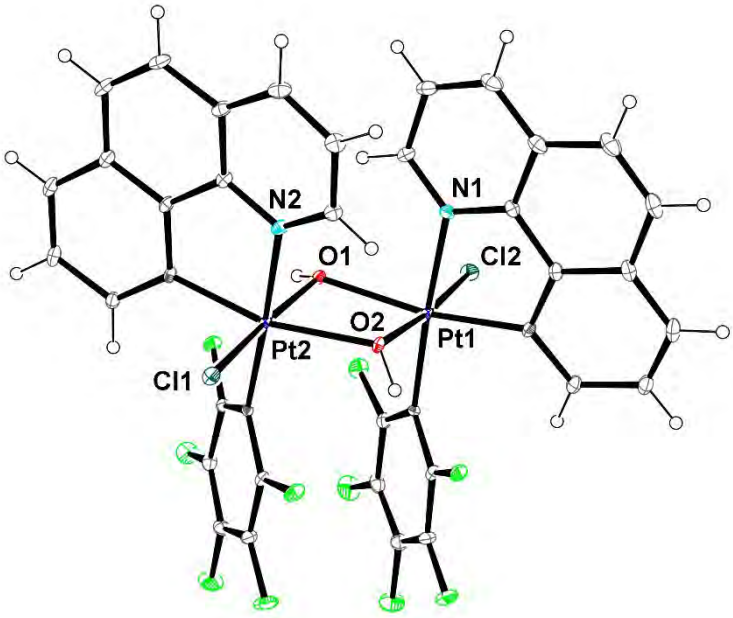

Figure E21. Thermal ellipsoid representation (30 % probability) of the crystal structure of **18**·2acetone.

X-RAY CHRYSTALLOGRAPHY EXPERIMENTAL DETAILS: CHAPTER 4

Yellow crystals were obtained by slow diffusion of *n*-hexane into a solution of the complex in CH_2Cl_2 (**20**·2.5CH_2Cl_2, -30 ºC) or CH_2Cl_2 (**19-O**·Et_2O, -30 ºC). X-ray intensity data were collected with a NONIUS-*k*CCD area-detector diffractometer, using graphite-monochromatic Mo-K_α radiation, and images processed using the DENZO and SCALEPACK suite of programs.[178] Structures were solved by Intrinsic Phasing using SHELXT[194] and refined by full-matrix least squares on F^2 with SHELXL.[194] The absorption correction was performed using MULTISCAN[188] with the WINGX program suite.[189] All non-hydrogen atoms were assigned anisotropic displacement parameters. The hydrogen atoms were constrained to idealized geometries fixing isotropic displacement parameters 1.2 times the U_{iso} value of their attached carbon for the aromatic and methylene hydrogens and 1.5 times for the methyl groups. For the complex **20**, disordered crystallization molecules of CH_2Cl_2 were observed but could not be adequately modelled and were removed from the model. Examination with PLATON[190] and SQUEEZE[190-191] revealed the presence of one void of 471 $Å^3$ in the unit cell containing 221 e^-, which fits with the presence of 5 molecules of CH_2Cl_2 in the unit cell giving rise to the stoichiometry (**20**·2.5CH_2Cl_2). Finally, the structures show some residual peaks greater than 1 e $Å^{-3}$ in the vicinity of the platinum and gold atoms but with no chemical meaning.

Table E.9: Crystallographic data for **19-O** and **20**.

	19-O·Et_2O	**20**·$2.5CH_2Cl_2$
Empirical formula	$C_{48}H_{40}F_5NO_2P_2Pt$	$C_{44}H_{30}AuClF_5NP_2Pt$
F_w	1014.84	1157.13
T (K)	173(1)	173(1)
crystal system, space group	Triclinic, P -1	Triclinic, P -1
a(Å)	10.9679(3)	10.8621(4)
b(Å)	10.9679(3)	13.4912(6)
c(Å)	16.1172(5)	16.9920(7)
α(deg)	70.501(2)	107.630(2)
β(deg)	73.2210(10)	106.287(2)
γ(deg)	87.162(2)	91.922(3)
volume (A^3)	2137.62(10)	2258.68(16)
Z	2	2
D_{calcd} (Mg/m^3)	1.577	1.701
absorption coefficient (mm^{-1})	3.419	6.517
F(000)	1008	1100
θ range for data collection (deg)	2.588 to 27.48	2.674 to 25.682
no of data // restraints // params	9639 / 0 / 532	8584 / 0 / 496
goodness-of-fit on F^2 [a]	1.041	1.049
final R indexes [I>2σ(I)] [a]	R1 = 0.0298, wR2 = 0.0696	R1 = 0.0454, wR2 = 0.1330
R indexes (all data) [a]	R1 = 0.0372, wR2 = 0.0723	R1 = 0.0556, wR2 = 0.1389
largest diff peak and hole ($e.Å^{-3}$)	0.917 and -1.649	3.884 and -2.215

[a] $R1 = \Sigma(|F_o| - |F_c|)/\Sigma|F_o|$; $wR2 = [\Sigma w(F_o^2 - F_c^2)^2/\Sigma wF_o^2]^{1/2}$; goodness of fit = $\{\Sigma[w(F_o^2 - F_c^2)^2]/(N_{obs} - N_{param}^{1/2}$; $w = [\sigma^2(F_o) + (g_1P)^2 + g_2P]^{-1}$; $P = [\max(F_o^2;0 + 2F_c^2]/3$.

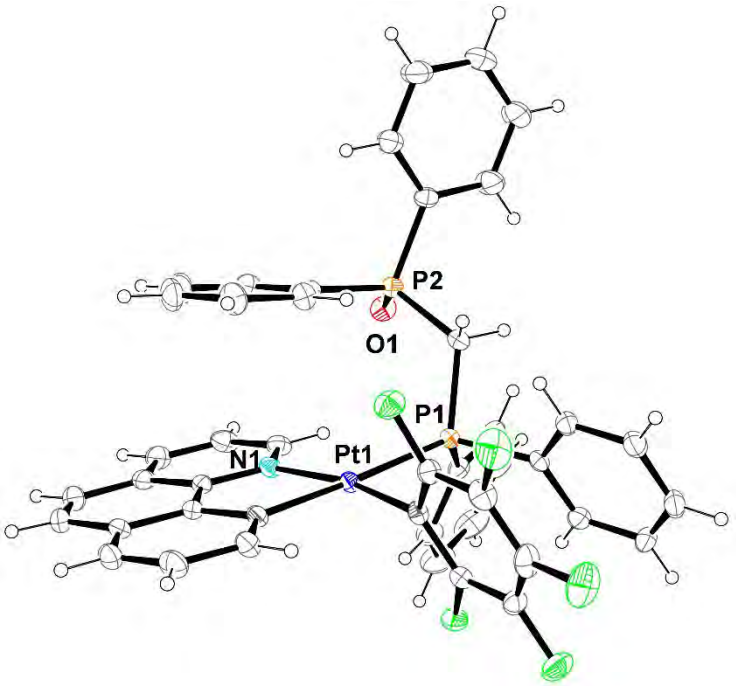

Figure E22. Thermal ellipsoid representation (30 % probability) of the crystal structure of **19-O**·Et_2O.

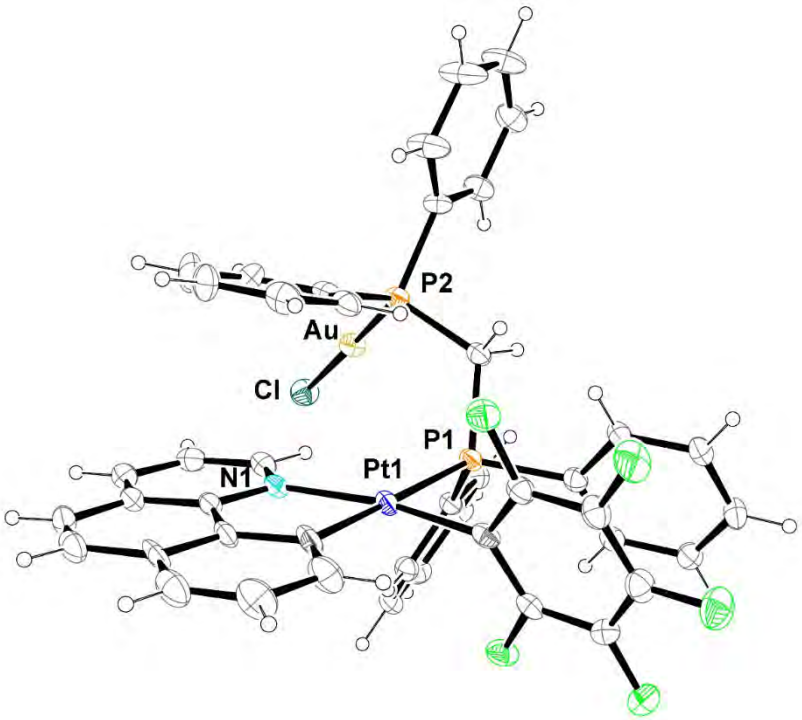

Figure E23. Thermal ellipsoid representation (30 % probability) of the crystal structure of **20**·2.5CH_2Cl_2.

Brooklyn College Stay

Titanocene-Gold Compounds Based on Highly Active Gold(I)-N-Heterocyclic Carbene Anticancer Agents

This section summarizes the research work carried out from February to July, 2017 at Brooklyn College – The City University of New York, under the supervision of Dr. María Contel. The stay at Brooklyn College was aimed to work on the broad topic of "Potential Metal-based cancer chemotherapeutics" with the project funded by the National Institutes of Health (US). More specifically, the main purpose of this project was the synthesis of new bimetallic bioactive molecules based on a Ti-Au scaffold with promising anticancer properties.

During the stay, we prepared the new titanocene-gold bimetallic compounds of the type $[(\eta^5\text{-}C_5H_5)_2TiMe(\mu\text{-mba})Au(NHC)]$ **2a** and **2b** (NHC = 1,3-dibenzyl-4,5-diphenylimidazol-2-ylidene, NHC-Bn; 1,3-diethyl-4,5-diphenylimidazol-2-ylidene, NHC-Et) bearing the ambidentate linker (-OC(O)-*p*-C_6H_4-S-) with a carboxylate and thiolate groups. These compounds are based on two highly active gold(I) compounds containing *N*-heterocyclic carbenes [AuX(NHC)] (NHC = NHC-Bn, X = Cl **a**; NHC = NHC-Et, X = Br **b**) described previously by Tacke *et al*. and Gust *et al*., respectively.[195]

Within this aim, the carbene thiolate gold (I) precursors [Au(Hmba)(NHC)] (NHC-Bn **1a**, NHC-Et **1b**), bearing the $Hmba^-$ group (H_2mba = 4-Mercaptobenzoic acid), were firstly synthetized by treatment of the halide [AuX(NHC)] with an equimolar mixture of H_2mba and KOH in ethanol/water (4:1) (Scheme A.1).

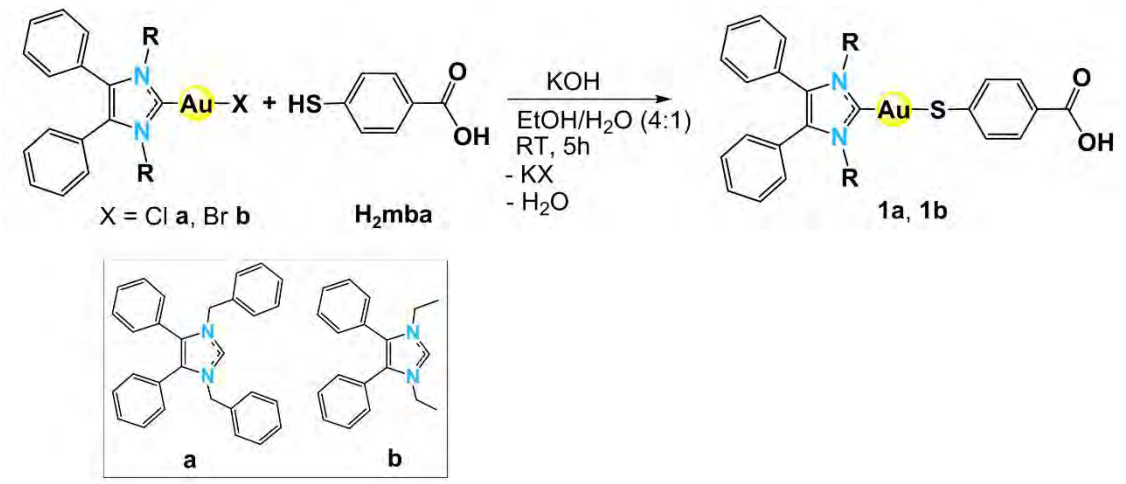

Scheme A.1. Preparation of complexes **1a** and **1b**.

The bimetallic Ti-Au complexes **2a** and **2b** were obtained as yellow solids by addition of a solution of **1a** or **1b** in thf dropwise over a solution of $[(\eta^5\text{-}C_5H_5)_2TiMe_2]$ in toluene (Scheme A.2), as was previously described by M. Contel's group for similar Ti-Au complexes.[162c, 196]

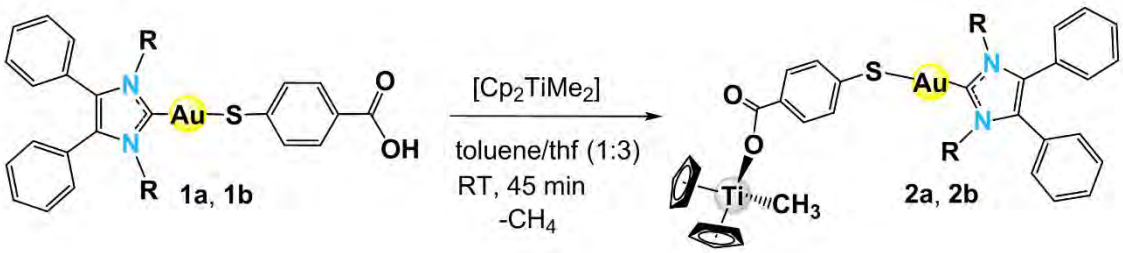

Scheme A.2. Preparation of $[(\eta^5\text{-}C_5H_5)_2TiMe(\mu\text{-mba})Au(NHC)]$ **2a** and **2b**.

All complexes (**1a**,**b** and **2a**,**b**) were characterized by NMR, ESI(+), IR spectroscopies and Elemental Analysis. The ^1H and $^{13}C\{^1H\}$ NMR spectra supported the proposed structures and the most significant proton and carbon signals were assigned (Figure A.1).

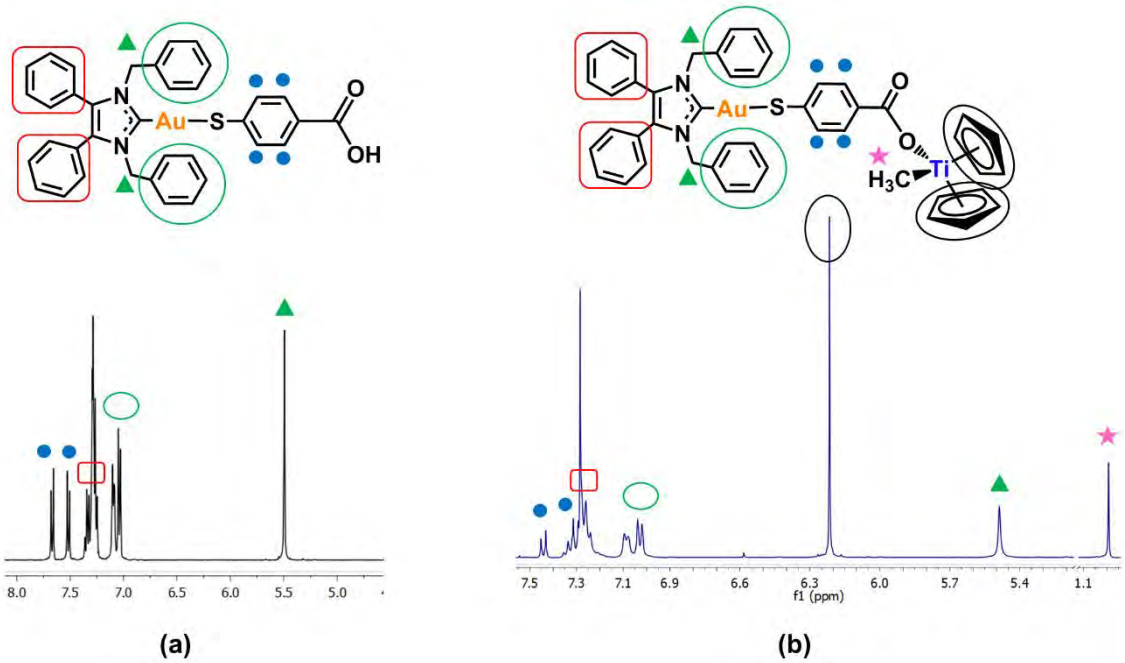

Figure A.1. ^1H NMR spectra of (a) **1a** and (b) **2a** complexes in $CDCl_3$.

The stability in dmso-d^6 and in a mixture dmso-d^6/PBS-D_2O (5:1) of the complexes was evaluated by ^1H NMR. Monitorization of the solutions at different times showed that the monometallic complexes were stable in dmso and in dmso/PBS solutions for more than 7 days. By contrast, the bimetallic derivatives **2a** and **2b** showed partial

hydrolysis and elimination of the cyclopentadienyl ligands over time, showing half-life values of 18 and 6 h, respectively (Figure A.2).

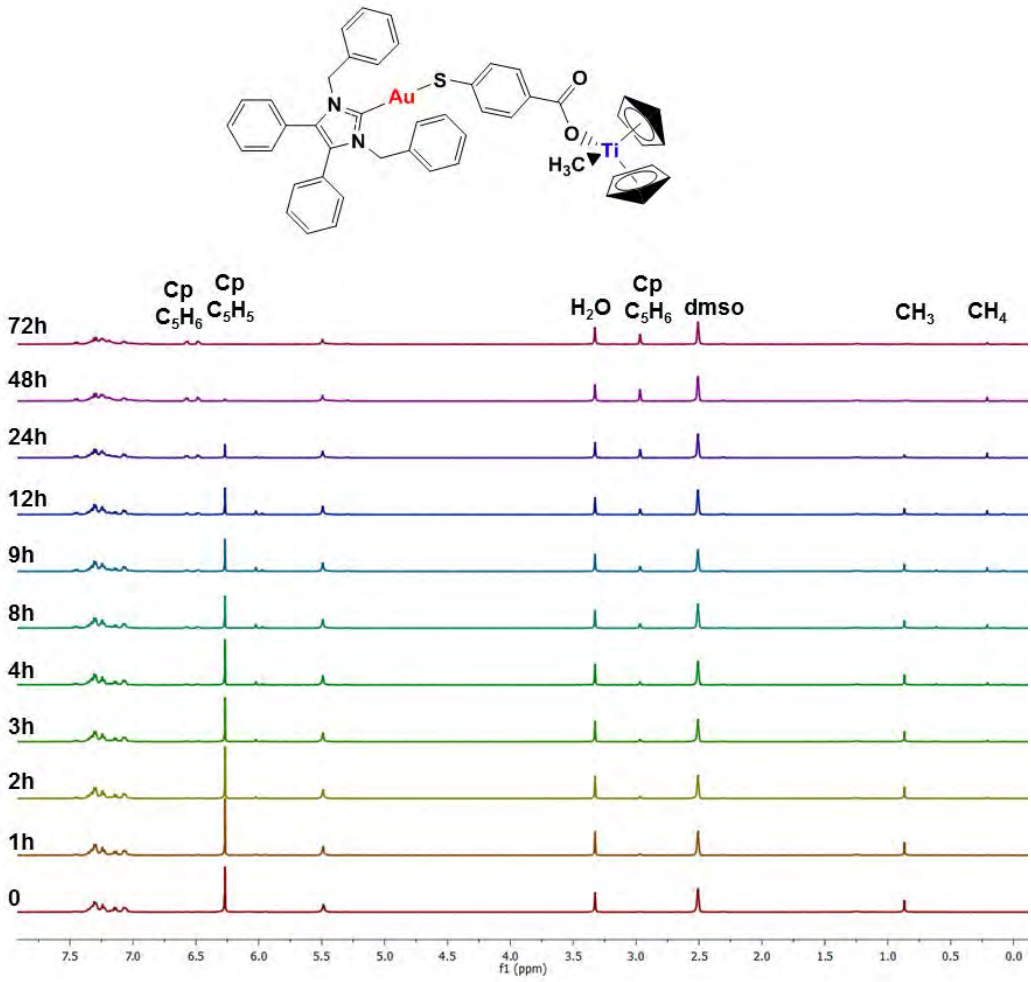

Figure A.2. ^{1}H NMR stability study of **2a** in dmso-d^{6}.

X-ray diffraction studies of both monometallic precursors **1a** and **1b** were carried out when I returned to the University of La Rioja (Figure A.3). Unfortunately, all attempts to obtain adequate crystals of the bimetallic **2a** or **2b** were infructuous.

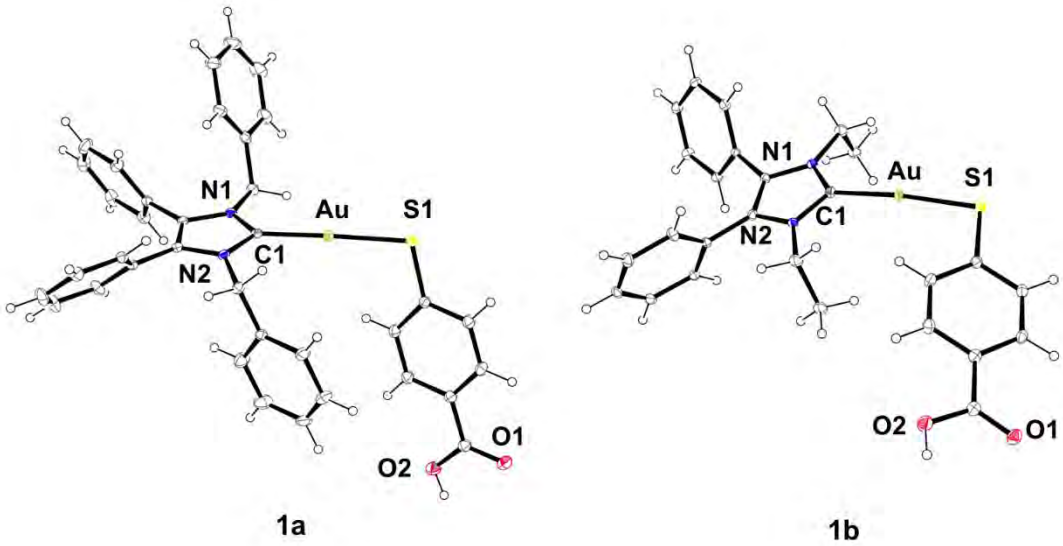

Figure A.3. ORTEP view of the molecular structures of **1a** and **1b**.

After my research work time was finished, the biological properties of all the compounds were evaluated by Maria Contel's research group. Thus, the cytotoxicity of **1a**, **1b**, **2a**, **2b**, the gold cytotoxic compounds [AuX(NHC)] **a**,**b**, and the reference compounds Auranofin (AF), *cis*-platin and Titanocene-Y (Ti-Y) were determined against human clear-cell renal carcinoma (Caki-1), human prostate cancer (PC3) cells and non-tumorigenic human fetal lung fibroblast (IMR90) cell line. The cytotoxicity assays revealed that the incorporation of the titanocene fragment improves or does not decrease the cytotoxicity in the human cancer cell lines Caki-1 and PC3. Moreover, the compounds were found to be more cytotoxic that the previously described Ti-Au compounds by Contel's group, containing non-optimized Gold(I)-N-heterocyclic fragments.[196c] Besides, they have demonstrated that the selected bimetallic compound **2a** has an improved pharmacological profile in terms of apoptosis, inhibition of migration, and inhibition of TrxR (thioredoxin reductase) and VEGF (vascular endothelial growth factor) in PC3 cell lines, in comparison to the monometallic bioactive gold compound **a** (Figure A.4).

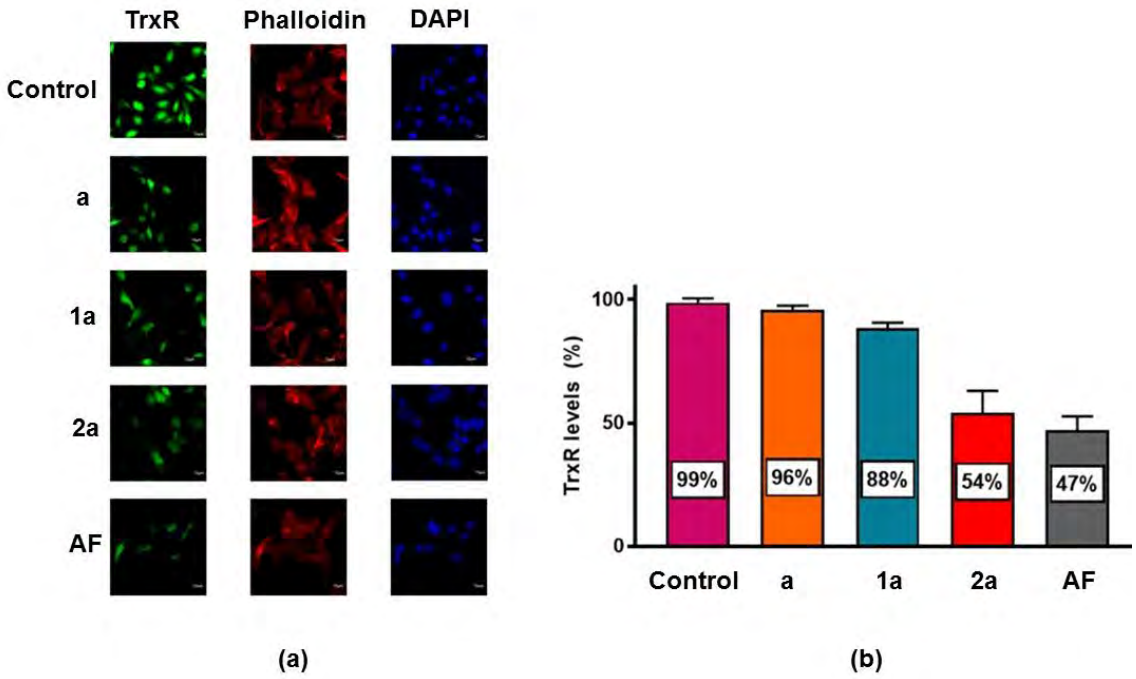

Figure A.4. (a) Immunofluorescent analysis of TrRx level upon treatment with control (0.1 % DMSO), **a**, **1a**, **2a** or Auranofin (**AF**) in 0.1% DMSO for 24 h. Thioredoxin reductase (green) in the PC3 cells and its levels are changed in response to treatment with compounds of interest. (b) Quantitative analysis of TrRx levels using ImageJ showing significant decreasing the enzyme level following exposure to **2a** and **AF** compared to control. All data in bar graphs represent mean ± SD of two independent experiments ($p < 0.05$).

Further characterization carried out by M. Contel's research group and theoretical calculations studies (Dr. Andrzej A. Jarzecki) support and confirm the proposed structures of the bimetallic complexes.

This work has recently led to the publication of the paper: **Preparation of Titanocene–Gold Compounds Based on Highly Active Gold(I)-N-Heterocyclic Carbene Anticancer Agents: Preliminary in vitro Studies in Renal and Prostate Cancer Cell Lines**. Natalia Curado, Nora Giménez, Kirill Miachin, Mélanie Aliaga-Lavrijsen, Mike A. Cornejo, Andrzej A. Jarzecki and María Contel. *ChemMedChem*, **2019**, 14, 1086 –1095.

Bibliografía

1. (a) Puttock, E. V.; Walden, M. T.; Williams, J. A. G., *Coord. Chem. Rev.* **2018**, *367*, 127; (b) Yersin, H.; Rausch, A. F.; Czerwieniec, R.; Hofbeck, T.; Fischer, T., *Coord. Chem. Rev.* **2011**, *255*, 2622; (c) Rausch, A. F.; Homeier, H. H. H.; Yersin, H., Organometallic Pt(II) and Ir(III) Triplet Emitters for OLED Applications and the Role of Spin–Orbit Coupling: A Study Based on High-Resolution Optical Spectroscopy. In *Photophysics of Organometallics. Top. Organomet. Chem.*, Lees, A. J., Ed. Springer, Berlín, Heidelberg: **2010**; Vol. 29, pp 193.
2. Baroncini, M.; Bergamini, G.; Ceroni, P., *Chem. Commun.* **2017**, *53*, 2081.
3. Bischoff, L.; Baudequin, C.; Hoarau, C.; Urriolabeitia, E. P., Chapter Two - Organometallic Fluorophores of d^8 Metals (Pd, Pt, Au). In *Advances in Organometallic Chemistry*, Pérez, P. J., Ed. Academic Press: **2018**; Vol. 69, pp 73.
4. Shafikov, M. Z.; Kozhevnikov, D. N.; Bodensteiner, M.; Brandl, F.; Czerwieniec, R., *Inorg. Chem.* **2016**, *55*, 7457.
5. Ruiz, S. Tesis Doctoral. Universidad de La Rioja, Logroño, **2014**.
6. Xiang, H.; Cheng, J.; Ma, X.; Zhou, X.; Chruma, J. J., *Chem. Soc. Rev.* **2013**, *42*, 6128.
7. (a) Fan, C.; Yang, C., *Chem. Soc. Rev.* **2014**, *43*, 6439; (b) Tang, M.-C.; Chan, A. K.-W.; Chan, M.-Y.; Yam, V. W.-W., Platinum and Gold Complexes for OLEDs. In *Photoluminescent Materials and Electroluminescent Devices*, Armaroli, N.; Bolink, H. J., Eds. Springer International Publishing: Cham, **2017**; pp 67.
8. Li, K.; Ming Tong, G. S.; Wan, Q.; Cheng, G.; Tong, W.-Y.; Ang, W.-H.; Kwong, W.-L.; Che, C.-M., *Chem. Sci.* **2016**, *7*, 1653.
9. (a) Yersin, H., Highly Efficient OLEDs with Phosphorescent Materials. Wiley-VCH: Weinheim, Germany, **2008**; pp458; (b) Gildea, L. F.; Williams, J. A. G., Iridium and platinum complexes for OLEDs. In *Organic Light-Emitting Diodes (OLEDs)*, Buckley, A., Ed. Woodhead Publishing: Cambridge, UK, **2013**; pp 77; (c) Cebrián, C.; Mauro, M., *Beilstein J. Org. Chem.* **2018**, *14*, 1459; (d) Choy, W. C. H.; Chan, W. K.; Yuan, Y., *Adv. Mater.* **2014**, *26*, 5368; (e) Fleetham, T.; Li, G.; Li, J., *Adv. Mater.* **2017**, *29*, 1601861; (f) Aliprandi, A.; Genovese, D.; Mauro, M.; Cola, L. D., *Chem. Lett.* **2015**, *44*, 1152; (g) Kalinowski, J.; Fattori, V.; Cocchi, M.; Williams, J. A. G., *Coord. Chem. Rev.* **2011**, *255*, 2401; (h) Visbal, R.; Gimeno, M. C., *Chem. Soc. Rev.* **2014**, *43*, 3551; (i) Zhou, G.; Wong, W.-Y.;

Yang, X., *Chem. Asian J.* **2011**, *6*, 1706; (j) Penconi, M.; Cazzaniga, M.; Panzeri, W.; Mele, A.; Cargnoni, F.; Ceresoli, D.; Bossi, A., *Chem. Mater.* **2019**, *31*, 2277.

10. (a) Zhong, J.-J.; Meng, Q.-Y.; Wang, G.-X.; Liu, Q.; Chen, B.; Feng, K.; Tung, C.-H.; Wu, L.-Z., *Chem. Eur. J.* **2013**, *19*, 6443; (b) Kim, J.-H.; Kim, J.-H., *J. Am. Chem. Soc.* **2012**, *134*, 17478; (c) Huang, X.; Meggers, E., *Acc. Chem. Res.* **2019**, *52*, 833; (d) Mede, T.; Jäger, M.; Schubert, U. S., *Chem. Soc. Rev.* **2018**, *47*, 7577; (e) Parasram, M.; Gevorgyan, V., *Chem. Soc. Rev.* **2017**, *46*, 6227; (f) Twilton, J.; Le, C.; Zhang, P.; Shaw, M. H.; Evans, R. W.; MacMillan, D. W. C., *Nature Rev. Chem.* **2017**, *1*, 0052; (g) You, Y.; Nam, W., *Chem. Soc. Rev.* **2012**, *41*, 7061.

11. (a) Xu, L.; Ho, C.-L.; Liu, L.; Wong, W.-Y., *Coord. Chem. Rev.* **2018**, *373*, 233; (b) Mills, I. N.; Porras, J. A.; Bernhard, S., *Acc. Chem. Res.* **2018**, *51*, 352; (c) Housecroft, C. E.; Constable, E. C., *Coord. Chem. Rev.* **2017**, *350*, 155; (d) Ho, C.-L.; Yu, Z.-Q.; Wong, W.-Y., *Chem. Soc. Rev.* **2016**, *45*, 5264; (e) Fresta, E.; Costa, R. D., *J. Mater. Chem. C* **2017**, *5*, 5643; (f) Jakubikova, E.; Bowman, D. N., *Acc. Chem. Res.* **2015**, *48*, 1441; (g) Bignozzi, C. A.; Argazzi, R.; Boaretto, R.; Busatto, E.; Carli, S.; Ronconi, F.; Caramori, S., *Coord. Chem. Rev.* **2013**, *257*, 1472; (h) Archer, S.; Weinstein, J. A., *Coord. Chem. Rev.* **2012**, *256*, 2530; (i) Marin, V.; Holder, E.; Hoogenboom, R.; Schubert, U. S., *Chem. Soc. Rev.* **2007**, *36*, 618; (j) Nazeeruddin, M. K.; Grätzel, M., Transition Metal Complexes for Photovoltaic and Light Emitting Applications. In *Photofunctional Transition Metal Complexes*, Yam, V. W. W., Ed. Springer Berlin Heidelberg: Berlin, Heidelberg, **2007**; pp 113; (k) Pashaei, B.; Shahroosvand, H.; Graetzel, M.; Nazeeruddin, M. K., *Chem. Rev.* **2016**, *116*, 9485.

12. (a) Yang, X.; Huang, Z.; Dang, J.; Ho, C.-L.; Zhou, G.; Wong, W.-Y., *Chem. Commun.* **2013**, *49*, 4406; (b) Guerchais, V.; Fillaut, J.-L., *Coord. Chem. Rev.* **2011**, *255*, 2448; (c) Saha, M. L.; Yan, X.; Stang, P. J., *Acc. Chem. Res.* **2016**, *49*, 2527; (d) Lo, K. K.-W.; Li, S. P.-Y.; Zhang, K. Y., *New J. Chem.* **2011**, *35*, 265; (e) Kumar, A.; Sun, S.-S.; Lees, A. J., *Coord. Chem. Rev.* **2008**, *252*, 922; (f) Amendola, V.; Fabbrizzi, L.; Foti, F.; Licchelli, M.; Mangano, C.; Pallavicini, P.; Poggi, A.; Sacchi, D.; Taglietti, A., *Coord. Chem. Rev.* **2006**, *250*, 273; (g) Zhao, Q.; Li, F.; Huang, C., *Chem. Soc. Rev.* **2010**, *39*, 3007; (h) Wenger, O. S., *Chem. Rev.* **2013**, *113*, 3686.

13. (a) Nguyen, T. N.; Ebrahim, F. M.; Stylianou, K. C., *Coord. Chem. Rev.* **2018**, *377*, 259; (b) Shum, J.; Leung, P. K.-K.; Lo, K. K.-W., *Inorg. Chem.* **2019**, *58*, 2231; (c) Zhang, Y.; Wang, Y.; Song, J.; Qu, J.; Li, B.; Zhu, W.; Wong, W.-Y., *Adv. Optical Mater.* **2018**, *6*, 1800466; (d) Zhang, K. Y.; Yu, Q.; Wei, H.; Liu, S.; Zhao, Q.; Huang, W., *Chem. Rev.* **2018**, *118*, 1770; (e) Lo, K. K.-W., Chapter Three - Luminescent Iridium(III) and Rhenium(I) Complexes as Biomolecular Probes and Imaging Reagents. In *Advances in Inorganic Chemistry*, van Eldik, R.; Hubbard, C. D., Eds. Academic Press: **2016**; Vol. 68, pp 97; (f) You, Y.; Cho, S.; Nam, W., *Inorg. Chem.* **2014**, *53*, 1804; (g) Zhao, Q.; Huang, C.; Li, F., *Chem. Soc. Rev.* **2011**, *40*, 2508; (h) Lo, K. K.-W.; Li, S. P.-Y., *RSC Adv.* **2014**, *4*, 10560; (i) Ma, D.-L.; He, H.-Z.; Leung, K.-H.; Chan, D. S.-H.; Leung, C.-H., *Angew. Chem. Int. Ed.* **2013**, *52*, 7666; (j) Caporale, C.; Massi, M., *Coord. Chem. Rev.* **2018**, *363*, 71; (k) Lee, L. C.-C.; Leung, K.-K.; Lo, K. K.-W., *Dalton Trans.* **2017,** *46*, 16357; (l) Mauro, M.; Aliprandi, A.; Septiadi, D.; Kehr, N. S.; De Cola, L., *Chem. Soc. Rev.* **2014**, *43*, 4144; (m) Fernández-Moreira, V.; Thorp-Greenwood, F. L.; Coogan, M. P., *Chem. Commun.* **2010**, *46*, 186.

14. (a) Chi, Y.; Chou, P. T., *Chem. Soc. Rev.* **2010**, *39*, 638; (b) Ladouceur, S.; Zysman-Colman, E., *Eur. J. Inorg. Chem.* **2013**, 2985; (c) Ulbricht, C.; Beyer, B.; Friebe, C.; Winter, A.; Schubert, U. S., *Adv. Mat.* **2009**, *21*, 4418; (d) Zanoni, K. P. S.; Coppo, R. L.; Amaral, R. C.; Murakami Iha, N. Y., *Dalton Trans.* **2015**, *44*, 14559; (e) Baranoff, E.; Curchod, B. F. E., *Dalton Trans.* **2015**, *44*, 8318; (f) Flamigni, L.; Barbieri, A.; Sabatini, C.; Ventura, B.; Barigelletti, F., Photochemistry and photophysics of coordination compounds: Iridium. In *Top. Curr. Chem.*, **2007**; Vol. 281, pp 143; (g) Chou, P.-T.; Chi, Y.; Chung, M.-W.; Lin, C.-C., *Coord. Chem. Rev.* **2011**, *255*, 2653; (h) Zamora, A.; Vigueras, G.; Rodríguez, V.; Santana, M. D.; Ruiz, J., *Coord. Chem. Rev.* **2018**, *360*, 34; (i) Chi, Y.; Chang, T.-K.; Ganesan, P.; Rajakannu, P., *Coord. Chem. Rev.* **2017**, *346*, 91; (j) Lo, K. K.-W., *Acc. Chem. Res.* **2015**, *48*, 2985; (k) Chen, Z. Q.; Bian, Z. Q.; Huang, C. H., *Adv. Mat.* **2010**, *22*, 1534; (l) Pal, A. K.; Hanan, G. S., *Chem. Soc. Rev.* **2014**, *43*, 6184; (m) Sun, Q.; Mosquera-Vazquez, S.; Suffren, Y.; Hankache, J.; Amstutz, N.; Lawson Daku, L. M.; Vauthey, E.; Hauser, A., *Coord. Chem. Rev.* **2015**, *282-283*, 87; (n) Barigelletti, F.; Flamigni, L., *Chem. Soc. Rev.* **2000**, *29*, 1.

15. (a) Williams, J. A. G., Photochemistry and photophysics of coordination compounds: Platinum. In *Top. Curr. Chem.*, **2007**; Vol. 281, pp 205; (b) Williams,

J. A. G.; Develay, S.; Rochester, D. L.; Murphy, L., *Coord. Chem. Rev.* **2008**, *252*, 2596; (c) Huo, S.; Carroll, J.; Vezzu, D. A. K., *Asian J. Org. Chem.* **2015**, *4*, 1210; (d) Strassner, T., *Acc. Chem. Res.* **2016**, *49*, 2680; (e) Muro, M. L.; Rachford, A. A.; Wang, X.; Castellano, F. N., *Top. Organomet. Chem.* **2010**, *29*, 159; (f) Zhao, J.; Ji, S.; Wu, W.; Wu, W.; Guo, H.; Sun, J.; Sun, H.; Liu, Y.; Li, Q.; Huang, L., *RSC Adv.* **2012**, *2*, 1712; (g) Vogler, A.; Kunkely, H., *Coord. Chem. Rev.* **2001**, *219-221*, 489.

16. (a) Pfenning, B. W., *Principles of Inorganic Chemistry*. Wiley: **2015**; (b) Fraga, S.; Karwowski, J.; Saxena, K. M. S., *Handbook of atomic data*. Elsevier Scientific Publishing Company: United States, 1976.
17. Kozhevnikov, V. N.; Durrant, M. C.; Williams, J. A. G., *Inorg. Chem.* **2011**, *50*, 6304.
18. (a) Yoshida, M.; Kato, M., *Coord. Chem. Rev.* **2018**, *355*, 101; (b) Ravotto, L.; Ceroni, P., *Coord. Chem. Rev.* **2017**, *346*, 62; (c) Wong, K. M.-C.; Yam, V. W.-W., *Acc. Chem. Res.* **2011**, *44*, 424; (d) Yam, V. W.-W.; Au, V. K.-M.; Leung, S. Y.-L., *Chem. Rev.* **2015**, *115*, 7589; (e) Gray, H. B.; Záliš, S.; Vlček, A., *Coord, Chem. Rev.* **2017**, *345*, 297; (f) Kim, D.; Brédas, J.-L., *J. Am. Chem. Soc.* **2009**, *131*, 11371.
19. Roundhill, D. M.; Gray, H. B.; Che, C. M., *Acc. Chem. Res.* **1989**, *22*, 55.
20. (a) Zhang, X.; Li, B.; Chen, Z. H.; Chen, Z. N., *J. Mater. Chem.* **2012**, *22*, 11427; (b) Kobayashi, A.; Kato, M., *Eur. J. Inorg. Chem.* **2014**, *2014*, 4469; (c) McConnell, A. J.; Wood, C. S.; Neelakandan, P. P.; Nitschke, J. R., *Chem. Rev.* **2015**, *115*, 7729; (d) Kato, M., *Bull. Chem. Soc. Jpn.* **2007**, *80*, 287.
21. (a) Sagara, Y.; Yamane, S.; Mitani, M.; Weder, C.; Kato, T., *Adv. Mater.* **2016**, *28*, 1073; (b) Xue, P.; Ding, J.; Wang, P.; Lu, R., *J. Mat. Chem. C* **2016**, *4*, 6688.
22. (a) Connick, W. B.; Henling, L. M.; Marsh, R. E.; Gray, H. B., *Inorg. Chem.* **1996**, *35*, 6261; (b) Kato, M.; Kosuge, C.; Morii, K.; Ahn, J. S.; Kitagawa, H.; Mitani, T.; Matsushita, M.; Kato, T.; Yano, S.; Kimura, M., *Inorg. Chem.* **1999**, *38*, 1638.
23. Maestri, M.; Sandrini, D.; Balzani, V.; Chassot, L.; Jolliet, P.; von Zelewsky, A., *Chem. Phys. Lett.* **1985**, *122*, 375.
24. Chassot, L.; Muller, E.; Von Zelewsky, A., *Inorg. Chem.* **1984**, *23*, 4249.
25. Sandrini, D.; Maestri, M.; Balzani, V.; Chassot, L.; Von Zelewsky, A., *J. Am. Chem. Soc.* **1987**, *109*, 7720.

26. (a) Lu, G.-Z.; Tu, Z.-L.; Liu, L.; Zheng, Y.-X.; Zhao, Y., *Dalton Trans.* **2019**, *48*, 1892; (b) Fereidoonnezhad, M.; Kaboudin, B.; Mirzaee, T.; Babadi Aghakhanpour, R.; Golbon Haghighi, M.; Faghih, Z.; Faghih, Z.; Ahmadipour, Z.; Notash, B.; Shahsavari, H. R., *Organometallics* **2017**, *36*, 1707; (c) Lanoë, P.-H.; Moreno-Betancourt, A.; Wilson, L.; Philouze, C.; Monnereau, C.; Jamet, H.; Jouvenot, D.; Loiseau, F., *Dyes Pigm.* **2019**, *162*, 967.

27. Berenguer, J. R.; Lalinde, E.; Moreno, M. T., *Coord. Chem. Rev.* **2018**, *366*, 69.

28. (a) Xu, H.; Chen, R.; Sun, Q.; Lai, W.; Su, Q.; Huang, W.; Liu, X., *Chem. Soc. Rev.* **2014**, *43*, 3259; (b) Xiao, L.; Chen, Z.; Qu, B.; Luo, J.; Kong, S.; Gong, Q.; Kido, J., *Adv. Mat.* **2011**, *23*, 926; (c) Farinola, G. M.; Ragni, R., *Chem. Soc. Rev.* **2011**, *40*, 3467; (d) Murphy, L.; Williams, J. A. G., Luminescent platinum compounds: From molecules to OLEDs. In *Top. Organomet. Chem.*, **2010**; Vol. 28, pp 75.

29. (a) Yang, X.; Yao, C.; Zhou, G., *Platinum Met. Rev.* **2013**, *57*, 2; (b) Campagna, S.; Puntoriero, F.; Nastasi, F.; Bergamini, G.; Balzani, V., *Top. Curr. Chem.* **2007**, *280*, 117; (c) Choi, W. J.; Choi, S.; Ohkubo, K.; Fukuzumi, S.; Cho, E. J.; You, Y., *Chem. Sci.* **2015**, *6*, 1454.

30. (a) Thorp-Greenwood, F. L.; Balasingham, R. G.; Coogan, M. P., *J. Organomet. Chem.* **2012**, *714*, 12; (b) Cutillas, N.; Yellol, G. S.; de Haro, C.; Vicente, C.; Rodríguez, V.; Ruiz, J., *Coord. Chem. Rev.* **2013**, *257*, 2784; (c) Baggaley, E.; Weinstein, J. A.; Williams, J. A. G., *Coord. Chem. Rev.* **2012**, *256*, 1762; (d) Lo, K. K. W.; Choi, A. W. T.; Law, W. H. T., *Dalton Trans.* **2012**, *41*, 6021; (e) Lo, K. K.-W.; Tso, K. K.-S., *Inorg. Chem. Front.* **2015**, *2*, 510.

31. (a) Ma, D.-L.; Ma, V. P.-Y.; Chan, D. S.-H.; Leung, K.-H.; He, H.-Z.; Leung, C.-H., *Coord. Chem. Rev.* **2012**, *256*, 3087; (b) Omae, I., *J. Organomet. Chem.* **2016**, *823*, 50.

32. Batema, G. D.; Lutz, M.; Spek, A. L.; van Walree, C. A.; de Mello Donegá, C.; Meijerink, A.; Havenith, R. W. A.; Pérez-Moreno, J.; Clays, K.; Büchel, M.; van Dijken, A.; Bryce, D. L.; van Klink, G. P. M.; van Koten, G., *Organometallics* **2008**, *27*, 1690.

33. (a) Zhang, J.; Zhou, L.; Al-Attar, H. A.; Shao, K.; Wang, L.; Zhu, D.; Su, Z.; Bryce, M. R.; Monkman, A. P., *Adv. Funct. Mater.* **2013**, *23*, 4667; (b) Kessler, F.; Costa, R. D.; Di Censo, D.; Scopelliti, R.; Orti, E.; Bolink, H. J.; Meier, S.;

Sarfert, W.; Gratzel, M.; Nazeeruddin, M. K.; Baranoff, E., *Dalton Trans.* **2012**, *41*, 180.

34. (a) Ruggi, A.; van Leeuwen, F. W. B.; Velders, A. H., *Coord. Chem. Rev.* **2011**, *255*, 2542; (b) Lincoln, R.; Kohler, L.; Monro, S.; Yin, H.; Stephenson, M.; Zong, R.; Chouai, A.; Dorsey, C.; Hennigar, R.; Thummel, R. P.; McFarland, S. A., *J. Am. Chem. Soc.* **2013**, *135*, 17161.
35. (a) Colombo, A.; Fiorini, F.; Septiadi, D.; Dragonetti, C.; Nisic, F.; Valore, A.; Roberto, D.; Mauro, M.; De Cola, L., *Dalton Trans.* **2015**, *44*, 8478; (b) Che, C.-M.; Zhang, J.-L.; Lin, L.-R., *Chem. Commun.* **2002**, 2556.
36. Cho, J.-Y.; Suponitsky, K. Y.; Li, J.; Timofeeva, T. V.; Barlow, S.; Marder, S. R., *J. Organomet. Chem.* **2005**, *690*, 4090.
37. Balashev, K. P.; Puzyk, M. V.; Kotlyar, V. S.; Kulikova, M. V., *Coord. Chem. Rev.* **1997**, *159*, 109.
38. (a) Brooks, J.; Babayan, Y.; Lamansky, S.; Djorovich, P. I.; Tsyba, I.; Bau, R.; Thompson, M. E., *Inorg. Chem.* **2002**, *41*, 3055; (b) Bossi, A.; Rausch, A. F.; Leitl, M. J.; Czerwieniec, R.; Whited, M. T.; Djurovich, P. I.; Yersin, H.; Thompson, M. E., *Inorg. Chem.* **2013**, *52*, 12403; (c) Colombo, A.; Dragonetti, C.; Marinotto, D.; Righetto, S.; Roberto, D.; Tavazzi, S.; Escadeillas, M.; Guerchais, V.; Le Bozec, H.; Boucekkine, A.; Latouche, C., *Organometallics* **2013**, *32*, 3890.
39. Zhao, J.; Feng, Z.; Zhong, D.; Yang, X.; Wu, Y.; Zhou, G.; Wu, Z., *Chem. Mater.* **2018**, *30*, 929.
40. (a) Arnal, L.; Fuertes, S.; Martín, A.; Sicilia, V., *Chem. Eur. J.* **2018**, *24*, 9377; (b) Luo, Y.; Xu, Y.; Zhang, W.; Li, W.; Li, M.; He, R.; Shen, W., *J. Phys. Chem. C* **2016**, *120*, 3462; (c) Lin, W.-J.; Naziruddin, A. R.; Chen, Y.-H.; Sun, B.-J.; Chang, A. H. H.; Wang, W.-J.; Hwang, W.-S., *Chem. Asian J.* **2015**, *10*, 728; (d) Soellner, J.; Strassner, T., *Organometallics* **2018**, *37*, 1821; (e) Bachmann, M.; Suter, D.; Blacque, O.; Venkatesan, K., *Inorg. Chem.* **2016**, *55*, 4733.
41. Cheng, G.; Chow, P.-K.; Kui, S. C. F.; Kwok, C.-C.; Che, C.-M., *Adv. Mater.* **2013**, *25*, 6765.
42. (a) Raoof, F.; Esmaeilbeig, A. R.; Nabavizadeh, S. M.; Niroomand Hosseini, F.; Kubicki, M., *Organometallics* **2013**, *32*, 3850; (b) Moustafa, M. E.; Boyle, P. D.; Puddephatt, R. J., *Organometallics* **2014**, *33*, 5402; (c) Maidich, L.; Cinellu, M. A.; Cocco, F.; Stoccoro, S.; Sedda, M.; Galli, S.; Zucca, A., *J. Organomet. Chem.*

2016, *819*, 76; (d) Crespo, M.; Font-Bardia, M.; Calvet, T., *Dalton Trans.* **2011**, *40*, 9431; (e) Nabavizadeh, S. M.; Amini, H.; Shahsavari, H. R.; Namdar, M.; Rashidi, M.; Kia, R.; Hemmateenejad, B.; Nekoeinia, M.; Ariafard, A.; Hosseini, F. N.; Gharavi, A.; Khalafi-Nezhad, A.; Sharbati, M. T.; Panahi, F., *Organometallics* **2011**, *30*, 1466; (f) Golbon Haghighi, M.; Rashidi, M.; Nabavizadeh, S. M.; Jamali, S.; Puddephatt, R. J., *Dalton Trans.* **2010**, *39*, 11396.

43. (a) Calvet, T.; Crespo, M.; Font-Bardia, M.; Gómez, K.; González, G.; Martínez, M., *Organometallics* **2009**, *28*, 5096; (b) Forniés, J.; Menjón, B.; Gómez, N.; Tomás, M., *Organometallics* **1992**, *11*, 1187.
44. Forniés, J.; Ibáñez, S.; Martín, A.; Gil, B.; Lalinde, E.; Moreno, M. T., *Organometallics* **2004**, *23*, 3963.
45. (a) Forniés, J.; Ibáñez, S.; Martín, A.; Sanz, M.; Berenguer, J. R.; Lalinde, E.; Torroba, J., *Organometallics* **2006**, *25*, 4331; (b) Forniés, J.; Ibáñez, S.; Lalinde, E.; Martín, A.; Moreno, M. T.; Tsipis, A. C., *Dalton Trans.* **2012**, *41*, 3439.
46. Berenguer, J. R.; Lalinde, E.; Moreno, M. T.; Sánchez, S.; Torroba, J., *Inorg. Chem.* **2012**, *51*, 11665.
47. Millán, G.; Giménez, N.; Lara, R.; Berenguer, J. R.; Moreno, M. T.; Lalinde, E.; Alfaro-Arnedo, E.; López, I. P.; Piñeiro-Hermida, S.; Pichel, J. G., *Inorg. Chem.* **2019**, *58*, 1657.
48. Martín, A.; Belío, Ú.; Fuertes, S.; Sicilia, V., *Eur. J. Inorg. Chem.* **2013**, 2231.
49. (a) Berenguer, J. R.; Lalinde, E.; Martín, A.; Moreno, M. T.; Ruiz, S.; Sánchez, S.; Shahsavari, H. R., *Chem. Commun.* **2013**, *49*, 5067; (b) Berenguer, J. R.; Lalinde, E.; Martín, A.; Moreno, M. T.; Ruiz, S.; Sánchez, S.; Shahsavari, H. R., *Inorg. Chem.* **2014**, *53*, 8770.
50. Berenguer, J. R.; Lalinde, E.; Martín, A.; Moreno, M. T.; Sánchez, S.; Shahsavari, H. R., *Inorg. Chem.* **2016**, *55*, 7866.
51. (a) Aseman, M. D.; Nabavizadeh, S. M.; Niroomand Hosseini, F.; Wu, G.; Abu-Omar, M. M., *Organometallics* **2018**, *37*, 87; (b) Vigalok, A., *Acc. Chem. Res.* **2015**, *48*, 238; (c) Puddephatt, R. J., *Angew. Chem. Int. Ed.* **2002**, *41*, 261; (d) Arias, A.; Forniés, J.; Fortuño, C.; Martín, A.; Latronico, M.; Mastrorilli, P.; Todisco, S.; Gallo, V., *Inorg. Chem.* **2012**, *51*, 12682; (e) Crespo, M.; Anderson, C. M.; Kfoury, N.; Font-Bardia, M.; Calvet, T., *Organometallics* **2012**, *31*, 4401; (f) Albert, J.; Bosque, R.; Crespo, M.; Granell, J.; Rodríguez, J.; Zafrilla, J., *Organometallics* **2010**, *29*, 4619.

52. (a) Crespo, M., *J. Organomet. Chem.* **2019**, *879*, 15; (b) Li, X.; Liu, Y.; Tian, H., *Bioinorg. Chem. Appl.* **2018**, *2018*, 18; (c) Deo, K. M.; Ang, D. L.; McGhie, B.; Rajamanickam, A.; Dhiman, A.; Khoury, A.; Holland, J.; Bjelosevic, A.; Pages, B.; Gordon, C.; Aldrich-Wright, J. R., *Coord. Chem. Rev.* **2018**, *375*, 148; (d) Gibson, D., *Dalton Trans.* **2016**, *45*, 12983; (e) Johnstone, T. C.; Wilson, J. J.; Lippard, S. J., *Inorg. Chem.* **2013**, *52*, 12234.

53. (a) Balashev, K. P.; Simon, J.; Ford, P. C., *Inorg. Chem.* **1991**, *30*, 859; (b) Shaw, P. A.; Clarkson, G. J.; Rourke, J. P., *Chem. Sci.* **2017**, *8*, 5547; (c) Blanco, N. G.; Maldonado, C. R.; Mareque-Rivas, J. C., *Chem. Commun.* **2009**, 5257; (d) Grice, K. A.; Scheuermann, M. L.; Goldberg, K. I., Five-Coordinate Platinum(IV) Complexes. In *Higher Oxidation State Organopalladium and Platinum Chemistry*, Canty, A. J., Ed. Springer Berlin Heidelberg: Berlin, Heidelberg, 2011; pp 1.

54. (a) Kirgan, R. A.; Sullivan, B. P.; Rillema, D. P., Photochemistry and Photophysics of Coordination Compounds: Rhenium. In *Photochemistry and Photophysics of Coordination Compounds II*, Balzani, V.; Campagna, S., Eds. Springer Berlin Heidelberg: Berlin, Heidelberg, 2007; pp 45; (b) Chi, Y.; Chou, P.-T., *Chem. Soc. Rev.* **2007**, *36*, 1421; (c) Fernández-Hernández, J. M.; Beltrán, J. I.; Lemaur, V.; Gálvez-López, M.-D.; Chien, C.-H.; Polo, F.; Orselli, E.; Fröhlich, R.; Cornil, J.; De Cola, L., *Inorg. Chem.* **2013**, *52*, 1812; (d) Longhi, E.; Cola, L. D., Iridium(III) Complexes for OLED Application. In *Iridium(III) in Optoelectronic and Photonics Applications*, **2017**; (e) Flamigni, L.; Collin, J. P.; Sauvage, J. P., *Acc. Chem. Res.* **2008**, *41*, 857.

55. Deaton, J. C.; Castellano, F. N., Archetypal Iridium(III) Compounds for Optoelectronic and Photonic Applications. In *Iridium(III) in Optoelectronic and Photonics Applications*.

56. Vivancos, Á.; Bautista, D.; González-Herrero, P., *Chem. Eur. J.* **2019**, *25*, 6014.

57. Expósito, J. E.; Álvarez-Paino, M.; Aullón, G.; Miguel, J. A.; Espinet, P., *Dalton Trans.* **2015**, *44*, 16164.

58. Chassot, L.; Von Zelewsky, A.; Sandrini, D.; Maestri, M.; Balzani, V., *J. Am. Chem. Soc.* **1986**, *108*, 6084.

59. (a) von Zelewsky, A.; Suckling, A. P.; Stoeckli-Evans, H., *Inorg. Chem.* **1993**, *32*, 4585; (b) Barigelletti, F.; Sandrini, D.; Maestri, M.; Balzani, V.; von Zelewsky,

A.; Chassot, L.; Jolliet, P.; Maeder, U., *Inorg. Chem.* **1988**, *27*, 3644; (c) Rendina, L. M.; Puddephatt, R. J., *Chem. Rev.* **1997**, *97*, 1735.

60. Thomas, S. W.; Venkatesan, K.; Müller, P.; Swager, T. M., *J. Am. Chem. Soc.* **2006**, *128*, 16641.
61. La Deda, M.; Crispini, A.; Aiello, I.; Ghedini, M.; Amati, M.; Belviso, S.; Lelj, F., *Dalton Trans.* **2011**, *40*, 5259.
62. Jenkins, D. M.; Bernhard, S., *Inorg. Chem.* **2010**, *49*, 11297.
63. Corbo, R.; Georgiou, D. C.; Wilson, D. J. D.; Dutton, J. L., *Inorg. Chem.* **2014**, *53*, 1690.
64. Ionescu, A.; Godbert, N.; Aiello, I.; Ricciardi, L.; La Deda, M.; Crispini, A.; Sicilia, E.; Ghedini, M., *Dalton Trans.* **2018**, *47*, 11645.
65. (a) Juliá, F.; García-Legaz, M.-D.; Bautista, D.; González-Herrero, P., *Inorg. Chem.* **2016**, *55*, 7647; (b) Parker, R. R.; Sarju, J. P.; Whitwood, A. C.; Williams, J. A. G.; Lynam, J. M.; Bruce, D. W., *Chem. Eur. J.* **2018**, *24*, 19010.
66. Juliá, F.; Bautista, D.; González-Herrero, P., *Chem. Commun.* **2016**, *52*, 1657.
67. (a) Juliá, F.; Bautista, D.; Fernández-Hernández, J. M.; González-Herrero, P., *Chem. Sci.* **2014**, *5*, 1875; (b) Juliá, F.; Aullón, G.; Bautista, D.; González-Herrero, P., *Chem. Eur. J.* **2014**, *20*, 17346; (c) Juliá, F.; González-Herrero, P., *Dalton Trans.* **2016**, *45*, 10599.
68. Lázaro, A.; Serra, O.; Rodríguez, L.; Crespo, M.; Font-Bardia, M., *New J. Chem.* **2019**, *43*, 1247.
69. Zhang, Y.; Meng, F.; You, C.; Yang, S.; Xiong, L.; Xiong, W.; Zhu, W.; Wang, Y.; Pei, Y.; Su, S., *Dyes and Pigments* **2017**, *142*, 457.
70. Molaee, H.; Nabavizadeh, S. M.; Jamshidi, M.; Vilsmeier, M.; Pfitzner, A.; Samandar Sangari, M., *Dalton Trans.* **2017**, *46*, 16077.
71. (a) Forniés, J.; Fortuño, C.; Gómez, M. A.; Menjón, B.; Herdtweck, E., *Organometallics* **1993**, *12*, 4368; (b) Arias, A.; Forniés, J.; Fortuño, C.; Martín, A.; Mastrorilli, P.; Todisco, S.; Latronico, M.; Gallo, V., *Inorg. Chem.* **2013**, *52*, 5493; (c) Menjón, B.; Martínez-Salvador, S.; Gómez-Saso, M. A.; Forniés, J.; Falvello, L. R.; Martín, A.; Tsipis, A., *Chem. Eur. J.* **2009**, *15*, 6371.
72. Sánchez, S. Tesis Doctoral. Universidad de La Rioja, Logroño, **2012**.
73. (a) Vedernikov, A. N., *Acc. Chem. Res.* **2012**, *45*, 803; (b) Powers, D. C.; Ritter, T., *Acc. Chem. Res.* **2012**, *45*, 840; (c) Vigalok, A., *Organometallics* **2011**, *30*, 4802; (d) Crespo, M., *Organometallics* **2012**, *31*, 1216; (e) Furuya, T.; Kamlet,

A. S.; Ritter, T., *Nature* **2011**, *473*, 470; (f) Lersch, M.; Tilset, M., *Chem. Rev.* **2005**, *105*, 2471; (g) Gallego, C.; Martínez, M.; Safont, V. S., *Organometallics* **2007**, *26*, 527; (h) Crosby, S. H.; Thomas, H. R.; Clarkson, G. J.; Rourke, J. P., *Chem. Commun.* **2012**, *48*, 5775; (i) Yahav-Levi, A.; Goldberg, I.; Vigalok, A.; Vedernikov, A. N., *Chem. Commun.* **2010**, *46*, 3324; (j) Dubinsky-Davidchik, I. S.; Goldberg, I.; Vigalok, A.; Vedernikov, A. N., *Chem. Commun.* **2013**, *49*, 3446; (k) Traversa, E.; Templeton, J. L.; Cheng, H. Y.; Mohadjer Beromi, M.; White, P. S.; West, N. M., *Organometallics* **2013**, *32*, 1938; (l) Crespo, M.; Martínez, M.; Nabavizadeh, S. M.; Rashidi, M., *Coord. Chem. Rev.* **2014**, *279*, 115; (m) Labinger, J. A., *Chem. Rev.* **2017**, *117*, 8483; (n) Shaw, P. A.; Rourke, J. P., *Dalton Trans.* **2017**, *46*, 4768.

74. Fernández, S.; Forniés, J.; Gil, B.; Gómez, J.; Lalinde, E., *Dalton Trans.* **2003**, 822.

75. (a) Forniés, J.; Lalinde, E., In *Comprehensive Organometallic Chemistry III*, Elsevier: Oxford, **2007**; Vol. 8, pp 611; (b) Cucciolito, M. E.; Ruffo, F., *Eur. J. Inorg. Chem.* **2012**, 599; (c) Sun, C.; Hudson, Z. M.; Chen, L. D.; Wang, S., *Angew. Chem. Int. Ed.* **2012**, *124*, 5769.

76. (a) Canty, A. J., *Dalton Trans.* **2009**, *10*, 10409; (b) Hartwig, J. F., *Nature* **2008**, *455*, 314; (c) Hickman, A. J.; Sanford, M. S., *Nature* **2012**, *484*, 177; (d) Powers, D. C.; Ritter, T., *Nature Chemistry* **2009**, *1*, 302; (e) Powers, D. C.; Benitez, D.; Tkatchouk, E.; Goddard, W. A.; Ritter, T., *J. Am. Chem. Soc.* **2010**, *132*, 14092; (f) Powers, D. C.; Xiao, D. Y.; Geibel, M. A. L.; Ritter, T., *J. Am. Chem. Soc.* **2010**, *132*, 14530; (g) Furuya, T.; Benitez, D.; Tkatchouk, E.; Strom, A. E.; Tang, P.; Goddard, W. A.; Ritter, T., *J. Am. Chem. Soc.* **2010**, *132*, 3793; (h) Yu, W.-Y.; Sit, W. N.; Lai, K.-M.; Zhou, Z.; Chan, A. S. C., *J. Am. Chem. Soc.* **2008**, *130*, 3304; (i) Wang, J.; Liu, B.; Zhao, H.; Wang, J., *Organometallics* **2012**, *31*, 8598; (j) Kim, M.; Kwak, J.; Chang, S., *Angew. Chem. Int. Ed.* **2009**, *48*, 8935.

77. (a) Wencel-Delord, J.; Dröge, T.; Liu, F.; Glorius, F., *Chem. Soc. Rev.* **2011**, *40*, 4740; (b) Satoh, T.; Miura, M., *Chem. Eur. J.* **2010**, *16*, 11212; (c) Zhu, C.; Wang, R.; Falck, J. R., *Chem. Asian J.* **2012**, *7*, 1502; (d) Song, G.; Wang, F.; Li, X., *Chem. Soc. Rev.* **2012**, *41*, 3651; (e) David, A.; Luciano, C.; Sonia, N.; Elena, S.; Esteban, P. U., *Curr. Org. Chem.* **2011**, *15*, 3441; (f) Wang, N.; Li, B.; Song, H.; Xu, S.; Wang, B., *Chem. Eur. J.* **2013**, *19*, 358; (g) Frutos-Pedreño, R.; González-

Herrero, P.; Vicente, J.; Jones, P. G., *Organometallics* **2013**, *32*, 1892; (h) Cuesta, L.; Soler, T.; Urriolabeitia, E. P., *Chem. Eur. J.* **2012**, *18*, 15178.

78. (a) Li, L.; Brennessel, W. W.; Jones, W. D., *J. Am. Chem. Soc.* **2008**, *130*, 12414; (b) Cabeza, J. A.; del Río, I.; García-Granda, S.; Riera, V.; Suárez, M., *Organometallics* **2004**, *23*, 3501.
79. Brent Young, G., In *Comprehensive Organometallic Chemistry II*, Elsevier: Oxford, **1995**; Vol. 9, pp 533.
80. (a) Chen, K.-Y.; Hsieh, C.-C.; Cheng, Y.-M.; Lai, C.-H.; Chou, P.-T., *Chem. Commun.* **2006**, 4395; (b) Riesgo, E. C.; Hu, Y.-Z.; Bouvier, F.; Thummel, R. P.; Scaltrito, D. V.; Meyer, G. J., *Inorg. Chem.* **2001**, *40*, 3413.
81. Baratta, W.; Ballico, M.; Baldino, S.; Chelucci, G.; Herdtweck, E.; Siega, K.; Magnolia, S.; Rigo, P., *Chem. Eur. J.* **2008**, *14*, 9148.
82. Parekh, N. M.; Maheria, K. C., *Med. Chem. Res.* **2012**, *21*, 4168.
83. Szadkowska, A.; Gstrein, X.; Burtscher, D.; Jarzembska, K.; Woźniak, K.; Slugovc, C.; Grela, K., *Organometallics* **2010**, *29*, 117.
84. Berenguer, J. R.; Fernández, J.; Giménez, N.; Lalinde, E.; Moreno, M. T.; Sánchez, S., *Organometallics* **2013**, *32*, 3943.
85. Zapata, F.; Caballero, A.; Espinosa, A.; Tárraga, A.; Molina, P., *Dalton Trans.* **2009**, 3900.
86. Yagyu, T.; Ohashi, J.-i.; Maeda, M., *Organometallics* **2007**, *26*, 2383.
87. Crosby, S. H.; Clarkson, G. J.; Deeth, R. J.; Rourke, J. P., *Organometallics* **2010**, *29*, 1966.
88. Khlebnikov, V.; Heckenroth, M.; Müller-Bunz, H.; Albrecht, M., *Dalton Trans.* **2013,** *42*, 4197.
89. (a) Cotton, F. A.; Falvello, L. R.; Han, S., *Inorg. Chem.* **1982**, *21*, 2889; (b) Elding, L. I.; Oskarsson, Å., *Inorg. Chim. Acta* **1987**, *130*, 209.
90. (a) Díez, A.; Forniés, J.; Larraz, C.; Lalinde, E.; López, J. A.; Martín, A.; Moreno, M. T.; Sicilia, V., *Inorg. Chem.* **2010**, *49*, 3239; (b) Vicente, J.; Arcas, A.; Gálvez-López, M.-D.; Jones, P. G., *Organometallics* **2006**, *25*, 4247; (c) Casas, J. M.; Forniés, J.; Fuertes, S.; Martín, A.; Sicilia, V., *Organometallics* **2007**, *26*, 1674.
91. (a) Forniés, J.; Gómez-Saso, M. A.; Martín, A.; Martínez, F.; Menjón, B.; Navarrete, J., *Organometallics* **1997**, *16*, 6024; (b) Casas, J.; Martín, A.; Oliva, J.; Tomás, M., *Inorg. Chim. Acta* **1995**, *229*, 291; (c) Deacon, G. B.; Lawrenz, E.

T.; Hambley, T. W.; Rainone, S.; Webster, L. K., *J. Organomet. Chem.* **1995**, *493*, 205.

92. Debaerdemaeker, T.; Roth, H.; Brune, H.-A., *J. Organomet. Chem.* **1991**, *412*, 243.

93. (a) Nabavizadeh, S. M.; Aseman, M. D.; Ghaffari, B.; Rashidi, M.; Hosseini, F. N.; Azimi, G., *J. Organomet. Chem.* **2012**, *715*, 73; (b) Jamali, S.; Nabavizadeh, S. M.; Rashidi, M., *Inorg. Chem.* **2008**, *47*, 5441.

94. Baya, M.; Belío, Ú.; Forniés, J.; Martín, A.; Perálvarez, M.; Sicilia, V., *Inorg. Chim. Acta* **2015**, *424*, 136.

95. Juliá, F.; González-Herrero, P., *J. Am. Chem. Soc.* **2016**, *138*, 5276.

96. Pearson, R. G., *J. Am. Chem. Soc.* **1963**, *85*, 3533.

97. Bondi, A., *J. Phys. Chem.* **1964**, *68*, 441.

98. (a) Baya, M.; Belío, Ú.; Martín, A., *Inorg. Chem.* **2013**, *53*, 189; (b) Lalinde, E.; Moreno, M. T.; Ruiz, S.; Sánchez, S., *Organometallics* **2014**, *33*, 3078.

99. (a) Mdleleni, M. M.; Bridgewater, J. S.; Watts, R. J.; Ford, P. C., *Inorg. Chem.* **1995**, *34*, 2334; (b) Stoccoro, S.; Cinellu, M. A.; Zucca, A.; Minghetti, G.; Demartin, F., *Inorg.Chim. Acta* **1994**, *215*, 17; (c) Fukuda, H.; Yamada, Y.; Hashizume, D.; Takayama, T.; Watabe, M., *Appl. Organomet. Chem.* **2009**, *23*, 154; (d) Lai, S. W.; Chan, M. C. W.; Cheung, K. K.; Che, C. M., *Organometallics* **1999**, *18*, 3327; (e) Jamali, S.; Kermanshahian, S., *Appl. Organomet. Chem.* **2017**, *31*, e3832.

100. Calligaris, M., *Coord. Chem. Rev.* **2004**, *248*, 351.

101. (a) Ai, Y.; Li, Y.; Ma, H.; Su, C.-Y.; Yam, V. W.-W., *Inorg. Chem.* **2016**, *55*, 11920; (b) Lalinde, E.; Moreno, M. T.; Lara, R.; López, I. P.; Alfaro-Arnedo, E.; Pichel, J. G.; Piñeiro-Hermida, S., *Chem. Eur. J.* **2018**, *24*, 2440.

102. Han, X.; Wu, L. Z.; Si, G.; Pan, J.; Yang, Q. Z.; Zhang, L. P.; Tung, C. H., *Chem. Eur. J.* **2007**, *13*, 1231.

103. (a) Liu, Y.; Guo, H.; Zhao, J., *Chem. Commun.* **2011**, *47*, 11471; (b) Chia, Y. Y.; Tay, M. G., *Dalton Trans.* **2014**, *43*, 13159; (c) Hofbeck, T.; Lam, Y. C.; Kalbáč, M.; Záliš, S.; Vlček, A.; Yersin, H., *Inorg. Chem.* **2016**, *55*, 2441.

104. (a) Masako, K., *Bull. Chem. Soc. Jpn.* **2007**, *80*, 287; (b) Varughese, S., *J. Mater. Chem. C* **2014**, *2*, 3499.

105. Forniés, J.; Giménez, N.; Ibáñez, S.; Lalinde, E.; Martín, A.; Moreno, M. T., *Inorg. Chem.* **2015**, *54*, 4351.

106. (a) Hong, Y.; Lam, J. W. Y.; Tang, B. Z., *Chem. Soc. Rev.* **2011**, *40*, 5361; (b) Fernández-Cestau, J.; Giménez, N.; Lalinde, E.; Montaño, P.; Moreno, M. T.; Sánchez, S., *Organometallics* **2015**, *34*, 1766.

107. (a) Tong, G. S. M.; Law, Y.-C.; Kui, S. C. F.; Zhu, N.; Leung, K. H.; Phillips, D. L.; Che, C.-M., *Chem. Eur. J.* **2010**, *16*, 6540; (b) Sesolis, H.; Dubarle-Offner, J.; Chan, C. K. M.; Puig, E.; Gontard, G.; Winter, P.; Cooksy, A. L.; Yam, V. W. W.; Amouri, H., *Chem. Eur. J.* **2016**, *22*, 8032.

108. Zhan, Y.; Zhao, J.; Yang, P.; Ye, W., *RSC Adv.* **2016**, *6*, 92144.

109. Rosenberg, B.; Vancamp, L.; Trosko, J. E.; Mansour, V. H., *Nature* **1969**, *222*, 385.

110. (a) Johnstone, T. C.; Suntharalingam, K.; Lippard, S. J., *Chem. Rev.* **2016**, *116*, 3436; (b) Galanski, M.; Jakupec, M. A.; Keppler, B. K., *Curr. Med. Chem.* **2005**, *12*, 2075.

111. (a) Brabec, V.; Hrabina, O.; Kasparkova, J., *Coord. Chem. Rev.* **2017**, *351*, 2; (b) Pages, B. J.; Garbutcheon-Singh, K. B.; Aldrich-Wright, J. R., *Eur. J. Inorg. Chem.* **2017**, 1613.

112. (a) Tsang, R. Y.; Al-Fayea, T.; Au, H. J., *Drug-Safety* **2009**, *32*, 1109; (b) Sullivan, M. J., *Cancer* **2009**, *115*, 5623; (c) Köberle, B.; Tomicic, M. T.; Usanova, S.; Kaina, B., *BBA Rev. Cancer* **2010**, *1806*, 172; (d) Meijer, C.; Mulder, N. H.; Timmer-Bosscha, H.; Sluiter, W. J.; Meersma, G. J.; de Vries, E. G. E., *Cancer Res.* **1992**, *52*, 6885.

113. (a) Fanelli, M.; Formica, M.; Fusi, V.; Giorgi, L.; Micheloni, M.; Paoli, P., *Coord. Chem. Rev.* **2016**, *310*, 41; (b) Wheate, N. J.; Walker, S.; Craig, G. E.; Oun, R., *Dalton Trans.* **2010**, *39*, 8113; (c) To, W.-P.; Zou, T.; Sun, R. W.-Y.; Che, C.-M., *Phil. Trans. R. Soc. A* **2013**, *371*, 20120126; (d) Wang, X.; Guo, Z., *Dalton Trans.* **2008**, 1521; (e) White, J. D.; Haley, M. M.; DeRose, V. J., *Acc. Chem. Res.* **2016**, *49*, 56; (f) Wilson, J. J.; Lippard, S. J., *Chem. Rev.* **2014**, *114*, 4470; (g) Wang, X.; Wang, X.; Guo, Z., *Acc. Chem. Res.* **2015**, *48*, 2622; (h) Cheung-Ong, K.; Song, K. T.; Ma, Z.; Shabtai, D.; Lee, A. Y.; Gallo, D.; Heisler, L. E.; Brown, G. W.; Bierbach, U.; Giaever, G.; Nislow, C., *ACS Chem. Biol.* **2012**, *7*, 1892; (i) Yang, M.; Bierbach, U., *Eur. J. Inorg. Chem.* **2017**, 1561.

114. (a) Omae, I., *Coord. Chem. Rev.* **2014**, *280*, 84; (b) Zamora, A.; Pérez, S. A.; Rodríguez, V.; Janiak, C.; Yellol, G. S.; Ruiz, J., *J. Med. Chem.* **2015**, *58*, 1320; (c) Jürgens, S.; Kühn, F. E.; Casini, A., *Curr. Med. Chem.* **2017**, *24*, 1; (d) Babak,

M. V.; Pfaffeneder-Kmen, M.; Meier-Menches, S. M.; Legina, M. S.; Theiner, S.; Licona, C.; Orvain, C.; Hejl, M.; Hanif, M.; Jakupec, M. A.; Keppler, B. K.; Gaiddon, C.; Hartinger, C. G., *Inorg. Chem.* **2018**, *57*, 2851; (e) Frezza, M.; Dou, Q. P.; Xiao, Y.; Samouei, H.; Rashidi, M.; Samari, F.; Hemmateenejad, B., *J. Med. Chem.* **2011**, *54*, 6166; (f) Zamora, A.; Gandioso, A.; Massaguer, A.; Buenestado, S.; Calvis, C.; Hernández, J. L.; Mitjans, F.; Rodríguez, V.; Ruiz, J.; Marchán, V., *ChemMedChem* **2018**, *13*, 1755.

115. Cutillas, N.; Martínez, A.; Yellol, G. S.; Rodríguez, V.; Zamora, A.; Pedreño, M.; Donaire, A.; Janiak, C.; Ruiz, J., *Inorg. Chem.* **2013**, *52*, 13529.

116. (a) Suryadi, J.; Bierbach, U., *Chem. Eur. J.* **2012**, *18*, 12926; (b) Liu, H.-K.; Sadler, P. J., *Acc. Chem. Res.* **2011**, *44*, 349; (c) Zou, T.; Liu, J.; Lum, C. T.; Ma, C.; Chan, R. C.-T.; Lok, C.-N.; Kwok, W.-M.; Che, C.-M., *Angew. Chem. Int. Ed.* **2014**, *53*, 10119; (d) Ruiz, J.; Vicente, C.; de Haro, C.; Espinosa, A., *Inorg. Chem.* **2011**, *50*, 2151.

117. (a) Sherman, S. E.; Lippard, S. J., *Chem. Rev.* **1987**, *87*, 1153; (b) Jamieson, E. R.; Lippard, S. J., *Chem. Rev.* **1999**, *99*, 2467; (c) Reedijk, J., *Platinum Met. Rev.* **2008**, *52*, 2.

118. Zhang, Y.; Luo, Q.; Zheng, W.; Wang, Z.; Lin, Y.; Zhang, E.; Lü, S.; Xiang, J.; Zhao, Y.; Wang, F., *Inorg. Chem. Front.* **2018**, *5*, 413.

119. A. Hilderbrand, S., Papkovsky, D. B., Ed. Humana Press: Totowa, NJ, **2010**; pp 17.

120. Solomatina, A. I.; Chelushkin, P. S.; Krupenya, D. V.; Podkorytov, I. S.; Artamonova, T. O.; Sizov, V. V.; Melnikov, A. S.; Gurzhiy, V. V.; Koshel, E. I.; Shcheslavskiy, V. I.; Tunik, S. P., *Bioconjugate Chem.* **2017**, *28*, 426.

121. (a) Barr, M. P.; Gray, S. G.; Hoffmann, A. C.; Hilger, R. A.; Thomale, J.; O'Flaherty, J. D.; Fennell, D. A.; Richard, D.; O'Leary, J. J.; O'Byrne, K. J., *PLoS One* **2013**, *8*, e54193; (b) Lopez-Ayllon, B. D.; Moncho-Amor, V.; Abarrategi, A.; de Cáceres, I. I.; Castro-Carpeño, J.; Belda-Iniesta, C.; Perona, R.; Sastre, L., *Cancer Med.* **2014**, *3*, 1099.

122. (a) Levasseur, L. M.; Slocum, H. K.; Rustum, Y. M.; Greco, W. R., *Cancer Res.* **1998**, *58*, 5749; (b) Hassan, S. B.; Jonsson, E.; Larsson, R.; Karlsson, M. O., *J. Pharmac. Exp. Ther.* **2001**, *299*, 1140.

123. (a) Sun, R. W.-Y.; Chow, A. L.-F.; Li, X.-H.; Yan, J. J.; Sin-Yin Chui, S.; Che, C.-M., *Chem. Sci.* **2011**, *2*, 728; (b) Sun, R. W.-Y.; Li, C. K.-L.; Ma, D.-L.; Yan,

J. J.; Lok, C.-N.; Leung, C.-H.; Zhu, N.; Che, C.-M., *Chem. Eur. J.* **2010**, *16*, 3097; (c) Sy, L.-K.; Yan, S.-C.; Lok, C.-N.; Man, R. Y. K.; Che, C.-M., *Cancer Res.* **2008**, *68*, 10229.

124. Martin, R. M.; Leonhardt, H.; Cardoso, M. C., *Cytometry Part A* **2005**, *67A*, 45.

125. (a) Tanley, S. W. M.; Schreurs, A. M. M.; Kroon-Batenburg, L. M. J.; Meredith, J.; Prendergast, R.; Walsh, D.; Bryant, P.; Levy, C.; Helliwell, J. R., *Acta Crystallogr Section D Biol Crystallogr.* **2012**, *68*, 601; (b) Uribe, P. M.; Mueller, M. A.; Gleichman, J. S.; Kramer, M. D.; Wang, Q.; Sibrian-Vazquez, M.; Strongin, R. M.; Steyger, P. S.; Cotanche, D. A.; Matsui, J. I., *PLoS One* **2013**, *8*, e55359.

126. (a) Shaw, P. A.; Phillips, J. M.; Clarkson, G. J.; Rourke, J. P., *Dalton Trans.* **2016,** *45*, 11397; (b) Omae, I., *Cyclometalation Reactions. Five-Membered Ring Products as Universal Reagents*. Springer: Japan, 2014; (c) Crosby, S. H.; Deeth, R. J.; Clarkson, G. J.; Rourke, J. P., *Dalton Trans.* **2011**, *40*, 1227; (d) Whitfield, S. R.; Sanford, M. S., *Organometallics* **2008**, *27*, 1683; (e) Albrecht, M., *Chem. Rev.* **2010**, *110*, 576.

127. (a) Luedtke, A. T.; Goldberg, K. I., *Inorg. Chem.* **2007**, *46*, 8496; (b) Zhao, S.-B.; Wu, G.; Wang, S., *Organometallics* **2008**, *27*, 1030; (c) Reinartz, S.; White, P. S.; Brookhart, M.; Templeton, J. L., *J. Am. Chem. Soc.* **2001**, *123*, 6425; (d) Kloek, S. M.; Goldberg, K. I., *J. Am. Chem. Soc.* **2007**, *129*, 3460.

128. (a) Shaw, P. A.; Phillips, J. M.; Newman, C. P.; Clarkson, G. J.; Rourke, J. P., *Chem. Commun.* **2015**, *51*, 8365; (b) Rivada-Wheelaghan, O.; Roselló-Merino, M.; Díez, J.; Maya, C.; López-Serrano, J.; Conejero, S., *Organometallics* **2014**, *33*, 5944; (c) Khaskin, E.; Zavalij, P. Y.; Vedernikov, A. N., *Angew. Chem. Int. Ed.* **2007**, *46*, 6309; (d) Kaspi, A. W.; Goldberg, I.; Vigalok, A., *J. Am. Chem. Soc.* **2010**, *132*, 10626; (e) Zhao, S.-B.; Becker, J. J.; Gagné, M. R., *Organometallics* **2011**, *30*, 3926.

129. Berenguer, J. R.; Pichel, J. G.; Giménez, N.; Lalinde, E.; Moreno, M. T.; Piñeiro-Hermida, S., *Dalton Trans.* **2015**, *44*, 18839.

130. Puddephatt, R. J., *Coord. Chem. Rev.* **2001**, *219–221*, 157.

131. Labinger, J.; Bercaw, J., H. In *Higher Oxidation State Organopalladium and Platinum Chemistry*, Canty, A. J., Ed. Springer: Berlín, Heidelberg, **2011**; Vol. 35, pp 29.

132. Newman, C. P.; Casey-Green, K.; Clarkson, G. J.; Cave, G. W. V.; Errington, W.; Rourke, J. P., *Dalton Trans.* **2007**, 3170.

133. Wang, N.; Hu, M.; Mellerup, S. K.; Wang, X.; Sauriol, F.; Peng, T.; Wang, S., *Inorg. Chem.* **2017**, *56*, 12783.

134. Biswas, A. N.; Das, P.; Bagchi, V.; Choudhury, A.; Bandyopadhyay, P., *Eur. J. Inorg. Chem.* **2011**, 3739.

135. (a) Anger, E.; Rudolph, M.; Norel, L.; Zrig, S.; Shen, C.; Vanthuyne, N.; Toupet, L.; Williams, J. A. G.; Roussel, C.; Autschbach, J.; Crassous, J.; Réau, R., *Chem. Eur. J.* **2011**, *17*, 14178; (b) Zhang, X.-P.; Liu, F.-Q.; Lai, J.-C.; Li, C.-H.; Li, A.-M.; You, X.-Z., *New J. Chem.* **2016**, *40*, 2628.

136. (a) Nastasi, F.; Puntoriero, F.; Serroni, S.; Campagna, S.; Olivier, J.-H.; Ziessel, R., *Dalton Trans.* **2014**, *43*, 17647; (b) Wu, W.; Zhao, J.; Guo, H.; Sun, J.; Ji, S.; Wang, Z., *Chem. Eur. J.* **2012**, *18*, 1961; (c) Sun, J.; Zhong, F.; Yi, X.; Zhao, J., *Inorg. Chem.* **2013**, *52*, 6299; (d) Chow, P.-K.; Cheng, G.; Tong, G. S. M.; Ma, C.; Kwok, W.-M.; Ang, W.-H.; Chung, C. Y.-S.; Yang, C.; Wang, F.; Che, C.-M., *Chem. Sci.* **2016**, *7*, 6083.

137. (a) Prier, C. K.; Rankic, D. A.; MacMillan, D. W. C., *Chem. Rev.* **2013**, *113*, 5322; (b) Eckenhoff, W. T.; Eisenberg, R., *Dalton Trans.* **2012**, *41*, 13004; (c) Schulz, D. M.; Yoon, T. P., *Science* **2014**, *343*, 1239176.

138. Singh-Rachford, T. N.; Castellano, F. N., *Coord. Chem. Rev.* **2010**, *254*, 2560.

139. Yang, C.-H.; Mauro, M.; Polo, F.; Watanabe, S.; Muenster, I.; Fröhlich, R.; De Cola, L., *Chem. Mat.* **2012**, *24*, 3684.

140. Li, J.; Djurovich, P. I.; Alleyne, B. D.; Yousufuddin, M.; Ho, N. N.; Thomas, J. C.; Peters, J. C.; Bau, R.; Thompson, M. E., *Inorg. Chem.* **2005**, *44*, 1713.

141. (a) Dang, W.; Yang, X.; Feng, Z.; Sun, Y.; Zhong, D.; Zhou, G.; Wu, Z.; Wong, W.-Y., *J. Mater. Chem. C* **2018**, *6*, 9453; (b) Adamovich, V.; Bajo, S.; Boudreault, P.-L. T.; Esteruelas, M. A.; López, A. M.; Martín, J.; Oliván, M.; Oñate, E.; Palacios, A. U.; San-Torcuato, A.; Tsai, J.-Y.; Xia, C., *Inorg. Chem.* **2018**, *57*, 10744; (c) Tamura, Y.; Hisamatsu, Y.; Kazama, A.; Yoza, K.; Sato, K.; Kuroda, R.; Aoki, S., *Inorg. Chem.* **2018**, *57*, 4571; (d) You, Y.; Han, Y.; Lee, Y.-M.; Park, S. Y.; Nam, W.; Lippard, S. J., *J. Am. Chem. Soc.* **2011**, *133*, 11488.

142. Janzen, D. E.; Mehne, L. F.; VanDerveer, D. G.; Grant, G. J., *Inorg. Chem.* **2005**, *44*, 8182.

143. Howarth, A. J.; Davies, D. L.; Lelj, F.; Wolf, M. O.; Patrick, B. O., *Inorg. Chem.* **2014**, *53*, 11882.

144. Li, Z.; Cui, P.; Wang, C.; Kilina, S.; Sun, W., *J. Phys. Chem. C* **2014**, *118*, 28764.

145. (a) Deng, J.-y.; Liu, Y.; Hu, Z.-y.; Zhu, M.-x.; Zhu, W.-g., *J. Cent. South Univ. Technol.* **2007**, *14*, 344; (b) Zheng, Y.; Batsanov, A. S.; Bryce, M. R., *Inorg. Chem.* **2011**, *50*, 3354.

146. (a) Vasilchenko, D.; Berdugin, S.; Tkachev, S.; Baidina, I.; Romanenko, G.; Gerasko, O.; Korenev, S., *Inorg. Chem.* **2015**, *54*, 4644; (b) Al-Baker, S.; Vollano, J. F.; Dabrowiak, J. C., *J. Am. Chem. Soc.* **1986**, *108*, 5643.

147. (a) Vasilchenko, D.; Tkachev, S.; Baidina, I.; Korenev, S., *Inorg. Chem.* **2013**, *52*, 10532; (b) Zhang, F.; Jennings, M. C.; Puddephatt, R. J., *Chem. Comm.* **2007**, 1496; (c) Azizpoor Fard, M.; Behnia, A.; Puddephatt, R. J., *Organometallics* **2017**, *36*, 4169.

148. Wu, W.; Wu, W.; Ji, S.; Guo, H.; Zhao, J., *Eur. J. Inorg. Chem.* **2010**, 4470.

149. Anthopoulos, T. D.; Frampton, M. J.; Namdas, E. B.; Burn, P. L.; Samuel, I. D. W., *Adv. Mater.* **2004**, *16*, 557.

150. (a) Hao, Z.; Meng, F.; Wang, P.; Wang, Y.; Tan, H.; Pei, Y.; Su, S.; Liu, Y., *Dalton Trans.* **2017**, *46*, 16257; (b) Hu, J.; Yip, J. H. K.; Ma, D.-L.; Wong, K.-Y.; Chung, W.-H., *Organometallics* **2009**, *28*, 51; (c) Su, N.; Meng, F.; Chen, J.; Wang, Y.; Tan, H.; Su, S.; Zhu, W., *Dyes Pigm.* **2016**, *128*, 68.

151. (a) Bodio, E.; Picquet, M.; Le Gendre, P., "Early–Late" Heterobimetallic Catalysis and Beyond. In *Homo- and Heterobimetallic Complexes in Catalysis: Cooperative Catalysis*, Kalck, P., Ed. Springer International Publishing: Cham, **2016**; pp 139; (b) Zanardi, A.; Mata, J. A.; Peris, E., *J. Am. Chem. Soc.* **2009**, *131*, 14531; (c) Sabater, S.; Mata, J. A.; Peris, E., *Organometallics* **2012**, *31*, 6450; (d) Zanardi, A.; Corberán, R.; Mata, J. A.; Peris, E., *Organometallics* **2008**, *27*, 3570.

152. (a) Curado, N.; Contel, M., Chap. 6 Heterometallic Complexes as Anticancer Agents. In *Metal-based Anticancer Agents*, The Royal Society of Chemistry: **2019**; pp 143; (b) Fernández-Moreira, V.; Gimeno, M. C., *Chem. Eur. J.* **2018**, *24*, 3345.

153. Crichton, R. R., Chapter 22 - Metals in Medicine and Metals as Drugs. In *Biological Inorganic Chemistry (Second Edition)*, Crichton, R. R., Ed. Elsevier: Oxford, **2012**; pp 415.

154. (a) Bertrand, B.; Williams, M. R. M.; Bochmann, M., *Chem. Eur. J.* **2018**, *24*, 11840; (b) Thota, S.; Rodrigues, D. A.; Crans, D. C.; Barreiro, E. J., *J. Med. Chem.* **2018**, *61*, 5805.

155. (a) Roder, C.; Thomson, M. J., *Drugs in R&D* **2015**, *15*, 13; (b) Rehder, D., Chap. 14 - Inorganics in medicine. In *Bioinorganic Chemistry*, Oxford University Press, **2014**.

156. (a) Schmidt, C.; Karge, B.; Misgeld, R.; Prokop, A.; Franke, R.; Brönstrup, M.; Ott, I., *Chem. Eur. J.* **2017**, *23*, 1869; (b) Yeo, C. I.; Ooi, K. K.; Tiekink, E. R. T., *Molecules* **2018**, *23*, 1410; (c) Nobili, S.; Mini, E.; Landini, I.; Gabbiani, C.; Casini, A.; Messori, L., *Med. Res. Rev.,* **2010**, *30*, 550; (d) Mirzadeh, N.; Reddy, T. S.; Bhargava, S. K., *Coord. Chem. Rev.* **2019**, *388*, 343.

157. (a) Svahn, N.; Moro, A. J.; Roma-Rodrigues, C.; Puttreddy, R.; Rissanen, K.; Baptista, P. V.; Fernandes, A. R.; Lima, J. C.; Rodríguez, L., *Chem. Eur. J.* **2018**, *24*, 14654; (b) Ott, I., *Coord. Chem. Rev.* **2009**, *253*, 1670; (c) Joao Carlos, L.; Laura, R., *Anti-Cancer Agents Med. Chem.* **2011**, *11*, 921; (d) Carboni, S.; Zucca, A.; Stoccoro, S.; Maiore, L.; Arca, M.; Ortu, F.; Artner, C.; Keppler, B. K.; Meier-Menches, S. M.; Casini, A.; Cinellu, M. A., *Inorg. Chem.* **2018**, *57*, 14852; (e) Curado, N.; Dewaele-Le Roi, G.; Poty, S.; Lewis, J. S.; Contel, M., *Chem. Commun.* **2019**, *55*, 1394.

158. Wenzel, M.; Bigaeva, E.; Richard, P.; Le Gendre, P.; Picquet, M.; Casini, A.; Bodio, E., *J. Inorg. Biochem.* **2014**, *141*, 10.

159. Christian, G. H.; Andrew, D. P.; Alexey, A. N., *Curr. Top. Med. Chem.* **2011**, *11*, 2688.

160. (a) Batchelor, L. K.; Păunescu, E.; Soudani, M.; Scopelliti, R.; Dyson, P. J., *Inorg. Chem.* **2017**, *56*, 9617; (b) Su, W.; Tang, Z.; Li, P.; Wang, G.; Xiao, Q.; Li, Y.; Huang, S.; Gu, Y.; Lai, Z.; Zhang, Y., *Dalton Trans.* **2016**, *45*, 19329.

161. (a) Manzotti, C.; Pratesi, G.; Menta, E.; Di Domenico, R.; Cavalletti, E.; Fiebig, H. H.; Kelland, L. R.; Farrell, N.; Polizzi, D.; Supino, R.; Pezzoni, G.; Zunino, F., *Clin. Cancer Res.* **2000**, *6*, 2626; (b) Oliveira, V. A.; Iglesias, B. A.; Auras, B. L.; Neves, A.; Terenzi, H., *Dalton Trans.* **2017**, *46*, 1660; (c) Petruzzella, E.; Braude, J. P.; Aldrich-Wright, J. R.; Gandin, V.; Gibson, D., *Angew. Chem. Int. Ed.* **2017**, *129*, 11697; (d) Malina, J.; Čechová, K.; Farrell, N. P.; Brabec, V., *Inorg. Chem.* **2019**, *DOI: 10.1021/acs.inorgchem.9b00254*; (e) Anderson, C. M.; Taylor, I. R.; Tibbetts, M. F.; Philpott, J.; Hu, Y.; Tanski, J. M., *Inorg. Chem.* **2012**, *51*, 12917;

(f) Herman, A.; Tanski, J. M.; Tibbetts, M. F.; Anderson, C. M., *Inorg. Chem.* **2008**, *47*, 274.

162. (a) Curado, N.; Giménez, N.; Miachin, K.; Aliaga-Lavrijsen, M.; Cornejo, M. A.; Jarzecki, A. A.; Contel, M., *ChemMedChem.* **2019**, *14*, 1086; (b) Ma, L.; Lin, X.; Li, C.; Xu, Z.; Chan, C.-Y.; Tse, M.-K.; Shi, P.; Zhu, G., *Inorg. Chem.* **2018**, *57*, 2917; (c) Fernández-Gallardo, J.; Elie, B. T.; Sadhukha, T.; Prabha, S.; Sanaú, M.; Rotenberg, S. A.; Ramos, J. W.; Contel, M., *Chem. Sci.* **2015**, *6*, 5269; (d) Bertrand, B.; Citta, A.; Franken, I. L.; Picquet, M.; Folda, A.; Scalcon, V.; Rigobello, M. P.; Le Gendre, P.; Casini, A.; Bodio, E., *J. Biol. Inorg. Chem.* **2015**, *20*, 1005; (e) Wenzel, M.; de Almeida, A.; Bigaeva, E.; Kavanagh, P.; Picquet, M.; Le Gendre, P.; Bodio, E.; Casini, A., *Inorg. Chem.* **2016**, *55*, 2544; (f) Massai, L.; Fernandez-Gallardo, J.; Guerri, A.; Arcangeli, A.; Pillozzi, S.; Contel, M.; Messori, L., *Dalton Trans.* **2015**, *44*, 11067; (g) Fernández-Gallardo, J.; Elie, B. T.; Sulzmaier, F. J.; Sanaú, M.; Ramos, J. W.; Contel, M., *Organometallics* **2014**, *33*, 6669; (h) González-Pantoja, J. F.; Stern, M.; Jarzecki, A. A.; Royo, E.; Robles-Escajeda, E.; Varela-Ramírez, A.; Aguilera, R. J.; Contel, M., *Inorg. Chem.* **2011**, *50*, 11099; (i) Wenzel, M.; Bertrand, B.; Eymin, M.-J.; Comte, V.; Harvey, J. A.; Richard, P.; Groessl, M.; Zava, O.; Amrouche, H.; Harvey, P. D.; Le Gendre, P.; Picquet, M.; Casini, A., *Inorg. Chem.* **2011**, *50*, 9472; (j) Elie, B. T.; Pechenyy, Y.; Uddin, F.; Contel, M., *J. Biol. Inorg. Chem.* **2018**, *23*, 399; (k) Fernández-Gallardo, J.; Elie, B. T.; Sanaú, M.; Contel, M., *Chem. Commun.* **2016**, *52*, 3155.

163. Pelletier, F.; Comte, V.; Massard, A.; Wenzel, M.; Toulot, S.; Richard, P.; Picquet, M.; Le Gendre, P.; Zava, O.; Edafe, F.; Casini, A.; Dyson, P. J., *J. Med. Chem.* **2010**, *53*, 6923.

164. Serratrice, M.; Maiore, L.; Zucca, A.; Stoccoro, S.; Landini, I.; Mini, E.; Massai, L.; Ferraro, G.; Merlino, A.; Messori, L.; Cinellu, M. A., *Dalton Trans.* **2016**, *45*, 579.

165. (a) Boselli, L.; Carraz, M.; Mazères, S.; Paloque, L.; González, G.; Benoit-Vical, F.; Valentin, A.; Hemmert, C.; Gornitzka, H., *Organometallics* **2015**, *34*, 1046; (b) Luengo, A.; Fernández-Moreira, V.; Marzo, I.; Gimeno, M. C., *Inorg. Chem.* **2017**, *56*, 15159.

166. Maidich, L.; Zuri, G.; Stoccoro, S.; Cinellu, M. A.; Zucca, A., *Dalton Trans.* **2014**, *43*, 14806.

167. Nabavizadeh, S. M.; Golbon Haghighi, M.; Esmaeilbeig, A. R.; Raoof, F.; Mandegani, Z.; Jamali, S.; Rashidi, M.; Puddephatt, R. J., *Organometallics* **2010**, *29*, 4893.

168. Brandys, M.-C.; Jennings, M. C.; Puddephatt, R. J., *J. Chem. Soc., Dalton Trans.* **2000**, 4601.

169. Ezquerro, C.; Sepúlveda, A. E.; Grau-Atienza, A.; Serrano, E.; Lalinde, E.; Berenguer, J. R.; García-Martínez, J., *J. Mat. Chem. C* **2017**, *5*, 9721.

170. Berenguer, J. R.; Lalinde, E.; Moreno, M. T.; Montaño, P., *Eur. J. Inorg. Chem.* **2012**, 3645.

171. Frisch, M. J.; Trucks, G. W.; Schlegel, H. B.; Scuseria, G. E.; Robb, M. A.; Cheeseman, J. R.; Scalmani, G.; Barone, V.; Mennucci, B.; Petersson, G. A.; Nakatsuji, H.; Caricato, M.; Li, X.; Hratchian, H. P.; Izmaylov, A. F.; Bloino, J.; Zheng, G.; Sonnenberg, J. L.; Hada, M.; Ehara, M.; Toyota, K.; Fukuda, R.; Hasegawa, J.; Ishida, M.; Nakajima, T.; Honda, Y.; Kitao, O.; Nakai, H.; Vreven, T.; Montgomery, J. A.; Peralta, J. E.; Ogliaro, F.; Bearpark, M.; Heyd, J. J.; Brothers, E.; Kudin, K. N.; Staroverov, V. N.; Kobayashi, R.; Normand, J.; Raghavachari, K.; Rendell, A.; Burant, J. C.; Iyengar, S. S.; Tomasi, J.; Cossi, M.; Rega, N.; Millam, J. M.; Klene, M.; Knox, J. E.; Cross, J. B.; Bakken, V.; Adamo, C.; Jaramillo, J.; Gomperts, R.; Stratmann, R. E.; Yazyev, O.; Austin, A. J.; Cammi, R.; Pomelli, C.; Ochterski, J. W.; Martin, R. L.; Morokuma, K.; Zakrzewski, V. G.; Voth, G. A.; Salvador, P.; Dannenberg, J. J.; Dapprich, S.; Daniels, A. D.; Farkas; Foresman, J. B.; Ortiz, J. V.; Cioslowski, J.; Fox, D. J., *Gaussian 09, Revision B.01*. Gaussian, Inc., Wallingford CT, **2010**.

172. (a) Becke, A. D., *Phys. Rev. A* **1988**, *38*, 3098; (b) Becke, A. D., *J. Chem. Phys.* **1993,** *98*, 5648; (c) Lee, C.; Yang, W.; Parr, R. G., *Phys. Rev. B* **1988**, *37*, 785.

173. Wadt, W. R.; Hay, P. J., *J. Chem. Phys.* **1985**, *82*, 284.

174. Barone, V.; Cossi, M., *J. Phys. Chem. A* **1998**, *102*, 1995.

175. O'Boyle, N. M.; Tenderholt, A. L.; Langner, K. M., *J. Comput. Chem.* **2008**, *29*, 839.

176. (a) Barone, V.; Cossi, M.; Tomasi, J., *J. Chem. Phys.* **1997**, *107*, 3210; (b) Cossi, M.; Scalmani, G.; Rega, N.; Barone, V., *J. Chem. Phys.* **2002**, *117*, 43.

177. Skripnikov, L., *Version **2016**, 4*.

178. Otwinowski, Z.; Minor, W., In *Methods in Enzymology*, Carter, C. V., Jr.; Sweet, R. M., Eds. Academic Press: New York, **1997**; Vol. 276A, p 307.

179. Hall, M. D.; Telma, K. A.; Chang, K.-E.; Lee, T. D.; Madigan, J. P.; Lloyd, J. R.; Goldlust, I. S.; Hoeschele, J. D.; Gottesman, M. M., *Cancer Res.* **2014**, *74*, 3913.

180. OECD. **2010**. Guidance Document on using Cytotoxicity Tests to Estimate Starting Doses for Acute Oral Systemic Toxicity Tests. No. 129, París, France. Available at: [http://www.oecd.org/env/testguidelines].

181. (a) Fereidoonnezhad, M.; Shahsavari, H. R.; Abedanzadeh, S.; Behchenari, B.; Hossein-Abadi, M.; Faghih, Z.; Beyzavi, M. H., *New J. Chem.* **2018**, *42*, 2385; (b) Fereidoonnezhad, M.; Shahsavari, H. R.; Lotfi, E.; Babaghasabha, M.; Fakhri, M.; Faghih, Z.; Faghih, Z.; Beyzavi, M. H., *Appl. Organomet. Chem.* **2018**, *32*, e4200.

182. (a) Edelstein, A.; Amodaj, N.; Hoover, K.; Vale, R.; Stuurman, N., Computer Control of Microscopes Using µManager. In *Current Protocols in Molecular Biology*, John Wiley & Sons, Inc.: **2010**; (b) Schindelin, J.; Arganda-Carreras, I.; Frise, E.; Kaynig, V.; Longair, M.; Pietzsch, T.; Preibisch, S.; Rueden, C.; Saalfeld, S.; Schmid, B.; Tinevez, J.-Y.; White, D. J.; Hartenstein, V.; Eliceiri, K.; Tomancak, P.; Cardona, A., *Nat Meth* **2012**, *9*, 676.

183. Usón, R.; Forniés, J.; Tomás, M.; Menjón, B., *Organometallics* **1985**, *4*, 1912.

184. Obeid, N.; Skulski, L., *Molecules* **2001**, *6*, 869.

185. Bai, W., *J. Lumin.* **2012**, *132*, 2847.

186. Edkins, R. M.; Fucke, K.; Peach, M. J. G.; Crawford, A. G.; Marder, T. B.; Beeby, A., *Inorg. Chem.* **2013**, *52*, 9842.

187. Sheldrick, G. M., *SHELX-97, a program for the refinement of crystal structures*. University of Göttingen: Germany, **1997**.

188. Blessing, R. H., *Acta Crystallogr.* **1995**, *A51*, 33.

189. Farrugia, L. J., *Appl. Crystallogr.* **1999**, *32*, 837.

190. Speck, A. L., *J. Appl. Cryst.* **2003**, *36*, 7.

191. Speck, A. L., *Acta Crystallogr., Sect C* **2015**, *71*, 9.

192. Parkin, I. P.; Slawin, A. M. Z.; Williams, D. J.; Woollins, J. D., *Inorg. Chim. Acta* **1990**, *172*, 159.

193. Sheldrick, G. M., *Acta Crystallogr., Sect. A: Found. Crystallogr.* **2015**, *71*, 3.

194. Sheldrick, G., *Acta Crystallogr., Sect. C* **2015**, *71*, 3.

195. (a) Hackenberg, F.; Müller-Bunz, H.; Smith, R.; Streciwilk, W.; Zhu, X.; Tacke, M., *Organometallics* **2013**, *32*, 5551; (b) Liu, W.; Bensdorf, K.; Proetto, M.; Abram, U.; Hagenbach, A.; Gust, R., *J. Med. Chem.* **2011**, *54*, 8605.

196. (a) Contel, M.; Fernandez-Gallardo, J.; Elie, B. T.; Ramos, J. W. (City University of New York). US Pat. No. US9315531, **2016**; (b) Elie, B. T.; Fernández-Gallardo, J.; Curado, N.; Cornejo, M. A.; Ramos, J. W.; Contel, M., *Eur. J. Med. Chem.* **2019**, *161*, 310; (c) Mui, Y. F.; Fernández-Gallardo, J.; Elie, B. T.; Gubran, A.; Maluenda, I.; Sanaú, M.; Navarro, O.; Contel, M., *Organometallics* **2016**, *35*, 1218.